Universität Bonn

Physikalisches Institut

Search for Neutral Higgs Bosons of the MSSM decaying to $\tau_{\text{had}}\,\tau_{\text{had}}$ in proton-proton collisions at $\sqrt{s} = 8$ TeV with the ATLAS detector

Federico Scutti

A search for the neutral Higgs bosons predicted by the Minimal Supersymmetric Standard Model, h, H and A, is presented in this thesis. It is based on a data sample with an integrated luminosity of $L_{\text{int}} = 19.5$ fb^{-1} from proton-proton collisions with a center-of-mass energy of $\sqrt{s} = 8$ TeV produced at the LHC and recorded by the ATLAS experiment in 2012. The search is performed in the decay channel with two tau leptons decaying hadronically, $h/H/A \to \tau_{\text{had}}\tau_{\text{had}}$. The selection of events is based on the kinematic and topological properties of a heavy neutral Higgs boson produced by $b\bar{b}$ annihilation and the gluon-gluon fusion production mechanisms.

The search significantly improves upon the sensitivity of previous searches, and leads the sensitivity of the $h/H/A \to \tau\tau$ combined search, where other tau decay modes are selected in the final state, for signal masses $m_A \gtrsim 350$ GeV.

As no significant excess is found, exclusion limits are set in the space of the two leading-order free parameters of the MSSM, m_A and tanβ. After the discovery of a Higgs boson in 2012, with a mass of $m_H = 125.09 \pm 0.24$ GeV, new phenomenological scenarios of the MSSM were proposed. In this search, exclusion limits are obtained for these various scenarios in the mass range $m_A = 170 - 1000$ GeV. Model-independent exclusion limits were also obtained for the cross-section of the production of a generic resonance, ϕ, by $b\bar{b}$ annihilation and gluon-gluon fusion. Excluded cross-sections at 95% confidence level are as high as $\sigma_{\text{excl.}}(b\bar{b} \to \phi \to \tau\tau) \approx 4.2$ pb and $\sigma_{\text{excl.}}(gg \to \phi \to \tau\tau) \approx 6.8$ pb at $m_\phi = 170$ GeV and $\sigma_{\text{excl.}}(b\bar{b} \to \phi \to \tau\tau) \approx 9.2$ fb and $\sigma_{\text{excl.}}(gg \to \phi \to \tau\tau) \approx 10$ fb at $m_\phi = 1000$ GeV.

Physikalisches Institut der
Universität Bonn
Nussallee 12
D-53115 Bonn

BONN-IR-2016-04
August 2016
ISSN-0172-8741

Search for Neutral Higgs Bosons of the MSSM decaying to $\tau_{\text{had}}\,\tau_{\text{had}}$ in proton-proton collisions at $\sqrt{s} = 8$ TeV with the ATLAS detector

Dissertation
zur
Erlangung des Doktorgrades (Dr. rer. nat.)
der
Mathematisch-Naturwissenschaftlichen Fakultät
der
Rheinischen Friedrich-Wilhelms-Universität Bonn

von
Federico Scutti
aus
Rom

Bonn, 2016

Dieser Forschungsbericht wurde als Dissertation von der Mathematisch-Naturwissenschaftlichen Fakultät der Universität Bonn angenommen und ist auf dem Hochschulschriftenserver der ULB Bonn `http://hss.ulb.uni-bonn.de/diss_online` elektronisch publiziert.

1. Gutachter:	Prof. Dr. Jochen Dingfelder
2. Gutachter:	Prof. Dr. Klaus Desch
Tag der Promotion:	15.07.2016
Erscheinungsjahr:	2016

Thesis Summary

A search for the neutral Higgs bosons h, H and A, predicted by the Minimal Supersymmetric Standard Model (MSSM), is presented in this thesis. It is based on a data sample with an integrated luminosity of $L_{\text{int}} = 19.5\ \text{fb}^{-1}$ from proton-proton collisions with a center-of-mass energy of $\sqrt{s} = 8$ TeV produced at the LHC and recorded by the ATLAS experiment in 2012. The search is performed in the decay channel with two tau leptons decaying hadronically, $h/H/A \to \tau_{\text{had}}\tau_{\text{had}}$.

The major background to hadronic tau decays are particle jets originating from the hadronisation of a quark or a gluon. In ATLAS, tau identification techniques have been developed using multivariate algorithms able to distinguish between a hadronic tau decay and a jet. However, the identification efficiency in simulated events needs to be corrected to match the efficiency in data, in order to achieve a meaningful comparison between collision data and simulated events. For this thesis, a fitting method has been developed for the measurement of the tau identification efficiency in data using the spectrum of the track multiplicity originating from charged particles in the hadronic tau decay. Correction factors for the efficiency in the simulation were measured with very competitive precision, ranging between $\approx 2\%$ and $\approx 5\%$ depending on the track multiplicity of the tau and the region of the detector.

In the $h/H/A \to \tau_{\text{had}}\tau_{\text{had}}$ search, the selection of events is based on the kinematic and topological properties of a heavy neutral Higgs boson produced by $b\bar{b}$ annihilation and gluon-gluon fusion production mechanisms. The selection is divided in two categories where events are required to fulfill two separate trigger requirements, a di-tau and a single-tau trigger. A higher signal efficiency and a lower multi-jet background contamination are achieved in the single-tau-trigger category, where tau leptons are triggered at higher transverse momenta with respect to the di-tau trigger. Data-driven techniques have been developed in both categories for the estimation of the dominant multi-jet contamination. Other background contributions are modelled using simulated events, including the abundant $Z/\gamma^* \to \tau\tau$ and the small $W \to \tau\nu$+jets contamination. In simulated backgrounds, jets that are reconstructed as a tau candidate are weighted using the tau mis-identification efficiency measured in data. This allows one to correct for the mis-modelling of the efficiency and to artificially increase the number of simulated events.

The sensitivity provided by the $h/H/A \to \tau_{\text{had}}\tau_{\text{had}}$ analysis is significantly enhanced with respect to previous ATLAS searches in this channel, and dominates the sensitivity of the combined $h/H/A \to \tau\tau$ search, where other tau decay modes are selected in the final state, for Higgs boson masses of $m_A \gtrsim 350$ GeV. As no significant excess is found, exclusion limits are set in the space of the two leading-order unpredicted parameters of the MSSM Higgs sector, the mass of the CP-odd Higgs boson, m_A, and the ratio between the vacuum expectation values of the two Higgs doublets, $\tan\beta$. After the discovery of a Higgs boson in 2012, with a mass of $m_H = 125.09 \pm 0.24$ GeV, new phenomenological scenarios of the MSSM were proposed. In this search, exclusion limits are obtained for these various scenarios in the mass range $m_A = 170 - 1000$ GeV. Model-independent exclusion limits were also obtained for the production cross-section of a generic resonance, ϕ, for both production modes. Excluded cross-sections at 95% confidence level vary with m_ϕ and are $\sigma_{\text{excl.}}(b\bar{b} \to \phi \to \tau\tau) \approx 4.2$ pb and $\sigma_{\text{excl.}}(gg \to \phi \to \tau\tau) \approx 6.8$ pb at $m_\phi = 170$ GeV and $\sigma_{\text{excl.}}(b\bar{b} \to \phi \to \tau\tau) \approx 9.2$ fb and $\sigma_{\text{excl.}}(gg \to \phi \to \tau\tau) \approx 10$ fb at $m_\phi = 1000$ GeV.

Contents

CHAPTER 1

Introduction

The scientific study of the main constituents of matter and their interactions is the main goal of particle physics. The idea that the universe is composed by fundamental constituents dates back to several hundreds of years B.C.. However, scientific investigations based on this underlying concept which led to the establishment of modern atomic theory, only go back to the 19th century. As experiments were performed over time, scientists gained insight into the structure of the atom itself, its nucleus structure, composed by protons and neutrons, and the distribution of electrons surrounding it.

Our current knowledge of the subatomic world is one of the most precise among scientific fields, and our theoretical description of such phenomena, called the Standard Model of particle physics (SM) [1–3], one of the most successful scientific theories. The Standard Model describes the universe in terms of a few fundamental particles composing matter divided in two groups called quarks and leptons, each of them subdivided in three generations. However, the complete picture also includes particles responsible for the fundamental forces we observe: the electromagnetic, weak and strong interactions. The gravitational force is left out of the SM as no successful quantum-mechanical description of this interaction has been proposed yet.

The highest energy particle physics facility nowadays is the *Large Hadron Collider* (LHC) [4], located near Geneva at CERN. The LHC has been designed to collide two proton beams at a center-of-mass energy of $\sqrt{s} = 14$ TeV, and was operated in 2011 and 2012 at $\sqrt{s} = 7$ TeV and $\sqrt{s} = 8$ TeV, respectively. One of the primary goals of the LHC is to shed light on the electroweak symmetry breaking mechanism, which describes how fundamental particles acquire mass. In the *Higgs mechanism* [5–10], the electroweak symmetry is broken spontaneously by the Higgs potential and a new scalar particle is predicted to exist, the Higgs boson.

On July 4 2012, the ATLAS and CMS experiments announced the discovery of a new particle consistent with the Higgs boson [11, 12]. Since then, as more data were collected and analyses refined, the SM nature of the new discovery seems to be confirmed, however, no conclusive evidence has been found yet to exclude alternative models.

The Standard Model of particle physics is a very successful theory although not complete. In particular the following open problems are relevant for the model related to the search presented in this thesis. The Higgs sector in the SM poses the so-called *hierarchy problem*. In short, the quantum corrections to the mass of the Higgs boson are found to diverge. The solution to this would be a fine-tuned cancellation between the bare value of the Higgs mass and its correction, which is regarded to be an undesirable feature of the theory. Direct observation of new phenomena has also motivated the speculation about new physics. Based on data from the WMAP and Plank space observatory [13, 14], we currently know that only 4.9%

of our universe is made of ordinary matter, while the remaining 68.3% of dark energy and 26.8% of dark matter, whose nature is yet to be identified. In the SM the parameters characterising the intensity of the fundamental interactions are found to have similar values at a high scale of the transferred momentum in the interaction ($Q \approx 10^{15}$ GeV). This feature may indicate the need for unification which would require new physics. Finally, the gravitational interaction needs to be described in a quantum-mechanical framework.

Among the most popular extensions of the Standard Model there is Supersymmetry, a theory relating the ordinary fermions and bosons with a new class of particles called superpartners, which are bosons and fermions, respectively. Supersymmetry can be a fundamental ingredient in theories addressing the previously mentioned problems, besides possibly providing a natural candidate for dark matter. Supersymmetric models require an extended Higgs sector with respect to the SM. In the Minimal Supersymmetric Standard Model (MSSM) the existence of three neutral physical states is predicted, two CP-even called h and H plus one CP-odd called A, and two electrically charged, $H^{\pm}$. Those states arise from the mixing of the degrees of freedom contained in two Higgs doublets required by the MSSM. The Higgs sector is characterised, at the leading order of perturbation theory, by two free parameters: the mass of the CP-odd state, m_A, and the ratio between the vacuum expectation values of the two Higgs doublets, called $\tan\beta$.

The topic of this thesis is the search for the neutral Higgs bosons predicted by the MSSM. The search is performed in the decay channel $h/H/A \to \tau_{\text{had}}\tau_{\text{had}}$ where τ_{had} refers to a decay of the τ (tau lepton) into hadrons and a neutrino. The analysed data were collected by the ATLAS experiment and amount to an integrated luminosity of 19.5 fb^{-1} from proton-proton collisions at $\sqrt{s} = 8$ TeV. The search for $h/H/A \to \tau\tau$ is motivated by the enhancement proportional to $\tan\beta$ of the MSSM Higgs bosons couplings to certain types of fermions. Other decay channels with enhanced couplings, like $h/H/A \to b\bar{b}$, present poor discrimination against the large background of jets originated from b quarks at the LHC.

Among di-tau decay channels, double hadronic decays occur $\approx 42\%$ of the time, therefore providing a comparative large sample to be analysed. The main challenge posed by this type of di-tau decays is the large multi-jet background originated by the hadronisation of quarks and gluons, abundantly produced at the LHC. A selection has been designed in order to suppress this background and separate it from the signal and dedicated background estimation techniques have been used depending on the mass hypothesis of the Higgs bosons.

This thesis is structured as follows. Chap. 2 introduces the Standard Model theoretical framework including the description of the electroweak symmetry breaking mechanism and the Higgs sector. The open problems of this theory are also discussed and the Minimal Supersymmetric Standard Model is introduced. Chap. 3 is an overview of the experimental status of MSSM Higgs searches including the most recent results from the LHC. Chap. 4 describes the Large Hadron Collider facility and the ATLAS experiment, while Chap. 5 discusses the detail of the reconstruction and identification of physical objects at ATLAS. Chap. 6 is dedicated to the reconstruction of tau leptons illustrating how these particles are reconstructed and discriminated from their major source of background, with particular attention devoted to the measurement of the tau identification correction factors, to be applied to the simulation, which was performed for this thesis. Chap. 7 describes the $h/H/A \to \tau_{\text{had}}\tau_{\text{had}}$ analysis, including the data and simulation samples used, background estimation techniques and the evaluation of the systematic uncertainties. In Chap. 8 the hypothesis test aimed at setting an exclusion limit on the signal hypothesis in the space of the free parameters of the theory is described. This test is performed by fitting the expected signal and background distributions to data. The validation of the fitting procedure is also presented in this chapter. Finally, Chap. 9 briefly reports the analyses performed in other di-tau decay channels, $h/H/A \to \tau_{\text{lep}}\tau_{\text{lep}}$ and $h/H/A \to \tau_{\text{lep}}\tau_{\text{had}}$, where τ_{lep} indicates the decay of the tau containing either a muon or an electron, and two neutrinos. This part also discusses the combination between all three

channels in the $h/H/A \to \tau\tau$ search aimed at setting an exclusion limit which depends on their joint sensitivity.

CHAPTER 2

Theory Overview

In the following, the overview of the theoretical framework for this thesis is presented. In Sec. 2.1, the Standard Model of particle physics (SM) is discussed, introducing the fundamental interactions and the particle content, as well as the underlying theoretical concepts. As this thesis will be focused on the Higgs boson sector, particular attention will be devoted to the description of the Higgs mechanism and the Higgs boson, firstly in the context of the SM. The search presented in this thesis is set for new Higgs bosons required by one of the most promising models of new physics, called Supersymmetry (SUSY), introduced in Sec. 2.2. The Higgs sector in Supersymmetry is more complex with respect to the SM one. The most simple extension of the SM, able to incorporate Supersymmetry, is the Minimal Supersymmetric Standard Model (MSSM), with minimal particle content with respect to the SM. This theory is discussed and motivated in Sec. 2.3, including a detailed illustration of the Higgs sector. A fundamental part of a search at a particle collider is the simulation of events, a necessary procedure to set the expectation of known processes and new signals. The main features of these simulation techniques are discussed in Sec. 2.4.

2.1 The Standard Model

The Standard Model of particle physics describes the fundamental forces in nature as a result of the interactions between few fundamental particles. This theory was developed starting from the second half of the 20th century and proved to be very successful through time. Experimental efforts continue nowadays to probe the SM predictions. The most important recent result is the discovery of a resonance consistent with the Higgs boson, a particle predicted in 1964 [5–10], and considered to be the last missing piece of evidence for the theory. In the following sections the SM is introduced based on the more detailed discussions in Ref. [15], [16], and [17].

2.1.1 Interactions and Particle Content

The present section introduces the interactions described by the SM and the particle content of the theory. Here, a description based on observable quantities and phenomena is given, paving the way to a more accurate mathematical treatment to be discussed in the following sections.

In nature we observe four fundamental forces: the gravitational, weak, electromagnetic and strong interactions. They result from the mediation of particles, the so-called *gauge bosons*, which have spin

Interaction	Gauge Boson	Mass / GeV	Range / m
Electromagnetic	γ (photon)	0	∞
Weak	$W^{\pm}$ (W bosons)	80.385 ± 0.015	$\approx 10^{-18}$
	Z^0 (Z boson)	91.1876 ± 0.0021	
Strong	$g_1, ..., g_8$ (gluons)	0	$\approx 10^{-15}$

Table 2.1: Summary of gauge bosons properties. Values are taken from Ref. [18].

$s = 1$, and are listed in Tab. 2.1. Particles which do not mediate the interactions are called *matter particles* which are fermions with spin $s = \frac{1}{2}$.

The relative intensity of the interactions we observe range between many orders of magnitude and can be expressed as a function of physical parameters, called couplings, related to the probability of the processes. Such couplings are found to depend on the energy scale of the interaction, as will be discussed in the following sections. Here, we will consider the so-called electroweak scale $\Lambda_{\mathrm{EW}} \approx 100$ GeV, relevant for processes tested at the LHC. The electromagnetic interaction is characterised by the coupling parameter $\alpha = e^2/4\pi\varepsilon_0\hbar c$, with $\alpha^{-1}(\Lambda_{\mathrm{EW}}) \approx 127.9$, containing the electron electric charge e. For the weak and strong interactions we have respectively $\alpha_W(\Lambda_{\mathrm{EW}}) \approx 2\alpha(\Lambda_{\mathrm{EW}})$ and $\alpha_S(\Lambda_{\mathrm{EW}}) \approx 7\alpha(\Lambda_{\mathrm{EW}})$. Gravity is by far the weakest, being $\approx 10^{-38}$ times weaker than the weak interaction, and therefore left out of the SM. Particle interactions mediated by gravity are not detectable at the energy scales probed at the LHC, but are expected to be as frequent as the other kind of interactions at much higher energies. Among gauge bosons, the photon (γ) mediates the electromagnetic interaction, W and Z bosons the weak one, and gluons (g) the strong interactions.

In a relativistic quantum theory like the Standard Model, energy can be converted into mass according to the Einstein relation $E = mc^2$. This implies that, for interacting particles, new states can be created during the interaction. In a quantum theory the Heisenberg uncertainty principle has to hold $\Delta E \Delta t \approx \hbar$. As a consequence, particles with a mass different from the equivalent energy of the interacting particles can be created for the time interval Δt. The more different the mass, the shorter Δt. As a consequence of this phenomenon, interactions mediated by massive gauge bosons have a limited range. The larger the mass of the boson, compared to the transferred momentum in the interaction, the shorter the range. All gauge boson masses and ranges are reported in Tab. 2.1. Similar to the case of the electric charge entering in the electromagnetic coupling parameter, all interactions are characterised by appropriate charges, which have to be conserved. We can assign to all particles in the SM quantum numbers associated with those charges. In the electromagnetic case, this quantum number is the electric charge of a particle Q which is expressed in units of the electron electric charge e.

Weak interactions conserve the quantum number I_3^W, the so-called *weak isocharge*, which can assume a set of discrete values. As will be discussed in the following sections, electromagnetic and weak interactions are connected to each other. This feature is represented by the quantum number Y, called *weak hypercharge*, and defined as

$$Y = Q - I_3^W \tag{2.1}$$

which is always conserved by the two processes.

Weak interactions violate *parity* (P), i.e. the probability of weak processes is not identical under reversal of the three-dimensional coordinates, called a *parity transformation*. If C represents a generic charge associated with a particle, weak interactions also violate the CP symmetry, i.e. they are not

invariant for a reversal of the charges joined to a parity transformation. Strong interactions are induced by the quantum number called *colour*, for which we have the three states *red* (r), *green* (g) and *blue* (b). For every particle in the SM there is a corresponding antiparticle with opposite quantum numbers.

The gauge bosons can interact with themselves if they carry charges. W bosons can interact with each other as well as with the Z, and thus have $I_3^W = \pm 1$ and $Q = \pm 1$. Photons and Z bosons are neutral and don't interact with themselves or with each other. Gluons carry colour charge in the form of superposition of states carrying colour and anticolour, yielding a total number of eight independent states, which interact with each other leading to a short range of the strong interaction, even though the gluon does not have a mass. This fundamental difference between the photon and the gluon leads to a different behaviour of the electromagnetic and strong couplings with increasing energy of the interaction. In the electromagnetic case, the electric charge is screened by virtual pairs of electrons and positrons, the electron antiparticle. This virtual pair arises by the decay of a virtual photon, γ^*. With increasing energy we are able to probe shorter distances around the charge and be less affected by the surrounding electron-positron cloud. For the strong interaction, a similar process occurs, but the gluons can couple to other gluons from the vacuum which add colour charge to the cloud. This leads to an increasing colour charge at larger distances, or decreasing energy (*confinement*), and diminishing at lower distances, or at higher energy (*asymptotic freedom*). The confinement is responsible for the fact that we do not observe free colour-charged states in nature.

In the Standard Model, matter particles are divided in leptons and quarks. All of them are fermions with spin $s = \frac{1}{2}$. They are reported in Tab. 2.2 and 2.3, which highlight their classification in three generations with different mass scales. Among the leptons, neutrinos only interact weakly, as they do not possess any electric charge, where all others also interact electromagnetically. Quarks interact weakly, electromagnetically and strongly. They carry colour charge as a superposition of states with different charges. Due to confinement, quarks form hadrons which are bound states of two or three so-called *valence quarks*. These hadrons are called mesons and baryons, respectively. Hadrons are always colour neutral. As the valence quarks interact strongly with each other, we can think of hadrons as composed also by gluons and other virtual quark pairs, the so-called *sea quarks*. Particles composing hadrons will be referred to as *partons*.

Partons remain confined in hadrons at low energies. However, when a high-energy interaction takes place, like proton-proton collisions at the LHC, they are excited beyond the energy levels characterising a bound state. As only colour-neutral states are observed in nature, all partons emerging from the interaction are forced to couple to other virtual partons and form new hadrons. This phenomenon is very common at the LHC and is called *hadronisation*.

2.1.2 Quantum Field Theory

In the following a detailed mathematical treatment is given of the Standard Model as a quantum field theory. Theories of fundamental particles and interactions are based on the variational principle of least action to derive equations of motion of the particles and define the structure of the interactions. The action is defined as

$$S = \int \mathrm{d}x^4 \mathcal{L}(\phi_a(x), \partial_\mu \phi_a(x)), \tag{2.2}$$

where $\mathcal{L}$ is the Lagrange density, the so-called *Lagrangian*, dependent on the generic field ϕ_a, and its space-time derivatives $\partial_\mu \phi_a(x)$ with respect to the components of the four-vector $x = (t, \mathbf{x})$, where t is the time coordinate and $\mathbf{x}$ is the three-dimensional space vector. Here a is an index representing the degrees of freedom of the system. A field is a function representing the particles we observe. Different particles are related to different fields. Equations of motions for the particles result from imposing $\delta S = 0$, with

	Leptons			Mass / GeV	Q	I_3^W	
I	electron-neutrino	$\begin{pmatrix}\nu_e\\ e\end{pmatrix}_L$	–	$< 0.225 \times 10^{-6}$	0	$\begin{pmatrix}\frac{1}{2}\\ -\frac{1}{2}\end{pmatrix}_L$	–
	electron		$(e)_R$	$(0.5109898928 \pm 0.000000011) \times 10^{-3}$	1		$(0)_R$
II	muon-neutrino	$\begin{pmatrix}\nu_\mu\\ \mu\end{pmatrix}_L$	–	$< 0.19 \times 10^{-3}$	0	$\begin{pmatrix}\frac{1}{2}\\ -\frac{1}{2}\end{pmatrix}_L$	–
	muon		$(\mu)_R$	$(105.6583668 \pm 0.0000038) \times 10^{-3}$	1		$(0)_R$
III	tau-neutrino	$\begin{pmatrix}\nu_\tau\\ \tau\end{pmatrix}_L$	–	$< 18.2 \times 10^{-3}$	0	$\begin{pmatrix}\frac{1}{2}\\ -\frac{1}{2}\end{pmatrix}_L$	–
	tau		$(\tau)_R$	1.77682 ± 0.00016	1		$(0)_R$

Table 2.2: Lepton content of the Standard Model. For each lepton generation the chiral components are broken down according to the weak interaction symmetries. The electric charge in units of the electron charge e, Q, is reported together with the weak isospin, I_3^W. Values are taken from Ref. [18].

	Quarks			Mass / GeV	Q	I_3^W		Colour Charge
I	up	$\begin{pmatrix}u\\ d\end{pmatrix}_L$	$(u)_R$	$(2.3 \pm 0.7) \times 10^{-3}$	$\frac{2}{3}$	$\begin{pmatrix}\frac{1}{2}\\ -\frac{1}{2}\end{pmatrix}_L$	$(0)_R$	r,g,b
	down		$(d)_R$	$(4.8 \pm 0.5) \times 10^{-3}$	$-\frac{1}{3}$		$(0)_R$	r,g,b
II	charme	$\begin{pmatrix}c\\ s\end{pmatrix}_L$	$(c)_R$	1.275 ± 0.025	$\frac{2}{3}$	$\begin{pmatrix}\frac{1}{2}\\ -\frac{1}{2}\end{pmatrix}_L$	$(0)_R$	r,g,b
	strange		$(s)_R$	$(95 \pm 5) \times 10^{-3}$	$-\frac{1}{3}$		$(0)_R$	r,g,b
II	top	$\begin{pmatrix}t\\ b\end{pmatrix}_L$	$(t)_R$	173.21 ± 0.87	$\frac{2}{3}$	$\begin{pmatrix}\frac{1}{2}\\ -\frac{1}{2}\end{pmatrix}_L$	$(0)_R$	r,g,b
	bottom		$(b)_R$	4.18 ± 0.03	$-\frac{1}{3}$		$(0)_R$	r,g,b

Table 2.3: Quark content of the Standard Model. For each quark generation the chiral components are broken down according to the weak interaction symmetries. The electric charge in units of the electron charge e, Q, is reported together with the weak isospin, I_3^W. Each quark can carry any of the three values of the colour charge, as indicated in the last column. Values are taken from Ref. [18].

respect to a variation of the field, and can be written as

$$\frac{\partial \mathcal{L}}{\partial \phi_a} = \partial_\mu \left(\frac{\partial \mathcal{L}}{\partial(\partial_\mu \phi_a)} \right), \qquad a = 1, \ldots, N. \tag{2.3}$$

Examples of Lagrangians describing a charged boson with spin $s = 0$, and a fermion with $s = \frac{1}{2}$, with mass m, are

$$\mathcal{L}_{\text{boson}} = \partial^\mu \phi^* \partial_\mu \phi - m^2 \phi^* \phi, \tag{2.4a}$$

$$\mathcal{L}_{\text{fermion}} = \overline{\psi}(i\gamma^\mu \partial_\mu - m)\psi. \tag{2.4b}$$

In (2.4), ϕ is a complex scalar field with two degrees of freedom and ψ a so-called *Dirac spinor* with four. The symbols γ^μ represent matrices defined in Ref. [15], and $\overline{\psi} = \psi^\dagger \gamma^0$, where $\psi^\dagger$ is the hermitian conjugate of the field. In Eq. (2.4) the symbols ϕ and ψ are related to the particles, while their respective antiparticles are represented by ϕ^* and $\overline{\psi}$.

A quantum field theory has to satisfy the following commutation relations between the fields and their conjugate moments

$$[\phi_a(\mathbf{x}, t), \pi_b(\mathbf{x}', t)] = i\hbar \delta_{ab} \delta(\mathbf{x} - \mathbf{x}') \tag{2.5a}$$

$$[\phi_a(\mathbf{x}, t), \phi_b(\mathbf{x}', t)] = [\pi_a(\mathbf{x}, t), \pi_b(\mathbf{x}', t)] = 0 \tag{2.5b}$$

where the conjugate moments are defined as

$$\pi_a(x) = \frac{\partial \mathcal{L}}{\partial(\partial_t \phi_a)}, \tag{2.6}$$

in which $\partial_t \phi_a$ is a time derivative.

2.1.3 Quantum Electrodynamics

Quantum electrodynamics (QED) introduces the photon in the Lagrangian of the free charged particles and describes its interactions with them. This is achieved by requiring invariance of Eq. (2.2) under the so-called *gauge* transformations of the photon field $\phi_a \equiv A_\mu$, representing a neutral spin $s = 1$ particle

$$A_\mu(x) \to A'_\mu(x) = A_\mu(x) + \partial_\mu f(x), \tag{2.7}$$

where $f(x)$ is a real arbitrary function. If we consider the interaction between a photon and a fermion with electric charge $q = eQ$, invariance is ensured if the Lagrangian has the form

$$\mathcal{L} = \mathcal{L}_{\text{fermion}} + \mathcal{L}_{\text{interaction}} = \overline{\psi}(i\gamma^\mu \partial_\mu - m)\psi - q\overline{\psi}\gamma^\mu \psi A_\mu \tag{2.8}$$

and the fermion fields undergo the transformations

$$\psi(x) \to \psi'(x) = \psi(x) e^{-iqf(x)} \approx [1 - iqf(x)]\psi(x), \tag{2.9a}$$

$$\overline{\psi}(x) \to \overline{\psi'}(x) = \overline{\psi}(x) e^{iqf(x)} \approx [1 + iqf(x)]\overline{\psi}(x), \tag{2.9b}$$

where the approximation is true for small values of the exponent. In other words, the Lagrangian has to be invariant under transformations of the group U(1).

The QED Lagrangian would not be complete without a term describing free photons, also invariant

under the transformation in Eq. (2.7), which we can write as

$$\mathcal{L}_{\text{photon}} = -\frac{1}{4}F^{\mu\nu}F_{\mu\nu} \quad \text{with} \quad F_{\mu\nu} = \partial_\mu A_\nu - \partial_\nu A_\mu. \tag{2.10}$$

QED represents the most simple example of a gauge theory, and is extended in the SM to include weak interactions in the way discussed in the next section.

2.1.4 Electroweak Unification

The first experimental evidence of weak interactions was established by the observation of processes mediated by the charged gauge bosons $W^\pm$. These particles couple to leptons and quarks selecting only one component of the Dirac field, indicated by ψ^{L}. This component is said to have a definite *chirality*, namely a left-handed one. Another component can be defined with a right-handed chirality, called ψ^{R}. They are defined as

$$\psi^{\text{L}}(x) = P_{\text{L}}\psi(x) = \frac{1}{2}(1-\gamma_5)\psi(x) \tag{2.11a}$$

$$\psi^{\text{R}}(x) = P_{\text{R}}\psi(x) = \frac{1}{2}(1+\gamma_5)\psi(x), \tag{2.11b}$$

where $\gamma_5 = i\gamma_0\gamma_1\gamma_2\gamma_4$. The structure of the interaction is such that we can arrange leptons or quarks fields into a so-called weak isospin doublet

$$\Psi^{\text{L}}(x) = \begin{pmatrix} \psi^{\text{L}}_{\mathcal{U}}(x) \\ \psi^{\text{L}}_{\mathcal{D}}(x) \end{pmatrix}, \tag{2.12}$$

where the symbols $\mathcal{U}$ and $\mathcal{D}$ indicate the up-type and down-type components, respectively, in the representation of a doublet transforming under the group SU(2). This representation is also used to display each lepton and quark generation in Tab. 2.2 and 2.3. On the other hand, we will treat the right-handed chirality states as only transforming under the U(1) group in a similar way as discussed for QED, so in Tab. 2.2 and 2.3 they are represented as a singlet. The $W^\pm$ bosons couple to fermion pairs with different isospin, which are purely left-handed chirality states. This coupling is responsible for maximal parity violation in weak interactions.

In the same way discussed for QED, the Lagrangian including the interaction term has to be invariant under the SU(2) transformations of isospin doublets

$$\Psi^{\text{L}}(x) \to \Psi'^{\text{L}}(x) = \Psi^{\text{L}}(x)e^{-ig\sigma_j\omega_j(x)} \tag{2.13a}$$

$$\overline{\Psi}^{\text{L}}(x) \to \overline{\Psi}'^{\text{L}}(x) = \overline{\Psi}^{\text{L}}(x)e^{ig\sigma_j\omega_j(x)}, \tag{2.13b}$$

where σ_j, with $j = 1, 2, 3$, are the Pauli matrices [15] which generate the transformation parametrised by the real function $\omega_j(x)$ and the coupling parameter g. Pauli matrices satisfy the commutation relation

$$[\sigma_i, \sigma_j] = 2i\varepsilon_{ijk}\sigma_k, \tag{2.14}$$

where ε_{ijk} is the completely antisymmetric tensor. In the case of weak interactions gauge bosons are represented by three real fields W^μ_i which transform like

$$W^\mu_i(x) \to W'^\mu_i(x) = W^\mu_i(x) + \partial^\mu\omega_i(x) - g\varepsilon_{ijk}\omega_j(x)W^\mu_k(x). \tag{2.15}$$

With part of the degrees of freedom provided by Eq. (2.15) we can write the two charged gauge bosons $W^{\pm}$ as

$$W^{\mu\pm}(x) = \frac{1}{\sqrt{2}}[W_1^{\mu}(x) \mp iW_2^{\mu}(x)]. \tag{2.16}$$

The remaining degrees of freedom allowed by Eq. (2.15) can be accommodated to represent a neutral current. However, this neutral current can couple to right-handed chirality states as well. For this reason, an extension of the model is required. This is done by introducing a further gauge field, B_μ, which transforms according to the U(1) symmetry, exactly as Eq. (2.7), and requiring all the fields to be invariant under transformations analogous to Eq. (2.9), if we replace $q = eQ$ with a weak charge $g'Y$, where Y is the weak hypercharge and g' a number parametrising the transformation analogous to e.

Electroweak unification requires the mixing

$$A^{\mu}(x) = \cos\theta_{\mathrm{W}} B^{\mu}(x) + \sin\theta_{\mathrm{W}} W_3^{\mu}(x) \tag{2.17a}$$

$$Z^{\mu}(x) = -\sin\theta_{\mathrm{W}} B^{\mu}(x) + \cos\theta_{\mathrm{W}} W_3^{\mu}(x) \tag{2.17b}$$

In Eq. (2.17), Z^μ is the field representing the Z^0 boson, and θ_{W}, called the Weinberg angle, mixes a purely left-handed interaction, represented by the W_3^μ field, with a universal one represented by B^μ. Experimentally we have $\sin^2\theta_{\mathrm{W}} = 0.2397 \pm 0.0013$ [18]. In Sec. 2.1.7 it will be seen how this angle is related to the masses of the gauge bosons. $\mathrm{U}(1)_Y$ transformations, related to the B_μ field, commute with $\mathrm{SU}(2)_L$ transformations, therefore the unification represented by Eq. (2.17), can be described by the joint group $\mathrm{SU}(2)_L \otimes \mathrm{U}(1)_Y$. In Tab. 2.2 and 2.3 the additional right-handed singlets interacting with the neutral currents are indicated together with their quantum numbers. Electroweak unification implies the relation

$$g\sin\theta_{\mathrm{W}} = g'\cos\theta_{\mathrm{W}} = e. \tag{2.18}$$

After electroweak unification the full interaction Lagrangian can be written as

$$\mathcal{L}_{\mathrm{interaction}} = -s_\mu A^\mu - \frac{g}{2\sqrt{2}}[J_\mu^{\mathrm{CC}} W^{\mu-} + \mathrm{h.\,c.}] - \frac{g}{\cos\theta_{\mathrm{W}}} J_\mu^{\mathrm{NC}} Z^\mu \tag{2.19}$$

where h.c. is the hermitian conjugate. In Eq. (2.19) the photon is coupled to the current s_μ, the charged vector bosons $W^\pm$ to J_μ^{CC} and the neutral vector boson Z^0 to J_μ^{NC}, defined as

$$s_\mu = q\overline{\psi}\gamma_\mu\psi \tag{2.20a}$$

$$J_\mu^{\mathrm{CC}} = \overline{\psi}_{\mathcal{D}}\gamma_\mu(1-\gamma^5)\psi_{\mathcal{U}} = \overline{\psi}^{\mathrm{L}}_{\mathcal{D}}\gamma_\mu\psi^{\mathrm{L}}_{\mathcal{U}} \tag{2.20b}$$

$$J_\mu^{\mathrm{NC}} = \overline{\psi}\gamma_\mu\frac{1}{2}(v_\psi - a_\psi\gamma^5)\psi. \tag{2.20c}$$

As evident from Eq. (2.20), the Z boson couples to a mixture of left-handed and right-handed states, as no pure $(1-\gamma_5)$ operator is involved. The coupling is parametrised by the coefficients v_ψ and a_ψ which depend on the particular fermion involved, and are defined as

$$v_\psi = I_3^W - 2Q\sin^2\theta_{\mathrm{W}}, \tag{2.21a}$$

$$a_\psi = I_3^W. \tag{2.21b}$$

It has to be pointed out that quarks participate in the weak interaction as a superposition of mass eigenstates in the current J_μ^{CC}. In other words a down-type quark in J_μ^{CC} coupling to an up-type quark j

can be written as

$$\psi'_{\mathcal{D},j} = \sum_{i=d,s,b} V_{ji}\psi_{\mathcal{D},i}, \qquad \text{where} \qquad j = u, c, t. \tag{2.22}$$

In Eq. (2.22), the numbers V_{ji} are elements of a unitary matrix called *Cabibbo-Kobayashi-Maskawa* (CKM) matrix [19, 20], parametrised by three angles and one complex phase, which accounts for the CP violation of weak interactions. The unitarity requirement corresponds to the following constraints

$$\sum_{i=u,c,t} |V_{ji}|^2 = \sum_{j=d,s,b} |V_{ji}|^2 = 1 \tag{2.23a}$$

$$\sum_{k} V_{jk}V^*_{ik} = 0. \tag{2.23b}$$

The CKM parameters are not a prediction of the SM and must be measured experimentally.

Similar to the quark case, recent experimental evidence has been collected [21] proving the mixing of neutrino mass eigenstates, necessary to explain the observed lepton-flavour violation in the neutrino sector, or *neutrino oscillations*. Neutrinos mix according to a unitary matrix called *Pontecorvo-Maki-Nakagawa-Sakata* (PMNS) [22, 23].

In addition to the interaction terms, the full Lagrangian includes the free field contributions. As for the case of the electromagnetic interaction, and assuming massless gauge bosons, we can write these terms with B_μ and W^i_μ with no mixing. Therefore we have

$$\mathcal{L}_B = -\frac{1}{4}B^{\mu\nu}B_{\mu\nu} \qquad \text{where} \qquad B^{\mu\nu} = \partial^\mu B^\nu - \partial^\nu B^\mu \tag{2.24a}$$

$$\mathcal{L}_F = -\frac{1}{4}F^{\mu\nu}_i F_{i\mu\nu} \qquad \text{where} \qquad F^{\mu\nu}_i = \partial^\mu W^\nu_i - \partial^\nu W^\mu_i + g\varepsilon_{ijk}W^\mu_j W^\mu_k. \tag{2.24b}$$

Unlike the QED case, the gauge bosons in the electroweak theory can interact with each other. This happens on account of the term $g\varepsilon_{ijk}$ in Eq. (2.24) (b), which couples bosons possessing a charge, therefore we observe the $W^\pm$ coupling to Z^0 and γ, as well as to each other.

Electroweak interactions conserve the total lepton number defined as

$$L = N_l - N_{\bar{l}} \qquad \text{where} \qquad l = e, \mu, \tau, \tag{2.25}$$

where the index l ($\bar{l}$) labels the different lepton (anti-lepton) generations.

2.1.5 Masses of Gauge Bosons and Fermions

In the previous section we left out the description of mass terms of gauge bosons and fermions. The reason for this is that these terms would violate the electroweak symmetries of the Lagrangian, an undesirable feature in a gauge theory, as will be explained later. We can try to add mass terms for gauge bosons as

$$\mathcal{L}^{\text{bosons}}_{\text{masses}} = \frac{1}{2}m^2_Z Z_\mu Z^\mu + m^2_W W^\dagger_\mu W^\mu. \tag{2.26}$$

Unfortunately, this term is not invariant under the transformations in Eq. (2.7) and (2.15). We can also introduce a mass term for fermions as

$$\mathcal{L}^{\text{fermion}}_{\text{mass}} = -m_f\overline{\psi}_f\psi_f. \tag{2.27}$$

Using the definitions in Eq. (2.11) we can expand it as

$$\mathcal{L}_{\text{mass}}^{\text{fermion}} = -m_f \overline{\psi}_f (P_{\text{R}} + P_{\text{L}}) \psi_f = m_f (\bar{\psi}_f^{\text{L}} \psi_f^{\text{R}} + \bar{\psi}_f^{\text{R}} \psi_f^{\text{L}}), \tag{2.28}$$

where the right-handed components transform under U(1), as in Eq. (2.9), but the left-handed ones under SU(2) ⊗ U(1), as in Eq. (2.13), as they are part of an isospin doublet. This difference causes again symmetry breaking. In Sec. 2.1.7 the Higgs mechanism will be presented, which allows the symmetries to be preserved and accounts for the mass terms.

2.1.6 Quantum Chromodynamics

In the Standard Model, quarks carry colour charge, as indicated in Tab. 2.3, and therefore interact strongly. Quantum chromodynamics describes the structure of the strong interaction utilising the symmetry group SU(3). This symmetry group has 8 generators, called λ matrices [15]. If we define $\hat{F}_i = \frac{1}{2}\lambda_i$, where $i = 1, \ldots, 8$, we have

$$[\hat{F}_i, \hat{F}_j] = i f_{ijk} \hat{F}_k \tag{2.29}$$

where f_{ijk} are completely antisymmetric real structure constants.

In the space of SU(3) transformations a quark state can be represented as

$$\Psi(x) = \begin{pmatrix} \psi_r(x) \\ \psi_g(x) \\ \psi_b(x) \end{pmatrix} \tag{2.30}$$

where r, g, b represent the three colour states. As in the electroweak case the Lagrangian is required to be invariant under the transformations

$$\Psi(x) \to \Psi'(x) = \Psi(x) e^{-i g_s \lambda_j \omega_j(x)}, \tag{2.31a}$$

$$\overline{\Psi}(x) \to \overline{\Psi}'(x) = \overline{\Psi}(x) e^{i g_s \lambda_j \omega_j(x)}. \tag{2.31b}$$

Complete invariance is obtained by introducing the eight gauge fields G_i^μ, which transform like

$$G_i^\mu(x) \to G'^\mu_i(x) = G_i^\mu(x) + \partial^\mu \omega_i(x) - g_s f_{ijk} \omega_j(x) G_k^\mu(x), \tag{2.32}$$

where the strong charge g_s has been introduced. As for the electroweak interaction, the appearance of the factor f_{ijk} in Eq. 2.32 leads to self interactions between the gauge bosons, the gluons. The interaction term in the Lagrangian can be written as

$$\mathcal{L}_{\text{interaction}} = -\frac{1}{2} g_s \overline{\Psi} \gamma_\mu \lambda_j \Psi G_j^\mu \tag{2.33}$$

and the gluon-only term as

$$\mathcal{L}_{\text{gluon}} = -\frac{1}{4} F_i^{\mu\nu} F_{i\mu\nu} \quad \text{where} \quad F_i^{\mu\nu} = \partial^\mu G_i^\nu - \partial^\nu G_i^\mu + g_s f_{ijk} G_j^\mu G_k^\nu. \tag{2.34}$$

In nature we do not observe free coloured states, but only colour singlets. A remarkable feature of QCD is the prediction of the composition of the hadrons in terms of quarks, based on the principle of colour confinement, which excludes single-quark, di-quark, and other fractionally charged states.

A fundamental property of QCD is flavour independence, which means that the strength of the

quark-gluon interaction is independent on the quark type. Also, QCD conserves the six quark flavour numbers

$$N_q = N(q) - N(\bar{q}) \quad \text{where} \quad q = u, d, s, \ldots \tag{2.35}$$

defined as the number of quarks minus the number of antiquarks of a given flavour q, which can be violated by electroweak interactions.

The QCD Lagrangian is SU(3) invariant, differently from the electroweak case. The SU(3) symmetry commutes with $\mathrm{SU}(2)_L \otimes \mathrm{U}(1)_Y$, making $\mathrm{SU}(3) \otimes \mathrm{SU}(2)_L \otimes \mathrm{U}(1)_Y$ the group suitable to describe all the interactions.

All interactions discussed so far conserve the *barion number* defined as

$$B = \frac{1}{3}\left(N_q - N_{\bar{q}'}\right). \tag{2.36}$$

2.1.7 The Higgs Mechanism

In Sec. 2.1.4 we introduced the Lagrangian describing electroweak interactions. The gauge bosons introduced in the theory, should remain massless in order to conserve the electroweak symmetries of the Lagrangian. Also fermions were treated as massless, as shown in Sec. 2.1.5. Invariance of the Lagrangian is fundamental if we want to keep the theory renormalisable. This requirement guarantees that all observable quantities can be computed with arbitrary degree of precision, i.e. to all orders in perturbation theory, avoiding divergences. In order to keep the theory renormalisable it is essential to introduce the masses by a mechanism which retains the gauge invariance of the Lagrangian. In this section we will describe a dynamical mechanism for electroweak symmetry breaking called the *Higgs mechanism*, ultimately responsible for all non-zero masses of gauge bosons, charged leptons and quarks[1].

The Higgs mechanism is based on a fundamental consideration about the energy levels of a system described by a Lagrangian $\mathcal{L}$ invariant under a certain group of transformations G. Regarding the potential related to such energy levels, two situations can occur. Firstly, if a given energy level is non-degenerate then the corresponding eigenstate is unique and invariant under the transformations of G. Secondly, the energy level might be degenerate and the corresponding eigenstates transform linearly into each other under G. In particular, we focus on the lowest energy levels of the system, i.e. the vacuum. In Fig. 2.1 a potential related to the second case is shown, which can be written as

$$V(\phi) = \mu^2|\phi|^2 + \lambda|\phi|^4 \quad \text{where} \quad \phi(x) = \frac{1}{\sqrt{2}}[\phi_1(x) + i\phi_2(x)] \tag{2.37}$$

with $\mu^2 < 0$ and $\lambda > 0$. Such a potential is invariant for $G \equiv \mathrm{U}(1)$. Looking at Fig. 2.1, it is clear that if we choose an arbitrary ground state this is not invariant under U(1), as this group consists of rotations in the (ϕ_1, ϕ_2) plane. However, we notice that no additional non-invariant term arises in $V(\phi)$ after this rotation. Then, if we insert $V(\phi)$ into $\mathcal{L}$ for a free massless boson, the U(1) symmetry will be violated by the choice of an arbitrary ground state, but the Lagrangian will still be invariant under U(1). Such a mechanism is called *spontaneous symmetry breaking*. In Eq. (2.37), a scalar field was chosen as its vacuum expectation value is invariant under Lorentz transformations. Due to the shape of the potential, this field has to have a non-vanishing vacuum expectation value

$$\langle\phi\rangle = \sqrt{\frac{-\mu^2}{2\lambda}} = \sqrt{\frac{1}{2}}\, v \tag{2.38}$$

[1] Neutrino masses are left out of this picture, as an extension of the SM or an additional non-invariant term in the Lagrangian [24], would be necessary to introduce them.

corresponding in Fig 2.1 to the distance between the minima and the origin in the (ϕ_1, ϕ_2) plane. From

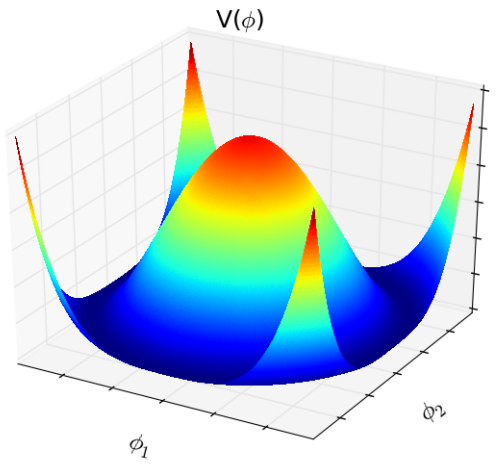

Figure 2.1: Qualitative sketch of the potential related to the spontaneous symmetry breaking mechanism in the case $G \equiv \mathrm{U}(1)$. Degenerate vacuum states form a circle around the origin, and transform into each other under a U(1) transformation.

the point of view of perturbation theory, we notice that orthogonal perturbations with respect to the origin of (ϕ_1, ϕ_2) lead to the existence of massless bosons, while radial perturbations to massive ones, both with spin $s = 0$. The latter will be relevant in the following to predict the existence of a new massive particle.

This simple picture of the case $G \equiv \mathrm{U}(1)$ has to be extended for $G \equiv \mathrm{SU}(2)_L \otimes \mathrm{U}(1)_Y$. In this case we should work with a weak isospin doublet of complex scalar fields, called the *Higgs field*

$$\Phi(x) = \begin{pmatrix} \phi^+(x) \\ \phi^0(x) \end{pmatrix} \tag{2.39}$$

We wish to extend the electroweak Lagrangian with the Higgs field and to include its interactions with the gauge bosons. This is achieved by the term

$$\mathcal{L}_{\text{Higgs}} = [\nabla^\mu \Phi]^\dagger [\nabla_\mu \Phi] - \mu^2 \Phi^\dagger \Phi - \lambda [\Phi^\dagger \Phi]^2 \tag{2.40}$$

where the symbol ∇^μ is the covariant derivative defined as

$$\nabla^\mu = \partial^\mu + ig\tau_j W_j^\mu / 2 + ig' Y B^\mu \tag{2.41}$$

Choosing a particular value for the ground state leads to spontaneous symmetry breaking, and without loss of generality we can choose

$$\Phi_0 = \frac{1}{\sqrt{2}} \begin{pmatrix} 0 \\ v \end{pmatrix} \tag{2.42}$$

where v is defined as in Eq. (2.38).

We would like to break the electroweak symmetry in such a way that the photon remains massless, therefore we require the state Φ_0 to be invariant only under the electromagnetic gauge transformations of

U(1). If we assign the value $Y = \frac{1}{2}$ to Φ, then Φ_0 would be invariant under

$$\Phi(x) \rightarrow \Phi'(x) = e^{-iQef(x)}\Phi(x) = e^{-i(Y+I_3^W)ef(x)}\Phi(x) \tag{2.43}$$

as desired.

Any possible value of the Higgs field can be represented by

$$\Phi(x) = \frac{1}{\sqrt{2}}\begin{pmatrix} \eta_1(x) + i\eta_2(x) \\ v + H(x) + i\eta_3(x) \end{pmatrix} \tag{2.44}$$

We decide to apply to this field a $SU(2)_L \otimes U(1)_Y$ gauge transformation, called *unitary gauge*, such that $\Phi(x)$ takes the form

$$\Phi(x) = \frac{1}{\sqrt{2}}\begin{pmatrix} 0 \\ v + H(x) \end{pmatrix} \tag{2.45}$$

The only degree of freedom left in $\Phi(x)$ after the gauge transformation is the field $H(x)$, generating a new massive particle, as it represents a radial oscillation. If we consider the Lagrangian for massless gauge bosons, insert Eq. (2.40), and transform the fields according to Eq. (2.17), we obtain

$$\begin{aligned}\mathcal{L}^{\text{bosons}} = &\underbrace{-\frac{1}{4}F^{\mu\nu}F_{\mu\nu}}_{\text{photon}} \underbrace{-\frac{1}{2}F_W^{\mu\nu}F_{W\mu\nu} + m_W^2 W_\mu^\dagger W^\mu}_{\text{W}^\pm\text{ bosons}} \\ &\underbrace{-\frac{1}{4}Z^{\mu\nu}Z_{\mu\nu} + \frac{1}{2}m_Z^2 Z_\mu^\dagger Z^\mu}_{\text{Z}^0\text{ boson}} \underbrace{-\frac{1}{2}(\partial^\mu H)(\partial_\mu H) + \frac{1}{2}m_H^2 H^2}_{\text{Higgs boson}} + \mathcal{L}^{\text{bosons}}_{\text{interaction}}\end{aligned} \tag{2.46}$$

The interactions between the Higgs and the gauge bosons can be written as

$$\mathcal{L}^{\text{Higgs-Gauge}} = \underbrace{\frac{vg^2}{2}W_\mu^\dagger W^\mu H + \frac{vg^2}{4\cos^2\theta_W}Z_\mu Z^\mu H}_{\text{trilinear couplings}} \underbrace{+\frac{g^2}{4}W_\mu^\dagger W^\mu H^2 + \frac{g^2}{8\cos^2\theta_W}Z_\mu Z^\mu H^2}_{\text{quadrilinear couplings}} \tag{2.47}$$

In Eq. (2.46), $F_W^{\mu\nu}$ and $Z^{\mu\nu}$ have analogous definitions with respect to $F^{\mu\nu}$, and the mass terms have been introduced as

$$m_W = \frac{1}{2}vg, \qquad m_Z = \frac{m_W}{\cos\theta_W}, \qquad m_H = \sqrt{-2\mu^2}. \tag{2.48}$$

The Lagrangian $\mathcal{L}^{\text{bosons}}$ contains a term related to neutral boson with spin zero called the *Higgs boson*. From Eq. (2.48), it is evident that gauge bosons have non-zero masses due to $v \neq 0$. From electroweak measurements [18] we have

$$v \approx 246 \text{ GeV}. \tag{2.49}$$

The mass of the Higgs boson is not predicted by the theory and can only be measured experimentally. It has recently been determined to be [25]

$$m_{H,\text{exp}} = 125.09 \pm 0.24 \text{ GeV} \tag{2.50}$$

Masses for leptons and quarks arise once we couple Φ with the fermions. In this coupling, terms not proportional to $H(x)$ are the mass terms. Also, if we focus for example only on leptons, we can write

interaction terms as

$$\mathcal{L}^{\text{Higgs–Leptons}} = -\frac{1}{v} m_l \bar{\psi}_l \psi_l H - \frac{1}{v} m_{\nu_l} \bar{\psi}_{\nu_l} \psi_{\nu_l} H \tag{2.51}$$

where the masses can be written as

$$m_l = v y_l \qquad m_{\nu_l} = v y_{\nu_l} \tag{2.52}$$

In Eq. (2.52), y_l and y_{ν_l} are called *Yukawa couplings* and parametrise the Higgs-fermion interactions. It has to be noticed here that the neutrino term in Eq. (2.51) not only couples to left-handed states, as required by total angular momentum conservation. As right-handed neutrinos are not observed, this raises questions on whether neutrino masses are actually generated via the Higgs couplings.

In Fig. 2.2 (left), the cross-section for the production of the SM Higgs boson at the LHC is reported for various processes, at center-of-mass energy of $\sqrt{s} = 8$ TeV. Feynman diagrams [15] for the different production modes are shown in Fig. 2.3. The SM Higgs boson decay probabilities to different final states, so-called *branching ratios* (BR), are shown on Fig. 2.2 (right). Couplings to massive fermions are enhanced due to Eq. (2.52). The dominant production mechanism is the *gluon-gluon fusion* (ggF),

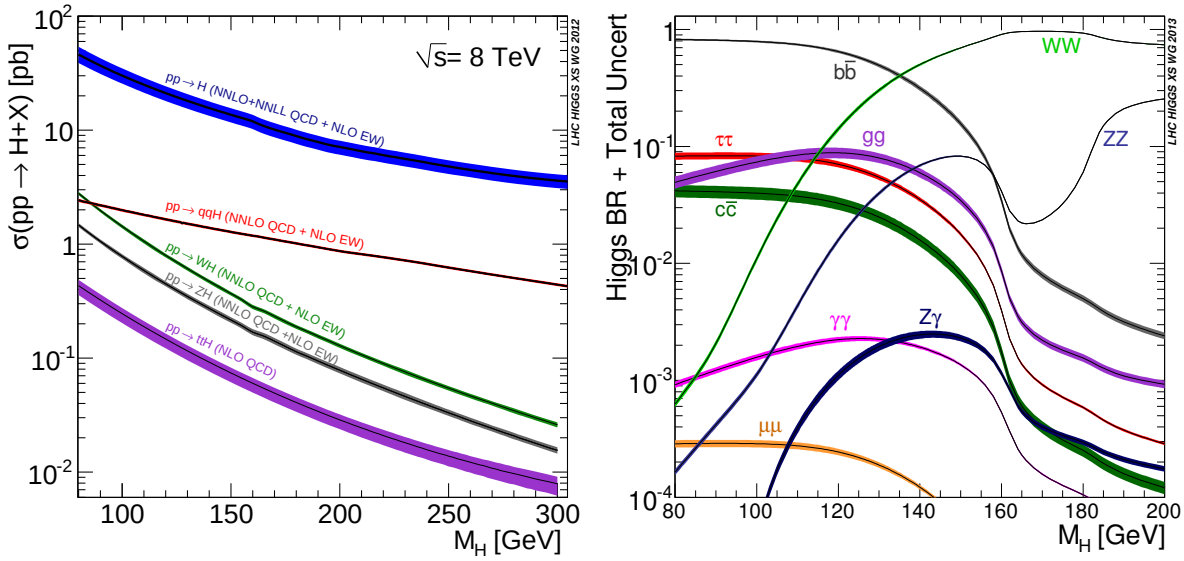

Figure 2.2: Production cross-sections for the SM Higgs boson at the LHC at $\sqrt{s} = 8$ TeV (left), and branching ratios for its decays (right) as a function of the Higgs boson mass. Plots are taken from Ref. [26].

reported in Fig. 2.3 (a), with the dominant contribution of the top quark in the quark loop. Other contributions come from *vector boson fusion* (VBF), in Fig. 2.3 (b), and the production in association with $W^{\pm}/Z$ (VH), Fig. 2.3 (c). Finally, the rate of associated production with top quarks, in Fig. 2.3 (d) and (e), is smaller due to the large top quark mass.

2.1.8 Fundamental Parameters of the Standard Model

In the previous sections the components of the Standard Model Lagrangian were described. Field interactions and their dynamics depend on a number of parameters not predicted by the theory but left to the experiments to determine. These are, for instance, masses and coupling constants. When performing experiments, the probability of a certain process to occur has to be computed, in order to set an expectation, as will be discussed in Sec. 2.4. This calculation is performed using the information contained in the Lagrangian in perturbation theory, i.e. the calculation is expanded up to a finite power

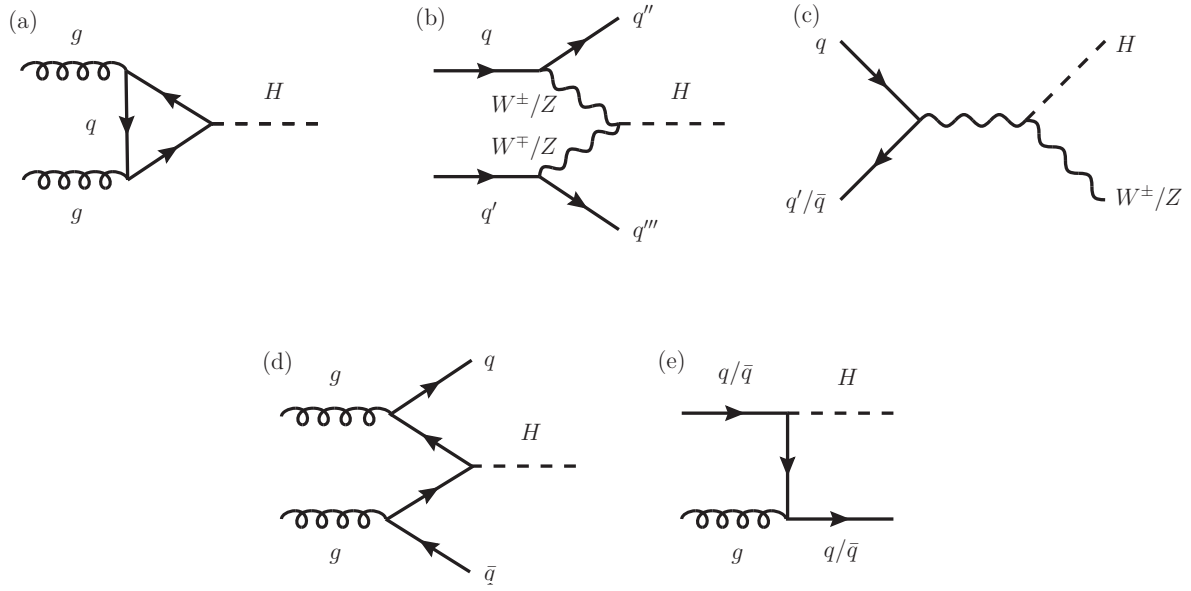

Figure 2.3: Feynman diagram representation of the SM Higgs boson production mechanisms at the LHC. The diagrams illustrate gluon-gluon fusion (a), vector boson fusion (b), production is association with a vector boson (c), and production in association with quark pairs (d) and a single quark (e).

of the fundamental couplings. This puts a limit on the number of vertices considered in the process, as depicted for instance in Fig. 2.3 and thus limits the accuracy of the prediction. Terms in the calculation beyond the leading order of the fundamental couplings are usually referred to as *radiative corrections*.

Some terms in the finite-order expansion might introduce divergences. In order to avoid this, the calculation is performed only up to a certain scale, Λ, of some physical parameter, such as the momentum, a technique called *regularisation* [15, 16]. This is considered to be acceptable only if Λ is much larger than the energy scale of the process. However, as Λ is not physically motivated, we wish to use a calculation scheme which does not depend on it.

Restoring a theory which is not dependent on such a scale to all orders in perturbation theory is a technique called *renormalisation* [15, 16], in which the physical quantities depend on Λ and reabsorb the divergences for $\Lambda \to \infty$. After renormalisation, whatever Λ value we consider, a certain value of the coupling dependent on the scale is predicted, which restores the theory for interactions beyond Λ. This will be possible to all orders in perturbation theory. As calculations are possible up to a finite order, a particular choice of the scale, called *renormalisation scale*, has to be introduced. As this choice is unphysical, it has to be taken into account when evaluating uncertainties on theoretical predictions.

In the Standard Model we can represent the couplings associated with the $U(1)_Y$, $SU(2)_L$ and SU(3) symmetry as a function of the transferred momentum in the interaction. According to the previous notation we can define $\alpha_1 = g'^2/4\pi$, $\alpha_2 = g^2/4\pi$ and $\alpha_3 = g_s^2/4\pi$. In Sec. 2.1.1, we have already introduced α_3 with the different name α_S. The trend of α_1, α_2 and α_3 as a function of the energy scale is determined by the so-called *renormalisation group* [16, 27] (RG), and is shown in Fig. 2.4. The dependency of the fundamental parameters on a certain scale is referred to as the *running* of the parameters.

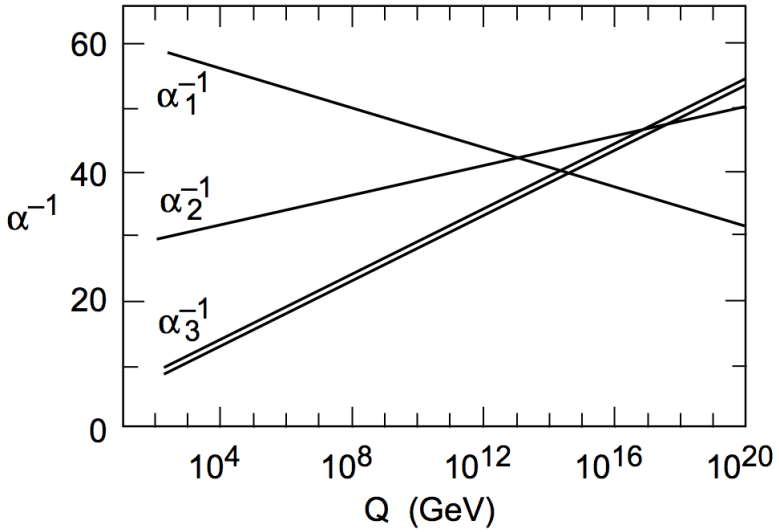

Figure 2.4: Standard Model couplings of the $\mathrm{SU}(3) \otimes \mathrm{SU}(2)_L \otimes \mathrm{U}(1)_Y$ symmetry group versus the transferred momentum, Q. The two lines in correspondence of α_3 represent the theoretical uncertainty. The plot is taken from Ref. [28].

2.1.9 Open Questions of the Standard Model

The Standard Model has been proven to be a successful theory in numerous experiments performed over several decades. Nevertheless, while providing a precise description of subatomic particles and their interactions, is still regarded to be incomplete and not the ultimate description of all the phenomena we observe. A list of open problems the SM does not address is given below.

Unification of forces : In Sec. 2.1.4 the unification of electromagnetic and weak interaction in the SM was discussed. However, this is not a unification in the sense that both couplings arise from a common source. In fact, the parameter θ_W has to be introduced to relate the couplings, which has to be experimentally determined. This is a reflection of the fact that electroweak interactions are described by the mere product of the groups $\mathrm{SU}(2)_L$ and $\mathrm{U}(1)_Y$. In a more appropriate unified description of interactions the group $\mathrm{SU}(2)_L \otimes \mathrm{U}(1)_Y$ would be part of a larger group G. Some of the transformations of G would then relate elements of the two groups, ultimately leading to a prediction for the relation between the couplings. We would like our unification to include the whole set of interactions, that is $G \supset \mathrm{SU}(3) \otimes \mathrm{SU}(2)_L \otimes \mathrm{U}(1)_Y$. This unification would then lead the running couplings to become identical at a certain energy scale and be unified beyond that point, their difference at lower scales being caused by some symmetry breaking mechanism. Unification is supported by the fact that we already predict similar values for the couplings at a certain energy scale, like shown in Fig. 2.4, which is unlikely to be a coincidence.

Gravity : At present, there is no satisfactory quantum theory for the gravitational interaction. The small coupling involved in gravitational processes also makes an experimental test particularly difficult. However, when gravitational effects are extrapolated to very high energies, they are predicted to have similar strength as the other forces. This may suggests that gravitation could be included in a unified quantum description. The typical energy scale beyond which gravity is regarded to have significant effects is the so-called *Plank scale* $M_\mathrm{P} \approx 10^{19}$ GeV.

Hierarchy problem and fine-tuning : As discussed in Sec. 2.1.8, the fundamental parameters of

the Standard Model show a scale dependence which has to be introduced to renormalise the interactions. The mass of the Higgs boson also shows this feature. If we consider for instance radiative corrections to m_H, due to creation and annihilation of fermion and anti-fermion pairs, we have

$$m^2_{H,\text{exp}} = m^2_H + \Delta m^2_H = m^2_H - \frac{g^2_f}{8\pi^2}\Lambda^2 + \dots \tag{2.53}$$

where g_f is the fermion-Higgs coupling, as in Eq. (2.52), and Λ is the scale introduced. There is no reason why Λ should be small, and, if we believe the SM to be reliable at any scale, it could assume very large values. If we extend its value up to large scales, for instance M_P, the magnitude of the corrections would be such that we will be forced to choose very large values of m_H, with very high precision, to obtain the experimentally measured mass and avoid the unnatural hierarchy $m_H \ll \Lambda$. This *fine-tuning* of the parameters is regarded to be undesirable in a theory, where a dynamical cancellation of the diverging corrections would be preferable.

Dark matter and dark energy : Cosmological observations [29, 30] support the existence of a particular kind of matter in the universe [31] which does not interact electromagnetically, but only through gravity and the weak force [32]. It amounts to 26.8% of the mass-energy of the universe [13, 14], and we refer to it as *dark matter*. Not dark matter candidate is provided by the Standard Model. In addition to this, evidence of an acceleration in the expansion of the universe [33, 34] points toward the existence of an unidentified source of energy commonly referred to as *dark energy* [35], making up 68.3% of the universe. Extensions of the SM or new theoretical frameworks are necessary to interpret these observations.

Anomalous magnetic moment : Higher-order corrections in QED are tested up to a very high precision, as in the case of the magnetic moment of the electron [36]. Nonetheless, the measurement of the analogous quantity for the muon, called $(g-2)_\mu$ [37], differs from the theoretical prediction, possibly indicating the presence of new physics.

Neutrino masses : Recent experimental results [21] indicate that neutrinos are massive particles. According to the SM description of spontaneous symmetry breaking this leads to the existence of right-handed neutrinos which are not observed by experiments. Accommodating non-interacting right-handed neutrinos would require an extension of the model.

Baryon-antibaryon asymmetry : The observable universe is composed mainly of baryonic matter rather than antimatter. While the universe is thought to be neutral with respect to all conserved charges, there is no consensus about what caused this asymmetry during the baryogenesis in the Big Bang [38].

All these problems require extensions of the Standard Model. One of the most prominent and best motivated is Supersymmetry.

2.2 Supersymmetry

As outlined in Sec. 2.1.9, the Higgs sector in the SM poses problems which are not possible to address in the same theoretical framework. Over time many theories have been proposed for the solution of these problems. Among them, Supersymmetry (SUSY) is one of the most popular. In the next sections a brief review of general SUSY is given, based on the more detailed documents Ref. [39–42]. Such

general introduction will serve to present the specific SUSY model relevant for this thesis, the Minimal Supersymmetric Standard Model.

2.2.1 Supersymmetry and the Hierarchy Problem

As mentioned in Sec. 1, Supersymmetry predicts the existence of a new set of particles, called *superpartners*, which mirror the Standard Model particles and differ from those by the value of their spin. In particular, fermionic degrees of freedom in the SM are mirrored by bosonic ones in SUSY and vice versa. Among the motivations for SUSY is the solution to the hierarchy problem mentioned in Sec. 2.1.9. If we compute the corrections to m_H coming from a fermion f in the SM we obtain

$$\Delta m_{H,f}^2 = N_f \frac{g_f^2}{8\pi^2}\left(-\Lambda^2 + 6m_f^2 \log\frac{\Lambda}{m_f} - 2m_f^2\right) + O\left(\frac{1}{\Lambda^2}\right) \tag{2.54}$$

where N_f is the number of fermion generations and g_f is proportional to the Yukawa coupling. Such terms are generated by the process illustrated in Fig. 2.5 (a), and are said to be *one-loop* corrections. Now,

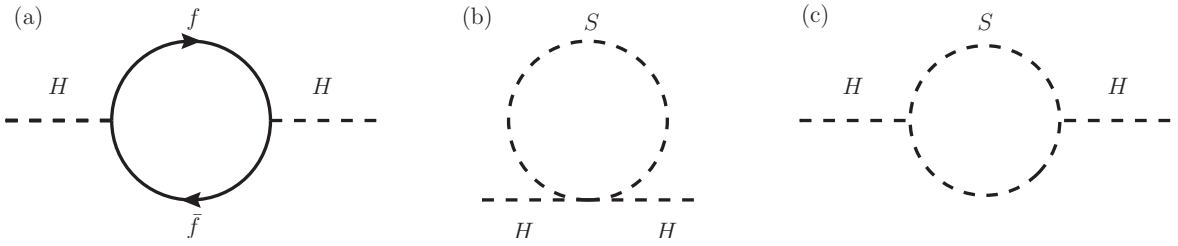

Figure 2.5: Feynman diagram representation of the one-loop interactions between the Higgs boson and a generic fermion (a), and a generic scalar boson (b) and (c).

if we assume the existence of a certain number of scalar particles N_S, represented by a real field, with masses m_S and linear and quadrilinear couplings to the Higgs boson given by $g_S v$ and g_S, respectively, they contribute to the correction by the amount

$$\Delta m_{H,S}^2 = N_S \frac{g_S}{16\pi^2}\left(-\Lambda^2 + 2m_S^2 \log\frac{\Lambda}{m_S}\right) - N_S \frac{g_S^2 v^2}{16\pi^2}\left(-1 + 2\log\frac{\Lambda}{m_S}\right) + O\left(\frac{1}{\Lambda^2}\right) \tag{2.55}$$

If we make the assumptions $g_f^2 = -g_S$ and $N_S = 2N_f$, we obtain

$$\Delta m_H^2 = N_f \frac{g_f^2}{4\pi^2}\left((m_f^2 - m_S^2)\log\frac{\Lambda}{m_S} + 3m_f^2 \log\frac{m_S}{m_f}\right) + O\left(\frac{1}{\Lambda^2}\right) \tag{2.56}$$

As can be seen from Eq. (2.56), if such a symmetry were exact, or in other words $m_f = m_S$, all the corrections to m_H would exactly cancel. However, we fail to observe superpartners at the energy scale of the Standard Model, therefore supersymmetry has to be broken. Logarithmic divergences in Eq. (2.56) do not present a hierarchy problem provided that the difference between m_f and m_S is not too large, i.e. in the order of a few TeV. This consideration motivates supersymmetry searches at the Large Hadron Collider, which is able to probe such energy scales.

We will see in the following sections how supersymmetry can also provide a particle candidate for dark matter, and allows for a unification of forces.

2.2.2 Supersymmetric Transformations and Lagrangian

A supersymmetry transformation relates fermionic and bosonic states. If we define Q as the generator of such a transformation, we can write

$$|\text{Fermion}\rangle = Q\,|\text{Boson}\rangle \qquad |\text{Boson}\rangle = Q\,|\text{Fermion}\rangle \tag{2.57}$$

According to the *Haag-Lopuszanski-Sohnius* and *Coleman-Mandula* theorems [43, 44], the operator Q and its hermitian conjugate $Q^\dagger$ must satisfy anticommutation and commutation relations of the form

$$\{Q_\alpha, Q^\dagger_{\dot\alpha}\} = -2\sigma^\mu_{\alpha\dot\alpha} P_\mu \tag{2.58a}$$

$$\{Q_\alpha, Q_\beta\} = 0 \qquad \{Q^\dagger_{\dot\alpha}, Q^\dagger_{\dot\beta}\} = 0 \tag{2.58b}$$

$$[Q_\alpha, P^\mu] = 0 \qquad [Q^\dagger_{\dot\alpha}, P^\mu] = 0 \tag{2.58c}$$

where P^μ is the momentum operator. The dotted indices refer to the right-handed degrees of freedom in a Dirac spinor, and the undotted to the left-handed ones. In the following, we will split each Dirac spinor in two *Weyl spinors* carrying only one type of such indices, with two degrees of freedom each. It has to be noted that the hermitian conjugate of any left-handed Weyl spinor is a right-handed Weyl spinor.

In a supersymmetric theory, particle states are represented as *supermultiplets*. Each supermultiplet contains both fermion and boson states which are known as *superpartners* of each other. Particles contained in the same supermultiplet have the same mass, before SUSY breaking, and share the same electric charge, weak isospin and colour. Each supermultiplet contains an equal number of bosonic, n_B, and fermionic, n_F, degrees of freedom. The simplest supermultiplet contains a Weyl spinor and a complex field, with $n_B = 2$, representing a fermion and a scalar boson, respectively. It is called a *chiral supermultiplet*. The supermultiplet that accommodates a spin $s = 1$ vector boson with zero mass, therefore with $n_B = 2$, and a Weyl spinor with $s = \frac{1}{2}$ is called a *gauge* supermultiplet.

Only chiral supermultiplets can contain fermions whose left-handed component transforms differently from the right-handed one, as is the case in the Standard Model. Therefore, these fermions should be arranged in separate supermultiplets with different complex scalar superpartners. Scalar superpartners of Standard Model leptons and quarks are called *sleptons* and *squarks*, while fermions in gauge supermultiplets with Standard Model gauge bosons are called *gauginos*. Unlike Standard Model fermions, right-handed and left-handed gauginos should transform in the same way. The complete list of particles predicted by the Minimal Supersymmetric Standard Model will be discussed in Sec. 2.3.

If we consider a chiral supermultiplet containing a left-handed Weyl spinor ψ and a complex scalar ϕ, we can write a Lagrangian which is invariant under supersymmetry transformations, which also contains interaction terms, as

$$\mathcal{L}_{\text{chiral}} = \underbrace{-\partial^\mu \phi^{*i} \partial_\mu \phi_i + i\psi^{\dagger i}\overline{\sigma}^\mu \partial_\mu \psi_i - W_i^* W^i}_{\text{kinetic}} \underbrace{-\frac{1}{2}\left(W^{ij}\psi_i\psi_j + W^*_{ij}\psi^{\dagger i}\psi^{\dagger j}\right)}_{\text{interaction}} \tag{2.59}$$

where

$$W^i = \frac{\partial W}{\partial \phi_i} \qquad W^{ij} = \frac{\partial^2 W}{\partial\phi_i \partial\phi_j} \qquad W = \frac{1}{2}M^{ij}\phi_i\phi_j + \frac{1}{6}y^{ijk}\phi_i\phi_j\phi_k \tag{2.60}$$

In Eq. (2.60) the repeated indices i, j run over the different fermion families, and W denotes the *superpotential*. The symbol M^{ij} is a symmetric mass matrix for the fermion fields and y^{ijk} a totally symmetric

symbol parametrising the interaction between a boson and two fermions, with the same physical meaning as the Yukawa coupling. The set of transformations under which $\mathcal{L}_{\text{chiral}}$ is invariant can be written as

$$\delta\phi_i = \epsilon\psi_i \qquad \delta\phi^{*i} = \epsilon^\dagger\psi^{\dagger i} \tag{2.61a}$$

$$\delta(\psi_i)_\alpha = -i(\sigma^\mu\epsilon^\dagger)_\alpha\partial_\mu\phi_i \qquad \delta(\psi^{\dagger i})_{\dot\alpha} = i(\epsilon\sigma^\mu)_{\dot\alpha}\partial_\mu\phi^{*i} \tag{2.61b}$$

where ϵ is an infinitesimal Weyl spinor parametrising the transformation[2]. It can be seen that, for the generic transformations written in Eq. (2.61), and for $X = \phi, \phi^*, \psi, \psi^\dagger$ the variation δX can be expressed as

$$[\epsilon Q + \epsilon^\dagger Q^\dagger, X] = -i\sqrt{2}\delta X \tag{2.62}$$

For the complete Lagrangian we should also consider the contribution of the gauge supermultiplets, featuring the gauge fields A^μ_a, where a is an index running over the number of generators of the gauge group, and the gauginos λ_a. Under an infinitesimal transformation in the adjoint representation [40] the fields transform as

$$A^\mu_a(x) \to A'^\mu_a(x) = A^\mu_a(x) + \partial^\mu\omega_a(x) - g f_{abc}\omega_b(x)A^\mu_c(x) \tag{2.63a}$$

$$\lambda_a(x) \to \lambda'_a(x) = \lambda_a(x) - g f_{abc}\omega_b(x)\lambda_c(x) \tag{2.63b}$$

where f_{abc} are the totally antisymmetric structure constants of the gauge group. A sensible Lagrangian should be invariant under the previous set of transformations as well as supersymmetry transformations. Therefore it can be written as

$$\mathcal{L}_{\text{total}} = \mathcal{L}_{\text{chiral}} \underbrace{-\frac{1}{4}F^a_{\mu\nu}F^{a\mu\nu} + i\lambda^{\dagger a}\overline{\sigma}^\mu\nabla_\mu\lambda^a}_{\text{gauge}} \underbrace{- \sqrt{2}g(\phi_i T^a\psi_i)\lambda^a - \sqrt{2}g\lambda^{\dagger a}(\psi^{\dagger i}T^a\phi_i) - \frac{1}{2}g^2(\phi^{*i}T^a\phi_i)(\phi^{*j}T^a\phi_j)}_{\text{gauge}-\text{chiral interactions}} \tag{2.64}$$

where the symbols $F^{\mu\nu}_a$ and $\nabla^\mu\lambda^a$ are defined as

$$F^{\mu\nu}_a = \partial^\mu A^\nu_a - \partial^\nu A^\mu_a + g f_{abc}A^\mu_b A^\nu_c \tag{2.65a}$$

$$\nabla^\mu\lambda^a = \partial^\mu\lambda^a + g f_{abc}A^\mu_b\lambda_c \tag{2.65b}$$

and the supersymmetry transformations of the gauge supermultiplet are[3]

$$\delta A^\mu_a = -\frac{1}{\sqrt{2}}\left(\epsilon^\dagger\overline{\sigma}^\mu\lambda_a + \lambda^\dagger_a\overline{\sigma}^\mu\epsilon\right) \tag{2.66a}$$

$$\delta\lambda^\alpha_a = \frac{i}{2\sqrt{2}}(\sigma_\mu\overline{\sigma}_\nu)^\alpha F^{\mu\nu}_a \tag{2.66b}$$

[2] In a rigorous presentation of the theory it should be pointed out that for a transformation on $(\psi_i)_\alpha$ an additional term arises which is proportional to an auxiliary bosonic field. This term is necessary to make Supersymmetry consistent as a quantum theory i.e. even when equations of motion are not satisfied [39]. However, this detail is inessential for this discussion and does not lead to a modification of the expression of the chiral Lagrangian given in Eq. (2.59).

[3] Similarly to what noted for Eq. (2.61), the reported transformations are incomplete as they lack an additional scalar component necessary for the off-shell consistency of the theory. Even in this case, this term does not appear in the lagrangian including interaction terms, and is not essential for this discussion.

Names	Supermultiplet Symbol	Spin 0	Spin $\frac{1}{2}$
squarks, quarks (× 3 generations)	Q	$(\tilde{u}\ \tilde{d})_L$	$(u\ d)_L$
	$\bar{u}$	$\tilde{u}_R^*$	$u_R^\dagger$
	$\bar{d}$	$\tilde{d}_R^*$	$d_R^\dagger$
sleptons, leptons (× 3 generations)	L	$(\tilde{\nu}\ \tilde{e})_L$	$(\nu\ e)_L$
	$\bar{e}$	$\tilde{e}_R^*$	$e_R^\dagger$
Higgs, higgsinos	H_u	$(H_u^+\ H_u^0)$	$(\tilde{H}_u^+\ \tilde{H}_u^0)$
	H_d	$(H_d^0\ H_d^-)$	$(\tilde{H}_d^0\ \tilde{H}_d^-)$

Table 2.4: Chiral supermultiplet content of the Minimal Supersymmetric Standard Model. Left-handed and right-handed fermionic degrees of freedom are arranged in different supermultiplets. In the symbol indicating supermultiplets originating from right-handed fermions, the bar does not indicate conjugation.

In Eq. (2.64), ordinary derivatives ∂_μ are replaced by the covariant derivative ∇_μ, and T^a are the generators of the gauge group. Here, only one group of such transformations has been considered, relative to the parameter g, but all the known symmetries of the Standard Model should be added.

2.3 The Minimal Supersymmetric Standard Model

The Higgs boson sector of interest for this thesis is an extended version of the SM one. In particular, its structure will be motivated by the general principles inspired by SUSY, discussed in Sec. 2.2. The Minimal Supersymmetric Standard Model (MSSM) is a supersymmetric extension of the Standard Model with minimal Higgs sector required. In the present section we will introduce and motivate the MSSM, with particular detail on the Higgs sector, and the Higgs boson phenomenology.

The supermultiplets of massless particles in the MSSM are illustrated in Tab. 2.4 for sfermions and in Tab. 2.5 for gauginos, where sparticles are marked by a tilde. Superpartners of fermions are scalar bosons carrying the L and R labels, referring to the chirality of their SM partner. No such label is used for the sneutrino as only left-handed neutrinos are observed. The symbols u and d are used for all three generations of up-type and down-type quarks, respectively, while e indicates all charged leptons. The bar on top of right-handed related supermultiplets is just a naming convention. Gauge interactions of particles in the same supermultiplet are the same. For instance, W bosons interact with $\tilde{u}_L$ and $\tilde{d}_L$, but not with $\tilde{u}_R$ and $\tilde{d}_R$.

The MSSM Higgs sector differs from the SM one. Due to the requirement of the cancellations of gauge anomalies introduced in the MSSM by the superpartner sector [39], we are forced to introduce two isospin doublets, $(H_u^+,\ H_u^0)$ and $(H_d^0,\ H_d^-)$ with $Y = \frac{1}{2}$ and $Y = -\frac{1}{2}$, respectively. The introduction of two Higgs doublets with different hypercharge is also necessary because, due to the structure of the MSSM, only a doublet with $Y = \frac{1}{2}$ can have the necessary Yukawa couplings to generate the masses of up-type quarks, and only a doublet with $Y = -\frac{1}{2}$ can generate the masses of down-type quarks and charged leptons. The fermionic superpartners of the Higgs bosons are called higgsinos. The MSSM is completely specified by the following choice of the superpotential

$$W_{\text{MSSM}} = \bar{u}\mathbf{y_u}QH_u - \bar{d}\mathbf{y_d}QH_d - \bar{e}\mathbf{y_e}LH_d + \mu H_u H_d \tag{2.67}$$

Names	Spin $\frac{1}{2}$	Spin 1
gluino, gluon	$\tilde{g}$	g
winos, W bosons	$\widetilde{W}^{\pm}$, $\widetilde{W}^{0}$	$W^{\pm}$, W^{0}
bino, B boson	$\widetilde{B}^{0}$	B^{0}

Table 2.5: Gauge supermultiplet content of the Minimal Supersymmetric Standard Model.

where μ is the higgsino mass, and summation over family and colour indices is implied. The $\mathbf{y_{u,d,e}}$ symbols are the Yukawa matrices, describing the mixing between the quarks, and determining the masses of quarks and leptons after electroweak symmetry breaking. We can decide to write the superpotential ignoring the contribution of the first and second generation of particles, which simplifies the form of the Yukawa matrices. We then obtain

$$W_{\text{MSSM}} \approx y_t(\bar{t}tH_u^0 - \bar{t}bH_u^+) - y_b(\bar{b}tH_d^- - \bar{b}bH_d^0) - y_\tau(\bar{\tau}\nu_\tau H_d^- - \bar{\tau}\tau H_d^0) + \mu(H_u^+ H_d^- - H_u^0 H_d^0) \tag{2.68}$$

2.3.1 R-parity

Supersymmetric models like the MSSM can provide a candidate for the non-baryonic dark matter observed in our universe. This is possible by imposing a new symmetry discussed in the following.

The superpotential in Eq. (2.67) is not written in the most general form, in the sense that other terms could be added which violate lepton number, L, and baryon number, B, defined in Eq. (2.25) and Eq. (2.36), respectively. However, they are known to be conserved in the energy range of current experiments. For example, we do not observe the proton decay which would require $\Delta L = 1$ and $\Delta B = 1$.

In the MSSM L and B are not assumed to be separately conserved. In the SM we do not make this assumption, rather it just happens that Lagrangian terms violating B and L are non-renormalisable. We also know that these quantum numbers are not conserved by non-perturbative electroweak effects [45]. Therefore, we introduce a new symmetry, involving both L and B, which results in the quantity called *R-parity*, $\mathcal{P}_R$, to be conserved. R-parity is defined as

$$\mathcal{P}_R = (-1)^{3(B-L)+2s}, \tag{2.69}$$

where s is the spin of the particle. The form of Eq. (2.69) is chosen such that sparticles have $\mathcal{P}_R = -1$ and SM particles $\mathcal{P}_R = 1$. If R-parity is exactly conserved, then there is no mixing between sparticles and particles. In addition to this, every interaction vertex contains an even number of sparticles. This has the following phenomenological consequences:

- The lightest supersymmetric particle, or LSP, is stable. If it is electrically neutral it only interacts weakly and can be considered to be a non-baryonic dark matter candidate.
- Each sparticle, other than an LSP, must decay into an odd number of LSPs.
- At collider experiments sparticles can only be produced in even numbers.

R-parity is conserved in the MSSM by definition.

2.3.2 Soft SUSY breaking in the MSSM

Sparticles have not been observed at energies probed by current experiments. This suggests that SUSY has to be broken. Unfortunately, no consensus has been reached on how to introduce this mechanism dynamically. In the MSSM, SUSY breaking is described by an effective additional term in the Lagrangian, where only mass terms of positive dimension are present in order to maintain the hierarchy between the electroweak and Planck scales. These terms are said to break SUSY *softly*, as they do not introduce quadratic divergences due to quantum corrections to scalar masses, therefore providing a solution to the hierarchy problem. In the MSSM, the soft SUSY-breaking part of the Lagrangian can be written as

$$\begin{aligned}\mathcal{L}_{\text{soft}}^{\text{MSSM}} = & \underbrace{-\frac{1}{2}\left(M_3\tilde{g}\tilde{g} + M_2\widetilde{W}\widetilde{W} + M_1\tilde{B}\tilde{B}\right) + \text{c. c.}}_{\text{gaugino masses}} \\ & \underbrace{\left(\tilde{\bar{u}}\mathbf{a_u}\tilde{Q}H_u - \tilde{\bar{d}}\mathbf{a_d}\tilde{Q}H_d - \tilde{\bar{e}}\mathbf{a_e}\tilde{L}H_d\right) + \text{c. c.}}_{\text{triliniear couplings}} \\ & \underbrace{-\tilde{Q}^\dagger\mathbf{m_Q^2}\tilde{Q} - \tilde{L}^\dagger\mathbf{m_L^2}\tilde{L} - \tilde{\bar{u}}\mathbf{m_{\bar{u}}^2}\tilde{\bar{u}}^\dagger - \tilde{\bar{d}}\mathbf{m_{\bar{d}}^2}\tilde{\bar{d}}^\dagger - \tilde{\bar{e}}\mathbf{m_{\bar{e}}^2}\tilde{\bar{e}}^\dagger}_{\text{sfermion masses}} \\ & \underbrace{-m_{H_u}^2 H_u^* H_u - m_{H_d}^2 H_d^* H_d - (bH_uH_d + \text{c. c.})}_{\text{Higgs sector}} \end{aligned} \quad (2.70)$$

where c.c. is the complex conjugate. All bold symbols in Eq. (2.70) represent matrices in generation space. The $\mathbf{a_{u,d,e}}$ matrices are in one-to-one correspondence with the Yukawa matrices. The masses M_3, M_2 and M_1 are the gluino, wino and bino masses, respectively. The symbol b is also a matrix with the dimension of a mass squared, however, it can be reduced to a real parameter by redefining the complex phases of the Higgs fields. The total number of parameters present in Eq. (2.70) are 105. In particular, if SUSY should be the solution to the hierarchy problem, the mass terms are expected to be very roughly at the scale $M_{\text{SUSY}} \approx 1$ TeV.

In the MSSM the running of the coupling parameters is modified by the contribution of additional particles in the loops. It is remarkable to see that the MSSM contains the right particle content that allows for a unification of the forces at $Q \approx 10^{16}$ GeV, as shown in Fig. 2.6, an additional motivation for SUSY. SUSY models other than the MSSM have been suggested in the attempt to break SUSY dynamically. In mSUGRA (minimal supergravity) [46], the gravitational interaction communicates SUSY breaking to the supersymmetric Standard Model. The graviton is predicted to have a superpartner, called gravitino. In gauge-mediated supersymmetry breaking models (GMSB), gauge interactions in the SM break SUSY.

2.3.3 Electroweak Symmetry Breaking in the MSSM

In this section, the Higgs sector in the MSSM is introduced. It is described by the following potential

$$V = (|\mu|^2 + m_{H_u}^2)|H_u^0|^2 + (|\mu|^2 + m_{H_d}^2)|H_d^0|^2 - (bH_u^0H_d^0 + \text{c. c.}) + \frac{1}{8}(g^2 + g'^2)(|H_u^0|^2 - |H_d^0|^2)^2, \quad (2.71)$$

where the charged degrees of freedom of the Higgs doublets have been eliminated without loss of generality. The CP symmetry is not spontaneously broken by this potential. Therefore, the Higgs mass states have a well-defined value of CP.

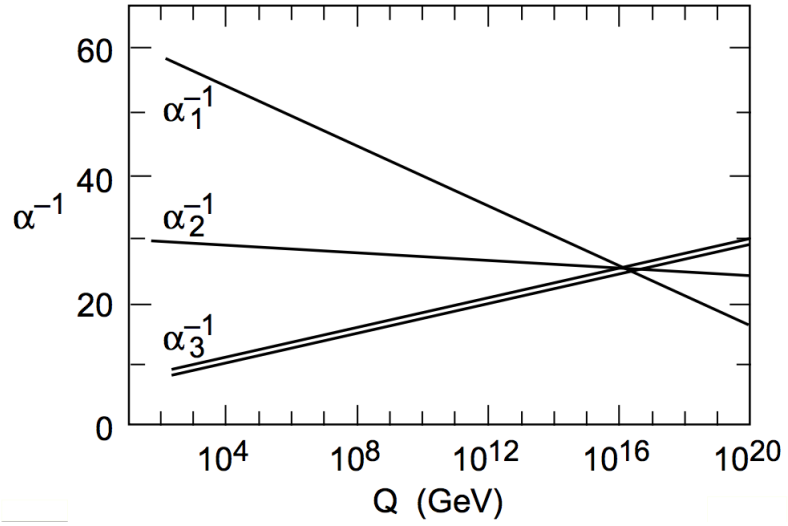

Figure 2.6: MSSM couplings of the $SU(3) \otimes SU(2)_L \otimes U(1)$ symmetry versus the transferred momentum. The two lines for α_3 represent the theoretical uncertainty. The plot is taken from Ref. [28].

The following conditions have to hold

$$2b < 2|\mu|^2 + m_{H_u}^2 + m_{H_d}^2 \tag{2.72a}$$

$$b^2 > (|\mu|^2 + m_{H_u}^2)(|\mu|^2 + m_{H_d}^2). \tag{2.72b}$$

The first condition is required for the potential to be bounded from below, and the second to require electroweak symmetry breaking by imposing $H_u^0 = H_d^0 = 0$ not to be a stable minimum.

We can now define, in analogy with Eq. (2.42),

$$\left\langle H_u^0 \right\rangle = \sqrt{\frac{1}{2}} v_u, \qquad \left\langle H_d^0 \right\rangle = \sqrt{\frac{1}{2}} v_d. \tag{2.73}$$

These two vacuum expectation values (VEV) have to satisfy the phenomenological relation

$$v_u^2 + v_d^2 = v^2 = \frac{4m_Z^2}{g^2 + g'^2} \approx (246 \text{ GeV})^2 \tag{2.74}$$

The ratio between v_u and v_d can be expressed as a function of an angle $\beta \in (0, \pi/2)$ as

$$\tan\beta = \frac{v_u}{v_d} = \frac{v\sin\beta}{v\cos\beta} \tag{2.75}$$

The two Higgs doublets in the MSSM correspond to eight real degrees of freedom. Out of these, three can be removed after a gauge transformation, as seen in Sec. 2.1.7, while the remaining five mix to give five mass eigenstates, two CP-even h^0, H^0, one CP-odd A^0 and two charged $H^\pm$. The mixing angle of the CP-even states is defined as $\alpha \in (-\pi/2, 0)$, while β defines the mixing in the CP-odd and charged sectors.

The following relations hold at leading order in perturbation theory

$$m^2_{A^0} = 2|\mu|^2 + m^2_{H_u} + m^2_{H_d}, \tag{2.76a}$$

$$m^2_{h^0,H^0} = \frac{1}{2}\left(m^2_{A^0} + m^2_{Z^0} \mp \sqrt{(m^2_{A^0} - m^2_{Z^0})^2 + 4m^2_Z m^2_{A^0}\sin^2(2\beta)}\right), \tag{2.76b}$$

$$m^2_{H^\pm} = m^2_{A^0} + m^2_W, \tag{2.76c}$$

$$\frac{\sin 2\alpha}{\sin 2\beta} = -\left(\frac{m^2_{H^0} + m^2_{h^0}}{m^2_{H^0} - m^2_{h^0}}\right), \qquad \frac{\tan 2\alpha}{\tan 2\beta} = \left(\frac{m^2_{A^0} + m^2_Z}{m^2_{A^0} - m^2_Z}\right). \tag{2.76d}$$

From the leading-order equations above we can see that two parameters introduced in the MSSM Higgs sector cannot be constrained. We choose these two to be m_A and $\tan\beta$.

In principle, all the masses above can be arbitrarily large, with the only exception of m_{h^0} which has an upper bound at the mass of the Z boson [41]. However, Eq. (2.76) does not include radiative corrections. These are dominated by the top and stop particles with diagrams analogous to Fig. 2.5. When they are included we can write

$$m^2_{h^0} < \underbrace{m^2_Z \cos^2(2\beta)}_{\text{leading order}} + \underbrace{\frac{3m_t^4}{2\pi^2 v^2 \sin^2\beta}\left[\log\frac{M_S^2}{m_t^2} + \frac{X_t^2}{2M_S^2}\left(1 - \frac{X_t^2}{6M_S^2}\right)\right]}_{\text{radiative corrections}} \tag{2.77}$$

In Eq. (2.77), we have $M_S = \frac{1}{2}(m_{\tilde{t}_1} + m_{\tilde{t}_2})$, where $\tilde{t}_{1,2}$ are the mass eigenstates of the stops, superposition of $\tilde{t}_R$ and $\tilde{t}_L$, and X_t is the stop mixing parameter to be introduced later. This equation holds in the so-called *decoupling limit* where $m_A \gg m_Z$, leading to h^0 couplings identical to the SM Higgs boson.

If we assume that all particles in the loops contributing to the corrections do not exceed 1 TeV, and include even higher-order corrections [47], we obtain an upper bound on the mass of the lightest Higgs boson of

$$m_{h^0} \lesssim 135 \text{ GeV}. \tag{2.78}$$

Higher-order corrections to m_h are of primary importance to decide upon the values assumed by the free MSSM parameters entering into it. This is particularly relevant after the discovery of a Higgs particle, which is presumably consistent with h. The discussion regarding the higher-order parameters will be the subject of the next two sections.

In the MSSM the masses of quarks and leptons and the CKM mixing parameters are determined not only by the Yukawa couplings but by $\tan\beta$ as well. In fact, at leading order we have

$$m_t = y_t v \sin\beta, \qquad m_b = y_b v \cos\beta, \qquad m_\tau = y_\tau v \cos\beta. \tag{2.79}$$

We notice that, to a good approximation, $y_b/y_t = (m_b/m_t)\tan\beta$ and $y_\tau/y_t = (m_\tau/m_t)\tan\beta$. Therefore, if $\tan\beta \gg 1$, y_b and y_τ are enhanced. Also, we notice that if $\sin\beta$ is too small y_t will be too large to be treated perturbatively. This leads to the requirement that $\tan\beta \gtrsim 1.2$. For a similar reason $\tan\beta \lesssim 60$ if y_b, y_τ should be small. MSSM Higgs bosons searches are therefore set in the $\tan\beta$ range between these two values.

The large number of free parameters in the MSSM can be reduced significantly, simplifying the phenomenological interpretation of searches. We can constrain the 105 parameters based on experimental results. In particular, no new sources of CP-violation should be introduced by the soft SUSY-breaking potential (2.70), therefore all the complex phases of the new parameters are assumed to be zero. No flavour-changing neutral currents (FCNC) are observed. Then, if we write the matrices **a** in Eq. (2.70)

as $\mathbf{a} = \mathbf{A}\mathbf{y}$ we can assume $\mathbf{A}$ to be diagonal and real. We notice that only squarks and sleptons of the third family can have large trilinear couplings, due to the proportionality of the Yukawa couplings to the masses of the fermions. In addition to this, squared-mass matrices are assumed to be diagonal with equal masses for the first and second generations, due to experimental constraints coming from the mixing of the mesons K^0 and $\bar{K}^0$ [48]. The previous set of assumptions are also supported by the fact that they lead to unification of the couplings as shown in Fig. 2.6.

After these assumptions we have reduced the number of MSSM parameters from 105 down to 19, which are

- m_A, $\tan\beta$: leading-order parameters.
- μ: higgsino mass parameter.
- M_1, M_2, M_3: the gaugino masses.
- $m_{Q_{1,2}}, m_{\bar{u}_{1,2}}, m_{\bar{d}_{1,2}}, m_{\bar{L}_{1,2}}, m_{\bar{e}_{1,2}}$: first and second generation sfermion masses.
- $m_{Q_3}, m_{\bar{u}_3}, m_{\bar{d}_3}, m_{L_3}, m_{\bar{e}_3}$: third generation sfermion masses.
- A_t, A_b, A_τ: third generation trilinear couplings.

Any search for MSSM Higgs bosons depend on a particular choice of these parameters, which we will refer to as a *benchmark scenario*. In Sec. 2.3.5 all relevant scenarios for the search discussed in this thesis will be presented and motivated.

Gauge eigenstates in the MSSM are not mass eigenstates, as also seen for the Higgs bosons. In Tab. 2.6, the full list of mass eigenstates is given. The mixing does not introduce new parameters with respect to the ones already mentioned. For sfermions, non-negligible mixing only occurs in the third generation, due to large Yukawa couplings. The stop sector is of particular importance for the radiative corrections to m_{h^0}, which depend on the off-diagonal term in the mixing matrix of the gauge eigenstates $m_t X_t = m_t(A_t - \mu\cot\beta)$. As we will see later, this term is crucial for the definition of a benchmark scenario. Benchmark scenarios include a choice of the values of the three gaugino masses. However, if these masses unify at a large energy scale, only M_3 and either M_2 or M_1 have to be defined in the scenario, as at the electroweak scale the following equality holds

$$M_1 = \frac{5}{3}\tan^2\theta_W M_2. \tag{2.80}$$

2.3.4 Neutral MSSM Higgs Bosons Phenomenology

In this and the following section we describe the phenomenology of the neutral MSSM Higgs sector, and discuss the definition of the benchmark scenarios relevant for this thesis. As already shown by the formulas in Eq. (2.76), there is a mass hierarchy between the three neutral Higgs bosons. The dependence of the mass of a generic neutral MSSM Higgs boson on m_A and $\tan\beta$ is illustrated in Fig. 2.7, which includes radiative corrections, for the particular scenario called $m^-_{h,\mathrm{mod}}$, to be discussed in Sec. 2.3.5. At the LHC, the MSSM neutral Higgs bosons are produced by the same mechanisms already illustrated in Fig. 2.3 for the SM case, with few important differences. Due to CP conservation the A boson does not couple to gauge bosons, and is therefore not produced by the processes illustrated in the diagrams (b) and (c). In the diagram in Fig. 2.3 (a), sfermions contribute in the loop as well as quarks, in particular the third-generation ones. In the MSSM the Higgs coupling to down-type fermions is enhanced by a factor

Names	Spin	P_R	Gauge Eigenstates	Mass Eigenstates
Higgs bosons	0	+1	H_u^0 , H_d^0 , H_u^+ , H_d^-	h^0 , H^0 , A^0 , $H^\pm$
Squarks	0	-1	$\tilde{u}_L$, $\tilde{u}_R$, $\tilde{d}_L$, $\tilde{d}_R$	(same)
			$\tilde{c}_L$, $\tilde{c}_R$, $\tilde{s}_L$, $\tilde{s}_R$	(same)
			$\tilde{t}_L$, $\tilde{t}_R$, $\tilde{b}_L$, $\tilde{b}_R$	$\tilde{t}_1$, $\tilde{t}_2$, $\tilde{b}_1$, $\tilde{b}_2$
Sleptons	0	-1	$\tilde{\nu}_e$, $\tilde{e}_L$, $\tilde{e}_R$	(same)
			$\tilde{\nu}_\mu$, $\tilde{\mu}_L$, $\tilde{\mu}_R$	(same)
			$\tilde{\nu}_\tau$, $\tilde{\tau}_L$, $\tilde{\tau}_R$	$\tilde{\nu}_\tau$, $\tilde{\tau}_1$, $\tilde{\tau}_2$
Neutralinos	$\frac{1}{2}$	-1	$\tilde{B}^0$, $\widetilde{W}^0$, $\tilde{H}_u^0$, $\tilde{H}_d^0$	$\tilde{N}_1$, $\tilde{N}_2$, $\tilde{N}_3$, $\tilde{N}_4$
Charginos	$\frac{1}{2}$	-1	$\widetilde{W}^\pm$, $\tilde{H}_u^+$, $\tilde{H}_d^-$	$\tilde{C}_1^\pm$, $\tilde{C}_2^\pm$
Gluinos	$\frac{1}{2}$	-1	$\tilde{g}$	(same)

Table 2.6: Mass eigenstates in the MSSM. The R-parity is quoted (P_R) , along with the original mixed gauge eigenstates. Mass eigenstates are numbered from lighter to heavier.

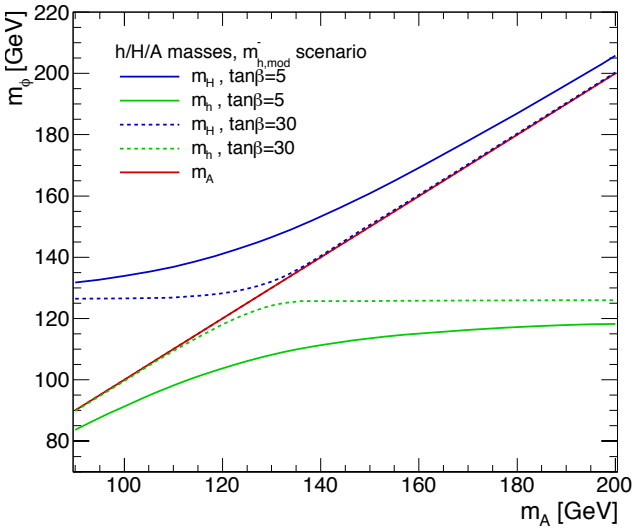

Figure 2.7: Masses of the neutral Higgs bosons in the MSSM. Here the $m_{h,\mathrm{mod}}^-$ scenario is assumed [49]. The plots are obtained with the program `FeynHiggs` [50–52]. The plots are obtained for $\tan\beta = 5, 30$.

Φ	$g_{\Phi\bar{u}u}$	$g_{\Phi\bar{d}d}$	$g_{\Phi VV}$	$g_{\Phi AZ}$	$g_{\Phi H^{\pm}W^{\mp}}$
H_{SM}	1	1	1	0	0
h	$\cos\alpha/\sin\beta$	$-\sin\alpha/\cos\beta$	$\sin(\beta-\alpha)$	$\cos(\beta-\alpha)$	$\mp\cos(\beta-\alpha)$
H	$\sin\alpha/\sin\beta$	$\cos\alpha/\cos\beta$	$\cos(\beta-\alpha)$	$-\sin(\beta-\alpha)$	$\pm\sin(\beta-\alpha)$
A	$\cot\beta$	$\tan\beta$	0	0	1

Table 2.7: Ratio between the MSSM Higgs bosons couplings and the Standard Model ones. The labels u and d represent all kinds of up-type and down-type fermions, respectively, while V represents either a W a Z.

of $\tan\beta$. Therefore, the diagrams in Fig. 2.3 (d) and (e) become dominant when b quarks are considered. The cross-sections for the production of the three neutral Higgs bosons are illustrated in Fig. 2.8, as a function of m_A at two values of $\tan\beta$. Differences in the Higgs couplings between the Standard Model and the MSSM are shown in Tab. 2.7 at the leading-order of the theory. In the decoupling limit, all leading-order couplings of the h boson reduce to the SM ones, for $\tan\beta \gg 1$. In the same limit, the H boson couplings approach the values of the A boson couplings in absolute value. Radiative corrections do not significantly alter this picture. Due to the enhancement with $\tan\beta$, the decay channels $h/H/A \to b\bar{b}$

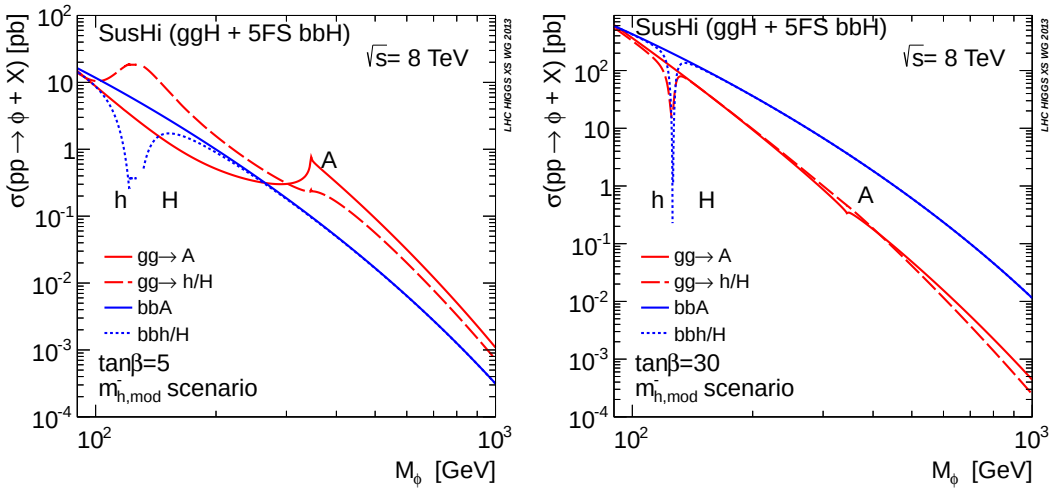

Figure 2.8: Cross sections for the production of the neutral Higgs bosons of the MSSM at the LHC with $\sqrt{s} = 8$ TeV. Here the $m^{-}_{h,\mathrm{mod}}$ scenario is assumed [49]. Plots are taken from Ref. [26] and obtained with the program `SusHi` Ref. [53]. The effect of different $\tan\beta$ is compared, with $\tan\beta = 5$ on the left and $\tan\beta = 30$ on the right.

and $h/H/A \to \tau^{+}\tau^{-}$ present a larger branching ratio with respect to the Standard Model prediction. The branching ratios are shown in Fig. 2.9 as a function of m_A at two values of $\tan\beta$.

2.3.5 MSSM Scenarios

An MSSM Higgs search has to rely on benchmark scenarios in which the higher-order parameters of the theory have been fixed. In this section, all the relevant scenarios considered for the $h/H/A \to \tau\tau$ search are presented. The following set of assumptions is common to all scenarios

- $m_t = 173.2$ GeV

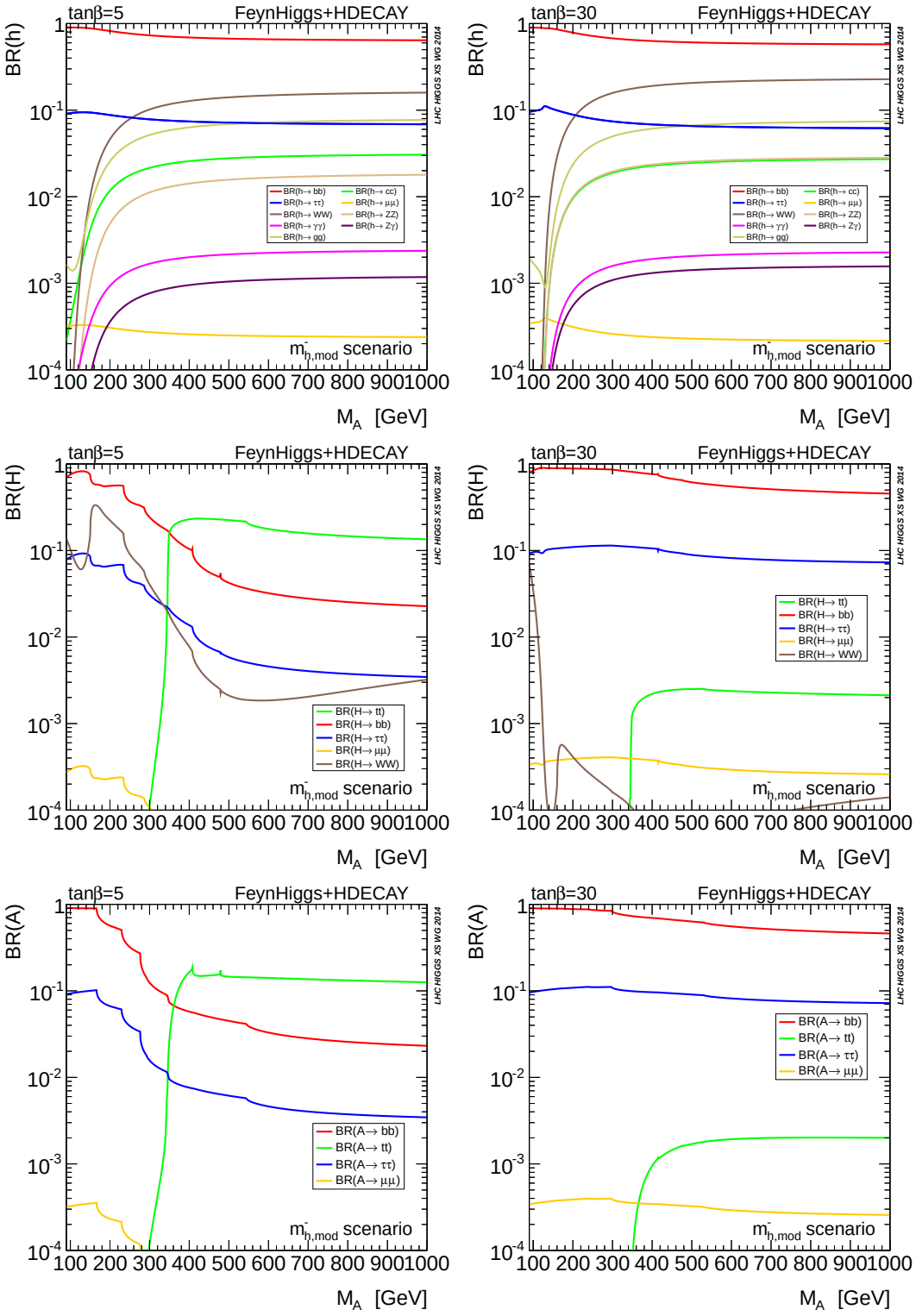

Figure 2.9: Branching ratios of neutral Higgs bosons in the MSSM. The $m_{h,\mathrm{mod}}^{-}$ scenario is assumed [49]. The plots are taken from Ref. [26] and are obtained with the programs `FeynHiggs` [50–52] and `HDECAY` [54]. The effect of different tanβ values is shown (tanβ = 5 on the left and tanβ = 30 on the right).

- $M_3 = 1500$ GeV
- $m_{Q_3} = m_{\bar{u}_3} = m_{\bar{d}_3} = M_{\text{SUSY}}$ and $m_{\bar{L}_3} = m_{\bar{e}_3}$
- $m_{Q_{1,2}} = m_{\bar{u}_{1,2}} = m_{\bar{d}_{1,2}} = 1500$ GeV and $m_{\bar{L}_{1,2}} = m_{\bar{e}_{1,2}} = 500$ GeV
- $A_f = 0 \;\; (f = c, s, u, d, \mu, e)$

It has to be noted that for the last two sets of assumptions the corresponding parameters only have a minor impact on the Higgs sector.

The results of a search for neutral MSSM Higgs bosons are often presented as exclusion bounds in the space of the leading-order free parameters of the theory, typically chosen to be m_A and $\tan\beta$. Previous to the Higgs boson discovery, the most popular scenario, called m_h^{max}, was designed to obtain the most conservative exclusion bounds on $\tan\beta$ at LEP experiments searches [55–57]. In the m_h^{max} scenario radiative corrections to m_h are maximised for fixed values of m_t and M_{SUSY}, such that the upper bound is obtained as in Eq. (2.78).

After the discovery, such a scenario allows only a small region to be available in the $(m_A, \tan\beta)$ plane. However, the MSSM parameters entering in the radiative corrections to m_h can be chosen in order to increase the available region in this two-parameter space. Such modifications affect the radiative corrections on m_h, lowering the upper bound of Eq. (2.77) down to $m_h < 125$ GeV [49]. In the scenarios called $m_{h,\text{mod}}^-$ and $m_{h,\text{mod}}^+$ this is achieved by altering m_h by the absolute value and sign of the X_t parameter, as reported in Tab. 2.8.

Another way to modify the bound on m_h is to decrease M_{SUSY}, necessarily leading to lighter stops and therefore lower M_S. For the *light-stop* scenario in Tab. 2.8 we have $m_{\tilde{t}_1} = 325$ GeV and $m_{\tilde{t}_2} = 670$ GeV. In this scenario μ and M_2 are modified according to the latest exclusion limits from LHC experiments.

In addition to the alteration on the m_h bound, another modification regards the decay rate $h \to \gamma\gamma$, as initial ATLAS and CMS measurements indicated an enhancement in this channel with respect to the Standard Model prediction. This enhancement has by now become weaker. Light staus might lead to such a modification, with a scale indicated in Tab. 2.8 in the *light-stau* scenario.

Finally, the *tau-phobic* scenario was proposed to motivate the initial lack of $H \to \tau\tau$ evidence from LHC experiments. Recent results from ATLAS [58] and CMS [59] make this motivation weak, as a 4σ excess has been observed in the $H \to \tau\tau$ search. The tau-phobic scenario induces modifications up to 20% of the Higgs decay in tau pairs in some regions of the parameter space, increasing it or enhancing it. The last two scenarios, even though no longer well motivated, were still considered for the search presented in this thesis.

2.4 Cross Section and Simulation of Events at Hadron Colliders

One of the most important physical observables in a particle physics experiment is the cross-section for a particular process. In the following, we illustrate how this quantity is defined and used in the simulation of events, which are widely exploited in order to model both new and SM processes.

We first consider the number of events produced in the collisions. The expected value for this quantity can be written as

$$N_{\text{exp}} = \sigma \int \mathrm{d}t L(t) \tag{2.81}$$

where σ is the cross-section of a physical process [15, 16] and the integral term is the so-called *integrated luminosity*, where the integration over time is performed of the quantity $L(t)$ called *instantaneous luminosity*. The cross-section is computed from the information contained in the Lagrangian and is

Parameters	Benchmark Scenarios			
	m_h^{max} / $m_{h,\text{mod}}^-$ / $m_{h,\text{mod}}^+$	*light-stop*	*light-stau*	*tau-phobic*
M_{SUSY}	1000 GeV	500 GeV	1000 GeV	1500 GeV
μ	200 GeV	350 GeV	500 GeV	2000 GeV
M_2	200 GeV	350 GeV	200 GeV	200 GeV
X_t	$2\ /\ -1.9\ /\ 1.5\ M_{\text{SUSY}}$	$2\ M_{\text{SUSY}}$	$1.6\ M_{\text{SUSY}}$	$2.45\ M_{\text{SUSY}}$
	$A_b = A_\tau = A_t$	$A_b = A_\tau = A_t$	$A_b = A_t,\ A_\tau = 0$	$A_b = A_t,\ A_\tau = 0$
$m_{\tilde{L}_3}, m_{\tilde{e}_3}$	1000 GeV	1000 GeV	245 GeV	500 GeV

Table 2.8: Summary of the parameters of the MSSM benchmark scenarios. Values are taken from Ref. [49].

related to the probability of the process to occur, while the instantaneous luminosity is a parameter of the collider. Assume that a collider produces head-on collisions of two bunches of particles at a certain frequency f_{coll}. We define the number of particles contained in these bunches as n_1 and n_2. If the bunches have the same transverse profiles, characterised by the horizontal and vertical widths σ_x and σ_y, respectively, we can write the instantaneous luminosity as

$$L = f_{\text{coll}} \frac{n_1 n_2}{4\pi\sigma_x\sigma_y} \tag{2.82}$$

Predictions of the cross-section for new and known processes are typically needed to interpret the data collected from the collisions. Simulated events are generated according to the probability of a process to occur, in a way illustrated in the following section.

2.4.1 Simulation of Hadronic Collisions

We focus our attention on the simulation of events originating from the scattering of protons, as relevant for LHC collisions, however, the following discussion also applies to a generic hadron-hadron scattering. This discussion will also serve to introduce the concept of a particle jet, one of the fundamental objects reconstructed in the events. The following overview is based on the more exhaustive documents [60–63].

As discussed in Sec. 2.1.1, hadrons are composed of partons. In simulating hadronic collisions, sequential steps are taken into account, starting from the partons in the initial state and ending with the particles observed in the detector. First of all, the momentum distributions of partons should be modelled by *parton distribution functions* (PDF). Knowing the kinematics of the initial state, the next step is the generation of the so-called *hard process* which requires detailed knowledge of the cross-sections involved for the particular interaction. After this, if coloured particles are produced, gluon radiation is emitted and a cascade of quarks and gluons is produced, called a *parton shower*. Particles generated at this step undergo *hadronisation* (cf. Sec. 2.1.1) and form colour-singlet states. Final states produced in the hard process might then decay in the detector, under the effect of the strong or electroweak interactions. If particles produced in the hard process have an electric charge, the radiation of photons must be taken into account. In Fig. 2.10, all the sequential steps considered by the simulation are shown. The hard process is characterised by a large transferred momentum between the initial partons. However, other interactions at lower momenta populate the event, which are part of the so-called *underlying event*. The

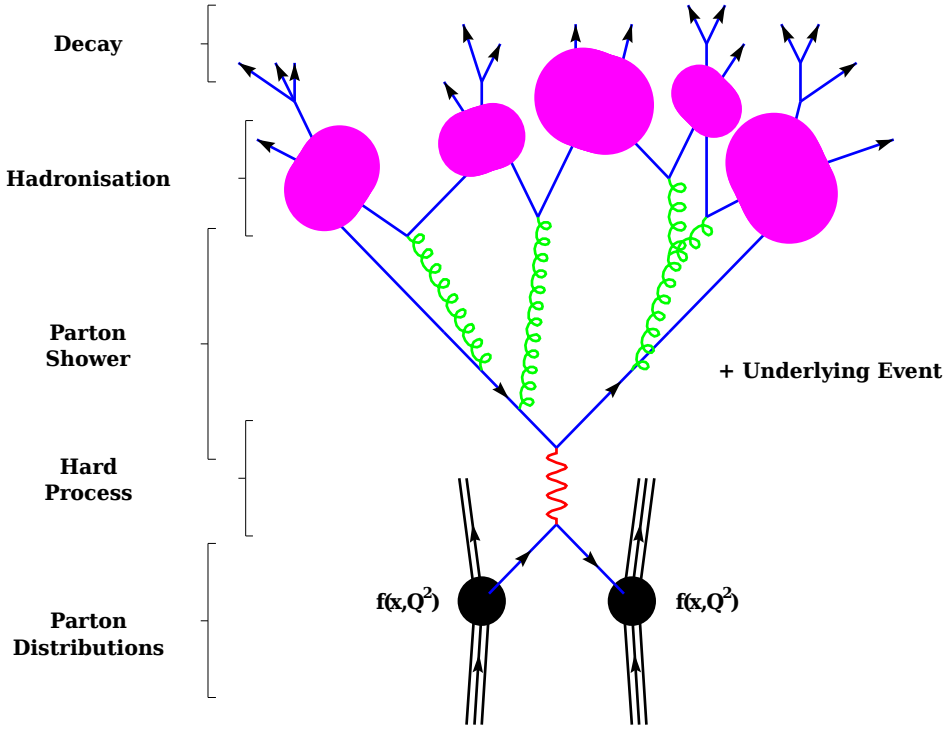

Figure 2.10: Illustration of all processes taken into account for the simulation of hadron collisions. The picture is taken from Ref. [64].

next sections will be dedicated to the details of all the steps mentioned. It is important to point out that only two interacting protons will be relevant for the following discussion, therefore ignoring for now the interactions of other protons in the same or different colliding bunches. Computer programs simulating the collisions are referred to as *generators*, which are based on Monte Carlo methods.

Hard Process

Interesting events produced in the collisions involve large momentum transfer, therefore, the core of the simulation has to focus on them. For such processes we are allowed to treat strong interactions perturbatively, as the asymptotic freedom, discussed in Sec. 2.1.1, guarantees that the coupling parameter α_S is small enough at high energies, thus making precision calculations possible. If we consider two partons i and j interacting inside two hadrons had_1 and had_2, respectively, and a final state n, we can write the cross-section of the interaction as

$$\begin{aligned}\sigma &= \sum_{i,j} \int_0^1 \mathrm{d}x_i \int_0^1 \mathrm{d}x_j \int f_i^{\text{had}_1}(x_i,\mu_F) f_j^{\text{had}_2}(x_j,\mu_F) \mathrm{d}\hat{\sigma}_{ij\to n}(\mu_F,\mu_R) \\ &= \sum_{i,j} \int_0^1 \mathrm{d}x_i \int_0^1 \mathrm{d}x_j \int \mathrm{d}\Phi_n f_i^{\text{had}_1}(x_i,\mu_F) f_j^{\text{had}_2}(x_j,\mu_F) \frac{1}{2\hat{s}} |\mathcal{M}_{ij\to n}|^2(\Phi_n,\mu_F,\mu_R) \end{aligned} \quad (2.83)$$

In Eq. (2.83), the transverse momenta with respect to the direction of the collision are neglected, as they are typically much smaller than the longitudinal component. Here, the index n represents the number of particles in the final state. In Eq. (2.83), we have introduced the parton distribution functions $f_i^{\text{had}_1}(x_i,\mu_F)$

and $f_j^{\text{had}_2}(x_j, \mu_F)$ which represent the density of probability to find two partons i and j inside the hadrons carrying momentum fractions $x_i = E_i/E_{\text{had}_1}$ and $x_j = E_j/E_{\text{had}_2}$. These functions depend on a scale of the transferred momentum $Q^2 = \mu_F$ called *factorisation scale*, corresponding to the energy scale at which we are able to resolve quarks and gluons inside the hadrons. A PDF cannot be determined by first principles, i.e. by perturbative calculations, rather it has to be measured experimentally. Different generators work with different PDF sets obtained by tuning a phenomenological model to data. The relevant PDF sets for this thesis, to be introduced later, are reviewed in Ref. [65]. The uncertainty deriving from the choice of the PDF set is typically evaluated comparing the result with different PDFs.

The quantity $\hat{\sigma}_{ij\to n}(\mu_F, \mu_R)$ is the parton-level cross-section for the process $i + j \to n$ and depends on μ_R, which is the renormalisation scale, introduced in Sec. 2.1.8, corresponding to the momentum scale at which the coupling parameter of the interaction has to be evaluated. The choice of the parameters μ_F and μ_R is not guided by any general principle, therefore an uncertainty has to be assigned to the chosen values. The differential parton-level cross-section $\mathrm{d}\hat{\sigma}_{ij\to n}$ depends on the momenta available in the final state phase space Φ_n. The integrated phase space might need to be reduced as far as regularisation is concerned, as discussed in Sec. 2.1.8.

The parton level process is represented by the so-called *matrix element* (ME) $|\mathcal{M}_{ij\to n}|^2$, which can be computed using the Lagrangian, and is averaged over the initial state colour and spin degrees of freedom. The factor $1/(2\hat{s}) = 1/(2x_i x_j s)$ is called the parton flux and contains the center-of-mass energy squared of the collision computed using the initial four-momenta $s = (p_i + p_j)^2$.

Eq. (2.83) holds to all orders in perturbation theory, however, commonly available simulations utilise mainly leading-order (LO) matrix elements, as complications arise when next-to-leading-order (NLO) terms are taken into account. The differential cross-section including LO and NLO contributions can be written as

$$\mathrm{d}\sigma^{\text{NLO}} = \mathrm{d}\Phi_n \left[\mathcal{B}(\Phi_n) + \alpha_S \mathcal{V}(\Phi_n)\right] + \mathrm{d}\Phi_{n+1} \alpha_S \mathcal{R}(\Phi_{n+1}) \tag{2.84}$$

where $\mathcal{B}$ is the LO term, while $\mathcal{V}$ and $\mathcal{R}$ are the NLO contributions. The so-called *virtual* term, $\mathcal{V}$, includes higher order loop corrections to $\mathcal{B}$, while the *real* term, $\mathcal{R}$, features an additional particle in the final state. The components of Eq. (2.84) include divergences. This problem can be addressed using regularisation as far as the LO term only is concerned. However, the loop contribution from $\mathcal{V}$ generates a diverging interference. This is not a concern as far as the $\mathcal{R}$ term is included, as divergences coming from $\mathcal{R}$ exactly cancel those from $\mathcal{V}$, for the inclusive observables of interest in a typical experiment. These divergences arise because two partons in the real emission can become collinear, or a parton is considered with vanishing momentum.

A NLO simulation is more accurate than a LO one. However, it is complicated by the fact that the mutually cancelling real and virtual divergences appear in integrals with different dimensions in $\mathrm{d}\Phi$, and are therefore difficult to treat numerically. Different methods exist to address this problem. However, the majority of generators, based on Monte Carlo integration, provide LO cross-sections. In this case, a correction can be applied, called a *k-factor*, derived by comparing the LO cross-section to a higher-order one for inclusive regions of the phase space. This kind of correction will be used in the analysis later described in this thesis.

Parton Shower

The description of the hard process given in the previous section is limited to a fixed-order in the perturbative expansion of the coupling parameter, α_S, if we consider the strong interactions. However, to give a complete exclusive description of the final products of the scattering we need to address their internal structure. This is achieved by using *parton shower* algorithms, which are formulated as an

evolution in the transferred momentum from the high scales associated with the hard process, which we will call $Q_{\max}$, down to a cut-off scale $Q_0 \approx 1$ GeV, where $\alpha_S \approx 1$ and QCD cannot be treated perturbatively. This evolution is performed by generating additional radiation in addition to the final state of the hard process simulated using the ME, using an approximated expression for the cross-section, which is

$$\mathrm{d}\sigma \approx \sigma_{\mathrm{ME}} \sum_{a\to bc}^{\text{all comb.}} \frac{\alpha_S}{2\pi}\frac{\mathrm{d}\theta^2}{\theta^2}\mathrm{d}z P_{a\to bc}(z,\phi)\frac{\mathrm{d}\phi}{2\pi}, \tag{2.85}$$

where $P_{a\to bc}$ is the so-called *splitting function*, which is associated with the probability that the parton a generated in the hard process subsequently decays in two other partons b and c. This function depends in general on the energy fraction $z = E_b/E_a$, and the azimuth of b with respect to the axis defined by a, called ϕ. In Eq. (2.85), θ represents the polar angle of the emitted parton. It is important to notice that Eq. (2.85) is only valid in the *soft/collinear approximation*, i.e. when z and θ are small. Different fundamental splitting functions are given for the different splitting possibilities $q \to qg$, $g \to q\bar{q}$ and $g \to gg$. Their expression can be found in Ref. [60], averaged over ϕ.

We can now build an iterative algorithm using Eq. (2.85), which is a completely general expression for a hard process to be accompanied by a collinear splitting. The final state of this process can be viewed as a new hard process to which we can apply a new collinear splitting, and so on. However, divergences arise for $z, \theta \to 0$. We notice, though, that in this limit b and c are indistinguishable from a, i.e. the transition $a \to b + c$ is identical to $a \to a$. We can address the divergence by introducing a resolution criterion, generating distributions of only resolvable partons. This can be done defining the cut-off Q_0^2 relative to the transferred momentum, as this can be approximated as $Q^2 \approx -4E_aE_b\sin^2(\theta/2)$.

The distribution we are interested in generating is the probability of the first split after the hard process $\mathcal{P}'_{q\to bc}$. If we call $F(Q^2_{\max}, Q^2)$ the probability of having no emission between $Q^2_{\max}$ and any lower scale Q^2, the first emission probability corresponds to its derivative with respect to Q^2. We have

$$\frac{\mathrm{d}\mathcal{P}'_{a\to bc}}{\mathrm{d}Q^2} = \frac{\mathrm{d}F(Q^2_{\max}, Q^2)}{\mathrm{d}Q^2} = F(Q^2_{\max}, Q^2)\frac{\mathrm{d}\mathcal{P}_{a\to bc}}{\mathrm{d}Q^2} \tag{2.86}$$

where the probability $\mathcal{P}_{a\to bc}$ is referred to a generic splitting and is determined by the so-called *Dokshitzer–Gribov–Lipatov–Altarelli–Parisi* (DGLAP) equation

$$\frac{\mathrm{d}\mathcal{P}_{a\to bc}}{\mathrm{d}Q^2} = \frac{\alpha_S}{2\pi Q^2}P(z)_{a\to bc}\mathrm{d}z \tag{2.87}$$

The function $F(Q^2_{\max}, Q^2)$ is obtained by solving Eq. (2.86), and is equal to

$$F(Q^2_{\max}, Q^2) = \exp\left(-\sum_{b,c}\int_{Q^2}^{Q^2_{\max}}\frac{\mathrm{d}k}{k}\int_{Q_0^2/k^2}^{1-Q_0^2/k^2}\frac{\alpha_S}{2\pi}P_{a\to bc}(z')\mathrm{d}z'\right) \tag{2.88}$$

The function $F(Q^2_{\max}, Q^2)$ should account for the probability of emitting no radiation, but the second integral contains the probability of the emission above the cut-off scale Q_0^2. This is not surprising, as the unitarity relation can be written as

$$\begin{aligned} 1 - \mathcal{P}(\text{resolvable radiation}) = \\ \mathcal{P}(\text{unresolvable}) + \mathcal{P}(\text{virtual correction}) = \mathcal{P}(\text{no radiation}) + \mathcal{P}(\text{virtual correction}) \end{aligned} \tag{2.89}$$

which relates the probability of resolvable processes to the quantity we are interested in, and where the

assumption $\mathcal{P}$(unresolvable) = $\mathcal{P}$(no radiation) has been utilised. From Eq. (2.88), we also deduce that virtual corrections are included in $F(Q^2_{\text{max}}, Q^2)$ as well.

In the evolution of the parton shower the parameter Q^2_{max} changes after every emission, in order to avoid double counting of the energy. The evolution continues, until no resolvable emissions are generated above Q^2_0. In the previous formulas the parameter α_S depends on Q^2, and Q_0 has to be chosen above the scale below which QCD becomes non-perturbative, $\Lambda_{\text{QCD}} \approx 200$ MeV. Therefore Q_0 becomes a physical parameter rather than a pure cut-off, and is chosen to be $Q_0 \approx 1$ GeV.

In general we refer to all the radiation emitted in the final state of the hard-process as *final-state radiation* (FSR), including QED processes. Any radiation emitted at the initial parton level is called *initial-state radiation* (ISR). The treatment of the ISR is complicated by the need to model the internal structure of the hadron and will not be discussed here. A detailed explanation can be found in Ref. [60].

Matching and Merging

In the previous two sections we have discussed two fundamental steps in the simulation of events containing radiation from strong interactions. Both present advantages and shortcomings. The integration of the matrix element allows one to simulate processes in a specific region of the phase space suitable for experimental needs, but high-order calculations involve divergences which are difficult to treat. On the other hand parton showers virtually include all orders of perturbation theory, due to unitarity considerations and their iterative character, but are only valid in the soft or collinear limits. Ideally we would like to combine the two methods. However, this is not a trivial task, because matrix element methods are inclusive, as they are used for the simulation of a final state with at least n final partons at a fixed order of α_S, while parton showers are exclusive, as they model exactly n partons in the final state approximately to all α_S orders. Also, care has to be taken to not double count some regions of phase space, or undercount them. Many algorithms have been proposed to address these problems, which are based on two main strategies. We call *matching* algorithms those approaches were higher-order corrections to an inclusive process are integrated with the parton shower. Other algorithms involve a *merging* scale, defined in terms of a resolution scale, where any parton produced above is generated with a corresponding higher-order ME, and any parton below with a parton shower.

Examples of NLO matching algorithms are implemented in `Powheg` [66], used in this thesis to model $h/H/A$ production via gluon-gluon fusion, and `MC@NLO` [67]. In these algorithms the LO matrix element is weighted to take into account higher-orders. An example of a merging algorithm is CKKW [68], which is used by the generator `Sherpa` [69], used in this thesis for the modelling of $h/H/A$ production in association with b quarks. Merging algorithms depend on the choice of the merging scale. This introduces a source of uncertainty, the estimation of which will be later discussed in this thesis.

Hadronisation

In the previous discussion we have illustrated the partonic level of the simulation. However, in physics experiments hadrons are observed. During the hadronisation phase all outgoing partons form hadrons at a typical energy scale of 1 GeV. This phase cannot be described from first principles, and phenomenological models have to be used, which involve ad-hoc parameters. These models are based on two approaches called the *string* and *cluster* fragmentation. They are implemented in the generators `Pythia` [70, 71] and either `Herwig` [72, 73] or `Sherpa`, respectively. The details of these models are beyond the scope of this thesis, however, a complete description is given in Ref. [60, 74].

Particle Decays

The final step of the simulation is the decay of the particles produced. The major complication to this task is the still incomplete knowledge about particle decays, for which measured branching ratios usually do not add up to 100%. Then, the available information which has been collected experimentally has to be complemented with a number of analytical methods. Standard generators typically include few matrix elements for hadron decays. More sophisticated simulation of hadronic decays are possible using specialised code to be interfaced to the generator. This is done for tau decays as well, with the package `TAUOLA` [75]. Other generators do include tau decays such as `Herwig++` [73] and `Sherpa` featuring also the description of spin effects. Radiative corrections to QED processes are modelled with the package called `PHOTOS` [76].

Underlying Event and Multiple Parton Interactions

The evolution of the hard process described so far regards the interaction of coloured particles bound in a colour-singlet state such as a proton. The remaining partons, which are themselves coloured, are therefore expected to hadronise or interact with each other. We refer to such a class of processes as the *underlying event* (UE) where all the radiation from the original hard interaction is excluded. Underlying event processes typically involve low transferred momenta, resulting in radiation with low transverse momentum with respect to the direction of the collision. However, the UE activity increases when selecting hard events. This happens because this kind of selection is biased toward those collisions where the two protons overlap, leading to a higher chance of *multiple parton interactions* (MPI). Physics generators can incorporate perturbative models of multiple interactions, like `Pythia`, `Sherpa` and `Herwig++`. Others, like `Herwig` need to be integrated with other programs like `Jimmy` [77]. In addition to the MPI, the whole underlying event needs to be modelled. Due to the soft nature of the interactions involved it is not possible to treat the UE perturbatively, rather phenomenological models have to be used featuring parameters which needs to be tuned with data. For this thesis the tunes called *Perugia* [78], *AUET2* [79] and *AUET2B* [80] are used. Further information on the underlying event and multiple interactions can be found in Ref. [81].

2.4.2 Particle Jets

The previous discussion has introduced the details of the simulation of hadron-hadron collisions, introducing the fundamental physics models. However, any practical use of these simulation techniques relies on reconstruction algorithms whose purpose is to provide an experimental definition of the physical objects composing an event. The final state of the parton shower has a composition in which most of the energy is carried by localised collinear bundles of partons called jets, whose structure is preserved after hadronisation. Jets are not fundamental objects defined by the theory, but only defined by reconstruction algorithms, which address the problem of what particles and momentum are to be assigned to a jet. In general, we require that these algorithms provide a way to compute jet cross-sections on the parton level to arbitrarily high-orders in perturbation theory, i.e. they should be *collinear and infrared safe*. This is achieved if the same result is obtained when replacing any partons with a collinear set of partons with the same total momentum or adding any number of infinitely soft partons in any direction. A general review of such algorithms is given in Ref. [82] and later in this thesis for our cases of interest.

CHAPTER 3

Experimental Status of MSSM Higgs Searches

The present chapter summarises the status of searches for the neutral Higgs bosons predicted by the MSSM. In Sec. 3.1, the discovery of a resonance consistent with the Higgs boson predicted by the Standard Model is discussed. In Sec. 3.2 a summary of the searches previous to the LHC experiments is discussed, while Sec. 3.3 and 3.4 illustrate the status of the direct searches at LHC experiments and the indirect experimental constraints on the MSSM Higgs sector, respectively.

3.1 Discovery of a Resonance Consistent with the Standard Model Higgs Boson

On 4 July 2012 the ATLAS and CMS collaborations announced the discovery of a new particle consistent with the Higgs boson predicted by the Standard Model [11, 12]. An excess in data corresponding to a significance of 5.1σ and 5σ for ATLAS and CMS, respectively, was observed. The sensitivity of the search was dominated by the decay channels with the best mass resolution, $H \to \gamma\gamma$ and $H \to ZZ^* \to 4l$. Combined datasets at different center-of-mass energies of $\sqrt{s} = 7$ TeV and $\sqrt{s} = 8$ TeV were used by the two experiments, with different integrated luminosities L_{int}: up to 4.8 fb^{-1} and 5.9 fb^{-1} for ATLAS, and 5.1 fb^{-1} and 5.3 fb^{-1} for CMS, respectively.

With increasing data samples, the sensitivity also from other channels increased. The combined sensitivity from all channels is shown in Fig. 3.1 on the left for the ATLAS experiment. The sensitivity of the search is dominated by the channels already mentioned, followed by the contributions of $H \to WW$, $H \to \tau\tau$ and $H \to b\bar{b}$, ordered from the most to the least sensitive. The last two modes are particularly challenging due to the difficult background situation involved.

More recent updates report evidence for $H \to WW \to lvlv$ and $H \to \tau\tau$ from ATLAS [58, 83] and CMS [59], while no evidence for $H \to b\bar{b}$ has been reported yet from the two collaborations [59, 84].

As indicated by Fig. 3.1, the significance of the excess is largest for a mass around 125 GeV. The current estimation of the mass has been published by ATLAS in Ref. [86], and is

$$m_{H,\,\text{ATLAS}} = 125.36 \pm 0.37\ (\text{stat.}) \pm 0.18\ (\text{syst.})\ \text{GeV} \tag{3.1}$$

while for CMS [59] the value is

$$m_{H,\,\text{CMS}} = 125.02 \pm 0.27\ (\text{stat.}) \pm 0.15\ (\text{syst.})\ \text{GeV} \tag{3.2}$$

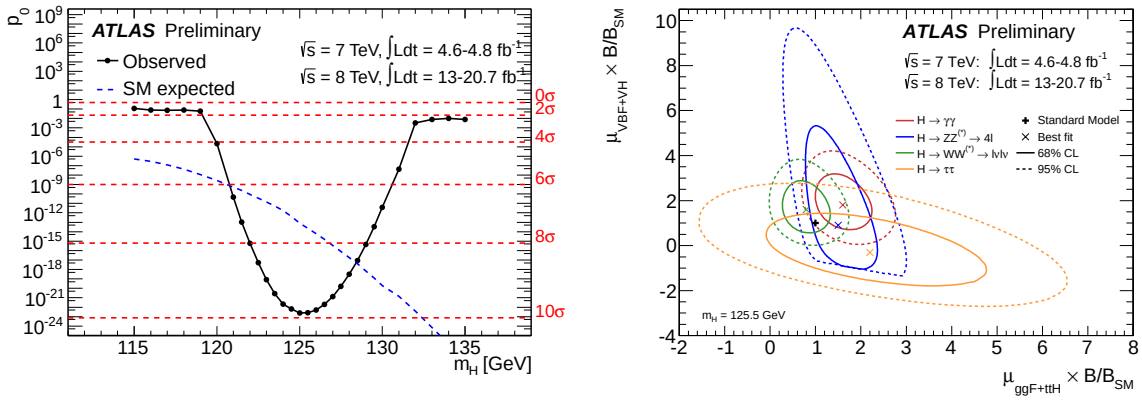

Figure 3.1: Left: local probability p_0 for a background-only experiment to be more signal-like than the observation, as a function of m_H. All channels mentioned in the text The channels $H \to \gamma\gamma$, $H \to ZZ^* \to 4l$, $H \to WW$, $H \to \tau\tau$ and $H \to b\bar{b}$ are combined. The dashed curve represents the median expected p_0 including the Standard Model Higgs boson hypothesis at that mass. Right: likelihood contours for all channels, for a mass hypothesis of $m_H = 125.5$ GeV. The values on the axes indicate the so-called *signal strength* which is the ratio between the measured cross-section of a specific production and decay mode and the value predicted by the SM. Both results are obtained by the ATLAS collaboration and are taken from Ref. [85].

The combination of the two measurements leads to the following estimate [25]

$$m_{H,\,\text{comb.}} = 125.09 \pm 0.21\ (\text{stat.}) \pm 0.11\ (\text{syst.})\ \text{GeV} \tag{3.3}$$

All these values have been measured using the two most sensitive channels. Contour plots for the mass estimate are shown in Fig. 3.2 for different confidence levels (CL) [87].

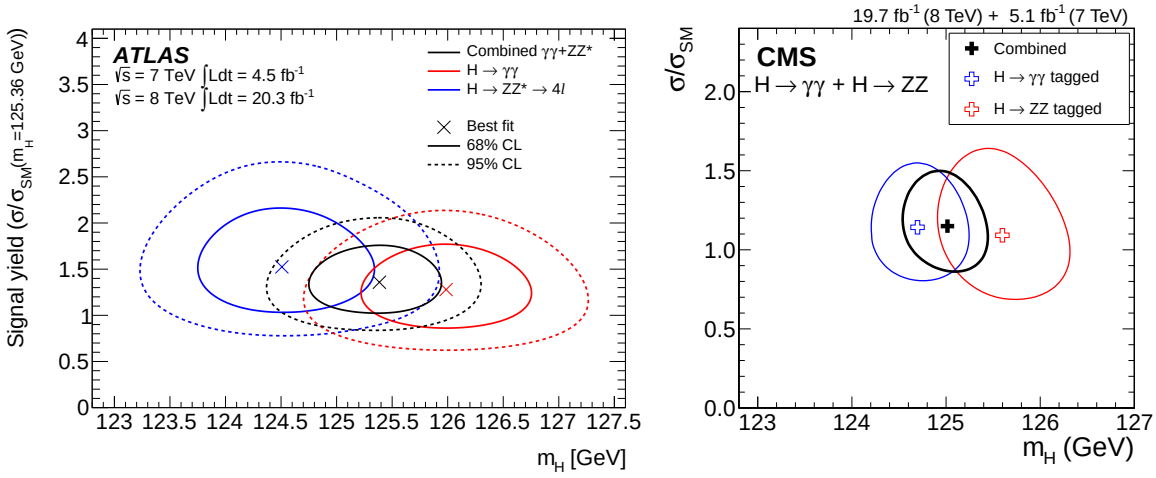

Figure 3.2: Left: likelihood contours as a function of the signal yield and m_H, for the channels $H \to \gamma\gamma$ and $H \to ZZ^* \to 4l$, from the ATLAS experiment [86]. The signal yield is normalised to the measured value $m_H = 125.36$ GeV. Right: 68% CL contour plots from the CMS experiment for the same decay channels [59]. The cross-section and the relevant branching ratios are set to the Standard Model expectation.

The measured cross-section of a process divided by its value predicted by the SM is the so-called *signal strength* μ. Recent analyses at ATLAS and CMS aim at measuring μ relative to the Higgs boson

production mechanisms. An example of such a measurement is illustrated in Fig. 3.1 (right) from the ATLAS experiment, showing the contribution of all channels. A similar study is reported by CMS in Ref. [59]. The present status of the μ measurement from all channels is shown in Fig. 3.3 for ATLAS on the left and CMS on the right. The plots are taken from Ref. [88] and [59], respectively.

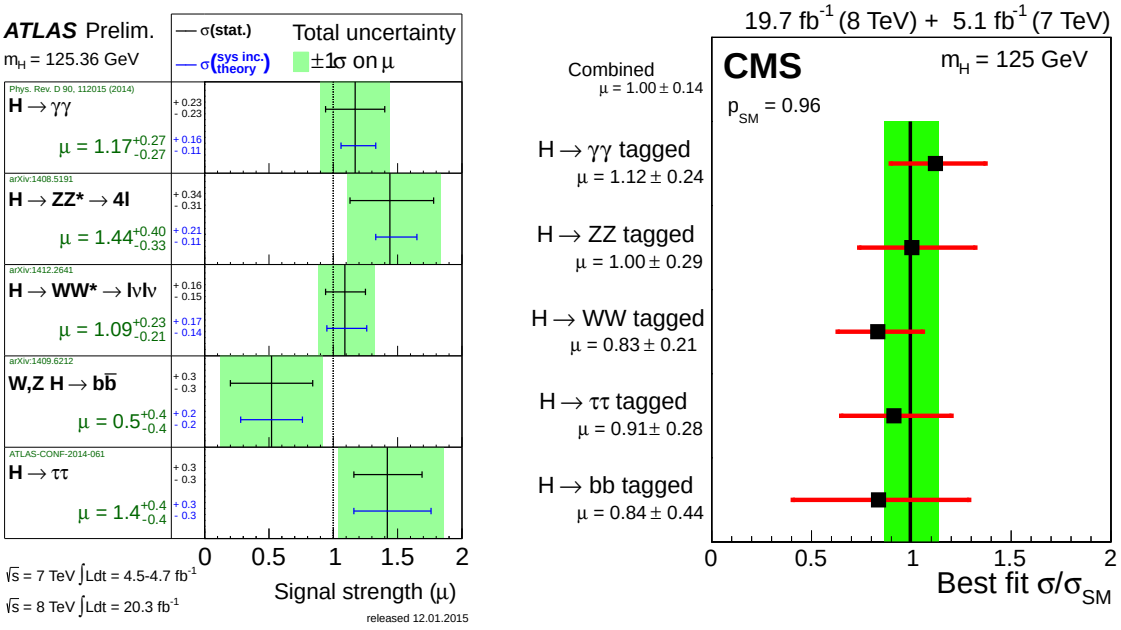

Figure 3.3: Summary of the signal strength measurements for the Higgs boson production and decays in the different channels, relative to a fixed m_H. The ATLAS plot on the left summarises the results from Ref. [58, 83, 84, 89, 90]. The CMS plot on the right is taken from Ref. [59].

3.2 Neutral MSSM Higgs Boson Searches at LEP and Tevatron

Previous to the LHC experiments, neutral MSSM Higgs bosons were searched for at the e^+e^- collider LEP (Large Electron-Positron) and at the Tevatron, a $p\bar{p}$ collider. At LEP the main production mechanisms are $e^+e^- \to (h/H)Z$ (*Higgs strahlung*) and $e^+e^- \to (h/H)A$ (*pair production*), where H production is prohibited by kinematics in a large part of the parameter space. The combined results from the LEP experiments, ALEPH, DELPHI, L3 and OPAL, are reported in Ref. [55]. The analyses were performed with datasets collected at center-of-mass energies in the range $\sqrt{s} = 91 - 209$ GeV, and with integrated luminosities in the range $L_{\text{int}} = 125 - 2400$ pb^{-1}.

Different decay channels are considered for different production modes. For Higgs strahlung the processes $Z \to q\bar{q}/\nu\bar{\nu}/e^+e^-/\mu^+\mu^-$ are used in association with Higgs decays into $b\bar{b}$. Higgs boson decays in $\tau\tau$ are considered only in conjunction with $Z \to q\bar{q}/\tau\tau$ decays. For the pair-production mode different combinations of the two Higgs boson decays into $b\bar{b}$ and $\tau\tau$ are considered.

The results of the search are interpreted in several MSSM scenarios, the most conservative being m_h^{max}, also relevant for this thesis. Exclusion limits in the plane $(m_A, \tan\beta)$ are shown in Fig. 3.4.

At the Tevatron the two experiments CDF and DØ performed searches with datasets from $p\bar{p}$ collisions at $\sqrt{s} = 1.96$ TeV. In Ref. [91], data with $L_{\text{int}} = 2.6$ fb^{-1} for CDF and $L_{\text{int}} = 5.2$ fb^{-1} for DØ were used. The production mechanism relevant for this search is $gb \to h/H/A\, b$ with the subsequent decay

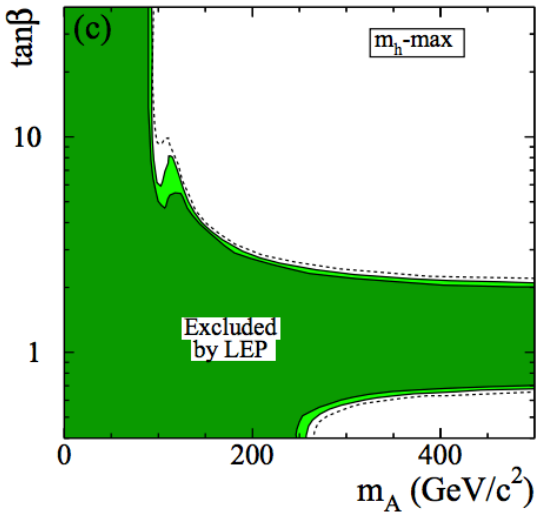

Figure 3.4: Exclusion limit in the $(m_A, \tan\beta)$ plane for combined LEP searches for neutral MSSM Higgs bosons. The dashed line indicates the boundaries of the exclusion at 95% CL. Dark green and light green indicate the observed exclusion at 99.7% and 95% CL, respectively. The limit is obtained for the m_h^{max} scenario with $\mu = -200$ GeV. The plot is taken from Ref. [55].

$h/H/A \to b\bar{b}$. The exclusion limits in the $(m_A, \tan\beta)$ plane are shown in Fig. 3.5 (left), including a comparison with the LEP limit.

In Ref. [92] another search is presented with $L_{\text{int}} = 1.8$ fb^{-1} and $L_{\text{int}} = 2.2$ fb^{-1} for CDF and DØ, respectively. The two production modes $gg \to h/H/A$ and $gg \to h/H/A\, b\bar{b}$ are relevant for this search, which focuses on the $\tau\tau$ decay modes of the Higgs bosons. The search is divided into categories distinguished by the decays of the tau leptons. These decays are usually indicated as $\tau_e\tau_\mu$, $\tau_e\tau_{\text{had}}$ and $\tau_\mu\tau_{\text{had}}$, where τ_{had} is the hadronic decay mode, and τ_e and τ_μ the leptonic ones, featuring respectively an electron or a muon plus two neutrinos. The corresponding exclusion limit is reported in Fig. 3.5 on the right. The DØ collaboration has also performed a combination of the previously mentioned $b\bar{b}$ decay channel and the searches in tau leptons in Ref. [93]. This study is performed with $L_{\text{int}} = 7.3$ fb^{-1}. Also, a search in the channel $\tau_{\text{had}}\tau_{\text{had}}$ is reported in Ref. [94] by CDF collaboration.

3.3 Neutral MSSM Higgs Boson Searches at the LHC

The following sections illustrate the status of the neutral Higgs boson searches at the LHC. Decays into fermions (ff) are considered in Sec. 3.3.1, while decay chains into other Higgs bosons are discussed in Sec. 3.3.2.

3.3.1 $h/H/A \to ff$ Searches

Neutral MSSM Higgs boson searches in di-fermion decays are particularly attractive in the $\tau\tau$ decay mode, as it offers a high branching ratio and better background separation with respect to the $b\bar{b}$ channel. Searches for $h/H/A \to \tau\tau$ have been performed by the ATLAS and CMS experiments. The most recent update from the ATLAS experiment, previous to the work presented in this thesis, is reported in Ref. [95], and relies on $L_{\text{int}} = 4.7 - 4.8$ fb^{-1} of data collected at $\sqrt{s} = 7$ TeV. The CMS result in Ref. [96] combines the datasets at $\sqrt{s} = 7$ TeV and $\sqrt{s} = 8$ TeV, with $L_{\text{int}} = 4.9$ fb^{-1} and $L_{\text{int}} = 19.7$ fb^{-1},

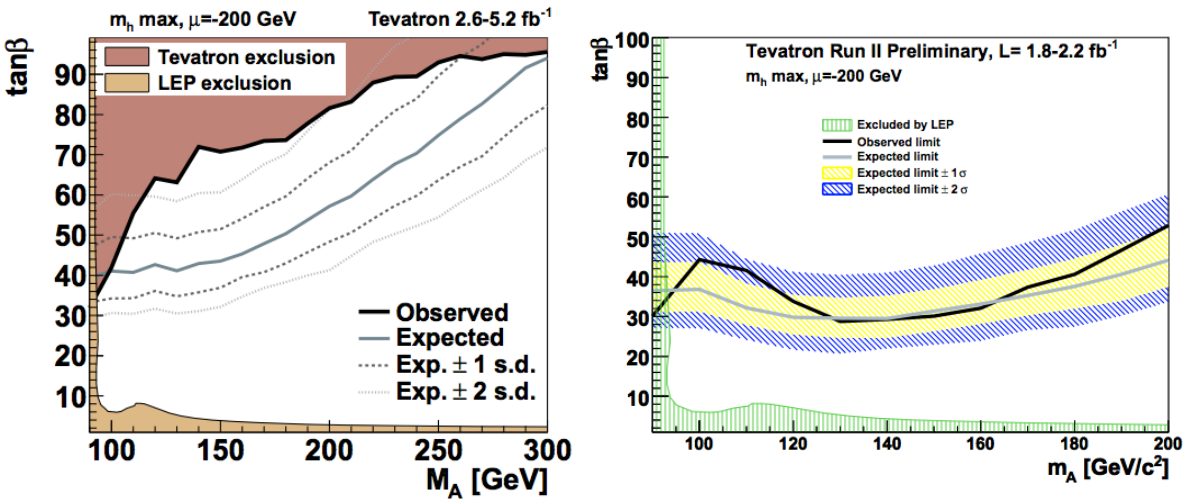

Figure 3.5: Exclusion limits at 95% CL in the $(m_A, \tan\beta)$ plane for neutral Higgs boson searches at the Tevatron. The left-hand plot shows the limit for the $b\bar{b}$ decay channel [91], and the right-hand plot for $\tau\tau$ [92].

respectively. Both searches include also the channel $h/H/A \to \mu\mu$, which allows for a precise estimate of the resonance mass, despite the lower branching ratio. The $\tau\tau$ search is optimised for different categories distinguished by the tau decay modes. These channels are $\tau_e\tau_\mu$, $\tau_e\tau_{\text{had}}$, $\tau_\mu\tau_{\text{had}}$ and $\tau_{\text{had}}\tau_{\text{had}}$. A further sub-categorisation is performed for each channel into a selection requiring the presence of a particle jet originating from the hadronisation of a b quark (*b-tagged* selection), and one vetoing such events (*b-vetoed* selection). These sub-channels target the dominant production mechanisms at the LHC, as seen in Sec. 2.3.4, the gluon-fusion mode and the associated production with b quarks.

The exclusion limits in the $(m_A, \tan\beta)$ plane set by the two analyses are shown in Fig. 3.6 and are obtained in the m_h^{max} scenario. The CMS collaboration performs the hypothesis test relative to the MSSM prediction of the different scenarios already discussed in Sec. 2.3.5. It has to be noticed that the CMS test is performed using a different definition of the *test statistic* [87], which quantifies the compatibility between data and the model, with respect to ATLAS. In the CMS case, the presence in data of the Higgs boson predicted by the SM penalises the significance of an excess, while in the ATLAS case it does not. The CMS plot in Fig. 3.6 also shows the region in the m_h^{max} scenario which is compatible with $m_h = 125$ GeV, bounded by the dashed contour at low $\tan\beta$. This region is larger for other scenarios already discussed in Sec. 2.3.5, in particular for the $m_{h,\text{mod}}^{+,-}$.

Upper bounds on the cross-section for a generic resonance ϕ are also derived in the two studies. The ATLAS one is reported in Fig. 3.7 on the right-hand side, for the b-tagged and b-vetoed selections. The left-hand plot shows the expected and observed exclusions set by the different channels in the ATLAS search.

Other di-fermion searches at the LHC have been performed by CMS in the channel $h/H/A \to b\bar{b}$ in Ref. [97]. The data used correspond to $L_{\text{int}} = 2.7 - 4.8$ fb^{-1} at $\sqrt{s} = 7$ TeV. The search targets the production mode with at least one b quark in the final state, and requires the presence of three b-tagged jets. The selection is divided into two categories. The all-hadronic category features only hadronic decays of the b quarks, while the semi-leptonic category requires the presence of at least one b quark including a muon among the decay products. No significant excess is observed among the expected background at 95% CL in the mass range $m_A = 90 - 350$ GeV.

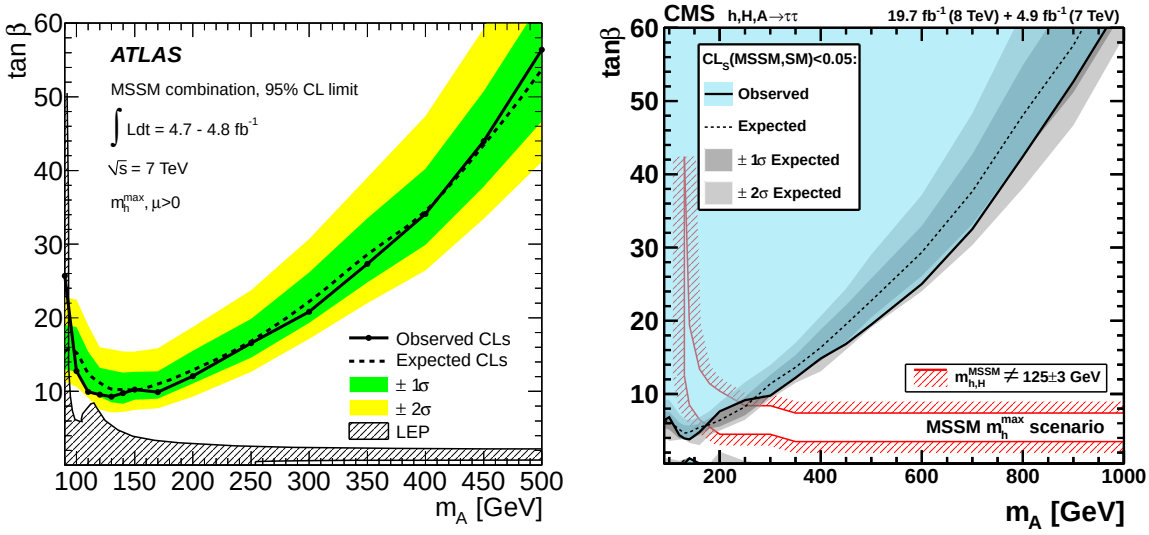

Figure 3.6: Exclusion limits in the $(m_A, \tan\beta)$ plane from $h/H/A \to \tau\tau/\mu\mu$ searches at ATLAS [95] and CMS [96]. The region above the lines is excluded at 95% CL. Both limits are obtained in the m_h^{max} scenario. The CMS plot also shows the region compatible with $m_h = 125 \pm 3$ GeV, relevant after the discovery of the Higgs boson.

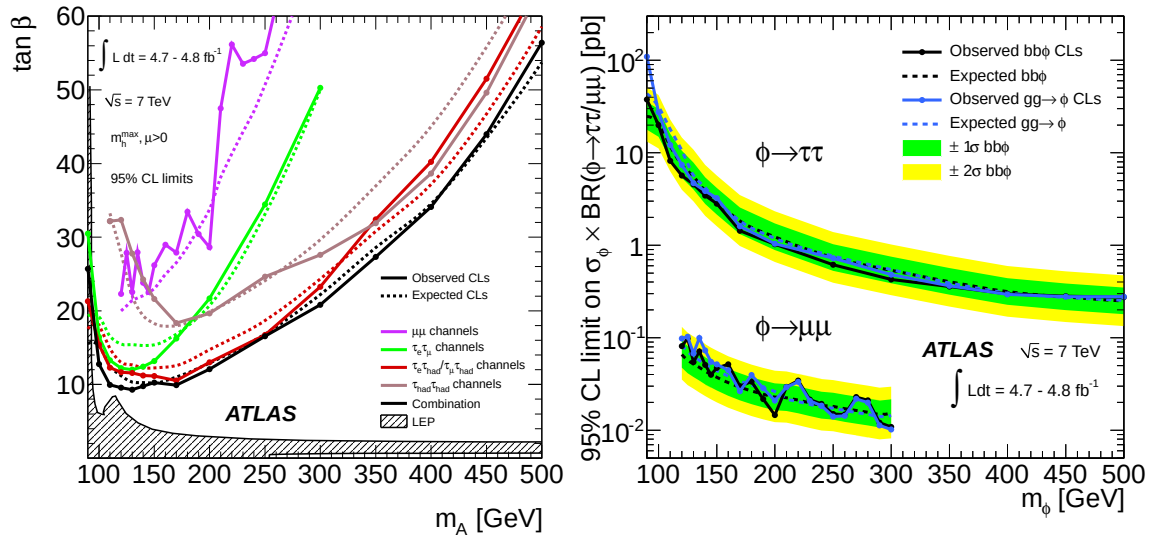

Figure 3.7: Left: observed and expected 95% CL exclusion limits from each channel in the $h/H/A \to \tau\tau/\mu\mu$ ATLAS search from Ref. [95]. Right: Excluded cross-section at 95% CL for the production of a generic resonance ϕ, requiring b-tagged jets ($bb\phi$) or vetoing them ($gg \to \phi$), and the subsequent decay in $\tau\tau$ or $\mu\mu$.

3.3.2 Other Neutral Higgs Boson Searches

Other than the di-fermion decay channel, LHC searches have been performed for neutral MSSM Higgs bosons coupling to each other. Therefore the decay mode $H \to hh$ has been considered for the ATLAS search in Ref. [98] and for the CMS one in Ref. [99] in the final state $hh \to \gamma\gamma b\bar{b}$. Both searches use data at $\sqrt{s} = 8$ TeV, with $L_{\text{int}} = 20$ fb^{-1} for ATLAS and $L_{\text{int}} = 19.7$ fb^{-1} for CMS. As many models, other than the MSSM, predict the existence of resonances with similar di-Higgs decays, the exclusion limit at 95% CL is set in a model-independent way. The ATLAS result excludes the cross-section of the process $pp \to \phi \to hh$ in the interval $m_\phi = 260 - 500$ GeV having fixed the $h \to \gamma\gamma/b\bar{b}$ branching ratios to the SM expectation. In the mentioned mass interval the expected exclusion lies in the range $\sigma_{\text{exp}} = 1.7 - 0.7$ pb and the observed in $\sigma_{\text{obs}} = 3.5 - 0.7$ pb. The CMS result excludes the cross-section for $pp \to \phi \to hh \to \gamma\gamma b\bar{b}$, while a constraint on m_h is used in the analysis, requiring compatibility with $m_h = 125.6 \pm 0.45$ GeV. For CMS we have $\sigma_{\text{exp}} = 3.14 - 0.43$ fb and $\sigma_{\text{obs}} = 3.98 - 0.33$ fb in the range $m_\phi = 260 - 1100$ GeV.

Another model-independent search is performed by CMS for the process $pp \to \phi \to hh \to b\bar{b}b\bar{b}$ in Ref. [100], using $L_{\text{int}} = 17.93$ fb^{-1} at $\sqrt{s} = 8$ TeV for masses $m_\phi = 270 - 1100$ GeV. The expected exclusion lies in the range $\sigma_{\text{exp}} \approx 6000 - 10$ fb, and no significant excess is observed.

Finally, the CMS search in Ref. [101] is performed for the decay chain $A \to Zh \to l\bar{l}b\bar{b}$, where the leptonic decays of the Z are either electrons or muons. The data sample used amounts to $L_{\text{int}} = 19.7$ fb^{-1} at $\sqrt{s} = 8$ TeV. Constraints on the mass of the Higgs boson and the Z are used. The model-independent cross-section exclusion in $m_\phi = 225 - 600$ GeV reveals a local excess at $m_\phi = 560$ GeV with a significance of 2.6σ, which is reduced to a global significance of 1.1σ after taking into account the *look-elsewhere-effect* [102]. Excluded cross-sections are in the range $\sigma \approx 18 - 2$ fb.

3.4 Indirect Constraints on the Neutral MSSM Higgs Boson

In addition to the direct searches already discussed, other measurements exist that are able to constrain the neutral MSSM Higgs sector.

The branching ratio of the decay $B_s \to \mu^+\mu^-$, where B_s is a meson composed of a b and an s quark, is sensitive to the existence of sparticles as well as additional Higgs bosons. The SM process is dominated by flavour changing neutral currents induced at 1-loop level and features a small branching ratio of $\approx 10^{-9}$. Effects predicted by the MSSM are dominated by the coupling between the heavy states H/A and a flavour changing neutral current $b \to s$ also induced at a 1-loop level. Evidence for the process $B_s \to \mu^+\mu^-$ was first reported by the LHCb collaboration in Ref. [103]. The most recent determination of its branching ratio comes from the combination of LHCb and CMS results [104] and is $\text{BR}(B_s \to \mu^+\mu^-) = (2.9 \pm 0.7) \times 10^{-9}$, compatible with the SM expectation. This measurement allows the high-tanβ portion of the $(m_A, \tan\beta)$ plane to be constrained. However, such a constraint is highly dependent on the MSSM scenario, as discussed in Ref. [105].

The process $B \to X_s\gamma$, where the meson X in the final state contains an s quark, also features a loop which could contain particles predicted in the MSSM. The BaBar experiment has recently updated its measurement of $\text{BR}(B \to X_s\gamma)$ [106], modifying the world average. The updated result is $\text{BR}(B \to X_s\gamma) = (3.43 \pm 0.22) \times 10^{-4}$ in very good agreement with the SM prediction. This measurement excludes the region in the $(m_A, \tan\beta)$ plane lower than $m_A \approx 300$ GeV as shown in Ref. [105].

The XENON100 collaboration has set stringent limits on the scattering cross-section between dark matter and nucleons, going as low as $\sigma < 2 \times 10^{-45}\text{cm}^2$ for dark matter masses of $O(100\text{ GeV})$ [107]. If we regard the dark matter candidate to be the lightest neutralino, the cross-section of its scattering on a proton strongly depends on the bino and higgsino masses M_1 and μ, respectively. If those particles are

maximally mixed ($M_1 \approx \mu$) we obtain the strongest constraint, ruling out tanβ values as high as tan$\beta \approx 60$ at $m_A \approx 1.2$ TeV [105].

The anomalous magnetic moment of the muon, $a_\mu = (g-2)_\mu/2$, is one of the most precise physical measurements. Its sensitivity to the MSSM comes from the contribution of sparticles in the loop corrections to it. Experimental results on a_μ show a deviation with respect to the SM expectation. The experimental value is $a_{\mu,\text{exp}} = 11659208.0 \pm 5.4$ (stat.) ± 3.3 (syst.) $\times 10^{-10}$ [37], while the SM expectation is $a_{\mu,\text{exp}} = 11659180.2.0 \pm 4.9$ (theor.) $\times 10^{-10}$ [108], corresponding to a significance of the discrepancy of $\approx 4\sigma$. The precise experimental determination challenges the theoretical uncertainties, therefore large effort is dedicated to improve both the SM and MSSM calculations as illustrated in Ref. [109].

3.4.1 MSSM Constraints from SM Higgs Coupling Measurements

More indirect constraints on the MSSM parameter space come from the measurement of the couplings and the mass of the Higgs particle discovered at the LHC. The ATLAS collaboration has published a study in Ref. [110] based on such measurements performed at $\sqrt{s} = 7$ TeV with $L_{\text{int}} = 4.8$ fb^{-1} and at $\sqrt{s} = 8$ TeV with $L_{\text{int}} = 20.3$ fb^{-1}. Those measurements have already been discussed in Sec. 3.1. This study relies on a simplified version of the MSSM [111, 112] where the mass mixing matrix of the CP-even states is exploited to express all the couplings as a function of only m_A and tanβ. This is possible after fixing the value of m_h to $m_h = 125.5$ GeV, which allows one to express all the relevant radiative corrections as a function of these two parameters. The resulting exclusion limit at 95% CL in the (m_A, tanβ) plane is shown in Fig. 3.8. The observed data are perfectly consistent with the decoupling limit of the MSSM, where $m_A \gg m_Z$ and the h boson couplings tend to the SM ones. It has to be pointed out that such a result is only valid in this simplified version of the MSSM.

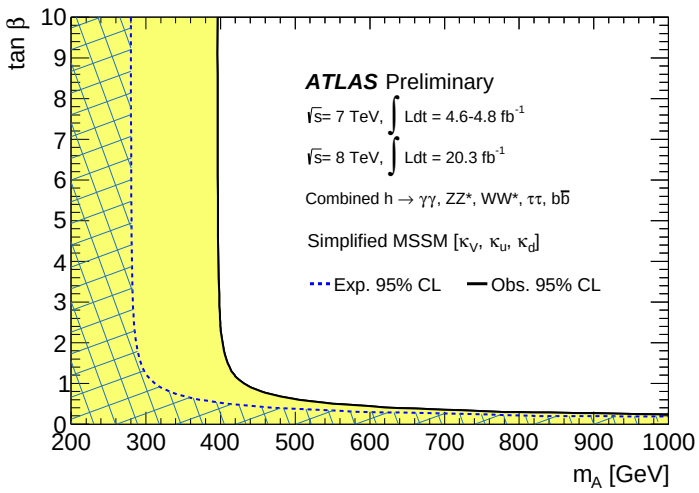

Figure 3.8: Exclusion limit at 95% CL in the (m_A, tanβ) plane, for a simplified version of the MSSM [111, 112], obtained using the measured couplings of the discovered Higgs boson to all the final states indicated in the plot. The limit is taken from Ref. [110].

CHAPTER 4

LHC and the ATLAS Experiment

New physics phenomena can be searched for at particle accelerators which produce collisions of particles at a fixed center-of-mass energy $\sqrt{s}$. The ability to generate collisions at high energies is fundamental to probe the energy scales where new physics might be discovered.

The most powerful particle collider to date is the *Large Hadron Collider* (LHC) located near Geneva, in Switzerland, at the *Conseil Européen pour la Recherche Nucléaire* (CERN). This machine can be operated at the highest energies ever achieved in the history of particle colliders. The search documented in this thesis is based on data collected with the ATLAS detector in the proton-proton collisions produced at the LHC.

The present chapter describes the LHC and the ATLAS experiment in detail. In Sec. 4.1, the accelerator is presented along with the details of its operation during the first period of data taking, the so-called Run-I. In Sec. 4.2, the ATLAS detector is described, and its relevant components, including the ATLAS trigger system. In Sec. 4.3, the simulation of the ATLAS detector is illustrated, to be integrated with the Monte Carlo simulation previously discussed in Sec. 2.4.

4.1 The Large Hadron Collider

The Large Hadron Collider [4] is a synchrotron [18] with a circumference of 26.7 km. It's located under the ground at a depth ranging between $\approx$ 50 m and $\approx$ 175 m. Two particle beams are accelerated inside adjacent ultra-high vacuum ($> 10^{-9}$ bar) cavities. Collisions can take place in four points of the accelerator where the four experiments are placed: ATLAS, CMS, LHCb and ALICE. Experiments other than ATLAS are discussed briefly in Sec. 4.1.1. The LHC is designed to accelerate beams of protons as well as heavy nuclei, typically lead ions (Pb). For protons, the designed center-of-mass energy of the collisions is $\sqrt{s} = 14$ TeV, with energetically symmetric beams. For heavy ions, energies up to 5.5 TeV per nucleon pair can be achieved.

At the LHC, particle beams are bent by a magnetic field created by 1232 super-conducting dipole magnets, with a length of 15 m each, operating at a temperature of 1.9 K. These magnets are designed to provide magnetic fields of 8.33 T. Super-conducting quadrupoles are used to focus or defocus the beam, each with a length of 7 m, and to compensate for the energy loss caused by synchrotron radiation [18]. The particles are accelerated using electric fields generated by 8 super-conducting cavities operating at a frequency of 400 MHz, which increase the beam energy by 485 keV per turn.

The acceleration of protons starts with their extraction from a bottle containing gaseous hydrogen which is ionised. After this, protons are injected in a linear accelerator (LINAC2) which brings their

energy to 50 MeV. They are then injected into a circular booster where they reach 1.4 GeV. Before being transferred to the LHC, protons are further accelerated by the Proton Synchrotron (PS) and by the Super Proton Synchrotron (SPS), where they reach 26 GeV and 450 GeV, respectively. In the PS a *bunch train* structure is generated, which is the one used for LHC collisions. At design conditions, this structure corresponds to 72 close bunches separated by a 25 ns spacing. They are grouped in *bunch trains* separated by a 320 ns time gap. Under these conditions, the bunch crossing occurs at a frequency of 40 MHz at the interaction points. However, the configuration is subject to changes and a 50 ns bunch spacing was used for collisions in 2011 and 2012. The proton acceleration chain at the LHC is schematically illustrated in Fig. 4.1. At design operation the LHC is filled with 39 bunch trains, therefore 2808 bunches per beam

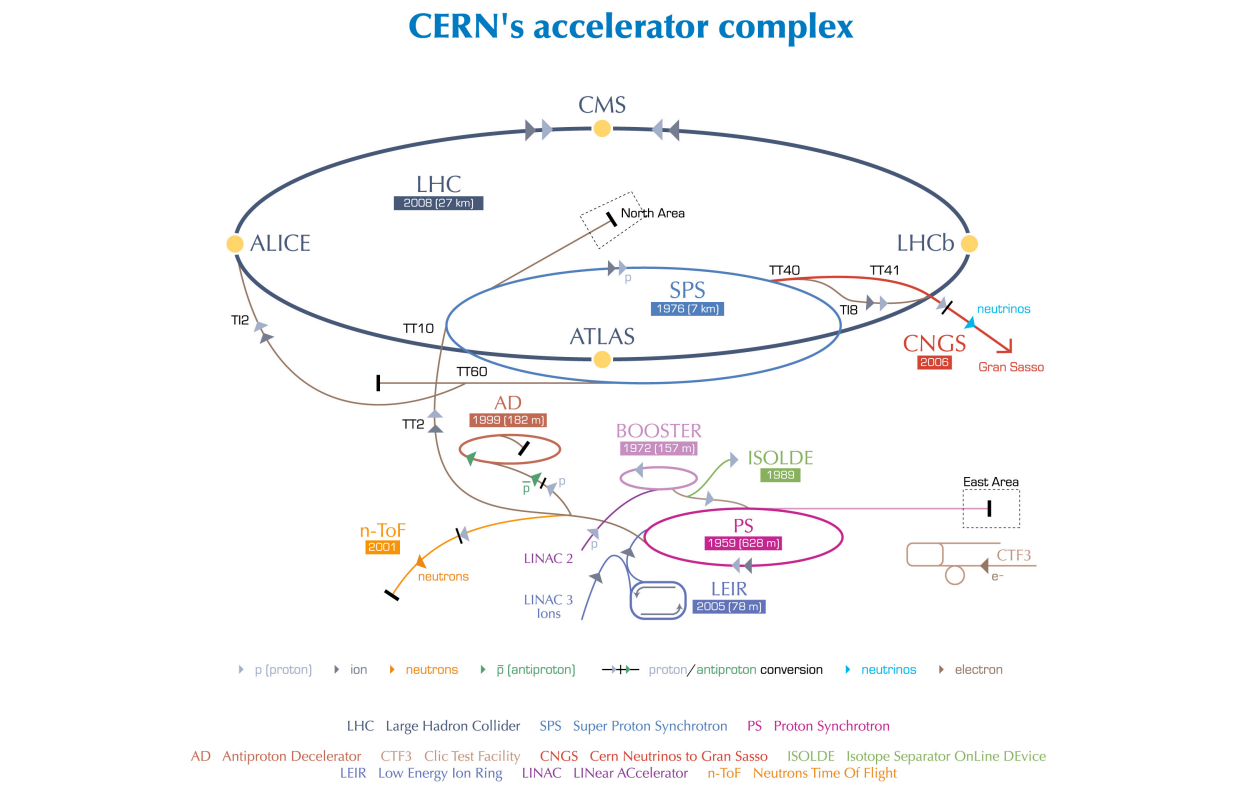

Figure 4.1: CERN accelerator complex including the LHC and the accelerators used for the beam injection: LINAC2, BOOSTER, PS and SPS. The image is taken from Ref. [113].

are collided, each of them containing approximately 10^{11} protons. Instantaneous luminosities as high as $L = 10^{34}$ cm^{-2} s^{-1} can be achieved at the interaction points where the two experiments ATLAS and CMS are located.

The high instantaneous luminosity reached at the LHC and the high energy of the beams are the most important factors making this machine very competitive. As illustrated by Eq. (2.81), the number of events produced, hence the statistical power of a search, is directly proportional to the luminosity. The trend of the cross-sections for the relevant processes produced in proton-(anti)proton collisions as a function of the center-of-mass energy is reported in Fig. 4.2, also indicating the Tevatron and the LHC design working points. The advantage coming from high interaction rates, however, comes at the expense of overlapping proton-proton interactions in the event, a phenomenon called *pile-up*. This occurs

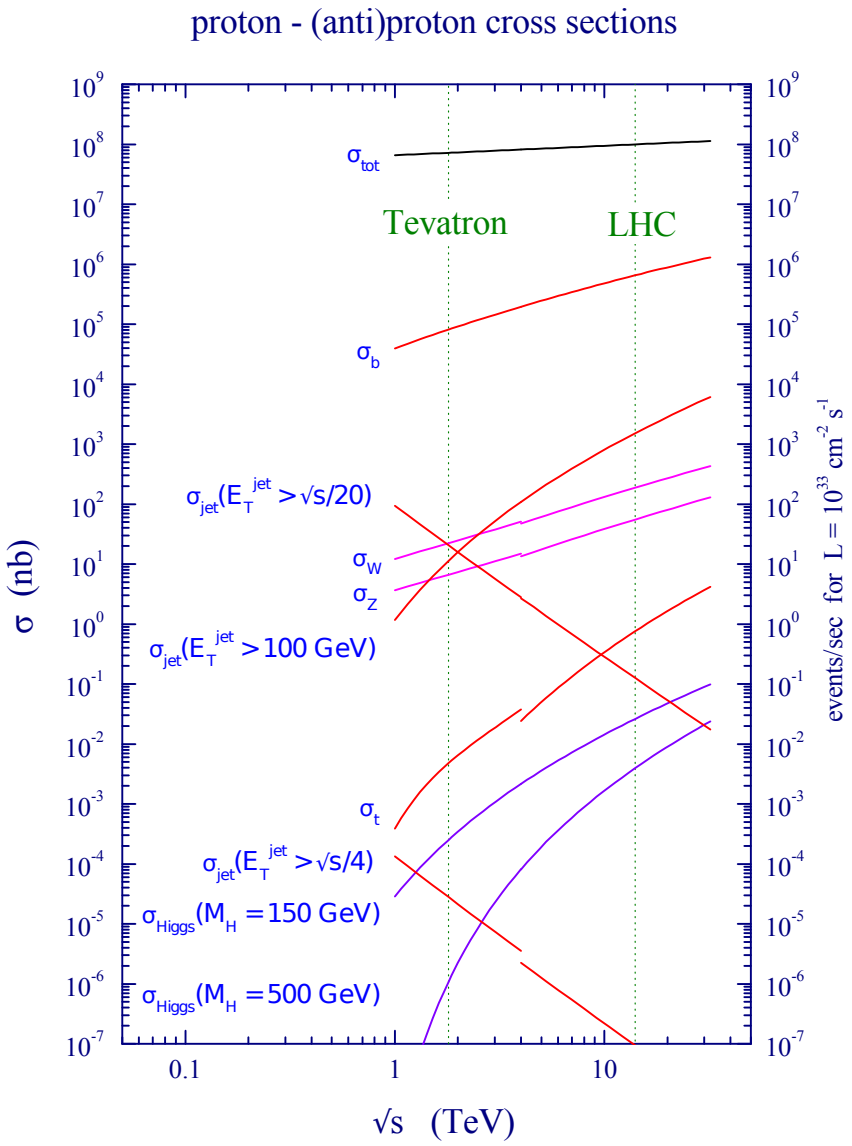

Figure 4.2: Cross-sections as a function of the center-of-mass energy for processes relevant at a proton-(anti)proton collider. The two vertical lines indicate the center-of-mass energies of the Tevatron (proton-antiproton at $\sqrt{s}$ = 1.96 TeV), and the LHC (proton-proton at $\sqrt{s}$ = 14 TeV.) The plot is taken from Ref. [114].

either in the same bunch crossing (*in-time pile-up*), or in different ones (*out-of-time pile-up*). The latter phenomenon is relevant if the signal acquisition by the detector is slower than the typical bunch spacing. In general, pile-up affects the reconstruction performance of the physical objects and has to be controlled.

4.1.1 LHC Experiments

The four experiments located at the collision points are designed for different purposes. The ATLAS [115] (*A Toroidal LHC ApparatuS*) and CMS [116] (*Compact Muon Solenoid*) experiments are multi-purpose detectors intended to pursue a broad physics program, performing precision measurements of known Standard Model processes, as well as probing the Higgs boson sector and searching for new physics phenomena. The two experiments make use of different arrangements of similar technologies for particle detection. The LHCb experiment [117] (*Large Hadron Collider beauty*) was designed to investigate hadrons containing b quarks, *b-hadrons*, with the purpose of studying CP violation as well as new physics in the b quark sector. The ALICE detector [118] (*A Large Ion Collider Experiment*) is specifically designed to collect data from Pb-Pb interactions, with the aim of studying the quark-gluon plasma [119], a new physical state where such particles are de-confined.

Further experiments at the LHC are TOTEM [120] (*TOTal Elastic and diffractive cross-section Measurement*), located near the CMS experiment and studying the low angle proton-proton scattering, and LHCf [121] (*Large Hadron Collider forward*), located on the beam line near the ATLAS experiment, which uses mesons from the collisions emitted in the forward direction to simulate cosmic rays in laboratory conditions. Finally, the MoEDAL experiment [122] (*MOnopole and Exotics Detector At the LHC*) performs the search for magnetic monopoles.

4.1.2 LHC Operation and Data Acquisition at ATLAS

LHC operations began in 2008 but soon stopped due to a connection failure of the magnets system. After this, data taking started in 2009 and stopped at the end of 2012 after completion of Run-I. During 2013/14, the LHC underwent an upgrade necessary to reach the design parameters of the machine and started operation again in early 2015 at $\sqrt{s} = 13$ TeV. During Run-I, data was recorded from proton-proton collisions at $\sqrt{s} = 900$ GeV and $\sqrt{s} = 2.36,\ 7,\ 8$ TeV. The total integrated luminosity delivered by the LHC was recorded by the ATLAS experiment with very high efficiency. In 2010, a total integrated luminosity of $L_{\text{int}} = 48.1$ pb^{-1} was provided by the accelerator and collected with 93.6% efficiency, followed by a heavy-ion run in winter 2012/11. Proton-proton collisions in 2011 at $\sqrt{s} = 7$ TeV were recorded by ATLAS with higher than 90% efficiencies, for a total integrated luminosity of $L_{\text{int}} = 5.08$ fb^{-1}, followed again by a further heavy-ion run. At the beginning of 2012, the center-of-mass energy was increased to $\sqrt{s} = 8$ TeV and a luminosity of $L_{\text{int}} = 22.8$ fb^{-1} was achieved by the LHC, allowing ATLAS to collect $L_{\text{int}} = 21.3$ fb^{-1} of data. The LHC delivered luminosity, and the one collected by the ATLAS experiment since the beginning of 2011, are reported in Fig. 4.3 [123].

As previously illustrated, high luminosities increase the amount of pile-up in the events. It has to be noted that the amount of pile-up generated at the LHC during Run-I exceeds the design values. This happened due to the higher number of protons per bunch with respect to the original plan, which allowed to achieve instantaneous luminosities as high as $L = 7.73$ cm^{-2} s^{-1}, even with a bunch spacing of 50 ns. Halving this spacing, i.e. achieving the original design, is one of the main challenges for the next run (Run-II). The average number of interactions per bunch crossing is reported in Fig. 4.4 [123]. The peak luminosities and number of interactions per bunch crossing are reported in Fig. 4.5, from the start of 2010 until the end of Run-I.

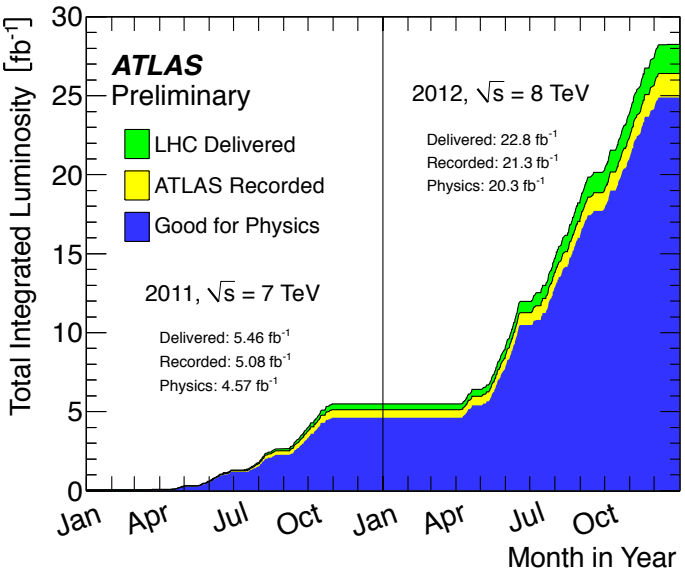

Figure 4.3: Cumulative luminosity from proton-proton collisions at the LHC as a function of time since the beginning of 2011. The plot includes the delivered luminosity by the LHC, the one recorded by the ATLAS experiment and the one flagged as usable for data analysis in ATLAS, due to full and correct operation of all subsystems, indicated as *Good for Physics*. The plot is taken from Ref. [123].

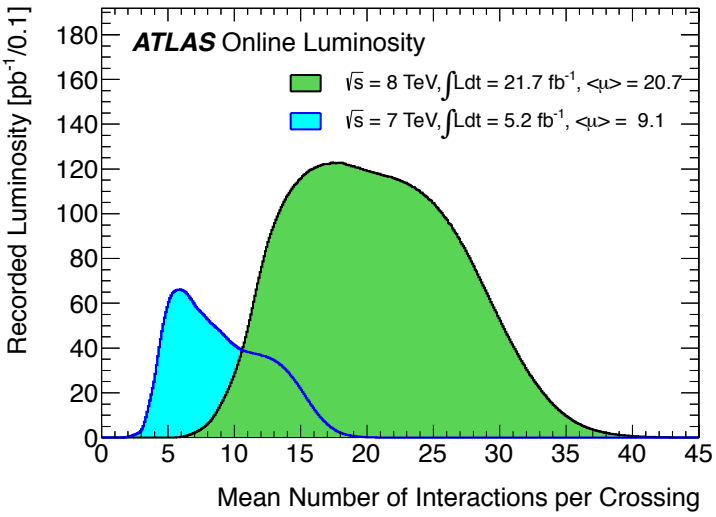

Figure 4.4: Mean number of interactions per bunch crossing, μ, for the data samples collected at $\sqrt{s} = 7$ TeV and $\sqrt{s} = 8$ TeV. The mean of the distributions is also indicated as $\langle\mu\rangle$. The plot is from Ref. [123].

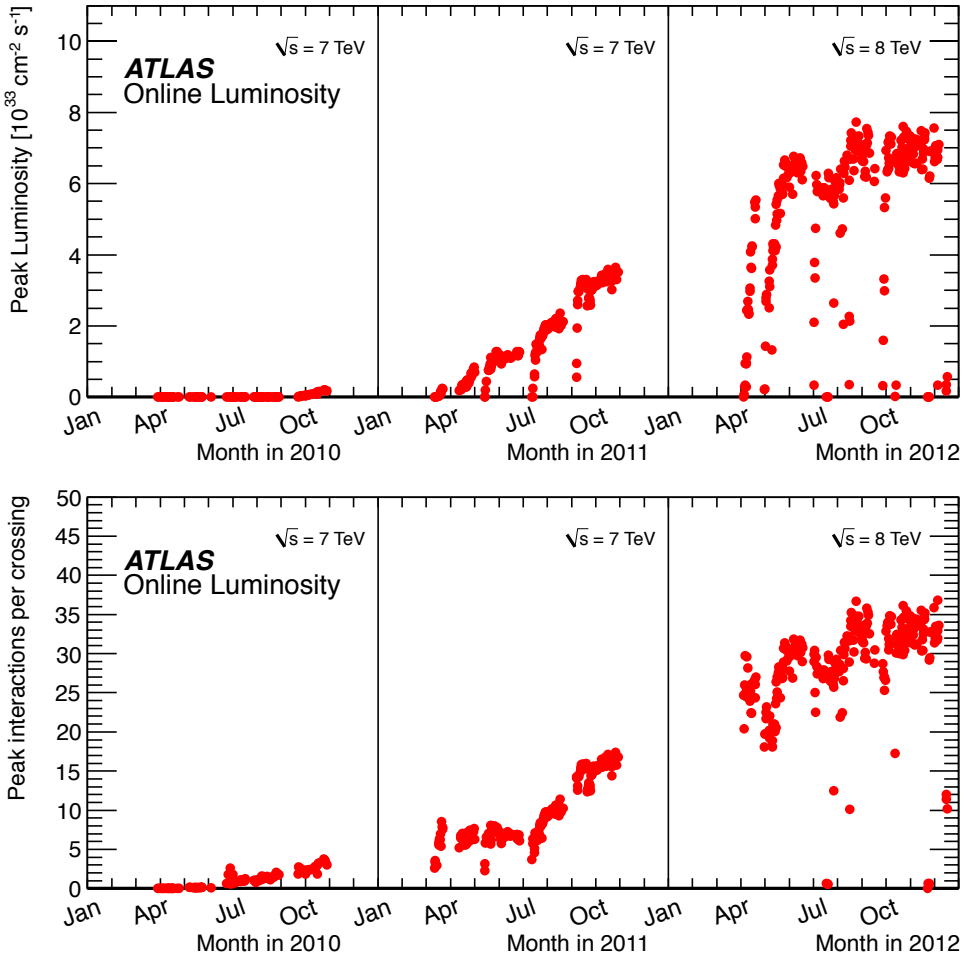

Figure 4.5: Upper plot: maximum instantaneous luminosity delivered to ATLAS in runs between 2010-2012. Lower plot: maximum mean number of interactions per bunch crossing for the same runs. The plots are from Ref. [123].

4.2 The ATLAS Detector

The ATLAS detector was designed to cope with a variety of experimental needs and has been optimised for high interaction rates, radiation doses, particle multiplicities and energies, as well as featuring subdetectors capable of precise measurements of energies and tracks. The detector is symmetric with respect to the plane orthogonal to the beam direction and containing the interaction point, and allows for a nearly complete coverage of the full solid angle (4π). The characteristics of the experiment were designed using the Standard Model Higgs boson signal as a benchmark, although they are compatible with a wide variety of other searches. The ATLAS experiment has been optimised for the following requirements:

- The electronics and the sensors have to be sufficiently fast and radiation-hard due to the demanding experimental conditions of the collisions at the LHC. High granularity of the detectors is also needed due to the high particle fluxes and to reduce the effects of pile-up.
- The geometrical acceptance of the detector should be as large as possible with an almost full solid

angle coverage.

- The subdetector closest to the interaction point, the inner-detector tracker (ID), should provide excellent charged-particle momentum resolution and reconstruction efficiency. This is of particular importance for tau leptons and b jets, i.e. the reconstruction of secondary vertices close to the interaction point.

- Excellent electromagnetic calorimetry for electron and photon identification and energy measurement. This has to be integrated with a very good hadronic calorimetry, in order to provide accurate jet and missing energy measurements.

- Good muon identification and momentum resolution in a wide range of momenta.

- The trigger rate for the processes of interest has to be kept at a reasonable level, requiring good background rejection while keeping high signal efficiencies.

The ATLAS detector, schematically illustrated in Fig. 4.6, is a large forward-backward symmetric structure approximately 25 m high and 44 m long. The central region is referred to as the *barrel*, while the forward and backward regions are called the *end-caps*.

The inner part of the detector is immersed in a solenoidal magnetic field generated by a thin superconducting solenoid surrounding the inner detector, which is able to generate a magnetic field of 2 T, with field lines parallel to the beam pipe. The inner detector is composed of high-resolution silicon semiconductor pixel and strip detectors, in the core, and straw-tube tracking detectors in the outer part, which are able to generate and detect transition radiation. This internal region is enclosed within a high-granularity liquid-argon (LAr) electromagnetic sampling calorimeter, which is surrounded by the hadronic calorimeter. The outermost part of the detector is the muon spectrometer, integrated within an eight-fold air-core magnetic system for the generation of a toroidal magnetic field. Excellent muon momentum resolution is achieved with three layers of high precision tracking chambers. The following sections describe all components of the ATLAS detector in more detail. This short review is based on Ref. [115, 124].

4.2.1 Coordinate System and Kinematic Variables

The ATLAS coordinate system relies on the definition of a three dimensional cartesian space $(x,\ y,\ z)$ where the origin is the interaction point. The x axis points towards the center of the LHC, the y axis upwards, and the z axis in the direction of the beam pipe. A cylindrical coordinate system is defined $(r,\ \theta,\ \phi)$, with $r = \sqrt{x^2 + y^2}$, the polar angle $\theta = \arctan(r/z)$ and the azimuthal angle $\phi = \arctan(y/x)$. Kinematic variables are defined in terms of their transverse components, as the longitudinal kinematics is poorly constrained due to the internal momenta of the partons inside the protons and the high boost of these particles along z. We will use the transverse momentum p_{T}, as defined in Tab. 4.1, as well as the transverse energy $E_{\mathrm{T}} = \sqrt{m^2 + p_{\mathrm{T}}^2}$ defined for an object with mass m. The *pseudo-rapidity*, defined in Tab. 4.1, is of particular importance, which is often used instead of the polar angle θ. Given the *rapidity* y, also defined in Tab. 4.1, we have that $y \to \eta$ for massless particles. The rapidity is invariant under a Lorentz transformation [15] along the z axis (*boost*). This is not true for the pseudo-rapidity, however, differences in pseudo-rapidity are invariant. Thanks to this property, we are able to work with distances in the $(\eta,\ \phi)$ space, ΔR, which are well defined independently of the longitudinal kinematics of the physical objects.

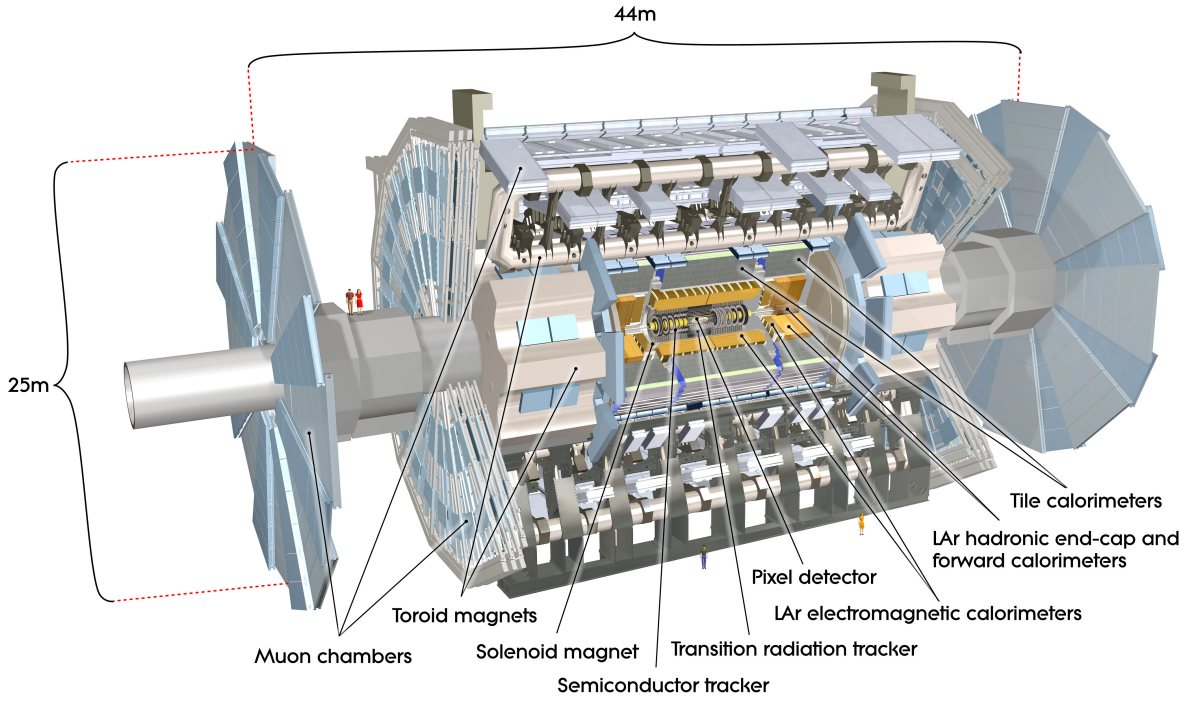

Figure 4.6: Schematic overview of the ATLAS detector with its subdetectors. From Ref. [115].

Variable	Definition
Four-momentum	$p = (E,\ p_x,\ p_y,\ p_z)$
Transverse momentum	$p_\mathrm{T} = \sqrt{p_x^2 + p_y^2}$
Polar angle	$\phi = \arctan\left(\frac{p_y}{p_x}\right)$
Azimuthal angle	$\theta = \arctan\left(\frac{p_\mathrm{T}}{p_z}\right)$
Rapidity	$y = \frac{1}{2}\ln\left(\frac{E+p_z}{E-p_z}\right)$
Pseudo-rapidity	$\eta = -\ln\left(\tan\frac{\theta}{2}\right)$
Azimuthal distance	$\Delta\phi = \min\{\lvert\phi - \phi'\rvert,\ \pi - \lvert\phi - \phi'\rvert\}$
Pseudo-rapidity distance	$\Delta\eta = \lvert\eta - \eta'\rvert$
(η, ϕ) distance	$\Delta R = \sqrt{(\Delta\eta)^2 + (\Delta\phi)^2}$

Table 4.1: Definition of variables relevant at ATLAS.

Another fundamental quantity relevant for the analysis is called the *missing transverse energy*, $\mathbf{E}_{\mathrm{T}}^{\mathrm{miss}}$. It is a vector in the transverse plane defined as

$$\mathbf{E}_{\mathrm{T}}^{\mathrm{miss}} = -\sum_{i} \mathbf{p}_{\mathrm{T},i}, \tag{4.1}$$

where the index i runs over all transverse momentum vectors associated with the objects in the event. The value of $|E_{\mathrm{T}}^{\mathrm{miss}}|$ vanishes if the kinematics of the event are balanced in the transverse plane. A non-vanishing value can be related to the presence of particles which escape detection, like neutrinos, which have low probability of interacting with the detector material. It can also be related to energy losses in the event or mis-reconstruction of particles.

4.2.2 The Inner Detector

The ATLAS inner detector (ID) is a tracking system covering the pseudo-rapidity region up to $|\eta| < 2.5$. It is built to provide excellent momentum resolution for measuring the primary vertex of proton-proton interactions and the decay vertex of particles with longer lifetimes [18], such as tau leptons or b-hadrons. It can also provide electron identification and separation from charged pions ($\pi^{\pm}$) for $|\eta| < 2.0$.

The ID is contained within a cylindrical structure, 7024 mm long, with a radius of 1150 mm, and immersed into a solenoidal magnetic field of 2 T, which curves the trajectories of the charged particles in the transverse plane, allowing their momenta to be measured. The lateral section of the ID is shown in Fig. 4.7. The layout of its subdetectors is illustrated in Fig. 4.8. The ID is composed of the *pixel layer*

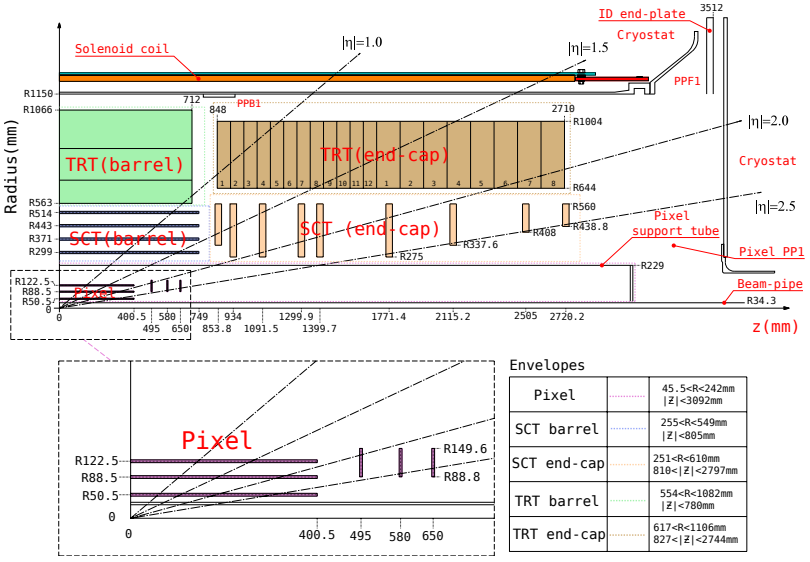

Figure 4.7: Quadrant of the ATLAS inner detector. The image is from Ref. [115].

and *silicon micro-strip* (SCT) detectors, located in the innermost region and capable of high-resolution pattern recognition achievable using discrete space-point measurements. At larger distances from the interaction point and in the region $|\eta| < 2.0$, the *transition radiation tracker* (TRT) is located, composed of many layers of straw-tubes [18, 125] filled with gas interleaved with transition radiation material. A more detailed presentation of all these ID components is given below.

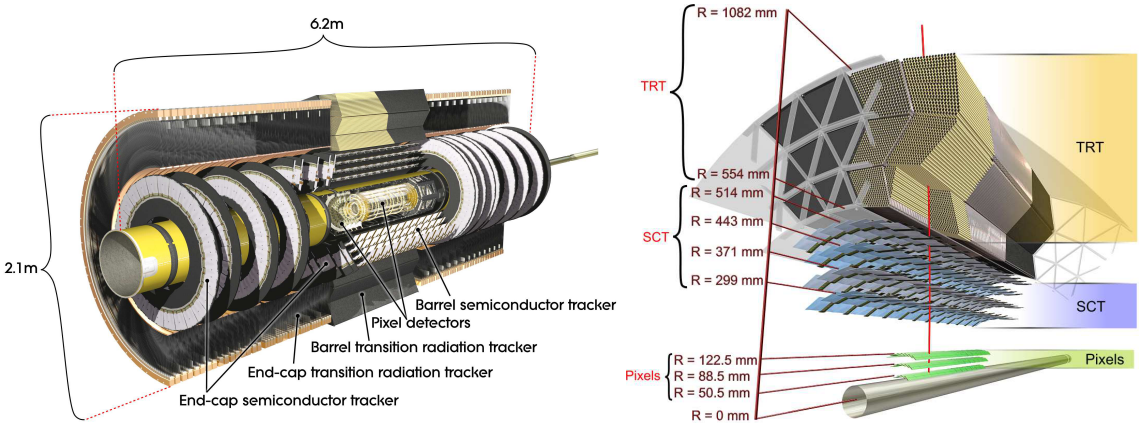

Figure 4.8: Left: the ATLAS inner detector. Right: barrel section of the inner detector illustrating the arrangement of its subcomponents starting from the LHC beam pipe. A typical track is represented by the red line. Both illustrations are from Ref. [115].

Pixel Detector

The ID subdetector closest to the interaction point is the pixel detector. This device consists of three coaxial cylindrical layers in the barrel and three concentrical discs in the end-cap, extending between 5 cm and 12 cm in the radial direction, and covering a pseudo-rapidity range of $|\eta| < 2.5$. The innermost layer in the barrel is called the *B-layer*, and provides crucial information to reconstruct secondary vertices, in particular those from b-hadrons. The entire device is composed of 80.4×10^6 Si sensors with a thickness of 250 μm distributed on 1744 modules. Each pixel has a nominal size of 50×400 μm^2. Each sensor contains a depletion region maintained by an electromagnetic potential up to $V_{\text{bias}} = 600$ V. In this region, ionisation occurs during the passage of a charged particle. The charges produced move under the effect of the electric field and generate a signal in the readout electronics, called a *hit*. A charged particle passing through the layers produces on average three hits in the pixel detector. Each hit has a resolution of 10 μm in the $r - \phi$ plane and 115 μm for both the z and r directions, measured in the barrel layers and the end-cap discs, respectively. The detector is operated at a temperature of 0° C, to suppress electronic noise.

Silicon Micro-strip Tracker

The silicon micro-strip tracker (SCT) is composed of four cylindrical layers in the barrel region plus nine discs in each of the end-caps, and covers a region up to $|\eta| = 2.5$, for at total active area of 63 m^2. The SCT consists of 4088 double-sided modules composed of two back-to-back sensors which are 6 cm long, for a total number of 15912 active sensors segmented in longitudinal strips with a pitch of 80 μm. The two sensors in a module are tilted by ±40 mrad with respect to each other, allowing for the measurement of the z coordinate in the barrel and r in the end-caps. The sensor thickness is approximately 285 μm. Each of them can be operated up to potentials $V_{\text{bias}} = 250 - 250$ V, required after ≈ 10 years of operation to maintain a good charge collection efficiency. Three-dimensional space-points are measured with an accuracy of 17 μm in the $r - \phi$ plane and 580 μm in either z, for the barrel, or r, for the end-cap. On average eight hits per track are provided by the SCT.

Transition Radiation Tracker

The transition radiation tracker (TRT) is built for tracking purposes as well as to provide electron identification and separation from charged mesons, in particular pions. The TRT is composed of 370000 drift tubes (*straws*) with a diameter of 4 mm and 144 cm long, and covers the pseudo-rapidity region up to $|\eta| = 2$. The straw tubes are made of kapton and are covered by a conductive film. They are aligned with the beam pipe in the barrel and arranged radially in the end-caps. Each tube is filled with a $Xe/CO_2/O_2$ gas mixture and contains at its center a gold-plated tungsten wire with a diameter of 30 μm. An electric field is present between the tube, serving as a cathode, and the anode wire. Electron-ion pairs are generated by an ionising charged particle in the gas and drift in the volume producing a signal. The coordinate measurement is performed using a drift-time measurement resulting in a spatial resolution of 130 μm on the distance between the charged particle track and the wire. No measurement of z is provided by the TRT.

The $e^{\pm}/\pi^{\pm}$ separation is achieved by using the energy depositions in the TRT. The straws are interleaved with fibers of polypropylen/polyethilen. When particles cross these layers, they emit photon radiation with an intensity proportional to the Lorentz γ factor, therefore inversely proportional to the mass of the particle. Given that $m_\pi \approx 273 m_e$, photons are suppressed for pions (or heavier particles) with respect to electrons. Two energy thresholds are then optimised for tracking and $e^{\pm}/\pi^{\pm}$ discrimination.

The poorer spatial resolution of the TRT, compared to the pixel detector or the SCT, is compensated by the large number of hits per track, which is 36 in total.

Material Budget

The material budget of the ID can significantly affect the tracking efficiency and the momentum resolution of charged particles. In addition to this, the following can happen:

- Electrons can lose their energy via photon emission before reaching the calorimeter.
- Approximately 40% of photons can convert into electron-positron pair before reaching the calorimeter.
- Hadrons can undergo inelastic hadronic interactions inside the ID volume.

These phenomena lead to an incorrect energy estimate of the initial particle by the calorimeters. For these reasons, the ID material and its effect have to be carefully modelled by the simulation. The ID material budget is illustrated in Fig. 4.9 as a function of $|\eta|$.

4.2.3 The Calorimeter

The purpose of the ATLAS calorimeter is to measure the energy of particles using the total absorption of the particle energy in a bulk of material followed by the measurement of the deposited energy. The energy deposition is mainly due to the ionisation of atoms in the material. On the other hand, particles like highly energetic photons, electrons and hadrons can interact with the material producing secondary particles which lead to a shower development. Calorimeters are optimised to detect electromagnetic and hadron showers and are referred to as *electromagnetic* (ECAL) and *hadronic* (HCAL) calorimeters, respectively.

The ATLAS calorimeter, including the ECAL and HCAL regions, is shown in Fig. 4.10 (left). The calorimeter region extends up to $|\eta| = 4.9$. The ECAL is characterised by a fine granularity and is ideally suited for precision measurements of electrons and photons, while the coarser segmentation of the HCAL

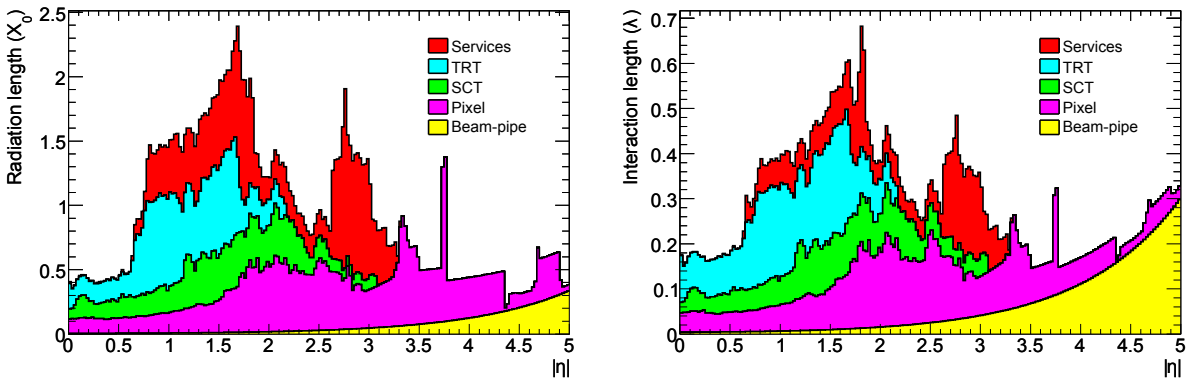

Figure 4.9: Material distribution in $|\eta|$ outside of the inner detector envelope, as seen by a straight track traversing the detector. The distribution is shown in units of the radiation length X_0 [18, 125] on the left, and interaction length λ [18, 125] on the right. Both distributions are averaged over ϕ. The plot is from Ref. [115].

is sufficient to provide good jet energy resolution and $\mathbf{E}_{\mathrm{T}}^{\mathrm{miss}}$ measurement. As particle showers have to be contained within the bulk of the calorimeter, the depth of this detector is an important design parameter. The thickness of the ATLAS ECAL is > 22 X_0 in the barrel and > 24 X_0 in the end-caps, where X_0 is the radiation length [18, 125], defined as the path length necessary to reduce the particle energy by $1/e$ due to photon radiation. The HCAL thickness is measured in units of the interaction length [18, 125], λ, defined as the mean path length required to reduce the number of particles in a shower by $1/e$, and amounts to 9.7 λ in the barrel and 10 λ in the end-cap.

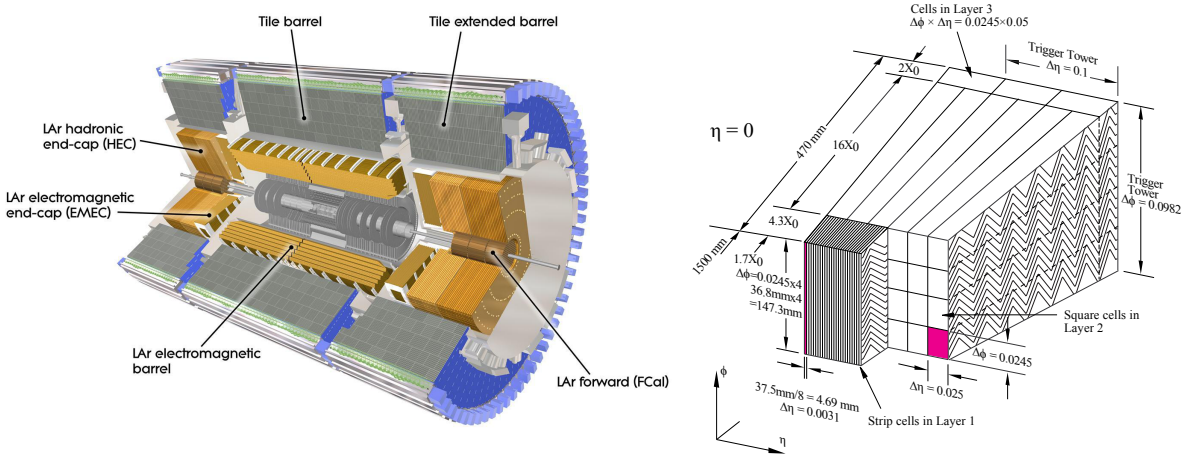

Figure 4.10: Left: Calorimeter system of the ATLAS experiment. Both the electromagnetic calorimeter (ECAL) and the hadronic calorimeter (HCAL) are shown. Right: Module of the ECAL illustrating its granularity. The values reported are for the barrel at $\eta = 0$. From Ref. [115].

Electromagnetic Calorimeter

The ATLAS ECAL is divided into a barrel region covering $|\eta| < 1.475$ and two end-cap regions covering $1.375 < |\eta| < 3.2$ (EMEC). The barrel region itself is composed of two half-barrels separated by a gap of 4 mm at $z = 0$, extending up to $|z| = 3.2$ m with a radial coverage of $r = 2.8 - 4$ m. Each end-cap section

is divided in two coaxial wheels, an external one covering $1.375 < |\eta| < 2.5$ and an internal one covering $1.375 < |\eta| < 3.2$. They are 63 cm thick and range from $r = 33$ cm to $r = 209.8$ cm.

The ATLAS ECAL is a *sampling* calorimeter, where only a fraction of the energy is detected, which is deposited in active layers alternated with layers of absorbing material. In the ECAL, the active material is LAr and the absorber is lead. The readout electronics uses kapton electrodes. The calorimeter has an accordion geometry, as shown in Fig. 4.10 on the right, in order to provide complete ϕ coverage without azimuthal cracks. In the barrel, the accordion waves are axial and run in ϕ, while in the end-cap they are parallel to the radial direction and run axially. As shown in the figure, the ECAL is divided in three regions with different granularities: the first one, called the *strip layer*, is finely segmented in η, the second is coarser, collecting the majority of the shower, while the third is the less segmented and collects only the tail of the shower. Fig. 4.10 shows the different granularities of the layers in $\Delta\phi \times \Delta\eta$, only for the barrel section. Coarser segmentations are used in the end-cap. Excellent energy resolution of approximately $\sigma_E/E = 10\%/\sqrt{E/\mathrm{GeV}} \oplus 0.7\%$ is provided by the ATLAS ECAL. The fine segmentation of the strip layer is particularly useful to identify the decays $\pi^0 \to \gamma\gamma$, which is relevant for the reconstruction and identification of the tau decay, as will be illustrated later.

As mentioned in Sec. 4.2.2, phenomena occurring upstream of the calorimeter region might lead to an incorrect energy estimate for electrons or photons. In order to correct for this, a *pre-sampler* detector is used in the region $|\eta| < 1.8$, consisting of a 1.1 (0.5) cm thick LAr layer in the barrel (end-caps). The pre-sampler is used to measure showers occurring before the calorimeter.

Hadronic Calorimeter

The hadronic calorimeter uses different technologies depending on the $|\eta|$ region. The so-called *tile calorimeter* is composed of a barrel and two end-cap sections, ranging over $|\eta| < 1.0$ and $0.8 < |\eta| < 1.7$, respectively. Radially, it extends from $r = 2.28$ m to $r = 4.25$ m, and is divided in depth in three layers with different thickness in λ. At $\eta = 0$ the total detector thickness is 9.7 λ. The depth in λ of the three layers as a function of $|\eta|$ is illustrated in Fig. 4.11. The tile calorimeter is a sampling calorimeter, where steel is used as the absorber and scintillating tiles as the active material, for a total amount of 64 modules divided azimuthally. Its granularity is coarser than for the ECAL, due to the larger dimension of hadronic showers compared to electromagnetic ones. The segmentation of the barrel cells is $\Delta\phi \times \Delta\eta = 0.1 \times 0.1$ for the first two layers, while the $\Delta\eta$ granularity is twice as coarse for the third layer.

In the forward region of the detector, the hadronic calorimeter is composed of two independent wheels per end-cap (*hadronic end-cap calorimeter*, HEC), behind the ECAL section. The HEC covers the range $1.5 < |\eta| < 3.2$. Each wheel is composed of 32 modules and divided into two layers. Also the HEC is a sampling calorimeter, where the absorbing material is copper and the active material liquid argon. Closer to the interaction point, the wheels are composed of 25 mm parallel copper plates, while for the outer wheels 50 mm plates are used. These plates have inner and outer radii of 0.475 m and 2.03 m, respectively. They are interleaved with 8.55 mm thick LAr gaps. The granularity of the HEC is $\Delta\phi \times \Delta\eta = 0.1 \times 0.1$ up to $|\eta| < 2.5$ and twice as coarse beyond.

The forward region of the end-cap ($3.1 < |\eta| < 4.9$) is covered by the *forward calorimeter* (FCal), which is a combined electromagnetic and hadronic sampling calorimeter using LAr as active material. The FCal is located 4.7 m away from the interaction point up to 6.1 m. It is composed of three layers where the first is optimised for electromagnetic showers, using copper as the absorber, and the last two for hadronic showers, where tungsten is utilised. Each layer is segmented in plates featuring holes into which electrode structures are inserted. They are composed of a coaxial rod and a tube made of absorber material, separated by LAr.

The typical hadron energy resolution provided by the HCAL is $\sigma_E/E = 50\%/\sqrt{E/\mathrm{GeV}} \oplus 3\%$ for the

barrel and end-cap regions, while for the forward calorimeter it is $\sigma_E/E = 100\%/\sqrt{E/\text{GeV}} \oplus 10\%$.

The material distribution of the entire calorimeter system, including both the electromagnetic and hadronic portions, is reported in Fig. 4.11, as a function of $|\eta|$ and in units of the interaction length. The entire calorimeter system has a thickness of at least 10 λ, providing good coverage in pseudo-rapidity, and good shower containment.

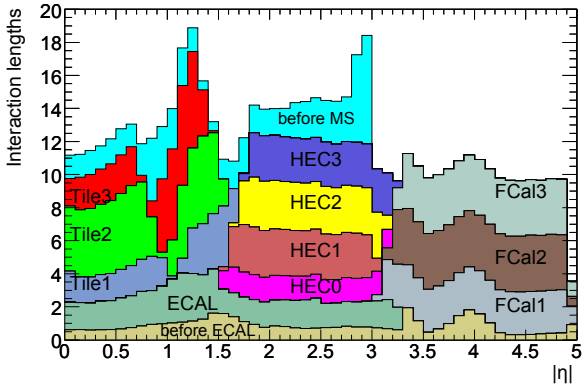

Figure 4.11: Material distribution of the ATLAS calorimeter system as a function of $|\eta|$ and in units of the interaction length λ. All layers of the hadronic calorimeter are shown separately. The material distribution before the calorimeter is indicated as "*before ECAL*". For completeness, the material distribution just outside the calorimeter, and in front of the muon spectrometer, is also included, indicated as "*before MS*". The plot is from Ref. [115].

4.2.4 The Muon Spectrometer

Outside the calorimeter, the ATLAS muon spectrometer (MS) is installed, which measures the muon momenta. The momentum of the muon is not significantly altered after traversing the calorimeter, due to the typical muon energies featured in LHC events, which make these leptons *minimum-ionising particles* [18]. The MS is immersed in a toroidal magnetic field, with field lines running mainly in the transverse plane, therefore bending the muon trajectories in a plane containing the beam pipe, the so-called *bending plane*. The magnetic field is generated by superconducting coils with an eight-fold geometry, as shown in Fig. 4.12 on the left, present in the barrel ($|\eta| < 1.4$) and in the end-caps ($1.6 < |\eta| < 2.7$). The bending power of the magnetic field, $\int B\text{d}l$, ranges from 1.5 Tm to 5.5 Tm in the barrel, and from 1.0 Tm to 7.5 Tm in the end-caps.

The MS uses different technologies for the muon tracking. Up to $|\eta| = 2.7$, *Monitored Drift Tube* chambers (MDT) provide a precision measurement of the muon trajectory in the bending plane. These detectors are present in three layers in the barrel and from three to four layers in the end-caps, as shown in Fig. 4.12 on the right. The chambers are composed of layers of aluminium drift tubes [18, 125], which are orthogonal to the beam pipe and run azimuthally. They have a diameter of 3 cm and contain a tungsten-rhenium wire functioning as the anode. The tubes are filled with an Ar/CO_2 gas mixture. The drift time of the ionisation products is converted into the distance between the muon track and the wire. The MDT chambers provide very high spatial resolution, approximately 35 μm, therefore an excellent monitoring of their alignment is required, which is achieved at the level of 30 μm by an optical system. Drift times of the ions in the gas of $\approx$ 700 ns are typical, therefore making this technology unsuitable for fast acquisition of events or for regions with large radiation fluxes.

In the forward region closer to the interaction point, covering $2.0 < |\eta| < 2.7$ and at $z \approx 7$ m, *Cathode Strip Chambers* (CSC) are used for tracking, which are multi-wire proportional chambers [18, 125] where two cathode plates are separated by a gap hosting anode wires radially oriented and immersed in an Ar/CO_2 gas mixture. Both cathodes are segmented, one parallel to the wires and the other orthogonal to it. A precision in r and ϕ coordinates of 40 μm and 5 mm, respectively, is achieved.

For the fast acquisition of events (*triggering*) and in order to measure the azimuthal coordinate of the tracks, *Resistive Plate Chambers* (RPC) [18, 125] are used in the barrel for $|\eta| < 1.05$ and in the forward region for $|\eta| < 2.0$. These detectors are mounted on two layers surrounding the middle MDT layer in the barrel and in one layer close to the outer MDT one. Each RPC is composed of two plates made of resistive material and hosting the electrodes, which are separated by a 2 mm gaseous gap where fast charge multiplication takes place after the passage of the ionising muon. The electrodes are segmented in the ϕ and z directions for a two-dimensional hit measurement with a precision of 10 mm in each dimension.

In the region of $1.05 < |\eta| < 2.4$, *Thin Gap Chambers* (TGC) are mounted to provide for the trigger and measure the azimuthal coordinate. The TGC detector is a multi-wire proportional chamber, with anode wires oriented in the azimuthal direction placed between radially segmented cathode plates. The hit resolution ranges approximately from 2 mm to 7 mm, for both the radial and azimuthal components.

The muon momentum resolution provided by the MS is a function of the momentum, and ranges approximately from 3% to 10% for 10 GeV $< p_T <$ 1000 GeV.

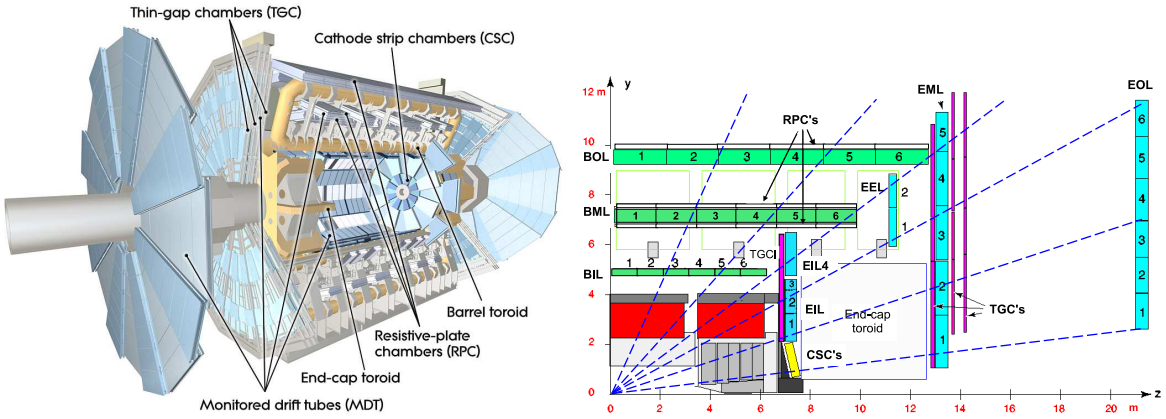

Figure 4.12: Left: Muon spectrometer of the ATLAS detector. The toroidal magnets are also shown. Right: Quadrant of the muon spectrometer showing the arrangement of its subdetectors. MDT chambers are present in the barrel in three layers (BIL, BML, BOL), and four layers in the end-cap (EIL, EEL, EML, EOL). RPC detectors are located near the two outermost MDT layers in the barrel, while four layers of TGC are present in the end-cap. The CSC tracking detector is located in the forward region closer to the interaction point and is indicated in yellow. The pictures are from Ref. [115].

4.2.5 The Forward Detectors

The whole set of ATLAS subdetectors includes forward devices dedicated to the measurement of the luminosity and other beam parameters. They are located along the beam pipe, outside of the ATLAS main volume and far away from the interaction point, as illustrated in Fig. 4.13. The two LUCID detectors (*LUminosity measurement using Cherenkov Integrating Detector*) are located 17 m away from the interaction point. They provide an online measurement of the instantaneous luminosity delivered to

ATLAS by measuring the number of inelastic proton-proton scatterings using an array of 20 Cherenkov tubes [125].

Farther away, the ALFA detectors are collocated (*Absolute Luminosity For ATLAS*), 240 m away from the interaction point. They measure the proton-proton elastic scattering amplitude, which can be related to the total cross-section using the *optical theorem* [15, 16]. These detectors are tracking detectors made of scintillating fibres located inside *Roman Pots* [18], which allow for a scintillator near the beam at variable distances, as close as 1 mm. The ALFA detectors can only be used in dedicated low instantaneous luminosity runs as they are not able to withstand the severe radiation conditions at full luminosity.

The ATLAS luminosity measurement relies on horizontal and vertical beam profile scans called *van der Meer scans* (vdM) [126]. A remarkable precision of ±1.8% [127] was achieved in 2011, while in 2012 a precision of ±2.8% was reached.

Finally, the *zero-degree calorimeter* (ZDC) is located at $z = \pm 140$ m and measures the centrality of heavy ion collisions. All detectors discussed in this section are shown in Fig. 4.13.

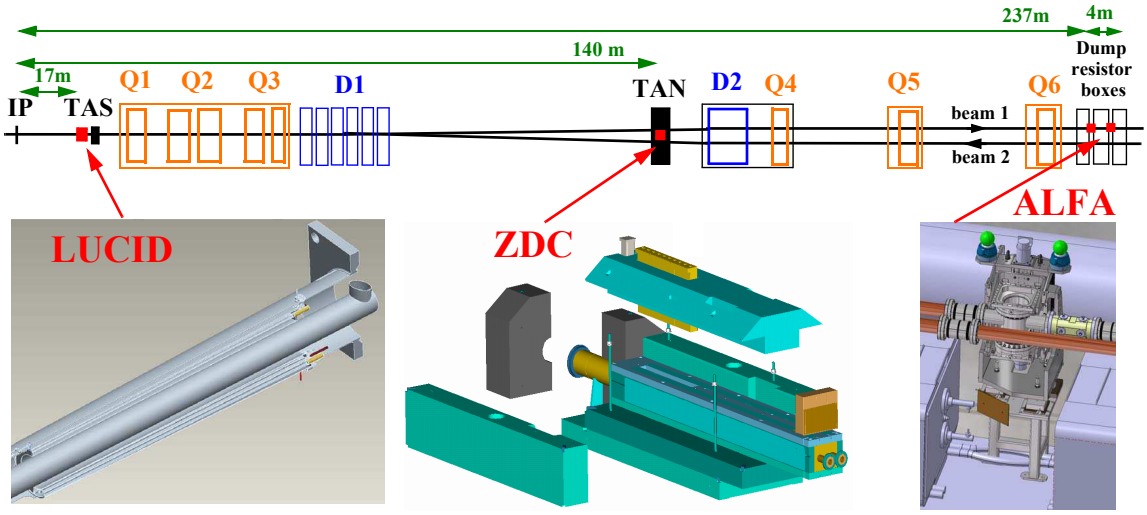

Figure 4.13: The ATLAS forward detector system. From Ref. [115].

4.2.6 The ATLAS Trigger System

With a collision rate of 40 MHz and a typical event size of few MB, it is impossible to store all the events produced in proton-proton collisions at the LHC. An online acquisition system able to select only interesting events has to be used, which is referred to as *trigger*. This system is divided in three levels with the purpose of reducing the recorded event rate down to ≈ 200 Hz at the end of the chain. These stages are called *Level-1 trigger* (L1), implementing a hardware-based decision, *Level-2 trigger* (L2) and *Event Filter* (EF), which are both software-based.

The L1 trigger takes hardware based decisions based on information coming from the calorimeters (L1Calo), the muon chambers (L1Muon) and the scintillators in the forward regions (Minimum Bias). The L1 searches for distinctive signatures of electrons, muons, tau leptons, jets as well as missing transverse energy. A decision is achieved within 2.5 μs by processing data with reduced granularity coming from the RPC and TGC detectors for muons, and from all the calorimeters for the other objects. The selected objects have to fulfill several topological and kinematic criteria to be selected. For instance, their p_{T} or E_{T} has to be larger than a certain threshold, or isolation in the (η, ϕ) plane might be required.

Different criteria are implemented in different *trigger menus*. The L1Calo information comes from the so-called *projective trigger towers*, which are calorimeter regions with reduced granularity, mostly $\Delta\phi \times \Delta\eta = 0.1 \times 0.1$ or larger. The information coming from L1Muon is organised in *roads* defined as conical regions where the hit coincidence coming from different RPC or TGC planes is searched for. The width of a road depends on the magnetic field and the p_{T} of the track. Results from the L1 subsystems are processed by the *Central Trigger Processor* (CTP) which implements a trigger menu based on logical combinations of the L1Calo and L1Muon subsystems. At this stage a pre-scale can be applied, which implements an artificially reduced "event acceptance" in order to make efficient use of the available bandwidth in situations where the luminosity or background conditions change. The L1 trigger supplies information organised in *Regions-of-Interest* (RoI), which consist of the coordinates of the object, as well as the set of criteria it satisfies. The output rate of L1 is $\approx$ 75 kHz.

The L2 trigger uses data with full granularity and relies on software algorithms to refine the selection by L1. At the L2 stage, 2% of the data from L1 are selected based on the RoI information. The nominal output rate of L2, 3.5 kHz, has been exceeded during Run-I where a rate of 5 kHz was achieved [128].

The last stage of the event selection is provided by the EF and works with fully reconstructed events. At this stage, similar algorithms to those used in the offline data analysis are used. The nominal processing time is 4 s per event, with an output rate of $\approx$ 200 Hz, which was also improved in Run-I to $\approx$ 500 Hz [128]. The output from the EF is then written to tape and can be used for physics analysis. The whole trigger chain is illustrated in Fig. 4.14.

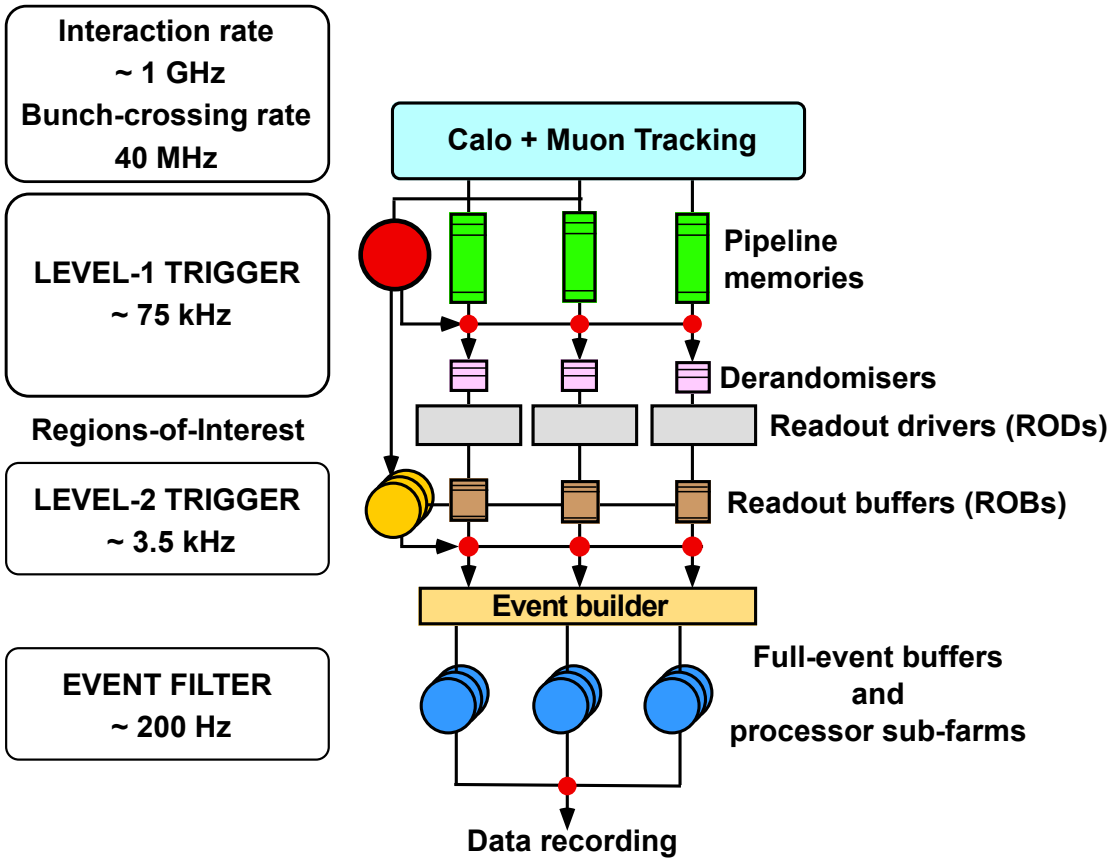

Figure 4.14: Diagram representing the various stages of the ATLAS trigger system. From Ref. [129].

4.3 The ATLAS Detector Simulation

In Sec. 2.4, the simulation of events produced in hadronic collisions was discussed. However, the discussion did not take into account the passage of the particles through the detector. At this intermediate stage of the simulation, simulated particles are referred to as *true particles*. The reconstruction of events in data relies on hits and energy deposits collected in the ATLAS detector. Monte Carlo simulated events have to be reconstructed using the same algorithms used for data, but the detector needs to be simulated in order to provide hit and energy deposit information. The simulation has to model the detector geometry and components, the interaction of the particles with the detector material and pile-up.

The full detector simulation is performed by `GEANT4` [130], a general tool used to simulate the passage of particles through matter, which relies on the complete detector geometry encoded in databases also containing the operation conditions for specific runs. The deposited energy is digitised, converting voltages and currents on a particular readout channel which raise above a certain preconfigured threshold. Pile-up is simulated overlapping different events, whose number depends on the luminosity and is Poisson-distributed. Simulated samples are not always produced after a data-taking period. For this reason the simulated pile-up conditions might need to be corrected using parameters measured in data after a given run.

The full simulation chain is very CPU-consuming and can take up to 15 minutes per event. Simulated samples, requiring a large number of events, can be obtained using a common dedicated framework called `ATLFAST2` [131], where a simplified detector model is used. In addition, the longitudinal and lateral profiles of the showers in the calorimeter are parametrised, rather than fully simulating the energy deposit of single particles.

CHAPTER 5

Object Reconstruction and Identification

In physics analyses we are interested in studying the properties of the events from collision data using comparisons to the simulation. It is important to understand these properties in order to improve the separation between signal and background. The lowest level of information provided by the detector consists of signals from its components, which are either hits or energy deposits. From this information we want to be able to reconstruct the physical objects in the event, meaning all the particles and their four-momenta.

In the present chapter we discuss how physical objects are reconstructed at the ATLAS experiment. The algorithms dedicated to this purpose are implemented in the ATLAS software called `ATHENA` [132]. The whole reconstruction chain reconstructs the particles starting from hits or energy deposits and using intermediate level objects such as tracks and clusters in the calorimeter.

These intermediate objects are the main building blocks of particle reconstruction. They also serve to discriminate between particles required in physics signatures and other particles which look similar in the detector, the so-called *fakes*. An example of fake relevant for this thesis is a jet, similar to the hadronic decay of a tau.

The process of discriminating between particles and their fakes is performed using dedicated algorithms which rely on variables providing discrimination between signal and background, and is known as *particle identification*. Reconstruction and identification are performed with the same algorithms in data and in the simulation but imperfections in the simulation might lead to deviations. Therefore, corrections to the simulated events are often necessary which have to be determined in dedicated studies using data.

In this chapter, the definition of intermediate-level objects is discussed in Sec. 5.1, 5.2 and 5.3, for tracks, vertices and calorimeter clusters, respectively. A brief presentation of the relevant objects for the $h/H/A \to \tau\tau$ analysis is then given, extended to those physical objects used by searches which are combined with $h/H/A \to \tau_{\text{had}}\tau_{\text{had}}$. In Sec. 5.4 and 5.5 muons and electrons are discussed, respectively. The reconstruction of jets and missing transverse energy is presented in Sec.5.6 and 5.7, respectively. Tau leptons are of particular importance for this thesis and are thus discussed in a separate chapter.

5.1 Tracks

In this section, only the reconstruction of tracks as measured by the inner detector is addressed, as those measured by the muon spectrometer are less relevant for this thesis. Tracks from the inner detector are also important to reconstruct primary and secondary vertices in the event. A complete review of all the algorithms used for tracking is given in Ref. [133].

Two main tracking methods are used in ATLAS, the *inside-out* and *outside-in* algorithms. The first step of the inside-out algorithm is the definition of three-dimensional hits from the pixel detector and SCT, which are called *space-point* objects. The two-dimensional hit position provided in the pixel sensors plane is integrated with the position of the sensors itself. For SCT sensors, only the azimuthal coordinate of the hit is measured, using the longitudinal segmentation of the module, while the module position itself, and the stereo angle between its two faces, allow for a determination of the remaining coordinates. A subset of these hits is then selected to *seed* the track-finding algorithm, which relies on a Kalman filter [134] to select track candidates. Many tracks are selected at this stage which have to be resolved, therefore, they are ranked in their likelihood to represent trajectories of real particles. This is done by assigning a score promoting tracks measured by more precise elements of the ID. Tracks falling below a certain quality selection are discarded. Finally, the last step of the algorithm extends the tracks into the TRT using the measurements from this subdetector, looking for compatibility between the two segments. The inside-out algorithm is the baseline for particle momenta $p_{\mathrm{T}} > 400$ MeV.

Situations might occur where seeds from the silicon detectors of the ID are not selected due to ambiguous hits or secondary decays of particles within the ID volume, such as K_S mesons or photon conversions. Also, due to mis-modelling of the material budget, particles might lose substantial energy outside of the silicon detectors, leading to a different track extrapolation in the TRT than predicted by the algorithm, which make the TRT matching inefficient. The outside-in algorithm is designed to cope with these cases, where track seeding starts from the TRT volume followed by back-tracking into the silicon region, relying on hits not selected to seed the inside-out algorithm.

In both algorithms all the points finally associated with the tracks are refitted [135]. Tracks are usually parametrised with the following vector:

$$\text{track parameters} = (d_0, z_0, \phi, \theta, q/p). \tag{5.1}$$

Parameters in this vector are defined with respect to the perigee point, i.e. the point of closest approach of the track with respect to the interaction point in the transverse plane. The distance between these two points is the *transverse impact parameter*, d_0, while z_0 is their longitudinal separation. The angles ϕ and θ also refer to the perigee point, while q/p is the ratio between the charge of the particle, measured by the track curvature, and its momentum. The selection of tracks in physics analyses requires them to satisfy quality criteria, such as a minimum number of hits in the silicon detectors, in order to further improve the quality of these objects. These requirements depend on the type of reconstructed particle.

5.2 Vertices

The algorithm for the reconstruction of primary vertices (PV) firstly selects reconstructed tracks based on quality criteria designed to reject those originating from secondary interactions. The algorithm, called *iterative vertex finding* [136] relies on the definition of the beam-spot center, i.e. the expected collision point determined by measurements of the beam position [137]. The z coordinate of the point of closest approach between the tracks and the beam-spot center is determined. The maximum of its distribution defines the seed vertex of the algorithm. At this point, the vertex is fitted using the seed position and the tracks around it. This step also serves to refit the tracks, constraining them to originate from the collision point. The fit down-weights outlier tracks with a weight which depends on the compatibility between the track and the vertex, as measured by a χ^2 variable [138]. After the fit, tracks with a χ^2 significance of 7σ are used to seed a new vertex. The procedure is repeated until no tracks are left in the event or no new vertex can be found. Vertices with less than two associated tracks are discarded.

Due to pile-up, more than one primary vertex is typically reconstructed in the event. For all tracks

associated with a vertex the quantity $\sum p_{\mathrm{T}}^2$ is calculated, and the primary vertex of the *hard scattering*, V_{HS}, is defined as the one with the largest $\sum p_{\mathrm{T}}^2$ value. All remaining primary vertices are referred to as pile-up vertices.

Physics analyses might need to further match reconstructed tracks to vertices, which is done using geometrical requirements. Usually, a selection of tracks with $\Delta z_0 \sin\theta \lesssim 1$ mm and $\Delta d_0 \lesssim 1$ mm with respect to the vertex position is performed.

5.3 Topological Clusters

Energy deposits in the calorimeter originating from jets or tau leptons decaying hadronically are reconstructed with the so-called *topological cluster algorithm* [139], which has the advantage of efficient noise suppression for clusters with a large number of associated cells. The main idea behind topological clustering is to group neighboring cells with energies significantly above the expected noise, leading to clusters with a variable number of associated cells. The algorithm is divided in two steps, called the *cluster maker* and *cluster splitter*.

During the clustering process, seed cells are defined as those where the signal to noise ratio r is above a large threshold. The ratio is defined as

$$r = \frac{E_{\mathrm{signal}}}{\sqrt{(\sigma_{\mathrm{noise}}^{\mathrm{electronic}})^2 + (\sigma_{\mathrm{noise}}^{\mathrm{pile-up}})^2}} \tag{5.2}$$

and the threshold is $t_{\mathrm{seed}} = 4$. In r, the pile-up noise is estimated from simulations and depends on η and the calorimeter module. Cells are considered over the entire extension of the calorimeter, but might also come from a portion of it as defined in a trigger RoI.

After the seed list is completed, all seed cells are ordered in descending order of r. Clusters are then formed by adding neighboring cells to each seed cell in turn, if they have $r > t_{\mathrm{neighbor}} = 2$ and are not in the seed list. Clusters are merged if a neighbor cell is adjacent to more than one seed. If $t_{\mathrm{neighbor}} > r > t_{\mathrm{cell}}$, with $t_{\mathrm{cell}} = 0$, the cell is added only to the seed with the higher r. After this iteration, the original seed list is discarded and the list of neighbors becomes the new seed list, which is considered for a further iteration. The algorithm is executed until the seed list is empty.

The second part of the algorithm, the cluster splitting, finds local maxima among the energy deposits clustered as previously described. This is done in order to separate individual particles showering in the calorimeter which do not typically lead to isolated clusters, especially in the end-caps and forward calorimeters. Firstly, local maximum cells are defined as the clustered ones with $E > 500$ MeV, at least four neighbouring cells and energy greater than any other neighboring cell. After this, clustering is performed similarly to what already described, but only considering previously clustered cells and without applying thresholds and cluster merging. In this process, cells could be associated with two clusters. These cells are then weighted according to the energy of the clusters and their distance with respect to the cluster centroids. The weights account for the probability of the shared cell to belong to either cluster.

When clusters are reconstructed they are calibrated at the *electromagnetic energy scale* (EM scale), which is defined as the calorimeter calibration suitable to restore the energy deposited by a purely electromagnetic shower. The EM scale is estimated in test-beam measurements. However, the ATLAS calorimeter is non-compensating, meaning that, depending on the nature of the shower (electromagnetic or hadronic) different signals in the detector are obtained, i.e. they have different response. While the EM scale is suitable to be used for electromagnetic showers, corrections have to be made to the deposits from

hadronic showers. During reconstruction, various cluster properties are determined, related to the shower shape and its energy density. Based on these, a probability for the cluster to be of electromagnetic or hadronic origin is assigned. In order to restore the correct energy scale of hadronic showers the *local cluster weighting* method (LCW) [140] is used. The calibration in LCW, often referred to as LC scale, is determined by comparing the reconstructed energy of simulated charged pions to their true energy, using the `GEANT4` software. According to the shower properties, the LCW method applies a weighted calibration to the cluster and its associated cells.

5.4 Muons

Muons are reconstructed and identified with the information collected by the muon spectrometer, the inner detector, and to a lesser extent by the calorimeter. According to the information available in the ID and MS, different muon algorithms are used [141], defining different reconstructed muon types. Muons are called *stand-alone* (SA) when the trajectory is reconstructed only in the MS. The track parameters at the interaction point are determined by extrapolating the track to the point of closest approach to the beam line, accounting for the energy loss in the calorimeter. SA muons are used to extend the acceptance in the region $2.5 < |\eta| < 2.7$, where the ID cannot provide a measurement. A muon is *segment-tagged* (ST) if, when reconstructed in the ID and extrapolated in the MS, it is associated with at least one local track segment in the MDT or CSC chambers. This method can be used to increase the reconstruction efficiency of muons for low-p_{T} ones, or in regions of reduced acceptance of the MS.

The majority of the muons are called *combined* (CB). Track reconstruction is performed independently in the ID and the MS and the two tracks are combined. The main algorithm implementing this method is called `STACO` [142], which uses the parameters vectors of the tracks, as measured by the ID and MS, to define a χ^2 variable including their covariance matrix. This variable is used to decide which pairs of segments are retained based on the quality of the match. The MS track parameters take into account the energy loss and multiple scattering [18, 125] in the calorimeter volume. The track parameters determined by `STACO` are the result of a statistical combination of the two track vectors.

Reconstructed muons are required to satisfy track quality requirements. One hit in the pixel detector and five in the SCT are required. At most two pixel and SCT sensors have to be traversed by the track without hits. At least nine TRT hits are required in the region of the full acceptance of this detector $0.1 < |\eta| < 1.9$.

Muon reconstruction efficiencies are measured with $Z \to \mu\mu$ events, using a *tag-and-probe* method [141], where the so-called *tag* muon is reconstructed and required to be within a maximum ΔR distance from a muon selected by the trigger, and another muon, the *probe*, is used to measure the efficiency. Very high reconstruction efficiencies are achieved of $\approx 99\%$ with a precision of $\approx 0.1\%$, for $|\eta| < 2.5$ and for $p_{\mathrm{T}} > 10$ GeV. The muon momentum scale and resolution are measured using $J/\Psi \to \mu\mu$, $\Upsilon \to \mu\mu$ and $Z \to \mu\mu$ events. The measured momentum scale is used to improve the agreement between data and simulation, and to reduce the uncertainties in physics analyses. Uncertainties on the scale depend on the pseudo-rapidity and are $\pm 0.05\%$ for $|\eta| < 1$ and increases up to 0.2% in the forward region.

5.5 Electrons

Electrons are reconstructed in the region $|\eta| < 2.47$ by matching the energy deposits in the electromagnetic calorimeter with a track in the inner detector. As electrons feature a more complex signature with respect to muons, identification is performed using multivariate techniques or *cut-based* decisions.

Electron reconstruction starts from energy deposits in the EM calorimeter which is divided into a grid of towers in the $\eta - \phi$ space. Seed clusters with energies above 2.5 GeV are considered by the *sliding window* algorithm [139]. Cluster reconstruction efficiencies above 95% for true electrons are achieved. Electrons might lose a significant amount of energy via photon radiation (*bremsstrahlung*) [18]. In this process, the radiated power is inversely proportional to the mass of the emitting particle, which implies that electrons lose a significant fraction of their energy via bremsstrahlung and more than any other particle.

Track reconstruction has to take into account for this phenomenon and provide high and uniform efficiency. Tracks are searched for in RoIs defined by the EM cluster positions and are measured by pattern recognition, as illustrated in Sec. 5.1, followed by a fit. The pattern recognition uses the pion hypothesis for energy loss in the detector material. This is complemented with a modified algorithm [143] which allows higher energy loss due to the contribution of photon radiation. If a track seed reconstructed with the usual algorithm does not lead to a segment satisfying quality criteria, and falls into an RoI, the modified method is used. Tracks are then fitted with either the pion or electron hypothesis using the ATLAS *global track fitter* [135]. After the fit, track matching to the EM cluster is performed based on a number of quality and geometrical requirements. Finally, the track parameters of the matched candidates are precisely re-estimated using an optimised electron track fitter, the *Gaussian Sum Filter* (GSF) [144], and a new matching is performed using the new track and tighter requirements, also including corrections for the energy deposit in the EM calorimeter [145].

Objects reconstructed at this stage include background due to jets and photon conversions. Electron identification exploits the separation power provided by variables related to the longitudinal and transverse shower shape, track properties and track-to-cluster matching quality, which provide separation between signal and background. A selection can be implemented using these quantities (*cut-based identification*) or a more refined *multi-variate analysis* (MVA) can be used based on a likelihood function. The latter combines the separation power of the different variables into a single *discriminant*. A selection in the distribution of the discriminant is the last step of the MVA identification. Depending on the required signal efficiency and background rejection, three working points are defined for both methods, which are called *loose*, *medium* and *tight*, in order of decreasing signal efficiency and increasing background rejection.

The reconstruction and identification efficiencies are determined with a tag-and-probe method using $Z \to ee$ and $J/\Psi \to ee$ events and is described in detail in Ref. [145] for the full data sample at $\sqrt{s} = 8$ TeV with $L_{\text{int}} = 20.3$ fb^{-1}. Averaged over η, the reconstruction efficiency is about 97%, for $p_{\text{T}} > 15$ GeV, and increases up to 99% at $p_{\text{T}} = 50$ GeV. For different p_{T} regions, maximum uncertainties up to $\approx 1.5\%$ are achieved. The identification efficiency, determined with respect to reconstructed electrons, is about 96% for the loose working point and 78% for the tight one, with a pile-up dependence below 4%. The background rejection, or inverse background efficiency, is ≈ 106.4 and ≈ 344.8 for the loose and tight working points, respectively. The total uncertainty for the identification efficiency ranges between 1% and 6% depending on the electron p_{T}.

5.6 Jets

Many algorithms for the reconstruction of jets are available [82], which have to satisfy the criteria outlined in Sec. 2.4.2. In ATLAS, the so-called anti-k_{T} algorithm [146] is used, which is implemented in the `FastJet` package [147]. The algorithm is available in different versions depending on its input objects, which are organised in a list for sequential recombination. These inputs could be stable simulated particles, making up *truth jets*, reconstructed tracks in the inner detector, composing *track jets*, or clusters

in the calorimeter leading to *calorimeter jets*. Only calorimeter jets are relevant for this thesis. For each pair of objects in this list, the quantities d_{ij} and d_{iB} are evaluated which are defined as

$$d_{ij} = \min\left(\frac{1}{p_{\mathrm{T}_i}^2}, \frac{1}{p_{\mathrm{T}_j}^2}\right)\frac{\Delta_{ij}^2}{R^2}, \qquad \text{where} \qquad \Delta_{ij}^2 = (y_i - y_j)^2 + (\phi_i - \phi_j)^2 \tag{5.3a}$$

$$\text{and} \qquad d_{iB} = \frac{1}{p_{\mathrm{T}_i}^2}, \tag{5.3b}$$

where R is a jet-radius parameter, usually a certain value of order one, and d_{iB} is called the *beam distance*. In this thesis, jets are reconstructed with $R = 0.4$. After the list is compiled, the minimum is found among all d_{ij} and d_{iB}, called $d_{\min}$. If $d_{\min}$ is a d_{ij}, the objects i and j are merged by summing up their four-momenta. If it is a beam distance, the object associated with it is considered to be a single jet and removed from the initial list. The procedure is iterated until no objects are present in the list. The anti-k_{T} algorithm has a number of advantages. First of all, it is infrared safe (Sec. 2.4.2). Due to this property the reconstruction performance of the jet is not significantly affected by the initial parton momentum. Also, it is collinear safe, i.e. it is robust against different particle multiplicities. The algorithm can be used with partons or reconstructed objects, allowing for direct comparison between theoretical predictions and experimental results. Also, the jet area in the $\eta - \phi$ space, as defined in Ref. [146], can be controlled with the parameter R, and is found to be approximately πR^2, which is of advantage when corrections to the jet properties have to be applied, e.g. due to pile-up. Finally, the anti-k_{T} algorithm is computationally fast.

As illustrated in Sec. 5.3, the energy of hadronic clusters is calibrated according to the LCW scheme. This method restores the correct energy deposit from hadrons with respect to the EM scale, and improves the energy resolution of the jet. However, this calibration alone is not sufficient to retrieve the correct energy of the initial parton which initiated the jet. A correction needs to be applied to determine the *jet energy scale* (JES). This has to be done for a number of reasons. Firstly, showers may not be completely contained in the calorimeter (*punch-through effect*), or be located in regions of the detector not completely instrumented or malfunctioning. Also, pile-up contributes to contaminate the jet with additional particles, or particles belonging to the jet may not be associated with it during reconstruction or not reach the calorimeter because their momenta is too low.

The JES is determined in four steps. First of all, a pile-up correction is applied [148, 149] using the number of primary vertices in the event N_{PV} and the expected number of interactions $\langle\mu\rangle$, as well as the jet area and the median p_{T} density of the event, which depends on the pile-up activity. The correction is found to be proportional to N_{PV} by a factor of ≈ 100 MeV. Secondly, the jet direction is corrected in order to make it point to the hard-scattering vertex instead of the nominal center of the ATLAS detector. The third step is the jet calibration itself, and is derived by comparing the visible energy of true jets in the simulation $E_{\text{vis jet}}^{\text{true}}$, which excludes the contribution from neutrinos, with the energy of the reconstructed jets $E_{\mathrm{LC}}^{\text{jet}}$ in both data and simulation. The response, $\mathcal{R}$, defined as

$$\mathcal{R} = \frac{E_{\mathrm{LC}}^{\text{jet}}}{E_{\text{vis jet}}^{\text{true}}} \tag{5.4}$$

is obtained as a function of the pseudo-rapidity. Energy calibration is followed by a pseudo-rapidity correction of the direction of the jet, derived in a similar way. The measurement of the JES and its uncertainties are described in Ref. [148, 150] for data collected during 2011 at $\sqrt{s} = 7$ TeV. Finally, due to the non-compensating nature of the calorimeter and the complex calorimeter geometry and material distribution, the JES needs to be validated *in-situ* to minimise the impact of eventual mis-modelling from

the simulation. This validation leads to the measurement of correction factors to be applied in addition to the JES. The validation is performed using di-jet events in data, where the momentum of a well-calibrated jet measured in a reference region $p_{\mathrm{T}}^{\mathrm{ref}}$ is compared with the other jet's momentum $p_{\mathrm{T}}^{\mathrm{probe}}$. The relative response is measured as

$$\frac{1}{c} = \frac{p_{\mathrm{T}}^{\mathrm{probe}}}{p_{\mathrm{T}}^{\mathrm{ref}}}. \tag{5.5}$$

Details on this measurement can be found in Ref. [151] for data collected at $\sqrt{s} = 8$ TeV. The measurement is performed for data and simulation, which is then corrected with a residual calibration factor $c_{\mathrm{data}}/c_{\mathrm{MC}}$. The in-situ calibration, determined in Ref. [151], is applied in addition to the JES measured at $\sqrt{s} = 7$ TeV. The relative response as a function of $p_{\mathrm{T}}^{\mathrm{avg}} = (p_{\mathrm{T}}^{\mathrm{probe}} + p_{\mathrm{T}}^{\mathrm{ref}})/2$ in the central and forward region is illustrated in Fig. 5.1, and its uncertainty in Fig. 5.2. The number of reconstructed

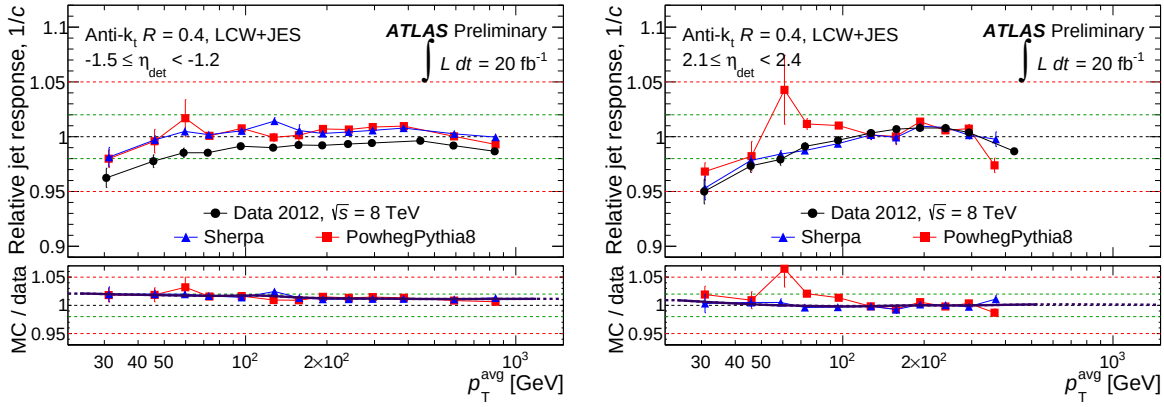

Figure 5.1: JES relative response as a function of the jet $p_{\mathrm{T}}^{\mathrm{avg}} = (p_{\mathrm{T}}^{\mathrm{probe}} + p_{\mathrm{T}}^{\mathrm{ref}})/2$ in a representative central portion of the detector (left) and in a forward portion (right). The lower inset shows the residual calibration factor measured for the MC simulation. A SHERPA sample is used. The plots are taken from Ref. [151].

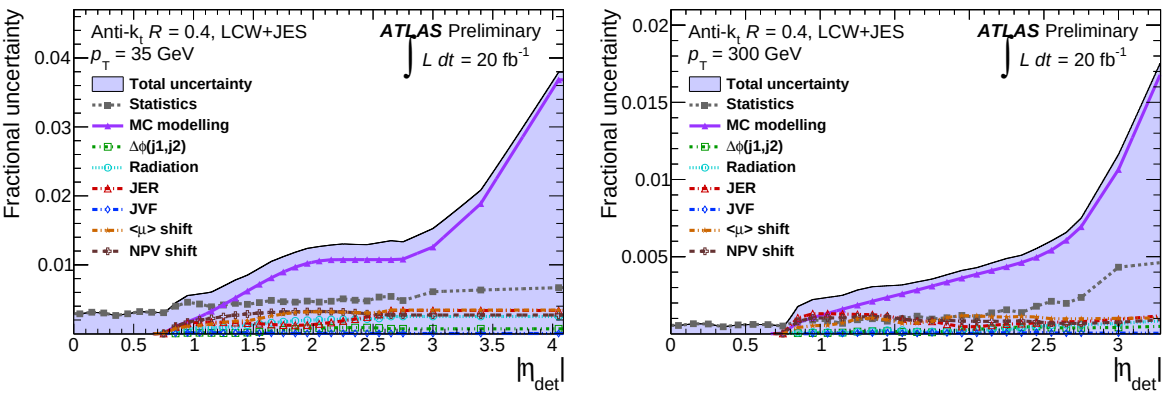

Figure 5.2: Uncertainties on the calibration factors c for a representative low-p_{T} value of the jet (left) and high-p_{T} (right) as a function of η. The different uncertainties are detailed in Ref. [151], where the plots are taken from.

jets depends on the amount of pile-up in the event. Pile-up subtraction helps reducing the number of reconstructed pile-up jets. However, this correction alone is not sufficient to suppress them completely due to localised fluctuations in the pile-up activity. Jets not originating from the hard-scattering vertex are rejected, using the tracks associated with each jet using topological requirements. To identify the

origin of jets, the *jet vertex fraction* (JVF) is used [149, 152], which is defined for a generic jet J and vertex V as

$$\mathrm{JVF}(J,V) = \frac{\sum_{i}^{N_{\mathrm{trk}}} p_{\mathrm{T},i}^{\mathrm{trk}}(J,V)}{\sum_{k}^{N_{\mathrm{PV}}} \sum_{i}^{N_{\mathrm{trk}}} p_{\mathrm{T},i}^{\mathrm{trk}}(J,V_k)}, \tag{5.6}$$

where i runs over all tracks matched to a vertex and a jet, and k over all primary vertices in the event. Only tracks from the inner detector with $p_{\mathrm{T}} > 500$ MeV are considered. This variable may be interpreted as an estimate of the fraction of the jet energy which is associated with a vertex, as illustrated schematically in Fig. 5.3. For physics analyses in 2012, with data taken at $\sqrt{s} = 8$ TeV, different selection criteria are

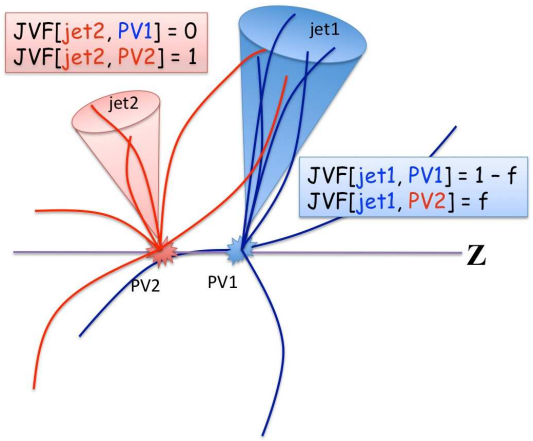

Figure 5.3: Schematic representation of the JVF principle. Tracks inside the cones in the drawing are considered matched to the respective jet. The picture is taken from Ref. [149].

used for the JVF variable computed for relevant jets and the hard-scattering vertex V_{HS} of the event, as defined in Sec. 5.2. Each analysis can choose between different values (JVF $> 0, 0.25, 0.5$) depending on the kinematic selection or the scope of the analysis itself.

Many physics analyses require the ability to identify jets originating from a b quark, a technique called *b-tagging*. This is achieved by using dedicated identification algorithms reviewed in Ref. [153]. The most commonly used flavour tagging algorithm in ATLAS is called MV1, which is calibrated in the simulation using $t\bar{t}$ events, as described in Ref. [154]. An overall efficiency of $\approx 70\%$ is achieved by the algorithm for b jets with $p_{\mathrm{T}} > 20$ GeV and $|\eta| < 2.5$. The mis-identification probability measurement for jets originating from other quarks, like c quarks, is illustrated in Ref. [155], and is approximately 0.7% depending on η and p_{T}. The identification of b jets is not used in the analysis presented in this thesis, however, it is used by the searches combined with it. These other searches define selections optimised for the two main production mechanisms of the neutral Higgs bosons in the MSSM, featuring the presence or absence of at least one b jet.

5.7 Missing Transverse Energy

As discussed in Sec. 4.2.1, the vectorial sum of the particle momenta in the transverse plane may not add up to zero, as required by momentum conservation. This is due to either the presence of undetected particles in the event, such as neutrinos, mis-measurements of the momenta, or losses of particles outside

the detector fiducial region. The missing transverse energy is defined as

$$E_{\mathrm{T}}^{\mathrm{miss}} = |\mathbf{E}_{\mathrm{T}}^{\mathrm{miss}}| = \sqrt{(E_x^{\mathrm{miss}})^2 + (E_y^{\mathrm{miss}})^2}. \tag{5.7}$$

It is reconstructed as discussed in Ref. [156] for 2012 data at $\sqrt{s} = 8$ TeV, and is measured using the energy deposits in the calorimeters and muons measured by the MS, as well as ST muons as defined in Sec. 5.4, and tracks in the ID from low-p_{T} particles not reaching the calorimeter. The energy deposits are associated with reconstructed and identified parent objects in a specific order, as indicated in the following formula

$$E_{x,y}^{\mathrm{miss}} = E_{x,y}^{\mathrm{miss,e}} + E_{x,y}^{\mathrm{miss},\gamma} + E_{x,y}^{\mathrm{miss},\tau} + E_{x,y}^{\mathrm{miss,jets}} + E_{x,y}^{\mathrm{miss,soft}} + E_{x,y}^{\mathrm{miss},\mu} \tag{5.8}$$

where only hadronic decays of the tau lepton are considered. The $E_{x,y}^{\mathrm{miss,soft}}$ term includes contributions from jets with $p_{\mathrm{T}} < 20$ GeV, calibrated with the LCW method, and tracks or clusters which are not associated with any object. If combined muons are used, their small energy loss in the calorimeter is subtracted from $E_{\mathrm{T}}^{\mathrm{miss}}$ to avoid double counting. Electrons and photons are calibrated to the EM scale, while tau leptons are calibrated as described in the following chapter. In order to characterise the $E_{\mathrm{T}}^{\mathrm{miss}}$ reconstruction performance, the following scalar variable is often used:

$$\sum E_{\mathrm{T}} = E_{\mathrm{T}}^{e} + E_{\mathrm{T}}^{\gamma} + E_{\mathrm{T}}^{\tau} + E_{\mathrm{T}}^{\mathrm{jets}} + E_{\mathrm{T}}^{\mathrm{miss,soft}}, \tag{5.9}$$

which is combined into the event variable

$$\sum E_{\mathrm{T}}(\mathrm{event}) = \sum E_{\mathrm{T}} + \sum p_{\mathrm{T}}^{\mu}. \tag{5.10}$$

Pile-up has a significant effect on the $E_{\mathrm{T}}^{\mathrm{miss}}$ reconstruction, especially concerning the soft term which can be affected by large fluctuations. Different methods are available for pile-up suppression, which are reviewed in Ref. [157]. Among them, the *soft term vertex fraction* (STVF) method is relevant for this thesis. This method uses tracks which are not associated with physics objects, but come from either the hard-scattering vertex V_{HS}, or from any other pile-up vertex. This correction is only applied to tracks with 500 MeV $< p_{\mathrm{T}} <$ 100 GeV, $|\eta| < 2.5$ and with more than 6 or 10 hits in the Pixel+SCT or Pixel+SCT+TRT systems respectively. The STVF variable is defined as

$$\mathrm{STVF} = \frac{\sum_{i}^{N_{\mathrm{trk}}} p_{\mathrm{T},i}^{\mathrm{trk}}(V_{\mathrm{HS}})}{\sum_{k}^{N_{\mathrm{PV}}} \sum_{i}^{N_{\mathrm{trk}}} p_{\mathrm{T},i}^{\mathrm{trk}}(V_k)}, \tag{5.11}$$

where, in the numerator, only tracks from the vertex V_{HS} are considered, while in the denominator all primary vertices are taken into account, including V_{HS}. The STVF variable is used as a factor to scale the soft contribution in Eq. (5.8). The pile-up correction is studied in $Z \to \mu\mu$ events, which do not feature genuine $E_{\mathrm{T}}^{\mathrm{miss}}$, apart from a small contribution coming from the p_{T} of the Z boson, and is shown in Fig. 5.4. A similar study for a selection of $W \to e\nu$ events, featuring genuine $E_{\mathrm{T}}^{\mathrm{miss}}$ from the neutrino, can be found in Ref. [157]. The $E_{\mathrm{T}}^{\mathrm{miss}}$ resolution as a function of N_{PV} for the two classes of events is reported in Fig. 5.5. The $E_{\mathrm{T}}^{\mathrm{miss}}$ resolution for $W \to e\nu$ and VBF $H \to \tau\tau$ is reported in Fig. 5.6. Systematic uncertainties on $E_{\mathrm{T}}^{\mathrm{miss}}$ come from the propagated uncertainties on all the physics objects this quantity is computed from. An additional uncertainty comes from the resolution and scale of the soft

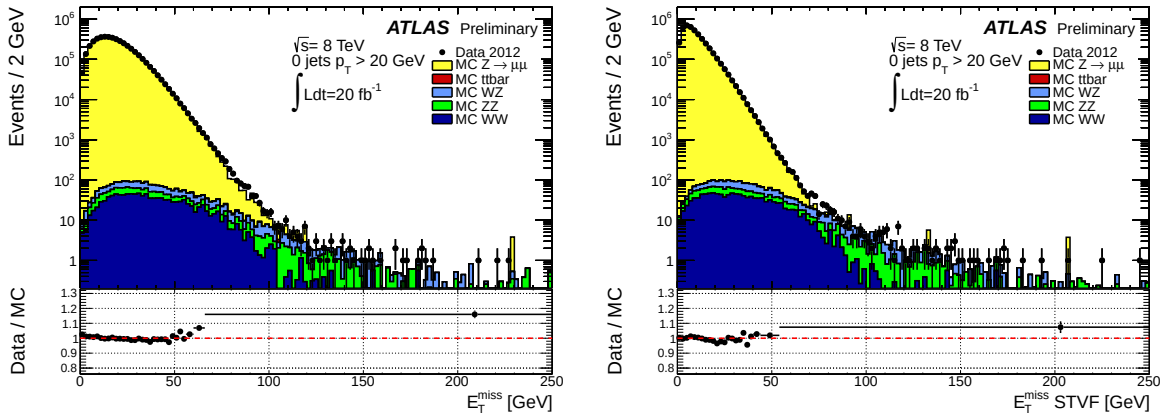

Figure 5.4: $E_{\mathrm{T}}^{\mathrm{miss}}$ distributions in simulated events from a $Z \to \mu\mu$ selection, where no additional jets are required. The plot on the left shows the distribution before the STVF correction, while the plot on the right is obtained after the correction. The plots are taken from Ref. [157].

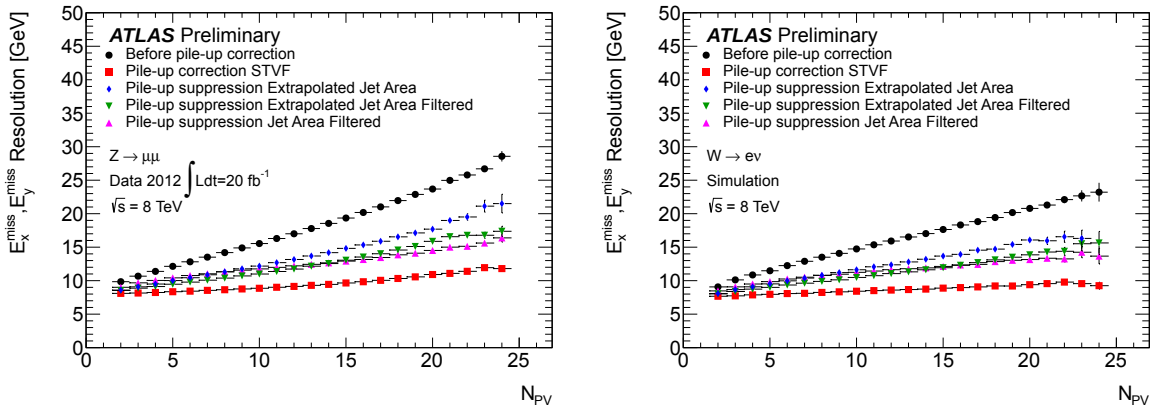

Figure 5.5: Resolution of the $E_{\mathrm{T}}^{\mathrm{miss}}$ components as a function of the number or primary vertices in the event for $Z \to \mu\mu$ (left) and $W \to e\nu$ (right) simulated events. The plots include the results for different methods other than STVF, all illustrated in Ref. [157]. The plots are taken from Ref. [157].

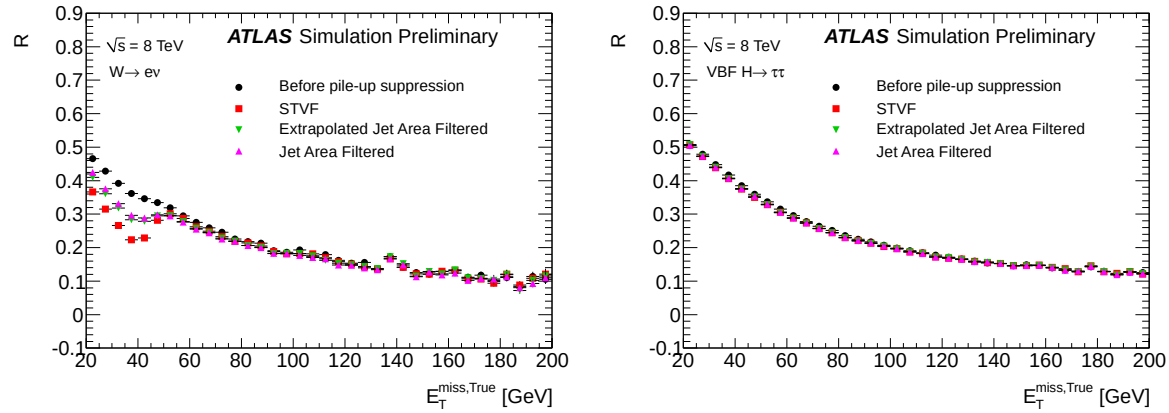

Figure 5.6: $E_{\mathrm{T}}^{\mathrm{miss}}$ resolution, $R = RMS(E_{\mathrm{T}}^{\mathrm{miss}}/E_{\mathrm{T}}^{\mathrm{miss,true}})/\left\langle E_{\mathrm{T}}^{\mathrm{miss}}/E_{\mathrm{T}}^{\mathrm{miss,true}}\right\rangle$, as a function of the true $E_{\mathrm{T}}^{\mathrm{miss}}$ in simulation for $W \to e\nu$ (left) and VBF $H \to \tau\tau$ (right) events. The plots are taken from Ref. [156].

term, which is studied in $Z \to \mu\mu$ events. Values as low as 1.4% on the scale and 0.7% on the resolution are obtained [157].

CHAPTER 6

Tau Leptons

Tau leptons are an important part in the physics programme of the ATLAS experiment. In the Standard Model, the decay $H_{\mathrm{SM}} \to \tau\tau$ features the second highest branching ratio available to study the coupling between the Higgs boson and fermions, as illustrated in Fig. 2.2. Many searches for physics beyond the Standard Model also include tau leptons in the final state, such as searches for heavy resonances, like $Z' \to \tau\tau$ [158], SUSY signals and MSSM Higgs searches. Tau leptons are of paramount importance for the search for $h/H/A \to \tau_{\mathrm{had}}\tau_{\mathrm{had}}$ presented in this thesis. The symbol τ_{had} refers to a tau lepton decaying to a combination of hadrons plus a neutrino, via the weak interaction. This kind of decay is dominant, as illustrated in Tab. 6.1, with $\mathrm{BR}(\tau_{\mathrm{had}}) \approx 65\%$. Leptonic decays featuring either an electron or a muon plus two neutrinos, τ_{lep}, are less likely to occur, having $\mathrm{BR}(\tau_{\mathrm{lep}}) \approx 35\%$. The tau is the heaviest lepton, with $m_\tau = 1.777$ GeV, and decays with a short lifetime, therefore also features a short characteristic decay length $c\tau_{\mathrm{lifetime}} \approx 87\ \mu$m. With such a short lifetime, tau leptons produced in the collisions are unlikely to reach the detector, therefore, leptonic decays of the tau are difficult to distinguish from the prompt production of muons or electrons in the collisions. Therefore, no attempt to identify these decays as a tau decay is made, instead, only hadronic decay modes are candidates for the identification process. Hadronic tau-decay modes are usually divided into two categories: the so-called *1-prong* decays, where only one charged hadron is produced, predominantly a pion, and *3-prong* decays, featuring three charged hadrons. A different number of neutral hadrons in the final state further characterises these decays, as illustrated in Tab. 6.1. The major source of background for hadronic decays of tau leptons are jets, however, also electrons and muons can mimic them. Separate identification techniques are designed to reject these backgrounds, which are discussed in the appendix.

The present chapter is structured as follows. In Sec. 6.1, tau reconstruction is discussed. Tau identification, or discrimination against jets, is performed with multivariate techniques illustrated in Sec. 6.2. The tau energy calibration is presented in Sec. 6.3. For this thesis, the measurement of the tau identification efficiency in data, and the corresponding calibration factors for the simulation, were performed using a tag-and-probe technique based on $Z \to \tau_\mu\tau_{\mathrm{had}}$ events. This measurement is presented in Sec. 6.4. Finally, the tau trigger is discussed in Sec. 6.5. The following chapter is based on Ref. [159–162], which document the tau reconstruction and energy calibration used in ATLAS in 2011 and 2012. Further details on discrimination techniques against electrons and muons are presented in App. B, which are relevant for the other channels that are later combined with the search described in this thesis.

Decay	Branching Ratio (%)
Leptonic Decay Modes	
$\tau^{\pm} \to \mu^{\pm}\nu_{\mu}\nu_{\tau}$	17.36
$\tau^{\pm} \to e^{\pm}\nu_{e}\nu_{\tau}$	17.85
Hadronic Decay Modes	
1-prong	
$\tau^{\pm} \to \pi^{\pm}\nu_{\tau}$	10.91
$\tau^{\pm} \to \pi^{\pm}\pi^{0}\nu_{\tau}$	25.52
$\tau^{\pm} \to \pi^{\pm}\pi^{0}\pi^{0}\nu_{\tau}$	9.27
$\tau^{\pm} \to \pi^{\pm}\pi^{0}\pi^{0}\pi^{0}\nu_{\tau}$	1.04
$\tau^{\pm} \to K^{\pm}\nu_{\tau}$ + neutral particles	1.57
3-prong	
$\tau^{\pm} \to \pi^{\pm}\pi^{\pm}\pi^{\mp}\nu_{\tau}$	9.32
$\tau^{\pm} \to \pi^{\pm}\pi^{\pm}\pi^{\mp}\pi^{0}\nu_{\tau}$	4.61
$\tau^{\pm} \to K^{\pm}\pi^{\pm}\pi^{\mp}\nu_{\tau}$ + neutral particles	0.48

Table 6.1: Summary of tau lepton decay modes and their branching ratios. Values are taken from Ref. [18].

6.1 Tau Reconstruction

Tau reconstruction uses the information collected by different detectors. Tracking and calorimeter information is combined and leads to the definition of a tau candidate called $\tau_{\text{had-vis}}$, emphasising that the reconstruction only considers the visible products of the decay, i.e. excludes neutrinos. In ATLAS, the $\tau_{\text{had-vis}}$ reconstruction is seeded by jets reconstructed as described in Sec. 5.6, but only calibrated with the LCW method, i.e. not applying any JES correction. These jets are all considered as $\tau_{\text{had-vis}}$ candidates. The following sections describe how tracks are associated with the tau and how their vertex is defined, in Sec. 6.1.1 and 6.1.2, respectively. The energy calibration of jets, previously described, is not appropriate for tau leptons, as these objects consist of a specific mixture of charged and neutral hadrons. Their calibration is derived independently of the JES and is illustrated in Sec. 6.3. The η and ϕ coordinates of $\tau_{\text{had-vis}}$ candidates are determined by the sum of the four-momenta of the clusters associated with the jet, assuming zero mass for each component, such that $p_{\text{T}} = E_{\text{T}} = E\sin\theta$. The η coordinate of the tau is finally corrected during the energy calibration procedure, as will be described later.

6.1.1 Tau Track Association

All jets with $p_{\text{T}} > 10$ GeV and $|\eta| < 2.5$ are considered. Tracks are associated with a $\tau_{\text{had-vis}}$ candidate if they are in the so-called *core cone* of the jet, i.e. within $\Delta R < 0.2$ with respect to the jet axis. They also have to satisfy the following criteria

- $p_{\text{T}} > 1$ GeV
- Number of pixel hits ≥ 2

- Number of pixel hits plus number of SCT hits ≥ 7
- $|\Delta z_0 \sin\theta| < 1.5$ mm
- $|\Delta d_0| < 1$ mm

where the z_0 and d_0 distances are measured with respect to the *tau vertex*, which is defined in the next section. The number of tracks n counted in the core cone is used to classify the tau as n-prong. Tracks are also counted within the so-called *isolation annulus*, $0.2 < \Delta R < 0.4$, useful for identification purposes, as described later. A schematic representation of a tau decay is shown in Fig. 6.1.

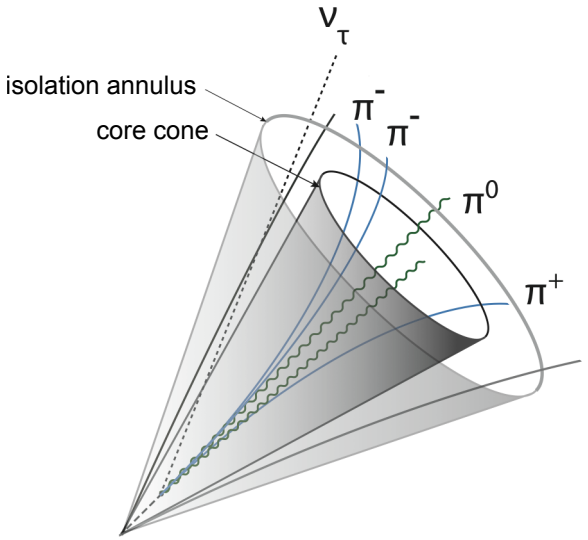

Figure 6.1: Schematic representation of a 3-prong tau decay of the type $\tau^- \to \pi^-\pi^-\pi^+\pi^0\nu_\tau$. The decay $\pi^0 \to \gamma\gamma$ is also shown. The picture includes a sketch of the isolation annulus and the core cone, defined in the main text.

6.1.2 Tau Vertex Association

Events must have a reconstructed hard-scattering vertex with at least three associated tracks. Such a vertex does not necessarily correspond to the origin of the tau, especially in events with many primary vertices. A dedicated algorithm is used to identify the best vertex hypothesis for each seed jet, which reduces the effect of pile-up and increases the reconstruction efficiency. This is due to the possibility to improve the track association which is sensitive to pile-up through the $|\Delta z_0 \sin\theta|$ requirement. The algorithm, called *Tau Jet Vertex Association* (TJVA) is described in detail in Ref. [162]. It uses all tracks associated with the candidate, as already described, but excluding the $|\Delta z_0 \sin\theta|$ and Δd_0 requirements. For each candidate, the vertex with the highest JVF value, as defined by Eq. (5.6), is defined as the tau vertex. The improvement provided by this algorithm is illustrated by Fig. 6.2, where the track selection efficiency is studied as a function of pile-up and compared to a version of the algorithm matching the tracks to the primary vertex. According to the pile-up conditions of 2012, in $Z \to \tau\tau$ events the tau vertex coincides with the hard-scattering vertex $\approx 90\%$ of the times, while in analyses requiring objects with higher p_{T} this happens in $\approx 99\%$ of the cases.

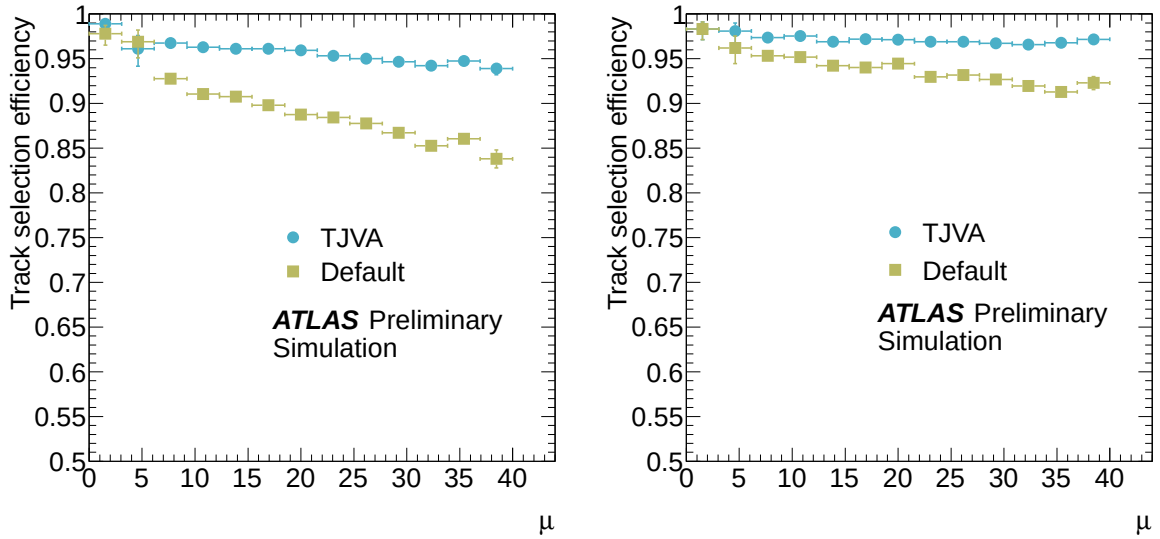

Figure 6.2: Track selection efficiencies of $\tau_{\text{had-vis}}$ candidates as a function of the expected number of interactions per bunch crossing μ. The plots are referred to 1-prong candidates (left) and 3-prong ones (right). The efficiency is studied in simulated $Z \to \tau\tau$ events. The default method uses tracks matched to the primary vertex, while TJVA uses the tau vertex. The plots are taken from Ref. [162].

6.1.3 π^0 Reconstruction in Tau Decays

The number of π^0 particles produced in the tau decay, and other variables related to them, is used in the identification process. A π^0 reconstruction algorithm was developed [163], which is based on calorimeter cluster information and is divided into two steps. These two separate steps utilise a multivariate technique, the so-called *Boosted Decision Trees* (BDT) [164, 165]. In the first stage, the number of neutral pions is estimated, N_{π^0}, using global features of the tau decay in the core cone. These properties are measured by a number of subdetectors including the pre-sampler and strip layer of the calorimeter, the calorimeter itself and the tracking system. All this information is combined into a BDT. If $N_{\pi^0} > 0$, the second step of the algorithm reconstructs π^0 candidates using up to two clusters among those in the core cone. The cluster properties are used to assign a π^0-*likeness* score to each cluster, which depends on the proportion of energy deposited in the pre-sampler and strip layer with respect to the energy deposited by charged pions. This is done after subtracting the contributions of pile-up, the underlying event and electronic noise, which are estimated in the isolation annulus. Only those clusters with the highest scores are kept, which will contribute to the definition of the tau variables used during identification. The additional information provided by π^0 reconstruction improves the separation power against jets.

6.2 Tau Identification

The reconstruction process provides little discrimination against the dominant background source for hadronically decaying tau leptons, i.e. jets initiated by a quark or a gluon, which have a very large production cross-section at the LHC, as shown in Fig. 4.2. However, jets typically feature higher track multiplicities than tau leptons, as well as a different energy deposit in the calorimeter, characterised by a wider shower shape compared to tau leptons due to less collimated particles. Therefore, we can define a set of variables based on these properties, which provide separation between the signal and the background.

These variables are used as input to a BDT algorithm which quantifies the combined separation in a discriminating variable called the *BDT score*. A selection on this score defines a working point for tau identification, with a characteristic signal efficiency and background rejection. The performance of the identification algorithm is optimised in order to achieve a stable signal efficiency as a function of pile-up and p_{T}. In the following, the identification algorithm and its performance are illustrated.

6.2.1 BDT Algorithm

BDT algorithms map the space of the input variables into regions which are more likely to be populated by signal or background. The mapping procedure, known as *training*, is based on two samples, known to be signal and background. Training is performed iteratively with the purpose of assigning weights to events in the samples, which depend on the performance of a previous classification, a technique called *boosting*. Boosting improves the performance of the classification, making the algorithm more robust against those events which are ambiguous to classify.

Separate BDT algorithms are used for 1-prong and 3-prong candidates, which use a different set of discriminating variables. The algorithms are trained with the *Toolkit for Multivariate Analysis* (TMVA) [166] software using a mixture of tau decays from simulated Z, W and Z' samples[1], while data are used for the background from collisions in 2012, selected with jet triggers. Only candidates with $p_{\mathrm{T}} > 15$ GeV and $|\eta| < 2.3$ are used. For the signal, a topological matching between the simulated and reconstructed $\tau_{\mathrm{had-vis}}$ candidates is utilised, by requiring them to be within $\Delta R < 0.2$ from each other. The distributions of all variables used by the identification algorithm and their definitions can be found in App. A.

6.2.2 Tau Identification Performance

The outcome of the BDT algorithm is called *BDT score*. This variable is distributed between zero and one, where background and signal events tend to have lower and higher scores, respectively. Tau identification is defined by a selection on the score, and three working points are defined. The signal efficiency is defined as the fraction of $\tau_{\mathrm{had-vis}}$ candidates that are found beyond a BDT threshold, for signal events matched to a true simulated tau and reconstructed with the same number of tracks as the simulated number of charged decay products. The background efficiency is defined in the same way, relative to background events. Three working points are defined, depending on the signal efficiency, called *loose*, *medium* and *tight*, ordered from highest to lowest efficiency. Their respective efficiency and background rejection, i.e. the inverse background efficiency, are shown in Fig. 6.3 for candidates with low-p_{T} (left) and high-p_{T} (right), the latter being particularly relevant for this thesis. The selection on the BDT score is chosen such that the signal efficiency is independent of the p_{T} of the $\tau_{\mathrm{had-vis}}$. The performance is also stable with respect to pile-up, as shown in Fig. 6.4, due to a careful choice of the discriminating variables used in the algorithm, relying on tracking and energy deposition in a narrow cone, as well as their correction for pile-up effects, a technique called *pile-up weighting* which is going to be introduced later.

[1] The Z' particle is a neutral gauge boson predicted by models including an electroweak extension of the Standard Model [167]. Its mass is believed to be much larger than the Z mass. Tau-related studies in ATLAS use simulated $Z' \to \tau\tau$ samples with $m_{Z'}$ between 250 GeV and 1250 GeV to study the high-p_{T} region of tau decays.

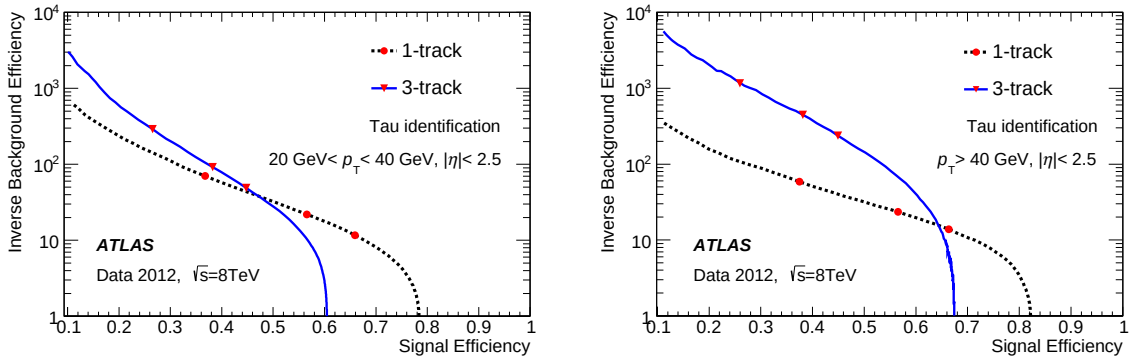

Figure 6.3: Inverse background efficiency as a function of the signal efficiency for the tau identification algorithm. Two curves are displayed referring to 1-prong and 3-prong candidates. The plots also show the definition of the three working points. Low-p_{T} candidates are considered for the plot on the left, and high-p_{T} ones on the right. The plots are taken from Ref. [159].

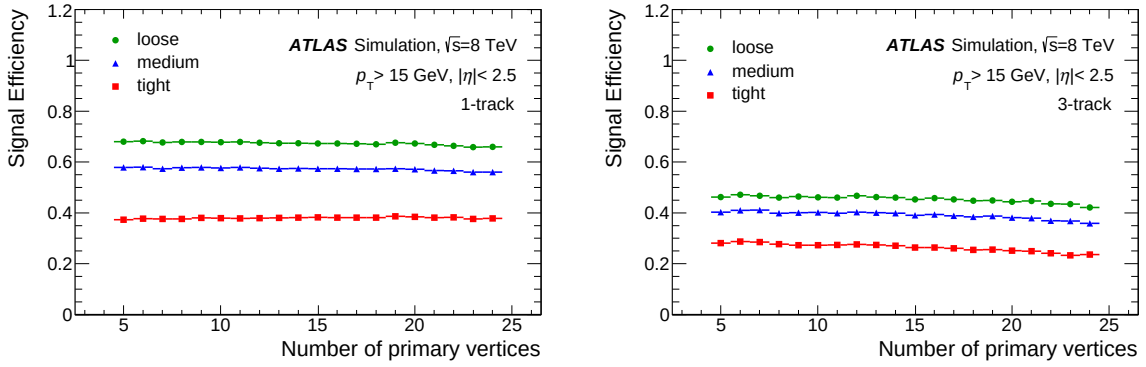

Figure 6.4: Signal efficiency as a function of pile-up for the BDT identification algorithm and for 1-prong (left) and 3-prong (right) candidates. The plots are taken from Ref. [159].

6.3 Tau Energy Scale

All clusters composing a tau candidate are calibrated to the LC scale. The correct tau energy scale (TES) has to be determined independently from the JES, as the $\tau_{\mathrm{had-vis}}$ consists of a specific mixture of hadrons. The calibration is performed using the simulation, and aims at eliminating any dependence of the response on η, the tau energy itself, pile-up and track multiplicity, as well as improving the energy resolution.

The response function for tau candidates is determined in a similar way as discussed for jets in Sec. 5.6, and is defined analogously to Eq. (5.4). It is a function of the reconstructed tau energy at the LC scale, E^{τ}_{LC}, pseudo-rapidity and the track multiplicity, and will be indicated as $\mathcal{R}(E^{\tau}_{\mathrm{LC}}, |\eta_{\mathrm{reco}}|, N_{\mathrm{trk}})$. Simulated events of the processes $Z \to \tau\tau$, $W \to \tau\nu$ and $Z' \to \tau\tau$ are used. Reconstructed candidates are selected by requiring $p_{\mathrm{T,LC}} > 15$ GeV, $|\eta| < 2.4$ and matching to a true tau with a visible $p_{\mathrm{T}} > 10$ GeV. In addition, they have to satisfy the medium identification requirement against jets and be at least $\Delta R = 0.5$ away from a jet. The distribution of the ratio $E^{\tau}_{\mathrm{LC}}/E^{\mathrm{true}}_{\mathrm{vis}}$ is obtained in intervals of $E^{\mathrm{true}}_{\mathrm{vis}}$, pseudo-rapidity and track multiplicity, and is fitted with a Gaussian function. In each interval, the mean value of E^{τ}_{LC} is also measured. Finally, empirically derived functions are used to fit the Gaussian mean determined

in the fit as a function of $\left\langle E_{\mathrm{LC}}^{\tau} \right\rangle$. The fit results are shown in Fig. 6.5. After the response curve is

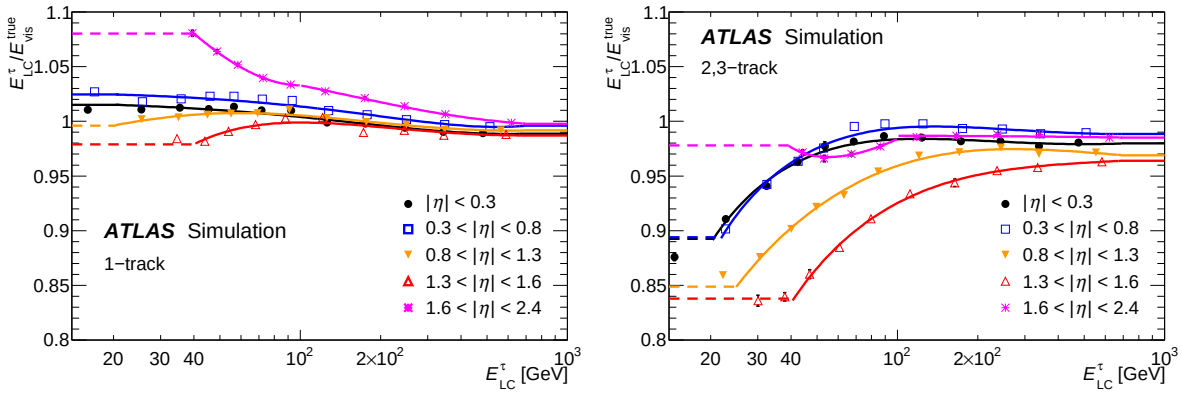

Figure 6.5: Response curves for 1-prong (left) and multi-prong (right) tau candidates, evaluated in intervals of pseudo-rapidity, as a function of the energy associated with the reconstructed tau candidate $\tau_{\mathrm{had-vis}}$. The plots are taken from Ref. [159].

measured, an additional correction to the pseudo-rapidity is applied, in order to correct for a bias arising from underestimated energy in the clusters, due to poorly instrumented regions. The correction is typically negligible and smaller than 1% in the transition region between the barrel and the end-cap. The correction is obtained from the average deviation of the reconstructed pseudo-rapidity with respect to the generated one, i.e. $\delta\eta_{\mathrm{bias}} = \langle |\eta_{\mathrm{reco}}| - |\eta_{\mathrm{true}}| \rangle$. Therefore, the correction is applied only as a function of the pseudo-rapidity

$$|\eta| = |\eta_{\mathrm{reco}}| - \delta\eta_{\mathrm{bias}}. \tag{6.1}$$

Finally, a pile-up correction $\delta E_{\mathrm{pile-up}}$ is measured which is proportional to the number of primary vertices. This is done with a linear fit versus N_{PV} performed in different regions of $|\eta_{\mathrm{reco}}|$ and for different track multiplicities, for the determination of the proportionality factor $A(|\eta_{\mathrm{reco}}|, N_{\mathrm{track}})$. The pile-up correction is written as

$$\delta E_{\mathrm{pile-up}} = A(|\eta_{\mathrm{reco}}|, N_{\mathrm{track}})(N_{\mathrm{PV}} - \langle N_{\mathrm{PV}} \rangle). \tag{6.2}$$

The correction increases with the absolute value of the pseudo-rapidity, and ranges between 90 MeV and 420 MeV per reconstructed vertex.

The final calibrated energy of the tau can then be written as

$$E_{\mathrm{reco}}^{\tau} = \frac{E_{\mathrm{LC}}^{\tau} - \delta E_{\mathrm{pile-up}}}{\mathcal{R}(E_{\mathrm{LC}}^{\tau}, |\eta_{\mathrm{reco}}|, N_{\mathrm{trk}})}. \tag{6.3}$$

The energy resolution of the tau after all corrections are applied is shown in Fig. 6.6.

6.3.1 Tau Energy Scale Uncertainties

Uncertainties on the TES come from the energy response of the calorimeter, the specific choice of the underlying event model, the detector description in the simulation and the calibration method itself, referred to as *non-closure* uncertainty.

The calorimeter response uncertainty can be estimated using single particle response measurements. The particle composition of the hadronic tau decay is taken from simulated $Z \to \tau\tau$ and $Z' \to \tau\tau$ events modelled with `Pythia8` [71] without pile-up, and is convoluted with the response of each hadron in the

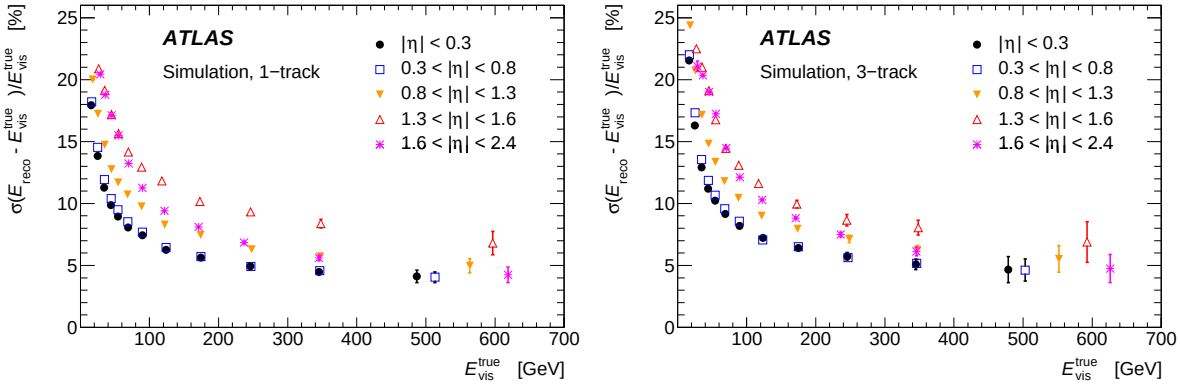

Figure 6.6: Energy resolution of tau leptons for 1-prong (left) and 3-prong (right) candidates. Curves corresponding to different pseudo-rapidities are shown. The resolution corresponds to the width of a Gaussian function from the fit to the distribution of $(E_{\text{reco}} - E_{\text{vis}}^{\text{true}})/E_{\text{vis}}^{\text{true}}$. The plots are taken from Ref. [159].

decay. This is done using a pseudo-experiment approach, where the energy scale is estimated from a set of pseudo-experiments, altering the single particle response and including the statistical and systematic uncertainties associated with it. The outcome of a set of 1000 pseudo-experiments is then fitted with a Gaussian function and its standard deviation is taken to represent the total TES uncertainty due to the calorimeter response, while its mean value is a bias.

The single particle response is estimated from three sources. For low-momentum hadrons with $p < 20$ GeV in the barrel ($|\eta| < 1.7$), or $p < 60$ GeV in the end-cap ($1.7 < |\eta| < 2.5$), in-situ measurements of E/p are used, where the energy is measured by the calorimeter and the momentum by the inner detector. For charged hadrons at high momenta with $|\eta| < 0.8$, the response is estimated from *Combined Test Beam* (CTB) measurements [168]. For particles with high momenta outside the central region, the simulation is used to determine the response. The uncertainty associated with the EM scale, mainly affecting the response of $\pi^0 \to \gamma\gamma$ decays, is constrained by $Z \to ee$ measurements to $\approx 1.5\%$ for the EM calorimeter, and by minimum ionising muons in the Tile calorimeter to $\approx 3\%$. The usage of in-situ measurements helps constraining the uncertainties associated with the interaction between the particles and the calorimeter and with the material in front of the calorimeter. As mentioned previously, after the TES is estimated from the set of pseudo-experiments, a bias might arise determined from a fit to the outcome of the pseudo-experiments. However, this is found to be within the estimated calorimeter response uncertainty, therefore it is quadratically added to the total uncertainty instead of performing a new correction.

Simulated interactions between hadrons and the calorimeter rely on specific models of the hadronic shower shape. Different choices of these models can lead to different energy densities in the shower, affecting the weights assigned by the LCW method, hence the uncalibrated energy of $\tau_{\text{had-vis}}$. To estimate the uncertainty coming from the hadronic shower choice, the nominal model *QGSP_BERT* [169–171] is compared to the *FTFP_BERT* [169, 172] model. For 1-prong and multi-prong tau decays, uncertainties of $\approx 0.5\%$ and $\approx 1\%$, respectively, are achieved.

The total uncertainty associated with the calorimeter response is estimated to be $\approx 1.5 - 2\%$ and $\approx 2 - 2.5\%$ respectively for 1-prong and multi-prong decays, depending on the transverse momentum and pseudo-rapidity region.

In addition to the calorimeter response, four more sources of uncertainty have to be considered: dead material in front of the calorimeter, the underlying event model, non-closure of the calibration method, and pile-up. To estimate the dead material contribution, the nominal sample is compared with

a simulation including extra amount of material. On average, an effect between $\approx 1\%$ and $\approx 2\%$ is found. The uncertainty due to the underlying event model is estimated using a different underlying event tune, and amounts to $\approx 1\%$. The non-closure effect is due to differences between the reconstructed and the true $\tau_{\text{had-vis}}$ energy when the calibration is applied to the same sample it is derived from. This effect is estimated to be $\approx 1\%$ and $\approx 2\%$ for 1-prong and multi-prong decays, respectively. The pile-up uncertainty is assigned independently of $|\eta|$. It is estimated by dividing the simulation sample in five intervals of $\langle N_{\text{PV}} \rangle$, from 0 to 40, and taking the largest variation of $(p_{\text{T}}^{\text{reco}} - p_{\text{T}}^{\text{true}})/p_{\text{T}}^{\text{true}}$.

All TES uncertainties are summarised in Fig. 6.7 as a function of the calibrated tau p_{T}, for the central region of the detector. More details about the TES uncertainty measurement can be found in Ref. [161].

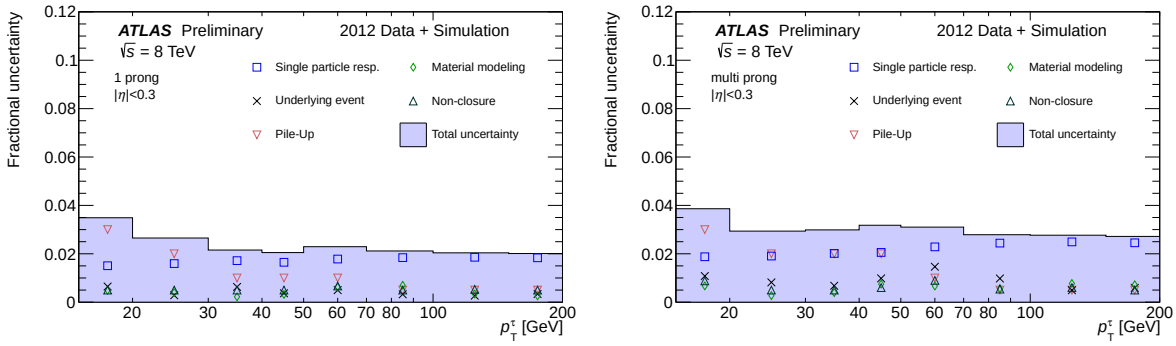

Figure 6.7: TES uncertainties for 1-prong (left) and multi-prong (right) tau decays as a function of the calibrated tau p_{T}. The magnitude of the different sources of uncertainty is shown separately. Their contribution is added quadratically and represented by the shaded area. The plots are taken from Ref. [161].

6.4 Tau Identification Efficiency in Data

The measurement of the identification efficiency in data and the derivation of its correction factors to be applied to the simulation are part of the work for this thesis. The measurement has been performed with $Z \to \tau_\mu \tau_{\text{had}}$ events from a tag-and-probe selection, referred to as the *muon channel*. The muon in the final state is the so-called *tag* while the hadronic decay of the tau is the *probe*, which is the object under study. This choice of decay and final state allows to select probe taus with good rejection against the large multi-jet contamination. In addition, muons are characterised by high trigger efficiencies. The final result has been combined with a similar and independent measurement using $Z \to \tau_e \tau_{\text{had}}$ events (*electron channel*). The following sections are dedicated to the details of the muon channel and the combination with the electron channel. This method has been developed with a portion of the full dataset collected at $\sqrt{s} = 8$ TeV, and updated with the full integrated luminosity in a second stage. The results discussed here refer to $L_{\text{int}} = 8.5$ fb^{-1} and are documented in Ref. [160], while the update is documented in Ref. [159] and is performed with $L_{\text{int}} = 20.3$ fb^{-1} of data.

The measurement utilises a fitting method, so-called *template fitting*, to determine the number of tau leptons in data before and after identification, $N^{\text{fit}}_{\text{before ID}}$ and $N^{\text{fit}}_{\text{after ID}}$, respectively. The efficiency is then determined as

$$\varepsilon_{\text{data}} = \frac{N^{\text{fit}}_{\text{after ID}}}{N^{\text{fit}}_{\text{before ID}}}. \tag{6.4}$$

The fit is performed to the tau track multiplicity distribution in data, which offers good separation power against the jet background.

The identification process could lead to different results in the simulation compared to data. For this reason, simulated events have to be rescaled with a correction factor, referred to as *scale factor* (SF), which is determined as

$$\mathrm{SF} = \frac{\varepsilon_{\mathrm{data}}}{\varepsilon_{\mathrm{MC}}} \tag{6.5}$$

where the efficiency in the simulation, $\varepsilon_{\mathrm{MC}}$, is derived from simulated events before the fit is performed.

6.4.1 Modified Track Counting

For the fitting method, the track multiplicity of the tau is determined with an alternative method to the standard one used for tau reconstruction, which only relies on the core cone $\Delta R \leq 0.2$, as described in Sec. 6.1.1. From now on, we will refer to the track multiplicity assessed with the standard method as $N_{\mathrm{track}}^{\mathrm{core}}$.

As jets initiated by a quark or a gluon feature tracks that are less collimated, the region outside the core cone can be used to improve the separation and include *outer tracks*, to be added to the *inner tracks* in the core. An annulus around the core is considered. For each track in the outer cone the distance parameter is computed

$$D^{\mathrm{outer}} = \frac{p_{\mathrm{T}}^{\mathrm{inner}}}{p_{\mathrm{T}}^{\mathrm{outer}}} \Delta R(\mathrm{inner}, \mathrm{outer}) \tag{6.6}$$

with respect to all tracks in the inner region. If any of the computed distances satisfies the requirement $D^{\mathrm{outer}} < D^{\mathrm{max}}$ the outer track is included. In the case of real tau leptons, additional tracks in the outer cone are likely to originate from pile-up. As these typically have a much lower p_{T} than tracks from the tau, they are rejected. However, outer tracks from a jet typically have a higher p_{T}. In addition, the p_{T} difference between tracks in the core cone and the outer region is smaller for jets than it is for tau leptons. For these reasons, outer tracks from jets are included by the algorithm. This algorithm, known as p_{T}*-correlated track counting* [160], estimates the number of additional tracks in the outer region, called $N_{\mathrm{track}}^{\mathrm{corr}}$. The total number of tracks is then used in the fit: $N_{\mathrm{track}}^{\mathrm{c+c}} = N_{\mathrm{track}}^{\mathrm{core}} + N_{\mathrm{track}}^{\mathrm{correlated}}$.

Three parameters influence the performance of the algorithm and the track multiplicity shape, which are the maximum distance D^{max}, the dimension of the annulus surrounding the core region, ΔR^{max}, and the minimum p_{T} of the tracks in the outer region. The choice of these parameters has been studied, based on a preliminary measurement of the efficiency using template fitting. The distributions for real tau leptons and the jet background are shown in Fig. 6.8, 6.9 and 6.10 and are determined using simulated $Z \rightarrow \tau_{\mu}\tau_{\mathrm{had}}$ and data events from a tag-and-probe selection as will be described later. As shown by the plots, the algorithm allows for a better separation between signal and background, as can be seen by comparing the $N_{\mathrm{track}}^{\mathrm{c+c}}$ spectra with the standard result. Using a preliminary template fitting, based on $L_{\mathrm{int}} = 4.5$ fb^{-1} of data at $\sqrt{s} = 8$ TeV, the uncertainty associated with the efficiency estimate is minimised with the choice $D^{\mathrm{max}} = 4$, $\Delta R^{\mathrm{max}} = 0.6$ and $p_{\mathrm{T}}^{\mathrm{outer}} > 500$ MeV, which are consequently chosen as the default parameters.

6.4.2 Selection

A sample of hadronically decaying tau leptons is obtained from a tag-and-probe selection of $Z \rightarrow \tau_{\mu}\tau_{\mathrm{had}}$ events. Muon triggers are used to select the muon. Events are considered if the trigger signals muons with $p_{\mathrm{T}}^{\mu} > 20$ GeV and a tight topological isolation, or with $p_{\mathrm{T}}^{\mu} > 24$ GeV and looser isolation. Well reconstructed muons are required to have $p_{\mathrm{T}}^{\mu} > 22$ GeV and $|\eta_{\mu}| < 2.4$. Muon isolation is also required to suppress the multi-jet background, by measuring the total transverse energy E_{T} in the region with

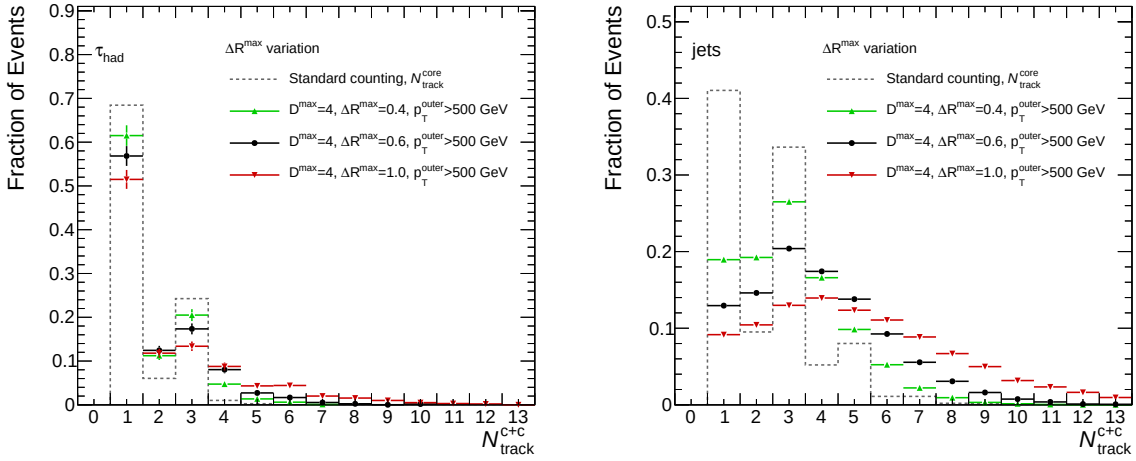

Figure 6.8: Variation versus $\Delta R^{\max}$ of the track multiplicity spectrum for tau leptons (left) and jets (right) determined with the alternative track counting. The track multiplicity spectrum obtained with the standard track counting is shown by the dashed line. The signal distributions are obtained using simulated events, while the jet track multiplicity is obtained from data. All distributions are normalised to unit area.

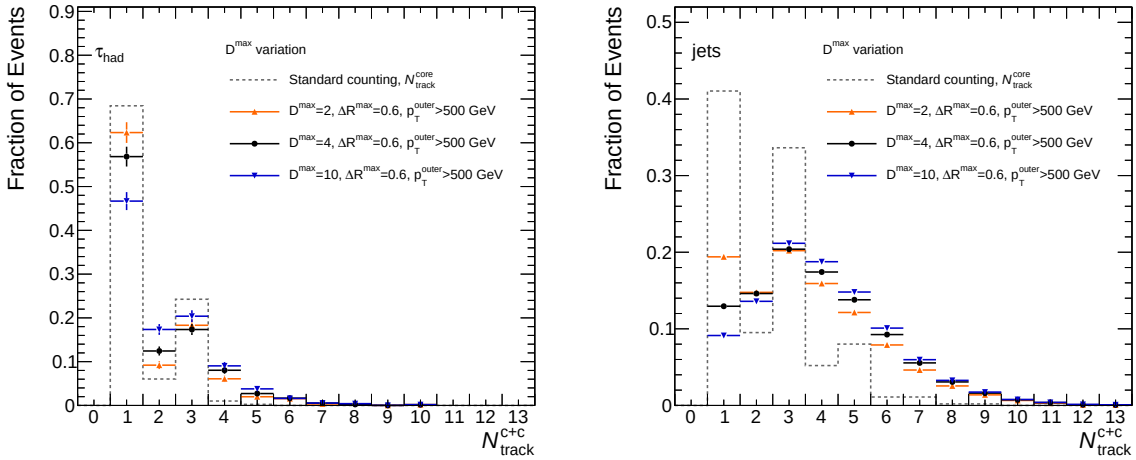

Figure 6.9: Variation versus $D^{\max}$ of the track multiplicity spectrum for tau leptons (left) and jets (right) determined with the alternative track counting. The track multiplicity spectrum obtained with the standard track counting is shown by the dashed line. The signal distributions are obtained using simulated events, while the jet track multiplicity is obtained from data. All distributions are normalised to unit area.

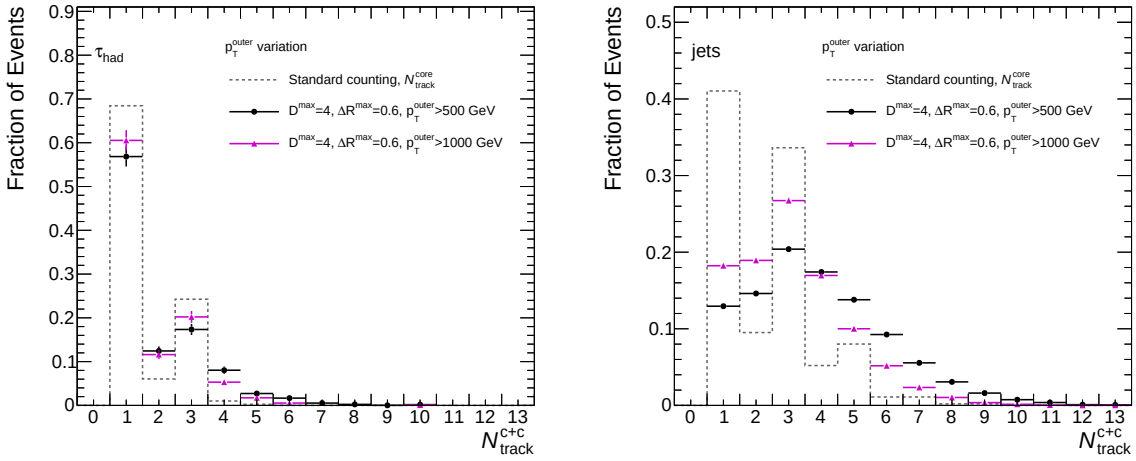

Figure 6.10: Variation versus $p_{\mathrm{T}}^{\mathrm{outer}}$ of the track multiplicity spectrum for tau leptons (left) and jets (right) determined with the alternative track counting. The track multiplicity spectrum obtained with the standard track counting is shown by the dashed line. The signal distributions are obtained using simulated events, while the jet track multiplicity is obtained from data. All distributions are normalised to unit area.

$0.05 < \Delta R < 0.2$ from the muon direction and requiring it to be less than 4% of p_{T}^{μ}. No additional tracks with $p_{\mathrm{T}} > 1$ GeV are allowed within $\Delta R < 0.4$ from the muon.

Hadronic tau decays are selected by requiring $p_{\mathrm{T}}^{\tau} > 20$ GeV, $|\eta_{\tau}| < 2.47$ and $N_{\mathrm{track}}^{\mathrm{core}} > 0$. The loose working point of the electron veto algorithm (cf. App. B.0.1) is also utilised if $N_{\mathrm{track}}^{\mathrm{core}} = 1$. The major portion of the jet background contamination comes from multi-jet events, and from those jets produced in association with $W \to \mu\nu$ events. In order to suppress the latter background the quantity $m_{\mathrm{T}} = \sqrt{2p_{\mathrm{T}}^{\mu}E_{\mathrm{T}}^{\mathrm{miss}}(1 - \cos\Delta\phi(\mu, E_{\mathrm{T}}^{\mathrm{miss}}))}$, called the *transverse mass*, is required to be below 50 GeV. For the same reason the requirements $\cos\Delta\phi(\mu, E_{\mathrm{T}}^{\mathrm{miss}}) + \cos\Delta\phi(\tau, E_{\mathrm{T}}^{\mathrm{miss}}) > -0.15$ and $\Delta\phi(\tau, \mu) > 2.4$ are applied.

In addition, the presence of a primary vertex with at least four associated tracks is required, no additional lepton other than the muon and the tau are allowed in the event, and the mass reconstructed with the muon and the $\tau_{\mathrm{had-vis}}$, called the *visible mass*, m_{vis}, has to be in the window 42 GeV $< m_{\mathrm{vis}}(\mu, \tau_{\mathrm{had-vis}}) < 82$ GeV. Finally, opposite electric charges between the tag and the probe are required.

The selection described above defines the region where the fit is performed to data. This region will be called the *opposite-sign* (OS) region referring to the charge correlation between the tag and the probe. As will be discussed in the following section, jets are modelled in the fit by using data selected in a control region where the tag and the probe have the same electric charge, the so-called *same-sign* (SS) region. Events in the SS region typically show a larger fraction of jets that originate from the hadronisation of a gluon compared to the OS region, where quark-initiated jets are more predominant. This charge correlation effect is introduced in the background by the presence of $W \to \mu\nu$ events with associated jets. As the jet model in the fit is obtained from the SS control region, it is important to check that this choice does not introduce a bias.

A potential bias could be caused by gluon-jet track multiplicities being higher than those of quark-jets, due to the higher colour charge of gluons. In order to reduce this effect, a selection is applied on the BDT score distribution. As gluons feature higher track multiplicities, gluon-originated jets are better separated from tau leptons than the quark-originated ones. Therefore, a BDT score of at least 0.3 is

required. This selection does not affect the signal efficiency, as shown in Fig. 6.11, where the BDT score distributions in the detector barrel and the end-cap are reported. The BDT score selection reduces the

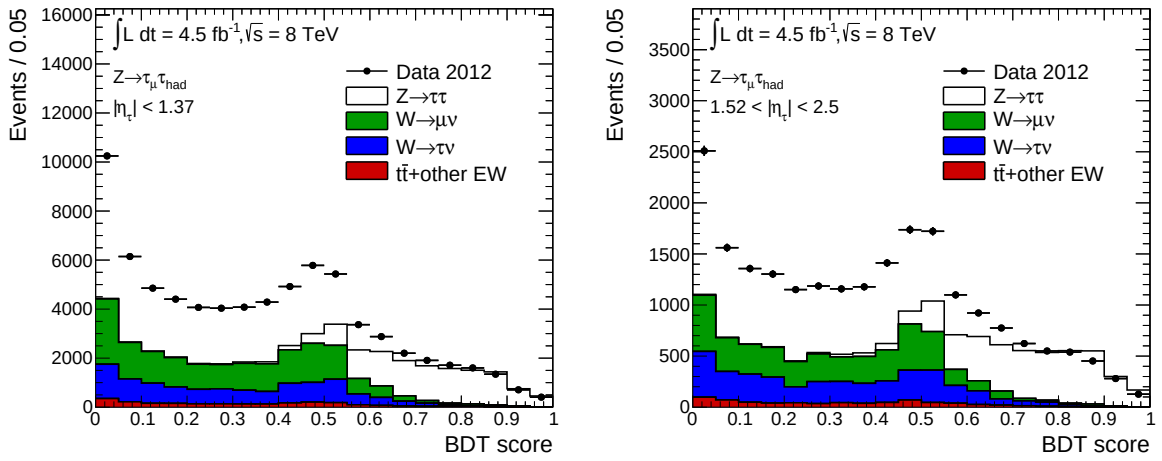

Figure 6.11: Distributions of the BDT score in the barrel (left) and in the end-cap (right), obtained with a data sample of $L_{\text{int}} = 4.5$ fb^{-1}. The large discrepancy between the data and the simulated contributions is caused by the lack of the multi-jet contribution, which is not shown here.

overall background in the OS region, while also reducing the discrepancy between the track multiplicity spectra from $W \to \mu\nu$ events between the OS and the SS region, as illustrated by Fig. 6.12. This allows for a completely data-driven estimate of the model for the jet track multiplicity in the fit, where the SS region does not show any significant bias with respect to the OS region. The summary of all the selection

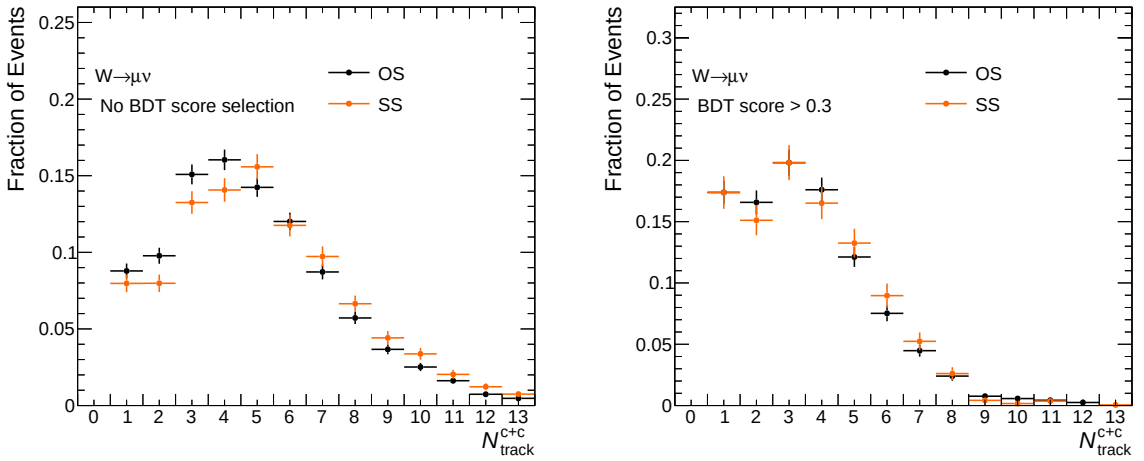

Figure 6.12: Shape comparison of the track multiplicity distributions for the $W \to \mu\nu$ background in the opposite-sign and same-sign regions before identification (left) and after (right). The shapes are obtained using simulated events. All distributions are normalised to unit area.

requirements used to define the relevant regions for the fitting method is given in Tab. 6.2. The table includes the definition of the regions where the fit is performed, as well as control regions used for the estimation of the jet background and its systematic uncertainty, which will be described later.

Selection Requirements	Fit Region	CR C (SS, Isolated)	CR B (OS, Anti-isolated)	CR D (SS, Anti-isolated)	$W \to \mu\nu$ CR
Tag Muon					
Identified muon	•	•	•	•	•
Muon triggers ($p_{\mathrm{T}}(\mu) > 20$ GeV + tight isolation or $p_{\mathrm{T}}(\mu) > 24$ GeV + loose isolation)	•	•	•	•	•
$p_{\mathrm{T}}(\mu) > 22$ GeV and $\lvert\eta(\mu)\rvert < 2.4$	•	•	•	•	•
Muon isolation (E_{T} in $0.05 < \Delta R < 0.2$ from muon direction less than 4% of $p_{\mathrm{T}}(\mu)$)	•	•	rev.	rev.	•
No other tracks with $p_{\mathrm{T}} > 1$ GeV within $\Delta R < 0.4$	•	•	•	•	•
Probe Tau					
$p_{\mathrm{T}}(\tau) > 20$ GeV and $\lvert\eta(\tau)\rvert < 2.47$	•	•	•	•	•
$N_{\mathrm{track}}^{\mathrm{core}} > 0$	•	•	•	•	•
Loose electron veto if $N_{\mathrm{track}}^{\mathrm{core}} = 1$	•	•	•	•	•
BDT score > 0.3	•	•	•	•	•
No tau-ID	• loose medium tight	• loose medium tight	• loose medium tight	• loose medium tight	• loose medium tight
Event Topology and Kinematic					
$\cos\Delta\phi(\mu, E_{\mathrm{T}}^{\mathrm{miss}}) + \cos\Delta\phi(\tau, E_{\mathrm{T}}^{\mathrm{miss}}) > -0.15$	•	•	•	•	rev.
$m_{\mathrm{T}} = \sqrt{2p_{\mathrm{T}}(\mu)E_{\mathrm{T}}^{\mathrm{miss}}(1 - \cos\Delta\phi(\mu, E_{\mathrm{T}}^{\mathrm{miss}}))} < 50$ GeV	•	•	•	•	rev.
$\Delta\phi(\tau, \mu) > 2.4$	•	•	•	•	•
One primary vertex with at least 4 associated tracks	•	•	•	•	•
No other reconstructed leptons in the event	•	•	•	•	•
42 GeV $< m_{\mathrm{vis}}(\mu, \tau) < 82$ GeV	•	•	•	•	•
Muon and tau with opposite electric charge	•	rev.	•	rev.	• / rev.

Table 6.2: Summary of the selection requirements defining the relevant regions of the fitting method, including the region where the fit is performed and control regions used for the estimation of the background and its uncertainty. In the table, the dot indicates the application of the requirement indicated in the list on the left. When a different requirement is imposed, it is explicitly indicated in the table. The reversal of a selection requirement is indicated as "rev.". The control regions used in the method and indicated as CR C, B and D, are named according to the convention used in Fig. 6.13 and 6.14.

6.4.3 Fitting Method and Choice of Templates

The tau identification efficiency in data is measured by a fit, which determines the number of real tau leptons in data before and after identification. To perform the fit, the track multiplicity distributions in data before and after identification are considered, which offer good discrimination power between the signal and the background. The signal is composed of real tau leptons, while the background is composed of the jet contamination and a small contribution from electrons. Both the signal and the background have to be modelled in the fit, i.e. they have to be included in the fitted functions before and after identification, $f_{\text{before ID}}(N_{\text{track}}^{\text{c+c}})$ and $f_{\text{after ID}}(N_{\text{track}}^{\text{c+c}})$, respectively. The signal and background models, also called *templates*, contribute to the fitted functions as

$$f_{\text{before ID}}(N_{\text{track}}^{\text{c+c}}) = N_\tau S_\tau(N_{\text{track}}^{\text{c+c}}) + N_{\text{jet}} B_{\text{jet}}(N_{\text{track}}^{\text{c+c}}) + N_e B_e(N_{\text{track}}^{\text{c+c}}) \tag{6.7a}$$

$$f_{\text{after ID}}(N_{\text{track}}^{\text{c+c}}) = \varepsilon_\tau N_\tau S'_\tau(N_{\text{track}}^{\text{c+c}}) + \varepsilon_{\text{jet}} N_{\text{jet}} B'_{\text{jet}}(N_{\text{track}}^{\text{c+c}}) + \varepsilon_e N_e B'_e(N_{\text{track}}^{\text{c+c}}). \tag{6.7b}$$

In Eq. (6.7), S_τ, B_{jet} and B_e represent the templates for signal, jets and electrons before identification, while S'_τ, B'_{jet} and B'_e refer to the respective templates after identification. The parameters determined by the fit are the number of events for each contribution before identification and the efficiencies. As the electron contribution is a minor one, the corresponding parameters are fixed using the simulation prediction. Hence, the fit only measures the signal and jet normalisations before ID, N_τ and N_{jet}, respectively, and their efficiencies ε_τ and ε_{jet}.

The question now arises about how to choose the different templates. The strategy used in the fit is to rely on the simulation to model real tau leptons and the minor electron background, while using a data-driven method to address the dominant jet background, for which no reliable simulation is available. The signal is modelled using simulated $Z \to \tau_\mu \tau_{\text{had}}$ events with `Pythia`, where reconstructed tau leptons are matched to the true simulated ones. The jet template consists of the $N_{\text{track}}^{\text{c+c}}$ data distribution in a region where the tag and the probe have opposite electric charges. The distributions in the fit regions before and after identification are illustrated by Fig. 6.13 (A) and 6.14 (A), respectively, for the medium working point of the ID algorithm and before the fit is performed. The data distributions in the same-sign control regions are also visible in Fig. 6.13 (B) and 6.14 (B) for the respective cases. The figures also show the jet background composition, which is dominated by the $W \to \mu\nu +$ jets and $W \to \tau\nu +$ jets contributions, together with multi-jet events, which are assumed to account for the large discrepancy between the data and the model. Other contributions, intended to be included in this model, are $Z \to \mu\mu$ + jets, where a jet is produced in association with the final state, and $t\bar{t}$ events, where the hadronically decaying tau and the muon are produced in top and anti-top decays. The electron contribution is mainly due to mis-identified electrons in the tau decay. This background is modelled using simulated $Z \to \tau_\mu \tau_{\text{had}}$ events, like the signal, but the reconstructed tau is required to fail the matching with the true one. This contribution amounts to only a small fraction of the events labelled as *other EW* in the figures.

The measurement of the efficiency is performed for inclusive track multiplicity, where no distinction is made between 1-prong and multi-prong decays, as well as for the exclusive case. The signal template in Eq. (6.7) is used for the inclusive measurement. In order to measure exclusive efficiencies, the signal template is split according to

$$S_\tau(N_{\text{track}}^{\text{c+c}}) = f S_{\text{1p}\,\tau}(N_{\text{track}}^{\text{c+c}}) + (1-f) S_{\text{mp}\,\tau}(N_{\text{track}}^{\text{c+c}}), \tag{6.8a}$$

$$S'_\tau(N_{\text{track}}^{\text{c+c}}) = f' S'_{\text{1p}\,\tau}(N_{\text{track}}^{\text{c+c}}) + (1-f') S'_{\text{mp}\,\tau}(N_{\text{track}}^{\text{c+c}}), \tag{6.8b}$$

where f and $(1-f)$ represent the fraction of 1-prong and multi-prong tau decays, respectively, before identification, and f' and $(1-f')$ are the corresponding fractions after identification. In order to simplify

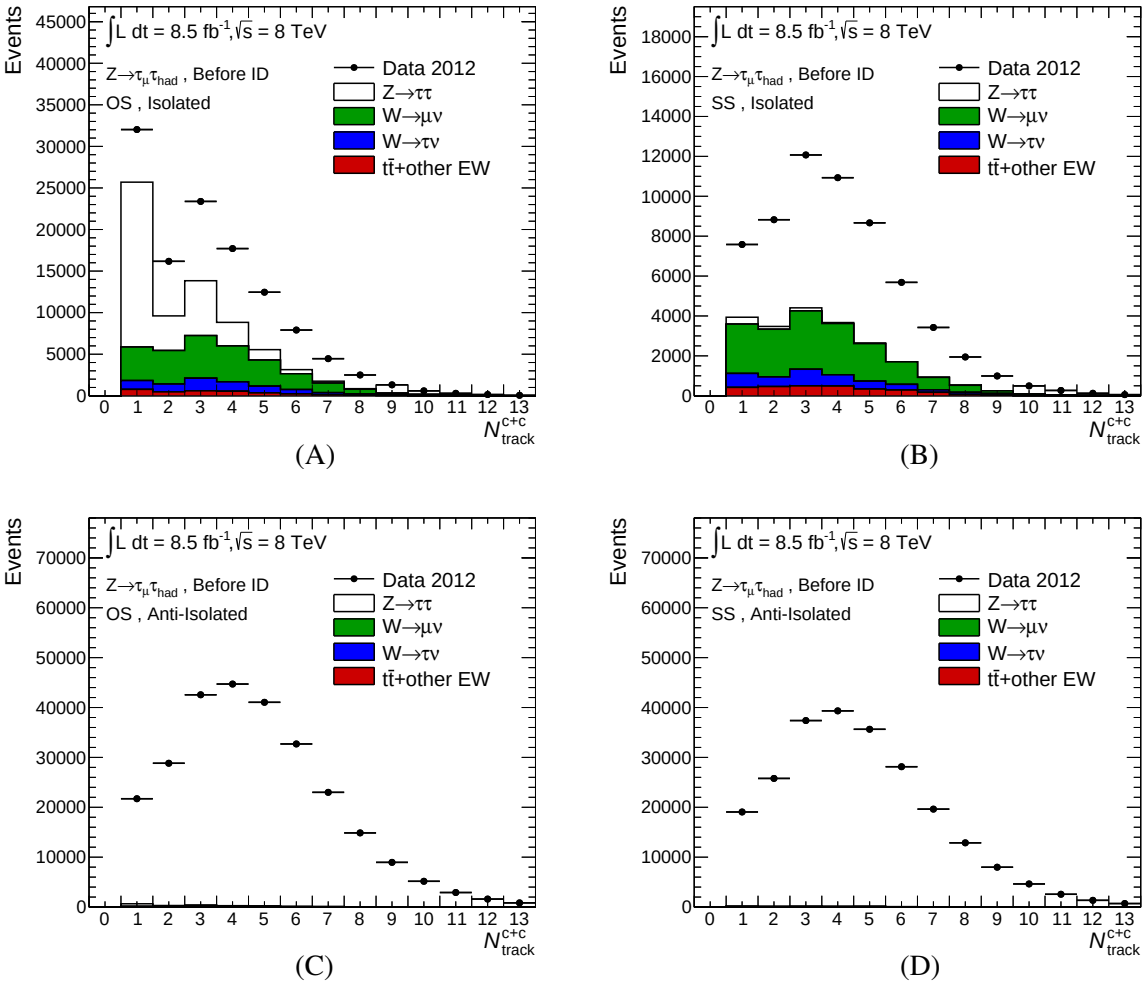

Figure 6.13: Signal and background distributions in all the regions relevant for the measurement of the tau identification efficiency in data. The distributions are shown *before identification* and no fit is performed. (A) Signal region chosen to perform the fit, also called opposite-sign region. (B) Control region chosen to model the jet contribution in the fit, which is the data distribution shown in the plot. (C) Control region for multi-jet events, where the isolation on the muon is reversed. (D) Control region for multi-jet events, where the tag and the probe have the same electric charge and isolation on the muon is reversed. All backgrounds shown are modelled with the simulation, choosing `Pythia` for $Z \to \tau\tau$ events, and `Alpgen` for other contributions. The discrepancy between data and the simulation is due to the multi-jet background, which is not shown here.

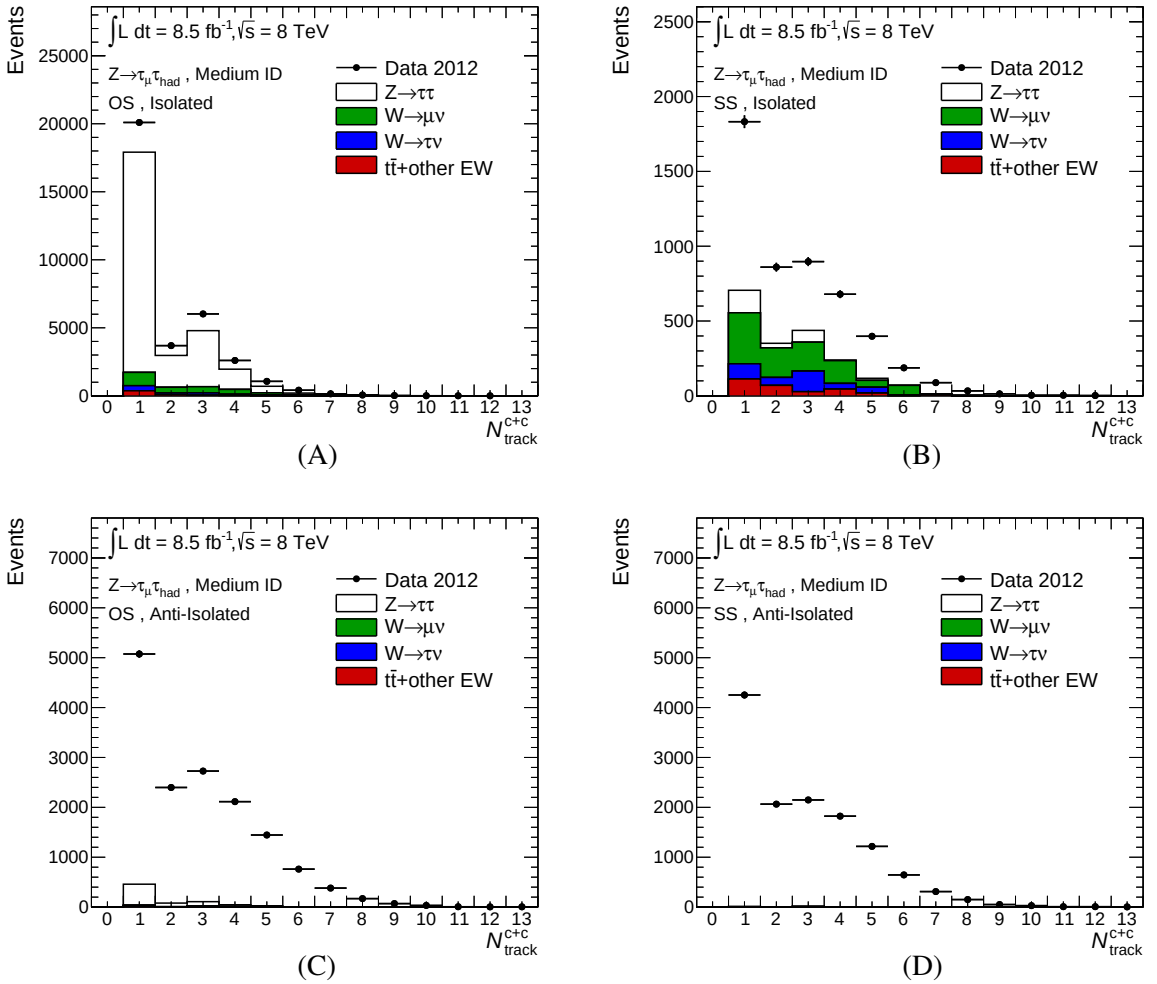

Figure 6.14: Signal and background distributions in all the regions relevant for the measurement of the tau identification efficiency in data. The distributions are shown *after identification* at the medium working point of the BDT algorithm and no fit is performed. (A) Signal region chosen to perform the fit, also called opposite-sign region. (B) Control region chosen to model the jet contribution in the fit, which is the data distribution shown in the plot. (C) Control region for multi-jet events, where the isolation on the muon is reversed. (D) Control region for multi-jet events, where the tag and the probe have the same electric charge and isolation on the muon is reversed. All backgrounds shown are modelled with the simulation, choosing `Pythia` for $Z \to \tau\tau$ events, and `Alpgen` for other contributions. The discrepancy between data and the simulation is due to the multi-jet background, which is not shown here.

the fit procedure and avoid instabilities, only f' is allowed to vary in the fit, while f is determined from the simulation. Potential fit instabilities can arise due to similarities between the shapes of the multi-prong signal and the jet background before identification. Fixing the proportion of the 1-prong and multi-prong contributions in this fit relies on the assumption that the reconstruction efficiency is well modelled by the simulation independently of the track multiplicity. The signal templates are obtained by requiring $N_{\text{track}}^{\text{core}} = 1$ and $N_{\text{track}}^{\text{core}} > 1$ for 1-prong and multi-prong decays, respectively. An example of the fit is shown in Fig. 6.15, where the signal template is split.

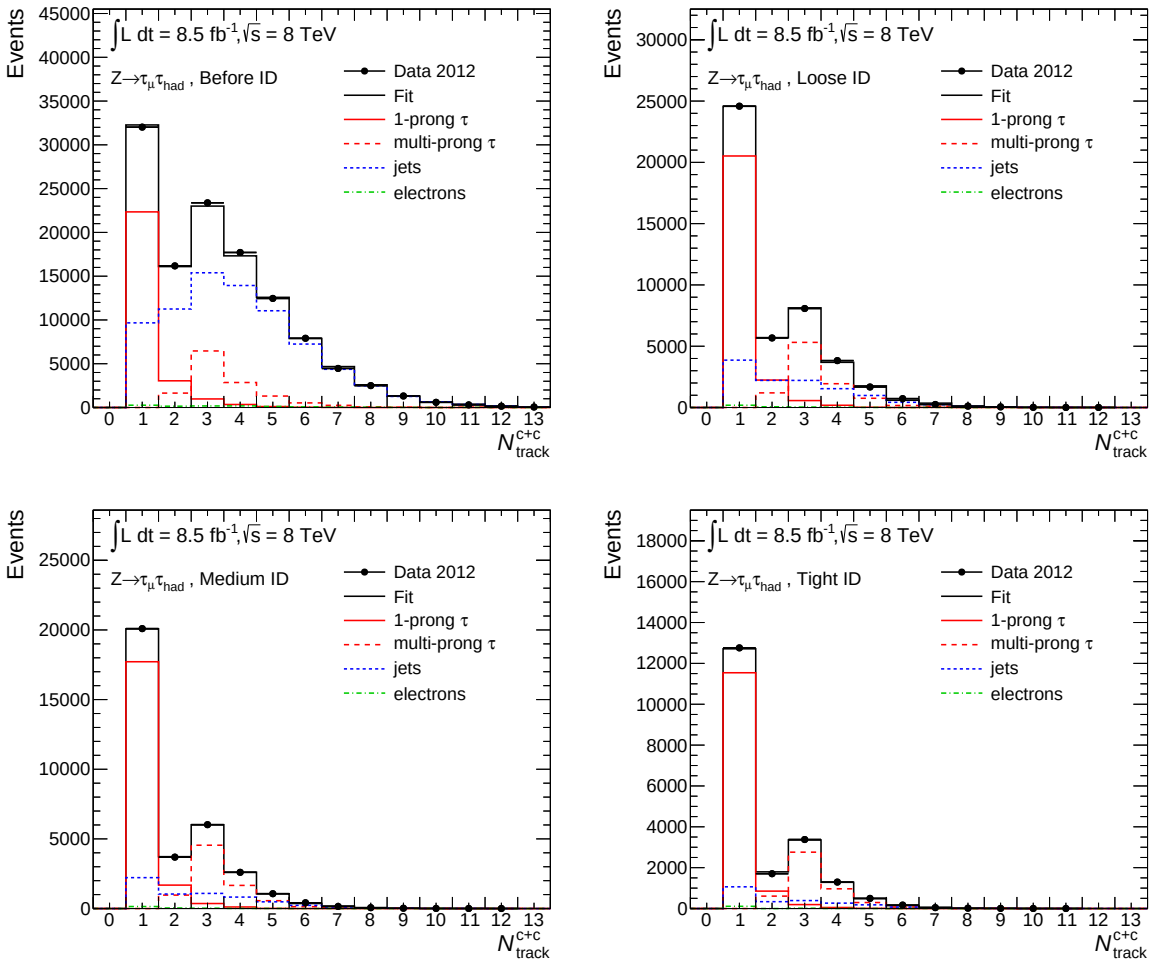

Figure 6.15: Fit of the track multiplicity distribution in data. All regions shown are fitted simultaneously. The signal is split into a 1-prong and a multi-prong component, which allows for the separate measurement of the respective efficiencies.

The efficiency and the corresponding scale factors are measured for 1-prong, multi-prong and inclusive decays of the tau. For each case, different pseudo-rapidity regions are considered: the barrel, the end-cap and the full η region.

6.4.4 Systematic Uncertainties

Systematic uncertainties have to be estimated, which are assigned to the choice of the templates. Individual systematic uncertainties are estimated altering each template shape, according to the systematic effect, and repeating the measurement. The relative uncertainty on the scale factor is then measured as

$$\Delta \mathrm{SF}_{\mathrm{syst.}}(\%) = \frac{\varepsilon_{\mathrm{nom.}} - \varepsilon_{\mathrm{syst.}}}{\varepsilon_{\mathrm{nom.}}} \tag{6.9}$$

where $\varepsilon_{\mathrm{nom.}}$ is the efficiency from the nominal fit and $\varepsilon_{\mathrm{syst.}}$ the one from the systematic variation.

Systematic uncertainties are estimated for the signal and the background. Signal uncertainties are assigned to the choice of the generator of simulated events, the tuning of the underlying event, the model of the detector material, the model of the hadronic shower and the effect of pile-up. The choice of the generator is accounted for by obtaining a signal template using `Alpgen` [173] instead of `Pythia`. The tuning of the underlying event is altered according to the *A2* tune [80]. The detector model is taken into account by including an additional amount of material in the simulation. The effect of the hadronic shower model is investigated by altering the shape according to the *FTFP_BERT* model or *QGSP*. To avoid double counting this effect, the largest variation between these two is considered. Simulated events might not reproduce well the effect of pile-up, hence, simulated distributions are modified using a weighting procedure based on a correction of the simulated $\langle\mu\rangle$ distribution to match the one in data. The correction has an uncertainty associated with it, which is propagated to the signal templates. In this case the uncertainty is estimated as $\Delta \mathrm{SF}_{\mathrm{pile-up}}(\%) = \pm|\Delta \mathrm{SF}_{\mathrm{up}}(\%) - \Delta \mathrm{SF}_{\mathrm{down}}(\%)|$.

In order to reduce the statistical uncertainty on the systematically altered signal templates, the nominal and altered shapes are obtained without applying the full tag-and-and probe selection, i.e. for $S_\tau^{\text{nom. no T\&P}}$ and $S_\tau^{\text{syst. no T\&P}}$, respectively. The nominal signal shape is then rescaled by the ratio $R^{\text{no T\&P}}(N_{\text{track}}^{\text{c+c}})$, defined as

$$R^{\text{no T\&P}}(N_{\text{track}}^{\text{c+c}}) = \frac{S_\tau^{\text{syst. no T\&P}}(N_{\text{track}}^{\text{c+c}})}{S_\tau^{\text{nom. no T\&P}}(N_{\text{track}}^{\text{c+c}})}. \tag{6.10}$$

The rescaled signal template can be written as

$$S_\tau^{\text{syst.}}(N_{\text{track}}^{\text{c+c}}) = R^{\text{no T\&P}}(N_{\text{track}}^{\text{c+c}}) S_\tau^{\text{nom.}}(N_{\text{track}}^{\text{c+c}}). \tag{6.11}$$

This method relies on the assumption that systematic effects are not correlated with the tag-and-probe selection itself. This is a reasonable assumption, as it is found that $R^{\text{no T\&P}}(N_{\text{track}}^{\text{c+c}})$, defined in Eq. (6.10), is consistent with $R^{\text{T\&P}}(N_{\text{track}}^{\text{c+c}})$ for all systematic uncertainties taken into account. This is illustrated in Fig. 6.16 showing a comparison of the two ratios obtained using the full tag-and-probe selection or discarding it. The ratio in Fig. 6.16 is obtained comparing the nominal `Pythia` sample with the `Alpgen` one, which corresponds to the leading alteration among the signal systematic uncertainties. The signal shapes $S_\tau^{\text{syst. no T\&P}}(N_{\text{track}}^{\text{c+c}})$ and $S_\tau^{\text{nom. no T\&P}}(N_{\text{track}}^{\text{c+c}})$, used to define $R^{\text{no T\&P}}(N_{\text{track}}^{\text{c+c}})$, are obtained including $Z \to \tau_{\text{had}}\tau_{\text{had}}$ events, in order to increase the available number of signal events. This is done by matching hadronically decaying tau leptons to true simulated taus, and imposing the same p_{T} requirements of the tag-and-probe selection. An example of the nominal signal template compared to the systematically altered ones is shown in Fig. 6.17, before and after medium identification.

The dominant systematic effect in the fitting method is due to the shape of the jet background. As mentioned in Sec. 6.4.2, a different proportion of gluon-initiated and quark-initiated tau candidates is present in the OS region, where the fit is performed, and in the SS region, where the jet shape is modelled. The requirement on the BDT score to be higher than 0.3 helps reducing this difference. Nonetheless, a

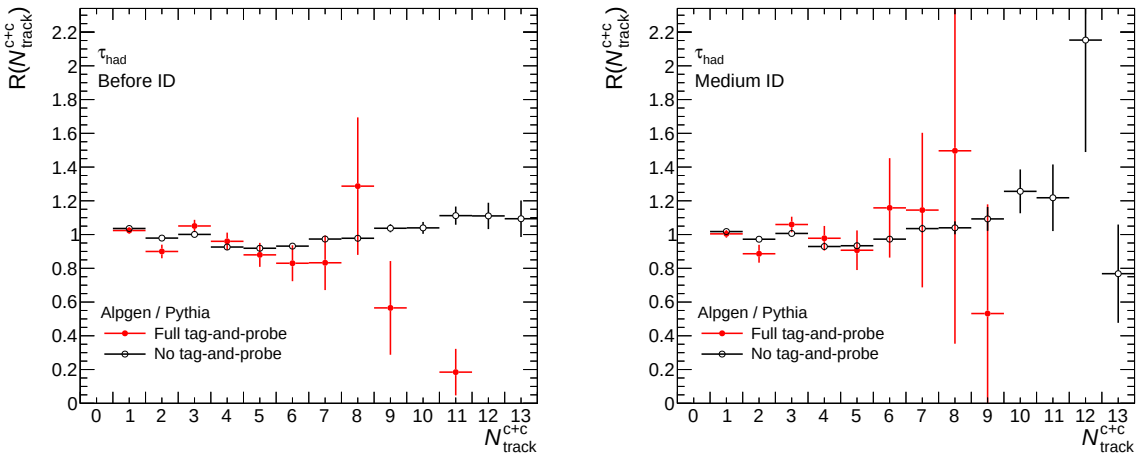

Figure 6.16: Ratios between signal templates obtained with `Alpgen` and `Pythia` before identification (left) and after (right). The plots show the comparison between the ratios of templates obtained applying the full tag-and-probe selection (red) or not (black). The uncertainty shown is only statistical.

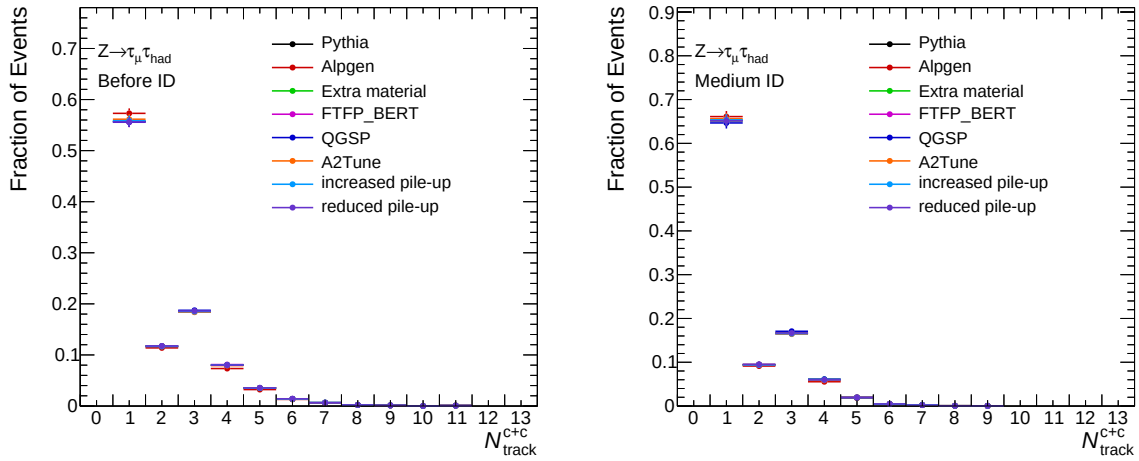

Figure 6.17: Nominal signal template compared to the systematically altered ones before identification (left) and after the medium one (right). All distributions are normalised to unit area.

systematic uncertainty has to be taken into account. To estimate the uncertainty the fit is repeated with an altered jet template reproducing the effect of a different proportion of quark and gluon-initiated jets with respect to the nominal template.

The method used to obtain the altered jet template relies on both data and simulation. The systematically altered jet template is obtained using all simulated contributions featuring tau candidates which are jets, as shown in Fig. 6.13 (B) and Fig. 6.14 (B), which are subtracted from data in the SS region. These contributions are dominated by W + jets events. Then, the remaining distribution, accounting only for multi-jet events, is rescaled with a data-driven factor, to take into account the different number of multi-jet events between the OS and SS regions. Two control regions, highly enriched in multi-jet events, are chosen for the measurement, which are defined by the same requirements applied to the OS and SS regions, but with reversed isolation on the muon tag (*anti-isolation*). The regions are shown in Fig. 6.13 (C,D) and 6.14 (C,D), before identification and after the medium requirement, respectively. The summary of the selection requirements imposed to define the control regions B, C and D are summarised in Tab. 6.2. The data-driven factor also alters the multi-jet shape, as it is measured as a function of $N_{\text{track}}^{\text{c+c}}$. Finally, the simulated contributions in the OS region are added to the shape. This procedure is summarised by the formula

$$B_{\text{jet}}^{\text{syst.}}(N_{\text{track}}^{\text{c+c}}) = \left(\text{data}_{\text{SS}}(N_{\text{track}}^{\text{c+c}}) - \sum_{i}^{\text{all sim.}} B_{i,\text{SS}}(N_{\text{track}}^{\text{c+c}})\right) \frac{\text{data}_{\text{OS}}^{\text{anti-iso}}(N_{\text{track}}^{\text{c+c}})}{\text{data}_{\text{SS}}^{\text{anti-iso}}(N_{\text{track}}^{\text{c+c}})} + \sum_{i}^{\text{all sim.}} B_{i,\text{OS}}(N_{\text{track}}^{\text{c+c}}). \quad (6.12)$$

In Eq. (6.12), the normalisation of the $W \to \mu\nu$ and $W \to \tau\nu$ contributions is obtained from data. Their simulated number of events is corrected to data in a control region enriched with $W \to \mu\nu$ events and defined by requiring $m_{\text{T}}(\mu, E_{\text{T}}^{\text{miss}}) > 50$ GeV and $\cos\Delta\phi(\mu, E_{\text{T}}^{\text{miss}}) + \cos\Delta\phi(\tau, E_{\text{T}}^{\text{miss}}) < -0.15$, i.e. reversed with respect to the nominal selection (cf. Tab. 6.2). An example distribution in this control region for the OS and SS selections, and before and after identification, is shown in Fig. 6.18 and 6.19, before any correction is applied to the simulation. The measurement is performed by rescaling the number of events of the two contributions to match the data, independently of $N_{\text{track}}^{\text{c+c}}$. The correction factor measured in

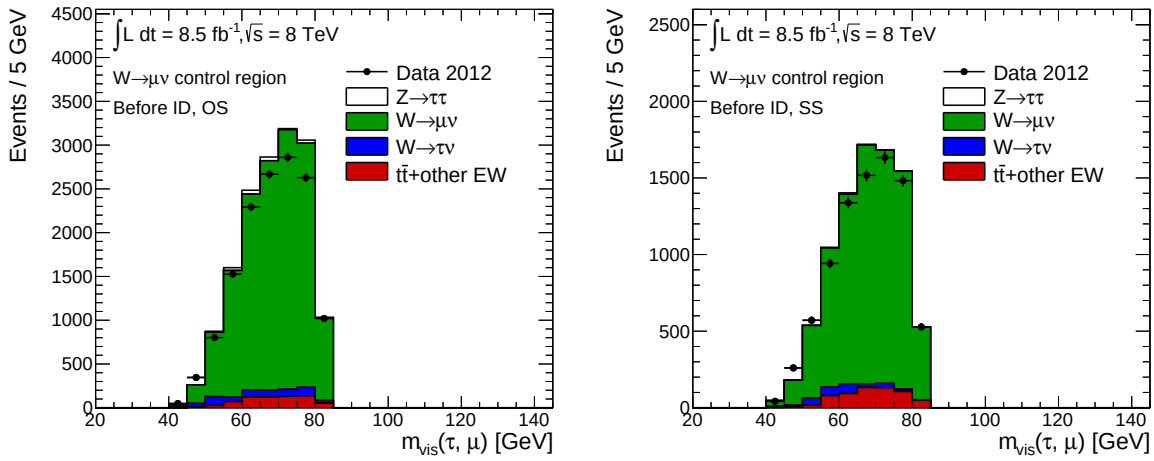

Figure 6.18: Control regions for the measurement of the normalisation correction factor to be applied to $W \to \mu\nu$ and $W \to \tau\nu$ simulated events. The plots show the opposite-sign (left) and same-sign (right) regions and are obtained before identification.

this region, called k_W, ranges between ≈ 1.2 and ≈ 0.73 depending on $|\eta|$, the charge product between the

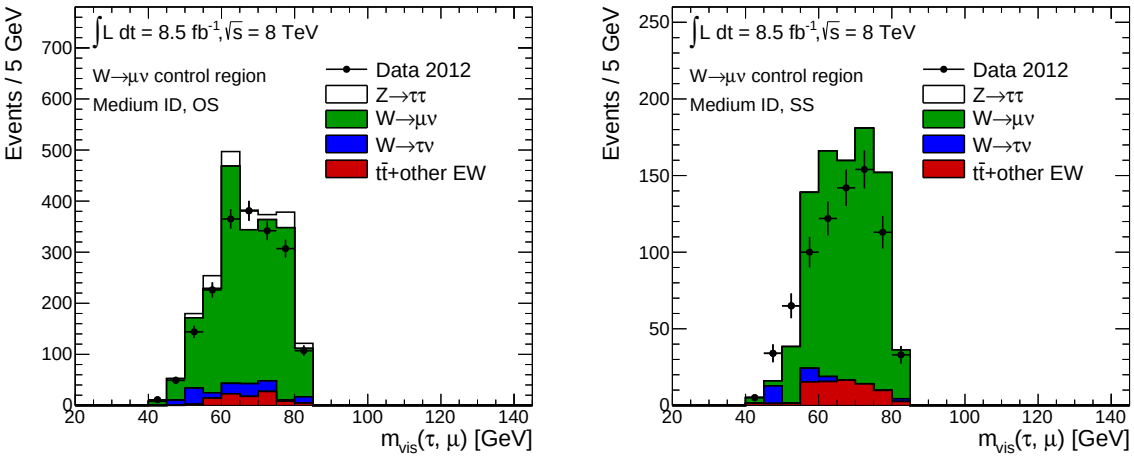

Figure 6.19: Control regions for the measurement of the normalisation correction factor to be applied to $W \to \mu\nu$ and $W \to \tau\nu$ simulated events. The plots show the opposite-sign (left) and same-sign (right) regions and are obtained after medium identification.

tag and the probe, and the ID working point. It has to be noted that the small signal contamination present in the control regions does not significantly alter the shape of the jet background and has negligible effect in the fit. The nominal and altered jet templates are compared in Fig. 6.20.

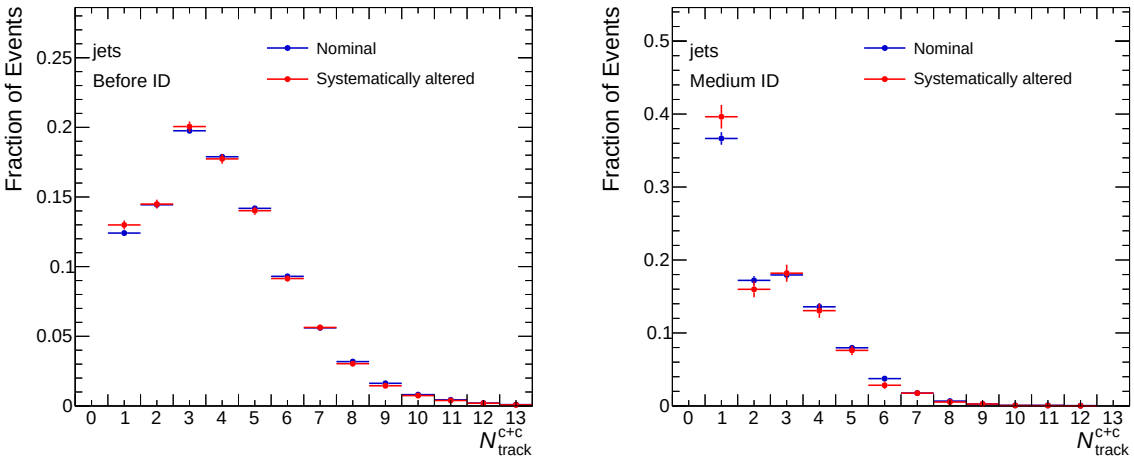

Figure 6.20: Comparison of the nominal and systematically altered jet templates before identification (left) and after the medium requirement (right). All distributions are normalised to unit area.

Finally, a systematic uncertainty is assigned to the choice of the electron template by conservatively altering its normalisation upward and downward by 100%. This conservative choice simplifies the treatment of the uncertainty and does not lead to a significant decrease in the precision of the measurement. The fit is repeated for the upward and downward variation and the uncertainty is estimated as $\Delta\mathrm{SF}_e(\%) = \pm|\Delta\mathrm{SF}_{\mathrm{up}}(\%) - \Delta\mathrm{SF}_{\mathrm{down}}(\%)|$. The full set of results are summarised in Tab. 6.3, and refer to the entire pseudo-rapidity range.

$Z \to \tau_\mu \tau_{\text{had}}$	ID Efficiency Scale Factors								
	Inclusive			1-prong			Multi-prong		
	Loose	Medium	Tight	Loose	Medium	Tight	Loose	Medium	Tight
Generator	0.4%	0.2%	0.6%	0.5%	0.5%	1.7%	2.6%	2.1%	2.2%
Hadronic shower	0.4%	0.5%	1.0%	0.3%	0.5%	1.0%	1.3%	1.5%	0.9%
UE tune	0.1%	0.1%	0.1%	0.1%	0.1%	0.1%	2.0%	2.2%	2.0%
Detector geometry	0.1%	0.1%	0.2%	0.1%	0.1%	0.2%	1.1%	2.3%	1.1%
Pile-up	0.2%	0.1%	0.1%	0.2%	0.2%	0.1%	0.5%	0.5%	0.6%
Jet shape	2.0%	2.3%	2.4%	1.4%	1.7%	1.9%	2.3%	2.5%	2.9%
Electrons	1.5%	0.4%	0.6%	1.3%	0.3%	0.5%	1.7%	0.6%	0.7%
$\Delta\text{SF}_{\text{syst.}}$	2.5%	2.4%	2.7%	2.0%	1.9%	2.3%	4.1%	4.3%	3.5%
$\Delta\text{SF}_{\text{stat.}}$	1.3%	1.5%	1.9%	1.3%	1.5%	1.9%	1.9%	2.1%	2.8%
$\Delta\text{SF}_{\text{stat.+syst.}}$	2.9%	2.8%	3.3%	2.4%	2.4%	3.0%	4.6%	4.8%	4.5%
SF	1.001	0.970	0.895	0.992	0.968	0.892	1.149	1.021	0.934

Table 6.3: Scale factors for the tau identification efficiency measured in data using a tag-and-probe selection of $Z \to \tau_\mu \tau_{\text{had}}$ events. The table includes the breakdown of the systematic uncertainty in its components, which are added in quadrature. The total SF uncertainty includes the statistical and systematic components which are added in quadrature.

6.4.5 The $Z \to \tau_e \tau_{\text{had}}$ channel

A similar measurement has been performed using a tag-and-probe selection of $Z \to \tau_e \tau_{\text{had}}$ events, i.e. in the electron channel, which relies on data collected at $\sqrt{s} = 8$ TeV with an integrated luminosity of $L_{\text{int}} = 10.5\ \text{fb}^{-1}$. Events are selected using similar requirements as for the muon channel, with only a few differences regarding the tag selection. An electron trigger requiring isolation and $E_{\text{T}} > 24$ GeV is used. The kinematic and topological requirements are also applied: 25 GeV $< p_{\text{T}}^e <$ 40 GeV and $|\eta_e| < 1.37$ or $1.52 < |\eta_e| < 2.47$. Isolation around the electron is required at the 8% level. The track multiplicity distribution of the probe tau is shown in Fig. 6.21, before and after medium identification. The fit models in the $Z \to \tau_e \tau_{\text{had}}$ and $Z \to \tau_\mu \tau_{\text{had}}$ channels are identical, featuring an identical choice of the control regions used for the jet template. The electron contribution in this channel, however, is dominated by $Z \to ee$ events, and the shape, as well as its normalisation, are taken from the simulation and fixed in the fit. An example of the fit in the electron channel is shown in Fig. 6.22, before and after identification. The systematic uncertainties for the measurement in the electron channel have identical sources as those already discussed for the muon channel, and are evaluated using similar methods. Further details about the electron channel can be found in Ref. [160].

6.4.6 Final Results and Combination

The scale factor measurements in the muon and electron channels are combined in the barrel, the end-cap, in the inclusive pseudo-rapidity region, and for each track multiplicity. The statistical combination of the two measurements is performed according to the prescriptions discussed in Ref. [174], which require the

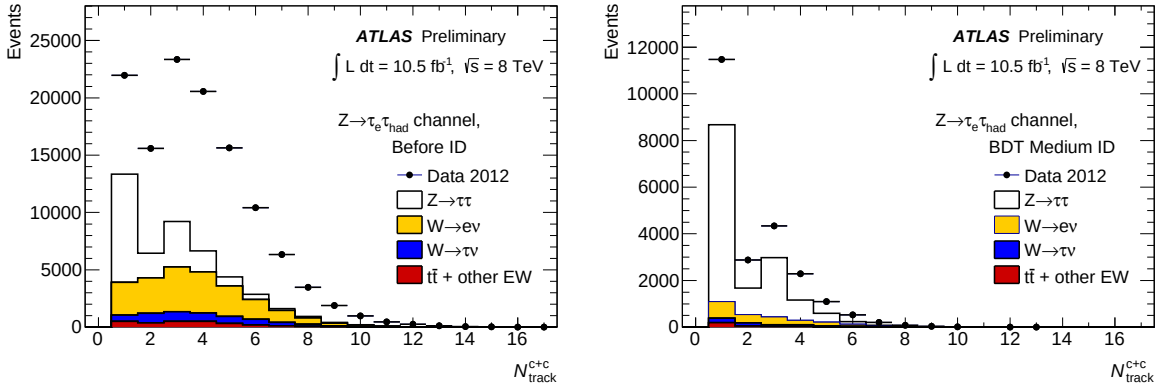

Figure 6.21: Track multiplicity distributions of the tau probe from a tag-and-probe selection of $Z \to \tau_e \tau_{\text{had}}$ events before identification (left) and after the medium requirement (right). Simulated signal events are obtained with the `Pythia` generator, while `Alpgen` is used for the other contributions. The large discrepancy between data and simulation is due to the multi-jet background which is not estimated.

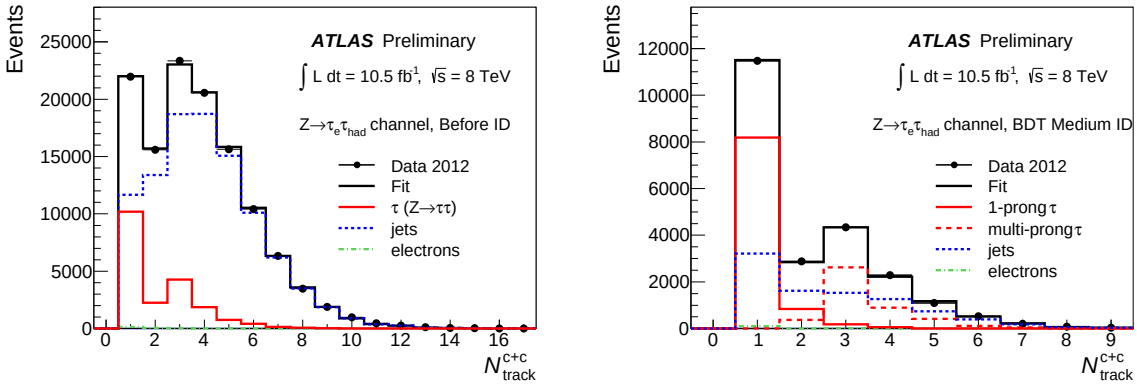

Figure 6.22: Fit to the track multiplicity distribution in data, using the template method in the electron channel. The fit is shown before identification (left) and after the medium requirement (right).

decomposition of the total uncertainties into a correlated and uncorrelated component. Each individual uncertainty is treated as 100% correlated between the two channels, as every systematic effect has the same origin and is evaluated in an analogous way. However, this does not necessarily lead to the same level of correlation between the total uncertainties associated with each channel. In order to compute the total degree of correlation, ρ_{total}, the following scheme is applied. We can write each uncertainty as σ_i which is evaluated for the two channels, c_μ and c_e. The correlation matrix between the measurements can be written as

$$\mathcal{M}_{\text{tot. corr.}}(c_\mu, c_e) = \sum_i^{\text{all unc.}} \begin{pmatrix} \sigma^2_{i,c_\mu} & \rho_i \sigma_{i,c_\mu} \sigma_{i,c_e} \\ \rho_i \sigma_{i,c_\mu} \sigma_{i,c_e} & \sigma^2_{i,c_e}. \end{pmatrix} \tag{6.13}$$

As all sources of uncertainty are treated as fully correlated, we have $\rho_i = 1$. The total degree of correlation between the measurements is then

$$\rho_{\text{total}} = \left(\sum_i^{\text{all unc.}} \sigma_{i,c_\mu} \sigma_{i,c_e} \right) \Bigg/ \left(\sqrt{\sum_i^{\text{all unc.}} \sigma^2_{i,c_\mu}} \sqrt{\sum_i^{\text{all unc.}} \sigma^2_{i,c_e}} \right), \tag{6.14}$$

$Z \to \tau_l \tau_{\text{had}}$	ID Efficiency SF Combination								
	Inclusive			1-prong			Multi-prong		
	Loose	Medium	Tight	Loose	Medium	Tight	Loose	Medium	Tight
SF($Z \to \tau_\mu \tau_{\text{had}}$)	1.001	0.970	0.895	0.992	0.968	1.892	1.149	1.021	0.934
uncorrelated syst.	2.0%	2.3%	2.4%	1.4%	1.7%	1.9%	2.6%	2.1%	2.2%
correlated syst.	1.6%	0.7%	1.3%	1.5%	0.7%	2.1%	3.9%	5.7%	5.3%
stat.	1.3%	1.5%	1.9%	1.3%	1.5%	1.9%	1.9%	2.1%	2.8%
syst.+stat.	2.9%	2.8%	3.3%	2.5%	2.4%	3.4%	5.1%	6.4%	6.4%
SF($Z \to \tau_e \tau_{\text{had}}$)	1.056	0.996	0.954	1.046	0.983	0.954	1.057	0.998	0.951
uncorrelated syst.	1.0%	2.8%	4.3%	0.5%	2.0%	3.0%	2.6%	5.1%	7.4%
correlated syst.	1.7%	1.8%	2.1%	1.9%	2.1%	2.3%	2.2%	2.2%	3.0%
stat.	1.5%	1.7%	2.3%	1.6%	1.8%	2.5%	2.3%	2.6%	3.5%
syst.+stat.	2.5%	3.8%	5.3%	2.5%	3.5%	4.5%	4.1%	6.2%	8.7%
SF combined	1.033	0.979	0.907	1.015	0.972	0.908	1.081	1.008	0.939
syst.	2.0%	2.1%	2.6%	1.8%	1.8%	2.7%	3.5%	4.8%	5.3%
stat.	1.0%	1.1%	1.5%	1.0%	1.2%	1.5%	1.5%	1.7%	2.2%
syst.+stat.	2.2%	2.4%	3.0%	2.1%	2.1%	3.1%	3.8%	5.1%	5.8%
ρ_{total}	0.387	0.121	0.159	0.457	0.182	0.310	0.418	0.326	0.282

Table 6.4: Combination of the tau identification scale factors as measured by the muon channel and the electron channel. The relative systematic uncertainties are split in a correlated and uncorrelated part. The total degree of correlation between the two measurements is reported as ρ_{total}. The statistical and systematic uncertainties are combined quadratically.

where the off-diagonal elements are considered in the numerator and the diagonal ones in the denominator. After computing ρ_{total} each scale factor measurement is decomposed as

$$\text{SF} \pm \Delta\text{SF}_{\text{stat.}} \pm \rho_{\text{total}} \Delta\text{SF}_{\text{syst.}} \pm (1 - \rho_{\text{total}}) \Delta\text{SF}_{\text{syst.}} \tag{6.15}$$

where the last two components are the correlated and uncorrelated uncertainties, respectively. A summary of the full combination is given in Tab. 6.4 for the full pseudo-rapidity range. The combination is also performed in the barrel and the end-cap, as illustrated in Fig. 6.23. The full set of results for all working points is reported in App. C.

6.5 Tau Trigger

The ATLAS trigger system was already introduced in Sec. 4.2.6. In this section the implementation of the tau trigger algorithm is discussed, as it is relevant for the main topic of this thesis, which follows the architecture already illustrated in Chap. 4. The tau reconstruction algorithm utilised by the trigger is

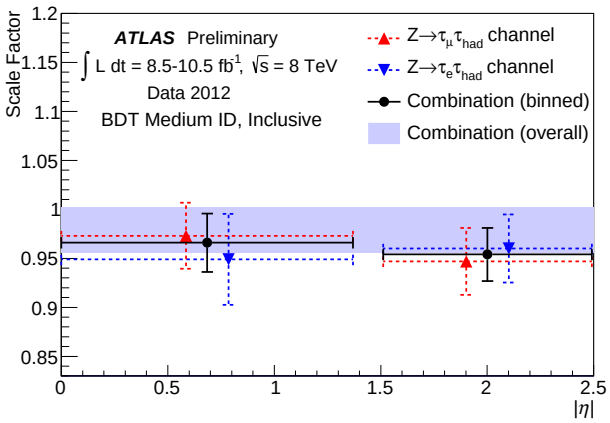

Figure 6.23: Tau identification efficiency scale factors measured by the muon and the electron channels in the barrel and the end-cap. Only the medium working point is shown here. The combined scale factors in the two regions are illustrated by the circles. The combination of the η-inclusive measurements is also shown (shaded area).

required to fulfill the requirements dictated by the reduced latency times available at the various trigger levels. In the following, the details of the various trigger stages will be outlined.

6.5.1 L1 Tau Trigger

The Level-1 trigger only relies on the calorimeter information, which is provided with reduced granularity. Energy deposits are considered in a core and in isolation regions of the EM and HCAL calorimeters composing the L1 Region-of-Interest (RoI). These are built from projective trigger towers with a granularity of $\Delta\eta \times \Delta\phi = 0.1 \times 0.1$ up to $|\eta| = 2.5$. The core region is built from 2×2 trigger towers. The tau energy is then estimated at the EM scale, considering the two neighboring most energetic towers in the core region for the EM calorimeter, and the whole core region in the HCAL. This scheme is depicted in Fig. 6.24. The region in the EM calorimeter just outside the core in the annulus between 0.2×0.2 and 0.4×0.4 serves to compute the EM isolation. Background suppression is required in order to reduce the trigger rate. This is achieved by requiring isolation at the level of 4 GeV for the lowest trigger E_{T} threshold of 8 GeV. No E_{T}-dependent isolation requirement can be implemented at L1, which causes an efficiency loss across the E_{T} threshold range between 11 GeV and 40 GeV. As this loss increases with the tau energy, no isolation is required for the highest threshold. No specific clustering algorithm nor energy calibration are exploited at L1, limiting the tau reconstruction efficiency and energy resolution at this stage.

6.5.2 L2 Tau Trigger

At Level-2, an RoI defined at L1 is considered in order to compute variables based on tracking and calorimeter information, which are used in an identification algorithm. The energy deposited by the tau is calibrated taking into account the subtraction of electronic and pile-up noise. A region around the L1 seed within $\Delta R < 0.4$ is used to compute the centre of the energy deposit weighting the cells according to their energy, while the total transverse energy of the tau is measured using only cells within $\Delta R < 0.2$ from this centre. Tracks are measured using a fast tracking algorithm [175] relying only on pixel and SCT hits. Tracks are considered if they have $p_{\mathrm{T}} > 1.5$ GeV and are within $\Delta R < 0.3$ of the tau axis, computed as previously mentioned. No vertex information is available at this stage. Therefore, the

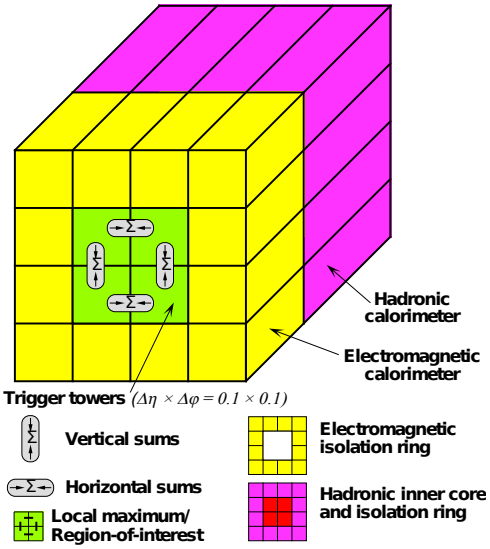

Figure 6.24: Schematic representation of an RoI at the Level-1 stage of the tau trigger algorithm. The separation between the core and isolation regions is highlighted. The picture is taken from Ref. [115].

track-based pile-up rejection relies on a Δz_0 requirement between the candidate track and the one with the highest p_{T}. The distribution of Δz_0 shows a peak consistent with the interaction point. Only tracks with -2 mm $< \Delta z_0 < 2$ mm and $\Delta R < 0.1$, with respect to the highest-p_{T} tracks, are considered in order to reject pile-up events. Isolation is track-based and requires that no track is reconstructed in the isolation region for 1-prong candidates. Multi-prong candidates are required to have a ratio between the total track p_{T} in the region $0.1 < \Delta R < 0.3$ to the one in $\Delta R < 0.1$ lower than 0.1.

At this point identification variables are defined similarly to what was already described in Sec. 6.2.1, with few differences. The f_{cent} variable is computed without a pile-up correction, and expanding the cone size to $\Delta R < 0.4$ in the denominator sum. The quantities f_{track} and R_{track} both consider tracks within $\Delta R < 0.3$ around the highest-p_{T} track. A background rejection factor of 10 is achieved by the algorithm, and a signal efficiency of $\approx 90\%$ at the medium working point.

6.5.3 Event Filter of the Tau Trigger

The Event Filter level of the tau trigger algorithm is similar to the tau reconstruction already discussed at the beginning of this chapter (*offline tau reconstruction*). Clustering is performed as described in Sec. 5.3, and calibration restores the tau energy scale. Both algorithms are run within an RoI. Track reconstruction is performed in the same region using a dedicated tracking algorithm. Vertex reconstruction is not available as tracking is limited to an RoI. Therefore, tracks are selected with different requirements with respect to the offline reconstruction in order to reduce the effect of pile-up. A Δz_0 requirement is used, similar to the L2 stage, which is $\Delta z_0 = 2$ mm with respect to the highest-p_{T} track. The requirement $\Delta d_0 < 2$ mm is also applied between the tracks and the vertex found within the RoI. The variables used for the identification algorithm illustrated in Sec. 6.2.1 are then computed, without applying any pile-up correction. In addition, variables relying on π^0 information are not used for the EF identification. This algorithm is trained using simulated $Z \to \tau\tau$, $W \to \tau\nu$ and $Z' \to \tau\tau$ events for the signal and multi-jet events from data for the background. The selected samples contain events passing the L1 trigger and with tau leptons that are matched with a reconstructed $\tau_{\mathrm{had-vis}}$ with $p_{\mathrm{T}} > 15$ GeV and $|\eta| < 2.2$. Truth matching is also required for the signal as well as the medium identification requirement of the offline

BDT algorithm. The performance of the tau identification used in the EF is illustrated in Fig. 6.25.

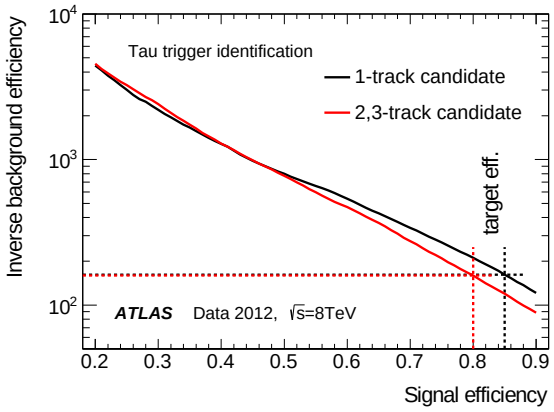

Figure 6.25: Background rejection as a function of the signal efficiency for the tau identification algorithm at the Event Filter. The target efficiencies and background rejections are highlighted by the dashed lines. The picture is taken from Ref. [159].

6.5.4 Trigger Efficiency in Data

The tau trigger efficiency is measured in data from a tag-and-probe selection of $Z \to \tau_\mu \tau_{\text{had}}$ events, in a similar way to what was already described in Sec. 6.4. However, the measurement is performed by requiring each candidate to pass the offline tau identification, therefore enhancing the relative signal fraction of the sample. The systematic uncertainty is dominated by the shape of the largest backgrounds, $W \to \mu\nu$ and multi-jet. Their contributions are estimated with a method similar to that described for the identification efficiency measurement, i.e. using data from a same-sign control region to model multi-jets, and rescaling the $W \to \mu\nu$ contribution with the k_W factor defined in Sec. 6.4.4. A control region for $t\bar{t}$ events is defined by requiring the presence of a jet originating from a b quark, dedicated to measure the $t\bar{t}$ normalisation in data. The $Z \to \mu\mu +$ jets contribution, where an associated jet in the final state is mis-identified as $\tau_{\text{had-vis}}$, is estimated from the simulation and normalised in a control region where the two muons have the same electric charge. The scale factors are measured as a function of the tau p_{T}, η and separately for 1-prong and 3-prong tau leptons. For this measurement, tau candidates are selected according to different offline BDT working points. Hence, scale factors are provided for different thresholds, as well as for different EF menus featuring different p_{T} thresholds, ranging from 20 GeV to 38 GeV. In addition, as the trigger algorithm configuration was subject to changes throughout data-taking in Run-I, the measurement is also performed for three different data-taking periods. In Fig. 6.26 and 6.27, data and simulation efficiencies are presented for 1-prong and 3-prong decays, respectively. The plots show the efficiency versus the tau p_{T} (*turn-on curve*) for the EF menu requiring $p_{\text{T}} > 38$ GeV, and are obtained for tau leptons passing the offline medium identification in the barrel ($|\eta| < 1.5$) and in the end-cap ($|\eta| > 1.5$). The plots also show the scale factors (lower insets). A detailed review of the measurement is given in Ref. [176], and all the resulting scale factors are reported in Ref. [177]. In general, in the p_{T} range from 30 GeV to 50 GeV, a total uncertainty of $\approx 2\%$ is achieved on the scale factors, which increases up to $\approx 8\%$ at $p_{\text{T}} \approx 100$ GeV and for $p_{\text{T}} < 30$ GeV, due to larger background contamination.

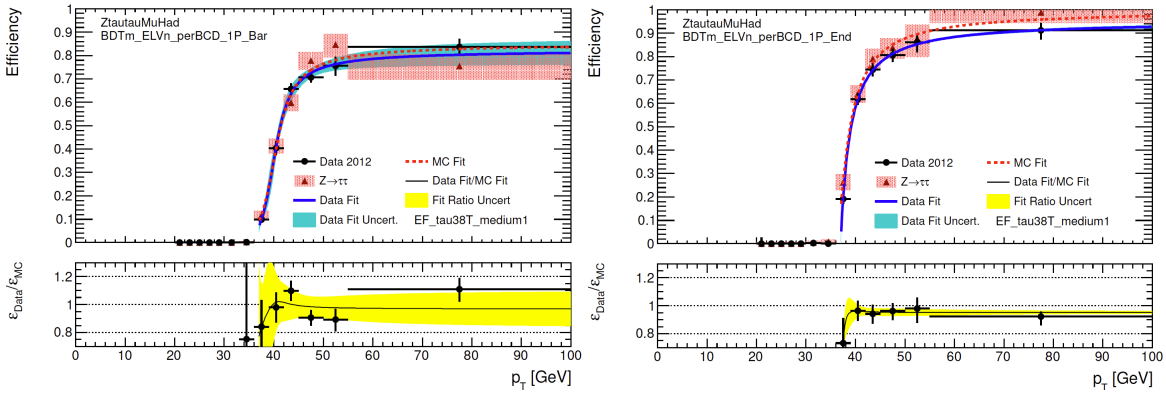

Figure 6.26: Trigger efficiencies in data and simulation as a function of the tau p_{T}, for 1-prong decays in the barrel (left) and the end-cap (right). The lower inset shows the scale factor, with statistical uncertainty obtained from data. The picture is taken from Ref. [177].

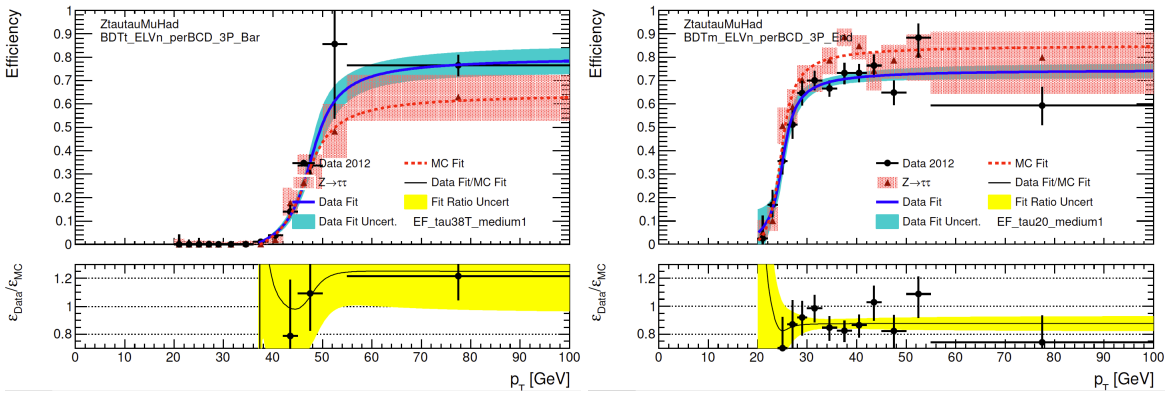

Figure 6.27: Trigger efficiencies in data and simulation as a function of the tau p_{T}, for multi-prong decays in the barrel (left) and the end-cap (right). The lower inset shows the scale factor, with statistical uncertainty obtained from data. The picture is taken from Ref. [177].

CHAPTER 7

MSSM $h/H/A \to \tau_{\text{had}}\tau_{\text{had}}$ analysis

The present chapter presents the search for $h/H/A \to \tau_{\text{had}}\tau_{\text{had}}$ decays, performed with $L_{\text{int}} = 19.5\ \text{fb}^{-1}$ of ATLAS data collected at $\sqrt{s} = 8$ TeV. The search only considers tau leptons decaying in the hadronic channel and is part of a larger search where different combinations of tau decays are considered. All search channels are later combined. The signal is searched for by selecting data events using kinematic and topological requirements, and by comparing data to the expected background, which has to be carefully estimated. The final state with two hadronic tau decays offers a high branching ratio of $\text{BR}(\tau\tau \to \text{hadrons}) \approx 42\%$.

The signal is searched for by requiring two tau leptons in the final state selected with a topological and kinematic configuration as required by the decay of a heavy neutral resonance. The $h/H/A \to \tau_{\text{had}}\tau_{\text{had}}$ search is performed in two event categories with different requirements. A different tau trigger is required for each category. A trigger featuring low-p_{T} thresholds on two taus is used to define a category where the selection is optimised in order to achieve better sensitivity in the hypothesis of Higgs bosons with low mass. Another trigger implementing a high-p_{T} threshold on only one tau is used to optimise a selection for high-mass signal. The two categories feature the same types of background contributions, however, with different relative compositions. The background is mainly composed of processes containing two objects in the final state which are either real tau leptons, jets mimicking tau decays, also referred to as *fake taus*, or a combination of the two. The dominant contribution is due to multi-jet events, where two jets are mis-identified as tau leptons. The background featuring real tau leptons is dominated by $Z/\gamma^* \to \tau\tau$. Other minor sources of background include $W \to \tau\nu$ + jets and $t\bar{t}$ events. Some background contributions are estimated with the help of simulation. However, this is not possible for multi-jets, given the complications in simulating QCD interactions. For this reason, data-driven techniques will be used to estimate the multi-jet background, and whenever possible to model backgrounds originating from jets.

This chapter is structured as follows. In Sec. 7.1 and 7.2 the signal and the backgrounds of the search are introduced, respectively. This includes details about the simulated samples relevant for their estimation and the evaluation of the systematic uncertainties. In Sec. 7.3, the pre-selection stage of the analysis is illustrated, where events are selected according to general requirements previous to the definition of categories. Events are further selected and assigned to two categories as described in Sec. 7.3.3. The different methods for multi-jet estimation are outlined in Sec. 7.4 and 7.5. The $Z/\gamma^* \to \tau\tau$ contribution is validated as described in Sec. 7.6. In Sec. 7.7, an overview is given of a weighting technique used to estimate the contribution of fake tau leptons. Systematic uncertainties affecting the data-driven estimation of backgrounds are discussed in the corresponding sections, while the remaining systematic uncertainties are discussed in Sec. 7.8. The results presented in this and the following chapter

are documented in Ref. [178].

7.1 Signal

The dominant production modes for neutral MSSM Higgs bosons are b-associated production, also called $b\bar{b}$ annihilation, and gluon-gluon fusion, for reasons explained in Sec. 2.3.4. They will be discussed in Sec. 7.1.1 and 7.1.2, respectively.

Simulated signal samples have been produced for each production mode in order to optimise the selection and to estimate the signal contribution. Events are generated for thirteen different mass hypotheses, m_A, in the range 170 − 1000 GeV. The value of tanβ not only affects the total cross-section, or equivalently the total number of expected events, but also the width of the mass spectrum, Γ. However, the width ranges roughly between 0.01 GeV and 10 GeV across the m_A − tanβ region of interest, i.e. it is much smaller than the experimental resolution on the mass of ≈ 30%. For this reason, no modification of the shape of the mass spectrum dependent on tanβ will be taken into account. The signal hypothesis for each value of the mass is tested for different values of tanβ between 3 and 60. An example of the generated invariant mass distributions for the signal samples in this analysis is given in Fig. 7.1. In

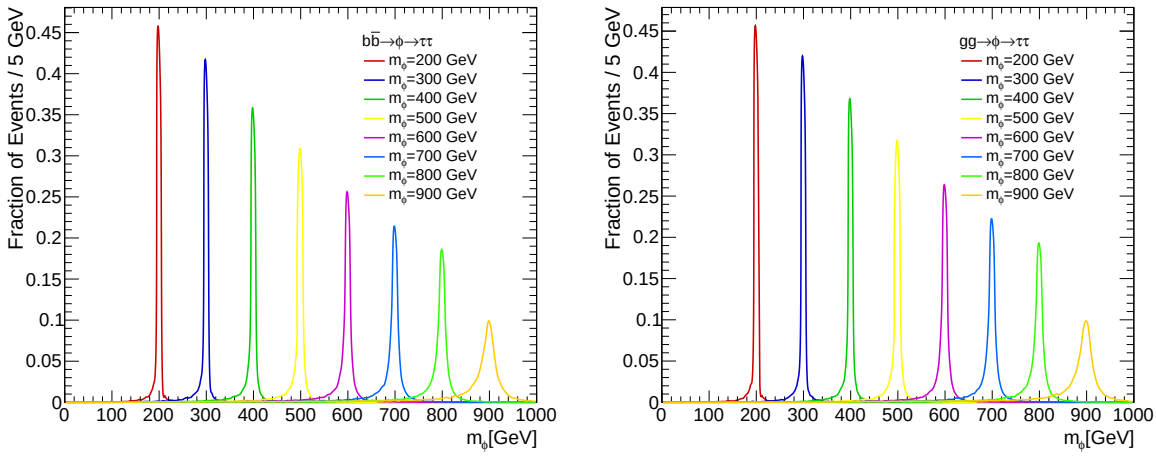

Figure 7.1: Spectra of the generated invariant mass for some of the signal samples used in the analysis. The mass spectrum for $b\bar{b}$ annihilation and gluon-gluon production are shown on the left and on the right, respectively. The distributions are normalised to unit area.

Fig. 7.2, an example of the p_{T} spectra for the highest-p_{T} and the lower-p_{T} tau lepton in the decay of the generated Higgs boson are given, referred to as the *leading tau* and the *sub-leading tau*, respectively.

7.1.1 MSSM neutral Higgs Production via $b\bar{b}$ Annihilation

As already illustrated in Sec. 2.3.4, the coupling between $b\bar{b}$ pairs and a generic neutral MSSM Higgs boson ϕ is enhanced for increasing values of tanβ, and is larger than for other down-type fermions pairs due to the relatively large mass of b quarks. Two computational schemes are available to determine the inclusive cross-section for producing ϕ bosons involving $b\bar{b}$ coupling. The calculation can be treated perturbatively, as the scale Λ_{QCD} below which this is no longer possible is much lower than m_b. In one scheme, the so-called *four-flavour scheme* (4FS) [179, 180], we can assume that b quarks do not contribute to the parton distribution functions of the protons. In this model, the processes $q\bar{q} \to \phi b\bar{b}$

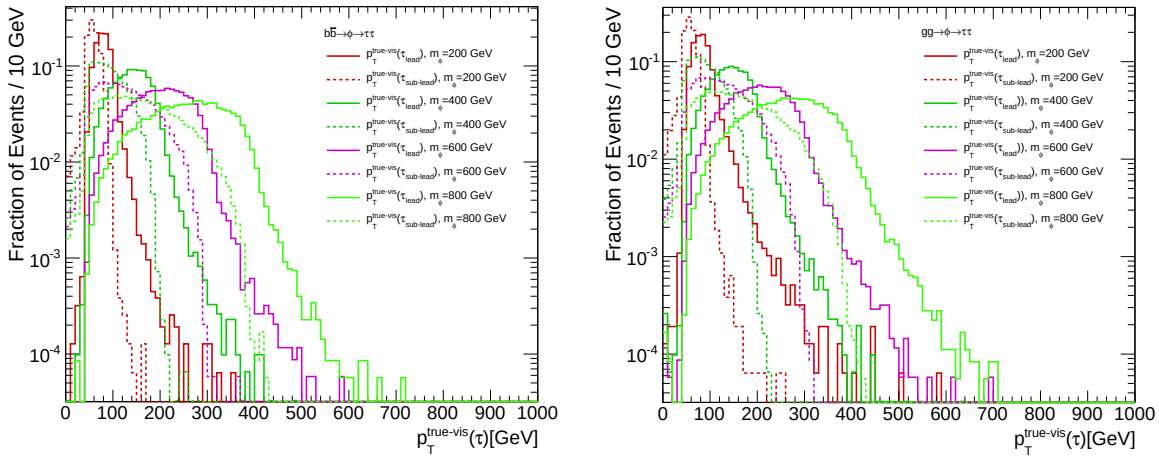

Figure 7.2: Spectra of the visible transverse momentum of true tau leptons in the decay of a simulated generic Higgs boson for a subset of the signal samples used. The highest-p_T and lower-p_T tau lepton are indicated as leading and sub-leading, respectively. The p_T spectra for $b\bar{b}$ annihilation and gluon-gluon fusion are on the left and on the right, respectively. The distributions are normalised to unit area.

and $gg \to \phi b\bar{b}$, illustrated in Fig. 7.3 (a) and (b), respectively, are dominant. However, the cross-section

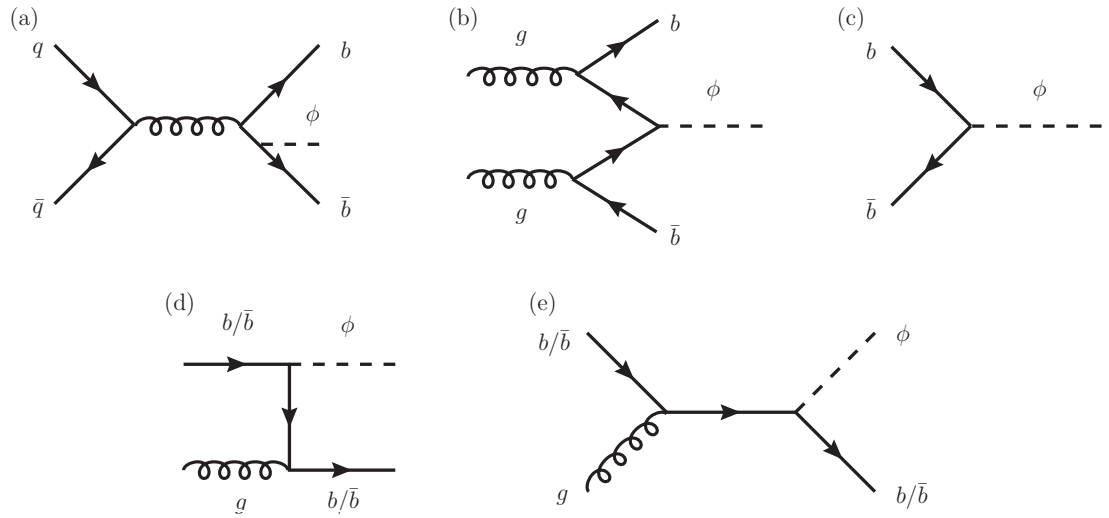

Figure 7.3: Example of the production modes for a generic neutral MSSM Higgs boson ϕ via $b\bar{b}$ annihilation.

for the latter is expressed as a sum involving logarithms of the form $\ln(\mu_F/m_b)$, originating from the nearly-collinear splitting of the gluons. This can lead to divergences if $m_\phi \gg 4m_b$, as the factorisation scale μ_F is chosen as $\mu_F \approx m_\phi/4$ [181–183]. If we introduce another scheme featuring b quarks in the partons, the so-called *five-flavour scheme* (5FS) [184, 185], the logarithms can be summed to all orders in perturbation theory. This is based on the assumption that the momentum transferred to the outgoing b quarks is small compared to their mass. In this case the leading-order production mode is the one depicted in Fig. 7.3 (c). In principle, if all orders would be taken into account, the two schemes would yield identical results. However, at any finite order, they include different parts of the complete

calculation, leading to different predictions. The two approaches are combined by a matching scheme called *Santander matching* [186]. As the 4FS and 5FS approaches provide a unique prediction of the cross-section in the limits $m_\phi/m_b \to 1$ and $m_\phi/m_b \to \infty$, respectively, the Santander scheme interpolates the two methods for very low and very high values of m_ϕ. This is done by weighting the prediction from the two methods using variable weights depending on m_ϕ. The cross-sections are combined according to

$$\sigma_{\text{Santander}} = \frac{\sigma_{\text{4FS}} + w\sigma_{\text{5FS}}}{1+w}, \tag{7.1}$$

where the total inclusive cross-sections from the 4FS and 5FS are included, and the weight is

$$w = \ln\left(\frac{m_\phi}{m_b}\right) - 2. \tag{7.2}$$

With this particular choice of w, both approaches get the same weight for $m_\phi \approx 100$ GeV, consistent with the fact that they lead to very similar predictions in this region. The uncertainty on the predicted cross-section comes from the linear combination of the individual uncertainties associated with the 4FS and 5FS approaches, according to Eq. (7.1). The individual uncertainties are due to the choice of μ_F, μ_R, α_S and the PDF set. In this thesis, theoretical uncertainties are estimated according to the prescriptions outlined in Ref. [187]. The cross-sections combined by the Santander matching are at NLO for the 4FS and NNLO for 5FS. Predictions for all MSSM scenarios illustrated in Sec. 2.3.5 are available. In this thesis, masses, couplings and branching ratios of the signal are predicted with the program `FeynHiggs` [50–52]. In Fig. 7.4, an example of the cross-sections $\sigma(b\bar{b} \to \phi) \times \text{BR}(\phi \to \tau\tau)$ is given as a function of m_A and for $\tan\beta = 15, 50$ in the m_h^{max} scenario. The plots also illustrate the cross-section uncertainty associated with the PDF set, α_S, μ_F and μ_R. In Fig. 7.5, the production cross-sections of A and H are illustrated in the $(m_A, \tan\beta)$ plane for the same scenario. The full summary of the cross-sections and their uncertainties for the $b\bar{b}$ annihilation production mode is reported in App. D, for the m_h^{max} scenario.

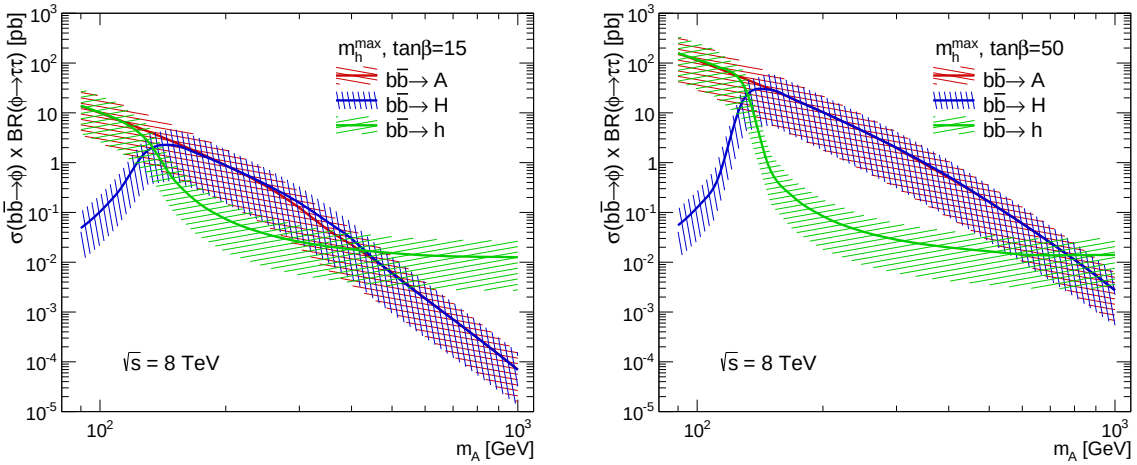

Figure 7.4: Cross-sections for the process $b\bar{b} \to \phi \to \tau\tau$ as a function of m_A and for $\tan\beta = 15$ (left) and $\tan\beta = 50$ (right) in the m_h^{max} scenario. The plots show also the uncertainty band associated with the PDF set, α_S, μ_F and μ_R uncertainties. Numerical values are obtained with `FeynHiggs` [50–52], implementing the Santander matching as illustrated in the text.

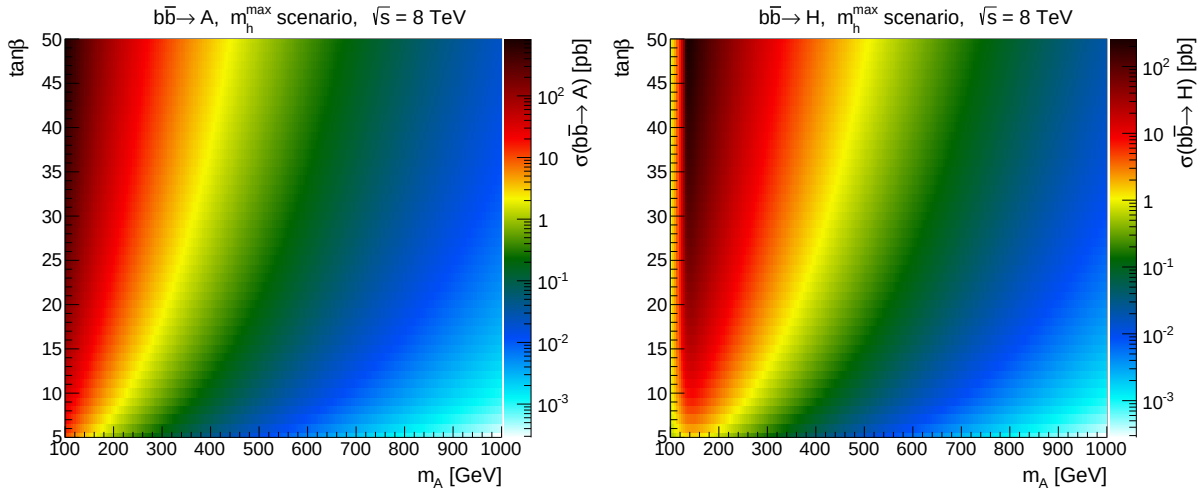

Figure 7.5: Cross-sections for the $b\bar{b} \to A$ (left) and $b\bar{b} \to H$ (right) production mechanisms in the $(m_A, \tan\beta)$ plane in the m_h^{max} scenario. The cross-sections have been computed with `FeynHiggs` [50–52] implementing the Santander matching as illustrated in the text.

All signal samples for the $b\bar{b}$ annihilation production mode in this thesis have been produced using the `Sherpa` generator [69]. This generator features all the leading-order matrix elements for processes of the form 2 partons $\to \tau\tau + n$, where $n \leq 3$ is the number of associated partons in the final state. Couplings between the Higgs bosons and quarks other than the b are not included. The `Sherpa` generator features its own parton shower and hadronisation model, as well as modelling the tau decay by itself. Finally, this generator uses the CKKW algorithm [68] in order to perform the merging of the parton shower and the matrix element, as discussed in Sec. 2.4.1, which is characterised by the scale $\Lambda_{\text{CKKW}} = \sqrt{20\ \text{GeV}/\sqrt{s}}$. The PDF set called CT10 [188] is used.

7.1.2 Signal Production in the Gluon-Gluon Fusion Mode

Higgs bosons do not couple directly to gluons, hence, a quark loop is always involved in the process $gg \to \phi$. Examples of gluon-gluon fusion (ggF) production mechanisms for a generic neutral Higgs boson in the MSSM at the LHC are shown in Fig. 7.6. In the Standard Model, the process shown in Fig. 7.6 (a) is largely dominated by the contribution of the top quark in the loop. However, in the MSSM the contribution of b quarks is also relevant, due to the dependence on $\tan\beta$ of the coupling between ϕ and $b\bar{b}$. The gluon-gluon fusion cross-sections are computed with `ggh@nnlo` [185] and `HIGLU` [189] taking into account the contribution of QCD processes at NNLO and the contribution of b quarks at NLO as well as their interference with a t loop, respectively. The contribution of squarks in the loop can be neglected, as it is suppressed by the factor $M_Z^2/M_{\tilde{q}}^2$ [190]. As for the $b\bar{b}$ annihilation production mode, uncertainties associated with the PDF set and α_S affect the prediction, and are evaluated by following the prescriptions in Ref. [187]. Fig. 7.7, illustrates the cross-sections for the process $\sigma(gg \to \phi) \times \text{BR}(\phi \to \tau\tau)$ as a function of m_A and for $\tan\beta = 15, 50$ in the m_h^{max} scenario. Uncertainties associated with the PDF set, α_S, μ_F and μ_R are also reported. In Fig. 7.8, the production cross-sections of A and H are shown, in the $(m_A, \tan\beta)$ plane for the m_h^{max} scenario. A full summary of the cross-sections and their uncertainties for the gluon-gluon fusion production mode is reported in App. D, for the m_h^{max} scenario. Signal events for the gluon-gluon fusion production are simulated with `Powheg` [66], which is interfaced to `Pythia8` for parton shower, hadronisation and model the tau decay. The PDF set used in the simulation is CT10.

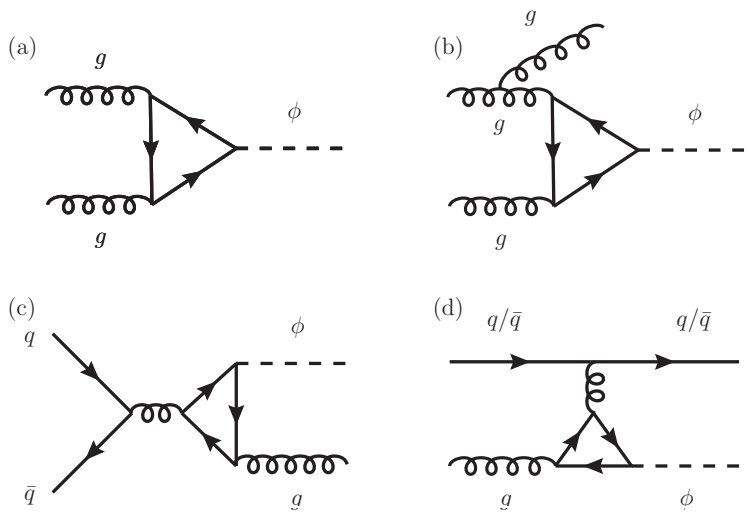

Figure 7.6: Examples of production modes for a generic neutral MSSM Higgs boson ϕ via gluon-gluon fusion.

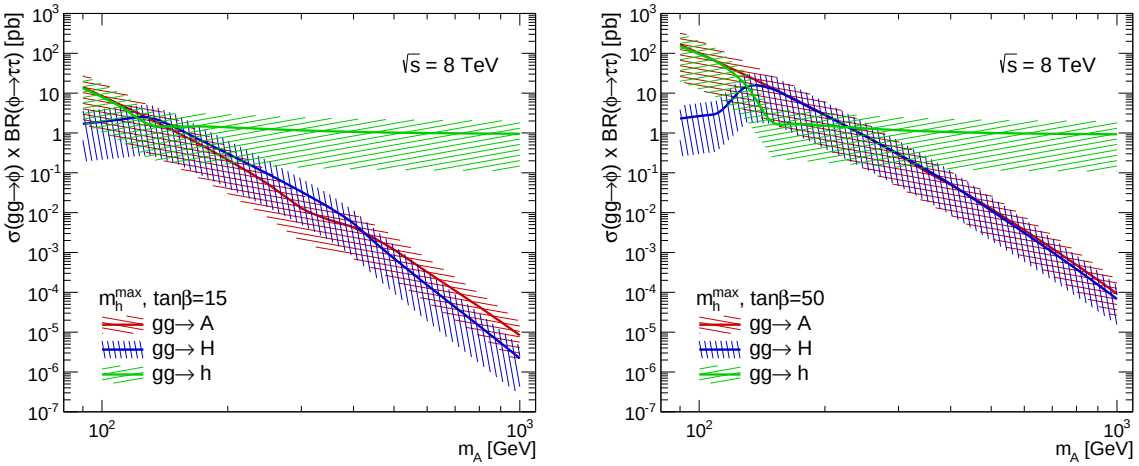

Figure 7.7: Cross-sections for the process $gg \to \phi \to \tau\tau$ as a function of m_A and for tanβ = 15 (left) and tanβ = 50 (right) in the m_h^{max} scenario. The plots show also the uncertainty band associated with the the PDF set, α_S, μ_F and μ_R uncertainties. The production cross-section is predicted with `ggh@nnlo` [185] and `HIGLU` [189], and `FeynHiggs` [50–52] is used for couplings and branching ratios.

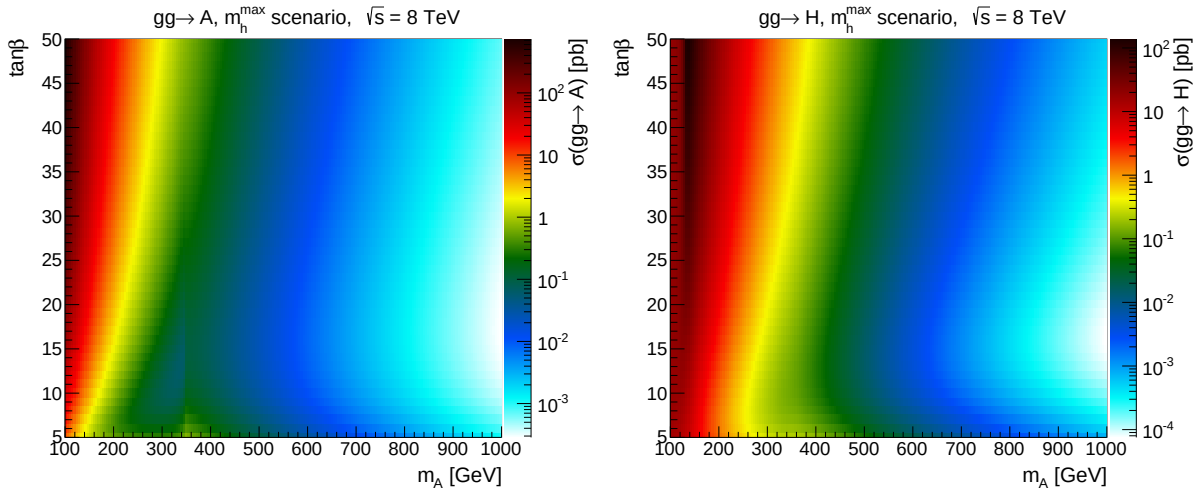

Figure 7.8: Cross-sections for the $gg \to A$ (left) and $gg \to H$ (right) production mechanisms in the $(m_A, \tan\beta)$ plane in the m_h^{max} scenario. The production cross-section is predicted with `ggh@nnlo` [185] and `HIGLU` [189].

7.2 Backgrounds

This section introduces the backgrounds to the signal previously discussed. In Sec. 7.2.1 the dominant multi-jet background is introduced, while the irreducible $Z/\gamma^* \to \tau\tau$ is presented in Sec. 7.2.2. In Sec. 7.2.3, $W \to \tau\nu$+jets events are discussed. Other minor contributions, including events featuring the top quark in the final state, are presented in Sec. 7.2.4 and 7.2.5. In Fig. 7.9 the production cross-sections of the main sources of backgrounds for the present search are reported, along with a variety of other cross-sections. This plot only serves as a general figure for comparison. All background cross-sections relevant for the analysis are reported in App. D.

7.2.1 Multi-jet Background

The high multi-jet production cross-section and the similarities between events with two hadronic tau decays and di-jet events, make this background particularly important. Examples of di-jet production modes at the LHC are illustrated in Fig. 7.10, showing some of the LO processes. However, this background might feature even a higher number of jets in the final state, as no requirement on the number of jets is posed by the analysis. As illustrated by Fig. 7.9, multi-jets have a much larger production cross-section at the LHC than the other backgrounds. For this reason, the usage of simulation for the estimation of this background is suboptimal, as any selection of resonant decay topologies would select only a small portion of the simulated events, leading to large shape uncertainties. In addition, as illustrated in Sec. 2.4.1, difficulties in the modelling of the parton shower, hadronisation, and choice of α_S make the modelling of QCD interactions non-trivial. In particular, the relative fraction of jets initiated by either a quark or a gluon can be mis-modelled, which would have a significant impact in the estimated tau mis-identification probability, which is critical for the present search. In both categories used in the analysis, multi-jets events are estimated from data, utilising requirements on the tau identification, as will be shown later in Sec. 7.5 and 7.4.

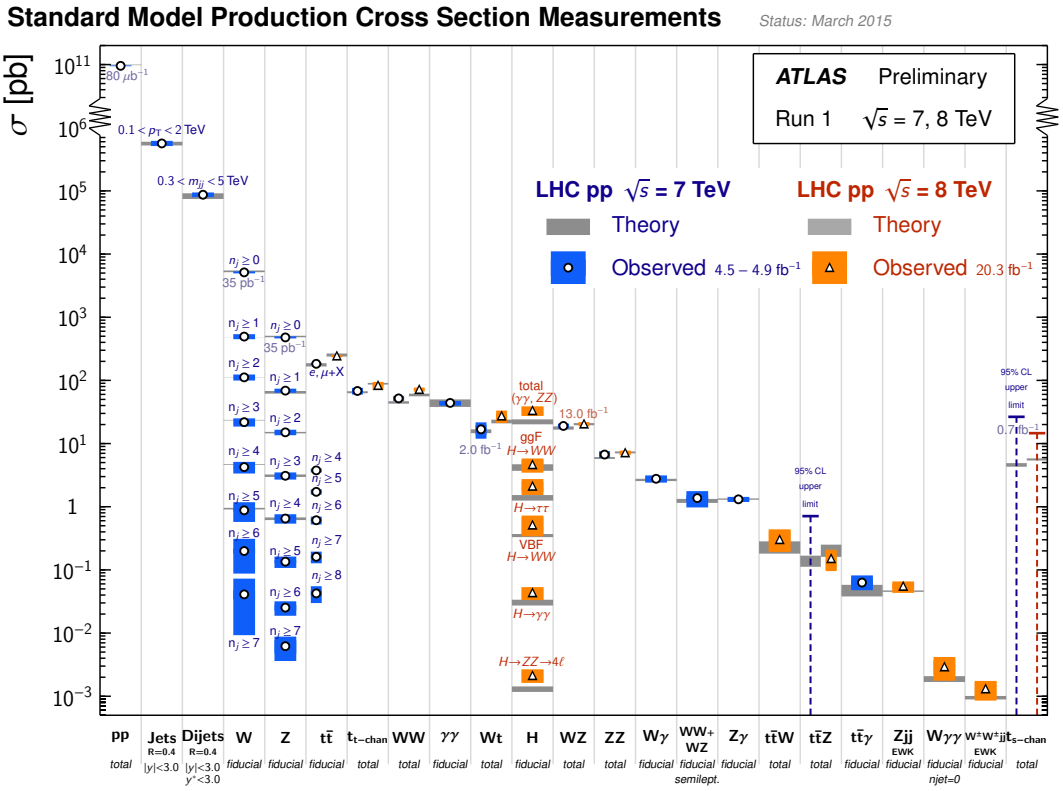

Figure 7.9: Cross-sections of relevant SM processes for in the ATLAS physics programme, as measured by the ATLAS experiments during Run-I. The theoretical cross-sections are marked in grey and compared to the measured values from collisions at $\sqrt{s} = 7$ TeV (blue points), and at $\sqrt{s} = 8$ TeV (orange points). The contribution labelled as Z includes Drell-Yan processes [191]. The symbols indicate the final state considered for the measurement. The plot is taken from Ref. [192].

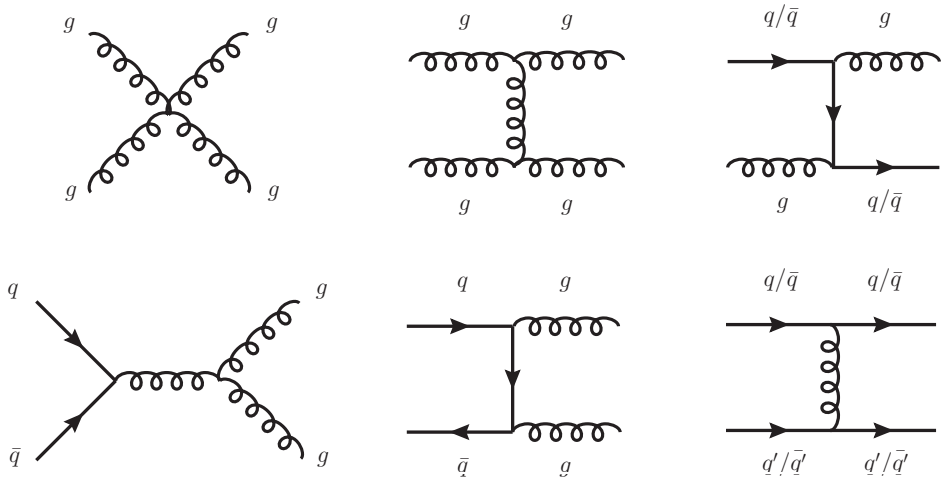

Figure 7.10: Examples of LO production modes for di-jet events.

7.2.2 $Z/\gamma^* \to \tau\tau$

The second largest background contribution in the search comes from di-tau decays originating from a Z boson, as well as from a virtual photon, γ^*. The decay has a branching ratio of $\mathrm{BR}(Z/\gamma^* \to \tau\tau) \approx 3.4\%$ [18]. This contribution is known as *Drell-Yan process* [191]. Due to the high-p_{T} selection on the tau leptons, events in the kinematic region of the peak in the spectrum of the invariant mass of the Z are rejected. Hence, only the high-mass portion of the spectrum is relevant for this analysis.

The production of the Z or γ^* features a coupling to $q\bar{q}$ pairs, as illustrated by the diagrams in Fig. 7.11. As the final state of this background contribution is identical to the signal, tau identification is not effective in reducing it. In addition, no control region for this contribution can be defined without a significant signal contamination or with a sufficiently large number of data events, hence prohibiting the usage of a data-driven technique. For this reason the $Z/\gamma^* \to \tau\tau$ background is estimated using simulated events. The simulation is performed with `Pythia 8.1` [71], which handles all stages of the simulation including the tau decay.

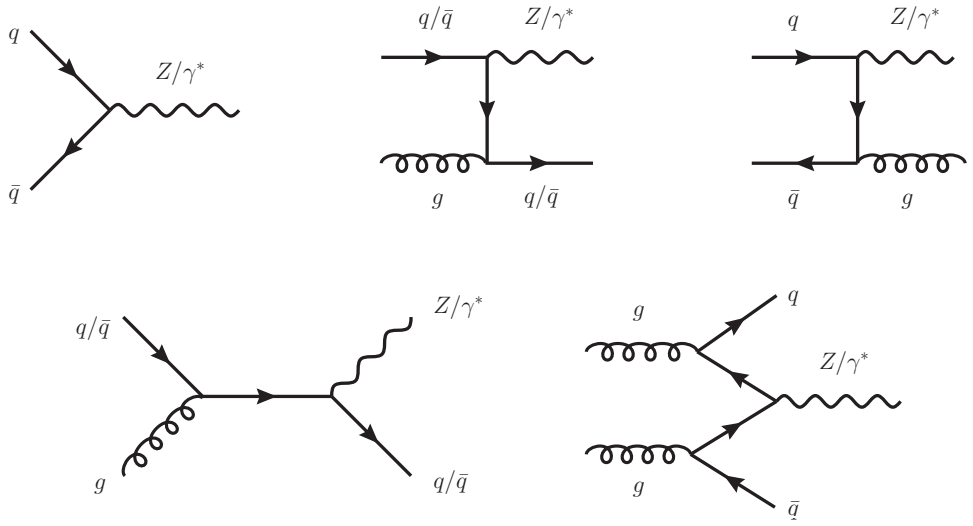

Figure 7.11: Examples of production modes for Z/γ^*.

The analysis is sensitive to the tail of the invariant di-tau mass spectrum. Therefore, a proper modelling of this background at high masses is critical. The total simulated sample consists of twelve simulated samples corresponding to exclusive regions of the di-tau invariant mass $m_{\tau\tau}^{\mathrm{true}}$ in the range $m_{\tau\tau}^{\mathrm{true}} = 60 - 2500$ GeV. The usage of these exclusive samples enhances the statistical power of the simulation in the tail of the $m_{\tau\tau}^{\mathrm{true}}$ distribution. The generator used for this analysis provides LO cross-sections, thus, a correction is needed to provide a prediction at NNLO, i.e. the k-factor already introduced in Sec. 2.4.1. This factor is applied as a function of the invariant mass of the simulated true tau leptons and is defined as $k = \sigma_{\mathrm{NNLO}}/\sigma_{\mathrm{LO}}$ where the NNLO cross-section is computed with `FEWZ 3.1.b2` [193, 194] and the LO one with `Pythia`.

The PDF set used in the simulation is CTEQ6L1 [195]. The distribution of the generated invariant mass for all the exclusive samples considered is reported in Fig. 7.12 (left), together with the transverse momentum distribution of the visible true tau leptons in the final state. In these plots the LO production cross-sections in the exclusive regions and the k-factor rescaling are taken into account. The k-factors are given in Fig. 7.13, which includes the uncertainty associated with the variation of α_S at 90% CL and the PDF set, which is altered using the MSTW prescriptions [196]. Further details on the simulation of

Drell-Yan events are reported in App. D.

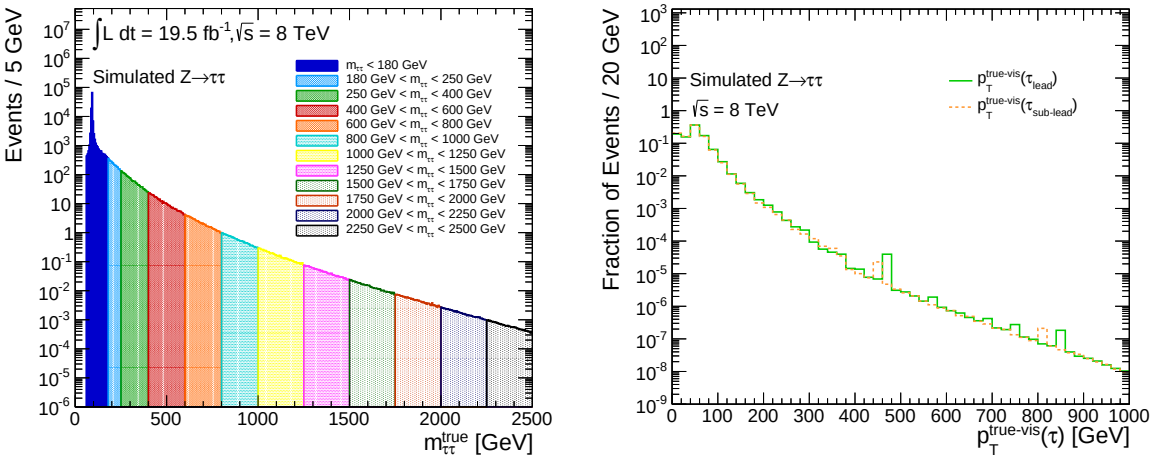

Figure 7.12: Left: mass spectrum of the generated resonance mass in the simulated $Z/\gamma^* \to \tau\tau$ production. Exclusive samples for different mass intervals are generated with `Pythia 8.1` [71]. The complete distribution is rescaled to the total integrated luminosity used in the analysis and the predicted cross-section, featuring k-factors for the NNLO prediction. Right: spectrum of the visible p_{T} of true leading and sub-leading taus from Z/γ^* decays. The distributions are normalised to unit area.

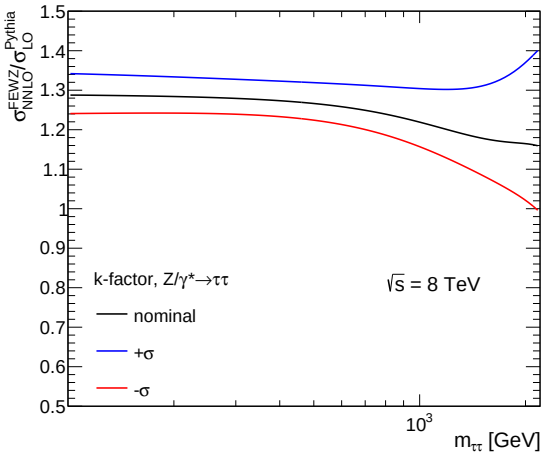

Figure 7.13: k-factor as a function of the resonance mass used to rescale the LO `Pythia` cross-section in order to achieve a NNLO prediction for $Z/\gamma^* \to \tau\tau$ events. The upward and downward variation is also shown, corresponding to the uncertainty from the PDF set and α_S. Numbers are obtained with `FEWZ 3.1.b2` [193, 194].

7.2.3 $W \to \tau\nu$ + jets

The production of a W boson in association with a jet is another source of background, if the W decays into a tau and a neutrino. This decay occurs with a branching ratio BR($W \to \tau\nu$) $\approx 11\%$ [18]. In these events two tau leptons are selected which arise from the real tau and a mis-identified jet. Even if tau identification rejects the vast majority of these events, the large W + jets production cross-section at the

LHC makes this background non-negligible. The dominant production modes are illustrated in Fig. 7.14 where the final state contains only one associated jet. As previously mentioned, the W boson and a quark-initiated associated jet feature a charge correlation. As the mis-identification probability for quark and gluon-initiated jets is different, and the signal region contains predominantly oppositely charged tau leptons, the origin of the jet has to be taken into account when estimating the mis-identification probability.

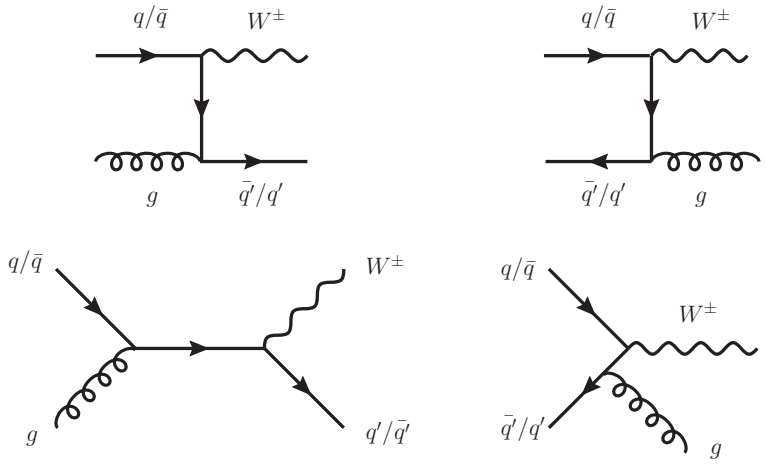

Figure 7.14: Examples of production modes for W + jets events.

The estimation of this background is partially data-driven. Simulated events are weighted with a mis-identification probability obtained from data, as will be described in Sec. 7.7.2. The simulation is performed using `Sherpa 1.4.1` [69], implementing the CKKW merging algorithm. This generator handles all steps of the simulation including the tau decay. The PDF set is CTEQ6L1 [195].

Events are simulated in five regions of the W boson transverse momentum, from $p_{\mathrm{T}}^{W} > 0$ GeV to $p_{\mathrm{T}}^{W} > 500$ GeV. For each region, exclusive samples are generated for different flavours of the quark initiating the associated jet. An exclusive simulation is performed depending on the flavour of the associated jet, which are obtained in the three cases (u, d, s), c and b quarks. Cross-sections are computed using `FEWZ` and are summarised in App. D.

7.2.4 $t\bar{t}$ and single-top

Another source of background is due to the production of $t\bar{t}$ and *single-top* events. Feynman diagrams for these processes are shown in Fig. 7.15. Due to the low production cross-sections at the LHC, this type of events corresponds to only a small contamination. The t quark decays in $t \to Wb$, with $\mathrm{BR}(t \to Wb) \approx 100\%$. In selected $t\bar{t}$ events, the two identified tau candidates might be real tau leptons, from the decays $W \to \tau\nu$, or might be fake taus most likely originating from a b-initiated jet, or a combination of the two cases. As b quarks hadronise into B mesons, or other b-hadrons, which have a lifetime roughly comparable to the one of the tau, they also lead to a displaced decay vertex, which increases their mis-identification probability. Simulated events are used to model this contribution, which are generated with `MC@NLO 4.01` [67], interfaced with `Herwig 6.52` [72, 197] for the simulation of the parton shower and hadronisation. Multiple interactions, discussed in Sec. 2.4.1, are modelled with `Jimmy 4.31` [77]. The PDF set is chosen to be CT10 [188]. The NNLO computation of the cross-section is performed with `top++ 2.0` [198–203], and uncertainties associated with the PDF set and the value

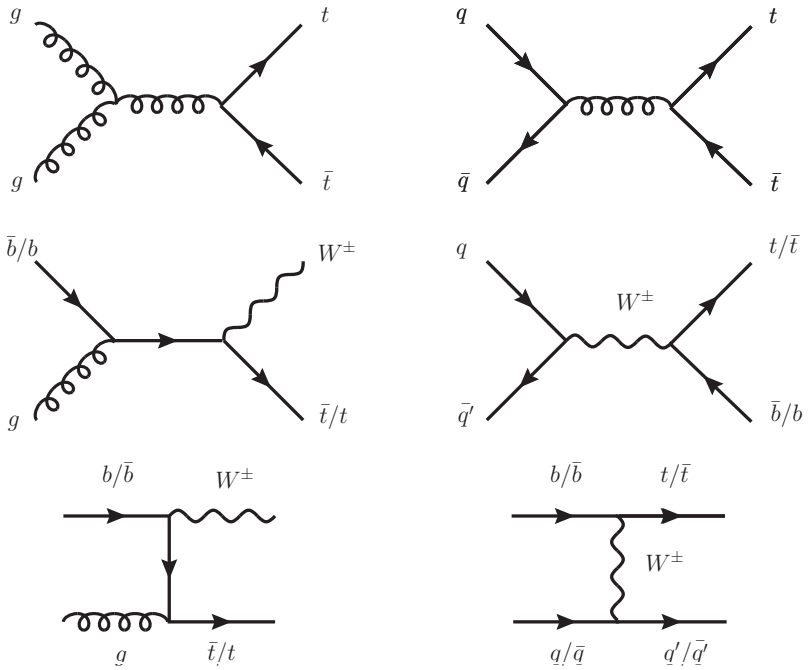

Figure 7.15: Examples of production modes for the $t\bar{t}$ background (upper row), and single-top background (lower rows). The *s*-channel and *t*-channel diagrams for single-top production are indicated by the middle row and lower row, respectively.

of α_S are evaluated according to the prescription of PDF4LHC [65]. The calculation also includes terms up to the *next-to-next-to-leading logarithm* (NNLL) of the perturbative expansion associated with gluons at low momenta. The computed cross-section is compatible with the value measured by ATLAS, reported in Fig. 7.9, $\sigma_{\text{obs}}(t\bar{t}) = 242.4 \pm 10.3$ pb [204], with a theoretical expectation of $\sigma_{\text{th}}(t\bar{t}) = 252.89 \pm 11.67(\text{PDF} + \alpha_S) \pm 7.51(\mu_F + \mu_R)$ pb. Events are simulated in two exclusive samples, one considering only hadronic decays of the W bosons and the other only leptonic decays.

Single-top production has a smaller cross-section than $t\bar{t}$ production, as illustrated in Fig. 7.9, where single-top is indicated as tW, if the final state features a W boson, or *t/s-chan* for the *t*-channel or *s*-channel exchange of an intermediate W boson [15, 18], respectively. For the tW final state, the cross-section is $\sigma_{\text{obs}}(tW) = 27.2 \pm 5.8$ pb [205] in good agreement with the theoretical prediction $\sigma_{\text{th}}(tW) = 22.4 \pm 1.5$ pb [206]. The dominant contribution to single-top production comes from *t*-channel W exchange, with $\sigma_{\text{obs}}(t\text{−chan}) = 82.6 \pm 12.1$ pb [207], where the theoretical prediction is $\sigma_{\text{th}}(t\text{−chan}) = 87.8 \pm 2.6$ pb [208]. A smaller contribution to the total single-top production cross-section comes from the *s*-channel exchange, with $\sigma_{\text{obs}}(s\text{−chan}) = 5.0 \pm 4.3$ pb [209] and $\sigma_{\text{th}}(s\text{−chan}) = 5.61 \pm 0.22$ pb [210]. As for the $t\bar{t}$ contribution, the single-top background is modelled with simulation. The tW and *s*-channel contributions are simulated with `MC@NLO` [211, 212] as previously described for $t\bar{t}$, interfaced with the same tools already mentioned. The *t*-channel is modelled with `AcerMC 3.8` [213] interfaced with `Pythia 6.421` [70] for parton showering and hadronisation. The PDF set used is CTEQ6L1 [195]. For both $t\bar{t}$ and single-top simulation the tau decay is modelled with `TAUOLA` [75].

Due to the small cross-section of the single-top contribution and the fact that the final state features at most one real tau from the W decay, only few events from this background are selected in the signal region. For convenience, the $t\bar{t}$ and single-top contributions will be merged in the following, and are referred to as the *top background*. More details about the simulation of this background are given in

App. D.

7.2.5 Other contributions

A number of other backgrounds contribute to the event yield in the signal region but only with a very small fraction. These are di-boson production, where WW or ZZ pairs are present in the final state, $Z/\gamma^* \to ll$ and $W \to l\nu$ + jets events, where $l = e, \mu$.

In di-boson events, two real tau leptons from WW can arise from the decay of each W boson, while in ZZ one Z boson can decay in two tau leptons and the other in two neutrinos. WZ final states might lead to various combinations of real tau leptons or tau fakes in the final state. However, the kinematic selection in the signal region largely suppresses this class of events, which rarely feature a pair of back-to-back tau leptons in the transverse plain. Also, the small cross-sections involved make the di-boson contribution small. Events are simulated with `Herwig 6.52` [197], which handles the parton shower and hadronisation, interfaced with `Jimmy 4.31` [77] to model multiple interactions. Tau decays are simulated with `TAUOLA`, while the chosen PDF set is CTEQ6L1 [195]. Cross-sections are computed at NLO with `MCMF` [214].

A contribution from $W \to l\nu$ + jets and $Z/\gamma^* \to ll$ is present in the analysis in particular in final states including electrons. Events containing either a reconstructed muon or electron are vetoed in the analysis, and only a small fraction of these backgrounds contaminate the signal region. Simulated events are used for their estimation. For $W \to l\nu$ + jets the same simulation is used as described in Sec. 7.2.3, while $Z/\gamma^* \to ll$ events are simulated with `Powheg` [66], where the parton shower and the hadronisation are simulated with `Pythia8` [71]. In a similar way as discussed in Sec. 7.2.2, the predicted cross-section has to be rescaled as a function of the generated di-lepton invariant mass, in order to provide a NNLO prediction, as the `Powheg` prediction is NLO. The k-factor is reported in Fig. 7.16, together with its upward and downward systematic variations resulting from the variation of the PDF set and the value of α_S. They are obtained with `FEWZ 3.1.b2`.

More details about the simulation of these additional contributions are given in App. D.

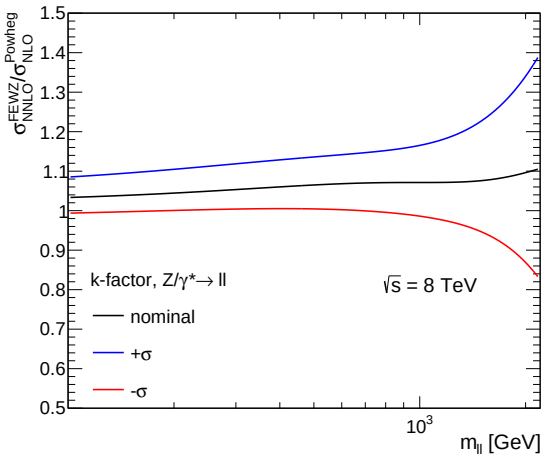

Figure 7.16: k-factors as a function of the resonance mass used to rescale the NLO `Powheg` cross-section in order to achieve an NNLO prediction for $Z/\gamma^* \to ll$ events. The upward and downward variation is also shown corresponding to the uncertainty from the PDF set and α_S. Numbers are obtained with `FEWZ 3.1.b2` [193, 194].

7.3 Selection of Events

This section illustrates the selection of events used in the analysis, which is divided into a pre-selection stage, discussed in Sec. 7.3.1, a set of general topological and kinematic requirements illustrated in Sec. 7.3.2, and the selection of events in two categories which are based on the trigger decision, presented in Sec. 7.3.3.

7.3.1 Pre-selection

Pre-selection includes a number of general requirements, referred to as *event cleaning*, aiming at removing those events collected in data-taking runs with non-perfect detector conditions or poorly reconstructed objects. Also, potential sources of fake hadronically decaying tau candidates from electrons or muons are removed with a dedicated *light-lepton veto*. An overview of the pre-selection requirements is given in the following. In this section, the overview of the pile-up weighting procedure is also given, aimed at correcting the effect of pile-up interactions in simulated events.

Event Cleaning

Each data-taking period is monitored in order to guarantee optimal detector conditions as well as good LHC operations status. Events fulfilling all the data-quality requirements are flagged by the ATLAS collaboration as good ones, which are used in this analysis. This includes the removal of events where sub-detectors could be flagged as temporarily unavailable. Noise-bursts or readout errors in the calorimeter system could lead to poorly reconstructed events, which are also flagged and not considered. Events are selected if they contain at least one reconstructed vertex with more than three associated tracks. This ensures that only pp collisions are selected, and removes spurious events that originate from e.g. proton collisions with the residual gas in the beam pipe or with components of the beam-halo [215], or cosmic-ray muons [18].

The missing transverse energy will be used in the selection of events. The determination of this quantity depends on reconstructed jets. However, these could be poorly reconstructed due to a number of reasons, including hardware problems, beam conditions and showers from cosmic rays overlapping with a jet. Sporadic noise-bursts in the HEC cells can lead to a reconstructed jet if neighboring cells feature coherent noise. Requirements on the fraction of energy deposited in the HEC and the pulse shapes are applied to flag these jets. Coherent noise is also induced by noise-bursts in the ECAL. Jets affected by this are flagged based on requirements on the pulse shapes and the *electromagnetic fraction*, f_{EM}, defined as the ratio between the energy deposited in the EM calorimeter and the sum of the energies deposited in the EM and HCAL calorimeters. Reconstructed jets from non-collision events are flagged using f_{EM}, the energy fraction in the pre-sampler, and the fraction of charged particles inside the jet. If events contain a flagged jet they are not considered for the analysis. Jets fulfilling the quality requirement must have $p_{\text{T}} > 20$ GeV.

Light-Lepton Veto

Events containing reconstructed electrons or muons are vetoed in this analysis to reject tau candidates originating from electrons or muons. Pre-selected events containing at least one electron or muon are not considered. The use of this veto in the $h/H/A \to \tau_{\text{had}}\tau_{\text{had}}$ channel also prevents any overlap with the other channels in the combined $h/H/A \to \tau\tau$ search, which utilise leptonic decay modes of the tau in the final state. In Tab. 7.2, a summary of the pre-selection requirements is given.

Period Name	Begin	End	Run Number Interval	Recorded L_{int} [pb^{-1}]	$\varepsilon_{\text{ATLAS}}$[%]	μ_{max}
A	Apr. 04	Apr. 20	200804–201556	910	98	30
B	May 01	Jun. 18	202660–205113	5594	98	31
C	Jul. 01	Jul. 24	206248–207397	1643	98	34
D	Jul .24	Aug. 23	207447–209025	3598	98	34
E	Aug. 23	Sep. 17	209074–210308	2863	98	36
G	Sep. 26	Oct. 08	211522–212272	1404	98	34
H	Oct. 13	Oct. 26	212619–213359	1655	98	35
I	Oct. 26	Nov. 02	213431–213819	1149	98	34
J	Nov. 02	Nov. 26	213900–215091	2941	98	35
L	Nov. 30	Dec. 06	215414–215643	983	98	36
M	Dec. 15	Dec. 16	216399–216432	14	97	12

Table 7.1: Summary of data taking periods during Run-I for pp collisions at $\sqrt{s}$ = 8 TeV in 2012. Each period is subdivided in runs where run numbers are indicated in the table. The data-taking efficiency from the ATLAS experiment, $\varepsilon_{\text{ATLAS}}$, is also indicated as well as the maximum number of average interactions per bunch-crossing, μ_{max}. Values are taken from Ref. [216].

Pile-up Weighting

Pile-up interactions are difficult to model in the simulation. As pile-up could significantly affect the distributions of the physical observables used in the analysis, Monte Carlo simulated distributions should be corrected to match the amount of pile-up observed in data. This is performed using a weighting procedure, where all simulated events are multiplied by a weight $w(\mu, P)$, which depends on the average number of interactions per bunch-crossing, μ, and the data-acquisition period, P. In Tab. 7.1, a summary of the data-taking periods in 2012 collisions at $\sqrt{s}$ = 8 TeV is given, featuring their total integrated luminosities and average number of pile-up interactions. In Fig. 7.17, the distributions of the average number of interactions per bunch-crossing μ is shown for the data from the four periods with the highest luminosity.

7.3.2 Topological and Kinematic Requirements

After pre-selection, a set of topological and kinematic requirements are applied to select tau leptons compatible with the decay of a heavy neutral resonance. Exactly two tau candidates are selected, with $p_{\text{T}} > 50$ GeV, one or three associated tracks, and opposite electric charge (*opposite-sign* requirement).

Due to the very large multi-jet cross-section at low momenta, little sensitivity is expected when the tau leptons in the decay have low p_{T}, hence likely to stem from a resonance with low mass. For this reason, the event selection in the $h/H/A \to \tau_{\text{had}}\tau_{\text{had}}$ channel mainly targets decays from a high-mass resonance. Two tau candidates are required to be emitted in opposite directions in the transverse plane, by rejecting events with $|\Delta\phi(\tau_{\text{lead}}, \tau_{\text{sub-lead}})| < 2.7$. In Tab. 7.2, a summary of the topological and kinematic requirements listed in this section is given.

In Fig. 7.18, distributions of events are shown, before the $\Delta\phi$ requirement is applied. In these distributions, the multi-jet contamination is estimated by simple subtraction of all other backgrounds which are estimated using the simulation with no data-driven correction applied. In Tab. 7.3, the event

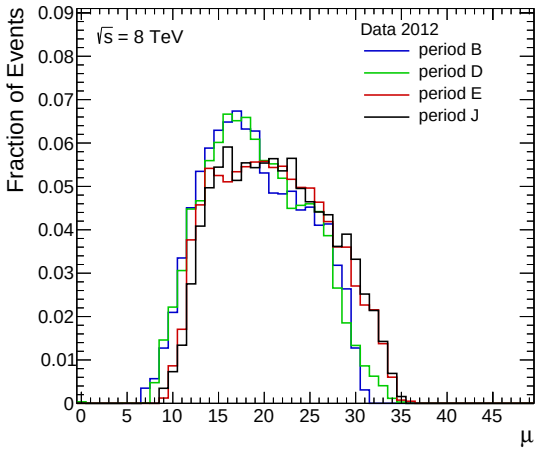

Figure 7.17: Average number of interactions per bunch-crossing in data corresponding to the four periods with the highest luminosity in 2012 data-taking.

$h/H/A \to \tau_{\text{had}}\tau_{\text{had}}$ Selection Requirements
Pre-selection
Event cleaning
At least one reconstruced primary vertex with > 3 associated tracks
Veto on events with poor jet reconstruction
Veto on events with reconstructed electrons or muons
Event Topology and Kinematic
Exactly two tau candidates
$N_{\text{track}}(\tau_{\text{lead/sub-lead}}) = 1$ or 3
$p_{\text{T}}(\tau_{\text{lead/sub-lead}}) > 50$ GeV
Leading and sub-leading tau candidates with opposite electric charge
$\lvert\Delta\phi(\tau_{\text{lead}}, \tau_{\text{sub-lead}})\rvert > 2.7$

Table 7.2: Summary of the pre-selection, topological and kinematic requirements applied in the $h/H/A \to \tau_{\text{had}}\tau_{\text{had}}$ analysis previous to the categorisation.

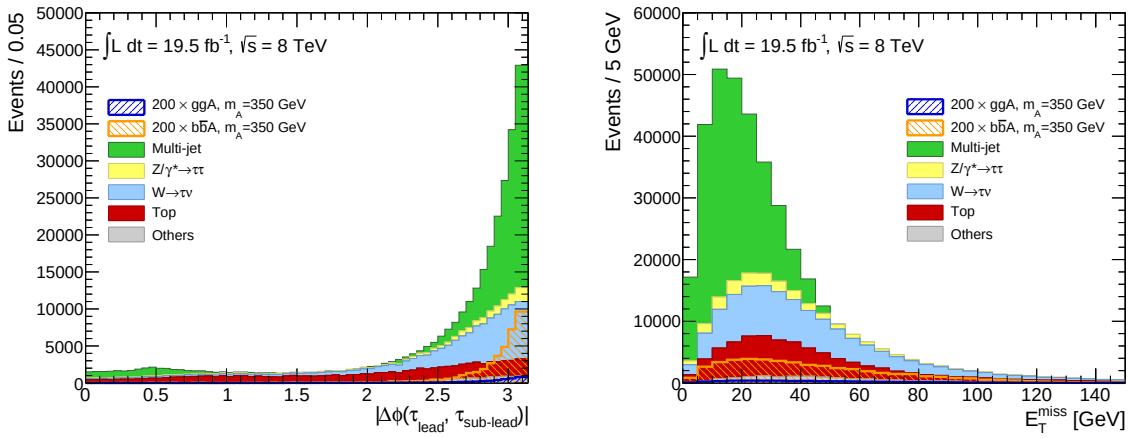

Figure 7.18: Distributions after pre-selection including topological and kinematic requirements, as discussed in the main text, with the exception of $|\Delta\phi(\tau_{\text{lead}}, \tau_{\text{sub-lead}})| < 2.7$. Left: absolute value of the azimuthal angular separation of the tau leptons in the event. Right: missing transverse energy in the event. In the plots, the multi-jet background is estimated as the difference between data and all other background contributions, which are estimated using the simulation. The signal shown in the plots is increased by a factor of 200 after normalising the expectation for $L_{\text{int}} = 19.5\ \text{fb}^{-1}$ at $\tan\beta = 20$.

	Pre-selection	$p_{\text{T}}(\tau_{\text{lead/sub-lead}}) > 50$ GeV	Opposite-sign	$\lvert\Delta\phi(\tau_{\text{lead}}, \tau_{\text{sub-lead}})\rvert > 2.7$
Background				
$Z\gamma^* \to \tau\tau$	59058 ± 253	32059 ± 256	19851 ± 197	10840 ± 141
$W \to \tau\nu$	442150 ± 958	141734 ± 561	93100 ± 461	55713 ± 373
Top	267626 ± 723	130322 ± 633	69062 ± 457	18604 ± 233
Others	315562 ± 951	27860 ± 316	15163 ± 238	7281.3 ± 174
Signal ($m_A = 350$ GeV, $\tan\beta = 20$)				
$b\bar{b} \to A$	377.2 ± 2.5	257.6 ± 2.6	243.4 ± 2.5	213.8 ± 2.3
$gg \to A$	40.15 ± 0.27	28.02 ± 0.27	25.99 ± 0.26	20.47 ± 0.23
Data	1533922 ± 1238	677172 ± 822	358722 ± 598	227093 ± 476

Table 7.3: Event yields for the background contributions, the data and the signal after pre-selection and the application of topological and kinematic requirements as discussed in Sec. 7.3.1 and 7.3.2, respectively. The table includes the statistical uncertainty. The multi-jet background is not included, as it is not yet estimated at this stage of the analysis. The expected amount of signal events is determined assuming the m_h^{max} scenario.

yield for each of the background contributions, the data and the signal are reported after pre-selection and the topological and kinematic requirements. For the signal, $m_A = 350$ GeV and $\tan\beta = 20$ is assumed. The results for all other mass points can be found in App. E.

7.3.3 Definition of Categories

Events in this analysis are classified in two categories where different tau triggers are utilised. At high m_A, the sensitivity of the entire $h/H/A \to \tau\tau$ search is dominated by the $h/H/A \to \tau_{\text{had}}\tau_{\text{had}}$ channel. This is possible thanks to the contribution to the $h/H/A \to \tau_{\text{had}}\tau_{\text{had}}$ sensitivity of a category where events are

selected using a single-tau trigger with a high-p_{T} threshold. A category utilising a di-tau trigger is also defined with low-p_{T} thresholds on the tau pair. Its sensitivity dominates the $h/H/A \to \tau_{\text{had}}\tau_{\text{had}}$ search for signal masses $m_A \lesssim 350$ GeV. The use of different tau triggers in the analysis allows for dedicated data-driven background estimation techniques for the multi-jet contribution, as will be discussed later.

Simulated events emulate the trigger decision. However, trigger menus are finalised using data, which is typically collected after a simulation campaign. Therefore, the trigger decision in simulated events might need to be re-emulated to avoid inconsistencies with data. However, this correction is not always possible if the necessary information for the re-emulation is not stored in the data format utilised by physics analyses. This happened in 2012 for collisions at $\sqrt{s} = 8$ TeV, where during period A no Δz_0 selection on the tracks utilised at trigger level was implemented. A Δz_0 requirement is present in simulated events, but the necessary tracking information needed for the re-emulation is not available. For this reason, period A is discarded and the total integrated luminosity used by this analysis is $L_{\text{int}} = 19.5$ fb^{-1}, instead of the full $L_{\text{int}} = 21.3$ fb^{-1} for the 2012 data sample.

Single-tau-trigger Category

The single-tau trigger, called `EF_tau125_medium1`, selects one hadronically decaying tau with $p_{\text{T}} > 125$ GeV, and applies medium identification on the candidate. This menu is seeded at L1 by `L1_TAU40`, where a candidate with $E_{\text{T}} > 40$ GeV is selected. Signal efficiencies for the single-tau trigger are illustrated in Fig. 7.19 (right), where the trigger-level tau lepton is matched to a true one.

Trigger threshold effects are avoided by requiring $p_{\text{T}}(\tau_{\text{lead}}) > 150$ GeV, while $p_{\text{T}}(\tau_{\text{sub-lead}}) > 50$ GeV is maintained. Given the high-p_{T} requirement of the trigger, multi-jet events are less abundant than in the di-tau-trigger category, therefore the loose working point is used when requiring identification of both tau candidates. Events selected by the single-tau trigger belong to the *single-tau-trigger category* (STT). The summary of the requirements defining the signal region of the STT category is given in Tab. 7.4.

Di-tau-trigger Category

The di-tau trigger used in this analysis, called `EF_2tau38T_medium1`, selects two hadronically decaying tau leptons with $p_{\text{T}} > 38$ GeV, identified according to the medium working point at the EF level. At L1 this menu is seeded by `L1_2TAU20`, selecting two tau candidates with $E_{\text{T}} > 20$ GeV. At L2, the tau is required to have a number of associated tracks between one and four. At the EF level, not more than three tracks are required. Signal efficiencies for the di-tau trigger are illustrated in Fig. 7.19 (left), obtained for simulated signal events where triggered tau leptons are matched to a true tau.

In addition to the trigger requirement, a few other selection criteria are applied. In order to improve the rejection of multi-jet events and avoid p_{T}-threshold effects from the trigger turn-on curves, the tau leptons must have $p_{\text{T}} > 50$ GeV. In order to avoid any overlap with the single-tau-trigger category, the requirement $p_{\text{T}}(\tau_{\text{lead}}) < 150$ GeV is applied. Reconstructed tau leptons have to be identified according to the medium working point of the identification algorithm. Given the presence of two neutrinos in the final state, the signal features higher $E_{\text{T}}^{\text{miss}}$ than multi-jet events. For this reason, $E_{\text{T}}^{\text{miss}} > 10$ GeV is required. Finally, the total sum of the scalar transverse energies of all objects in the event, $\sum E_{\text{T}}$ as defined in Eq. 5.9, is required to be above 160 GeV. This is also effective in removing multi-jet events, as they are preferentially produced in collisions with lower transferred energies than the signal. Events selected by this trigger will be referred in the following as *di-tau-trigger category* (DTT). The summary of the selection requirements defining the DTT signal region is given in Tab. 7.8.

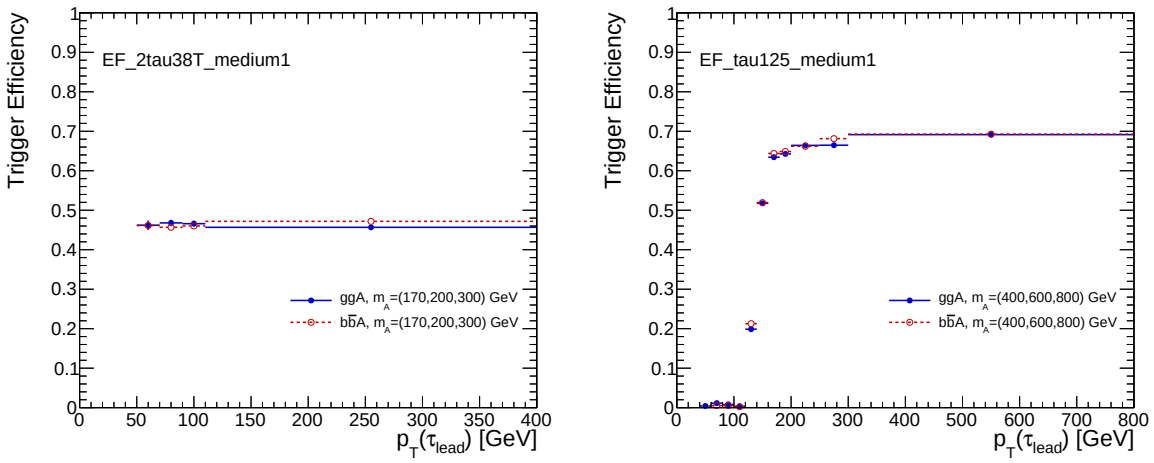

Figure 7.19: Trigger efficiencies for the `EF_2tau38T_medium1` menu (left), and the `EF_tau125_medium1` (right) menu, measured with signal samples as a function of the leading tau p_{T}. Only pre-selection is applied plus the requirement $p_{\mathrm{T}} > 50$ GeV for both tau candidates. The trigger-level tau lepton is geometrically matched to a true one. The efficiencies shown in the plots are the combined efficiencies measured with several signal samples at different values of m_A, as indicated in the plots.

7.4 Multi-jet Background Estimation in the Single-Tau Trigger Category

As illustrated in Fig. 7.19, the single-tau trigger has a higher signal efficiency than the di-tau trigger. In addition, due to the higher p_{T} threshold, the rejection of the multi-jet contribution is significantly enhanced. These features make the single-tau trigger category the most sensitive in the combined $h/H/A \to \tau\tau$ analysis for masses $m_A \gtrsim 350$ GeV, where the leading sensitivity is provided by the $h/H/A \to \tau_{\mathrm{had}}\tau_{\mathrm{had}}$ channel.

The use of a single-tau trigger allows one to define a multi-jet background estimation method which is completely data-driven and relies on a control region particularly rich in multi-jet events. This method is based on a weighting technique applied to events found in a control region defined using identical requiremnts with respect to the signal region, but where the sub-leading tau candidate fails identification. The summary of the requirements defining this control region is given in Tab. 7.4, where it is called $\mathrm{CR}_{\mathrm{multi-jet}}$.

In Fig. 7.20 and 7.21, the distributions of the tau identification BDT score for the leading and sub-leading tau candidates in the STT selection are shown before any identification is applied. The loose ID working point used in the STT category corresponds approximately to a 0.6 threshold on the score. As becomes evident from the BDT distributions, events below this threshold, used in the weighting technique, are dominated by multi-jet events.

The event weight applied to events in $\mathrm{CR}_{\mathrm{multi-jet}}$ is called the *fake-factor*, f_{fake}, and is defined as

$$f_{\mathrm{fake}} = \frac{N_{\mathrm{pass\ ID}}(p_{\mathrm{T}}, N_{\mathrm{trk}})}{N_{\mathrm{fail\ ID}}(p_{\mathrm{T}}, N_{\mathrm{trk}})}, \tag{7.3}$$

where $N_{\mathrm{pass\ ID}}$ and $N_{\mathrm{fail\ ID}}$ are the number of tau candidates above and below the loose working point threshold, measured as a function of the candidate p_{T} and track multiplicity, respectively. Fake-factors are measured in a data-driven way from a tag-and-probe selection of di-jet events, as will be described in

STT Selection Requirements	STT signal region	$CR_{\text{multi-jet}}$ (multi-jet estimation)	VR1 (multi-jet validation)	VR2 (multi-jet estimation for validation)
Single-tau trigger ($p(\tau) > 125$ GeV + medium trigger-level tau-ID)	•	•	•	•
$p_{\text{T}}(\tau_{\text{lead}}) > 150$ GeV	•	•	•	•
Leading and sub-leading tau candidates with opposite electric charge	•	•	rev.	rev.
Loose tau-ID on leading tau	•	•	•	•
Loose tau-ID on sub-leading tau	•	rev.	•	rev.

Table 7.4: Summary of the selection requirements defining the relevant regions of the STT category. In the table, the dot indicates the application of the requirement indicated in the list on the left. When a requirement is reversed it is explicitly indicated in the table by "rev.". The region indicated as $CR_{\text{multi-jet}}$ is the control region used for the estimation of multi-jet events. The regions indicated as VR1 and VR2 are defined to validate the estimation of the multi-jet bakcground.

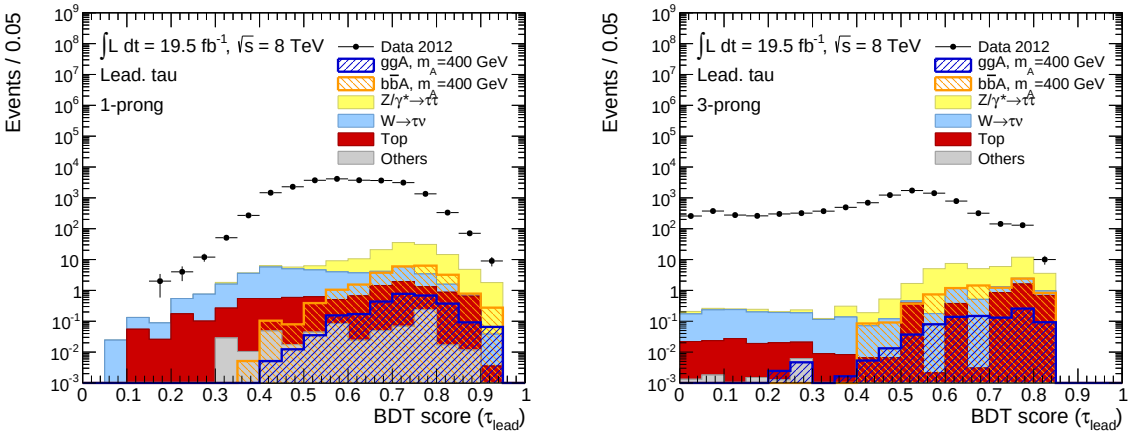

Figure 7.20: Distributions of the BDT score for the leading tau lepton for 1-prong (left) and 3-prong (right) candidates. All selection requirements of the STT category are applied with the exception of the tau identification. The multi-jet contribution is not estimated.

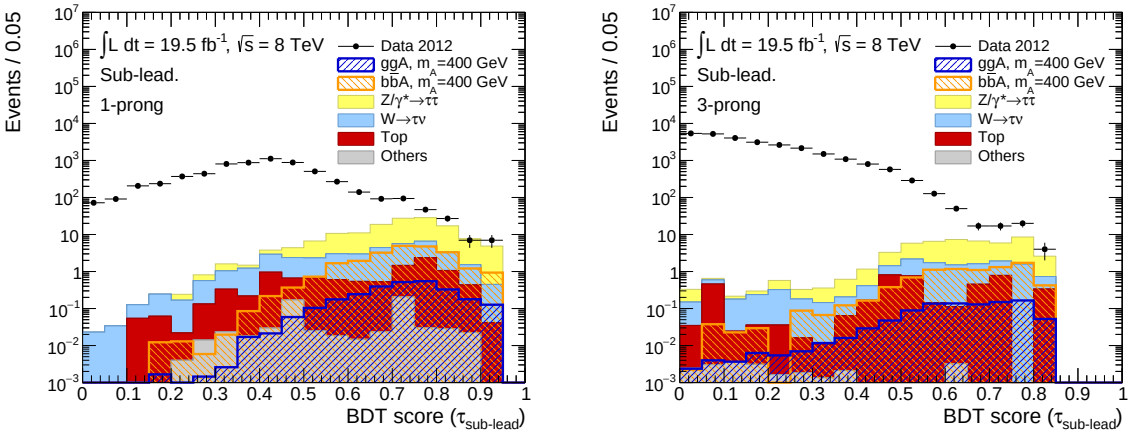

Figure 7.21: Distributions of the BDT score for the sub-leading tau lepton for 1-prong (left) and 3-prong (right) candidates. All selection requirements of the STT category are applied with the exception of the tau identification. The multi-jet contribution is not estimated.

Tag-and-Probe Di-jet Selection Requirements
Pre-selection (cf. Tab. 7.2)
Single-jet triggers (p_{T}(jet) > 110, 145, 180, 220, 360 GeV)
At least two tau candidates with $p_{\text{T}}(\tau) > 50$ GeV
p_{T}(tag) > 150 GeV
Tight electron veto on tag jet
$p_{\text{T}}(\text{probe})/p_{\text{T}}(\text{tag}) \geq 0.3$

Table 7.5: Summary of the requirements applied in the di-jet tag-and-probe selection for the measurement of the fake-factors used in the STT category for the multi-jet background estimation.

the next section.

7.4.1 Measurement of Fake-factors

Fake-factors are measured using a tag-and-probe selection of di-jet events in data. Events are pre-selected as described in Sec. 7.3.1, with no opposite-sign requirement to reduce the statistical uncertainty. Many single-jet triggers with different p_{T} thresholds are used. Some of these triggers feature pre-scale factors, which artificially increase their event rejection, given the very large multi-jet production cross-section, especially the low-p_{T} ones. Different thresholds from p_{T}(jet) = 110 GeV to p_{T}(jet) = 360 GeV are implemented.

The selection used for di-jet events in data is as similar as possible to the selection of the STT category. At least two reconstructed tau candidates are required with $p_{\text{T}} > 50$ GeV. The probe object is the lowest-p_{T} one, while the tag is required to have $p_{\text{T}} > 150$ GeV. Electrons from $Z/\gamma^* \to ee$ + jets might contaminate the selection. To reduce this contribution, the tag is required to pass the electron veto according to the tight working point (cf. App. B.0.1). In addition, the requirement $p_{\text{T}}(\text{probe})/p_{\text{T}}(\text{tag}) \geq 0.3$ is applied to reduce the p_{T} imbalance between the two objects. Events in the STT category indeed have high values of this p_{T} ratio, as illustrated in Fig. 7.22, where the distributions of $p_{\text{T}}(\tau_{\text{sub-lead}})/p_{\text{T}}(\tau_{\text{lead}})$ are shown for the STT signal region (upper-left), the control region chosen to weight multi-jet events, $\text{CR}_{\text{multi-jet}}$, (upper-right), and two additional control regions which are relevant for the validation of the multi-jet estimation, VR1 and VR2. All these regions are defined in Tab. 7.4. The summary of the requirements applied in the tag-and-probe di-jet selection is given in Tab. 7.5.

The selection on $p_{\text{T}}(\text{probe})/p_{\text{T}}(\text{tag})$ reduces the contribution of multi-jet events where more than two jets are present in the event, thus increasing the fraction of di-jet events which are likely to be the dominant multi-jet contribution in the STT selection. This is important, as the relative fraction of quark and gluon-initiated probes is likely to be very different in the two classes of multi-jet events, leading to a significant effect on the fake-factors.

If multi-jet events contaminate the selection used in the fake-factor measurement, it is important to check whether this has an effect on the fake-factors. For this reason, the measurement is repeated distinguishing between different additional jet multiplicities, where a number of additional reconstructed jets in the event between zero and four is required. This measurement is illustrated in Fig. 7.23. No significant dependence on the number of additional jets is visible. A large statistical uncertainty can be seen for the zero-jet measurement at low p_{T} due to the requirement on the p_{T} balance rejecting events

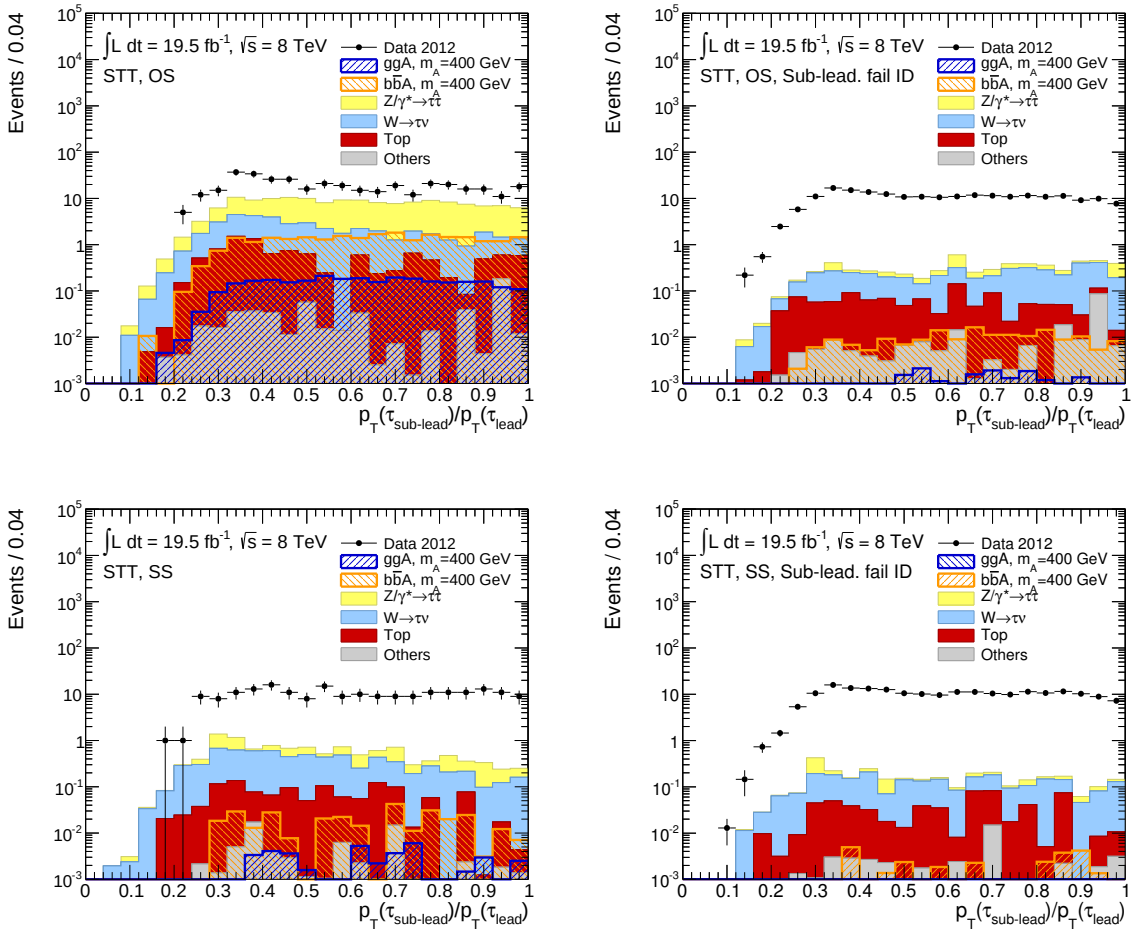

Figure 7.22: Distributions of the ratio between the p_{T} of the sub-leading and leading tau leptons in the STT selection for the signal region and three control regions. The upper row shows the distribution for the signal region (left) and a control region where the sub-leading candidate is required to fail identification (right), defined in Tab. 7.4, where it is called $\mathrm{CR}_{\mathrm{multi-jet}}$. The lower row shows analogous regions, where the two candidates are required to have the same charge. They are also defined in Tab. 7.4, where they are called VR1 and VR2, corresponding to the lower plots on the left and the right, respectively. No multi-jet contribution is estimated in the plots.

with missing additional jets at low momenta.

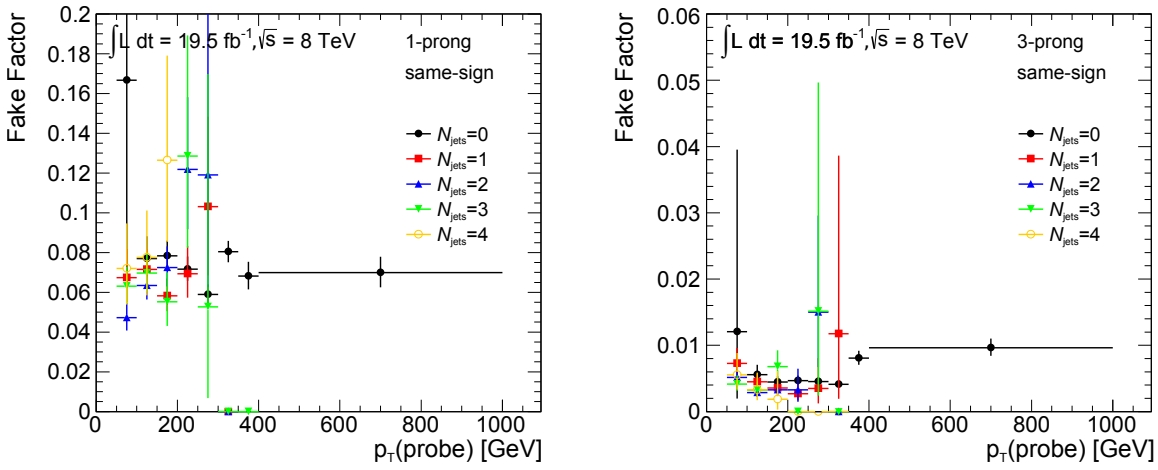

Figure 7.23: Fake-factors measured as a function of the probe jet p_T from a di-jet tag-and-probe selection of events in data. The plots show the comparison of measurements where different numbers of additional jets are required in the event. The measurement is obtained for 1-prong (left) and 3-prong (right) fake candidates, applying a same-sign requirement for the tag and the probe.

Fake-factors are measured with single-jet triggers. However, in the STT signal region and in the control region used to estimate the multi-jet background, events are selected by a single-tau trigger. Multi-jet events selected by the tau trigger might feature a different relative fraction of quark and gluon-initiated jets, with respect to those selected by jet triggers, or a contribution from real tau leptons. Thus, fake-factors measured using the di-jet tag-and-probe selection might not be applicable to the STT analysis, where events in $\text{CR}_{\text{multi-jet}}$ are selected by the signle-tau trigger. To check for an eventual bias, fake-factors measured from di-jet events using single-jet and single-tau triggers are compared in Fig. 7.24, as a function of p_T(probe). Different fake-factors are obtained depending on the charge-product between the tag and the probe jet. At high p_T the available number of events selected by the single-tau trigger decreases due to the isolation requirement at the trigger level, not applied by the jet triggers. Same-sign fake-factors measured with the di-jet and single-tau triggers do not show a significant discrepancy as a function of p_T(probe), while opposite-sign ones differ in the low-p_T regions. This low-p_T discrepancy is likely to be caused by a contamination from $Z/\gamma^* \to \tau\tau$ + jets events in di-jet events selected by the single-tau trigger in the tag-and-probe selection. However, same-sign fake-factors measured with the two different triggers agree within the statistical uncertainties, indicating that no bias is found. In addition, same-sign and opposite-sign fake-factors measured with single-jet triggers are in agreement.

In the nominal STT selection, quark-initiated fakes are more likely to be triggered by the single-tau trigger than gluon-initiated ones. This implies that $\text{CR}_{\text{multi-jet}}$ is more enriched in gluon-initiated jets. As this feature is not present in the di-jet tag-and-probe selection, it is important to investigate the effect of altering the fake composition. This is performed by applying a selection on the BDT score of the tag, simulating the effect of the tau trigger. The effect is illustrated by the plots in Fig. 7.25, obtained by applying the same-sign requirement to avoid any $Z/\gamma^* \to \tau\tau$ contamination. The plots show no significant effect, which increases the confidence in the nominal measurement.

Nominal fake-factors are measured without applying any requirement on the charge-product between the tag and the probe. As illustrated by the checks discussed in this section, this does not result in a bias of the measurement, but contributes to reduce the statistical uncertainty. However, a charge-product requirement is applied when evaluating the systematic uncertainty, as will be explained in Sec. 7.4.2. The

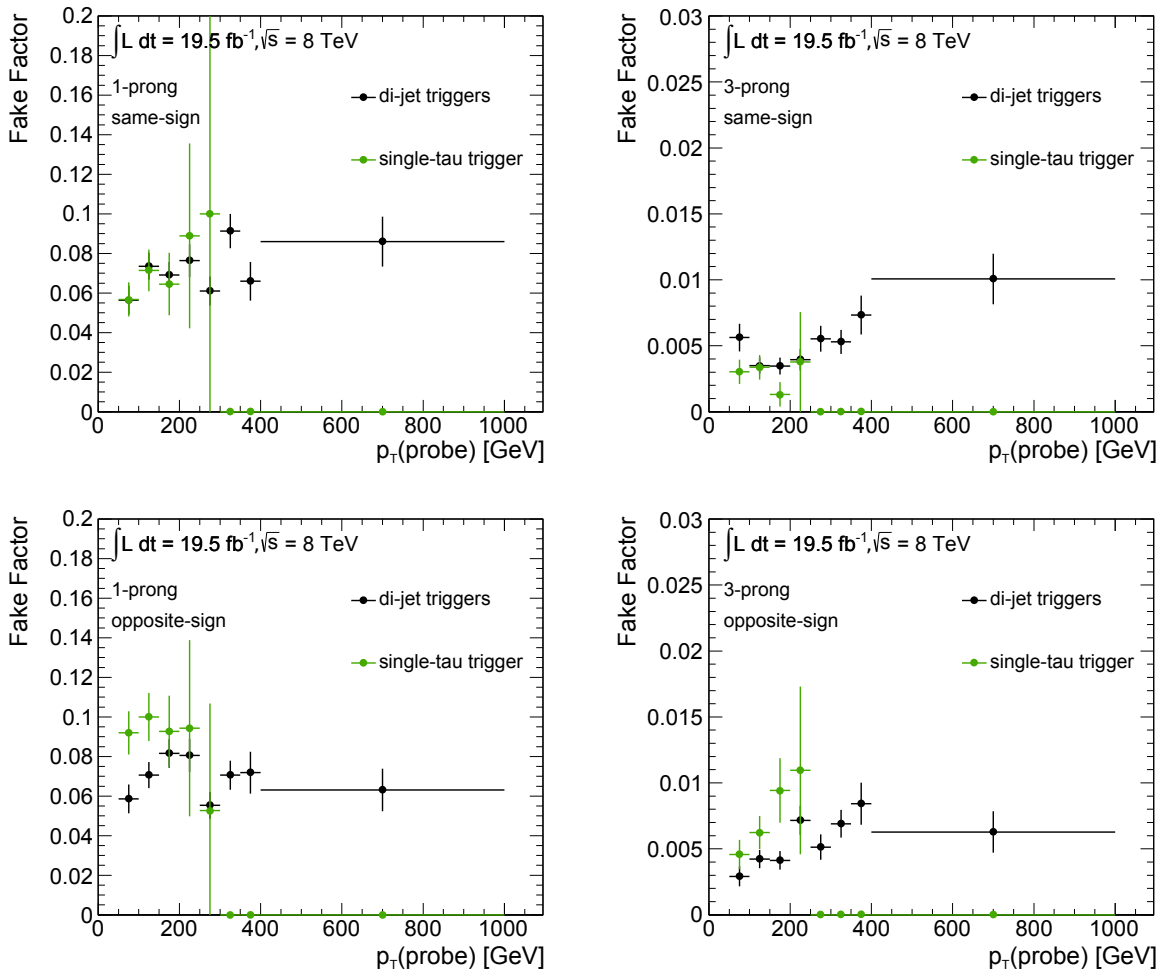

Figure 7.24: Fake-factors measured as a function of the probe jet p_{T} from a di-jet tag-and-probe selection in data. The comparison of the measurement performed using di-jet triggers is shown with respect to the single-tau trigger one. The plots on the left and the right are obtained for 1-prong and 3-prong candidates, respectively. A same-sign and opposite-sign requirement is applied to the candidates in the upper and lower plots, respectively.

events yield for backgrounds and the signal contamination in $\mathrm{CR}_{\mathrm{multi-jet}}$ are reported in Tab. 7.6.

7.4.2 Uncertainty on STT Multi-jet Estimation

Fake-factors measured for opposite-sign or same-sign tag and probe are consistent with the inclusive ones within the statistical uncertainty. However, as can be seen in Fig. 7.26, opposite-sign fake-factors tend to be larger than same-sign ones. This can be due to a contribution of real tau leptons in the tag-and-probe di-jet selection from $Z/\gamma^* \rightarrow \tau\tau$ decays, or, even more likely, of quark-initiated jets which are more similar to a hadronically decaying tau lepton than gluon-initiated ones. Therefore, a systematic uncertainty on the estimate is assessed by comparing the opposite-sign and same-sign fake-factors as a function of p_{T}. Their difference with respect to the inclusive measurement is computed. The largest deviation is taken to represent one standard deviation of the nominal measurement due to systematic effects. When this difference is smaller than the statistical uncertainty on the nominal estimate, the statistical uncertainty is used instead. The uncertainty evaluated in this way amounts to $6-30\%$, depending on p_{T} and the track

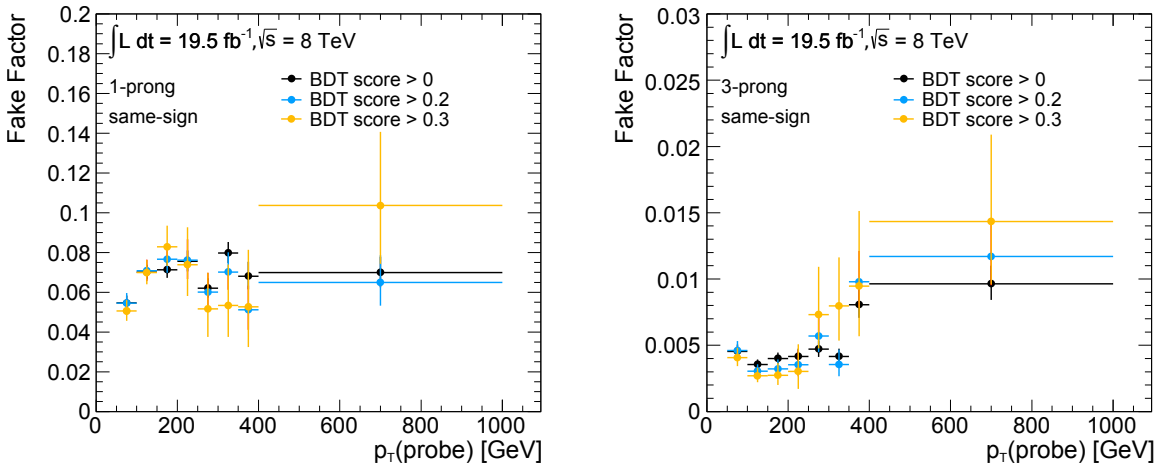

Figure 7.25: Fake-factors measured as a function of the probe jet p_{T} from a di-jet tag-and-probe selection of events in data. The plots show the comparison between measurements where different requirements on the BDT score of the tag jet are used. The measurement is obtained for 1-prong fake candidates (left) and 3-prong ones (right), applying a same-sign requirement between the tag and the probe to avoid any $Z/\gamma^* \to \tau\tau$ contamination.

	STT Control Regions	
	$\text{CR}_{\text{multi-jet}}$ (OS, $\tau_{\text{sub-lead}}$ fails loose ID)	VR2 (SS, $\tau_{\text{sub-lead}}$ fails loose ID)
Background		
$Z/\gamma^* \to \tau\tau$	1.44 ± 0.28	0.65 ± 0.17
$W \to \tau\nu$	3.63 ± 0.22	1.94 ± 0.14
Top	1.01 ± 0.11	0.57 ± 0.11
Others	0.202 ± 0.088	0.0438 ± 0.0099
Signal (m_A = 400 GeV, tanβ = 20)		
$b\bar{b} \to A$	0.174 ± 0.012	0.0291 ± 0.0048
$gg \to A$	0.021 ± 0.0015	0.00316 ± 0.00055
Data	14814 ± 122	13971 ± 118

Table 7.6: Events yields for the simulated backgrounds and data in the control regions used for the estimation of multi-jet events in the STT category. The regions are indicated as $\text{CR}_{\text{multi-jet}}$ and VR2, respectively, following the convention used in Tab. 7.4. They are used for the nominal multi-jet estimation and its validation, respectively. The symbol OS refers to the opposite-sign requirement on the electric charge of the candidates, while the SS symbol to the same-sign one. In this table, the contribution of the multi-jet background is not included. In these control regions, it is simply assumed to be the difference between the data and the sum of all other backgrounds. The statistical uncertainty on the yields is indicated in the table. The signal is estimated assuming tanβ = 20 in the m_h^{max} scenario.

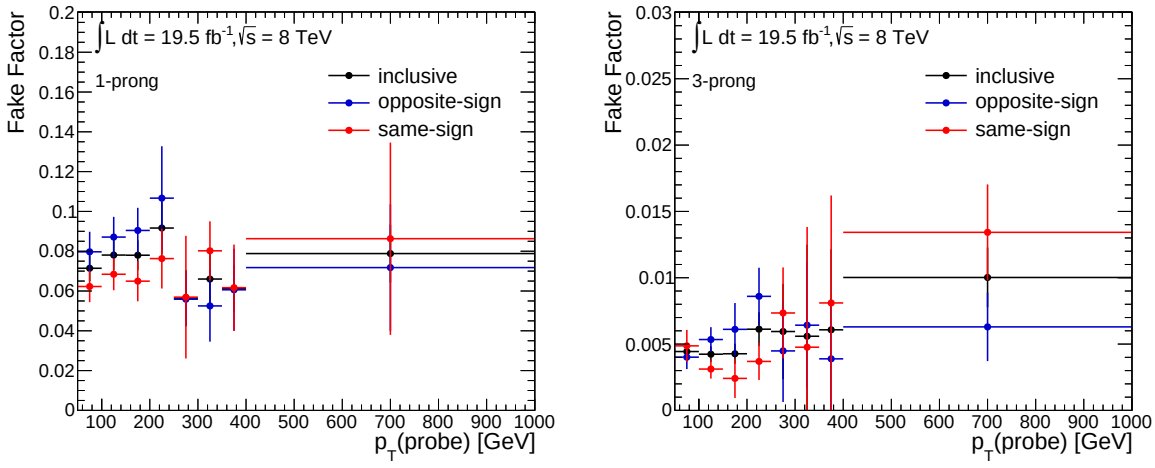

Figure 7.26: Fake-factors measured for 1-prong (left) and 3-prong (right) candidates obtained inclusively and applying an opposite-sign or same-sign requirement.

multiplicity. The systematically altered multi-jet estimate is taken using fake-factors varied upward and downward by one standard deviation. The nominal fake-factors and their total uncertainty as a function of p_{T} are illustrated in Fig. 7.27.

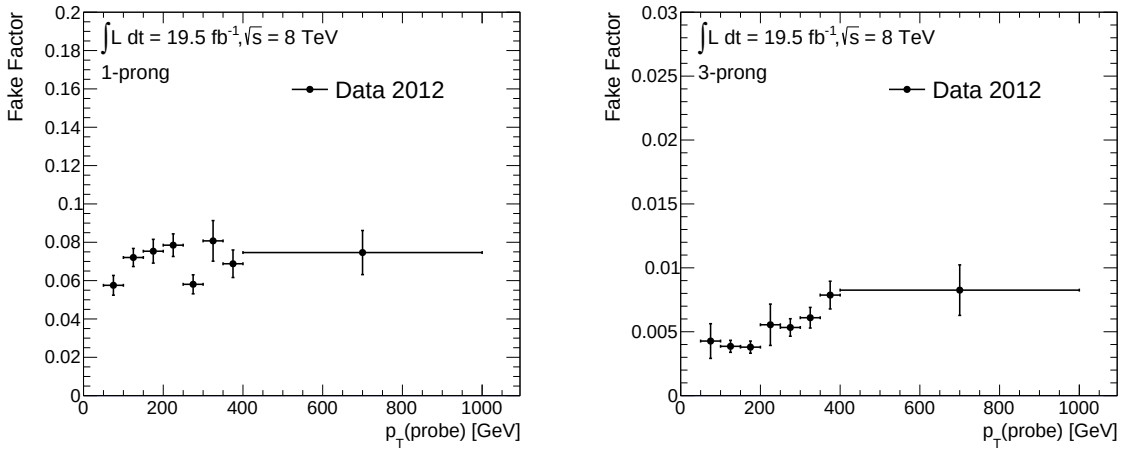

Figure 7.27: Nominal fake-factors as a function of the probe jet p_{T}. The uncertainty corresponds to the statistical and systematic uncertainties.

7.4.3 Validation of Multi-jet estimation in the Single-tau Trigger Category

In order to validate the multi-jet estimation outlined in Sec. 7.4, a control region is chosen using a selection which does not significantly distort the kinematic and topological properties of the signal region, while containing a negligible amount of signal. This is done by using the nominal selection of the STT category, but replacing the opposite-sign requirement with the same-sign one. The estimation of the multi-jet background is then performed with the fake-factor method applied to same-sign events. The

summary of the requirements defining the regions used to validate the multi-jet estimate in the STT category is given in Tab. 7.4. In the table, the region used for the validation and the one used to estimate multi-jet events for the validation are called VR1 and VR2, respectively.

In Fig. 7.28 - 7.32, tau lepton variables as well as global event and mass variables in VR1 are presented, where the multi-jet contribution is estimated after applying the nominal fake-factors to events in VR2. A good agreement between the data and the estimated background is observed. The events yields of the various contributions in VR2 are reported in Tab. 7.6. All contributions in the validation region VR1 are given in Tab. 7.7.

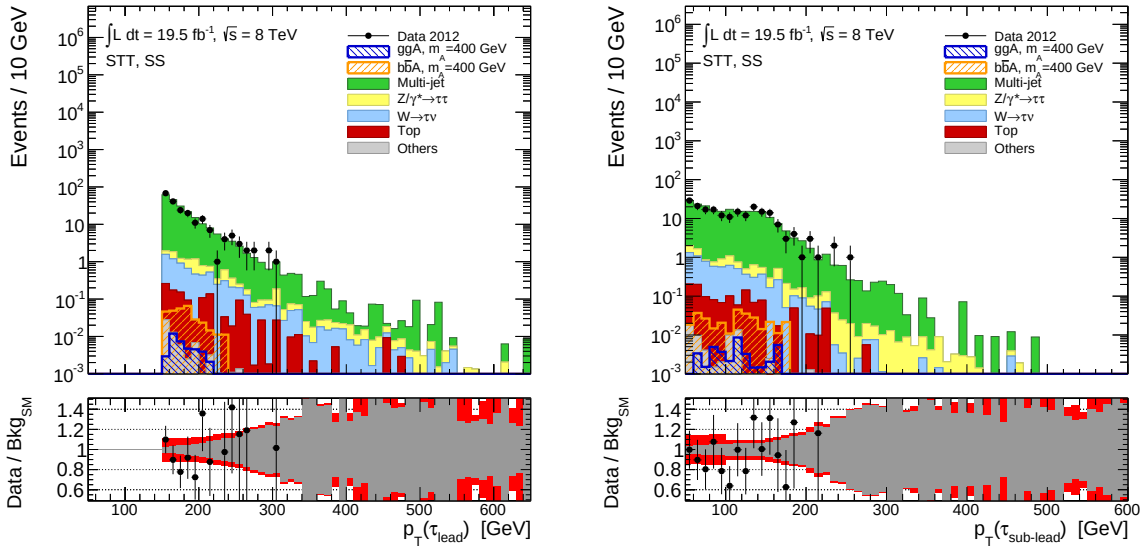

Figure 7.28: Distributions of $p_{\text{T}}(\tau)$ for the leading (left) and sub-leading (right) candidates in the STT multi-jet validation region VR1, where the two tau candidates satisfy the same-sign requirement. The lower plots illustrate the ratio between the data and the total expected background. The grey band shows the statistical uncertainty on the expected background and the red one the effect of all systematic uncertainties added quadratically. The signal contamination is estimated assuming $\tan\beta = 20$ in the m_h^{max} scenario.

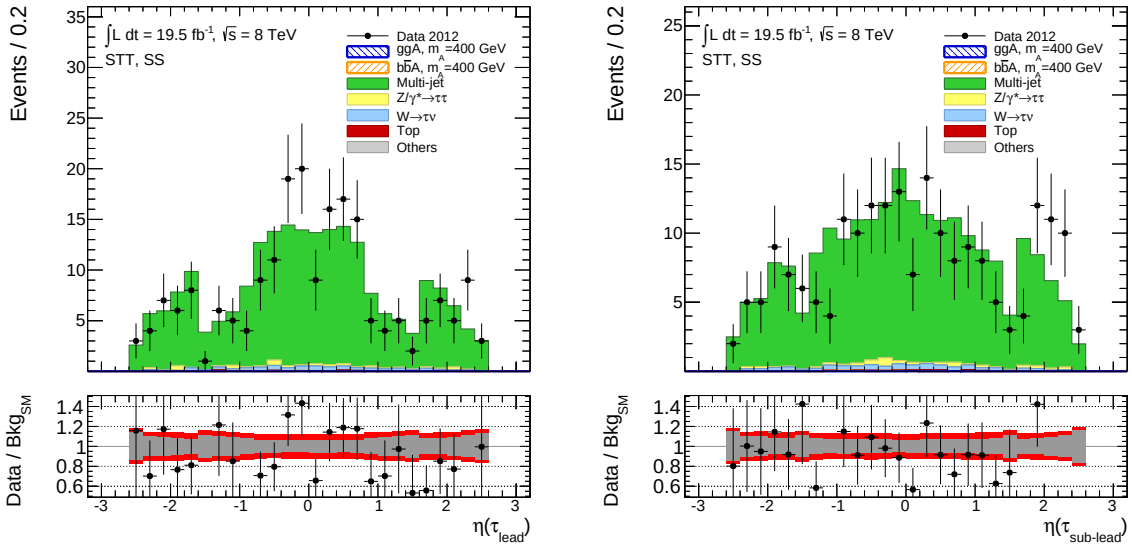

Figure 7.29: Distributions of $\eta(\tau)$ for the leading (left) and sub-leading candidates (right) in the STT multi-jet validation region VR1, where the two tau candidates satisfy the same-sign requirement. The lower plots illustrate the ratio between the data and the total expected background. The grey band shows the statistical uncertainty on the expected background and the red one the effect of all systematic uncertainties added quadratically. The signal contamination is estimated assuming $\tan\beta = 20$ in the m_h^{max} scenario.

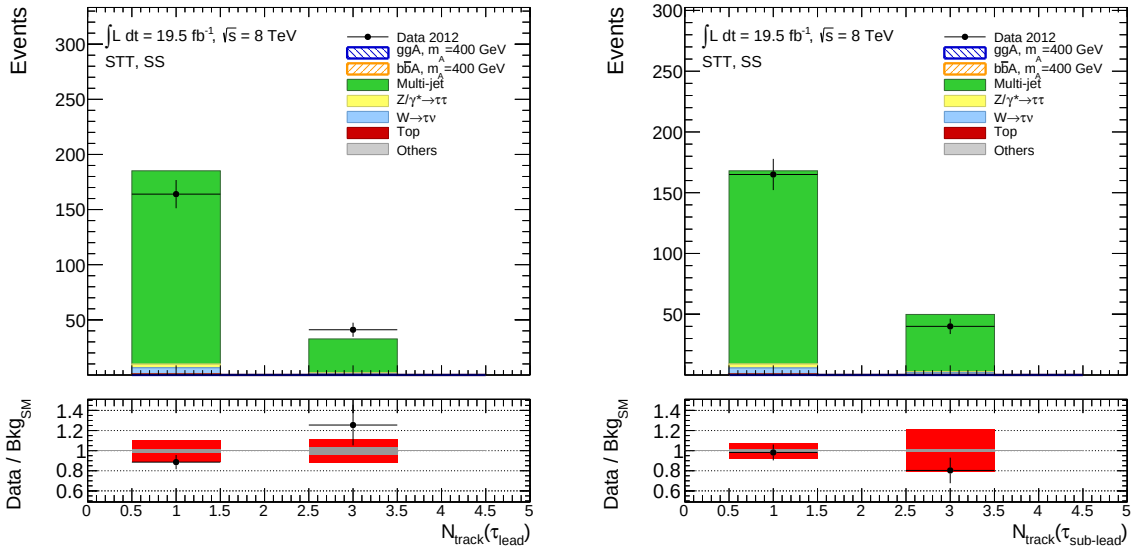

Figure 7.30: Distributions of track multiplicities for the leading (left) and sub-leading candidates (right) in the STT multi-jet validation region VR1, where the two tau candidates satisfy the same-sign requirement. The lower plots illustrate the ratio between the data and the total expected background. The grey band shows the statistical uncertainty on the expected background and the red one the effect of all systematic uncertainties added quadratically. The signal contamination is estimated assuming $\tan\beta = 20$ in the m_h^{max} scenario.

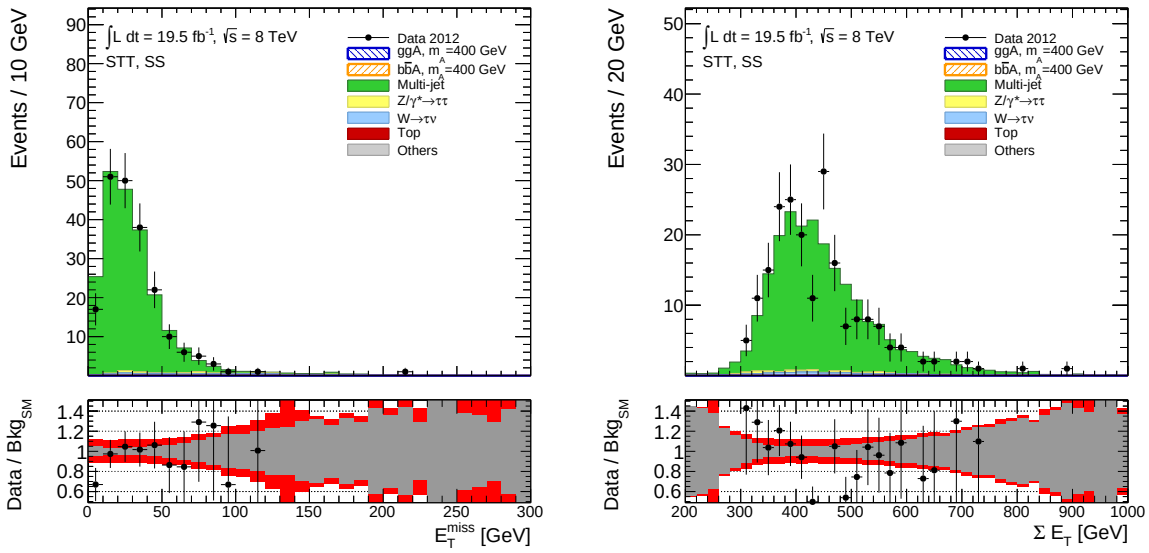

Figure 7.31: Distributions of $E_{\text{T}}^{\text{miss}}$ (left) and $\sum E_{\text{T}}$ (right) in the STT multi-jet validation region VR1, where the two tau candidates satisfy the same-sign requirement. The lower plots illustrate the ratio between the data and the total expected background. The grey band shows the statistical uncertainty on the expected background and the red one the effect of all systematic uncertainties added quadratically. The signal contamination is estimated assuming $\tan\beta = 20$ in the m_h^{max} scenario.

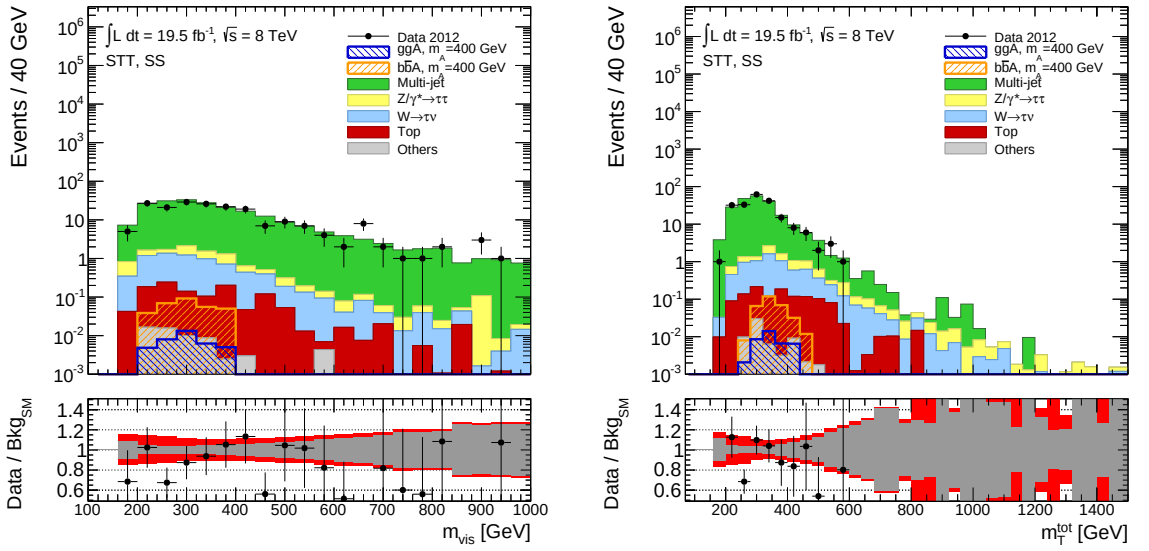

Figure 7.32: Distributions of m^{vis} (left) and $m_{\text{T}}^{\text{tot}}$ (right) in the STT multi-jet validation region VR1, where the two tau candidates satisfy the same-sign requirement. The lower plots illustrate the ratio between the data and the total expected background. The grey band shows the statistical uncertainty on the expected background and the red one the effect of all systematic uncertainties added quadratically. The signal contamination is estimated assuming $\tan\beta = 20$ in the m_h^{max} scenario.

	STT Validation Region VR1 (SS, $\tau_{\text{sub-lead}}$ passes loose ID)
Background	
Multi-jet	206.2 ± 3.3
$Z/\gamma^* \to \tau\tau$	4.21 ± 0.52
$W \to \tau\nu$	6.14 ± 0.28
Top	1.17 ± 0.15
Others	0.066 ± 0.018
Signal (m_A = 400 GeV, tanβ = 20)	
$b\bar{b} \to A$	0.305 ± 0.060
$gg \to A$	0.0380 ± 0.0078
Data	205 ± 14
Total SM	217.8 ± 3.3

Table 7.7: Events yields for all backgrounds, data and the signal contamination in the multi-jet validation region in the STT category, where the two tau candidates satisfy the same-sign requirement. The region is indicated as VR1, according to the convention used in Tab. 7.4. The statistical uncertainty is shown in the table. The signal is estimated assuming tanβ = 20 in the m_h^{max} scenario.

7.5 Multi-jet Background Estimation in the Di-tau-trigger Category

In the di-tau-trigger category, the multi-jet background is estimated with a method similar to one already discussed in Sec. 6.4.4. It is usually referred to as *ABCD method*, where each letter stands for a different region of the event selection, region A being the signal one. The multi-jet shape is modelled using data events from a control region (B) identical to the signal region, but requiring the two tau leptons to have the same electric charge. All other contributions are subtracted, which are modelled using simulated events where fake taus are weighted as described in Sec. 7.7. However, multi-jet events selected in this way might not amount to the correct event yield in the signal region. To predict the correct normalisation the other two control regions are used. In the di-tau trigger selection the requirement $E_{\text{T}}^{\text{miss}} > 10$ GeV is the most effective in suppressing multi-jets. By reversing it, a sample of multi-jet events is obtained with very little background contamination. The regions C and D are defined, which are analogous to A and B, but require $E_{\text{T}}^{\text{miss}} < 10$ GeV. The selection requirements defining the relevant regions of the ABCD method are summarised in Tab. 7.8.

Assuming that the relative proportion of multi-jet events in regions C and D are the same as in A and B, the ratio between the number of data events in C and D is computed, which is called $R_{\text{OS/SS}}$, after subtracting all other contributions. We can write

$$R_{\text{OS/SS}} = \frac{N^C_{\text{data}} - N^C_{\text{sim.}}}{N^D_{\text{data}} - N^D_{\text{sim.}}} \tag{7.4}$$

Where $N_{\text{sim.}}$ is the number of expected events for the sum of all backgrounds, excluding multi-jets, which are estimated using the simulation. $R_{\text{OS/SS}}$ is used to rescale the multi-jet description from region B. This method relies on the assumption that $R_{\text{OS/SS}}$ does not depend on $E_{\text{T}}^{\text{miss}}$, i.e. that $R_{\text{OS/SS}}$ measured in the low-$E_{\text{T}}^{\text{miss}}$ control regions can be used to model multi-jet events in the high-$E_{\text{T}}^{\text{miss}}$ regions. A

systematic uncertainty will be later introduced associated with this assumption. To summarise, the multi-jet background is estimated as

$$N_{\text{multi-jet}}(x) = R_{\text{OS/SS}} \left(N^{B}_{\text{data}}(x) - N^{B}_{\text{sim.}}(x) \right) \tag{7.5}$$

where x is the discriminating variable used to perform the fit for the hypothesis test in the $h/H/A \to \tau_{\text{had}}\tau_{\text{had}}$ channel. This is chosen to be the *total transverse mass* of the di-tau system defined as

$$m_{\text{T}}^{\text{tot}} = \sqrt{2p_{\text{T}}(\tau_{\text{lead}})|E_{\text{T}}^{\text{miss}}|F_1 + 2p_{\text{T}}(\tau_{\text{sub-lead}})|E_{\text{T}}^{\text{miss}}|F_2 + 2p_{\text{T}}(\tau_{\text{lead}})p_{\text{T}}(\tau_{\text{sub-lead}})F_3} \tag{7.6}$$

where

$$F_1 = 1 - \cos\Delta\phi(\tau_{\text{lead}}, E_{\text{T}}^{\text{miss}}), \tag{7.7a}$$

$$F_2 = 1 - \cos\Delta\phi(\tau_{\text{sub-lead}}, E_{\text{T}}^{\text{miss}}), \tag{7.7b}$$

$$F_3 = 1 - \cos\Delta\phi(\tau_{\text{lead}}, \tau_{\text{sub-lead}}). \tag{7.7c}$$

The $m_{\text{T}}^{\text{tot}}$ variable corresponds to the mass of a particle determined using the topology and kinematic of its decay products determined in the transverse plane. In this case, the leading and sub-leading tau leptons are taken into account, as well as $E_{\text{T}}^{\text{miss}}$ to account for the neutrinos in the tau decays.

Systematic uncertainties for the ABCD method are evaluated by comparing the nominal value of $R_{\text{OS/SS}}$ with one determined using two additional control regions, alternative to C and D, called E and F, where the tau identification reversal is used instead of $E_{\text{T}}^{\text{miss}} < 10$ GeV. The selection requirements defining the control regions E and F are summarised in Tab. 7.8. The uncertainty on $R_{\text{OS/SS}}$ is the largest affecting the multi-jet estimate in the DTT category. However, the estimate is also affected by all other systematic uncertainties evaluated for the simulated backgrounds subtracted from the control regions. This will be discussed in detail in Sec. 7.5.1.

In Fig. 7.33, the $m_{\text{T}}^{\text{tot}}$ distributions for all the regions considered for the ABCD method are shown, including the signal one as well as E and F. The events yield for all backgrounds and data in all the control regions is reported in Tab. 7.9.

7.5.1 Uncertainty on DTT Multi-jet Estimation

The multi-jet estimation method utilised in the DTT category and illustrated in Sec. 7.5 relies on the assumption that the transfer factor, $R_{\text{OS/SS}}$, measured to determine the normalisation of multi-jets in the signal region, does not depend on $E_{\text{T}}^{\text{miss}}$. This is important because the signal region is defined by $E_{\text{T}}^{\text{miss}} > 10$ GeV, while $R_{\text{OS/SS}}$ is measured using control regions with $E_{\text{T}}^{\text{miss}} < 10$ GeV. To verify this assumption, the transfer factor is measured using two alternative control regions, where the nominal $E_{\text{T}}^{\text{miss}}$ requirement of the signal region is used, but both tau candidates are required to fail loose identification. The event yield and background composition of the alternative control regions is illustrated in Tab. 7.9, where the fail-ID opposite-sign and same-sign regions are called E and F, respectively. A difference of $\approx 5.4\%$ is found in the measured $R_{\text{OS/SS}}$ value, which is taken into account as an uncertainty on the multi-jet event yield.

In addition to the effect on the multi-jet normalisation, another source of uncertainty is considered which affects the $m_{\text{T}}^{\text{tot}}$ shape of this background. In principle, the $m_{\text{T}}^{\text{tot}}$ shape in the signal region could be different with respect to the shape in the control region where it is estimated. To get a handle on this difference, $R_{\text{OS/SS}}$ is measured as a function of $m_{\text{T}}^{\text{tot}}$ using the two methods where the control regions are defined with the high-$E_{\text{T}}^{\text{miss}}$ and fail-ID criteria. The transfer factor as a function of $m_{\text{T}}^{\text{tot}}$, as determined

DTT Selection Requirements	DTT signal region	CR B	CR C	CR D	CR E / VR A'	CR F / VR B'	VR C'	VR D'
Di-tau trigger ($p_{\mathrm{T}}(\tau_{\mathrm{lead/sub-lead}}) > 38$ GeV + medium trigger-level tau-ID)	•	•	•	•	•	•	•	•
$p_{\mathrm{T}}(\tau_{\mathrm{lead.}}) < 150$ GeV	•	•	•	•	•	•	•	•
Leading and sub-leading tau candidates with opposite electric charge	•	rev.	•	rev.	•	rev.	•	rev.
Medium tau-ID on leading tau	•	•	•	•	fail loose	fail loose	fail loose	fail loose
Medium tau-ID on sub-leading tau	•	•	•	•	fail loose	fail loose	fail loose	fail loose
$E_{\mathrm{T}}^{\mathrm{miss}} > 10$ GeV	•	•	rev.	rev.	•	•	rev.	rev.
$\sum E_{\mathrm{T}} > 160$ GeV	•	•	•	•	•	•	•	•

Table 7.8: Summary of the selection requirements defining the relevant regions of the DTT category. In the table, the dot indicates the application of the requirement indicated in the list on the left. When a requirement is reversed it is explicitly indicated in the table by "rev.". The control regions CR B, C, and D are used for the nominal estimation of the multi-jet background, while CR E and F for the estimation of the its systematic uncertainty. The validation regions VR A', B', C' and D' are also defined, which are used to validate the multi-jet estimation. The definition of CR E and F, and VR A' and B' is the same, as indicated in the table.

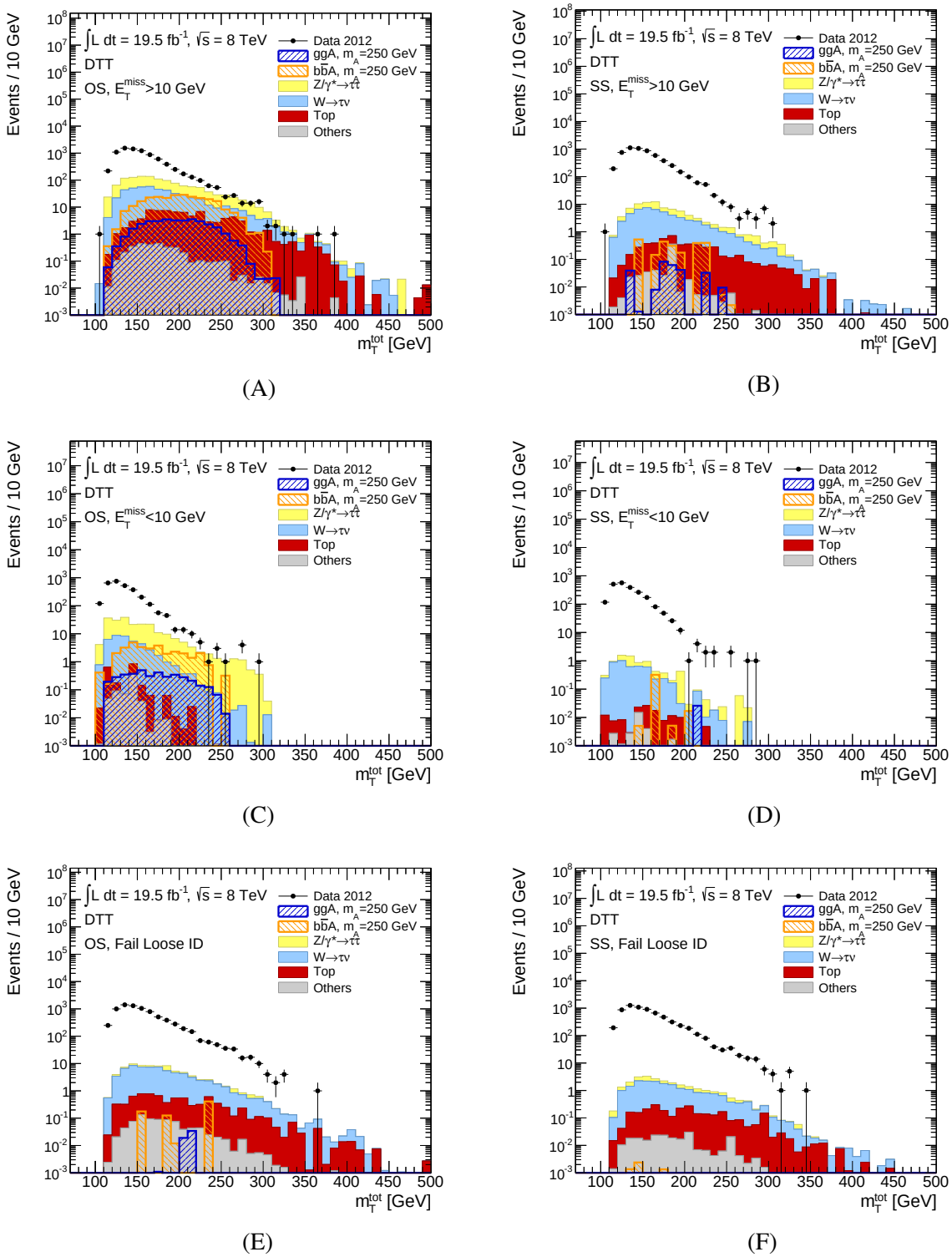

Figure 7.33: Distributions of m_T^{tot} in the DTT signal region and in the control regions used in the ABCD method. The OS and SS symbols refer to the opposite-sign and same-sign requirement on the electric charges of the tau candidates, respectively. The letters below the plots indicate the name of the region as defined in the ABCD method. Here, two additional regions are reported, E and F, which are relevant for the estimation of the systematic uncertainty on $R_{OS/SS}$, which are defined requiring the two tau leptons to fail the loose identification requirement. The multi-jet background is not estimated in these plots. The signal is estimated using cross-sections for $\tan\beta = 20$ in the m_h^{max} scenario.

	DTT Control Regions				
	B	C	D	E	F
Background					
$Z/\gamma^* \to \tau\tau$	30.2 ± 3.2	180 ± 14	3.05 ± 0.49	11.4 ± 1.8	6.18 ± 0.61
$W \to \tau\nu$	48.0 ± 1.4	39.0 ± 2.7	4.67 ± 0.57	62.5 ± 1.9	16.97 ± 0.69
Top	4.38 ± 0.21	1.21 ± 0.69	0.104 ± 0.031	6.84 ± 0.44	2.55 ± 0.19
Others	0.57 ± 0.33	0.629 ± 0.328	0.028 ± 0.012	0.855 ± 0.053	0.234 ± 0.023
Signal (m_A = 250 GeV, tanβ = 20)					
$b\bar{b} \to A$	2.40 ± 0.71	31.56 ± 2.48	0.34 ± 0.32	0.72 ± 0.36	0.0061 ± 0.0031
$gg \to A$	0.279 ± 0.084	3.898 ± 0.331	0.026 ± 0.025	0.055 ± 0.038	0.00070 ± 0.00031
Data	5627 ± 75	2889 ± 54	2194 ± 47	7603 ± 87	6545 ± 81

Table 7.9: Events yield for the backgrounds and data in the control regions used to estimate the multi-jet contribution in the ABCD method. The nominal control regions are indicated as B, C and D, while E and F are used to estimate the systematic uncertainty on $R_{\mathrm{OS/SS}}$. The control regions are named according to the same convention used in Tab. 7.8. The statistical uncertainty on the number of events is also indicated in the table. The estimate of the multi-jet contribution is not shown in the table. The signal contamination is estimated assuming the m_h^{max} scenario.

by the two methods, is illustrated in Fig. 7.34. The two trends shown in Fig. 7.34 are fitted with a linear

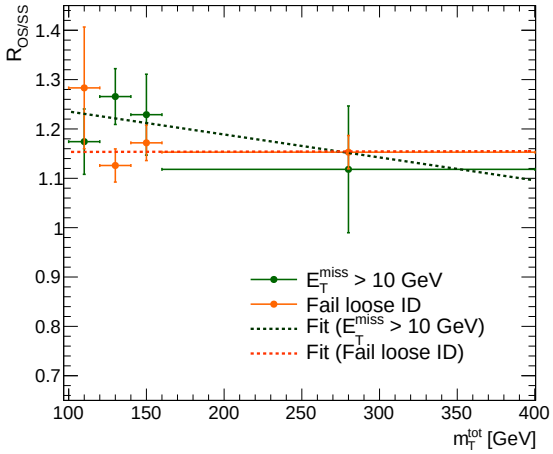

Figure 7.34: Multi-jet transfer factor $R_{\mathrm{OS/SS}}$, used for multi-jet estimation in the DTT category, measured as a function of $m_{\mathrm{T}}^{\mathrm{tot}}$. Different estimation methods are compared, based on different definitions of the regions used. They rely on either the $E_{\mathrm{T}}^{\mathrm{miss}} < 10$ GeV or the fail-loose-ID criterion. The linear fits used to address the multi-jet shape systematic uncertainty are also shown.

function where only the slope parameter is allowed to vary. The slope can be written as

$$C = \frac{R_{\mathrm{OS/SS}}(m_{\mathrm{T}}^{\mathrm{tot}}) - \langle R_{\mathrm{OS/SS}} \rangle}{m_{\mathrm{T}}^{\mathrm{tot}} - \langle m_{\mathrm{T}}^{\mathrm{tot}} \rangle} \tag{7.8}$$

where $\langle R_{\mathrm{OS/SS}} \rangle$ is the standard estimate of $R_{\mathrm{OS/SS}}$ as measured in the ABCD method, and $\langle m_{\mathrm{T}}^{\mathrm{tot}} \rangle$ is the mean of the $m_{\mathrm{T}}^{\mathrm{tot}}$ distribution in the control regions C and D, or alternatively E and F. Both $\langle R_{\mathrm{OS/SS}} \rangle$ and

	$\langle R_{\text{OS/SS}} \rangle$	$\langle m_{\text{T}}^{\text{tot}} \rangle_{\text{OS}}$	$\langle m_{\text{T}}^{\text{tot}} \rangle_{\text{SS}}$	C_{fit}
$E_{\text{T}}^{\text{miss}} < 10$ GeV	1.220 ± 0.035	132.22 ± 0.39	132.45 ± 0.41	$(-4.6 \pm 8.2) \times 10^{-4}$
Fail loose ID	1.154 ± 0.019	155.62 ± 0.35	155.54 ± 0.37	$(0.0 \pm 2.6) \times 10^{-4}$

Table 7.10: Fit parameters and fit results for the estimation of the multi-jet systematic shape uncertainty in the DTT category. The statistical uncertainties are also indicated for each value.

$\langle m_{\text{T}}^{\text{tot}} \rangle$ are fixed in the fit. Their values are reported in Tab. 7.10 along with the value of C as determined by the fit.

A systematic uncertainty on the shape is finally assessed by computing the maximum difference between the nominal $R_{\text{OS/SS}}$ measurement and the two estimates determined by the linear fit as a function of $m_{\text{T}}^{\text{tot}}$. This difference is regarded to be one signed standard deviation of the uncertainty assigned to the multi-jet shape.

7.5.2 Validation of Multi-jet estimation in the Di-tau-trigger Category

The multi-jet model has to be validated by checking the agreement between data and the expected background in control regions with negligible signal contamination. This is done by using another version of the ABCD method, where all regions are defined as in Sec. 7.5, but the two tau leptons are required to fail identification. In order to decrease the signal contamination as much as possible, the two candidates are required to fail the loose working point instead of the medium one used in the di-tau trigger selection. The summary of the requirements defining the control regions used for multi-jet validation in the DTT category is given in Tab. 7.8.

In Fig. 7.35, 7.36 and 7.37 the distributions of transverse momenta, pseudo-rapidity and track multiplicity of the two tau leptons are shown, while in Fig. 7.38 the $E_{\text{T}}^{\text{miss}}$ and ΣE_{T} variables are shown. The $m_{\text{T}}^{\text{tot}}$ variable along with the di-tau visible mass are shown in Fig. 7.39. Good agreement between the data and the expectation is observed, indicating a reliable multi-jet model. The events yields for all backgrounds and the signal contamination are reported in Tab. 7.11 for the validation regions used in the alternative ABCD method.

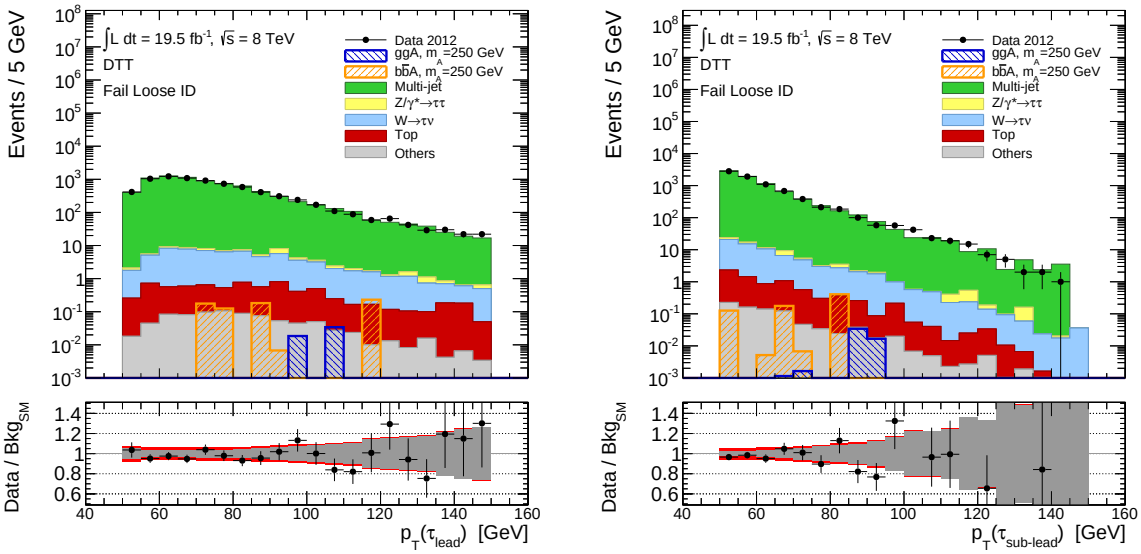

Figure 7.35: Distributions of $p_{\mathrm{T}}(\tau)$ for the leading (left) and sub-leading tau candidates (right) in the DTT multi-jet validation region, defined inverting the loose identification requirement on both tau candidates. The lower plots illustrate the ratio between the data and the total expected background. The grey band shows the statistical uncertainty on the expected background and the red one the effect of all systematic uncertainties added quadratically. The signal contamination is estimated assuming $\tan\beta = 20$ in the m_h^{max} scenario.

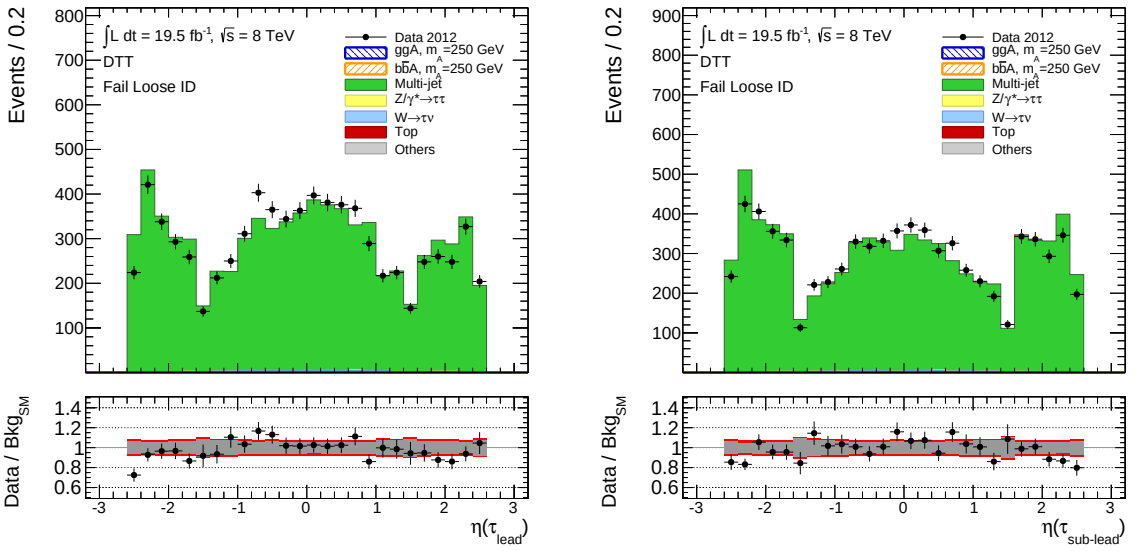

Figure 7.36: Distributions of $\eta(\tau)$ for the leading (left) and sub-leading tau candidates (right) in the DTT multi-jet validation region, defined inverting the loose identification requirement on both tau candidates. The lower plots illustrate the ratio between the data and the total expected background. The grey band shows the statistical uncertainty on the expected background and the red one the effect of all systematic uncertainties added quadratically. The signal contamination is estimated assuming $\tan\beta = 20$ in the m_h^{max} scenario.

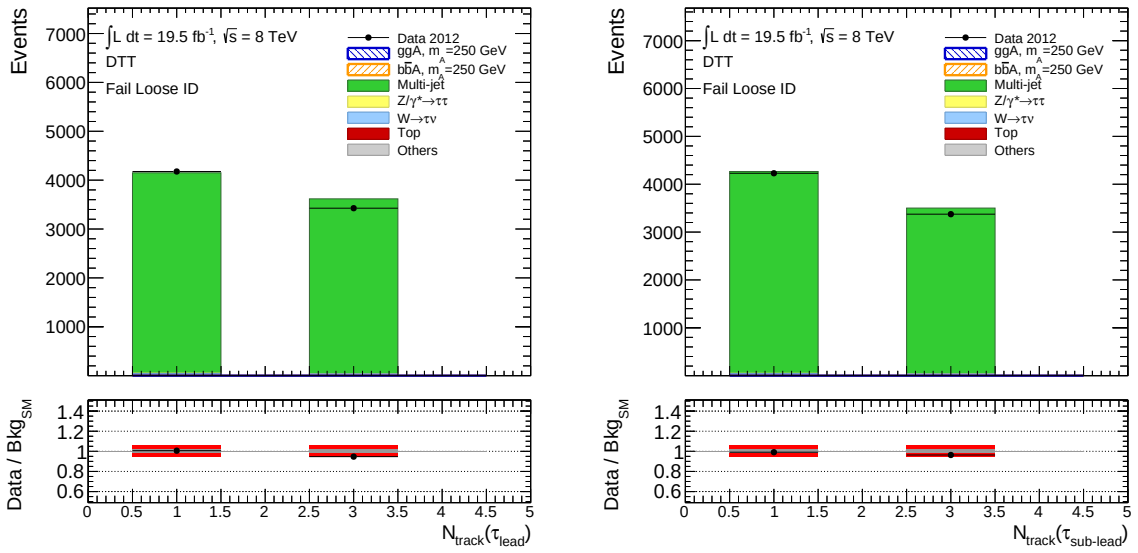

Figure 7.37: Distributions of track multiplicities for the leading (left) and sub-leading tau candidates (right) in the DTT multi-jet validation region, defined inverting the loose identification requirement on both tau candidates. The lower plots illustrate the ratio between the data and the total expected background. The grey band shows the statistical uncertainty on the expected background and the red one the effect of all systematic uncertainties added quadratically. The signal contamination is estimated assuming $\tan\beta = 20$ in the m_h^{max} scenario.

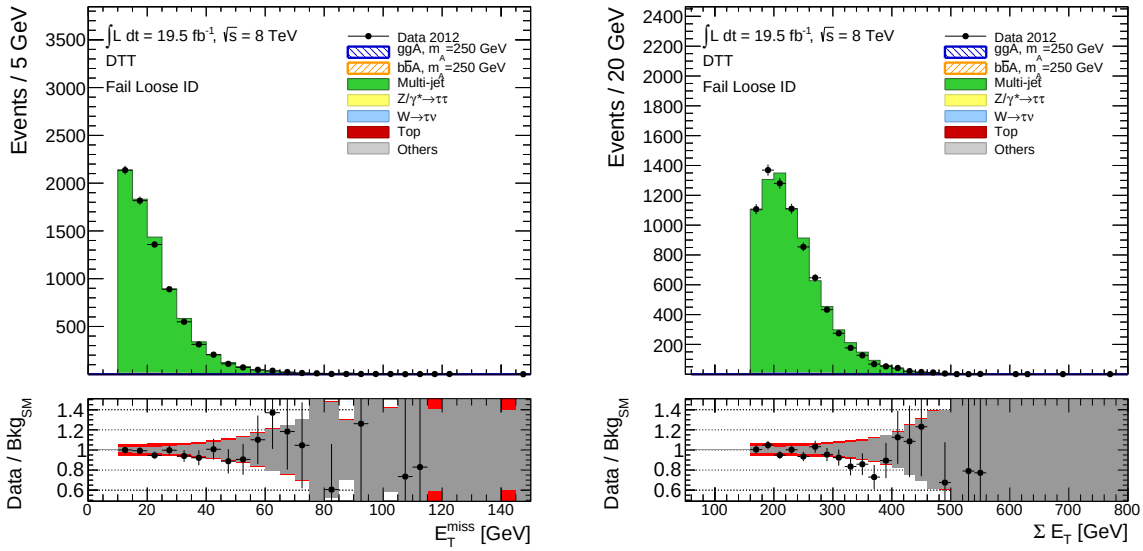

Figure 7.38: Distributions of $E_{\text{T}}^{\text{miss}}$ (left) and $\sum E_{\text{T}}$ (right) in the DTT multi-jet validation region, defined inverting the loose identification requirement on both tau candidates. The lower plots illustrate the ratio between the data and the total expected background. The grey band shows the statistical uncertainty on the expected background and the red one the effect of all systematic uncertainties added quadratically. The signal contamination is estimated assuming $\tan\beta = 20$ in the m_h^{max} scenario.

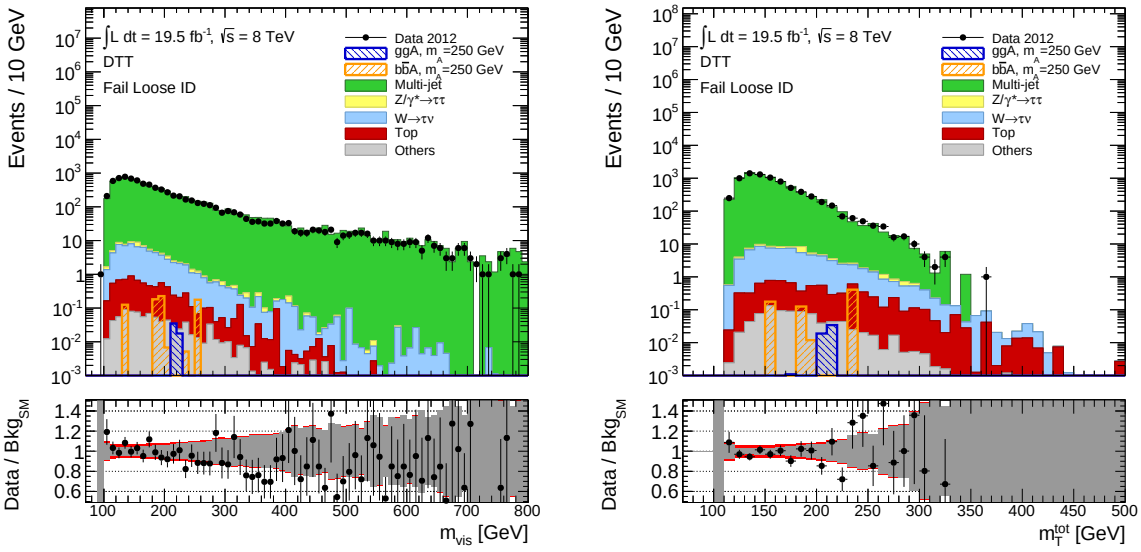

Figure 7.39: Distributions of m^{vis} (left) and $m_{\text{T}}^{\text{tot}}$ (right) in the DTT multi-jet validation region, defined inverting the loose identification requirement on both tau candidates. The lower plots illustrate the ratio between the data and the total expected background. The grey band shows the statistical uncertainty on the expected background and the red one the effect of all systematic uncertainties added quadratically. The signal contamination is estimated assuming $\tan\beta = 20$ in the m_h^{max} scenario.

	DTT Validation Regions			
	A'	B'	C'	D'
Background				
Multi-jet	7681 ± 95	-	-	-
$Z/\gamma^* \to \tau\tau$	11.4 ± 1.8	6.18 ± 0.61	1.01 ± 0.22	0.64 ± 0.16
$W \to \tau\nu$	62.5 ± 1.9	16.97 ± 0.69	6.69 ± 0.81	1.19 ± 0.14
Top	6.84 ± 0.44	2.55 ± 0.19	0.229 ± 0.034	0.102 ± 0.018
Others	0.855 ± 0.053	0.234 ± 0.023	0.058 ± 0.011	0.0153 ± 0.0037
Signal ($m_A = 250$ GeV, $\tan\beta = 20$)				
$b\bar{b} \to A$	0.72 ± 0.36	0.0061 ± 0.0031	0.0 ± 0.0	0.0 ± 0.0
$gg \to A$	0.055 ± 0.038	0.00070 ± 0.00031	0.0 ± 0.0	0.0 ± 0.0
Data	7603 ± 87	6545 ± 81	2919 ± 54	2471 ± 50
Total SM	7767 ± 95	-	-	-

Table 7.11: Events yields for the backgrounds and data in the control regions used to validate the multi-jet background in the DTT category. The control regions are defined analogously to the nominal ABCD definition, but requiring the two tau leptons to fail the loose identification requirement. The name of the regions A', B', C' and D' is defined in analogy to those in the nominal ABCD method, and follows the same naming convention used in Tab. 7.8, where they are defined. The statistical uncertainty on the number of events is also indicated in the table. The signal contamination is estimated assuming the m_h^{max} scenario.

7.6 $Z/\gamma^* \to \tau\tau$ Validation

The $Z/\gamma^* \to \tau\tau$ contribution is the second most important background in this analysis. Its final state is identical to the signal and it is very difficult to suppress or to define a signal-free control region for a data-driven estimation. For this reason, it is estimated using simulated events. However, it is desirable to check the reliability of this estimation. A control region is defined with low signal and multi-jet contamination, for events selected by the di-tau trigger and with $p_{\text{T}}(\tau_{\text{lead/sub-lead}}) > 50$ GeV, where the decaying resonance is produced with significant transverse momentum. No back-to-back requirement is applied, instead the two candidates have to satisfy $\cos\Delta\phi(\tau_{\text{lead}}, \tau_{\text{sub-lead}}) > 0.2$ and must have opposite electric charge. Also, the $E_{\text{T}}^{\text{miss}}$, which is mainly due to the neutrinos, should point in the same direction of the sum of the momenta of the two taus, therefore, events are selected with $\cos\Delta\phi(E_{\text{T}}^{\text{miss}}, \tau_{\text{sub-lead}}) > 0$. The two tau leptons must have $\Delta R(\tau_{\text{lead}}, \tau_{\text{sub-lead}}) < 1.5$. Finally, $E_{\text{T}}^{\text{miss}} > 10$ GeV is required. The summary of all the requirements defining the control region for $Z/\gamma^* \to \tau\tau$ validation is given in Tab. 7.12

In this control region, the multi-jet contamination is estimated using a method similar to the one described in Sec. 7.5, where the multi-jet shape is taken from a same-sign control region, but the transfer factor is the same determined in Sec. 7.5. In Fig. 7.40, 7.41 and 7.42, distributions of the two tau leptons are shown, while in Fig. 7.43, and 7.44 global variables of the event are shown. As can be seen by these distributions, this control region is not suitable for background estimation given the low number of events and the different kinematics with respect to the signal region. Nevertheless the comparison between data and the estimated background indicates a reliable estimate. The event yield for all contributions in the $Z/\gamma^* \to \tau\tau$ validation region is reported in Tab. 7.13.

Selection Requirements of the $Z/\gamma^* \to \tau\tau$ Validation Region
Di-tau trigger ($p_{\text{T}}(\tau_{\text{lead./sub-lead.}}) > 38$ GeV + medium trigger-level tau-ID)
$p_{\text{T}}(\tau_{\text{lead/sub-lead}}) > 50$ GeV
Leading and sub-leading tau candidates with opposite electric charge
$\cos\Delta\phi(\tau_{\text{lead}}, \tau_{\text{sub-lead}}) > 0.2$
$\cos\Delta\phi(E_{\text{T}}^{\text{miss}}, \tau_{\text{sub-lead}}) > 0$
$\Delta R(\tau_{\text{lead}}, \tau_{\text{sub-lead}}) < 1.5$
$E_{\text{T}}^{\text{miss}} > 10$ GeV

Table 7.12: Summary of the requirements defining the control region used for the validation of the $Z/\gamma^* \to \tau\tau$ background.

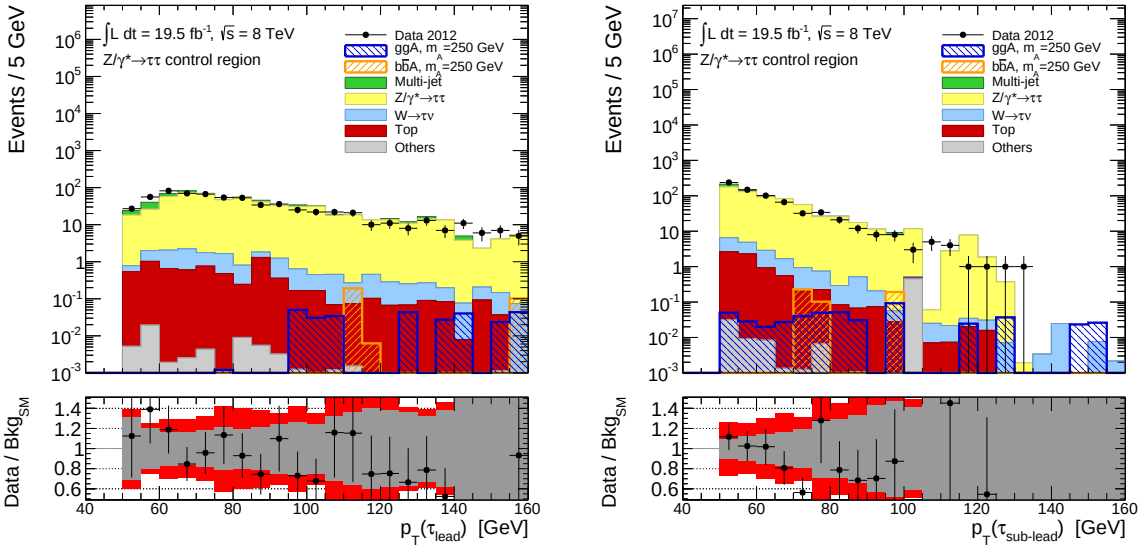

Figure 7.40: Distributions of $p_{\mathrm{T}}(\tau)$ for the leading (left) and sub-leading tau candidates (right) in the $Z/\gamma^* \to \tau\tau$ validation region. The lower plots illustrate the ratio between the data and the total expected background. The grey band shows the statistical uncertainty on the expected background and the red one the effect of all systematic uncertainties added quadratically. The signal contamination is estimated assuming $\tan\beta = 20$ in the m_h^{max} scenario.

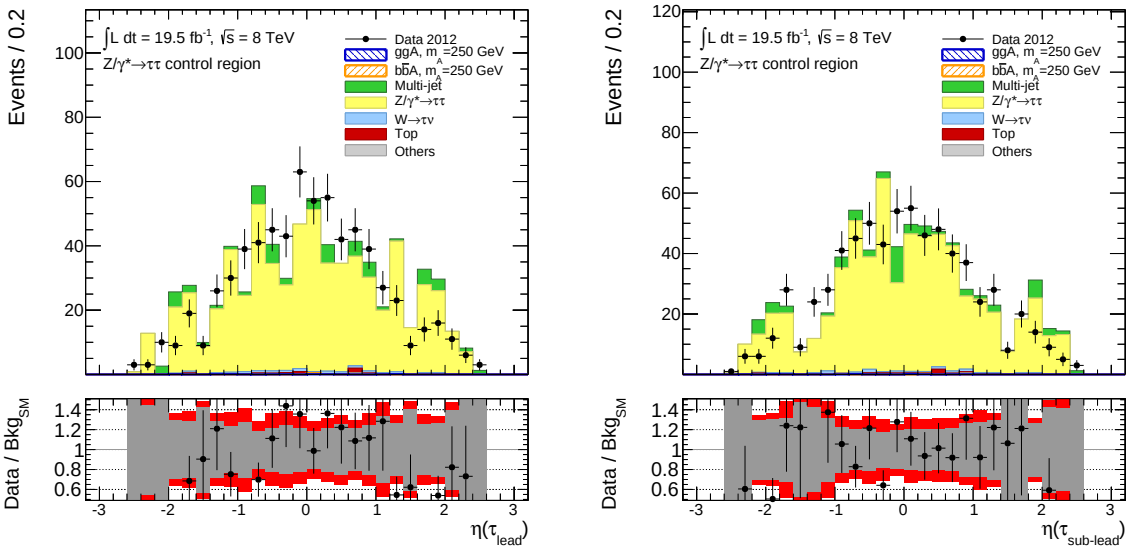

Figure 7.41: Distributions of $\eta(\tau)$ for the leading (left) and sub-leading tau candidates (right) in the $Z/\gamma^* \to \tau\tau$ validation region. The lower plots illustrate the ratio between the data and the total expected background. The grey band shows the statistical uncertainty on the expected background and the red one the effect of all systematic uncertainties added quadratically. The signal contamination is estimated assuming $\tan\beta = 20$ in the m_h^{max} scenario.

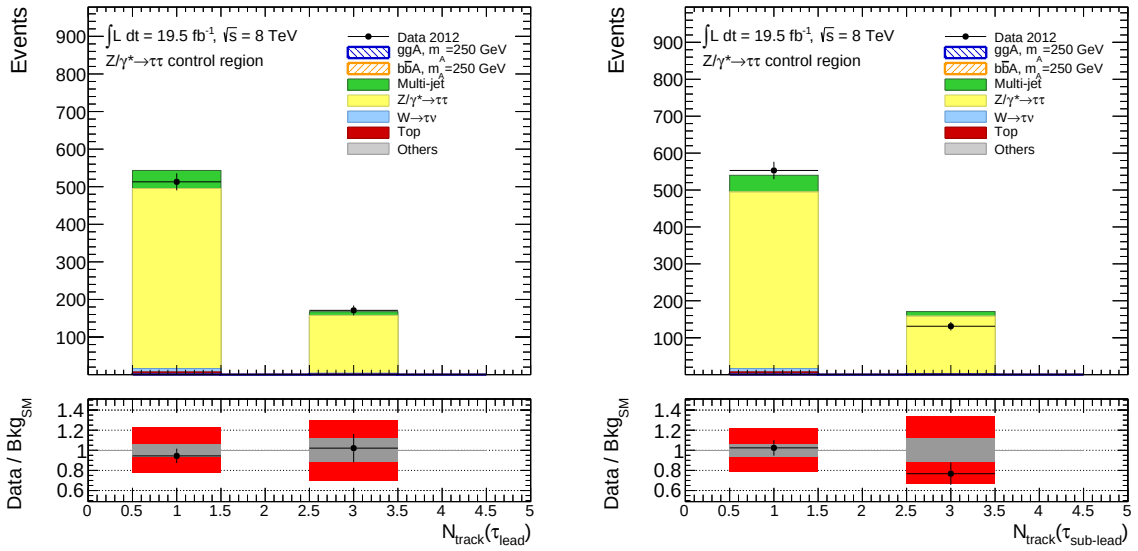

Figure 7.42: Distributions of track multiplicities for the leading (left) and sub-leading tau candidates (right) in the $Z/\gamma^* \to \tau\tau$ validation region. The lower plots illustrate the ratio between the data and the total expected background. The grey band shows the statistical uncertainty on the expected background and the red one the effect of all systematic uncertainties added quadratically. The signal contamination is estimated assuming $\tan\beta = 20$ in the m_h^{max} scenario.

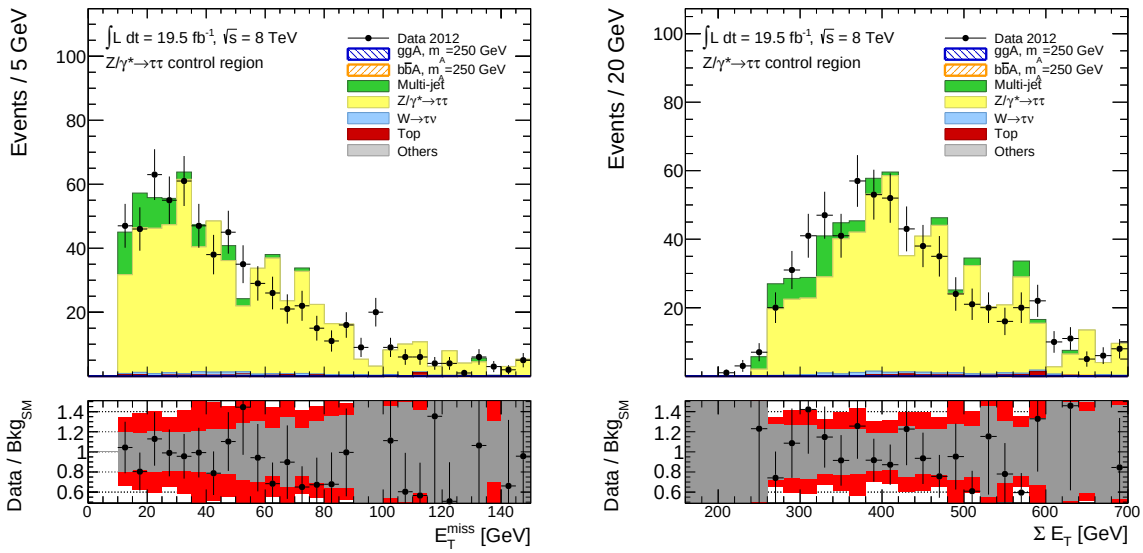

Figure 7.43: Distributions of $E_{\text{T}}^{\text{miss}}$ (left) and $\sum E_{\text{T}}$ (right) in the $Z/\gamma^* \to \tau\tau$ validation region. The lower plots illustrate the ratio between the data and the total expected background. The grey band shows the statistical uncertainty on the expected background and the red one the effect of all systematic uncertainties added quadratically. The signal contamination is estimated assuming $\tan\beta = 20$ in the m_h^{max} scenario.

	$Z/\gamma^* \to \tau\tau$ Validation Region Selection			
	$\cos\Delta\phi(\tau_{\text{lead}}, \tau_{\text{sub-lead}}) > 0.2$	$E_{\text{T}}^{\text{miss}} > 10$ GeV	$\cos\Delta\phi(E_{\text{T}}^{\text{miss}}, \tau_{\text{sub-lead}}) > 0$	$\Delta R(\tau_{\text{lead}}, \tau_{\text{sub-lead}}) < 1.5$
Background				
Multi-jet	-	-	-	57.9 ± 9.8
$Z/\gamma^* \to \tau\tau$	904 ± 44	852 ± 43	717 ± 39	633 ± 37
$W \to \tau\nu$	42.4 ± 1.9	40.9 ± 1.9	21.1 ± 1.1	11.79 ± 0.72
Top	26.7 ± 2.2	26.1 ± 2.2	14.0 ± 1.8	7.1 ± 1.2
Others	1.85 ± 0.64	1.84 ± 0.64	0.82 ± 0.53	0.51 ± 0.45
Signal ($m_A = 250$ GeV, $\tan\beta = 20$)				
$b\bar{b} \to A$	1.68 ± 0.57	1.68 ± 0.57	1.66 ± 0.57	0.53 ± 0.31
$gg \to A$	1.54 ± 0.21	1.51 ± 0.21	1.31 ± 0.19	0.57 ± 0.13
Data	1427 ± 37	1300 ± 36	855 ± 29	684 ± 26
Total SM	-	-	-	710 ± 39

Table 7.13: Events yields for the backgrounds and data in the control region used to validate the $Z/\gamma^* \to \tau\tau$ contribution at each step of the selection. The statistical uncertainty on the number of events is also indicated. The signal contamination is estimated assuming the m_h^{max} scenario.

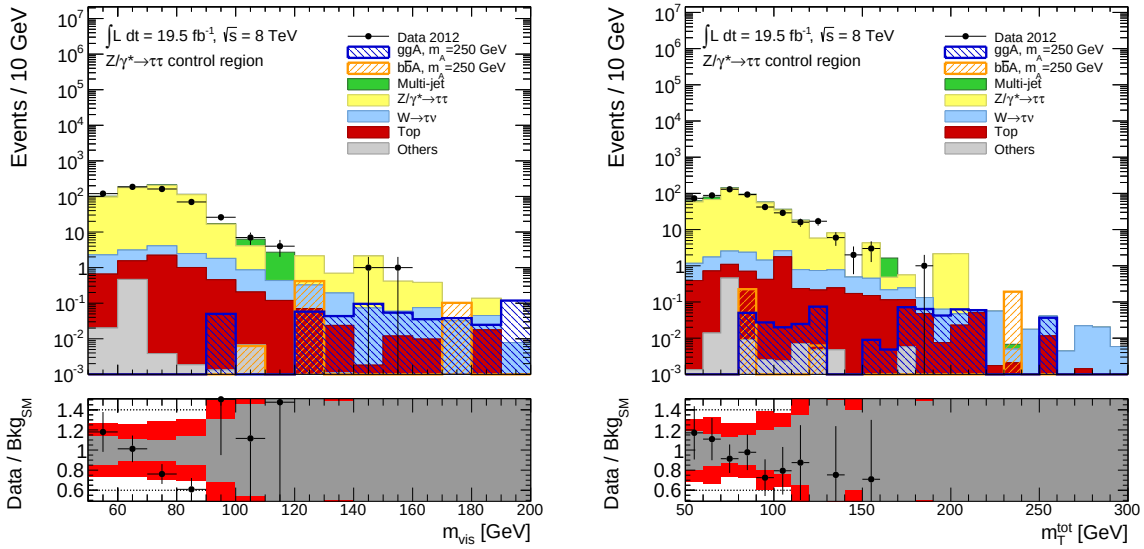

Figure 7.44: Distributions of m^{vis} (left) and $m_{\text{T}}^{\text{tot}}$ (right) in the $Z/\gamma^* \to \tau\tau$ validation region. The lower plots illustrate the ratio between the data and the total expected background. The grey band shows the statistical uncertainty on the expected background and the red one the effect of all systematic uncertainties added quadratically. The signal contamination is estimated assuming $\tan\beta = 20$ in the m_h^{max} scenario.

7.7 Weighting of Simulated Fake Tau Candidates

With the exception of the multi-jet contribution, all backgrounds in this search are estimated using simulation. However, the jet-to-tau mis-identification probability might be mis-modelled in the simulation, as previously discussed in this thesis. Thus, backgrounds with one or more jets in the final state might be significantly mis-modelled, for instance W + jets, as illustrated in Fig. 7.45. For this reason, a method relying on data has been used in this analysis for the estimation of these backgrounds.

The method is based on a weighting technique for fake taus. If a tau candidate in simulation is not matched to a true tau, no identification is applied. Instead, a weight is assigned to the event corresponding to the mis-identification probability of the object. This quantity is measured in data using a selection of $W \to \mu\nu$+jets events, by counting data events before and after identification. The choice of $W \to \mu\nu$+jets events is justified by the fact that its fake tau composition is very similar to $W \to \tau\nu$+jets events, which is the major source of fake taus after the multi-jet background in this search. Mis-identification probabilities are measured as a function of the p_{T} and track multiplicity of the tau candidate, as well as distinguishing between the two cases where a fake tau candidate has been triggered or not. The latter distinction is important as identification is also performed at the trigger level. Finally, mis-identification probabilities are also measured depending on the sign of the charge-product of the candidates, which is useful for background estimation in same-sign control regions already described.

7.7.1 $W \to \mu\nu$ + jets Control Region

To measure the mis-identification probabilities, the number of fake taus from $W \to \mu\nu$ + jets events is measured in data before and after tau identification in a $W \to \mu\nu$+jets control region. In this control region, events are selected by either of the two muon triggers named `EF_mu24i_tight` and `EF_mu36_tight`,

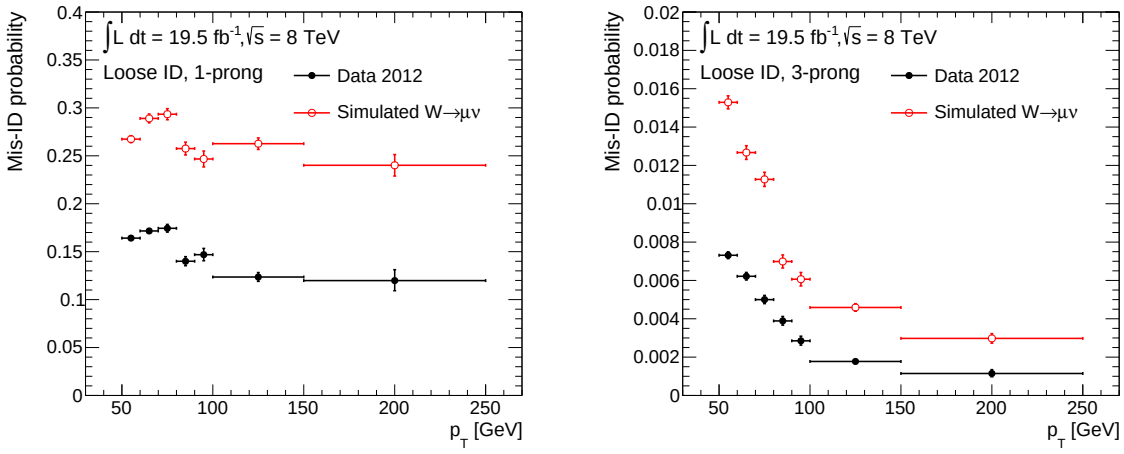

Figure 7.45: Mis-identification probability for 1-prong (left) and 3-prong (right) fake tau candidates as measured in data and in simulated $W \to \mu\nu$ + jets events, applying the loose identification requirement.

Selection Requirements of the $W \to \mu\nu$ + jets Control Region
Muon triggers ($p_{\mathrm{T}}(\mu) > 24$ GeV + isolation and tight identification or $p_{\mathrm{T}}(\mu) > 36$ GeV + tight identification)
Pre-selected muon with $p_{\mathrm{T}}(\mu) > 26$ GeV
Muon isolation (E_{T} in $0.05 < \Delta R < 0.2$ from muon direction less than 6% of $p_{\mathrm{T}}(\mu)$)
Veto on events with ≥ 1 reconstructed electron
Veto on events with > 1 reconstructed muon
$p_{\mathrm{T}}(\mu) > 40$ GeV
One tau candidate with $p_{\mathrm{T}}(\tau) > 50$ GeV
$\cos\Delta\phi(\mu, E_{\mathrm{T}}^{\mathrm{miss}}) + \cos\Delta\phi(\tau, E_{\mathrm{T}}^{\mathrm{miss}}) < -0.15$

Table 7.14: Summary of the selection requirements defining the $W \to \mu\nu$+jets control region for the measurements of the tau mis-identification efficiency.

selecting muons with transverse momenta $p_{\mathrm{T}}(\mu) > 24$ GeV and $p_{\mathrm{T}}(\mu) > 36$ GeV, respectively, identified according to the tight working point. The first trigger also requires muon isolation at the EF level. Isolation at the trigger level is track-based and requires that the ratio between the sum of the p_{T} of the tracks measured by the ID within $\Delta R < 0.2$ around the muon and $p_{\mathrm{T}}(\mu)$ is less than 12%. At this stage, offline muons are required to have $p_{\mathrm{T}}(\mu) > 26$ GeV and a calorimetric isolation $E_{\mathrm{T}}^{\Delta R<0.2}/p_{\mathrm{T}} < 6\%$, reducing the amount of muons from semi-leptonic b-hadron decays found inside jets. Events with at least one reconstructed electron are rejected, as well as those containing two muons. A further requirement on the muon momentum, $p_{\mathrm{T}}(\mu) > 40$ GeV, reduces the number of multi-jet events. One reconstructed tau candidate with $p_{\mathrm{T}}(\tau) > 50$ GeV is required in the event, which is due to a jet faking a tau lepton. Similarly to what was discussed in Sec. 6.4.2, the two azimuthal angle distances $\Delta\phi(\mu, E_{\mathrm{T}}^{\mathrm{miss}})$ and $\Delta\phi(\tau, E_{\mathrm{T}}^{\mathrm{miss}})$ are exploited by the requirement $\cos\Delta\phi(\mu, E_{\mathrm{T}}^{\mathrm{miss}}) + \cos\Delta\phi(\tau, E_{\mathrm{T}}^{\mathrm{miss}}) < -0.15$. The selection imposed to define the $W \to \mu\nu$+jets control region is summarised in Tab. 7.14.

An example of distributions in this control region at various stages of the selection are illustrated

in Fig. 7.46. The total number of events for each contribution in the control region at various stages of the selection is reported in Tab. 7.15. A high purity sample of $W \to \mu\nu$ + jets events is obtained, with $W \to \mu\nu$+jets making up $\approx 87\%$ of the selected sample. The background is mainly composed of $t\bar{t}$ and single-top events, amounting to $\approx 8\%$. A minor contribution arises from $Z \to \mu\mu$ + jets. The impact of these backgrounds on the measured mis-identification probability is small and covered by the uncertainties.

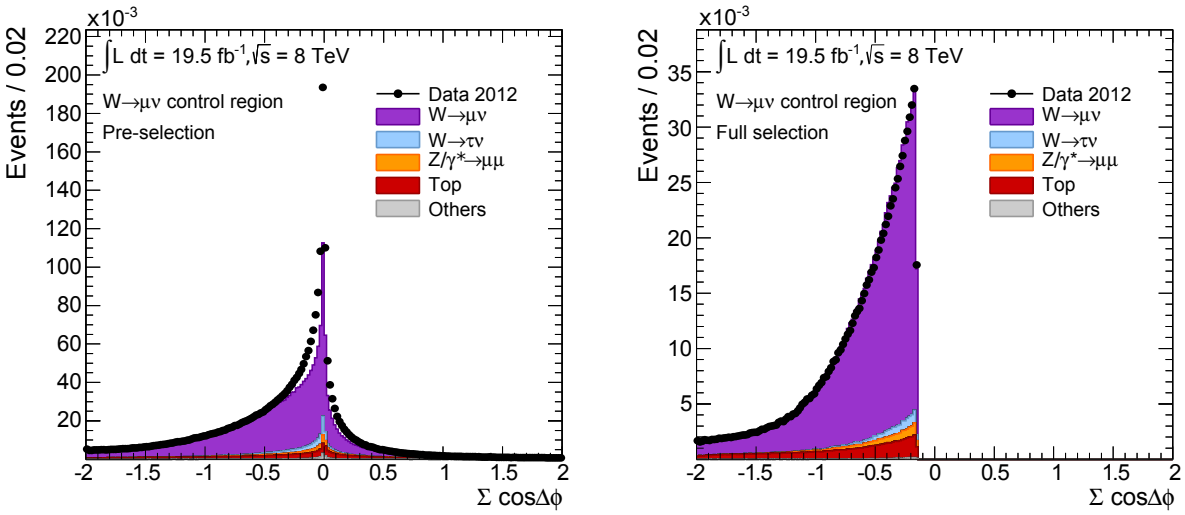

Figure 7.46: Distribution of $\Sigma_{l=\mu,\tau}\cos\Delta\phi(l, E_{\text{T}}^{\text{miss}})$ in the $W \to \mu\nu$ + jets control region at the pre-selection stage (left) and after the full selection (right). The pre-selection stage corresponds to the muon trigger requirement as indicated in Tab. 7.15. Multi-jet events are not estimated in the plots.

7.7.2 Tau Mis-identification Probability Measurement

The mis-identification probability for hadronic tau decays, f_{data}, is measured in a completely data-driven way, using data events in the control region introduced before. It is defined as

$$f_{\text{data}} = \frac{N^{\tau}_{\text{after ID (and trig.)}}(p_{\text{T}}, N_{\text{trk}}, \mu \times \tau \text{ charge sign})}{N^{\tau}_{\text{before ID (and trig.)}}(p_{\text{T}}, N_{\text{trk}}, \mu \times \tau \text{ charge sign})} \tag{7.9}$$

where N^{τ} is the number of tau candidates in data. In every event, only the tau candidate with the highest p_{T} is selected. Different levels of tau-ID are considered, which are loose and medium. As the identification algorithm running at trigger level is identical for all menus, only the trigger decision from `EF_2tau38T_medium1` is considered for this measurement. The obtained mis-identification probabilities are illustrated in Fig. 7.47 and 7.48, with and without the trigger requirement, respectively. Because of the charge correlation already mentioned in Sec. 6.4.2, mis-identification probabilities measured with the opposite-sign requirement are typically higher than those measured using the same-sign requirement, and are mainly due to the mis-identification of quark-initiated jets.

The fake tau composition in $W \to \mu\nu$ + jets events is very similar to the $W \to \tau\nu$ + jets case. However, the measured mis-identification probabilities are used to weight all non-multi-jet contributions, where the relative fraction of quark and gluon-initiated fake taus can significantly differ with respect to W + jets. This relative fraction can significantly influence the mis-identification probability, therefore, it is important to check that it is comparable between W + jets and the other backgrounds. This check is

	$W \to \mu\nu$ Control Region Selection							
	Muon triggers	Electron veto	$p_{\mathrm{T}}(\mu) > 26$ GeV	Di-muon veto	Muon isolation	$N_\tau = 1$	$p_{\mathrm{T}}(\mu) > 40$ GeV	$\Sigma\cos\Delta\phi < 0.15$
$W \to \mu\nu$	87.8×10^6	87.7×10^6	80.2×10^6	80.1×10^6	76.8×10^6	18.2×10^5	13.5×10^5	78.5×10^4
$Z/\gamma^* \to \mu\mu$	12.1×10^6	12.0×10^6	11.4×10^6	38.9×10^5	37.4×10^5	63.1×10^3	49.3×10^3	21.5×10^3
$W \to \tau\nu$	30.8×10^5	30.7×10^5	22.5×10^5	22.4×10^5	21.4×10^5	98.9×10^3	48.4×10^3	19.0×10^3
Top	73.4×10^4	64.3×10^4	60.8×10^4	49.3×10^4	41.0×10^4	21.1×10^4	15.2×10^4	74.6×10^3
Others	62.9×10^4	58.2×10^4	46.4×10^4	42.1×10^4	39.8×10^4	33.6×10^3	19.4×10^3	76.7×10^2
Data	18.4×10^7	18.3×10^7	15.3×10^7	14.2×10^7	93.3×10^6	93.3×10^6	16.8×10^5	89.9×10^4

Table 7.15: Event yields for all expected contributions and the data in the $W \to \mu\nu$ + jets control region, at each step of the selection.

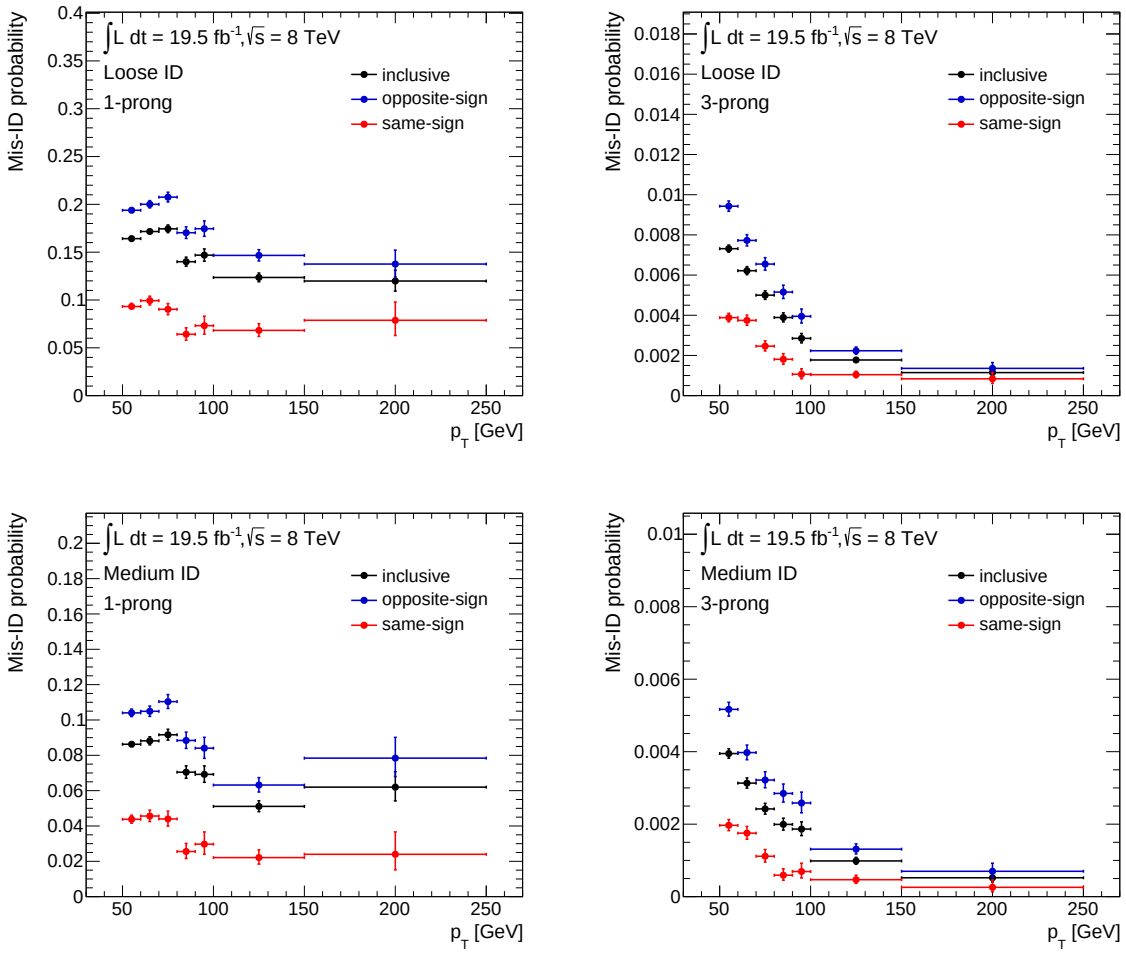

Figure 7.47: Mis-identification probabilities for fake tau candidates measured using data events selected in a $W \to \mu\nu$ + jets control region. The plots on the left and the right are obtained for 1-prong and 3-prong candidates, respectively. The loose and medium identification requirements are used for the upper and lower plots, respectively.

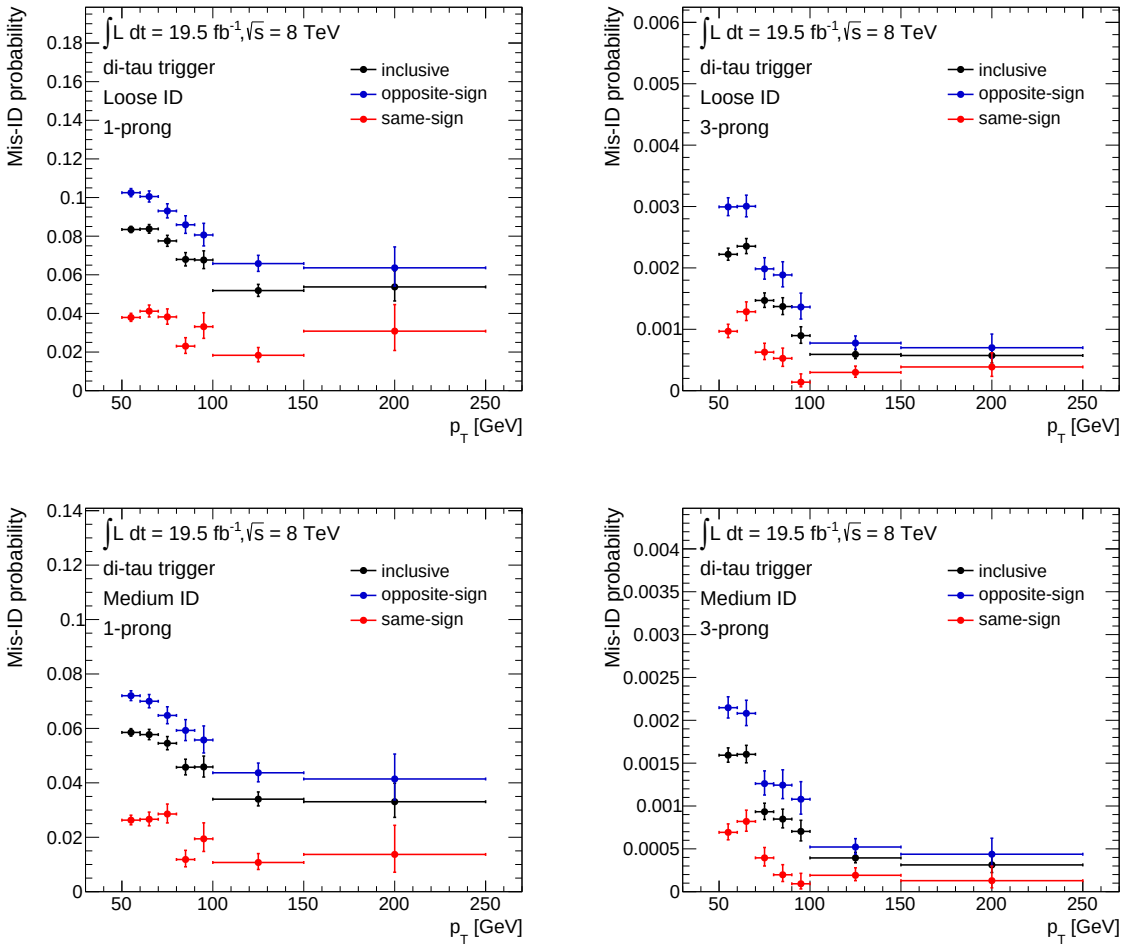

Figure 7.48: Mis-identification probabilities for fake tau candidates measured using data events selected in a $W \rightarrow \mu\nu$ + jets control region. The plots on the left and the right are obtained for 1-prong and 3-prong candidates, respectively. The loose and medium identification requirements are utilised for the upper and lower plots, respectively. The di-tau trigger requirement is also applied.

illustrated in Fig. 7.49, showing the fraction of quark-initiated jets in the final state of different background contributions, including $W \to \tau\nu$+jets.

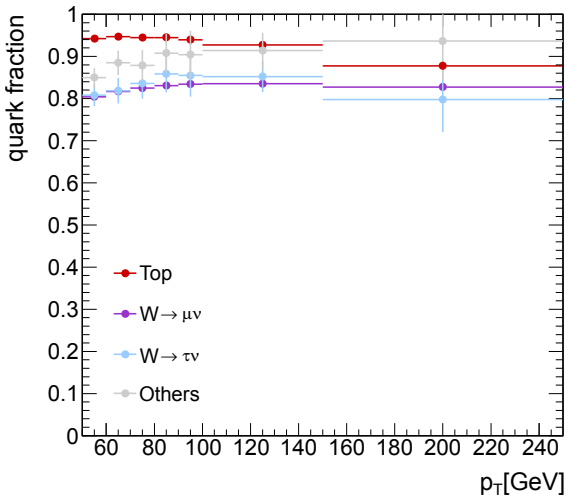

Figure 7.49: Fraction of jets originating from quarks in different background contributions, including $W \to \mu\nu$+jets, obtained using the true information in inclusive simulated events.

7.7.3 Uncertainty on the Tau Mis-identification Probability

Fake tau candidates in $W \to \mu\nu$ + jets events originate from quarks or gluons. However, the relative proportion of the two might differ between $W \to \mu\nu$+jets and other sources of background. In this analysis, the assumption is made that this proportion is similar between $W \to \mu\nu$+jets and $W \to \tau\nu$+jets events, as confirmed by Fig. 7.49. Motivated by this assumption, the uncertainty considered on the mis-identification probability for the weighting of $W \to \tau\nu$ + jets is only the statistical one. Other backgrounds, such as $t\bar{t}$, are likely to differ significantly in the proportion between quark and gluon-initiated fake tau candidates. For this reason, a conservative 60% uncertainty on the mis-identification probability is propagated during weighting, motivated by the observed difference between the weights measured in opposite-sign and same-sign events, as shown in Fig. 7.47 and 7.48. This large uncertainty does not reduce the sensitivity of the analysis in a significant way because of the very small amount of these backgrounds.

7.8 Systematic Uncertainties

The sensitivity of the analysis to the presence of signal is affected by statistical and systematic uncertainties. The statistical uncertainty is due to the finite number of events, both for the data and the simulation. Systematic uncertainties arise due to imperfections in the model of the signal and the background and their reconstruction. Systematic uncertainties are also assigned to the background estimation techniques. Uncertainties can influence both the normalisation and the $m_{\text{T}}^{\text{tot}}$ shape of the signal or the background.

This section illustrates the sources of systematic uncertainty considered in this analysis and the methods used to estimate their effects. Experimental and theoretical uncertainties will be discussed in the following. Experimental uncertainties, discussed in Sec. 7.8.1, are mainly due to the background estimation techniques, reconstruction and calibration of the objects and the effect of pile-up. Theoretical

uncertainties, discussed in Sec. 7.8.2, affect the cross-sections and shapes of distributions for the signal and the backgrounds.

The TES is among the leading sources of uncertainty for the signal and for backgrounds featuring real tau leptons, together with the tau trigger and the tau identification uncertainties. The dominant uncertainty on the multi-jet background comes from the method used for its estimation and is assigned to the fake-factors in the STT category and to the $R_{\mathrm{OS/SS}}$ factor in the DTT category. The uncertainty on the mis-identification probability is dominant for those backgrounds where fake tau leptons are simulated, like $W \to \tau\nu$+jets, the top background and the other minor background contributions. Other experimental uncertainties affect all backgrounds and the signal, like the track reconstruction efficiency in the STT category, or the JES and $E_{\mathrm{T}}^{\mathrm{miss}}$ resolution and scale in the DTT category.

The impact of each systematic uncertainty will be illustrated in the next section as the relative variation in the number of expected events for either the background or the signal. In addition, systematic effects will also be quantified in the next chapter by estimating their impact on the fitted amount of signal in the final hypothesis test.

7.8.1 Experimental Uncertainties

Tau Energy Scale

The tau energy is calibrated as discussed in Sec. 6.3. Due to the use of a p_{T}-based selection in this analysis, the uncertainty associated with the energy calibration influences the event yield. It also affects the shape of the $m_{\mathrm{T}}^{\mathrm{tot}}$ distribution. As the uncertainty on a single tau is measured as a function of $p_{\mathrm{T}}(\tau)$, its pseudo-rapidity and its track multiplicity, this uncertainty is applied as a shift in $p_{\mathrm{T}}(\tau)$, where the TES is varied upward and downward coherently for all tau leptons, independent on p_{T}, i.e. the TES is treated as correlated over the whole p_{T} range. Recommendations are only available up to $p_{\mathrm{T}}(\tau) \approx 200$ GeV. Above this threshold, the TES and the uncertainties associated to it are assumed to not change, based on studies performed with γ + jets events [217]. Depending on the p_{T}, the tau track multiplicity and the $|\eta|$ region of the detector, the uncertainty on the TES amounts to $\approx 2-4\%$. The TES uncertainty is evaluated separately for real tau leptons in the simulation and fake tau candidates.

Tau Trigger Efficiency

The tau-trigger efficiency and its uncertainties have been measured as described in Sec. 6.5.4. A tag-and-probe method using $Z \to \tau\tau$ events is used, similar to the method utilised for the tau ID efficiency. Therefore, prescriptions to treat uncertainties are only available up to $p_{\mathrm{T}}(\tau) = 100$ GeV. For this reason, no simulation correction factors are applied to tau leptons beyond this threshold. Rather, a conservative uncertainty of 10% covers any mis-modelling for $p_{\mathrm{T}}(\tau) > 100$ GeV. This is based on the maximum deviation of the correction factors from unity observed at lower p_{T}, as can be seen in Fig. 6.26.

Tau Identification

The tag-and-probe method for the estimation of the tau identification correction factors has been illustrated in Sec. 6.4. It only provides uncertainties up to $p_{\mathrm{T}}(\tau) \approx 100$ GeV, as $Z \to \tau\tau$ events are used. Given the much higher transverse momenta involved in this search, a different estimation has to be performed. For $p_{\mathrm{T}}(\tau) \gtrsim 100$ GeV and up to $p_{\mathrm{T}}(\tau) \approx 800$ GeV, there is no abundant source of tau leptons in data to be used for testing the simulation. However, the problem that has to be addressed is whether there is any degradation in the tau-ID efficiency correction at high p_{T}. Any degradation in the response is mainly

caused by either a mis-modelling of the tau decay, or of the detector response. Any effect from these sources will be considered to increase the uncertainty, which is measured as described in Sec. 6.4.

As far as the tau decay is concerned, the assumption is made that no degradation in the simulation is present at high p_{T}. To get a handle on this assumption different configurations of the simulation are used, as described in Ref. [158, 218], where $Z' \to \tau\tau$ decays with $m_{Z'} = 1000$ GeV are modelled. Five simulated samples have been produced. One is obtained with `Pythia`, using *QGSP_BERT* to model the hadronic shower, while other two are obtained using *QGSP* and *FTFP_BERT* instead. A different detector geometry with additional material is used in another simulation. Finally, a different underlying event tune, *A2* [80], is considered. For all these simulated samples the tau identification efficiency is measured for reconstructed candidates as a function of $p_{\text{T}}(\tau)$ with respect to the loose working point. This measurement is shown in Fig. 7.50, showing the 1-prong and 3-prong efficiencies. Reconstructed tau leptons are matched to a true tau within $\Delta R < 0.2$. As shown in the pictures, consistent efficiencies are measured in the various cases, even at higher p_{T}, indicating no degradation due to the decay model.

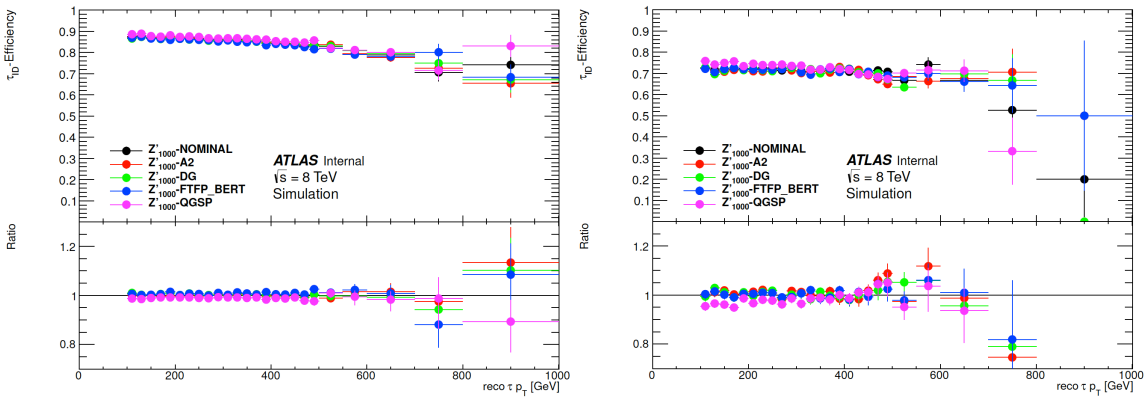

Figure 7.50: Tau identification efficiency for the loose working point as a function of p_{T} of the reconstructed candidate. Simulated events from different Z' samples with $m_{Z'} = 1000$ GeV are used for this measurement, each of them accounting for a different systematic effect. Efficiencies for 1-prong (left) and 3-prong (right) candidates are shown. The lower plots show the ratio between the measurement using the specific sample and the nominal simulation setup. The plots are taken from Ref. [218].

In order study the robustness of the detector response at high p_{T}, the mis-identification probability of jets is measured in data and simulation using di-jet events. These events are selected using similar requirements as those described in Sec. 7.4.1. A data sample selected with single-jet triggers and corresponding to $L_{\text{int}} = 20.3$ fb^{-1} is used. Two jets are selected, the tag and the probe, which are required to be back-to-back in the transverse plane, $\cos\Delta\phi(\text{tag}, \text{probe}) < -0.95$. A p_{T}-balance requirement is applied $|(p_{\text{T}}(\text{tag}) - p_{\text{T}}(\text{probe}))/p_{\text{T}}(\text{tag})| < 0.05$. This selection targets jets originating from leading-order processes at high energies, therefore avoiding low-p_{T} gluon radiation which is difficult to model. Electron contamination is reduced by applying an electron veto to the probe, and excluding reconstructed jets in the region $1.37 < |\eta| < 1.52$, where electron identification is more difficult due to the presence of non-instrumented regions of the detector. Only probe jets with one or three associated tracks are considered. Simulated events are obtained with `Pythia`, in exclusive samples for different jet p_{T} ranges. Details about the samples are reported in Ref. [158, 218]. An overall good agreement is observed between the simulation and the data. However, the ϕ distribution, presented in Fig. 7.51, shows an excess in data for $\phi(\text{probe}) \approx -2$. The reason for this is a broken pixel module in the inner detector, which causes an inefficiency in the track reconstruction for jets with high track multiplicities, resulting in an enhanced number of reconstructed jets with one or three tracks. The excess is present because the broken sensor is

not modeled in the simulation. For this measurement, the probe jet is required to be outside the region $-2.5 < \phi(\text{probe}) < -2.0$. As the tau identification does not depend on ϕ, a negligible effect is expected.

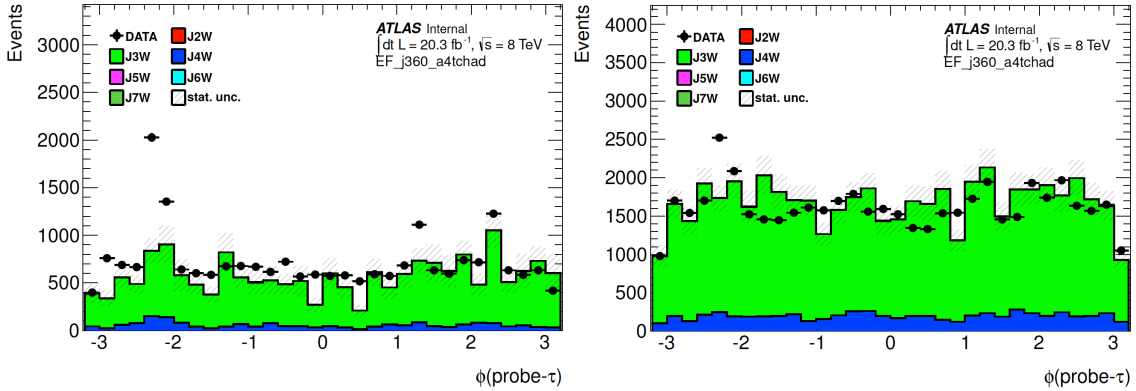

Figure 7.51: Distributions of the polar angle of the probe jet for 1-prong candidates (left) and 3-prong ones (right). In the legend, JXW (with X = 2 − 7) refers to different simulated samples where di-jet events are simulated in exclusive regions of p_{T}, from p_{T} = 80 GeV to p_{T} = 2000 GeV. The plots are taken from Ref. [218].

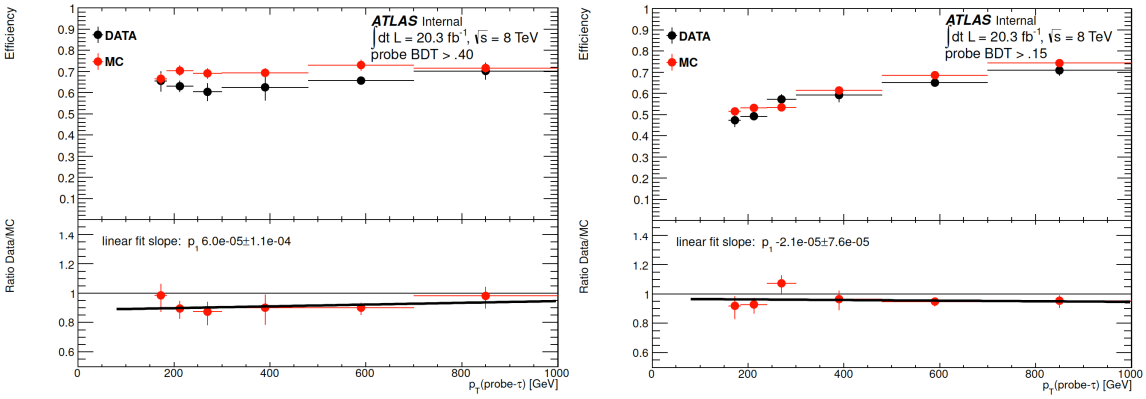

Figure 7.52: Mis-identification probability as a function of the probe jet p_{T} for 1-prong (left) and 3-prong (right) tau candidates. The comparison between the data and the simulation is shown. A selection is applied on the BDT score which reproduces the effect of the loose tau identification. The lower plots show the ratio between the data and the simulation as well as the linear fit performed. The plots are taken from Ref. [218].

The mis-identification probability measured with reconstructed probe jets in data and simulation is illustrated in Fig. 7.52, as a function of p_{T}(probe) for 1-prong and 3-prong candidates. A selection is required on the BDT score in order to obtain a mis-identification probability comparable to the loose working point of tau identification. As expected, a discrepancy is observed, likely due to the mis-modelling of jets. However, no significant deterioration of the mis-identification probability is observed with increasing p_{T}. This increases the level of confidence that no deterioration in the response for real tau leptons is to be expected at high p_{T}. To quantify the agreement between data and simulation, a linear fit to the ratio between the mis-identification probabilities is performed. It is found that the slope is consistent with zero. The uncertainty on the slope is used to increase the uncertainty on the tau-ID efficiency determined in Sec. 6.4, $\Delta\varepsilon_{\tau-\mathrm{ID,low-p_T}}$, as a function of p_{T}. To avoid an extreme increase of the uncertainty at high p_{T}, $\Delta\varepsilon_{\tau-\mathrm{ID}}$, a cut-off is used. For this, a constant fit is performed and the uncertainty on the determined constant is taken as an upper bound for $\Delta\varepsilon_{\tau-\mathrm{ID}}$. The identification efficiency uncertainty for

$p_{\text{T}}(\tau) > 100$ GeV can then be written as

$$\Delta\varepsilon^{1-\text{prong}}_{\tau-\text{ID}}(p_{\text{T}}) = \Delta\varepsilon^{1-\text{prong}}_{\tau-\text{ID,low}-p_{\text{T}}} + 0.011\%/\text{ GeV} \times (p_{\text{T}} - 100\text{ GeV}), \tag{7.10a}$$

$$\Delta\varepsilon^{3-\text{prong}}_{\tau-\text{ID}}(p_{\text{T}}) = \Delta\varepsilon^{3-\text{prong}}_{\tau-\text{ID,low}-p_{\text{T}}} + 0.0076\%/\text{ GeV} \times (p_{\text{T}} - 100\text{ GeV}), \tag{7.10b}$$

where $\Delta\varepsilon^{1-\text{prong}}_{\tau-\text{ID}}$ and $\Delta\varepsilon^{3-\text{prong}}_{\tau-\text{ID}}$ have an upper bound of 2.3% and 1.5%, respectively. More details about this measurement can be found in Ref. [218].

Track Reconstruction Efficiency at High p_{T}

It has been shown [158] that the track reconstruction efficiency for 3-prong tau leptons at high momenta decreases. This is due to track-merging effects, where overlapping tracks cannot be resolved due to hits being very close to each other in the inner detector. The collimation of the tracks of tau candidates increases with increasing tau p_{T}, therefore this effect becomes relevant at high energies. The fraction of reconstructed candidates with two, three or four tracks as a function of the tau transverse momentum is shown in Fig. 7.53 for simulated 3-prong decays. Different reconstructed track multiplicities are compared. As visible in the plot, for $p_{\text{T}}(\tau) > 150$ GeV, the fraction of wrongly reconstructed track multiplicities increases. In particular the fraction of 2-prong tau leptons increases due to track-merging effects. The simulation has been proven to be consistent with data in modelling the effect of hits shared

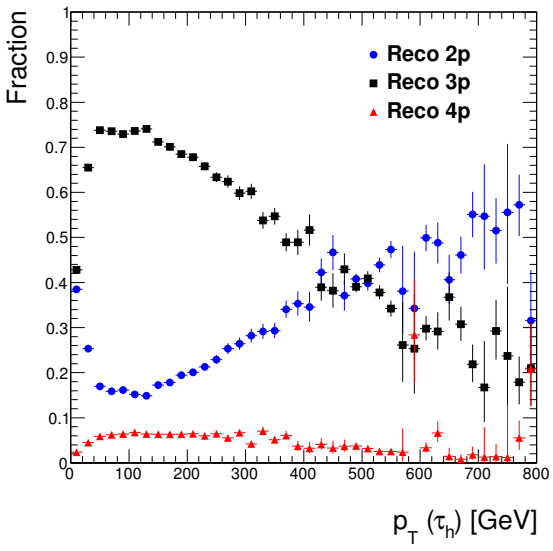

Figure 7.53: Fraction of simulated 3-prong tau leptons reconstructed as 2-prong, 3-prong and 4-prong, as a function of the reconstructed $p_{\text{T}}(\tau)$. The plot is taken from Ref. [158].

by more than one track in the inner detector, which leads to track merging [219]. A conservative estimate of 50% on the tracking efficiency loss for 3-prong candidates is assumed [219], which is confirmed by the plot in Fig. 7.53. The degradation becomes significant for $p_{\text{T}} > 150$ GeV, and increases by $\approx 10\%$ every $\Delta p_{\text{T}} \approx 100$ GeV. The following prescription is used

$$\Delta\varepsilon^{3-\text{prong}}_{\text{tracking}}(p_{\text{T}}) = 0 \quad \text{for} \quad p_{\text{T}}(\tau) \leq 150\text{ GeV}, \tag{7.11a}$$

$$\Delta\varepsilon^{3-\text{prong}}_{\text{tracking}}(p_{\text{T}}) = 0.05 \times (p_{\text{T}}(\tau)/\text{ GeV} - 150)\% \quad \text{for} \quad p_{\text{T}}(\tau) > 150\text{ GeV}. \tag{7.11b}$$

Jet Energy Scale

The measurement of the jet energy scale has been discussed in Sec. 5.6, along with all the sources of uncertainty associated with it. The uncertainties depend on the jet p_{T} and η and amount to $\approx 5\%$. Their measurement is discussed in detail in Ref. [148, 151]. Sources of uncertainty include pile-up, the contribution of other close jets and the flavour composition of the hadrons composing them. In this analysis, no selection criterium is applied to jets. However, the topology and kinematic of the jets in the event is relevant for the $E_{\mathrm{T}}^{\mathrm{miss}}$ calculation, as illustrated in Sec. 5.7. Therefore, the JES uncertainty can affect the missing transverse energy. However, this uncertainty only has a minor effect in the analysis.

Missing Transverse Energy

The determination of the missing transverse energy in the events has been detailed in Sec. 5.7. As $E_{\mathrm{T}}^{\mathrm{miss}}$ is computed using all objects in the event, its uncertainty is influenced by the uncertainties on all objects, including their energy scale and resolution. The evaluation of this effect is performed by recalculating $E_{\mathrm{T}}^{\mathrm{miss}}$ after varying the kinematic and topology of all objects according to their systematic uncertainties. Another source of $E_{\mathrm{T}}^{\mathrm{miss}}$ uncertainty comes from the soft term, defined in Eq. (5.8). The energy resolution and scale of the soft term is studied in $Z \to \mu\mu$ events and propagated to the $E_{\mathrm{T}}^{\mathrm{miss}}$ estimate, as detailed in Ref. [157].

Luminosity

The luminosity is measured by the forward detectors introduced in Sec. 4.2.5. The procedure is illustrated in Ref. [127]. In 2012, the total uncertainty on the estimate of the luminosity is 2.8%. All background contributions and the signal are affected by this uncertainty, which is also propagated to the data-driven estimate of multi-jets, as simulated backgrounds are subtracted in the control regions.

7.8.2 Cross-section and Acceptance Uncertainties

In this section, the uncertainty on the cross-sections used to normalise signal and background samples is discussed, as well as the acceptance uncertainty, which has an impact on the probability for events to pass the selection in the STT and DTT categories.

Cross-section Uncertainty on $Z/\gamma^* \to ll$

Backgrounds from $Z/\gamma^* \to ll$ are estimated with simulation, using programs discussed in detail in Sec. 7.2.2 for $Z/\gamma^* \to \tau\tau$ and in 7.2.5 for other final states. This estimate is affected by the uncertainty on the k-factor used for the NNLO cross-sections. The dependence of the k-factors on the resonance mass are visible in Fig. 7.13 (left) and 7.16, along with their uncertainty. Uncertainties arise from the choice of the PDF set and the values of α_S, and are computed with the program `FEWZ 3.1.b2` using the MSTW prescriptions. The effect depends on the generated mass of the resonance, and is at most $\approx 10\%$.

Cross-section Uncertainty on $W \to \tau\nu$ + jets

The control region used to measure the tau mis-identification probability can be used to constrain the prediction of the cross-section for $W \to \tau\nu$ + jets events. This is of great advantage in reducing the uncertainty, which would be $\approx 27\%$ using only the theoretical predictions. This uncertainty is constrained by applying the mis-identification probability to all fake tau candidates in simulated events found in the

$W \to \mu\nu$ + jets control region defined in Sec. 7.7.1. A good agreement is found, indicating a reliable cross-section prediction. The largest background not from W + jets in this region comes from $t\bar{t}$ events, and amounts to $\approx 10\%$. As discussed in Sec. 7.7.3, the mis-identification probability uncertainty has a 60% effect on the normalisation of this background. Propagating the uncertainty in $t\bar{t}$ events in this region to the W + jets normalisation results in a $\approx 6\%$ effect. This number is then assumed to be the cross-section uncertainty for $W \to \tau\nu$ + jets.

Cross-section Uncertainty on $t\bar{t}$ and single-top

Cross-sections for $t\bar{t}$ and single-top events are computed as discussed in Sec. 7.2.4, and are found to be in good agreement with measurements. Uncertainties associated with the calculation come from the choice of the PDF set and value of α_S. They are evaluated according to the prescriptions in Ref. [220], and amount to $\approx 10\%$ for $t\bar{t}$ and $\approx 13\%$ for single-top events.

Cross-section Uncertainty on Di-boson events

A total cross-section uncertainty of 5% is assigned to di-boson events such as WW, WZ and ZZ production, based on previous ATLAS results [221].

Acceptance Systematic Uncertainties

Alterations in basic parameters of the simulation can affect the acceptance of the analysis, due to alterations they induce on the kinematic properties of the final state. The impact of this uncertainty is evaluated using different simulated samples where these properties are altered. Effects considered are associated with the variation of the PDF set, the initial and final state radiation, the renormalisation scale and the factorisation one. After each variation is applied, the event yield is measured and its difference with respect to the nominal one is considered as the uncertainty. The systematically altered event yield is obtained at the generator level using the *RIVET* framework [222]. All contributions are added in quadrature.

Only four different representative mass points are chosen for the signal samples, in order to reduce significantly this computationally demanding process. Also, only the main simulated backgrounds $Z/\gamma^* \to \tau\tau$ and $W \to \tau\nu$ + jets are considered. The nominal PDF set is replaced in the new simulations in order to alter the nominal one. The nominal PDF set for `Sherpa` and `Powheg` generators is CT10 [188], which is altered using CTEQ6L1 [220]. This set is the nominal one for `Pythia` samples, for which NNPDF21NLO [220] is considered as a systematic variation.

Another source of uncertainty is the choice of the merging scale featured by the nominal algorithm, altering the amount of initial and final state radiation predicted. As illustrated in Sec. 7.1.1, the `Sherpa` generator relies on the CKKW algorithm to perform merging, which uses the scale $\Lambda_{\text{CKKW}} = \sqrt{20\ \text{GeV}/\sqrt{s}}$. Upward and downward variations of this scale are considered, setting the values $\Lambda_{\text{CKKW}} = \sqrt{30\ \text{GeV}/\sqrt{s}}$ and $\Lambda_{\text{CKKW}} = \sqrt{15\ \text{GeV}/\sqrt{s}}$. For `Powheg` the initial and final state radiation can be tuned using dedicated parameters which have been altered according to ATLAS prescriptions [220].

The nominal choice of the renormalisation and factorisation scales, μ_R and μ_F, respectively, depends on the sample considered. For the gluon-gluon production mode of the signal the choice $\mu_R = \mu_F = m_\phi$ is adopted [187]. The $b\bar{b}$ annihilation process relies on two approaches, the four-flavour and five-flavour schemes, as illustrated in Sec. 7.1.1. The choice adopted in each case is $\mu_R = 4\mu_F = m_\phi$ for the 5FS and $\mu_R = \mu_F = m_\phi/4$ for the 4FS. All other samples rely on the assumption $\mu_R = \mu_F = m_\phi$. The uncertainty

associated with the choice of μ_R and μ_F is estimated by altering their values by 10% and 50%, respectively. This shift is applied upward and downward. In all samples the variations are treated as uncorrelated, with the exception of `Powheg`, where they are both varied upward or downward simultaneously.

7.9 Results

As can be seen from Fig. 7.54 (left), the fraction of generated signal events accepted in the DTT category has a maximum at $m_A \approx 300$ GeV. Beyond this peak a migration to the STT category is observed, due to the requirement $p_T(\tau_{lead}) < 150$ GeV. Also, the DTT category features a lower acceptance than the STT one, due to the tighter tau selection and the different trigger.

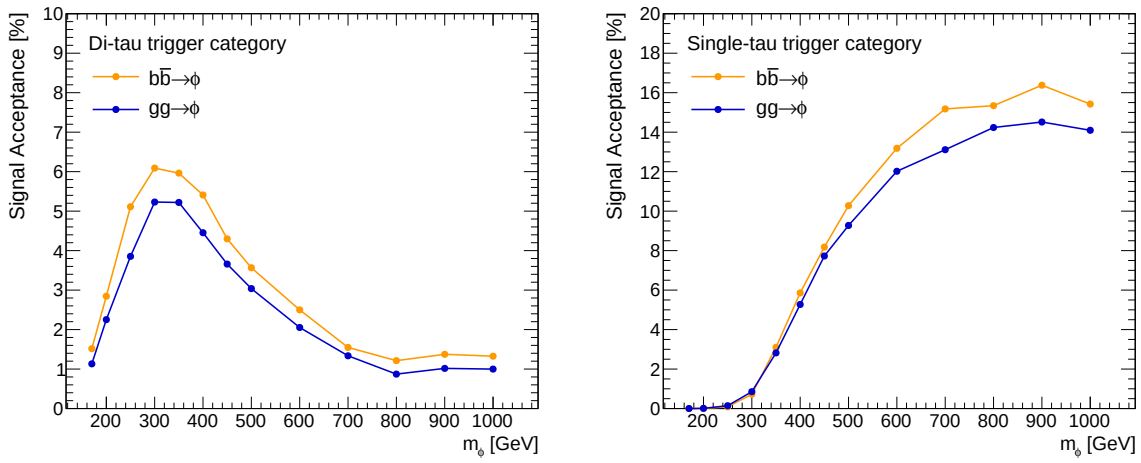

Figure 7.54: Signal acceptance in the DTT (left) and the STT (right) categories for the two production modes $b\bar{b}$ annihilation and gluon-gluon fusion.

After the background estimation is performed and validated, the expected contributions are compared with data. This is shown in Fig. 7.55 - 7.59, for key distributions in the DTT signal region. The number of events in the DTT category after each selection stage is reported in Tab. 7.16 for the backgrounds, the data and the signal. As the selection in the DTT category is optimised for low m_A, the point $m_A = 250$ GeV and $\tan\beta = 20$ is assumed for the signal. The results for other mass points can be found in App. E.

The dominant systematic uncertainty in the DTT category is the multi-jet normalisation, followed by the TES and the trigger uncertainties, affecting backgrounds with real taus.

In Tab. 7.17, the effect of the experimental systematic uncertainties on the event yields for every contribution is illustrated. The chosen signal point for the table is $m_A = 250$ GeV and $\tan\beta = 20$. Cross-section uncertainties for the full set of signal mass points are reported in App. D, while the effect of the other systematic uncertainties is reported in App. E.

Distributions in the STT signal region are shown in Fig. 7.60 - 7.64. The number of background, data and signal events in the STT signal region is reported in Tab. 7.18. For the signal, $m_A = 400$ GeV and $\tan\beta = 20$ is assumed. The results for all other mass points can be found in App. E. The signal acceptance in the STT category is illustrated in Fig. 7.54 (right). It increases with the signal mass and is higher than for the DTT category due to the more inclusive selection and the higher trigger efficiency. The STT systematic uncertainties are given in Tab. 7.19. The chosen signal point is $m_A = 400$ GeV and $\tan\beta = 20$. Systematic uncertainties for the full set of signal mass points are reported in App. E.

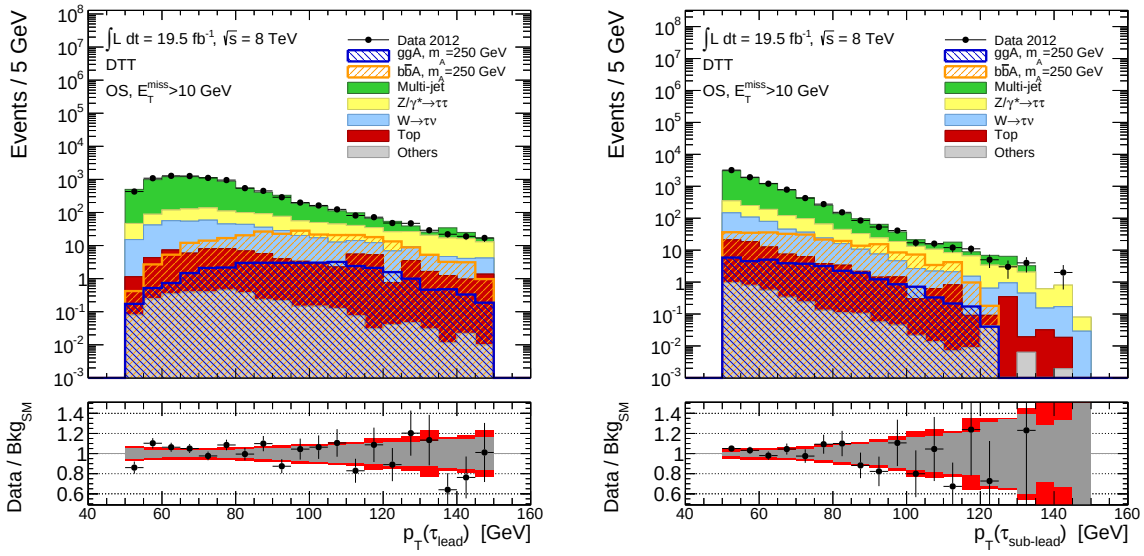

Figure 7.55: Distributions of $p_{\text{T}}(\tau)$ for the leading (left) and sub-leading (right) candidates in the DTT signal region. The lower plots illustrate the ratio between the data and the total expected background. The grey band shows the statistical uncertainty on the expected background and the red one the effect of all systematic uncertainties added quadratically. The signal is estimated assuming $\tan\beta = 20$ in the m_h^{max} scenario.

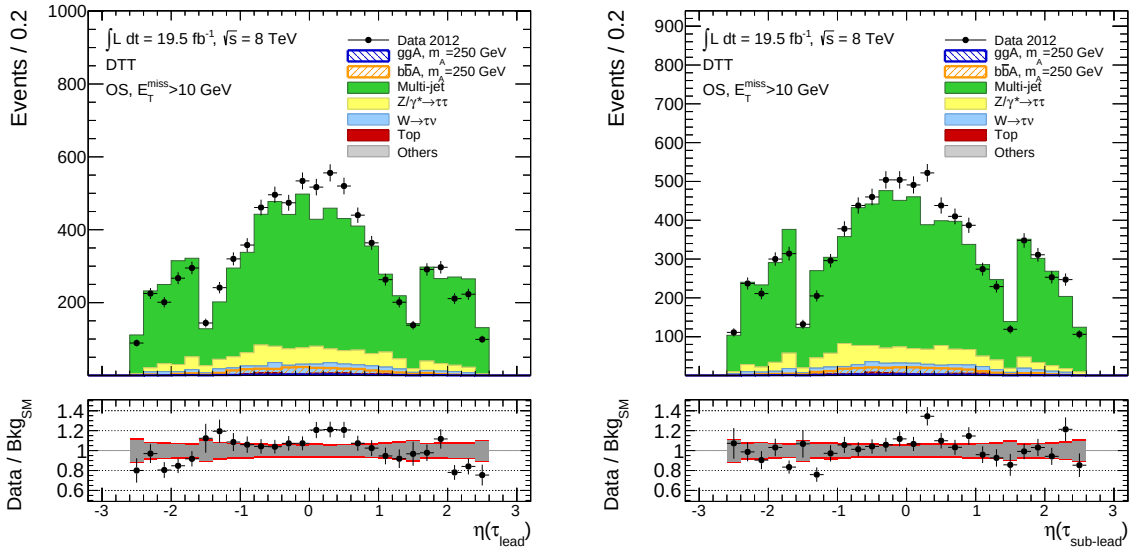

Figure 7.56: Distributions of $\eta(\tau)$ for the leading (left) and sub-leading (right) candidates in the DTT signal region. The lower plots illustrate the ratio between the data and the total expected background. The grey band shows the statistical uncertainty on the expected background and the red one the effect of all systematic uncertainties added quadratically. The signal is estimated assuming $\tan\beta = 20$ in the m_h^{max} scenario.

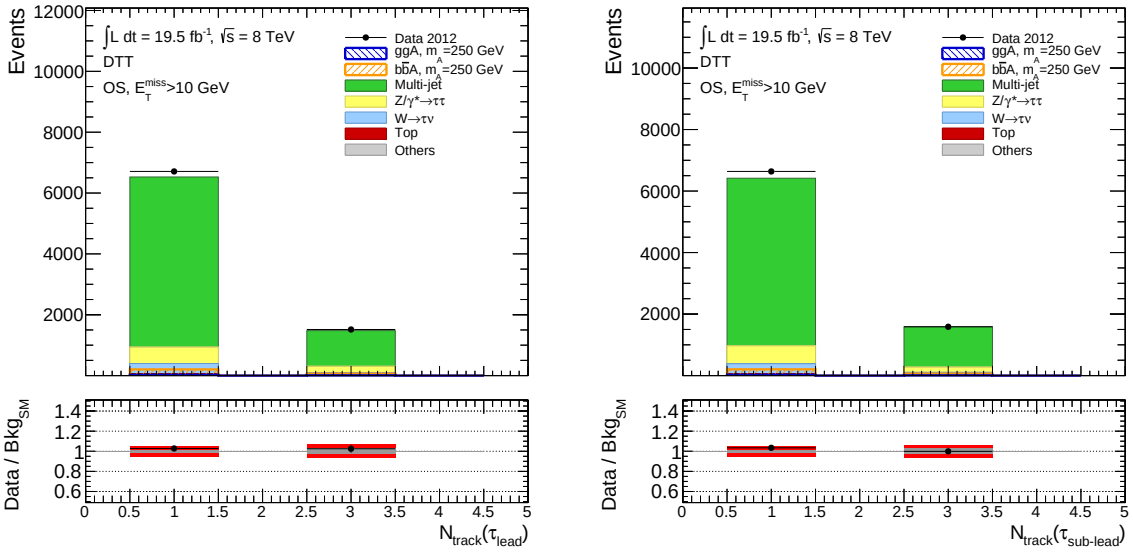

Figure 7.57: Distributions of track multiplicities for the leading (left) and sub-leading (right) candidates in the DTT signal region. The lower plots illustrate the ratio between the data and the total expected background. The grey band shows the statistical uncertainty on the expected background and the red one the effect of all systematic uncertainties added quadratically. The signal is estimated assuming $\tan\beta = 20$ in the m_h^{max} scenario.

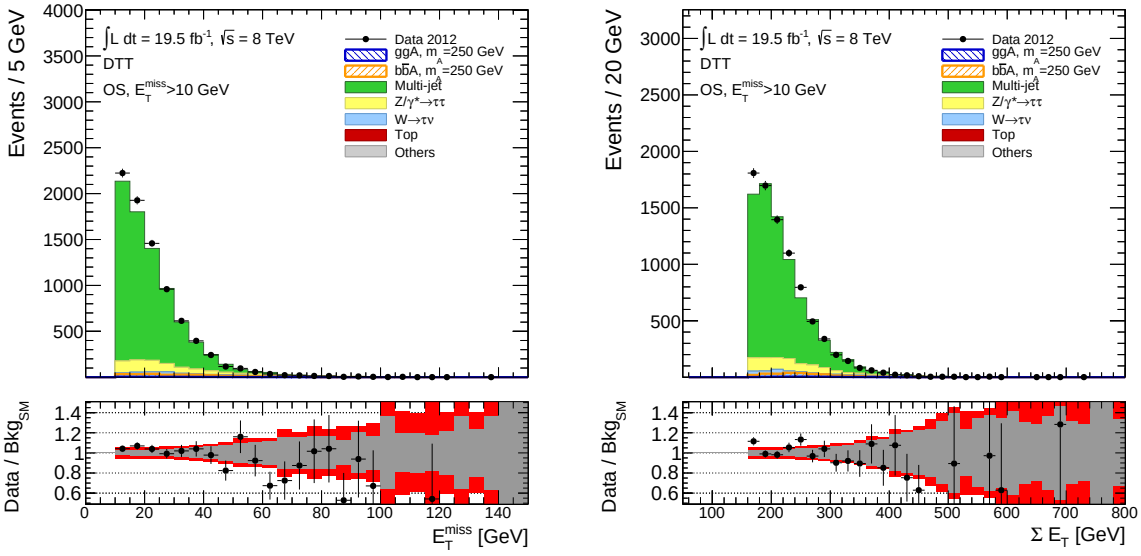

Figure 7.58: Distributions of $E_{\text{T}}^{\text{miss}}$ (left) and $\sum E_{\text{T}}$ (right) in the DTT signal region. The lower plots illustrate the ratio between the data and the total expected background. The grey band shows the statistical uncertainty on the expected background and the red one the effect of all systematic uncertainties added quadratically. The signal is estimated assuming $\tan\beta = 20$ in the m_h^{max} scenario.

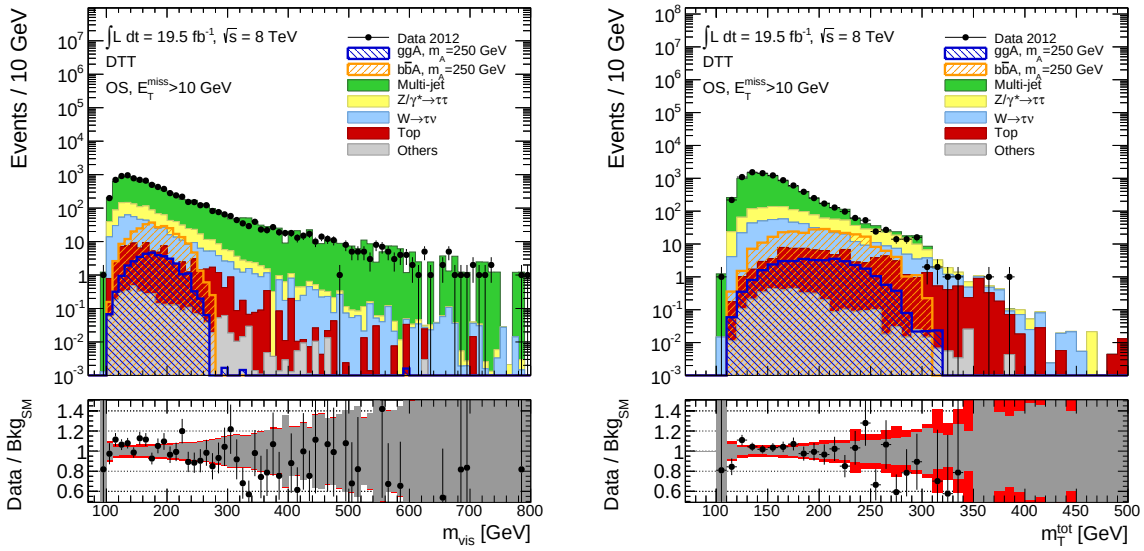

Figure 7.59: Distributions of m^{vis} (left) and $m_{\text{T}}^{\text{tot}}$ (right) in the DTT signal region. The lower plots illustrate the ratio between the data and the total expected background. The grey band shows the statistical uncertainty on the expected background and the red one the effect of all systematic uncertainties added quadratically. The signal is estimated assuming $\tan\beta = 20$ in the m_h^{max} scenario.

	DTT Selection				
	Di-tau trigger	$p_{\text{T}}(\tau_{\text{lead}}) < 150$ GeV	Medium tau-ID	$E_{\text{T}}^{\text{miss}} > 10$ GeV	$\Sigma E_{\text{T}} > 160$ GeV
Background					
Multi-jet	-	-	-	-	6765 ± 92
$Z/\gamma^* \to \tau\tau$	8631 ± 132	8143 ± 129	1196 ± 37	904 ± 30	752 ± 25
$W \to \tau\nu$	56409 ± 382	52880 ± 379	512.9 ± 9.7	462.6 ± 9.1	408.7 ± 7.9
Top	18535 ± 234	16708 ± 222	77.6 ± 4.9	76.4 ± 4.9	76.4 ± 4.9
Others	7282 ± 174	6807 ± 159	4.38 ± 0.39	3.68 ± 0.22	3.42 ± 0.21
Signal ($m_A = 250$ GeV, $\tan\beta = 20$)					
$b\bar{b} \to A$	422.1 ± 9.2	415.1 ± 9.1	312.2 ± 7.8	276.3 ± 7.4	264.9 ± 7.2
$gg \to A$	56.3 ± 1.2	54.3 ± 1.2	38.9 ± 1.0	34.71 ± 0.96	33.97 ± 0.95
Data	85816 ± 293	85316 ± 292	15294 ± 124	10291 ± 101	8225 ± 91
Total SM	-	-	-	-	8005 ± 95

Table 7.16: Event yields for the background contributions, the data and the signal at each stage of the selection in the DTT category. The quoted uncertainty is statistical. The multi-jet background is estimated only at the final step of the selection. The expected number of signal events is determined assuming the m_h^{max} scenario.

	DTT Systematic Uncertainties [%]							
	Multi-jet	$Z/\gamma^* \to \tau\tau$	$W \to \tau\nu$	Top	Others	Total SM	$b\bar{b} \to \phi$	$gg \to \phi$
Expected Events	6765 ± 92	752 ± 25	408.7 ± 7.9	76.4 ± 4.9	3.42 ± 0.21	8005 ± 95	264.9 ± 7.2	33.97 ± 0.95
$R_{OS/SS}$	±5.4	-	-	-	-	±4.6	-	-
		-	-	-	-		-	-
TES true tau	-0.8	+9.9	+4.9	+3.6	+0.6	±1.2	+2.8	+2.4
	+0.4	-9.5	-3.4	-2.3	-0.01		-2.4	-3.8
TES fake tau	-0.06	+0.2	+3.4	+1.3	+6.1	±0.1	-	-
	+0.08	-0.3	-2.7	-0.8	-3.9		-	-
Trigger low-p_T	-1.5	+16.9	+10.4	+12.3	+0.7	±2.3	+14.7	+14.9
	+1.6	-18.4	-12.2	-13.5	-0.9		-15.9	-16.4
Trigger high-p_T	-0.1	±3.1	±0.7	±2.9	±0.1	±0.3	+5.1	+4.8
	+0.1						-4.9	-4.7
Tau-ID	-0.5	+6.6	±3.6	+5.1	±0.3	±0.8	+6.6	+6.7
	+0.5	-6.4		-4.9			-6.4	-6.4
Mis-ID reweighting	-0.4	±4.8	+5.2	+29.4	+15.4	±0.6	-	-
	+0.4		-4.9	-25.9	-11.3		-	-
JES	+0.2	+0.6	+2.1	+0.07	+2.8	±0.3	+0.5	-0.2
	-0.3	-0.8	-2.3	-0.23	-2.1		-0.4	-0.4
E_T^{miss} resolution	+0.1	+0.6	-0.2	+0.03	+0.5	±0.1	-0.5	-0.03
	-0.05	-0.1	-0.08	-0.05	+0.07		+0.04	-0.1
E_T^{miss} scale	-0.1	∓0.2	-0.4	-0.02	∓0.05	±0.1	-0.2	+0.3
	+0.06		-	-0.03			+0.02	-0.09
Cross-section	±0.32	+3.94	±6.0	±8.3	±5.1	±0.5	+12.1	+13.9
		-3.32	-	-		-	-16.1	-14.8
Acceptance	±1.15	±15.0	±19.4	-	-	±1.9	±4.7	±1.8
				-	-			

Table 7.17: Systematic uncertainties in the DTT category presented as a relative variation in the expected number of events for each contribution. The chosen signal point is m_A = 250 GeV and tanβ = 20. Systematic uncertainties discussed in the main text that are negligible in the DTT category are not included. The upward and downward variations in the event yield are shown in the upper and lower rows, respectively, for the case of asymmetric systematic effects. Each uncertainty is also propagated to the total SM expectation.

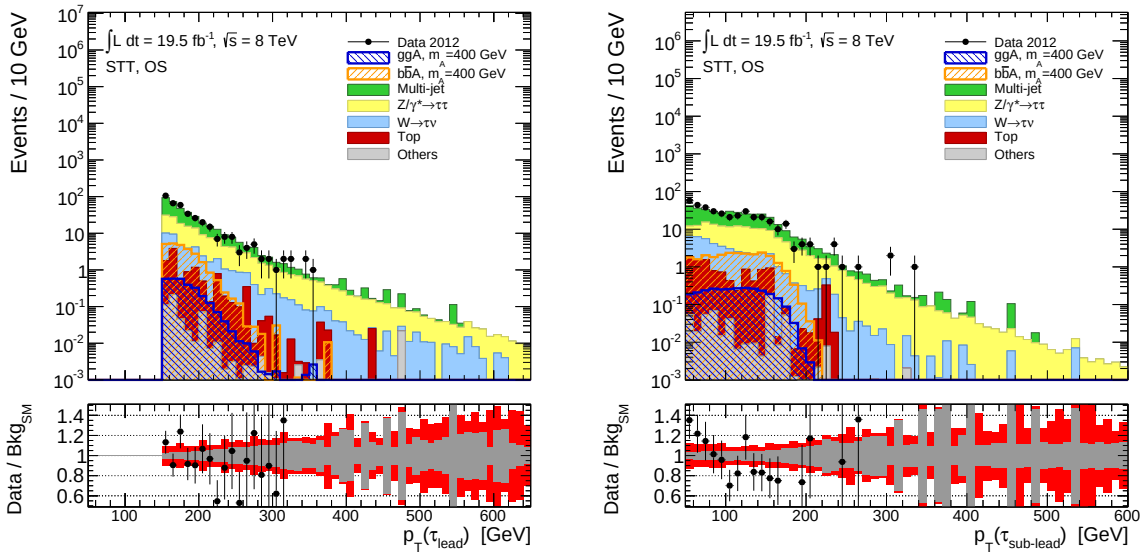

Figure 7.60: Distributions of $p_{\text{T}}(\tau)$ for the leading (left) and sub-leading (right) candidates in the STT signal region. The lower plots illustrate the ratio between the data and the total expected background. The grey band shows the statistical uncertainty on the expected background and the red one the effect of all systematic uncertainties added quadratically. The signal is estimated assuming $\tan\beta = 20$ in the m_h^{max} scenario.

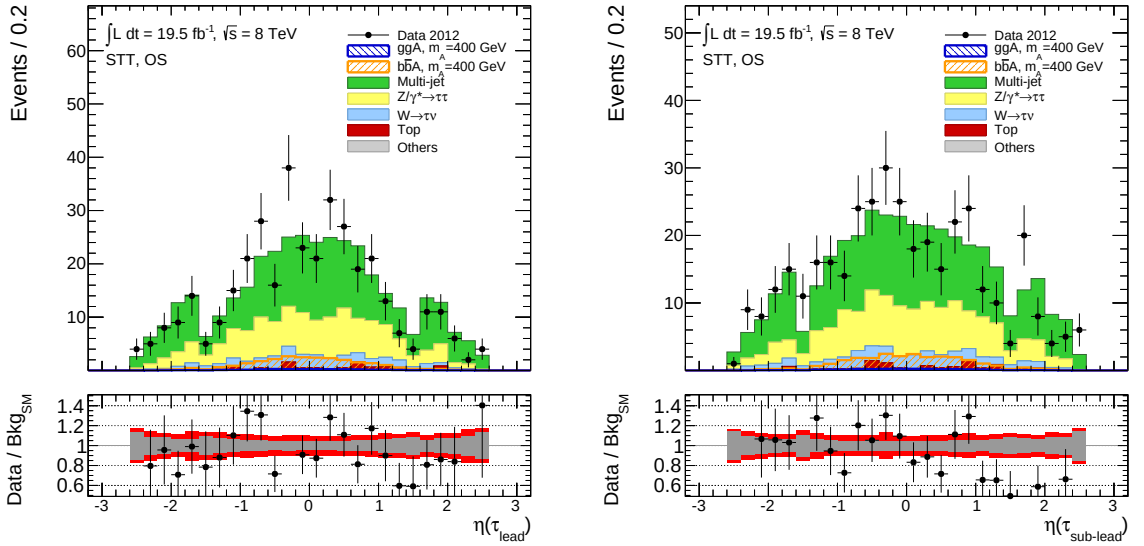

Figure 7.61: Distributions of $\eta(\tau)$ for the leading (left) and sub-leading (right) candidates in the STT signal region. The lower plots illustrate the ratio between the data and the total expected background. The grey band shows the statistical uncertainty on the expected background and the red one the effect of all systematic uncertainties added quadratically. The signal is estimated assuming $\tan\beta = 20$ in the m_h^{max} scenario.

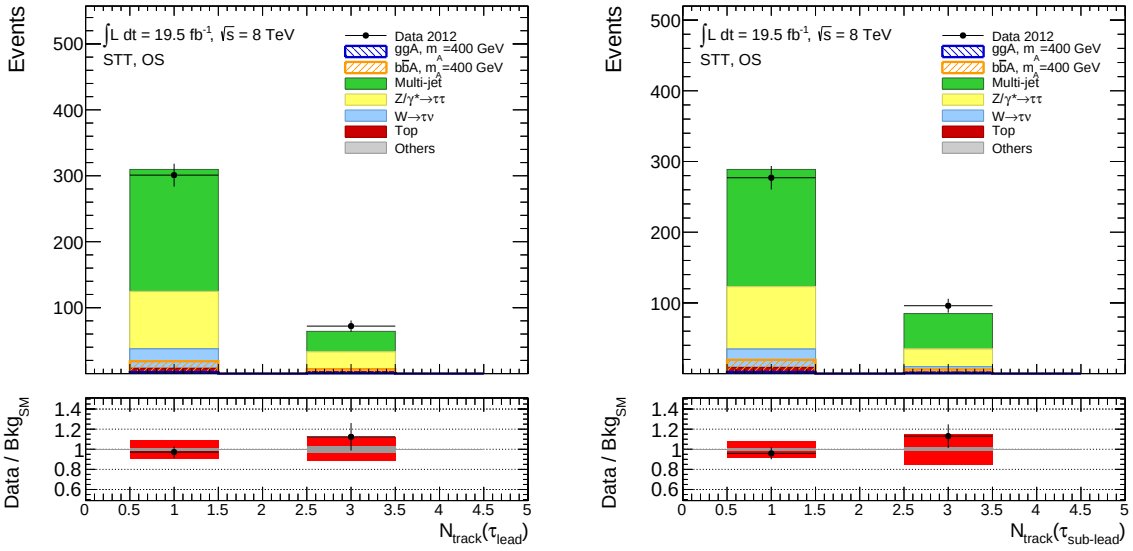

Figure 7.62: Distributions of track multiplicities for the leading (left) and sub-leading (right) candidates in the STT signal region. The lower plots illustrate the ratio between the data and the total expected background. The grey band shows the statistical uncertainty on the expected background and the red one the effect of all systematic uncertainties added quadratically. The signal is estimated assuming $\tan\beta = 20$ in the m_h^{max} scenario.

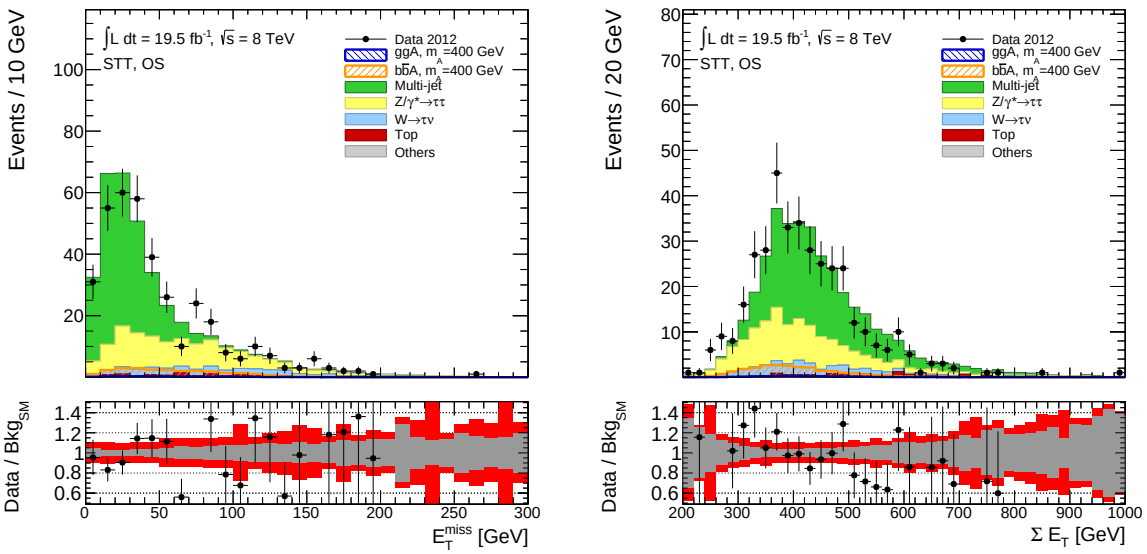

Figure 7.63: Distributions of $E_{\text{T}}^{\text{miss}}$ (left) and $\sum E_{\text{T}}$ (right) in the STT signal region. The lower plots illustrate the ratio between the data and the total expected background. The grey band shows the statistical uncertainty on the expected background and the red one the effect of all systematic uncertainties added quadratically. The signal is estimated assuming $\tan\beta = 20$ in the m_h^{max} scenario.

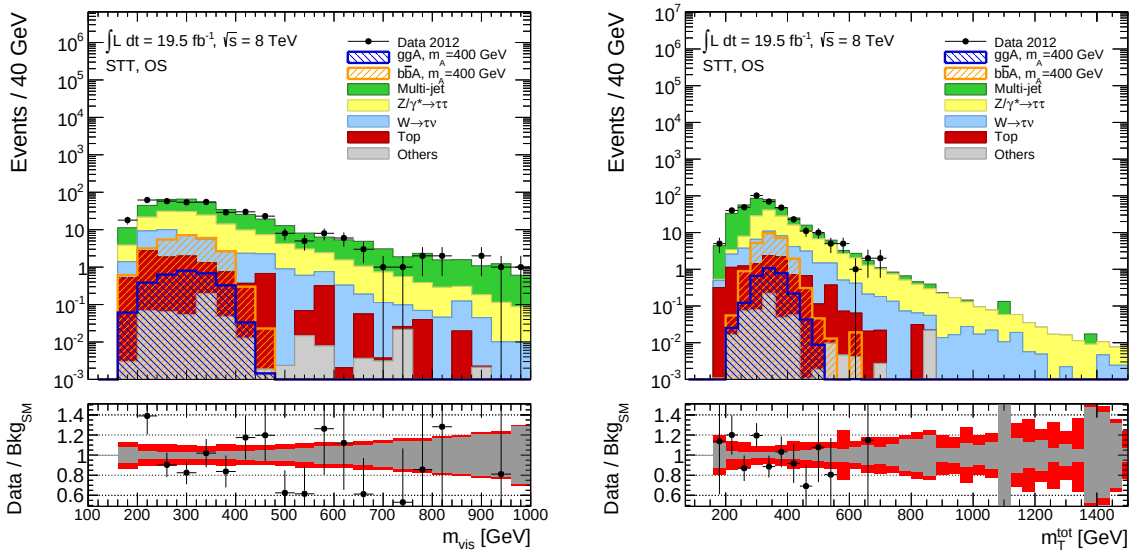

Figure 7.64: Distributions of m^{vis} (left) and $m_{\text{T}}^{\text{tot}}$ (right) in the STT signal region. The lower plots illustrate the ratio between the data and the total expected background. The grey band shows the statistical uncertainty on the expected background and the red one the effect of all systematic uncertainties added quadratically. The signal is estimated assuming $\tan\beta = 20$ in the m_h^{max} scenario.

	STT Selection		
	Single-tau trigger	$p_{\text{T}}(\tau_{\text{lead}}) > 150$ GeV	Loose tau-ID
Background			
Multi-jet	60178 ± 245	33322 ± 182	216.1 ± 3.3
$Z/\gamma^* \to \tau\tau$	952 ± 90	485 ± 27	113.3 ± 2.4
$W \to \tau\nu$	35383 ± 280	3349 ± 48	33.6 ± 1.0
Top	17325 ± 231	1792 ± 73	10.2 ± 1.4
Others	7268 ± 174	475 ± 70	0.54 ± 0.19
Signal ($m_A = 400$ GeV, $\tan\beta = 20$)			
$b\bar{b} \to A$	42.78 ± 0.74	32.97 ± 0.65	25.31 ± 0.56
$gg \to A$	4.914 ± 0.090	3.873 ± 0.080	2.926 ± 0.068
Data	60178 ± 245	33322 ± 182	373 ± 19
Total SM	121106 ± 479	39423 ± 215	373.7 ± 4.4

Table 7.18: Event yields for the background contributions and the data at each stage of the selection in the STT category. The quoted uncertainty is statistical. The multi-jet background is estimated only at the final step of the selection. The expected number of signal events is determined assuming the m_h^{max} scenario.

	STT Systematic Uncertainties [%]							
	Multi-jet	$Z/\gamma^* \to \tau\tau$	$W \to \tau\nu$	Top	Others	Total SM	$b\bar{b} \to \phi$	$gg \to \phi$
Expected Events	216.1 ± 3.3	113.3 ± 2.4	33.6 ± 1.0	10.2 ± 1.4	0.54 ± 0.19	373.7 ± 4.4	25.31 ± 0.56	2.926 ± 0.068
Fake Factor	±11.3	-	-	-	-	±6.6	-	-
TES true tau	-	+7.2	+5.9	+20.3	-	±2.3	+6.1	+6.6
	-	-6.1	-3.8	-9.0	-		-6.7	-6.0
TES fake tau	-	+0.6	+6.9	+3.2	+5.4	±0.7	-	-
	-	-0.1	-5.8	-1.4	-8.0		-	-
Trigger high-p_T	-	±9.8	±2.4	±7.5	-	±3.0	±10.0	±10.0
Tau-ID	-	±6.5	±3.4	±5.2	±0.3	±2.0	+6.5	+6.5
	-						-6.3	-6.3
Mis-ID reweighting	-	±1.7	+14.8	+33.0	+21.0	±1.3	-	-
	-		-12.8	-28.0	-14.7		-	-
Track reco. eff.	-	±0.7	±0.2	±0.4	-	±0.2	±0.4	±0.4
Cross-section	-	+4.32	±6.0	±8.9	±4.8	±1.4	+13.3	+18.7
	-	-3.54	-	-	-		-15.1	-16.8
Acceptance	-	±6.3	±14.7	-	-	±2.3	±13.2	±1.5
	-			-	-			

Table 7.19: Systematic uncertainties in the STT category presented as a relative variation in the expected number of events for each contribution. The chosen signal point is m_A = 400 GeV and tanβ = 20. Systematic uncertainties discussed in the main text that are negligible in the STT category are not included. The upward and downward variations in the event yield are shown in the upper and lower rows, respectively, for the case of asymmetric systematic effects. Each uncertainty is also propagated to the total SM expectation.

As can be seen in Fig. 7.56, a local excess of events is present in the data in the pseudo-rapidity distribution of the two tau leptons for $\eta_{\tau_{\text{lead/sub-lead}}} \approx 0.4$ in the DTT signal region. This feature, albeit not significant for the sensitivity and well within the total uncertainties, is addressed in Sec. 7.9.1.

7.9.1 Pseudo-rapidity Distributions in the DTT Category

The pseudo-rapidity distributions of the leading and sub-leading tau leptons in the DTT category show an excess of events in the range $\eta \in [0, 0.6]$. This effect does not lead to an excess when the final hypothesis test is performed. However, it is important to investigate whether it has an impact on the sensitivity of the analysis, or, in other words, if the m_T^{tot} distribution is affected by this excess. To do so, the ABCD method illustrated in Sec. 7.5 is altered, and the $R_{\text{OS/SS}}$ factor is measured in 16 exclusive regions of η, dividing the η distributions for each tau lepton in four regions defined by the boundaries $\eta < -1$, $\eta \in [-1, 0]$, $\eta \in [0, 1]$ and $\eta > 1$. The measured factors are illustrated in Fig. 7.65. They are applied to the distributions in each of the exclusive regions, which are then summed to obtain the total multi-jet estimation in the signal region. This leads to the η distributions shown in Fig. 7.66. As can be seen in the

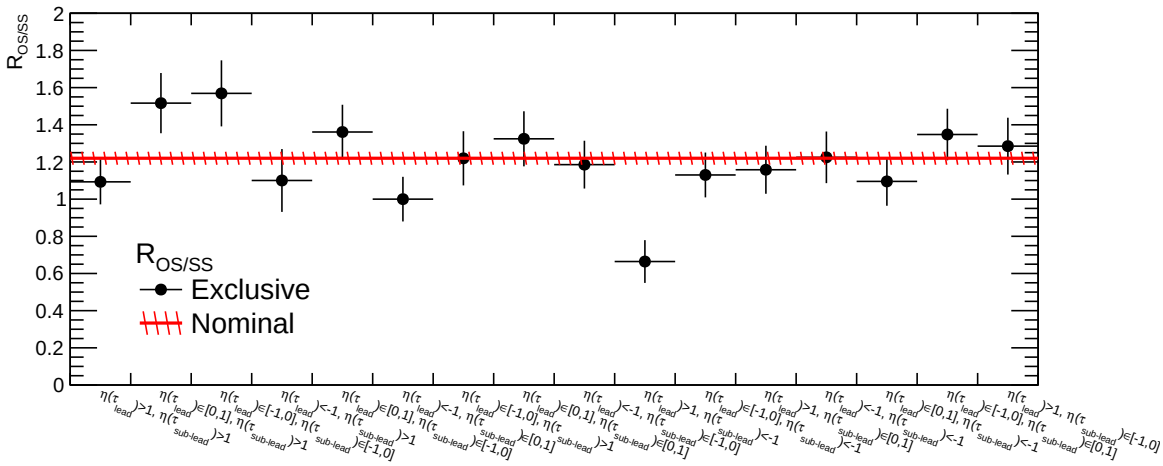

Figure 7.65: $R_{\text{OS/SS}}$ factors measured in exclusive regions of η for the leading and sub-leading tau candidates. The statistical uncertainty is shown for each point. The plot includes the nominal value of $R_{\text{OS/SS}}$ measured over the η range, with its statistical uncertainty.

figures, the expected backgrounds show a better agreement with the data than in the nominal estimation. However, the $m_{\text{T}}^{\text{tot}}$ distribution obtained with this alternative method does not show a significant difference with respect to the nominal one, as can be seen in Fig. 7.67. As no significant difference is observed in the variable used for the hypothesis test, no change in the nominal sensitivity is expected.

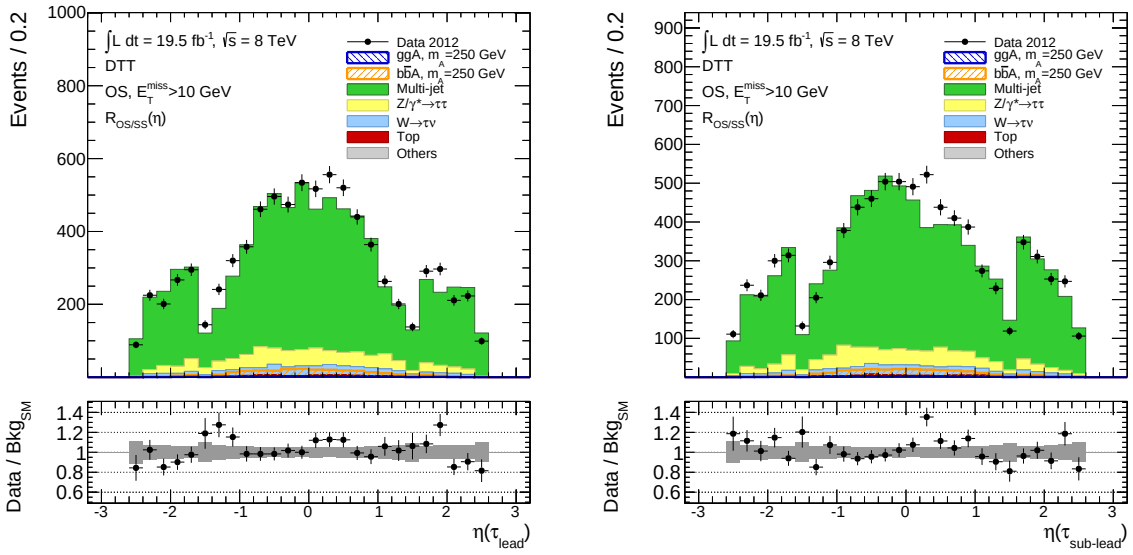

Figure 7.66: Distributions of $\eta(\tau)$ for the leading (left) and sub-leading (right) candidates in the DTT signal region, where the multi-jet contribution is estimated measuring $R_{\mathrm{OS/SS}}$ in exclusive η regions. The lower plots illustrate the ratio between the data and the total expected background. Only the statistical uncertainty is shown. The signal contamination is estimated assuming $\tan\beta = 20$ in the m_h^{max} scenario.

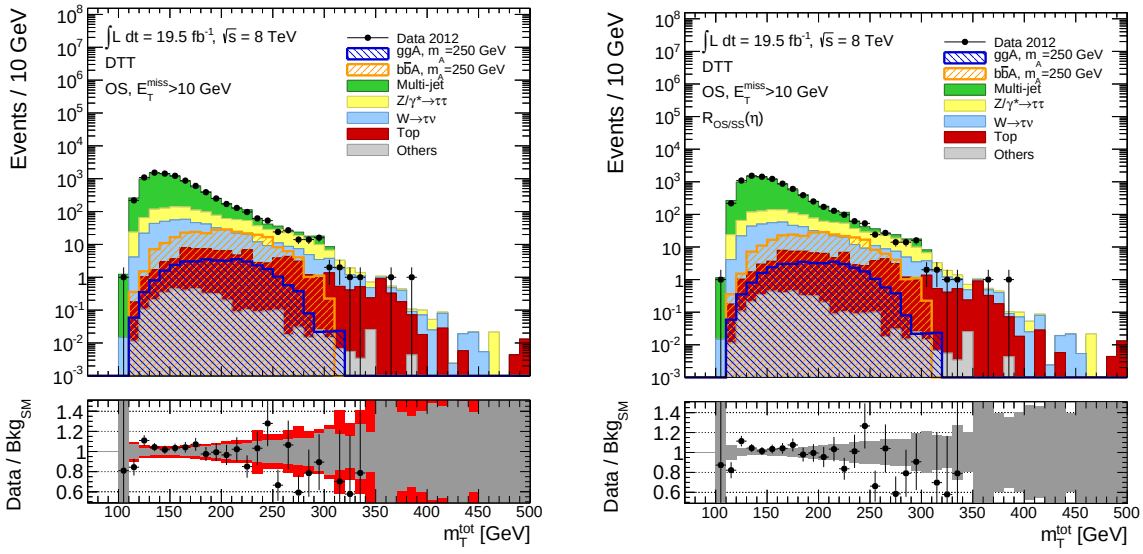

Figure 7.67: Distributions of $m_{\mathrm{T}}^{\mathrm{tot}}$ for the nominal multi-jet estimation technique (left) and the altered one (right), where $R_{\mathrm{OS/SS}}$ is measured in exclusive regions of η. Only the statistical uncertainty is shown in the lower plot on the right.

CHAPTER 8

Exclusion Limits

In the present chapter the background prediction and the signal hypothesis are compared to data for the selected sample and the background estimates discussed in the previous chapter to check if a significant excess in data is present. This comparison, called *hypothesis testing*, is based on principles discussed in Sec. 8.1. The signal hypothesis is tested in the (m_A, tanβ) plane, rejecting portions of it incompatible with the observed data. As a result, an *exclusion limit* in the (m_A, tanβ) plane is set. Hypothesis testing is implemented in the analysis using a fit, whose model is discussed in Sec. 8.2. The final results are illustrated in Sec. 8.3, and the fit is validated as presented in Sec. 8.4. The results presented in this chapter are documented in Ref. [178].

8.1 Hypothesis Testing

In this section, all the fundamental quantities necessary for the evaluation of exclusion limits are introduced. They pertain the underlying procedure of hypothesis testing, where the outcome depends on the assumed confidence level, which is going to be introduced at the end of this section.

Hypothesis testing [18, 87] quantifies the agreement between the observed outcome of an experiment and the expectation by evaluating a probability called *p-value* [87]. This number depends on the assumptions we make on the expectation and will be computed in the following using the distributions obtained in the previous chapter. We can write the number of expected events in these distributions as

$$\mathrm{E}[n_i] = \mu s_i + b_i \tag{8.1}$$

where $\mathrm{E}[n_i]$ is the expected number of events in bin number i of the histograms while s_i and b_i are the number of expected signal and background events, respectively. The expected number of signal events is scaled by the factor μ, called the *signal strength*, which quantifies the abundance of the signal, and assumes values between 0 and 1, representing the absence of any signal and the nominal expectation, respectively. We can write the p-value for a certain value of μ as

$$p_\mu = P(q_\mu \geq q_{\mu,\mathrm{obs}}|\mu) = \int_{q_{\mu,\mathrm{obs}}}^{\infty} f(q_\mu|\mu)\mathrm{d}q_\mu. \tag{8.2}$$

In Eq. (8.2), the variable q_μ, called a *test statistic*, depends on μ and quantifies the agreement between the model and the data. The definition of q_μ will be presented later in this chapter. This variable is distributed according to the probability density $f(q_\mu|\mu)$, which describes the distribution of q_μ under the assumption

of a certain signal strength. Assuming that this function is known, hypothesis testing relies on an estimate of $q_{\mu,\text{obs}}$, which is the value of the test statistic computed using the data collected by the experiment. In the limits that will be presented later, results based on $q_{\mu,\text{obs}}$ will be called *observed exclusion*.

The test statistic assumes positive values by definition. Larger values of $q_{\mu,\text{obs}}$, or smaller p-values, indicate worse compatibility between the data and the model. A qualitative illustration of how p-values are computed can be seen in Fig. 8.1 on the left. In particle physics, p-values are typically converted into a corresponding significance Z, utilised to quantify potential excesses in data. It is defined as

$$Z = \Phi^{-1}(1 - p), \tag{8.3}$$

where Φ^{-1} is the inverse of the cumulative distribution of a standard Gaussian function [18, 87]. It follows that Z can be measured in units of a Gaussian standard deviation σ.

The previously defined variables are useful to introduce the concept of *confidence level* (CL) [87], which is a probability defined as

$$\text{CL} = 1 - p', \tag{8.4}$$

where p', called the *significance level*, is computed as illustrated in Eq. (8.2), but replacing the lower bound of the integral with a predefined threshold $q_{\mu,\text{thr}}$, and corresponds to the probability of wrongly rejecting the hypothesis. A confidence level CL= 95% is chosen to exclude the presence of signal in data. In terms of p-values, this corresponds to $p_\mu < 0.05$, relative to the hypothesis that some signal is present in data in addition to the background, i.e. $\mu > 0$, which will be indicated as H_{s+b}.

Stricter requirements on the confidence level are placed for discovery than for signal exclusion. A discovery is based on the rejection of the *background-only* hypothesis, indicated as H_b, corresponding to $\mu = 0$. If the observed p-value for H_b, called p_0, is found to be below a certain threshold, a significant excess is regarded to be present in the data, which might indicate new physics. The particle physics community has agreed to establish such threshold at $p = 2.87 \times 10^{-7}$, or $Z = 5\sigma$. This corresponds to a confidence level of CL= 99.99994%. The estimate of p_0 is performed with the distribution $f(q_0|0)$ and estimating $q_{0,\text{obs}}$. It is important to notice that q_0 is not necessarily a special case of q_μ with $\mu = 0$.

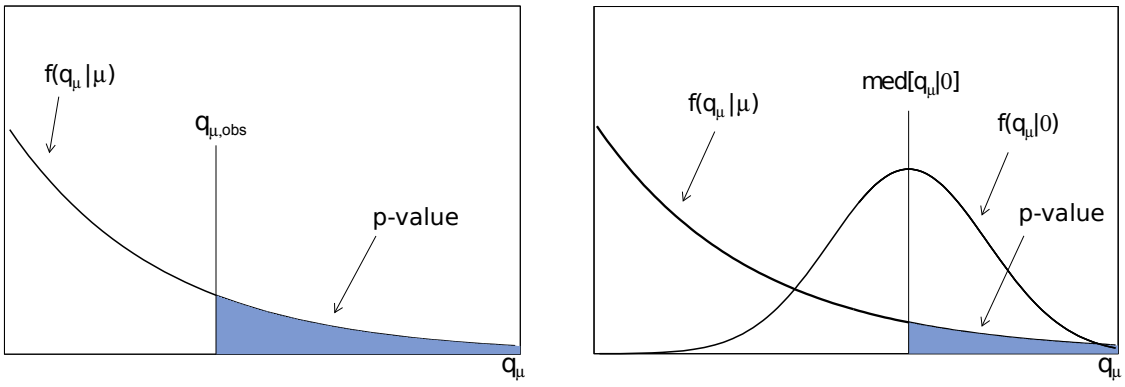

Figure 8.1: Qualitative examples of different evaluations of the p-values in the case of the observed limit (left) and the expected one (right). The plots are taken from Ref. [223].

8.1.1 Sensitivity of a Search

The limits that will be presented in the following will include an *expected exclusion*, which depends on the sensitivity of the search. The sensitivity quantifies our ability to reject a signal hypothesis in case only background is present in the data. It is estimated by comparing the distribution of q_μ for $\mu = 0$ with the corresponding distributions for all other assumptions, as illustrated in Fig. 8.1 on the right for a generic signal strength μ. The median [18, 87] of the distributions $f(q_\mu|0)$ is computed, and a p-value is estimated for $f(q_\mu|\mu)$ by using such median instead of $q_{\mu,\text{obs}}$. As for the case of signal exclusion, we can decide to set CL= 95%. The μ value corresponding to $p_\mu \leq p'$ is excluded.

In the limits that will be presented, a standard deviation is assigned to the expected exclusion, corresponding to two bands at the $\pm 1\sigma$ and $\pm 2\sigma$ levels. These are obtained by considering the values of the test statistic that correspond to the appropriate quantiles of the $f(q_\mu|0)$ distribution, instead of its median.

8.1.2 Definition of Test Statistic

After discussing the principles of hypothesis testing and introducing the quantities that characterise exclusion limits, the problem remains how to define and compute the test statistic.

Assuming that the expectation for the signal and background does not depend on any parameter, like for instance μ in Eq. (8.1), the *Neyman-Person* lemma [224] can be used for the definition of the most powerful test statistic. This power can be quantified as follows. Assuming a generic hypothesis H_α and a certain confidence level, we define a threshold value q_{thr} for a test statistic q such that $P(q < q_{\text{thr}}|H_\alpha) = p'$. We assume an alternative hypothesis H_β, which is accepted if $q > q_{\text{thr}}$, rejecting H_α. We would like to achieve a minimal value for the probability $P(q \geq q_{\text{thr}}|H_\beta)$, corresponding to a high test power. This is possible if

$$q = \frac{\mathcal{L}(H_\alpha)}{\mathcal{L}(H_\beta)}, \tag{8.5}$$

where $\mathcal{L}$ is the so-called *likelihood* [87]. For our purposes, we would like to parametrise both hypotheses H_{s+b} and H_b as a function of μ. We then define the likelihood

$$\mathcal{L}(\mu) = \prod_{i=1}^{N_{\text{bins}}} \text{Pois}(n_i|\mu s_i + b_i) = \prod_{i=1}^{N_{\text{bins}}} \frac{(\mu s_i + b_i)^{n_i}}{n_i!} e^{-(\mu s_i + b_i)}. \tag{8.6}$$

In Eq. (8.6), $\text{Pois}(n_i|\mu s_i + b_i)$ is the *Poisson probability* [87] of observing n_i events in each bin of the data histogram while expecting $\mu s_i + b_i$ events.

Using the Neyman-Person lemma, the optimal choice for the definition of a test statistic suitable for setting exclusion limits has been investigated in Ref. [223], addressing the problem of parametrising any hypothesis, including a variable signal strength and a set of uncertainties. The effect of the systematic and statistical uncertainties can be incorporated in the likelihood. This alters the expression of the signal and the background event yield in each of the bins, which can be written as $s_i(\boldsymbol{\theta})$ and $b_i(\boldsymbol{\theta})$ where the vector $\boldsymbol{\theta}$ is introduced to parametrise the effect of the uncertainties. The definition of $\boldsymbol{\theta}$ will be discussed later. Each element of this vector is usually referred to as a *nuisance parameter* (NP). In general, different sets of nuisance parameters could affect different contributions, so the most general notation would be $s_i(\boldsymbol{\theta}_s)$ and $b_i(\boldsymbol{\theta}_b) = b_{1,i}(\boldsymbol{\theta}_{b_1}) + ... + b_{N_{\text{bkg}},i}(\boldsymbol{\theta}_{b_{N_{\text{bkg}}}})$, where the sum of all backgrounds is considered. However, here the same vector of nuisance parameters has been written for the signal and the background to reduce clutter.

Uncertainties are constrained in the likelihood depending on their nominal bound. This is done by

introducing an auxiliary multiplicative term which only depends on the vector $\boldsymbol{\theta}$. This term could be viewed as the contribution to the analysis of all those auxiliary measurements performed to constrain the uncertainties. For example, in the case of an auxiliary tag-and-probe technique for the measurement of a systematic uncertainty, this approach corresponds to considering the histograms utilised by the tag-and-probe measurement as coming from a control region of the analysis. However, to simplify things, these are treated as correlated with the signal region only via the nuisance parameters corresponding to the uncertainties that the tag-and-probe method constrains. As a consequence, in the most general formalism, the auxiliary likelihood will have a Poissonian form. The total likelihood is then defined as

$$\mathcal{L}_(\mu, \boldsymbol{\theta}) = \mathcal{L}_{\text{nom}}(\mu, \boldsymbol{\theta}) \times \mathcal{L}_{\text{aux}}(\boldsymbol{\theta}) = \prod_{i=1}^{N_{\text{bins}}} \frac{(\mu s_i(\boldsymbol{\theta}) + b_i(\boldsymbol{\theta}))^{n_i}}{n_i!} e^{-(\mu s_i(\boldsymbol{\theta}) + b_i(\boldsymbol{\theta}))} \times \prod_{j=1}^{M_{\text{bins}}} \frac{a_j(\boldsymbol{\theta})^{m_j}}{m_j!} e^{-a_j(\boldsymbol{\theta})}, \quad (8.7)$$

where the dependence of the signal and the background on $\boldsymbol{\theta}$ has been highlighted in the nominal likelihood and in the auxiliary one. In the latter, $\mathrm{E}[m_j] = a_j(\boldsymbol{\theta})$ is the expected number of events in bin j of the distributions of the auxiliary measurement. In practice, approximations are used for the form of $\mathcal{L}_{\text{aux}}(\boldsymbol{\theta})$ used in the actual fit, which will be introduced later.

We define the quantity

$$\lambda(\mu) = \frac{\mathcal{L}(\mu, \hat{\hat{\boldsymbol{\theta}}})}{\mathcal{L}(\hat{\mu}, \hat{\boldsymbol{\theta}})}, \quad (8.8)$$

called the *profile likelihood ratio* [87, 223]. In Eq. (8.8), the symbol $\hat{\hat{\boldsymbol{\theta}}}$ indicates the set of nuisance parameters which maximises $\mathcal{L}(\mu, \boldsymbol{\theta})$ for a fixed value of μ. It depends on μ and is called a *conditional maximum-likelihood estimate* [87] of the nuisance parameters. The quantities $\hat{\mu}$ and $\hat{\boldsymbol{\theta}}$ are the μ and $\boldsymbol{\theta}$ values which maximise $\mathcal{L}(\mu, \boldsymbol{\theta})$, respectively, and do not depend on each other. This is called an *unconditional maximum-likelihood estimate* of the parameters. We notice that $\hat{\mu}$ is an effective estimator of μ and is not constrained to be positive.

Using the profile likelihood ratio, a test statistic has been proposed in Ref. [223], which is used by the ATLAS experiment to set exclusion limits:

$$q_\mu = \begin{cases} -2\ln\left[\mathcal{L}\left(\mu, \hat{\hat{\boldsymbol{\theta}}}(\mu)\right) / \mathcal{L}\left(0, \hat{\boldsymbol{\theta}}(0)\right)\right], & \text{if } \hat{\mu} < 0 \\ -2\ln\left[\mathcal{L}\left(\mu, \hat{\hat{\boldsymbol{\theta}}}(\mu)\right) / \mathcal{L}\left(\hat{\mu}, \hat{\boldsymbol{\theta}}\right)\right], & \text{if } 0 \leq \hat{\mu} \leq \mu \\ 0, & \text{if } \hat{\mu} > \mu \end{cases} \quad (8.9)$$

No general rule can be formulated for the optimal definition of a test statistic depending on a set of parameters. However, approximations can be made for the functional form of Eq. (8.8) for a sufficiently large data sample. This result, called the *Wald approximation* [225], shows that q_μ is a monotonic function of $\hat{\mu}$, as well as q. This means it is optimal in the absence of uncertainties, or approximately so for well constrained ones.

The Wald approximation also allows one to express the observed and expected upper limits on the signal strength μ_{up}, obtained with q_μ for a certain confidence level, which can be written as

$$\mu_{\text{up}}^{\text{obs}} = \hat{\mu} + \sigma\Phi^{-1}(1 - p') \quad (8.10a)$$

$$\mu_{\text{up}}^{\text{exp}\pm N\sigma} = \mu + \sigma\left(\Phi^{-1}(1 - p') \pm N\right). \quad (8.10b)$$

Here σ is the standard deviation of the distribution of $\hat{\mu}$, which is Gaussian. Asymptotic formulae also allow one to express σ as a function of $\hat{\mu}$. In Eq. (8.10), N indicates the number of standard deviations

considered for the expected exclusion and μ the hypothesised signal strength.

Expressions for the distributions of q_μ are also obtained using the Wald approximation and are reported in Ref. [223]. In the following we will refer to these results as *asymptotic formulae* for q_μ. These formulae greatly simplify the limit setting procedure, which in the most general formulation would require the generation of a large number of simulated experiments in order to obtain the distributions.

8.1.3 Method for Exclusion

The previous sections illustrate the general procedure of hypothesis testing. However, specific methods have been formulated to address problems recurring in particle physics. For this search a particular technique called CL_s *method* [226] is used. This method has been formulated to prevent spurious signal exclusions in situations where the distributions $f(q_\mu|\mu)$ and $f(q_\mu|0)$ are not well separated from each other, i.e. when the distribution of q_μ under the signal+background hypothesis is very similar compared to the one in the background-only prediction. In such cases, it is preferable to base the test not on the usual p-value alone, but to compare its value to another quantity related to the background-only distribution. For this reason we define the following variable:

$$\mathrm{CL}_s = \frac{p_\mu}{1 - p_b}. \tag{8.11}$$

In Eq. (8.11), the variable p_b is defined as the integral of $f(q_\mu|0)$ in the range $q_\mu \in [0, q_{\mu,\mathrm{obs}}]$. In Fig. 8.2, a qualitative example is shown of how CL_s is computed. It is easy to see that when the two distributions

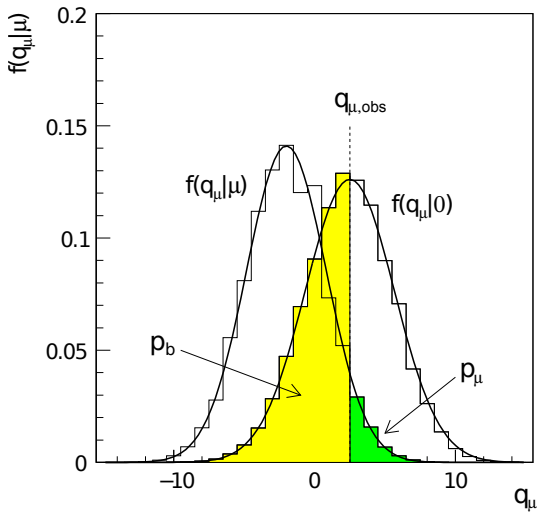

Figure 8.2: Qualitative example of how the CL_s value is determined. The plot includes the distribution of the test statistic in the case of the background-only hypothesis $f(q_\mu|0)$, and the signal+background one $f(q_\mu|\mu)$ The plot is taken from Ref. [223].

in Fig. 8.2 approach each other, the CL_s value increases. For the exclusion limits presented in this chapter, the CL_s value, rather than p_μ, is compared to the significance level p' to reject the signal hypothesis. This is done assuming a confidence level of 95%, i.e. excluding the signal hypothesis when $\mathrm{CL}_s < 0.05$.

8.2 Fit Model

The procedure outlined in the previous sections is implemented in this analysis using fits of the estimated signal and background distributions to the observed data. The definition of the test statistic relies on the profile likelihood ratio defined in Eq. (8.8), hence, likelihood fits are used. These fits estimate the unconditional parameters, $\hat{\mu}$ and $\hat{\boldsymbol{\theta}}$, and the conditional one, $\hat{\hat{\boldsymbol{\theta}}}$, by maximising the respective likelihood functions in which they appear, for each hypothesis of μ. This method is referred to as the *maximum likelihood estimate* (MLE) [87] of the parameters. The contribution of different histograms from the different signal regions in the DTT and STT categories is included simultaneously in the fit by simply defining a combined product likelihood:

$$\mathcal{L}_{\text{comb}}(\mu, \boldsymbol{\theta}) = \mathcal{L}_{\text{DTT}}(\mu, \boldsymbol{\theta}_{\text{DTT}}) \times \mathcal{L}_{\text{STT}}(\mu, \boldsymbol{\theta}_{\text{STT}}). \tag{8.12}$$

The form of Eq. (8.12), implies that the fit procedure takes correctly into account systematic correlations across different bins or channels of the analysis, which might depend on the same nuisance parameter.

In order to simplify the numerical treatment of the maximisation procedure and guarantee the same result, the likelihood functions are transformed monotonically according to $\mathcal{L} \rightarrow -2\ln(\mathcal{L})$ (*negative log-likelihood*, NLL). The principle of MLE then corresponds to the minimisation of the NLL. The procedure is now simplified, as a product has been transformed into a sum, and exponential terms into simple factors. Later in the chapter, likelihood profiles will be shown, whose minima correspond to the best estimate of the parameters.

The NP vector $\boldsymbol{\theta}$ can be divided into two components, which we will call $\boldsymbol{\alpha}$, for the modelling of the systematic uncertainties, and $\boldsymbol{\gamma}$ for the treatment of the statistical ones. The following two sections illustrate how these two vectors affect the model of the signal and backgrounds in Eq. (8.7) and how the auxiliary likelihood term is defined. These notions will be used when discussing the validation of the fit performed to obtain the exclusion limits.

8.2.1 Model of Systematic Uncertainties

First of all, we discuss the dependence of the signal and the background on the nuisance parameters associated to the systematic uncertainties, arranged in the vector $\boldsymbol{\alpha}$. By definition, the nominal expected number of events in each bin of the signal regions corresponds to the choice $\alpha_k = 0$ for each element of $\boldsymbol{\alpha} = (\alpha_1, ..., \alpha_{N_{\text{sys}}})$. We will call this number of events c_i^0, for a generic contribution c. In addition, the systematic variation within one standard deviation of each uncertainty presented in Sec. 7.8 is represented by the values $\alpha_k = \pm 1$ corresponding to an upward and downward variation, respectively.

The nuisance parameters can affect both the normalisation and the shape of the $m_{\text{T}}^{\text{tot}}$ distributions of the signal and the background. If we take into account both effects simultaneously at the 1σ level, we can define the expected number of events in each bin i of the distributions as $c_{i,k}^{\pm}$, relative to the uncertainty k. An upward or downward variation in the number of events does not necessarily correspond to a shift in α_k in the same direction.

A computational scheme has to be provided in order to parametrise the variation in the number of events as a function of $\boldsymbol{\alpha}$. The appropriate choices of these schemes for both the shape and the normalisation effects are discussed in Ref. [227] and are referred to as the *piecewise linear* $L(\boldsymbol{\alpha})$ and *exponential* $E(\boldsymbol{\alpha})$

interpolations, respectively. They are defined by the following equations:

$$c_i(\boldsymbol{\alpha}) = \underbrace{\left(c_i^0 + \sum_{k=1}^{N_{\text{sys}}} L_{i,k}(\alpha_k)\right)}_{\text{shape effect}} \underbrace{\left(\prod_{k=1}^{N_{\text{sys}}} E_k(\alpha_k)\right)}_{\text{normalisation effect}} \tag{8.13}$$

where

$$L_{i,k}(\alpha_k) = \begin{cases} \alpha_k(\phi_k^+ c_{i,k}^+ - c_i^0), & \text{if } \alpha_k \geq 0 \\ \alpha_k(c_i^0 - \phi_k^- c_{i,k}^-), & \text{if } \alpha_k < 0 \end{cases} \tag{8.14}$$

$$\phi_k^+ = \sum_{i=1}^{N_{\text{bins}}} c_i^0 \Big/ \sum_{i=1}^{N_{\text{bins}}} c_{i,k}^+ \tag{8.15a}$$

$$\phi_k^- = \sum_{i=1}^{N_{\text{bins}}} c_i^0 \Big/ \sum_{i=1}^{N_{\text{bins}}} c_{i,k}^- \tag{8.15b}$$

and

$$E_k(\alpha_k) = \begin{cases} \left(\sum_{i=1}^{N_{\text{bins}}} c_{i,k}^+ \Big/ \sum_{i=1}^{N_{\text{bins}}} c_i^0\right)^{\alpha_k}, & \text{if } \alpha_k \geq 0 \\ \left(\sum_{i=1}^{N_{\text{bins}}} c_i^0 \Big/ \sum_{i=1}^{N_{\text{bins}}} c_{i,k}^-\right)^{\alpha_k}, & \text{if } \alpha_k < 0 \end{cases} \tag{8.16}$$

The factors $\phi_k^\pm$ are defined in order to maintain the normalisation of the original distributions once the linear interpolation is applied.

The total likelihood in Eq. (8.7) includes an auxiliary factor $\mathcal{L}_{\text{aux}}(\boldsymbol{\theta})$. As far as systematic uncertainties are concerned, this portion of the total likelihood represents a constraint on the nuisance parameters determined by the set of auxiliary measurements which estimate the $\pm 1\sigma$ systematic effect, as already illustrated in Sec. 8.1.2. In general, a Poissonian constraint should be used to incorporate these measurements into the main analysis, as previously illustrated. However, this is an extremely unpractical procedure. The effect of the auxiliary measurements is modelled by assuming that only the relevant nuisance parameters constrained by those measurements are correlated with the signal region of the analysis. As a result, only those parameters are considered to enter the expression of $\mathcal{L}_{\text{aux}}(\boldsymbol{\theta})$. Also, the *central limit theorem* [87] is used to approximate the Poissonian form of each auxiliary constraint. Each NP is then allowed to vary according to a Gaussian distribution centered at the nominal value and variance determined by the auxiliary measurement. According to our parametrisation of the nuisance parameters these nominal values and variances correspond to 0 and 1, respectively. We can therefore write

$$\mathcal{L}_{\text{sys}}(\boldsymbol{\alpha}) = \prod_{k=1}^{N_{\text{sys}}} \text{Gauss}(\alpha_k|0,1) = \prod_{k=1}^{N_{\text{sys}}} \frac{e^{-\alpha_k^2/2}}{\sqrt{2\pi}}, \tag{8.17}$$

where $\text{Gauss}(\alpha_k|0,1)$ represents a Gaussian distribution centered at zero with unit variance.

8.2.2 Model of Statistical Uncertainties

The effect of the statistical uncertainties can be modelled by an additional set of nuisance parameters, which we will call $\boldsymbol{\gamma}$. In the most general fit model, a different vector for each contribution should be considered. However, this would considerably complicate the fitting procedure. Therefore, a single

nuisance parameter is assumed to represent the statistical fluctuations in the number of events for the sum of all backgrounds in each bin. This approximation is summarised by the following equation:

$$b_i(\boldsymbol{\alpha}, \boldsymbol{\gamma}_i) = b_{1,i}(\boldsymbol{\alpha}, \gamma_{b_1,i}) + ... + b_{N_{\text{bkg}},i}(\boldsymbol{\alpha}, \gamma_{b_{N_{\text{bkg}},i}}) = \gamma_i \left(b_{1,i}(\boldsymbol{\alpha}) + ... + b_{N_{\text{bkg}},i}(\boldsymbol{\alpha}) \right) = \gamma_i b_i(\boldsymbol{\alpha}). \tag{8.18}$$

To further simplify the model, only bins where the statistical uncertainty is larger than 5% are considered for the introduction of a corresponding γ_i. This simplifies the fit and has negligible impact on the result [227]. In addition, no statistical uncertainty is considered for signal events, which are characterised by smaller statistical uncertainties than the background.

For the systematic uncertainties, each component of $\boldsymbol{\gamma}$ has to be constrained with a term which will appear in $\mathcal{L}_{\text{aux}}(\boldsymbol{\theta})$. This is done using a very similar approach to the one illustrated in Sec. 8.2.1 and leading to Eq. (8.17).

Each background contribution can be thought of as the sum of weighted events. The weights could come from background estimation techniques, e.g. the tau mis-identification probabilities, or correspond to overall multiplicative factors, such as the luminosity, applied to simulated events. Unweighted background events b' could be thought of as representing auxiliary measurements following a Poissonian distribution with expectation value $\mathrm{E}[b_i'] = \gamma_i b_i'$ for the number of events in each bin i. This Poissonian constraint would enter the expression of $\mathcal{L}_{\text{aux}}(\boldsymbol{\theta})$. However, an approximation has to be made for b_i'. As this number of events is usually unknown, the statistical uncertainty in each bin, σ_i, is used to estimate it. This leads to

$$b_i' = \frac{1}{\sigma_i^2}, \tag{8.19}$$

which is true for all Poissonian-distributed numbers of events. In Eq. (8.19), b_i' is the sum of all backgrounds. This treatment of the constraint is also consistent under the assumption that all weights applied to the backgrounds act as an effective overall rescaling of the total background distribution.

The value of b_i' determined in Eq. (8.19) is not an integer, inconsistent with the assumption of a Poissonian distribution. To resolve this problem, a different constraint is assumed for the auxiliary measurement, namely a Gamma distribution [87, 227] is utilised. We therefore obtain

$$\mathcal{L}_{\text{stat}}(\boldsymbol{\gamma}) = \prod_{j=1}^{N_{\text{stat}}} \text{Gamma}\left(\gamma_j \middle| b_j' + 1, \frac{1}{b_j'}\right) = \prod_{j=1}^{N_{\text{stat}}} \frac{{\gamma_j}^{b_j'} e^{-\gamma_j}}{\Gamma(b_j' + 1)}, \tag{8.20}$$

where the index j runs over all N_{stat} elements of the $\boldsymbol{\gamma}$ vector, a subset of the number of bins, and $\Gamma(x) = \int_0^\infty u^{x-1} e^{-u} \mathrm{d}u$.

Having obtained the expression for the auxiliary constraint on the systematic and statistical nuisance parameters, the full auxiliary likelihood term appearing in Eq. (8.7) can be expressed as

$$\mathcal{L}_{\text{aux}}(\boldsymbol{\theta}) = \mathcal{L}_{\text{sys}}(\boldsymbol{\alpha}) \times \mathcal{L}_{\text{stat}}(\boldsymbol{\gamma}). \tag{8.21}$$

8.2.3 Fitting Procedure

Before presenting the results a few details will be given in this section regarding the fitting procedure.

Observed and Expected Exclusion

In the following, the exclusion limits will be presented for a 95% confidence level for the hypothesis test. The plots will include the observed and expected exclusion limits. The observed limit is the result of the procedure outlined in Sec. 8.1, where the value of $q_{\mu,\text{obs}}$ is determined using a likelihood fit to data for a certain hypothesis of μ. In practice, this involves two likelihood fits, conditional and unconditional, to determine the numerator and denominator of $\lambda(\mu)$ in Eq. (8.8), respectively, which enters in the definition of q_μ in Eq. (8.9).

The expected exclusion limit depends on the sensitivity of a search, introduced in Sec. 8.1.1. The procedure outlined there requires the estimation of the median of the distribution $f(q_\mu|0)$. As illustrated in Ref. [223], asymptotic formulae can be used to approximate this value, greatly simplifying the test procedure. In practice, the median value med$[f(q_\mu|0)]$ is obtained by using a fit to the so-called *Asimov dataset* [223]. This dataset is defined as the sum of all expected backgrounds in correspondence of the estimate of $\boldsymbol{\theta}$ resulting from a conditional fit to data assuming $\mu = 0$, which can be written as $\boldsymbol{\theta}_{\text{Asimov}} = \hat{\hat{\boldsymbol{\theta}}}(\mu = 0)$. The usage of the Asimov dataset greatly simplifies the standard procedure for hypothesis testing, where the distribution of $f(q_\mu|0)$ should be obtained using a *pseudo-experiment approach* which is computationally demanding. This procedure will be described in the following, and it is used to validate the fit results for only one m_A and tanβ point.

Treatment of Systematic Uncertainties

As illustrated in Sec. 8.2.1, systematic uncertainties could affect the normalisation and the shape of the expected distributions. In the fit model, shape uncertainties are considered based on a compatibility test between the upward and downward altered distributions and the nominal one for each expected signal and background sample. The compatibility is measured using the *Kolmogorov-Smirnov* test [87], based on the evaluation of the probability for two distributions to arise from the same probability density, p_{KS}. For each signal and background contribution all systematic effects are tested against the nominal expectation. If $p_{\text{KS}} < 0.8$, the systematic effect is implemented in the fit model also as a shape uncertainty, as discussed in Sec. 8.2.1. Fig. 8.3, shows an example of signal distributions in the DTT (left) and STT (right) categories, where the TES alteration leads to a significant shift in the $m_{\text{T}}^{\text{tot}}$ shape. Significant alterations of the shape are only observed for the signal distribution in both categories and relative to the TES and trigger uncertainties. As a consequence, no shape systematic uncertainty is implemented for any of the backgrounds except for the shape uncertainty associated with the $R_{\text{OS/SS}}$ transfer factor for the rescaling of the multi-jet contribution in the DTT category, discussed in Sec. 7.5.1. Despite the high value of $p_{\text{KS}} \approx 0.9$ measured for this shape alteration, this choice is motivated by a conservative approach on the multi-jet estimate in the DTT category.

In the following, a series of plots and studies will be presented to investigate the modelling of the nuisance parameters in the fit. For reference, Tab. 8.1 gives the naming convention chosen for the nuisance parameters in this analysis. .

8.3 Results

Exclusion limits are set in two different ways. One for the MSSM Higgs interpretation, referred to as *model-dependent* exclusion, and one where no model restrictions are imposed on the production and decay of a generic resonance, referred to as *model-independent*. The following two sections describe the signal model and the results for these two cases.

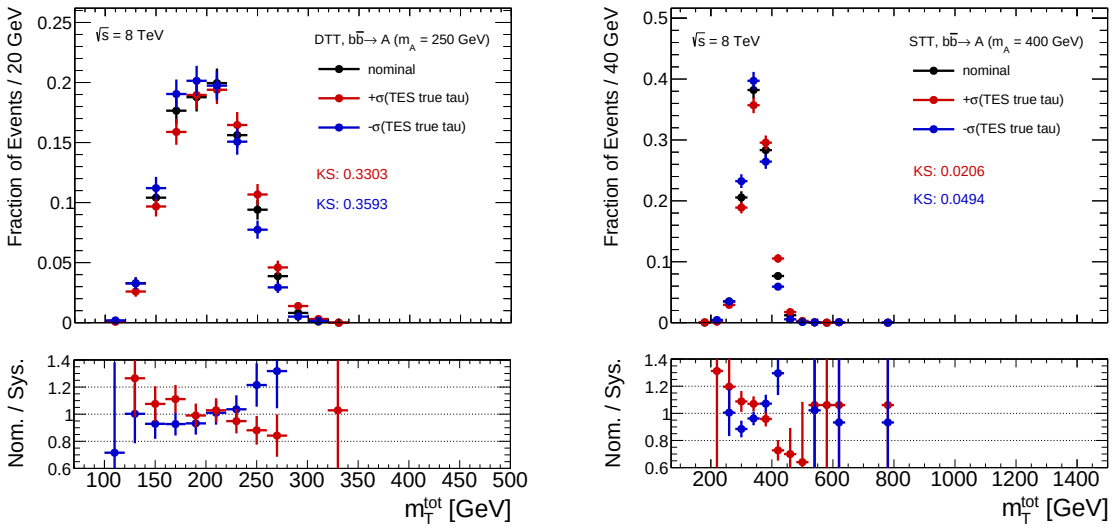

Figure 8.3: Distributions of $m_{\mathrm{T}}^{\mathrm{tot}}$ for two signal samples in the DTT (left) and STT (right) categories for the $b\bar{b}$ annihilation production. The plots show the nominal distribution and the two distributions corresponding to an upward (red) and downward (blue) variation of the TES uncertainty. A significant difference between the altered shapes and the nominal one is observed as indicated by the p_{KS} values reported in the plots for the two variations.

Systematic Uncertainty	Nuisance Parameter Symbol
Tau energy scale for real tau leptons	TES_REAL
Tau energy scale for fake tau leptons	TES_FAKE
Tau trigger for $p_{\mathrm{T}}(\tau) > 100$ GeV	TAU_TRIG_HIPT
Tau trigger for $p_{\mathrm{T}}(\tau) \leq 100$ GeV	TAU_TRIG_LOWPT
Tau identification	TAU_ID
Mis-identification probability for W + jets events	TAU_MISID
Mis-identification probability for non - W + jets events	TAU_MISID60
Track reconstruction efficiency for 3-prong tau leptons	TAU_3PRECO
Multi-jet normalisation in DTT category	R_OSSS
Multi-jet shape in DTT category	R_OSSS_SHAPE
Multi-jet normalisation in STT category	FAKE_FACTOR
Luminosity	LUMI
Missing transverse energy	MET
k-factor applied to $Z/\gamma^* \rightarrow \tau\tau/ll$ events	K_FACTOR
Cross-section uncertainty for contribution x	XS_x
Acceptance uncertainty for contribution x	Q2_x

Table 8.1: Summary of nuisance parameters and their names used in this analysis.

8.3.1 Model-dependent Exclusion

The model-dependent exclusion relies on a signal modelled in accordance with the MSSM prediction and is set in the $(m_A, \tan\beta)$ plane. In principle, the signal should include the contribution of all three Higgs bosons h, H and A produced by the two mechanisms discussed in Sec. 7.1. However, due to the very low signal acceptance at lower masses, as illustrated in Fig. 7.54, no h contribution is added to the signal model, which would only contribute with a small number of events. For instance, in the DTT category and for $m_A = 130$ GeV only $N_{\text{exp}}(gg \to h \to \tau_{\text{had}}\tau_{\text{had}}) \approx 6.4$ and $N_{\text{exp}}(b\bar{b} \to h \to \tau_{\text{had}}\tau_{\text{had}}) \approx 0.2$ signal events are expected assuming the m_h^{max} scenario.

The limit is obtained by determining the excluded signal strength μ_{excl} using the CL_s method in a grid of m_A and $\tan\beta$ values, which are

$$m_A = (170, 200, 250, 300, 350, 400, 450, 500, 600, 700, 800, 900, 1000)\ \text{GeV}, \tag{8.22a}$$

$$\tan\beta = (3, 4, 5, 8, 10, 13, 16, 20, 23, 26, 30, 35, 40, 45, 50, 55, 60). \tag{8.22b}$$

For each mass point the production and decay of only one Higgs boson is simulated for each production mechanism. For this reason, the entire signal model is built by just combining mass spectra at different mass points, out of the same simulated set. These are selected from those which agree best with the MSSM mass dispersion relations, as in Eq. (2.76), for the $(m_A, \tan\beta)$ point taken into account. As mentioned in Sec. 7.1, any variation in $\tan\beta$ is assumed to not change the shape of the signal, but only its normalisation. The combination of all mass spectra corresponding to the two production mechanism is then represented by one signal strength μ.

A point in the $(m_A, \tan\beta)$ space is excluded if $\mu_{\text{excl}} < 1$. This is illustrated in Fig. 8.4 for limit curves obtained at $m_A = 350$ GeV as a function of $\tan\beta$, where the excluded $\tan\beta$ region is computed by interpolating the grid results across $\mu_{\text{excl}} = 1$. Exclusion limits are computed in all MSSM scenarios

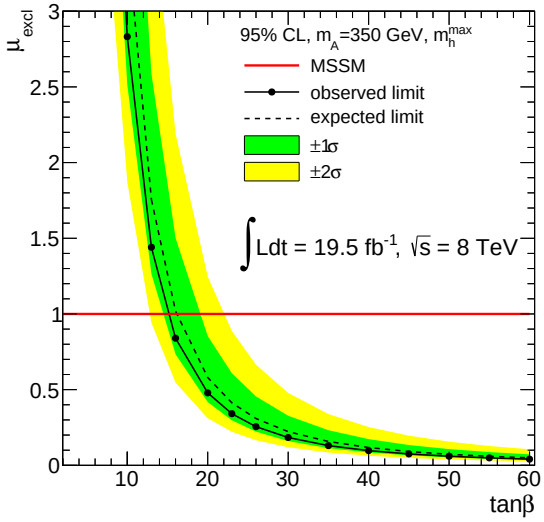

Figure 8.4: Example for the interpolation of the excluded signal strength, μ_{excl}, as a function of $\tan\beta$ for $m_A = 350$ GeV. The red line indicates the MSSM prediction in the m_h^{max} scenario, which is excluded by the curves if they assume values below it.

illustrated in Sec. 2.3.5. In Fig. 8.5, the exclusion for the m_h^{max} scenario is presented. This scenario is disfavoured by the measured value of the Higgs boson mass. Nevertheless, is still instructive to do

comparisons between current searches and previous ones, e.g. at LEP, as also mentioned in Sec. 2.3.5. The curves in Fig 8.5, represent upper bounds on the allowed parameter region at CL=95%. Cross-section uncertainties on the signal production are not included in the fit model. However, the observed exclusion is computed again for upward and downward variations of the cross-section. These additional observed limits are shown as curves surrounding the nominal observed limit.

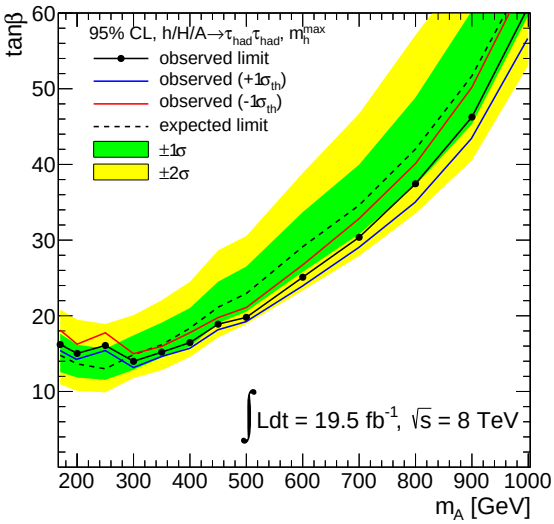

Figure 8.5: Exclusion limit in the m_h^{max} scenario of the MSSM. The area above each curve is excluded at 95% CL. The blue and the red lines represent the observed exclusion determined after varying the signal cross-section upward and downward, respectively, within its uncertainty.

At lower masses the sensitivity of the search is dominated by the DTT category, up to $m_A \approx 350$ GeV where the contribution of the STT channel starts to become dominant. This effect is illustrated in Fig. 8.6, where only the expected limit is shown. The plot also illustrates the decrease in sensitivity due to the effect of the systematic uncertainties. Systematic uncertainties in the DTT category have the largest effect on the sensitivity at lower masses. The dominant systematic uncertainties in the DTT category are those associated with the multi-jet background and the trigger at low momenta. At higher masses the largest effect comes from the trigger and tau identification, which are the dominant uncertainties in the STT category. Alternative MSSM scenarios are considered beyond m_h^{max}. The limits computed assuming the $m_{h,\text{mod}}^{+}$ and $m_{h,\text{mod}}^{+}$ scenarios are shown in Fig. 8.7 on the left and right, respectively. Limits for the remaining scenarios discussed in Sec. 2.3.5 are shown in App. F.0.2.

8.3.2 Model-independent Exclusion

Limits are also provided in a model-independent way for each production mechanism, to investigate the presence of a generic resonance ϕ in the data. The cross-section exclusion for the production and decay of ϕ is set as a function of its mass. Only one signal sample is considered for the signal in correspondence of a mass hypothesis. Predicted signal events are rescaled to account for a total production cross-section and decay branching ratio of 1 pb. In this way, the excluded value of μ represents the exclusion on these observables.

Exclusion limits for the two production mechanisms are reported in Fig. 8.8. They feature a very similar sensitivity, as a consequence of the similar signal acceptances presented in Fig. 7.54.

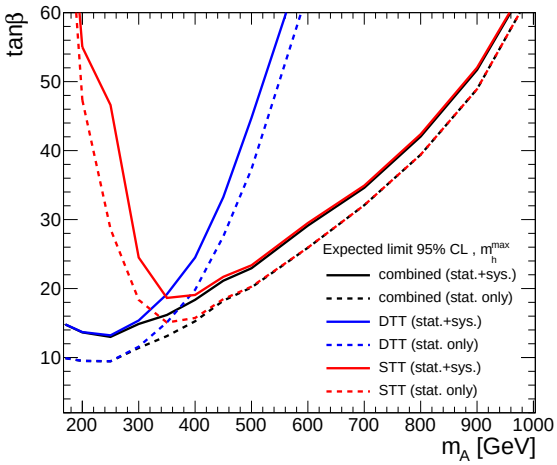

Figure 8.6: Expected exclusion limits in the m_h^{max} scenario for the DTT (blue) and STT (red) categories, as well as their combination (black). The limits are obtained considering only the statistical uncertainty in the fit model (dashed lines) and including the effect of the systematic uncertainties (continuous lines). The effect of the systematic uncertainties increases toward lower masses.

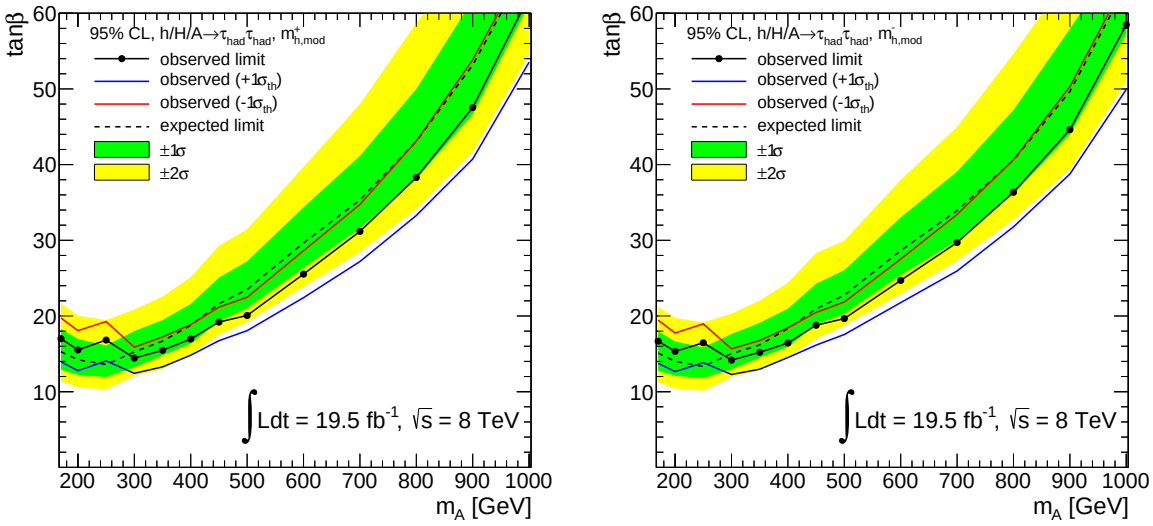

Figure 8.7: Exclusion limits at 95% CL in the $m^{+}_{h,\text{mod}}$ (left) and $m^{-}_{h,\text{mod}}$ (right) scenarios of the MSSM. The blue and the red lines represent the observed exclusion determined after varying the signal cross-section upward and downward, respectively, within its uncertainty.

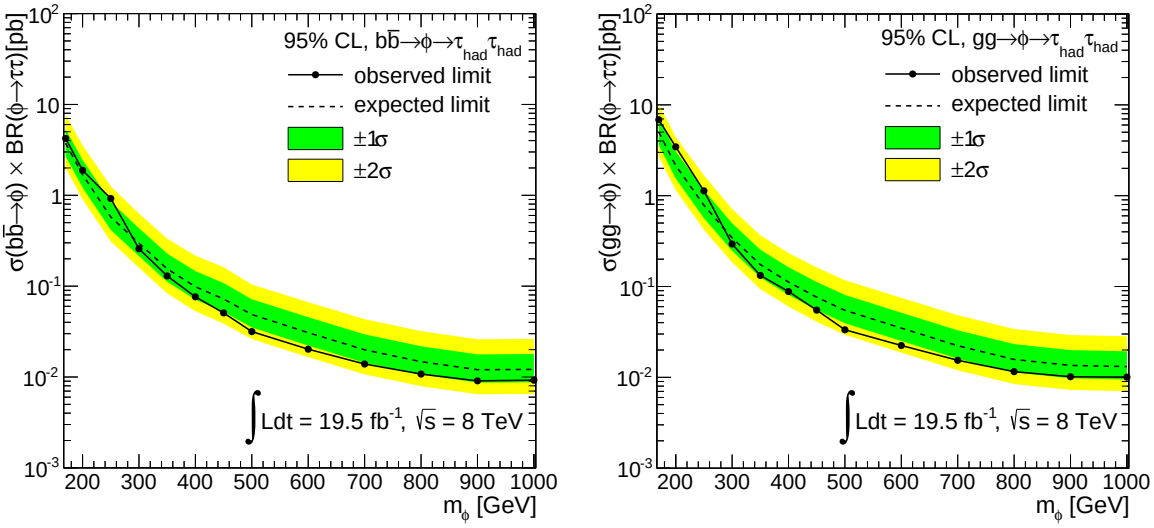

Figure 8.8: Model independent exclusion limits at 95% CL. The curves represent the excluded cross cross-section for the production and decay of a generic Higgs boson ϕ produced via $b\bar{b}$ annihilation (left) and gluon-gluon fusion (right).

8.4 Fit Validation

In this section studies to validate the fitting procedure are presented. These studies are mainly focused on the nuisance parameters associated with the systematic uncertainties implemented in the likelihood. They include tests to check whether the appropriate model is implemented for the nuisance parameters, a measurement of their correlations, and their impact on the fitted signal strength.

8.4.1 Profiling of Nuisance Parameters

Nuisance parameters are constrained in the likelihood function using a Gaussian term, as illustrated in Eq. (8.17). It is important to check that this model is consistent with the fitting procedure, which should not alter the Gaussian profile of each parameter. Alterations might result in multiple minima of the NLL and lead to ambiguous results. If the minimisation procedure is consistent with the model, the NLL profile is found to be parabolic as a function of a single nuisance parameter, as a consequence of its Gaussian constraint. The value of the likelihood at its minimum is irrelevant and can be subtracted, leading to the definition of $\ln(\mathcal{L}) - \ln(\mathcal{L}_{\min}) = \Delta\ln(\mathcal{L})$, which is equal to zero at the minimum. The contour of this new parabolic profile, where the function assumes a value of one, corresponds to the uncertainty determined by the minimisation procedure on a nuisance parameter which we will call $\hat{\sigma}_k^{\min}$, referring to the uncertainty k. The minimum of this function corresponds to the estimate of the nuisance parameter itself, $\hat{\alpha}_k^{\min}$.

In Fig. 8.9, two NLL profiles are presented for two of the dominant systematic uncertainties in the analysis, the TES and the tau trigger. These profiles are the results of an unconditional fit to data assuming $m_A = 400$ GeV and $\tan\beta = 20$. Both profiles feature a smooth trend, with no double minima, indicating no problems in the minimisation. Similar trends are observed for the other parameters. A line is drawn in the plots indicating the $\hat{\sigma}_k^{\min}$ contour of the nuisance parameters. In correspondence of the line, bounds of $\approx \pm 1$ are observed for the two nuisance parameters considered, indicating that the fit does

not over-constrain the uncertainty on the nuisance parameter beyond the nominal 1σ level.

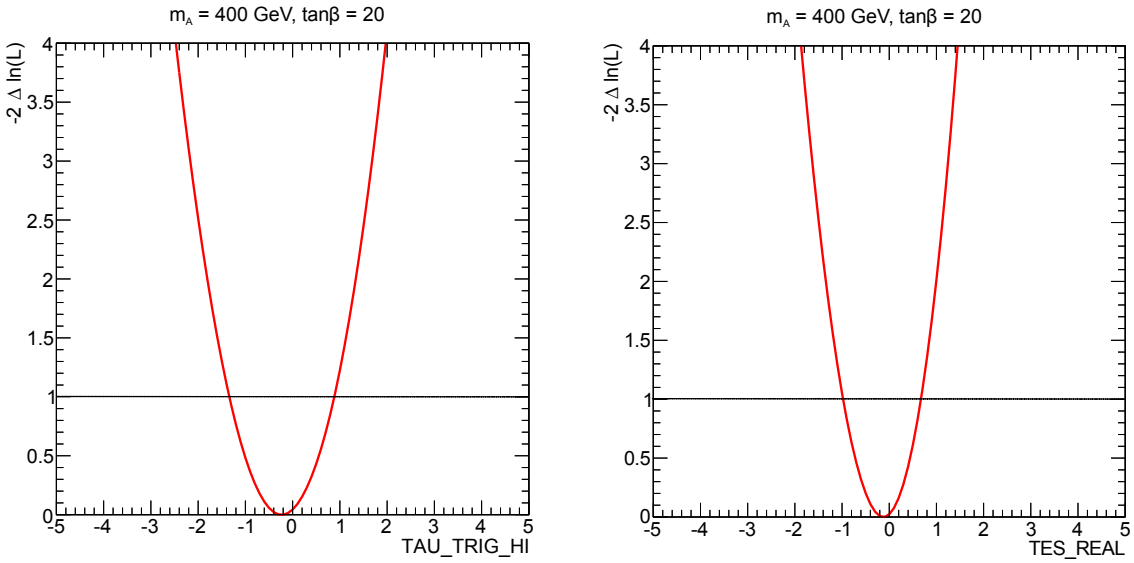

Figure 8.9: Likelihood profiles determined from an unconditional fit to data for the tau trigger uncertainty at high-p_{T} (left) and the TES (right). The horizontal line corresponds to the contour defining the uncertainty of the nuisance parameter determined by the fit $\hat{\alpha}_k^{\mathrm{min}} \pm 1\hat{\sigma}_k^{\mathrm{min}}$. The point $m_A = 400$ GeV and $\tan\beta = 20$ has been used.

In order to provide exclusion limits, the asymptotic approximation is used. In the most general version of this hypothesis test, a pseudo-experiment approach should be applied [228], where the distribution of the test statistic is not approximated, rather it is obtained by repeating the fit many times after altering the model by randomly varying each of the nuisance parameters according to their constraint. This random alteration is called a *pseudo-experiment*. As the pseudo-experiment approach represents the most general method to set limits, it is used in this thesis, rather than the likelihood profiles, to investigate constraints and final fitted NP values.

A non-problematic fitting procedure is guaranteed if the fitted nuisance parameters are distributed according to a Gaussian model. The distribution of the fitted nuisance parameters is checked for the systematic uncertainties by plotting the following variable

$$\Delta\alpha_k = \frac{\alpha_k^{\mathrm{min}} - \alpha_k^{\mathrm{nom}}}{\sigma_k^{\mathrm{min}}}, \tag{8.23}$$

where α_k^{min} is the fitted value of the nuisance parameter in each of the pseudo-experiments, α_k^{nom} the nominal one used to generate the distributions and σ_k^{min} the uncertainty on α_k^{min} obtained from the fit. According to the Gaussian model in the likelihood of Eq. 8.17, the distribution of $\Delta\alpha_k$ should be centered at zero and have a standard deviation of one. To check the consistency of the model, 10000 pseudo-experiments are generated and an unconditional likelihood fit to data is performed each time. In Fig. 8.10, the $\Delta\alpha_k$ distributions for the TES and tau trigger uncertainties are plotted. The figures include a Gaussian fit using the function $\mathrm{Gauss}(\Delta\alpha_k|0,1)$, which describes the distributions well. The Gaussian mean and standard deviation are an estimate of $\hat{\alpha}_k^{\mathrm{min}}$ and $\hat{\sigma}_k^{\mathrm{min}}$, respectively, and they should be consistent with the parameter of the likelihood profile previously mentioned. The full set of fitted distributions can be found in App. F.0.1. The gaussian means might be shifted with respect to the nominal value of zero.

These shifted values, called the *pulls*, are summarised in Fig. 8.11.

Overall, the fitted mean does not show a significant deviation from the nominal value, being always within the 1σ band. This indicates that the fit does not significantly alter each background component using the nuisance parameters, indicating that the nominal values of the scales, for instance the TES or the tau identification scale factors, are estimated well. An exception is the normalisation of the multi-jet background in the DTT category, represented by the factor $R_{\mathrm{OS/SS}}$. In Fig. 8.11, it can be seen that the fit prefers a larger number of multi-jet events, as it increases the nominal estimate by approximately 80% of its nominal uncertainty, therefore increasing the number of multi-jet events by $\approx 4.4\%$. Also, the $\approx 5\%$ uncertainty on $R_{\mathrm{OS/SS}}$ is constrained by the fit to nearly half of this value. The constraint indicates that the normalisation uncertainty for the multi-jet background is conservative. This could be a concern if the fit was trying to accommodate more multi-jet events, which would lead to a bias on the values of other parameters, in particular the signal strength. In other words, to make sure that no bias is introduced, we have to check the correlation matrix between the parameters and $\hat{\mu}$. The correlations are illustrated in Fig. 8.12, for an unconditional fit to data at the point $m_A = 400$ GeV and $\tan\beta = 20$.

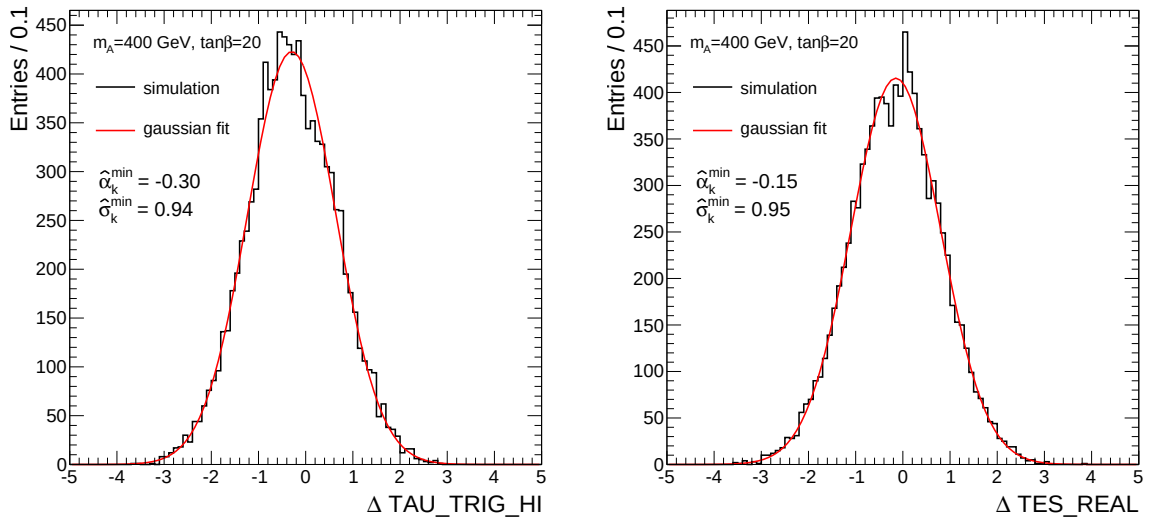

Figure 8.10: Distributions of $\Delta\alpha_k$, defined in the main text, for the tau trigger uncertainty at high-p_{T} (left) and the TES (right). The distributions obtained with pseudo-experiments are fitted with a Gaussian function in order to determine $\hat{\alpha}_k^{\mathrm{min}}$ and $\hat{\sigma}_k^{\mathrm{min}}$, whose values are indicated in the plots. The point $m_A = 400$ GeV and $\tan\beta = 20$ has been used.

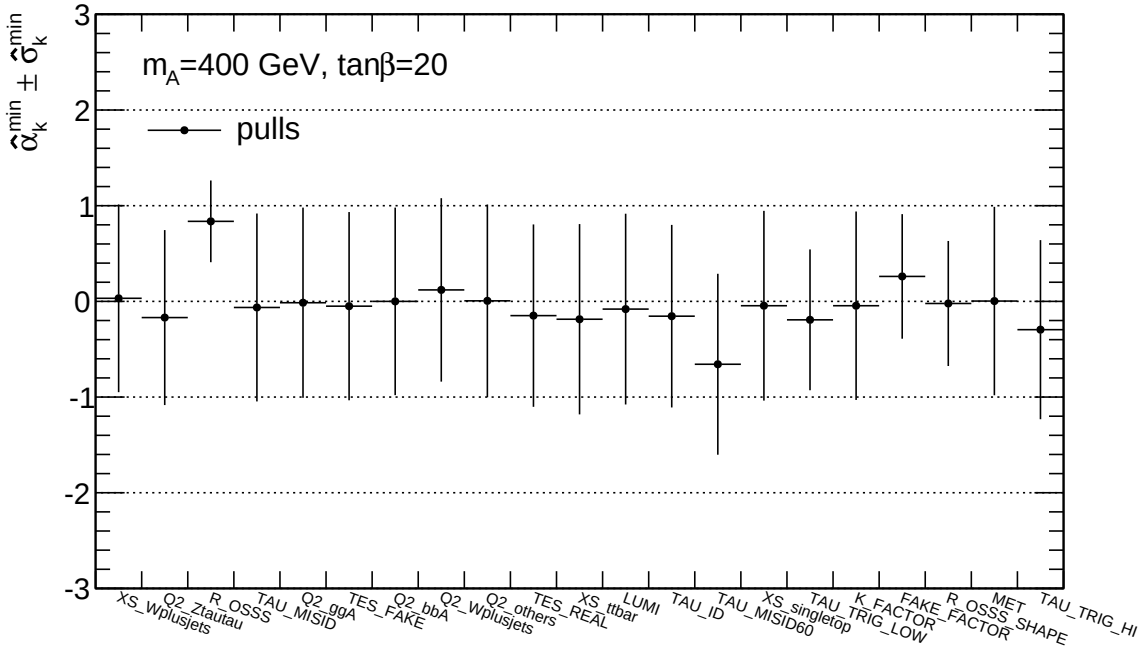

Figure 8.11: Full set of fitted values for $\hat{\alpha}_k^{\min}$ and $\hat{\sigma}_k^{\min}$, for all systematic uncertainties, determined with pseudo-experiments. The point $m_A = 400$ GeV and tan$\beta = 20$ has been used.

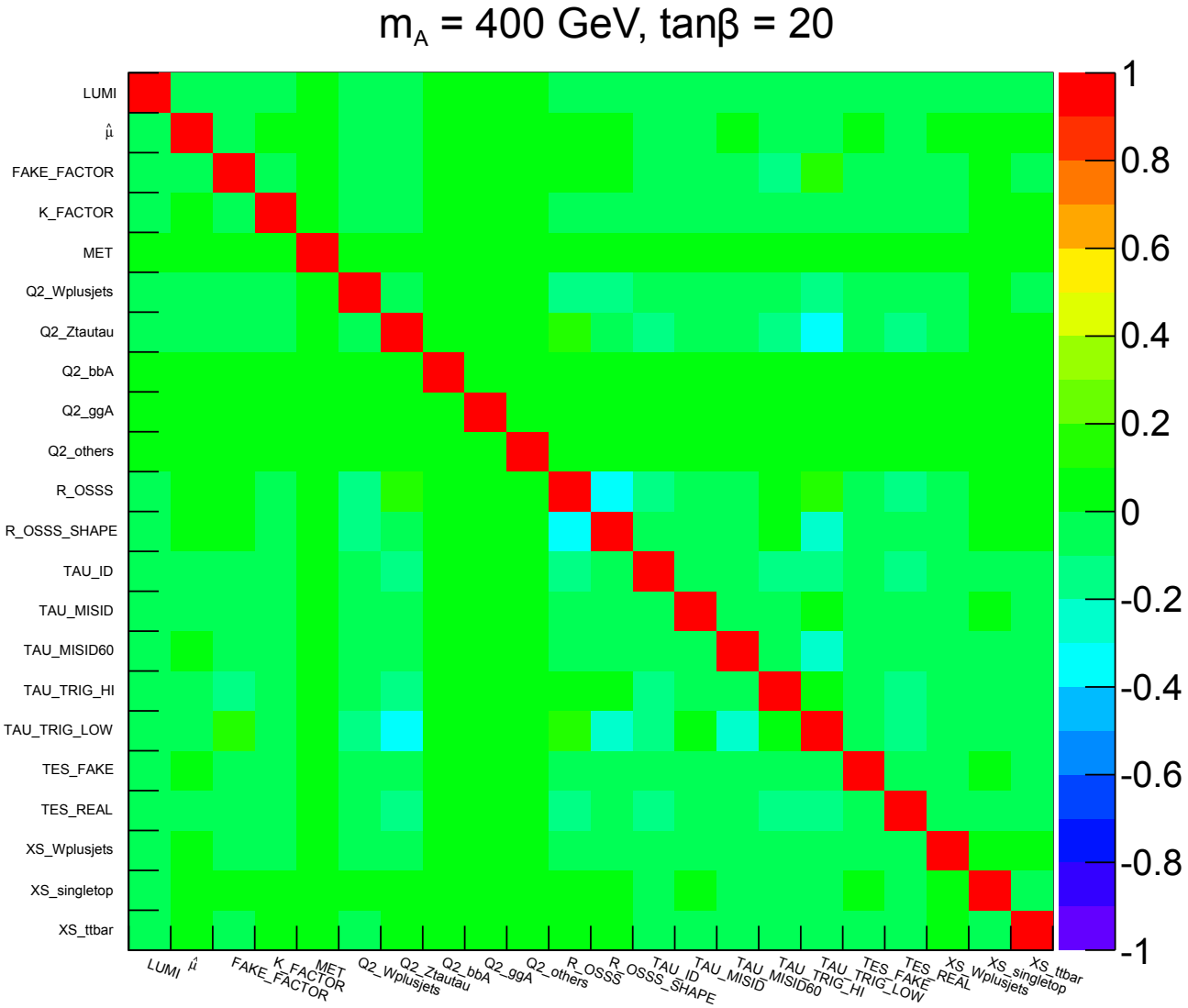

Figure 8.12: Correlation matrix of the systematic uncertainties obtained from an unconditional fit to data for $m_A = 400$ GeV and tan$\beta = 20$. Systematic uncertainties are named according to the nomenclature defined in Tab. 8.1.

The correlation matrix does not reveal a problematic amount of correlation between the nuisance parameters. The fitted signal strength $\hat{\mu}$ is not correlated with any of the uncertainties.

Only two cases are present of correlations below $\approx 40\%$. This degree of correlation is not problematic and arises from expected features in the fit. In the first case, R_OSSS and R_OSSS_SHAPE are correlated by $\approx -38\%$. This is expected, as they are two non-independent components of the same uncertainty, as the value of $R_{\mathrm{OS/SS}}$ is used for the evaluation of the shape systematic uncertainty, as illustrated in Eq. (7.8). In the second case, the $Z/\gamma^* \rightarrow \tau\tau$ acceptance and low-p_{T} component of the tau trigger uncertainties, Q2_Ztautau and TAU_TRIG_LOW, respectively, are correlated by $\approx -36\%$. Also this is expected, because, as shown in Tab. 7.17, these are the largest uncertainties on $Z/\gamma^* \rightarrow \tau\tau$ and have similar magnitudes. As both are implemented only as a normalisation parameter in the fit, they similarly compete with each other to alter the normalisation of this background.

8.4.2 Ranking of Systematic Uncertainties

In the previous chapter, the impact of the systematic uncertainties on the expected number of events for signal and background was presented, and summarised in Tab. 7.17. However, the impact on the expected number of events is not the most relevant quantity to determine the effect of the systematic uncertainties on the exclusion limit. As the exclusion relies on a fitting procedure, the impact of the systematic uncertainties on the fitted signal strength, $\hat{\mu}$, has to be determined. This is done separately for each uncertainty.

In order to measure the effect of the systematic uncertainty k on $\hat{\mu}$, the following procedure is used:

1. Perform an unconditional fit to the Asimov dataset to measure the nominal value of the signal strength $\hat{\mu}_0$.
2. Find the $\pm\hat{\sigma}_k^{\mathrm{min}}$ contour for the nuisance parameter $\hat{\alpha}_k$ based on the measured likelihood profile, as illustrated in Fig. 8.9.
3. Fix the value of $\hat{\alpha}_k$ at the upper and lower 1σ limits, i.e. $\hat{\alpha}_k^{\mathrm{min}} \pm \hat{\sigma}_k^{\mathrm{min}}$ in turn.
4. Repeat the unconditional fit allowing the other nuisance parameters and μ to vary, in order to estimate two additional values of the signal strength $\hat{\mu}_{\pm}$ for the upper and lower bounds on the systematic contour.
5. Estimate the systematic impact on $\hat{\mu}$ as $\pm\sigma_{\hat{\mu}} = \pm\hat{\mu}_0 \mp \hat{\mu}_{\pm}$

These steps are performed in order to estimate the so-called *post-fit* systematic impact on $\hat{\mu}$, as step 2 makes use of the post-fit likelihood profile measured in step 1.

A similar kind of measurement is also performed to investigate the *pre-fit* systematic impact on $\hat{\mu}$. This is done by repeating step 3 using the nominal systematic boundary before any fit constraint, which is simply $\pm 1\sigma_k^{\mathrm{nom}} = \pm 1$. In the case the fit is not able to constrain a systematic uncertainty, the post-fit and pre-fit systematic impacts on $\hat{\mu}$ are the same. In Fig. 8.13, the pre-fit and post-fit impacts on $\hat{\mu}$ are reported, together with the nominal and constrained boundaries on the nuisance parameters. Each uncertainty is ranked from top to bottom according to the magnitude of the post-fit impact, i.e. $|+\sigma_{\hat{\mu}}| + |-\sigma_{\hat{\mu}}|$. Further ranking plots for other mass points and tanβ values are in App. F.0.3.

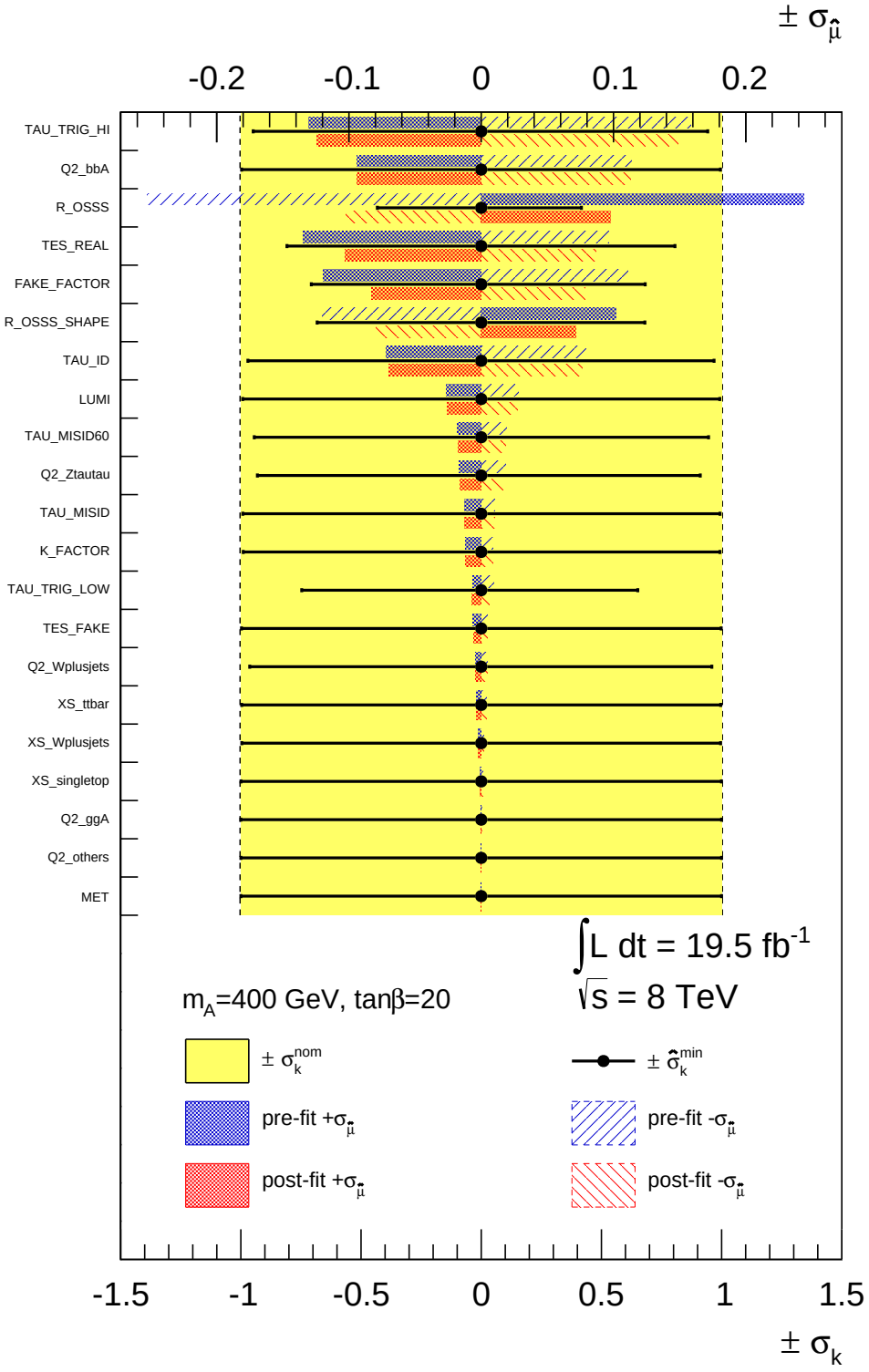

Figure 8.13: Summary of the impact of systematic uncertainties on $\hat{\mu}$ determined from an unconditional fit to the Asimov dataset. The point $m_A = 400$ GeV and $\tan\beta = 20$ has been used. Systematic uncertainties are ranked from top to bottom on the left axis according to the post-fit impact shown in red. The upper axis illustrates the scale of $\sigma_{\hat{\mu}}$. The plot also includes the values of $\hat{\sigma}_k^{\min}$, shown in black, determined from the post-fit likelihood contours. The nominal pre-fit bound on each nuisance parameter is also shown and represented by the yellow region. The scale of the post-fit and pre-fit systematic contours is shown by the lower axis.

CHAPTER 9

MSSM $h/H/A \to \tau\tau$ analysis

In Chap. 7 and 8 the MSSM $h/H/A \to \tau_{\text{had}}\tau_{\text{had}}$ analysis was discussed, which is intended as one of the channels in a wider $h/H/A \to \tau\tau$ search including other combinations of decay modes of the tau, also including leptonic decays. At lower masses, from $m_A = 200$ GeV downwards, the $h/H/A \to \tau_{\text{had}}\tau_{\text{had}}$ channel starts to lose sensitivity due to selection criteria aimed at rejecting the abundant multi-jet background. The low-mass region of the MSSM Higgs hypothesis is probed by the other channels, which are presented in this chapter. Their selections and background estimation techniques are briefly outlined in the following. In Sec. 9.1, the $h/H/A \to \tau_\mu\tau_e$ analysis with two leptonic tau decays is presented. In Sec. 9.2, the $h/H/A \to \tau_{\text{lep}}\tau_{\text{had}}$ channel is discussed, where both hadronic and leptonic tau decays are considered in the final state. Finally, Sec. 9.3 presents the combination of all three channels in the search and the combined exclusion limits. The combination of all three channels and the final limit derivation is part of the work performed for this thesis, while the searches for $h/H/A \to \tau_\mu\tau_e$ and $h/H/A \to \tau_{\text{lep}}\tau_{\text{had}}$ is not. All results are documented in Ref. [178].

9.1 MSSM $h/H/A \to \tau_\mu\tau_e$ channel

In the $h/H/A \to \tau_\mu\tau_e$ channel, final states where each tau decays into two neutrinos and two light leptons are selected. Only final states where these two light leptons have different flavours (e and μ) are considered. Masses in the range $m_A = 90 - 200$ GeV are taken into account for the signal hypothesis. In this range the $h/H/A \to \tau_\mu\tau_e$ search offers competitive sensitivity, despite the low branching ratio of $\text{BR}(\tau + \tau \to \mu\bar{\nu}_\mu\nu_\tau + e\bar{\nu}_e\nu_\tau) \approx 6\%$, due to the very low multi-jet contamination. The major source of background in this channel are $Z/\gamma^* \to \tau\tau$ events. Further backgrounds come from $t\bar{t}$ and single-top events. This search uses $L_{\text{int}} = 20.3\ \text{fb}^{-1}$ of collected data.

9.1.1 Selection

Tau decays with leptons of different flavours are required to reduce the abundant $Z/\gamma^* \to ll$ background. Events are selected using single-electron or electron-muon triggers, imposing a momentum threshold on the leptons of $p_{\text{T}}(e) > 24$ GeV or $p_{\text{T}}(e) > 12$ GeV and $p_{\text{T}}(\mu) > 8$ GeV, respectively. Events are required to contain exactly one isolated electron and one isolated muon with opposite electric charges. The lepton momenta have to satisfy the offline requirement $p_{\text{T}}(e) > 15$ GeV and $p_{\text{T}}(\mu) > 10$ GeV. Events in the window 15 GeV $< p_{\text{T}}(e) <$ 25 GeV are selected by the electron-muon trigger, while at higher momenta they are selected by the single-electron trigger. A veto is imposed on events containing a hadronically

decaying tau identified with the loose identification criterion.

For the further selection, two categories targeting the two main production mechanisms are introduced. A *tag category* and a *veto category* are defined, based on the presence or absence of a b-tagged jet, respectively.

Events in the tag category are required to contain exactly one b-tagged jet. The dominant background contribution in this category are $t\bar{t}$ and single-top events. In order to reject them, a number of kinematic requirements is applied. The azimuthal angle between the leptons must satisfy $\Delta\phi(\mu, e) > 2.0$. Also, $\sum_{l=\mu,e} \cos(\phi(l) - \phi(E_{\mathrm{T}}^{\mathrm{miss}})) > -0.2$ is required. The scalar sum of the transverse momenta for all jets with $p_{\mathrm{T}}(\mathrm{jet}) > 30$ GeV has to be lower than 100 GeV, and the scalar sum of lepton momenta, including $E_{\mathrm{T}}^{\mathrm{miss}}$, has to be below 125 GeV.

In the veto category, events featuring b-tagged jets are rejected. Kinematic requirements are loosened due to a lower $t\bar{t}$ and single-top contamination. Therefore, the requirements $\Delta\phi(\mu, e) > 1.6$ and $\sum_{l=\mu,e} \cos(\phi(l) - \phi(E_{\mathrm{T}}^{\mathrm{miss}})) > -0.4$ are imposed.

9.1.2 Background Estimation

Events from the $Z/\gamma^* \to \tau\tau$ process are an important source of background, especially in the veto category where they dominate. This contribution is modelled using the so-called *embedding technique* [229]. In this method $Z/\gamma^* \to \mu\mu$ events are used, which are selected from data. The muon signature, consisting of tracks and energy deposits in calorimeter cells, is replaced by the signature of a simulated tau decay. The tau decay is modelled with the program `TAUOLA` [75]. This procedure offers the advantage of a data-driven model of the event kinematics, leaving to the simulation only the tau decay and its detector response. Di-muon events are selected by requiring two isolated muons within $|\eta| < 2.5$, $p_{\mathrm{T}}(\mu_{\mathrm{lead}}) > 20$ GeV, $p_{\mathrm{T}}(\mu_{\mathrm{sub-lead}}) > 15$ GeV and an invariant mass $m_{\mu\mu} > 40$ GeV. Events at lower invariant masses, i.e. $m_{\tau\tau} < 40$ GeV, are modelled using events simulated with `Alpgen`. The normalisation of the $Z/\gamma^* \to \tau\tau$ contribution is estimated using the `FEWZ` [193, 194] estimate of its cross-section at NNLO, together with an estimate of the muon selection efficiency performed using the simulation.

Two uncertainties are related to the embedding method, namely, the one associated with the muon selection, which is estimated by altering the muon isolation requirement, and one associated with the energy subtraction from calorimeter cells associated with the muon. Their combined impact on the normalisation of $Z/\gamma^* \to \tau\tau$ events is 1.3% in the tag category, and 0.1% for the b-veto category. The dominant uncertainty, however, is associated with the normalisation of this background and amounts to an alteration on the number of expected events of $\approx 5.0\%$ for both categories.

The $t\bar{t}$ background is estimated from the simulation. However, the predicted number of events are normalised according to the data event yield in a control region defined by requiring the presence of two b-tagged jets in the event. Single-top events are estimated using the simulation only. The dominant systematic uncertainties on the $t\bar{t}$ and single-top contributions come from the JES and b-tagging efficiency in the tag category, amounting to $\approx 6\%$ and $\approx 3\%$, respectively, and the b-tagging efficiency and cross-section uncertainty in the veto selection, $\approx 12\%$ and $\approx 5.5\%$, respectively.

The multi-jet contamination is the third most significant contamination. It is estimated from data using an ABCD method similar to the one described in Sec. 7.5. The control region B, from which the multi-jet shape is taken, is defined by requiring two leptons with the same electric charge. The control regions C and D are defined for the measurement of the multi-jet normalisation, and require opposite and same charges, respectively, while also imposing an anti-isolation criterion on both leptons. The main systematic uncertainty on the multi-jet contribution comes from the ABCD method, and is estimated by altering the anti-isolation criterion used to define regions C and D. This has an impact of $\approx 7\%$ for both categories in the analysis.

In Fig. 9.1, the $m_{\tau\tau}$ mass distributions of the $h/H/A \to \tau_\mu\tau_e$ channel are presented for the tag channel (left) and the veto channel (right). The mass variable utilised by this search differs from the one used in the $h/H/A \to \tau_{\text{had}}\tau_{\text{had}}$ analysis. The presence of two neutrinos in the final state affects the mass resolution significantly. Therefore, a more advanced reconstruction technique is used, called the *Missing Mass Calculator* (MMC) [230] algorithm. In this technique the missing momentum is assumed to be entirely caused by the presence of the neutrinos. The two-dimensional space of the angles between the $E_{\text{T}}^{\text{miss}}$ vector and the visible momenta of the two tau leptons is scanned to look for the most likely configuration in the event. This configuration is determined with the help of input PDFs obtained with simulated tau decays. A mass resolution of $\approx 30\%$ is achieved at $m_A = 150$ GeV.

As two neutrinos are present in the $h/H/A \to \tau_{\text{had}}\tau_{\text{had}}$ final state, the MMC algorithm has also been considered for the $m_{\tau\tau}$ mass reconstruction. However, no significant improvement has been observed at lower masses and a decrease in sensitivity is observed for high masses, compared to the use of $m_{\text{T}}^{\text{tot}}$. The reason for this is due to the fact that multi-jet events typically have lower transverse momenta than the signal. For this reason, a variable relying purely on the transverse kinematics, like $m_{\text{T}}^{\text{tot}}$, will improve the separation between the signal and this particular background, which will be more peaked at lower masses. The predicted number of background and signal events in the signal regions, together with the

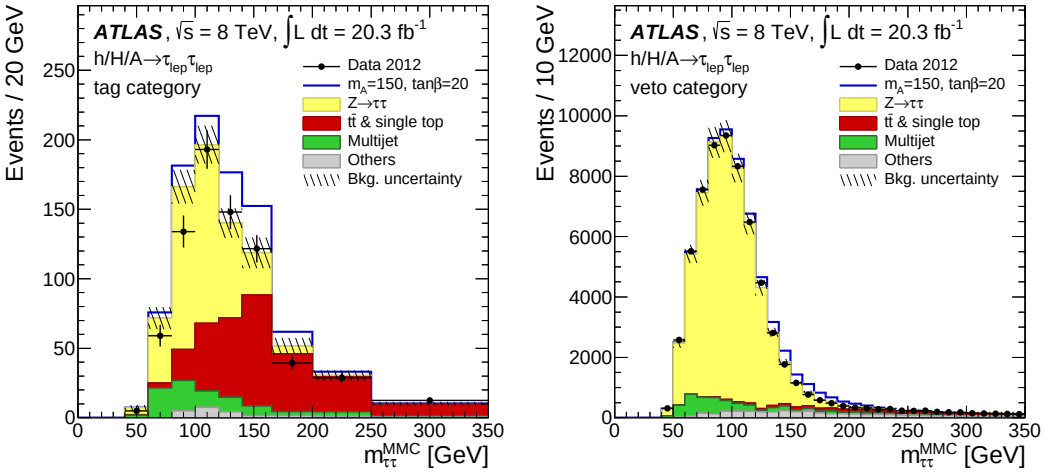

Figure 9.1: Mass distributions in the signal regions of the $h/H/A \to \tau_\mu\tau_e$ channel. The variable called $m_{\tau\tau}^{\text{MMC}}$ corresponds to the invariant mass estimate of the di-tau system from the MMC algorithm as explained in the main text. The tag and veto categories are shown on the left and on the right, respectively. The uncertainty band shown on top of the total expected background includes the statistical and systematic uncertainties, where all sources are added in quadrature. The signal model is plotted on top of the total background and includes both production mechanisms at $m_A = 150$ and $\tan\beta = 20$. The plots are taken from Ref. [178].

observed number of data events, are reported in Tab. 9.1 for the two categories.

9.2 MSSM $h/H/A \to \tau_{\text{lep}}\tau_{\text{had}}$ channel

In the $h/H/A \to \tau_{\text{lep}}\tau_{\text{had}}$ channel the leptonic decay of only one tau is taken into account, considering both electron and muons in the final state, while the other tau decays hadronically. This is the channel with the highest total branching ratio, being $\text{BR}(\tau+\tau \to \mu\bar{\nu}_\mu\nu_\tau + \text{hadrons}) \approx 23\%$ and $\text{BR}(\tau+\tau \to e\bar{\nu}_e\nu_\tau + \text{hadrons}) \approx 23\%$. The analysis offers competitive sensitivity across the mass range $m_A = 90 - 1000$ GeV.

$h/H/A \to \tau_\mu\tau_e$ Categories		
	Tag	Veto
Signal (m_A = 150 GeV, tanβ = 20)		
$h \to \tau\tau$	8.7 ± 1.9	244 ± 11
$H \to \tau\tau$	65 ± 14	882 ± 45
$A \to \tau\tau$	71 ± 15	902 ± 48
$Z/\gamma^* \to \tau\tau$	418 ± 28	54700 ± 3800
Multi-jet	100 ± 21	4180 ± 670
$t\bar{t}$ and single-top	421 ± 46	2670 ± 360
Others	25.8 ± 7.4	4010 ± 280
Total SM	965 ± 59	65500 ± 3900
Data	904	65917

Table 9.1: Event yields for the expected signal and background and for the observed data in the tag and veto categories of the $h/H/A \to \tau_\mu\tau_e$ channel. The signal expectation is split into the contribution from each neutral Higgs boson in the MSSM. The uncertainties on the number of events include the statistical and systematic components, added quadratically. Values are taken from Ref. [178].

The dominant background contamination is the irreducible $Z/\gamma^* \to \tau\tau$ contamination, followed by W + jets, $t\bar{t}$ and single-top, and multi-jet backgrounds. A different optimisation of the selection is performed depending on the mass hypothesis as discussed in the next section. The analysis uses $L_{\text{int}} = 20.3\ \text{fb}^{-1}$ of ATLAS data.

9.2.1 Selection

Events are selected using single-electron and single-muon triggers, both featuring lepton p_{T} thresholds of 24 GeV. An offline requirement of $p_{\text{T}}(l) > 26$ GeV is imposed, as well as $p_{\text{T}}(\tau_{\text{had}}) > 20$ GeV. The light lepton and the tau have to be oppositely charged and a medium tau identification is required for the hadronic tau decay, together with an electron and a muon veto (cf. App. B) to reject light leptons mis-reconstructed as tau candidates. A veto on events with additional electrons or muons is applied.

The analysis is divided into three categories. Both a tag and a veto category are used to optimise the selection for $m_A < 200$ GeV, while only one category, the so-called *high-mass category*, is used for $m_A \geq 200$ GeV.

In the tag category, events containing at least one b-jet are selected. Events containing further jets with $p_{\text{T}}(\text{jet}) > 30$ GeV are rejected, in order to reduce the $t\bar{t}$ background. For the same reason the selection criterion $m_{\text{T}}(l, E_{\text{T}}^{\text{miss}}) < 45$ GeV is imposed. In the veto selection, all events containing at least one b-jet are rejected. In order to reduce the W + jets contribution, two kinematic requirements are applied. First of all, $m_{\text{T}}(l, E_{\text{T}}^{\text{miss}}) < 60$ GeV, and secondly $\Delta\phi(\tau_{\text{had}}, E_{\text{T}}^{\text{miss}}) + \sum_{l=\mu,e} \Delta\phi(l, E_{\text{T}}^{\text{miss}}) < 3.3$. In the muon channel of the veto category, a further event veto is applied for events with 70 GeV $< m_{\text{vis}}(\mu, \tau_{\text{had}}) <$ 112 GeV and with 1-prong tau candidates with an electromagnetic fraction of $f_{\text{EM}} < 0.1$, to further reject events where a muon is mis-reconstructed as a tau.

The last requirement is also utilised in the high-mass category. In this category the visible decay products are required to be back-to-back in the transverse plane by imposing $\Delta\phi(l, \tau_{\text{had}}) > 2.4$. Hadronic tau decays tend to deposit a higher fraction of their energy as visible component in the detector compared

to leptonic ones, due to the presence of only one neutrino in the final state. In the high-mass category, this property is exploited by imposing a momentum imbalance requirement: $p_{\mathrm{T}}(\tau_{\mathrm{had}}) - p_{\mathrm{T}}(l) > 45$ GeV.

In the low-mass categories the electron and muon channels are treated separately in the final hypothesis test, while they are merged in the high mass category in order to improve the statistical significance.

9.2.2 Background Estimation

The dominant $Z/\gamma^* \to \tau\tau$ background is estimated using the embedding technique illustrated in Sec. 9.1.2, and normalised in an analogous way. The dominant uncertainty on the $Z/\gamma^* \to \tau\tau$ background is associated with its normalisation, amounting to $\approx$ 7.5% on the predicted number of events for all categories, followed by the TES ranging between $\approx$ 3.5% and $\approx$ 9.8% depending on the category.

Events from W + jets, $t\bar{t}$, single-top and the less abundant $Z/\gamma^* \to ll$ + jets production contribute to the background due to the presence of an additional jet faking the hadronic tau decay. They are estimated using simulation. However, their normalisation is derived by comparing simulated events with data in control regions enriched in these backgrounds. Different control regions are defined for each category and background. The dominant systematic uncertainties on W + jets, $t\bar{t}$ and single-top come from the estimate of their normalisations and are obtained by altering the selection of the control regions. Their relative impact varies between $\approx 12 - 17\%$ for W + jets and is $\approx$ 8.0% for $t\bar{t}$ and single-top combined, depending on the category.

Events from $Z/\gamma^* \to ee$ + jets also contribute to the background if one of the electrons fakes a hadronically decaying tau lepton. Simulated events are then weighted with the electron-to-tau mis-identification probability, which is measured as illustrated in App. B.1.

An ABCD method is used in the $h/H/A \to \tau_{\mathrm{lep}}\tau_{\mathrm{had}}$ channel to estimate the multi-jet contribution, where different definitions of the three auxiliary control regions B, C and D are used depending on the category. However, region B is always defined by imposing a same-charge requirement between the tau and the light lepton, while an anti-isolation criterion on the latter is always used for regions C and D. The systematic uncertainty on the multi-jet normalisation is estimated by altering the anti-isolation criterion, resulting in an uncertainty of $\approx$ 6% on the expected number of multi-jet events.

As mass estimator in the $h/H/A \to \tau_{\mathrm{lep}}\tau_{\mathrm{had}}$ analysis also the MMC is used. In Fig. 9.2, the final $m_{\tau\tau}$ distributions for the tag (left) and veto (right) categories are illustrated. In Fig. 9.3, the final distribution for the high-mass category is reported. The predicted number of events in each signal region for the signal and background, along with the observed data, are reported in Tab. 9.2 and 9.3 for the low-mass and high-mass categories, respectively.

9.3 MSSM $h/H/A \to \tau\tau$ Combination

As previously stated, the combination of the three channels in the search depends on their sensitivity for different mass hypotheses. Below $m_A = 200$ GeV, only $h/H/A \to \tau_\mu\tau_e$ and $h/H/A \to \tau_{\mathrm{lep}}\tau_{\mathrm{had}}$ are combined, while above that value, only $h/H/A \to \tau_{\mathrm{had}}\tau_{\mathrm{had}}$ and $h/H/A \to \tau_{\mathrm{lep}}\tau_{\mathrm{had}}$ are combined. The signal model for the model-dependent and model-independent exclusion presented in this section is analogous to the one discussed in Sec. 8.3.1 and 8.3.2.

The final exclusion in the $(m_A, \tan\beta)$ plane is illustrated in Fig. 9.4 on the left for the m_h^{max} scenario. On the right, the observed and expected limits are shown separately for each channel in the search. The $h/H/A \to \tau_{\mathrm{had}}\tau_{\mathrm{had}}$ channel dominates the sensitivity of the combined search for $m_A > 300$ GeV, while in the intermediate mass range, 100 GeV $< m_A \leq 300$ GeV, the $h/H/A \to \tau_{\mathrm{lep}}\tau_{\mathrm{had}}$ channel is the most sensitive. For masses $m_A \leq 100$ GeV, the $h/H/A \to \tau_{\mathrm{lep}}\tau_{\mathrm{lep}}$ channel is the dominant one, with rapidly

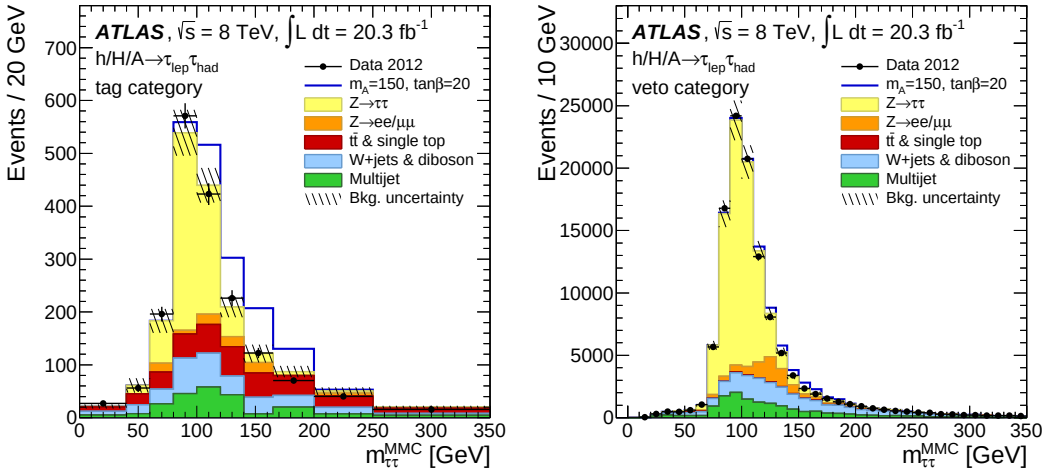

Figure 9.2: Mass distributions in the signal regions of the low-mass categories of the $h/H/A \to \tau_{\text{lep}}\tau_{\text{had}}$ channel. The variable called $m_{\tau\tau}^{\text{MMC}}$ corresponds the invariant mass estimate of the di-tau system from the MMC algorithm as explained in the main text. The tag and veto categories are illustrated by the plot on the left and right, respectively. The uncertainty band shown on top of the total expected background includes the statistical and systematic uncertainties, where all sources are added in quadrature. The signal model is plotted on top of the total background and includes both production mechanisms at $m_A = 150$ and $\tan\beta = 20$. The plots are taken from Ref. [178].

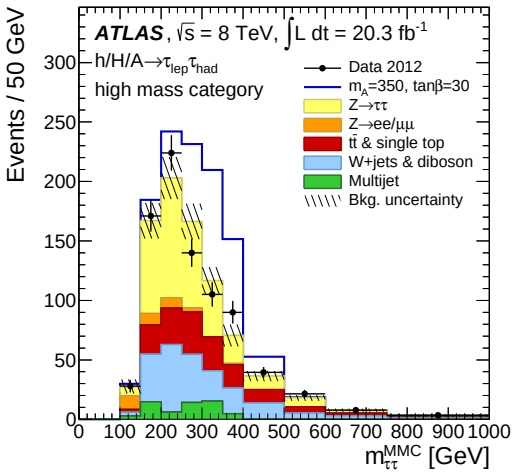

Figure 9.3: Mass distribution in the high-mass signal region of the $h/H/A \to \tau_{\text{lep}}\tau_{\text{had}}$ channel. The variable called $m_{\tau\tau}^{\text{MMC}}$ corresponds the invariant mass estimate of the di-tau system from the MMC algorithm as explained in the main text. The uncertainty band shown on top of the total expected background includes the statistical and systematic uncertainties, where all sources are added in quadrature. The signal model is plotted on top of the total background and includes both production mechanisms at $m_A = 350$ and $\tan\beta = 30$. The plot is taken from Ref. [178].

$h/H/A \to \tau_{\text{lep}}\tau_{\text{had}}$ Low-mass Categories				
	Tag		Veto	
	e channel	μ channel	e channel	μ channel
Signal (m_A = 150 GeV, tanβ = 20)				
$h \to \tau\tau$	10.5 ± 2.8	10.5 ± 2.6	194 ± 13	192 ± 14
$H \to \tau\tau$	86 ± 26	86 ± 24	836 ± 60	822 ± 61
$A \to \tau\tau$	94 ± 29	94 ± 27	840 ± 64	825 ± 62
$Z/\gamma^* \to \tau\tau$	403 ± 39	425 ± 42	31700 ± 2800	38400 ± 3300
$Z/\gamma^* \to ll$	72 ± 24	33 ± 14	5960 ± 920	2860 ± 510
W + jets	158 ± 44	185 ± 58	9100 ± 1300	9800 ± 1400
Multi-jet	185 ± 35	66 ± 31	11700 ± 490	3140 ± 430
$t\bar{t}$ and single-top	232 ± 36	236 ± 34	533 ± 91	535 ± 98
Di-boson	9.1 ± 2.3	10.0 ± 2.5	466 ± 40	468 ± 42
Total SM	1059 ± 81	955 ± 86	59500 ± 3300	55200 ± 3600
Data	1067	947	60351	54776

Table 9.2: Event yields for the expected signal and background and for the observed data in the tag and veto categories of the $h/H/A \to \tau_{\text{lep}}\tau_{\text{had}}$ channel. The signal expectation is split into the contribution from each neutral Higgs boson in the MSSM. The uncertainties on the number of events include the statistical and systematic components, added quadratically. Values are taken from Ref. [178].

$h/H/A \to \tau_{\text{lep}}\tau_{\text{had}}$ High-mass Category	
Signal (m_A = 350 GeV, tanβ = 30)	
$h \to \tau\tau$	5.60 ± 0.68
$H \to \tau\tau$	157 ± 13
$A \to \tau\tau$	152 ± 13
$Z/\gamma^* \to \tau\tau$	380 ± 50
$Z/\gamma^* \to ll$	34.9 ± 7.3
W + jets	213 ± 40
Multi-jet	57 ± 20
$t\bar{t}$ and single-top	184 ± 26
Di-boson	30.1 ± 4.8
Total SM	900 ± 72
Data	920

Table 9.3: Event yields for the expected signal and background and for the observed data in the high-mass category of the $h/H/A \to \tau_{\text{lep}}\tau_{\text{had}}$ channel. The signal expectation is split into the contribution from each neutral Higgs boson in the MSSM. The uncertainties on the number of events include the statistical and systematic components, added quadratically. Values are taken from Ref. [178].

decreasing sensitivity at higher masses due to the lower branching ratio with respect to the other channels.

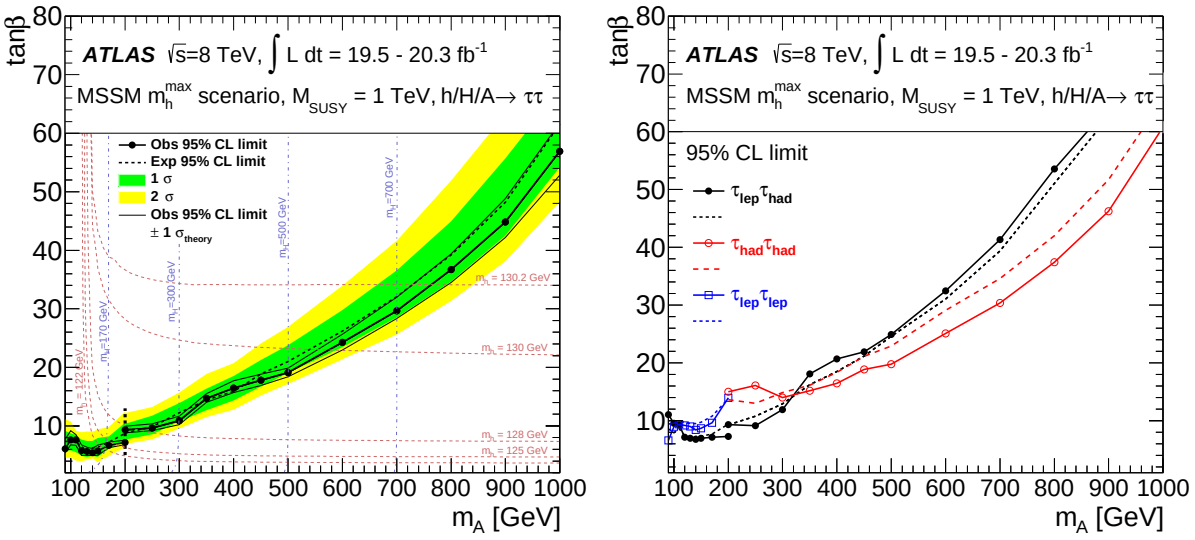

Figure 9.4: Exclusion limits in the $(m_A, \tan\beta)$ plane of the MSSM obtained assuming the m_h^{max} scenario. The effect of the theoretical uncertainties is represented in the plot on the left by the black lines surrounding the observed limit, which are obtained by recomputing the observed exclusion after an upward and downward alteration of the signal cross-section. On the same plots the red and blue lines illustrate the contour of the $(m_A, \tan\beta)$ plane where m_h and m_H, respectively, assume the values indicated along the curves. The vertical dashed line in the plot at $m_A = 200$ GeV illustrates the separation between the low-mass and high-mass combinations. While the low-mass expected exclusion is always obtained for $m_A < 200$ GeV and the high-mass one for $m_A \geq 200$ GeV, the quoted observed limit at $m_A = 200$ GeV is considered to be the most stringent among the two different combinations, which, in this scenario, comes from the low-mass analysis. The graph on the right illustrates the expected and observed exclusion limits for each channel in the combined analysis. The plots are taken from Ref. [178].

In Fig. 9.5, the exclusion limits in the $(m_A, \tan\beta)$ plane are shown for the $m_{h,\text{mod}}^{+}$ (left) and $m_{h,\text{mod}}^{-}$ (right) scenarios. In Fig. 9.4 and 9.5 red and blue lines are shown, which correspond to the contours of the $(m_A, \tan\beta)$ plane where m_h and m_H, respectively, assume the values indicated on the same lines. These contours are scenario dependent, and, by comparison between the figures, it is evident that a larger portion of the $(m_A, \tan\beta)$ plane is compatible with the hypothesis of $m_h \approx 125$ GeV in the $m_{h,\text{mod}}^{+}$ and $m_{h,\text{mod}}^{-}$ scenarios than it is in the m_h^{max}.

All the other additional scenarios proposed in the MSSM are also considered for the limit setting. The full list of plots is available in Ref. [178]. The model-independent exclusion plots are presented in Fig. 9.6 for the two production mechanisms.

The major sources of systematic uncertainty in the final combination are presented in Tab. 9.4 and 9.5, respectively for the low-mass and high-mass combinations at $m_A = 150$ GeV and $\tan\beta = 5.7$ and $m_A = 350$ GeV and $\tan\beta = 15$. They are listed in a similar fashion as discussed in Sec. 8.4.2, ranking from top to bottom in decreasing order of their post-fit impact on the fitted signal strength.

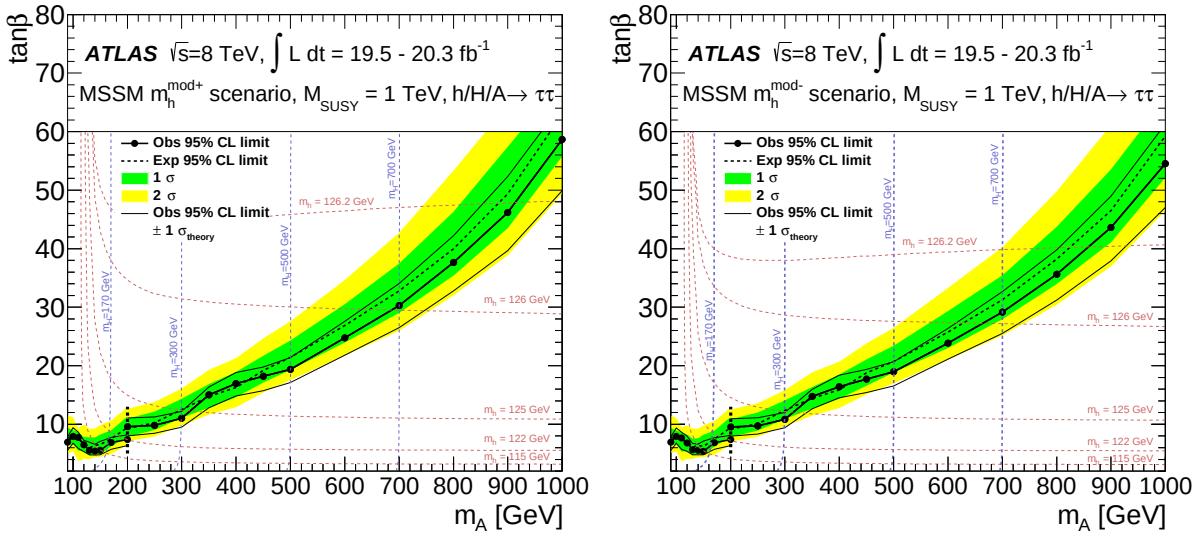

Figure 9.5: Exclusion limits in the $(m_A, \tan\beta)$ plane of the MSSM obtained assuming the $m^{+}_{h,\mathrm{mod}}$ (left) and $m^{-}_{h,\mathrm{mod}}$ (right) scenarios. The effect of the theoretical uncertainties is represented by the black lines surrounding the observed limits, which are obtained by recomputing the observed exclusion after an upward and downward alteration of the signal cross-sections. On the same plots the red and blue lines illustrate the contour of the $(m_A, \tan\beta)$ plane where m_h and m_H, respectively, assume the values indicated along the curves. The vertical dashed line at $m_A = 200$ GeV in the plots illustrates the separation between the low-mass and high-mass combinations. While the low-mass expected exclusion is always obtained for $m_A < 200$ GeV and the high-mass one for $m_A \geq 200$ GeV, the quoted observed limit at the $m_A = 200$ GeV is considered to be the most stringent among the two different combinations, which, in this case, comes from the low-mass analysis. The plots are taken from Ref. [178].

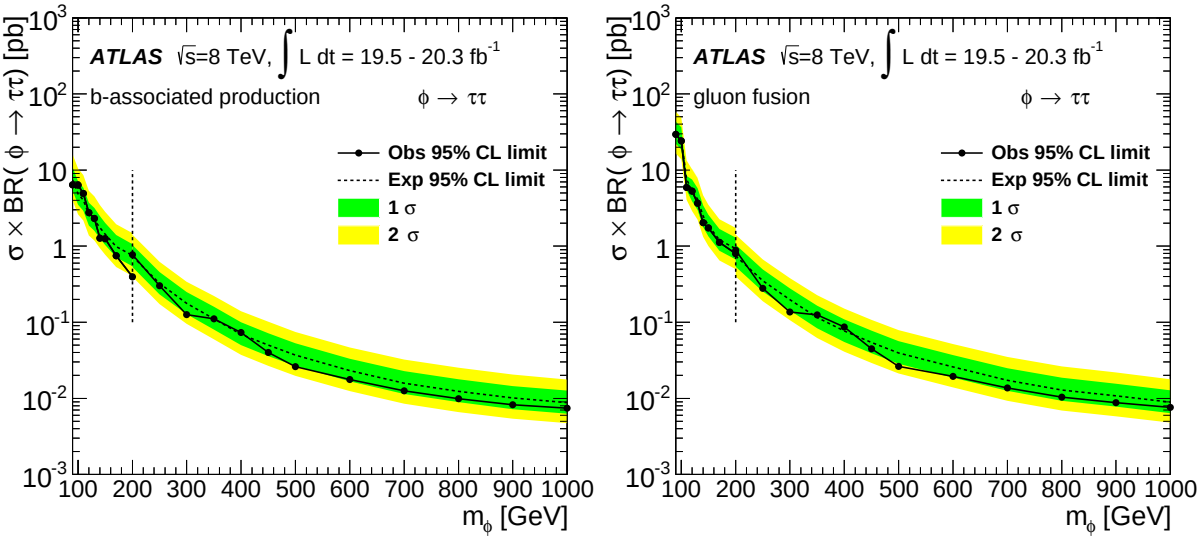

Figure 9.6: Model-independent exclusion limits of the combined analysis. The limit on the $b\bar{b}$ annihilation production mode, here called b-associated production, is shown on the left, while the one for the gluon-gluon fusion production mode is on the right. The plots are taken from Ref. [178].

$h/H/A \to \tau_e\tau_\mu + \tau_{\text{lep}}\tau_{\text{had}}$ at $m_A = 150$ GeV, tan$\beta = 5.7$	
Systematic Uncertainty	Relative Effect on $\hat{\mu}$ (%)
Lepton-to-tau mis-identification probability	14
TES	12
JES+JER	11
Electron reconstruction and identification	8.1
Backgrounds cross-sections and acceptances	7.5
Luminosity	7.4
Muon reconstruction and identification	7.2
b-tagging	6.6
Jet-to-tau mis-identification probability	6.2
Multi-jet shape and normalisation	6.1
$Z \to \tau\tau$ embedding	5.3
Signal acceptance	2.0
Electron+muon trigger	1.5
Tau identification	0.8

Table 9.4: Relative impact of systematic uncertainties on the fitted signal strength for the low-mass combination. The systematic uncertainties listed in the table do not always correspond to a single nuisance parameter in the fit model as some systematic effects on $\hat{\mu}$ are added quadratically. Here the point $m_A = 150$ GeV and tan$\beta = 5.7$ has been used. Values are taken from Ref. [178].

$h/H/A \to \tau_{\text{had}}\tau_{\text{had}} + \tau_{\text{lep}}\tau_{\text{had}}$ at $m_A = 350$ GeV, tan$\beta = 14$	
Systematic Uncertainty	Relative Effect on $\hat{\mu}$ (%)
TES	15
Multi-jet shape and normalisation	9.8
Tau identification	7.9
Jet-to-tau mis-identification probability	7.6
Tau trigger	7.4
Backgrounds cross-sections and acceptances	6.6
Signal acceptance	4.7
Luminosity	4.1
$Z \to \tau\tau$ embedding	1.2
Electron and muon identification	0.7

Table 9.5: Relative impact of systematic uncertainties on the fitted signal strength for the high-mass combination. The systematic uncertainties listed in the table do not always correspond to a single nuisance parameter in the fit model as some systematic effects on $\hat{\mu}$ are added quadratically. Here the point $m_A = 350$ GeV and tan$\beta = 15$ has been used. Values are taken from Ref. [178].

CHAPTER 10

Summary and Conclusions

The discovery of a resonance consistent with the Higgs boson predicted by the Standard Model of particle physics was announced by the ATLAS and CMS experiments in July 2012 [11, 12]. The discovery of this particle, with a mass of $m_H = 125.09 \pm 0.24$ GeV, has started a new era in particle physics. While the Higgs boson is one of the key elements to complete our picture of the fundamental constituents of matter, many observations and open questions in the Standard Model suggest to push the investigation beyond this theory. Measurements of the properties of the Higgs boson have been performed at the LHC and will continue to be an important part of its future physics programme. These measurements are compatible with predictions from extensions of the Standard Model proposed to address unsolved issues with the theory. The model taken into account in this thesis is the Minimal Supersymmetric Standard Model, where the Higgs sector is extended to include three neutral Higgs states h, H and A, and two charged states, $H^{\pm}$. In the MSSM, the discovered particle could arise from the neutral Higgs sector.

In this thesis, the search for the neutral Higgs bosons predicted by the MSSM has been discussed, which was performed with a data sample of $L_{\text{int}} = 19.5$ fb^{-1} collected by the ATLAS experiment from LHC proton-proton collisions at $\sqrt{s} = 8$ TeV. This search focuses on di-tau decays of these particles, which offer a large branching ratio and a better separation from background compared to the dominant decay into pairs of b quarks. For this thesis, the di-tau decay channel where both tau leptons decay hadronically, $h/H/A \to \tau_{\text{had}}\tau_{\text{had}}$, was studied. This decay channel offers a high branching ratio and is part of a combined search in which also other decay channels of the tau leptons are considered. The $h/H/A \to \tau_{\text{had}}\tau_{\text{had}}$ channel has been shown to provide the best sensitivity for high masses of the Higgs bosons, $m_A \gtrsim 350$ GeV.

A fundamental requirement of the analysis is a good discrimination between the hadronic decay of a tau and particle jets initiated by quarks or gluons. The jet background is very abundant in proton-proton collisions, therefore discrimination techniques have been developed to help improve the separation between the tau signal and the jet background. These techniques, based on multivariate algorithms, are applied to both data and simulated events to identify hadronic tau decays. However, the identification efficiency in the simulation might be mis-modelled. For this thesis, a method to calibrate the tau identification efficiency for simulated events has been developed based on a fit to the tau track multiplicity spectrum in data before and after identification. The identification efficiency measured by the fit is then compared to the simulated one in order to derive correction factors provided as a function of the pseudo-rapidity and the track multiplicity of the tau. Systematic uncertainties on the correction have been estimated and are dominated by the model of the jet background in the fit. The fitting method significantly improved the precision of the measured correction factors compared with the previous

ATLAS measurement, lowering the total uncertainty from ≈ 5% to ≈ 2%. The correction factors provided with this method helped reducing the uncertainty associated with the tau identification efficiency in all searches featuring hadronic tau decays, particularly the one reporting evidence for di-tau decays of a scalar boson consistent with the Higgs particle [58].

The search discussed in this thesis greatly improved upon the sensitivity of previous ATLAS searches in the $h/H/A \to \tau_{\text{had}}\tau_{\text{had}}$ channel [95]. In the search, events are selected with topological and kinematic requirements compatible with the di-tau decay of a heavy neutral resonance produced by $b\bar{b}$ annihilation or gluon-gluon fusion production modes. Two categories are defined, where events are triggered by either a single-tau or a di-tau trigger, with high and low p_{T} thresholds, respectively, on the tau candidates. In the single-tau-trigger category the signal acceptance is higher than in the di-tau-trigger category, due to the trigger selection. In addition to this, it offers a better multi-jet rejection compared to the di-tau-trigger category, due to the higher p_{T} threshold.

The multi-jet background is the dominant one and is estimated with data in both categories. In the single-tau-trigger category, a multi-jet control region offering a high number of multi-jet events is used. The multi-jet contribution in the signal region is estimated by weighting events in this control region using weights measured in data with a di-jet tag-and-probe selection. In the di-tau trigger category, three control regions are defined for the measurement of the multi-jet $m_{\text{T}}^{\text{tot}}$ shape and normalisation in the signal region.

Other contributions to the total background include $Z/\gamma^* \to \tau\tau$ and $W \to \tau\nu$+jets events. The analysis is affected by the $Z/\gamma^* \to \tau\tau$ background mainly due to its off-peak events away from the Z resonance peak. Dedicated simulated samples are used to model the tail of the $Z/\gamma^* \to \tau\tau$ invariant mass distribution, which improves the statistical power for this background expectation with respect to an on-peak simulation only. The $W \to \tau\nu$+jets contribution is estimated using a weighting technique applied to simulated fake tau candidates where simulated events are not rejected when failing tau identification, but corrected using a weight measured from data in a $W \to \mu\nu$ + jets control region. This allows one to conserve the statistical power of the simulated sample, while, at the same time, correcting the simulation for a possible mis-modelling of the jet-to-tau mis-identification probability.

The sensitivity of the $h/H/A \to \tau_{\text{had}}\tau_{\text{had}}$ channel dominates the combined search for high Higgs masses, $m_A \gtrsim 350$ GeV. The combined $h/H/A \to \tau\tau$ search at ATLAS makes use of the combined statistical power of the $h/H/A \to \tau_\mu\tau_e$ and $h/H/A \to \tau_{\text{lep}}\tau_{\text{had}}$ channels. Mainly due to the contribution of the $h/H/A \to \tau_{\text{had}}\tau_{\text{had}}$, the ATLAS exclusion limit in the $(m_A, \tan\beta)$ plane is currently the most sensitive in the high-mass region [178]. Compared to the current CMS result [96], the ATLAS expected exclusion is stronger by ≈ 2% to ≈ 20% for mass values from m_A = 400 GeV to m_A = 1000 GeV. A similar difference is seen in the observed exclusion limits. Even though the two fit models are not directly comparable, as a different test statistic is used in the hypothesis test (cf. Sec. 3.3.1), the presented search is still the most sensitive at high mass.

Many MSSM scenarios, proposed after the discovery of the new resonance, have been investigated in the analysis. While the most conservative m_h^{max} has become disfavoured after the measurements of the Higgs mass of $m_H \approx 125$ GeV, it has nonetheless been considered in this thesis in order to allow for a comparison with previous results. Less conservative scenarios, like $m_{h,\text{mod}}^{+}$ and $m_{h,\text{mod}}^{-}$, however, while being more compatible with the measured Higgs boson mass value, do not lead to an observed excess. Also these new scenarios have been investigated.

Exclusion limits have also been set in a model independent way, providing an excluded cross-section at 95% confidence level on the $b\bar{b}$ annihilation and the gluon-gluon fusion production modes of a generic neutral resonance, ϕ. The excluded cross-sections decrease with the value of the resonance mass and are $\sigma_{\text{excl.}}(b\bar{b} \to \phi \to \tau\tau) \approx 4.2$ pb and $\sigma_{\text{excl.}}(gg \to \phi \to \tau\tau) \approx 6.8$ pb at m_ϕ = 170 GeV and $\sigma_{\text{excl.}}(b\bar{b} \to \phi \to \tau\tau) \approx 9.2$ fb and $\sigma_{\text{excl.}}(gg \to \phi \to \tau\tau) \approx 10$ fb at m_ϕ = 1000 GeV. These limits are of

paramount importance to theorists who investigate new models and can probe new parameter spaces with the excluded cross-sections.

Research is continuing at the ATLAS and CMS experiments after the start of Run-II at $\sqrt{s} = 13$ TeV. The increase in the centre-of-mass energy opens up interesting prospects for the $h/H/A \to \tau\tau$ search, especially at high m_A. In fact, background cross-sections will increase very roughly by a factor of ≈ 3, but production cross-sections for A and H will both increase by a factor in the range from ≈ 2 to ≈ 7 for $m_A = 100$ GeV and $m_A = 1000$ GeV, respectively. The sensitivity of the combined $h/H/A \to \tau\tau$ analysis presented in this thesis is expected to be achieved already with $L_{\text{int}} \approx 5$ fb^{-1}, expected to be collected within 2016. Given these projections, the high-mass region of the MSSM parameter space will be the main focus of the new search, where the $h/H/A \to \tau_{\text{had}}\tau_{\text{had}}$ channel will be the one with the dominant sensitivity across the vast majority of the m_A range.

New prospects for tau lepton reconstruction will also be taken into account for future ATLAS searches. An improved tau reconstruction is available in Run-II, taking into account the topological and kinematic configuration of the hadronic tau decay products, which will particularly benefit tau identification and the $h/H/A \to \tau_{\text{had}}\tau_{\text{had}}$ search. Thanks to this, searches for di-tau resonances will also have the possibility to address spin correlations of the two tau leptons, especially in the channel where both taus decay hadronically, due to the presence of only two neutrinos.

For future $h/H/A \to \tau\tau$ searches, the interpretation of the results will be updated. The MSSM phenomenological scenarios considered in this thesis will continue to provide a useful benchmark for the presentation of final results, however, further scenarios have been proposed [111], which are less dependent on assumptions on the next-to-leading-order MSSM parameters of the Higgs sector, and fix the value of the mass of the lightest MSSM Higgs boson at the measured Higgs boson mass.

If no discovery is made in the next LHC runs, a significant portion of the available MSSM parameter space will close. However, if signal of new physics, such as additional Higgs bosons, will be found, our picture of the fundamental constituents of matter will significantly change, opening a new era of scientific investigations.

Bibliography

[1] S. L. Glashow, *Partial Symmetries of Weak Interactions*, Nucl. Phys. **22** (1961) 579–588 (cit. on p. 1).

[2] S. Weinberg, *A Model of Leptons*, Phys. Lett. **19** (1967) 1264–1266 (cit. on p. 1).

[3] A. Salam and J. Ward, *Weak and Electromagnetic Interactions*, Nuovo Cimento **11** (1959) 568–577 (cit. on p. 1).

[4] L. Evans and P. Bryant, *LHC Machine*, JINST **3** (2008) S08001 (cit. on pp. 1, 49).

[5] F. Englert and R. Brout, *Broken symmetry and the mass of gauge vector mesons*, Phys. Rev. Lett. **13** (1964) 321–323 (cit. on pp. 1, 5).

[6] P. W. Higgs, *Broken symmetries, massless particles and gauge fields*, Phys. Lett. **12** (1964) 132–133 (cit. on pp. 1, 5).

[7] P. W. Higgs, *Broken symmetries and the masses of gauge bosons*, Phys. Rev. Lett. **13** (1964) 508–509 (cit. on pp. 1, 5).

[8] P. W. Higgs, *Spontaneous symmetry breakdown without massless bosons*, Phys. Rev. **145** (1966) 1156–1163 (cit. on pp. 1, 5).

[9] G. Guralnik, C. Hagen and T. Kibble, *Global conservation laws and massless particles*, Phys. Rev. Lett. **13** (1964) 585–587 (cit. on pp. 1, 5).

[10] T. Kibble, *Symmetry breaking in non-Abelian gauge theories*, Phys. Rev. **155** (1967) 1554–1561 (cit. on pp. 1, 5).

[11] ATLAS Collaboration, *Observation of a new particle in the search for the Standard Model Higgs boson with the ATLAS detector at the LHC*, Phys. Lett. B **716** (2012) 1–29, arXiv:1207.7214 [hep-ex] (cit. on pp. 1, 41, 207).

[12] CMS Collaboration, *Observation of a new boson at a mass of 125 GeV with the CMS experiment at the LHC*, Phys. Lett. B **716** (2012) 30–61, arXiv:1207.7235 [hep-ex] (cit. on pp. 1, 41, 207).

[13] G. Hinshaw et al., *Five-Year Wilkinson Microwave Anisotropy Probe Observations: Data Processing, Sky Maps, and Basic Results*, Astrophysical Journal Supplement **180** (2009) 225–245, arXiv:0803.0732 [astro-ph] (cit. on pp. 1, 20).

[14] Plank Collaboration, *Planck 2013 results. XVI. Cosmological parameters* (2014), arXiv:1303.5076 [astro-ph.CO] (cit. on pp. 1, 20).

[15] F. Mandl and G. Shaw, *Quantum Field Theory*, 2nd ed., Wiley, 2010 (cit. on pp. 5, 9, 10, 13, 17, 18, 33, 55, 64, 120).

[16] M. E. Peskin and D. Schroeder, *An Introduction to Quantum Field Theory*, Westview Press, 1995 (cit. on pp. 5, 18, 33, 64).

[17] A. Djouadi,
The Anatomy of Electro-Weak Symmetry Breaking. I: The Higgs bosons in the Standard Model,
Phys. Rept. **457** (2008) 1–216, arXiv:hep-ph/0503172v2 (cit. on p. 5).

[18] J. Beringer et al. (Particle Data Group), *Review of Particle Physics*,
Phys. Rev. D **86** (2012) 010001
(cit. on pp. 6, 8, 11, 16, 49, 57, 60, 62–64, 70, 71, 80, 117, 118, 120, 122, 177–179).

[19] N. Cabibbo, *Unitary Symmetry and Leptonic Decays*, Phys. Rev. Lett. **10**.12 (1963) 531–533 (cit. on p. 12).

[20] M. Kobayashi and T. Maskawa, *CP-Violation in the Renormalizable Theory of Weak Interaction*, Prog. Theor. Phys. **49**.2 (1973) 652–657 (cit. on p. 12).

[21] T2K Collaboration, *Observation of Electron Neutrino Appearance in a Muon Neutrino Beam*, Phys. Rev. Lett. **112** (2014) 061802, arXiv:1311.4750 [hep-ex] (cit. on pp. 12, 20).

[22] B. Pontecorvo, *Neutrino Experiments and the Problem of Conservation of Leptonic Charge*, Soviet Physics JETP **26** (1968) 984 (cit. on p. 12).

[23] Z. Maki, M. Nakagawa and S. Sakata, *Remarks on the Unified Model of Elementary Particles*, Prog. Theor. Phys. **28**.5 (1962) 870–880 (cit. on p. 12).

[24] F. R. Klinkhamer, *Neutrino mass and the Standard Model*,
Mod. Phys. Lett. A **28** (2013) 1350010, arXiv:1112.2669 [hep-ph] (cit. on p. 14).

[25] ATLAS and CMS Collaborations, *Combined Measurement of the Higgs Boson Mass in pp Collisions at $\sqrt{s} = 7$ TeV and 8 TeV with the ATLAS and CMS Experiments*,
Phys. Rev. Lett. **114** (2015) 191803, arXiv:1503.07589 [hep-ex] (cit. on pp. 16, 42).

[26] LHC Higgs Cross Section Working Group, S. Dittmaier et al.,
LHC Higgs Cross Section Working Group Twiki, [Online; accessed 19-January-2015], 2015,
URL: https://twiki.cern.ch/twiki/bin/view/LHCPhysics/LHCHXSWG
(cit. on pp. 17, 31, 32).

[27] M. Gell-Mann and F. E. Low, *Quantum Electrodynamics at Small Distances*,
Phys. Rev. **95** (1954) 1300 (cit. on p. 18).

[28] M. E. Peskin, *Beyond the Standard Model* (1997), arXiv:hep-ph/9705479 (cit. on pp. 19, 27).

[29] V. C. Rubin and W. K. Ford,
Rotation of the Andromeda Nebula from a Spectroscopic Survey of Emission Regions,
Astrophysical Journal **159** (1970) 379 (cit. on p. 20).

[30] V. Rubin, W. K. Thonnard and N. Ford, *Rotational Properties of 21 Sc Galaxies with a Large Range of Luminosities and Radii from NGC 4605 (R = 4kpc) to UGC 2885 (R = 122kpc)*,
Astrophysical Journal **238** (1980) 471 (cit. on p. 20).

[31] F. Zwicky, *On the Masses of Nebulae and of Clusters of Nebulae*,
Astrophysical Journal **86** (1937) 217 (cit. on p. 20).

[32] C. J. Copi, D. N. Schramm and M. S. Turner,
Big-Bang Nucleosynthesis and the Baryon Density of the Universe (1995),
arXiv:astro-ph/9407006 (cit. on p. 20).

[33] G. Paál, I. Horváth and B. Lukács, *Inflation and compactification from Galaxy redshifts?*, Astrophysics and Space Science **191** (1992) 107–124 (cit. on p. 20).

[34] R. Durrer, *What do we really know about Dark Energy?*, Phil. Trans. R. Soc. A **369**.1957 (2011) 5102–5114, arXiv:1103.5331 [astro-ph] (cit. on p. 20).

[35] P. J. E. Peebles and B. Ratra, *The cosmological constant and dark energy*, Reviews of Modern Physics **75** (2003) 559–606, arXiv:astro-ph/0207347 (cit. on p. 20).

[36] D. Hanneke, S. Fogwell Hoogerheide and G. Gabrielse, *Cavity Control of a Single-Electron Quantum Cyclotron: Measuring the Electron Magnetic Moment*, Phys. Rev. A **83** (2011) 052122, arXiv:1009.4831 [physics.atom-ph] (cit. on p. 20).

[37] Muon (g-2) Collaboration, *Final report of the E821 muon anomalous magnetic moment measurement at BNL*, Phys. Rev. D **73** (2006) 072003, arXiv:hep-ex/0602035 (cit. on pp. 20, 48).

[38] S. W. Hawking and G. F. R. Ellis, *The Large Scale Structure of Space-Time*, Cambridge University Press, 1973 (cit. on p. 20).

[39] S. P. Martin, *Supersymmetry Primer* (2011), arXiv:hep-ph/9709356v6 (cit. on pp. 20, 23, 24).

[40] I. J. R. Aitchinson, *Supersymmetry and the MSSM: An Elementary Introduction* (2005), arXiv:hep-ph/0505105v1 (cit. on pp. 20, 23).

[41] A. Djouadi, *The Anatomy of Electro-Weak Symmetry Breaking. II: The Higgs bosons in the Minimal Supersymmetric Model*, Phys. Rept. **459** (2008) 1–241, arXiv:hep-ph/0503173v2 (cit. on pp. 20, 28).

[42] K. A. Olive, *Introduction to Supersymmetry: Astrophysical and Phenomenological Constraints* (1999), arXiv:hep-ph/9911307v1 (cit. on p. 20).

[43] S. Coleman and J. Mandula, *All Possible Symmetries of the S Matrix*, Phys. Rev. **159** (1967) 1251 (cit. on p. 22).

[44] R. Haag, J. T. Lopuszański and M. Sohnius, *All possible generators of supersymmetries of the S-matrix*, Nucl. Phys. B **88** (1975) 257–274 (cit. on p. 22).

[45] G. 't Hooft, *Symmetry Breaking through Bell-Jackiw Anomalies*, Phys. Rev. Lett. **37** (1976) 8 (cit. on p. 25).

[46] A. Chamseddine, R. Arnowitt and P. Nath, *Locally Supersymmetric Grand Unification*, Phys. Rev. Lett. **49** (1982) 970 (cit. on p. 26).

[47] G. Degrassi, S. Heinemeyer, W. Hollik, P. Slavich, G. Weiglein, *Towards High-Precision Predictions for the MSSM Higgs Sector*, Eur. Phys. J. C **28** (2002) 133–143, arXiv:hep-ph/0212020 (cit. on p. 28).

[48] A. Djouadi et al., *The Minimal Supersymmetric Standard Model: Group Summary Report* (1999), arXiv:hep-ph/9901246v1 (cit. on p. 29).

[49] M. Carena et al., *MSSM Higgs Boson Searches at the LHC: Benchmark Scenarios after the Discovery of a Higgs-like Particle*, Eur. Phys. J. C **73** (2013) 2552, arXiv:1302.7033 [hep-ph] (cit. on pp. 30–34).

[50] T. Hahn et al., *FeynHiggs: A program for the calculation of MSSM Higgs-boson observables*, Comput. Phys. Comm. **180** (2009) 1426–1427 (cit. on pp. 30, 32, 112–114).

[51] S. Heinemeyer, W. Hollik and G. Weiglein, *The Masses of the neutral CP-even Higgs bosons in the MSSM: Accurate analysis at the two loop level*, Eur. Phys. J. C **9** (1999) 343–366, arXiv:hep-ph/9812472 [hep-ph] (cit. on pp. 30, 32, 112–114).

[52] M. Frank et al., *The Higgs boson masses and mixings of the complex MSSM in the Feynman-diagrammatic approach*, JHEP **02** (2007) 047, arXiv:hep-ph/0611326 [hep-ph] (cit. on pp. 30, 32, 112–114).

[53] R. Harlander, S. Liebler and H. Mantler, *SusHi: A program for the calculation of Higgs production in gluon fusion and bottom-quark annihilation in the Standard Model and the MSSM*, Comput. Phys. Comm. **184** (2013) 1605–1617, arXiv:1212.3249 [hep-ph] (cit. on p. 31).

[54] A. Djouadi, J. Kalinowski and M. Spira, *HDECAY: a Program for Higgs Boson Decays in the Standard Model and its Supersymmetric Extension*, Comput. Phys. Comm. **108** (1998) 56–74, arXiv:hep-ph/9704448 (cit. on p. 32).

[55] ALEPH, DELPHI, L3, OPAL Collaborations, *Search for Neutral MSSM Higgs Bosons at LEP*, Eur. Phys. J. C **47** (2006) 547–587, arXiv:hep-ex/0602042 (cit. on pp. 33, 43, 44).

[56] M. Carena, S. Heinemeyer, C.E.M. Wagner, G. Weiglein, *Suggestions for Improved Benchmark Scenarios for Higgs-Boson Searches at LEP2* (1999), arXiv:hep-ph/9912223 (cit. on p. 33).

[57] M. Carena, S. Heinemeyer, C.E.M. Wagner, G. Weiglein, *Suggestions for Benchmark Scenarios for MSSM Higgs Boson Searches at Hadron Colliders*, Eur. Phys. J. C **26** (2003) 601–607, arXiv:hep-ph/0202167 (cit. on p. 33).

[58] ATLAS Collaboration, *Evidence for the Higgs-boson Yukawa coupling to tau leptons with the ATLAS detector*, JHEP **04** (2015) 117, arXiv:1501.04943 [hep-ex] (cit. on pp. 33, 41, 43, 208).

[59] CMS Collaboration, *Precise determination of the mass of the Higgs boson and tests of compatibility of its couplings with the standard model predictions using proton collisions at 7 and 8 TeV* (2014), arXiv:1412.8662 [hep-ex] (cit. on pp. 33, 41–43).

[60] A. Buckley et al., *General-purpose event generators for LHC physics* (2011), arXiv:1101.2599v1 [hep-ph] (cit. on pp. 34, 37, 38).

[61] T. Sjöstrand, *Monte Carlo Generators* (2006), arXiv:hep-ph/0611247v1 (cit. on p. 34).

[62] C. Reuschle, *Event simulation for colliders - A basic overview* (2014), arXiv:1411.7321 [hep-ph] (cit. on p. 34).

[63] M. H. Seymour, M. Marx, *Monte Carlo Event Generators* (2013), arXiv:1304.6677 [hep-ph] (cit. on p. 34).

[64] M. Dobbs, , J. B. Hansen, *The HepMC C++ Monte Carlo event record for High Energy Physics*, Comput. Phys. Comm. **134** (2001) 41–46 (cit. on p. 35).

[65] M. Botje, J. Butterworth, A. Cooper-Sarkar, A. de Roeck, J. Feltesse, S. Forte, A. Glazov, J. Huston, R. McNulty, T. Sjostrand, R. Thorne, *The PDF4LHC Working Group Interim Recommendations* (2011), arXiv:1101.0538 [hep-ph] (cit. on pp. 36, 120).

[66] P. Nason, *A New Method for Combining NLO QCD with Shower Monte Carlo Algorithms*, JHEP **0411** (2004) 040, arXiv:hep-ph/0409146 (cit. on pp. 38, 113, 121).

[67] S. Frixione, B. R. Webber, *Matching NLO QCD computations and parton shower simulations*, JHEP **0206** (2002) 029, arXiv:hep-ph/0204244 (cit. on pp. 38, 119).

[68] S. Catani, F. Krauss, R. Kuhn, B. R. Webber, *QCD matrix elements + parton showers*, JHEP **0111** (2001) 063, arXiv:hep-ph/0109231 (cit. on pp. 38, 113).

[69] T. Gleisberg, S. Hoeche, F. Krauss, M. Schoenherr, S. Schumann, F. Siegert, J. Winter, *Event generation with SHERPA 1.1*, JHEP **0902** (2009) 007, arXiv:0811.4622 [hep-ph] (cit. on pp. 38, 113, 119).

[70] T. Sjöstrand, S. Mrenna, P. Skands, *PYTHIA 6.4 Physics and Manual*, JHEP **0605** (2006) 026, arXiv:hep-ph/0603175 (cit. on pp. 38, 120).

[71] T. Sjöstrand, S. Mrenna, P. Skands, *A Brief Introduction to PYTHIA 8.1*, Comput. Phys. Comm. **178** (2008) 852–867, arXiv:0710.3820 [hep-ph] (cit. on pp. 38, 85, 117, 118, 121).

[72] G. Marchesini, B. R. Webber, *Simulation of QCD coherence in heavy quark production and decay*, Nucl. Phys. B **330** (1990) 261–283 (cit. on pp. 38, 119).

[73] M. Bähr, S. Gieseke, M. H. Seymour, *Simulation of multiple partonic interactions in Herwig++*, JHEP **0807** (2008) 076, arXiv:0803.3633 [hep-ph] (cit. on pp. 38, 39).

[74] B. Andersson, G. Gustafson, G. Ingelman, T. Sjöstrand, *Parton fragmentation and string dynamics*, Phys. Rep. **97** (1983) 31–145 (cit. on p. 38).

[75] S. Jadach, J. H. Kühn, Z. Wąs, *TAUOLA - a library of Monte Carlo programs to simulate decays of polarized τ leptons*, Comp. Phys. Comm. **64** (1991) 275–299 (cit. on pp. 39, 120, 198).

[76] P. Golonka, Z. Wąs, *PHOTOS Monte Carlo: a precision tool for QED corrections in Z and W decays*, Eur. Phys. J. C **45** (2006) 97–107, arXiv:hep-ph/0506026 (cit. on p. 39).

[77] J.M.Butterworth, J.R.Forshaw, M.H.Seymour, *Multiparton Interactions in Photoproduction at HERA*, Z. Phys. C **72** (1996) 637–646, arXiv:hep-ph/9601371 (cit. on pp. 39, 119, 121).

[78] P. Z. Skands, *Tuning Monte Carlo Generators: The Perugia Tunes*, Phys. Rev. D **82** (2010) 074018, arXiv:1005.3457v5 [hep-ph] (cit. on p. 39).

[79] ATLAS Collaboration, *New ATLAS event generator tunes to 2010 data*, tech. rep. ATL-PHYS-PUB-2011-008, CERN, May 2011, URL: https://cdsweb.cern.ch/record/1345343 (cit. on p. 39).

[80] ATLAS Collaboration, *Further ATLAS tunes of PYTHIA6 and Pythia 8*, tech. rep. ATL-PHYS-PUB-2011-014, CERN, Nov. 2011, URL: https://cds.cern.ch/record/1400677 (cit. on pp. 39, 97, 160).

[81] T. Sjöstrand, P. Skands, *Multiple Interactions and the Structure of Beam Remnants*, JHEP **0403** (2004) 053, arXiv:hep-ph/0402078v2 [hep-ph] (cit. on p. 39).

[82] G. P. Salam, *Towards Jetography*, Eur. Phys. J. C **67** (2010) 637–686, arXiv:0906.1833 [hep-ph] (cit. on pp. 39, 71).

[83] ATLAS Collaboration,
Observation and measurement of Higgs boson decays to WW^* with the ATLAS detector (2014), arXiv:1412.2641 [hep-ex] (cit. on pp. 41, 43).

[84] ATLAS Collaboration, *Search for the $b\bar{b}$ decay of the Standard Model Higgs boson in associated $(W/Z)H$ production with the ATLAS detector*, JHEP **01** (2015) 069, arXiv:1409.6212 [hep-ex] (cit. on pp. 41, 43).

[85] ATLAS Collaboration, *Combined coupling measurements of the Higgs-like boson with the ATLAS detector using up to 25* fb^{-1} *of proton-proton collision data*, tech. rep. ATLAS-CONF-2013-034, CERN, Mar. 2013, URL: https://cds.cern.ch/record/1528170 (cit. on p. 42).

[86] ATLAS Collaboration, *Measurement of the Higgs boson mass from the $H \to \gamma\gamma$ and $H \to ZZ^* \to 4l$ channels with the ATLAS detector using 25* fb^{-1} *of pp collision data*, Phys. Rev. D **90** (2014) 052004, arXiv:1406.3827 [hep-ex] (cit. on pp. 41, 42).

[87] G. Cowan, *Statistical Data Analysis*, Clarendon press, 1998 (cit. on pp. 42, 45, 177–180, 182–185).

[88] ATLAS Collaboration, *Summary plots from the ATLAS Higgs physics group*, [Online; accessed 27-January-2015], 2015, URL: https://atlas.web.cern.ch/Atlas/GROUPS/PHYSICS/CombinedSummaryPlots/HIGGS/ (cit. on p. 43).

[89] ATLAS Collaboration,
Measurements of Higgs boson production and couplings in the four-lepton channel in pp collisions at center-of-mass energies of 7 and 8 TeV with the ATLAS detector, Phys. Rev. D **91** (2015) 012006, arXiv:1408.5191 [hep-ex] (cit. on p. 43).

[90] ATLAS Collaboration, *Measurement of Higgs boson production in the diphoton decay channel in pp collisions at center-of-mass energies of 7 and 8 TeV with the ATLAS detector*, Phys. Rev. D **90** (2014) 112015, arXiv:1408.7084 [hep-ex] (cit. on p. 43).

[91] CDF and DØ Collaborations,
Search for Neutral Higgs Bosons in Events with Multiple Bottom Quarks at the Tevatron (2012), arXiv:1207.2757 [hep-ex] (cit. on pp. 43, 45).

[92] CDF and DØ Collaborations, *Combined CDF and D0 upper limits on MSSM Higgs boson production in tau-tau final states with up to* 2.2 fb^{-1} (2010), arXiv:1003.3363 [hep-ex] (cit. on pp. 44, 45).

[93] DØ Collaboration, *Search for Higgs bosons of the minimal supersymmetric standard model in $p\bar{p}$ collisions at* $\sqrt{s} = 1.96$ TeV (2011), arXiv:1112.5431 [hep-ex] (cit. on p. 44).

[94] CDF Collaboration,
Search for New Physics Using High Mass Tau Pairs from 1.96 TeV Proton-Antiproton Collisions, Phys. Rev. Lett. **95** (2005) 131801, arXiv:hep-ex/0506034 (cit. on p. 44).

[95] ATLAS Collaboration, *Search for the neutral Higgs bosons of the Minimal Supersymmetric Standard Model in pp collisions at* $\sqrt{s} = 7$ TeV *with the ATLAS detector*, JHEP **02** (2013) 95, arXiv:1211.6956 [hep-ex] (cit. on pp. 44, 46, 208).

[96] CMS Collaboration,
Search for neutral MSSM Higgs bosons decaying to a pair of tau leptons in pp collisions, JHEP **10** (2014) 160, arXiv:1408.3316 [hep-ex] (cit. on pp. 44, 46, 208).

[97] CMS Collaboration, *Search for a Higgs boson decaying into a b-quark pair and produced in association with b quarks in proton-proton collisions at 7 TeV*, Phys. Lett. B **722** (2013) 207, arXiv:1302.2892 [hep-ex] (cit. on p. 45).

[98] ATLAS Collaboration, *Search For Higgs Boson Pair Production in the $\gamma\gamma b\bar{b}$ Final State using pp Collision Data at $\sqrt{s} = 8$ TeV from the ATLAS Detector* (2014), arXiv:1406.5053 [hep-ex] (cit. on p. 47).

[99] CMS Collaboration, *Search for the resonant production of two Higgs bosons in the final state with two photons and two bottom quarks*, tech. rep. CMS-PAS-HIG-13-032, CERN, Apr. 2014, URL: https://cds.cern.ch/record/1697512 (cit. on p. 47).

[100] CMS Collaboration, *Search for narrow resonant pair production of the Higgs boson in the final state with four bottom quarks*, tech. rep. CMS-PAS-HIG-14-013, CERN, Aug. 2014, URL: https://cds.cern.ch/record/1748425 (cit. on p. 47).

[101] CMS Collaboration, *Search for a pseudoscalar boson A decaying into a Z and an h boson in the $l\bar{l}b\bar{b}$ final state*, tech. rep. CMS-PAS-HIG-14-011, CERN, Nov. 2014, URL: https://cds.cern.ch/record/1969698 (cit. on p. 47).

[102] E. Gross and O. Vittels, *Trial factors for the look elsewhere effect in high energy physics*, Eur. Phys. J. C **70** (2010) 525–530, arXiv:1005.1891 [physics.data-an] (cit. on p. 47).

[103] LHCb Collaboration, *First evidence for the decay $B_s \to \mu^+\mu^-$*, Phys. Rev. Lett. **110** (2013) 021801, arXiv:1211.2674 [hep-ex] (cit. on p. 47).

[104] CMS and LHCb Collaborations, *Combination of results on the rare decays $B_s \to \mu^+\mu^-$ from the CMS and LHCb experiments*, tech. rep. CMS-PAS-BPH-13-007; LHCb-CONF-2013-012; CERN-LHCb-CONF-2013-012, CERN, June 2014, URL: https://cds.cern.ch/record/1564324 (cit. on p. 47).

[105] W. Altmannshofer, M. Carena, N. R. Shah, F. Yu, *Indirect probes of the MSSM after the Higgs discovery*, JHEP (2013) 160, arXiv:1211.1976 [hep-ph] (cit. on pp. 47, 48).

[106] BaBar Collaboration, *Measurement of $B(B \to X_s\gamma)$, the $B \to X_s\gamma$ photon energy spectrum, and the direct CP asymmetry in $B \to X_{s+d}\gamma$ decays*, Phys. Rev. D **86** (2012) 112008, arXiv:1207.5772 [hep-ex] (cit. on p. 47).

[107] XENON100 Collaboration, *Dark Matter Results from 225 Live Days of XENON100 Data*, Phys. Rev. Lett. **109** (2012) 181301, arXiv:1207.5988 [hep-ex] (cit. on p. 47).

[108] F. Jegerlehner, A. Nyffeler, *The Muon g-2*, Phys. Rep. **477** (2009) 1–110, arXiv:0902.3360 [hep-ph] (cit. on p. 48).

[109] H. G. Fargnoli, C. Gnendiger, S. Paßehr, D. Stöckinger, H. Stöckinger-Kim, ed., *Two-loop corrections to $(g-2)_\mu$ in the SM and the MSSM*, Proceedings of Science, July 2014, arXiv:1407.1501 [hep-ph] (cit. on p. 48).

[110] ATLAS Collaboration, *Constraints on New Phenomena via Higgs Coupling Measurements with the ATLAS Detector*, tech. rep. ATLAS-CONF-2014-010, CERN, Mar. 2014, URL: http://cds.cern.ch/record/1670531 (cit. on p. 48).

[111] A. Djouadi, L. Maiani, G. Moreau, A. Polosa, J. Quevillon, V. Riquer, *The post-Higgs MSSM scenario: Habemus MSSM?*, Eur. Phys. J. C **73** (2013) 2650, arXiv:1307.5205 [hep-ph] (cit. on pp. 48, 209).

[112] L. Maiani, A. Polosa, V. Riquer, *Bounds to the Higgs Sector Masses in Minimal Supersymmetry from LHC Data*, Phys. Lett. B **724** (2013) 274–277, arXiv:1305.2172 [hep-ph] (cit. on p. 48).

[113] CERN, *The CERN accelerator complex*, [Online; accessed 23-March-2015], 2015, URL: https://cds.cern.ch/record/1260465 (cit. on p. 50).

[114] J.M. Campbell, J.W. Huston, W.J. Stirling, *Hard Interactions of Quarks and Gluons: a Primer for LHC Physics*, Rept. Prog. Phys **70** (2007) 89, arXiv:hep-ph/0611148 (cit. on p. 51).

[115] ATLAS Collaboration, *The ATLAS Experiment at the CERN Large Hadron Collider*, JINST **3** (2008) S08003 (cit. on pp. 52, 55–58, 60, 62–64, 105).

[116] CMS Collaboration, *The CMS experiment at the CERN LHC*, JINST **3** (2008) S08004 (cit. on p. 52).

[117] LHCb Collaboration, *The LHCb Detector at the LHC*, JINST **3** (2008) S08005 (cit. on p. 52).

[118] ALICE Collaboration, *The ALICE experiment at the CERN LHC*, JINST **3** (2008) S08002 (cit. on p. 52).

[119] W. A. Zajc, *The Fluid Nature of Quark-Gluon Plasma*, Nucl. Phys. A **805** (2008) 283–294, arXiv:0802.3552 [nucl-ex] (cit. on p. 52).

[120] TOTEM Collaboration, *The TOTEM Experiment at the CERN Large Hadron Collider*, JINST **3** (2008) S08007 (cit. on p. 52).

[121] LHCf Collaboration, *The LHCf detector at the CERN Large Hadron Collider*, JINST **3** (2008) S08006 (cit. on p. 52).

[122] MoEDAL Collaboration, *Technical Design Report of the MoEDAL Experiment*, tech. rep. CERN-LHCC-2009-006, CERN, June 2009, URL: http://cds.cern.ch/record/1181486 (cit. on p. 52).

[123] ATLAS Collaboration, *LuminosityPublicResults*, [Online; accessed 22-March-2015], 2015, URL: https://twiki.cern.ch/twiki/bin/view/AtlasPublic/LuminosityPublicResults (cit. on pp. 52–54).

[124] ATLAS Collaboration, *ATLAS detector and physics performance: Technical Design Report, 1*, tech. rep. CERN-LHCC-99-014, CERN, May 1999, URL: https://cds.cern.ch/record/391176 (cit. on p. 55).

[125] C. Grupen and B. Shwartz, *Particle Detectors*, 2nd ed., Cambridge University Press, 2008 (cit. on pp. 57, 60, 62–64, 70).

[126] S. van der Meer, *Calibration of the effective beam height in the ISR*, tech. rep. CERN-ISR-PO-68-31, CERN, 1968, URL: https://cds.cern.ch/record/296752 (cit. on p. 64).

[127] ATLAS Collaboration, *Improved luminosity determination in pp collisions at $\sqrt{s}$ = 7 TeV using the ATLAS detector at the LHC*, Eur. Phys. J. C **73** (2013) 2518, arXiv:1302.4393 [hep-ex] (cit. on pp. 64, 163).

[128] R. Hauser,
The ATLAS Data Acquisition and High Level Trigger Systems: Experience and Upgrade Plans,
tech. rep. ATL-DAQ-PROC-2012-073, CERN, Nov. 2012,
URL: http://cds.cern.ch/record/1497132 (cit. on p. 65).

[129] R. Achnenbach et al., *The ATLAS Level-1 Calorimeter Trigger*, JINST **3** (2008) P03001
(cit. on p. 65).

[130] S. Agostinelli et al., *Geant4:a simulation toolkit*, Nucl. Inst. and Meth. A **506** (2003) 250–303
(cit. on p. 66).

[131] ATLAS Collaboration, *ATLFAST 2.0 a fast simulation package for ATLAS*,
tech. rep. ATL-PHYS-98-131, CERN, Nov. 1998,
URL: https://cds.cern.ch/record/683751 (cit. on p. 66).

[132] ATLAS Collaboration, *ATLAS Computing: technical design report*,
tech. rep. CERN-LHCC-2005-022, CERN, 2005,
URL: https://cds.cern.ch/record/837738 (cit. on p. 67).

[133] ATLAS Collaboration,
Concepts, Design and Implementation of the ATLAS New Tracking (NEWT),
tech. rep. ATL-COM-SOFT-2007-002, CERN, Mar. 2007,
URL: https://cdsweb.cern.ch/record/1020106 (cit. on p. 67).

[134] R. E. Kalman, *A New Approach to Linear Filtering and Prediction Problems*,
J. Fluids Eng. **82** (1960) 35–45 (cit. on p. 68).

[135] T. G. Cornelissen et al., *The global χ^2 track fitter in ATLAS*,
J. Phys.: Conf. Ser. **119** (2008) 032013 (cit. on pp. 68, 71).

[136] ATLAS Collaboration, *Performance of primary vertex reconstruction in proton-proton collisions at $\sqrt{s}$ = 7 TeV in the ATLAS experiment*, tech. rep. ATLAS-CONF-2010-069, CERN, July 2010,
URL: https://cdsweb.cern.ch/record/1281344 (cit. on p. 68).

[137] ATLAS Collaboration, *Characterization of Interaction-Point Beam Parameters Using the pp Event-Vertex Distribution Reconstructed in the ATLAS Detector at the LHC*,
tech. rep. ATLAS-CONF-2010-027, CERN, May 2010,
URL: https://cds.cern.ch/record/1277659 (cit. on p. 68).

[138] W. Waltenberger, R. Frühwirth, P. Vanlaer, *Adaptive vertex fitting*, J. Phys. G **34** (2007) N343
(cit. on p. 68).

[139] W. Lampl et al., *Calorimeter Clustering Algorithms: Description and Performance*,
tech. rep. ATL-LARG-PUB-2008-002, CERN, Apr. 2008,
URL: https://cds.cern.ch/record/1099735 (cit. on pp. 69, 71).

[140] T. Barillari et al., *Local Hadronic Calibration*, tech. rep. ATL-LARG-PUB-2009-001-2,
CERN, Dec. 2008, URL: https://cds.cern.ch/record/1112035 (cit. on p. 70).

[141] ATLAS Collaboration, *Measurement of the muon reconstruction performance of the ATLAS detector using 2011 and 2012 LHC proton-proton collision data*, Eur. Phys. J. C **74** (2014) 3130,
arXiv:1407.3935 [hep-ex] (cit. on p. 70).

[142] ATLAS Collaboration, *Expected Performance of the ATLAS Experiment* (2009),
arXiv:0901.0512 [hep-ex] (cit. on p. 70).

[143] R. Früwirth et al., *Application of Kalman filtering to track and vertex fitting*, Nucl. Inst. and Meth. A **262** (1987) 444–450 (cit. on p. 71).

[144] ATLAS Collaboration, *Improved electron reconstruction in ATLAS using the Gaussian Sum Filter-based model for bremsstrahlung*, tech. rep. ATLAS-CONF-2012-047, CERN, May 2012, URL: https://cdsweb.cern.ch/record/1449796 (cit. on p. 71).

[145] ATLAS Collaboration, *Electron efficiency measurements with the ATLAS detector using the 2012 LHC proton-proton collision data*, tech. rep. ATLAS-CONF-2014-032, CERN, June 2014, URL: https://cds.cern.ch/record/1706245 (cit. on p. 71).

[146] M. Cacciari, G. P. Salam, G. Soyez, *The anti-k_t jet clustering algorithm*, JHEP **0804** (2008) 063, arXiv:0802.1189 [hep-ph] (cit. on pp. 71, 72).

[147] M. Cacciari, G. P. Salam, and G. Soyez, *FastJet user manual*, Eur. Phys. J. C **72** (2011) 1896, arXiv:1111.6097 [hep-ph] (cit. on p. 71).

[148] ATLAS Collaboration, *Jet energy measurement and its systematic uncertainty in proton-proton collisions at $\sqrt{s}$ = 7 TeV with the ATLAS detector*, Eur. Phys. J. C **75** (2015) 17, arXiv:1406.0076 [hep-ex] (cit. on pp. 72, 163).

[149] ATLAS Collaboration, *Pile-up subtraction and suppression for jets in ATLAS*, tech. rep. ATLAS-CONF-2013-083, CERN, Aug. 2013, URL: http://cds.cern.ch/record/1570994 (cit. on pp. 72, 74).

[150] ATLAS Collaboration, *Jet energy measurement with the ATLAS detector in proton-proton collisions at $\sqrt{s}$ = 7 TeV*, Eur. Phys. J. C **73** (2013) 2034, arXiv:1112.6426 [hep-ex] (cit. on p. 72).

[151] ATLAS Collaboration, *Data-driven determination of the energy scale and resolution of jets reconstructed in the ATLAS calorimeters using dijet and multijet events at $\sqrt{s}$ = 7 TeV*, tech. rep. ATLAS-CONF-2015-017, CERN, Apr. 2015, URL: http://cds.cern.ch/record/2008678 (cit. on pp. 73, 163).

[152] D. W. Miller, A. Schwartzman, D. Su, *Jet-Vertex Association Algorithm*, tech. rep. ATL-COM-PHYS-2008-008, CERN, Jan. 2008, URL: https://cds.cern.ch/record/1082880 (cit. on p. 74).

[153] ATLAS Collaboration, *Commissioning of the ATLAS high-performance b-tagging algorithms in the 7 TeV collision data*, tech. rep. ATLAS-CONF-2011-102, CERN, July 2011, URL: https://cds.cern.ch/record/1369219 (cit. on p. 74).

[154] ATLAS Collaboration, *Calibration of b-tagging using dileptonic top pair events in a combinatorial likelihood approach with the ATLAS experiment*, tech. rep. ATLAS-CONF-2014-004, CERN, Feb. 2014, URL: https://cds.cern.ch/record/1664335 (cit. on p. 74).

[155] ATLAS Collaboration, *Calibration of the performance of b-tagging for c and light-flavour jets in the 2012 ATLAS data*, tech. rep. ATLAS-CONF-2014-046, CERN, June 2014, URL: https://cds.cern.ch/record/1741020 (cit. on p. 74).

[156] ATLAS Collaboration, *Performance of Missing Transverse Momentum Reconstruction in ATLAS studied in Proton-Proton Collisions recorded in 2012 at 8 TeV*,
tech. rep. ATLAS-CONF-2013-082, CERN, Aug. 2013,
URL: https://cds.cern.ch/record/1570993 (cit. on pp. 75, 76).

[157] ATLAS Collaboration, *Pile-up Suppression in Missing Transverse Momentum Reconstruction in the ATLAS Experiment in Proton-Proton Collisions at $\sqrt{s}$ = 8 TeV*,
tech. rep. ATLAS-CONF-2014-019, CERN, May 2014,
URL: https://cds.cern.ch/record/1702055 (cit. on pp. 75–77, 163).

[158] ATLAS Collaboration, *A search for high-mass resonances decaying to $\tau^+\tau^-$ in pp collisions at $\sqrt{s}$ = 8 TeV with the ATLAS detector* (2015), arXiv:1502.07177 [hep-ex]
(cit. on pp. 79, 160, 162).

[159] ATLAS Collaboration, *Identification and energy calibration of hadronically decaying tau leptons with the ATLAS experiment in pp collisions at $\sqrt{s}$ = 8 TeV*,
Eur. Phys. J. C **75** (2014) 303, arXiv:1412.7086 [hep-ex]
(cit. on pp. 79, 84–87, 106, 227–231, 234, 235).

[160] ATLAS Collaboration,
Identification of the Hadronic Decays of Tau Leptons in 2012 Data with the ATLAS Detector,
tech. rep. ATLAS-CONF-2013-064, CERN, July 2013,
URL: http://cds.cern.ch/record/1562839 (cit. on pp. 79, 87, 88, 101, 235).

[161] ATLAS Collaboration,
Determination of the tau energy scale and the associated systematic uncertainty in proton-proton collisions at $\sqrt{s}$ = 8 TeV with the ATLAS detector at the LHC in 2012,
tech. rep. ATLAS-CONF-2013-044, CERN, Apr. 2013,
URL: http://cds.cern.ch/record/1544036 (cit. on pp. 79, 87).

[162] ATLAS Collaboration, *Performance of the Reconstruction and Identification of Hadronic Tau Decays in ATLAS with 2011 Data*, tech. rep. ATLAS-CONF-2012-142, CERN, Oct. 2012,
URL: http://cds.cern.ch/record/1485531 (cit. on pp. 79, 81, 82).

[163] M. T. McDonald, *A Cluster-based Approach to Reconstructing π^0s in τ Decays*,
[Online; accessed 24-April-2015], 2012,
URL: https://indico.cern.ch/event/194235/material/slides/0?contribId=2
(cit. on p. 82).

[164] L. Breiman, J. Friedman, R. Olshen, and C. Stone, *Classification and Regression Trees*,
Chapman & Hall, 1984 (cit. on p. 82).

[165] Y. Freund and R. E. Schapire,
A Decision-Theoretic Generalization of On-Line Learning and an Application to Boosting,
J. Comput. Syst. Sci. **55** (1997) 119–139 (cit. on p. 82).

[166] A. Hoecker et al., *TMVA - Toolkit for Multivariate Data Analysis*, PoS **040** (2007),
arXiv:physics.data-an/0703039 (cit. on p. 83).

[167] T. G. Rizzo, *Z' Phenomenology and the LHC* (2006), arXiv:hep-ph/0610104 (cit. on p. 83).

[168] ATLAS Collaboration,
Study of the Response of the Hadronic Barrel Calorimeter in the ATLAS Combined Test-beam to Pions of Energies from 20 to 350 GeV for Beam Impact Points from 0.2 to 0.65,
tech. rep. ATL-TILECAL-PUB-2009-007, CERN, Apr. 2009,
URL: http://cds.cern.ch/record/1172156 (cit. on p. 86).

[169] H. W. Bertini,
Intranuclear-Cascade Calculation of the Secondary Nucleon Spectra from Nucleon-Nucleus Interactions in the Energy Range 340 to 2900 MeV and Comparisons with Experiment,
Phys. Rev. **188** (1969) 1711 (cit. on p. 86).

[170] G. Folger, J.P. Wellisch, *String Parton Models in Geant4* (2003), arXiv:nucl-th/0306007 (cit. on p. 86).

[171] M. Blann, B. L. Berman, and T. T. Komoto,
Precompound-model analysis of photonuclear reactions, Phys. Rev. C **28** (1983) 2296 (cit. on p. 86).

[172] B. Andersson, G. Gustafson, B. Nilsson-Almqvist, *A model for low-p_T hadronic reactions with generalizations to hadron-nucleus and nucleus-nucleus collisions*,
Nuclear Physics B **281** (1987) 289–309 (cit. on p. 86).

[173] M.L. Mangano, F.Piccinini, A.D. Polosa, M.Moretti, R. Pittau,
ALPGEN, a generator for hard multiparton processes in hadronic collisions,
JHEP **0307** (2003) 001, arXiv:hep-ph/0206293 (cit. on p. 97).

[174] M. G. Cox, C. Eiø, G. Mana, F. Pennecchi,
The generalized weighted mean of correlated quantities, Metrologia **43** (2006) S268 (cit. on p. 101).

[175] ATLAS Collaboration, *Performance of the ATLAS Trigger System in 2010*,
Eur. Phys. J. C **72** (2012) 1849, arXiv:1110.1530 [hep-ex] (cit. on p. 104).

[176] P. Rados, [Online; accessed 18-May-2015], 2013,
URL: https://indico.cern.ch/event/239543/material/slides/0?contribId=6 (cit. on p. 106).

[177] P. Rados, *2013 Tau Trigger Scale Factors*, [Online; accessed 18-May-2015], 2013,
URL: https://indico.cern.ch/event/242060/material/slides/1?contribId=3 (cit. on pp. 106, 107).

[178] ATLAS Collaboration, *Search for neutral Higgs bosons of the minimal supersymmetric standard model in pp collisions at $\sqrt{s}$ = 8 TeV with the ATLAS detector*, JHEP **11** (2014) 056,
arXiv:1409.6064 [hep-ex] (cit. on pp. 110, 177, 197, 199, 200, 202–206, 208).

[179] S. Dittmaier, M. Krämer, M. Spira,
Higgs Radiation off Bottom Quarks at the Tevatron and the LHC,
Phys. Rev. D **70** (2004) 074010, arXiv:hep-ph/0309204 (cit. on p. 110).

[180] S. Dawson, C.B. Jackson, L. Reina, D. Wackeroth,
Exclusive Higgs Boson Production with bottom quarks at Hadron Colliders,
Phys. Rev. D **69** (2004) 074027, arXiv:hep-ph/0311067 (cit. on p. 110).

[181] D. Rainwater, M. Spira, D. Zeppenfeld,
Higgs boson production at hadron colliders: Signal and background processes (2001),
arXiv:hep-ph/0203187 (cit. on p. 111).

[182] T. Plehn, *Charged Higgs Boson Production in Bottom-Gluon Fusion*, Phys. Rev. D **67** (2003) 014018, arXiv:hep-ph/0206121 (cit. on p. 111).

[183] F. Maltoni, Z. Sullivan, S. Willenbrock, *Higgs-Boson Production via Bottom-Quark Fusion*, Phys. Rev. D **67** (2003) 093005, arXiv:hep-ph/0301033 (cit. on p. 111).

[184] R. V. Harlander, W. B. Kilgore, *Higgs boson production in bottom quark fusion at next-to-next-to-leading order*, Phys. Rev. D **68** (2003) 013001, arXiv:hep-ph/0304035 (cit. on p. 111).

[185] R. Harlander and W. B. Kilgore, *Next-to-Next-to-Leading Order Higgs Production at Hadron Colliders*, Phys. Rev. Lett. **88** (2002) 201801, arXiv:hep-ph/0201206 [hep-ph] (cit. on pp. 111, 113–115).

[186] R. Harlander, M. Krämer and M. Schumacher, *Bottom-quark associated Higgs-boson production: reconciling the four- and five-flavour scheme approach* (2011), arXiv:1112.3478 [hep-ph] (cit. on p. 112).

[187] LHC Higgs Cross Section Working Group, *Handbook of LHC Higgs Cross Sections: 1. Inclusive Observables* (2011), arXiv:1101.0593 [hep-ph] (cit. on pp. 112, 113, 164).

[188] H.-L. Lai, M. Guzzi, J. Huston, Z. Li, P. M. Nadolsky, J. Pumplin, C.-P. Yuan, *New parton distributions for collider physics*, Phys. Rev. D **82** (2010) 074024, arXiv:1007.2241 [hep-ph] (cit. on pp. 113, 119, 164).

[189] M. Spira, *HIGLU: A Program for the Calculation of the Total Higgs Production Cross Section at Hadron Colliders via Gluon Fusion including QCD Corrections* (1995), arXiv:hep-ph/9510347 (cit. on pp. 113–115).

[190] LHC Higgs Cross Section Working Group, *Handbook of LHC Higgs Cross Sections: 3. Higgs Properties* (2013), arXiv:1307.1347 [hep-ph] (cit. on p. 113).

[191] S. D. Drell, T. M. Yan, *Massive Lepton-Pair Production in Hadron-Hadron Collisions at High Energies*, Phys. Rev. Lett. **25** (1970) 316 (cit. on pp. 116, 117).

[192] ATLAS Collaboration, *Summary plots from the ATLAS Standard Model physics group*, [Online; accessed 31-May-2015], 2015, URL: https://atlas.web.cern.ch/Atlas/GROUPS/PHYSICS/CombinedSummaryPlots/SM/ (cit. on p. 116).

[193] R. Gavin, Y. Li, F. Petriello, S. Quackenbush, *FEWZ 2.0: A code for hadronic Z production at next-to-next-to-leading order*, Comput. Phys. Commun. **182** (2011) 2388–2403, arXiv:1011.3540 [hep-ph] (cit. on pp. 117, 118, 121, 198).

[194] Y. Li, F. Petriello, *Combining QCD and electroweak corrections to dilepton production in FEWZ* (2012), arXiv:1208.5967 [hep-ph] (cit. on pp. 117, 118, 121, 198).

[195] P. M. Nadolsky, H.-L. Lai, Q.-H. Cao, J. Huston, J. Pumplin, D. Stump, W.-K. Tung, C.-P. Yuan, *Implications of CTEQ global analysis for collider observables*, Phys. Rev. D **78** (2008) 013004, arXiv:0802.0007 [hep-ph] (cit. on pp. 117, 119–121).

[196] A.D. Martin, W.J. Stirling, R.S. Thorne, G. Watt, *Uncertainties on α_S in global PDF analyses and implications for predicted hadronic cross sections*, Eur. Phys. J C **64** (2009) 653–680, arXiv:0905.3531 [hep-ph] (cit. on p. 117).

[197] G. Corcella et al., *HERWIG 6.5 Release Note* (2005), arXiv:hep-ph/0210213 (cit. on pp. 119, 121).

[198] M. Cacciari, M. Czakon, M. L. Mangano, A. Mitov, P. Nason, *Top-pair production at hadron colliders with next-to-next-to-leading logarithmic soft-gluon resummation* (2011), arXiv:1111.5869 [hep-ph] (cit. on p. 119).

[199] M. Czakon, A. Mitov, *Top++: a program for the calculation of the top-pair cross-section at hadron colliders* (2011), arXiv:1112.5675 [hep-ph] (cit. on p. 119).

[200] M. Czakon, A. Mitov, *NNLO corrections to top-pair production at hadron colliders: the all-fermionic scattering channels* (2012), arXiv:1207.0236 [hep-ph] (cit. on p. 119).

[201] M. Czakon, P. Fiedler, A. Mitov, *The total top quark pair production cross-section at hadron colliders through $O(\alpha_S^4)$*, Phys. Rev. Lett. **110** (2013) 252004, arXiv:1303.6254 [hep-ph] (cit. on p. 119).

[202] M. Czakon, A. Mitov, *NNLO corrections to top pair production at hadron colliders: the quark-gluon reaction*, JHEP **1380** (2013), arXiv:1210.6832 [hep-ph] (cit. on p. 119).

[203] M. Czakon, A. Mitov, *NNLO corrections to top-pair production at hadron colliders: the all-fermionic scattering channels*, JHEP **1254** (2012), arXiv:1207.0236 [hep-ph] (cit. on p. 119).

[204] ATLAS Collaboration, *Measurement of the $t\bar{t}$ production cross-section using $e\mu$ events with b-tagged jets in pp collisions at $\sqrt{s} = 7$ and 8 TeV with the ATLAS detector*, Eur. Phys. J C **74** (2014) 3109, arXiv:1406.5375 [hep-ex] (cit. on p. 120).

[205] ATLAS Collaboration, *Measurement of the cross-section for associated production of a top quark and a W boson at $\sqrt{s} = 8$ TeV with the ATLAS detector*, tech. rep. ATLAS-CONF-2013-100, CERN, Sept. 2013, URL: https://cds.cern.ch/record/1600799 (cit. on p. 120).

[206] N. Kidonakis, *Two-loop soft anomalous dimensions for single top quark associated production with a W^- or H^-*, Phys. Rev. D **82** (2010) 054018, arXiv:1005.4451 [hep-ph] (cit. on p. 120).

[207] ATLAS Collaboration, *Measurement of the Inclusive and Fiducial Cross-Section of Single Top-Quark t-Channel Events in pp Collisions at $\sqrt{s} = 8$ TeV*, tech. rep. ATLAS-CONF-2014-007, CERN, Mar. 2014, URL: https://cds.cern.ch/record/1668960 (cit. on p. 120).

[208] N. Kidonakis, *Next-to-next-to-leading-order collinear and soft gluon corrections for t-channel single top quark production*, Phys. Rev. D **83** (2011) 091503, arXiv:1103.2792 [hep-ph] (cit. on p. 120).

[209] ATLAS Collaboration, *Search for s-channel single top-quark production in proton-proton collisions at $\sqrt{s} = 8$ TeV with the ATLAS detector*, Phys. Lett. B **740** (2015) 118, arXiv:1410.0647 [hep-ex] (cit. on p. 120).

[210] N. Kidonakis, *NNLL resummation for s-channel single top quark production*, Phys. Rev. D **81** (2010) 054028, arXiv:1001.5034 [hep-ph] (cit. on p. 120).

[211] S. Frixione, E. Laenen, P. Motylinski, B.R. Webber, *Single-top production in MC@NLO*, JHEP **0603** (2006) 092, arXiv:hep-ph/0512250 (cit. on p. 120).

[212] S. Frixione, E. Laenen, P. Motylinski, B. Webber, C. D. White, *Single-top hadroproduction in association with a W boson*, JHEP **0807** (2008) 029, arXiv:0805.3067 [hep-ph] (cit. on p. 120).

[213] B. P. Kersevan, E. Richter-Wąs, *The Monte Carlo Event Generator AcerMC 2.0 with Interfaces to PYTHIA 6.2 and HERWIG 6.5*, Comp. Phys. Comm. **184** (2013) 919–985, arXiv:hep-ph/0405247 (cit. on p. 120).

[214] J. M. Campbell, R. K. Ellis, *Update on vector boson pair production at hadron colliders*, Phys. Rev. D **60** (1999) 113006, arXiv:hep-ph/9905386 (cit. on p. 121).

[215] ATLAS Collaboration, *Data-Quality Requirements and Event Cleaning for Jets and Missing Transverse Energy Reconstruction with the ATLAS Detector in Proton-Proton Collisions at a Center-of-Mass Energy of $\sqrt{s} = 7$ TeV*, tech. rep. ATLAS-CONF-2010-038, CERN, July 2010, URL: https://cds.cern.ch/record/1277678 (cit. on p. 122).

[216] ATLAS Collaboration, *ATLAS Data Summary*, [Online; accessed 5-June-2015], 2015, URL: https://atlas.web.cern.ch/Atlas/GROUPS/DATAPREPARATION/DataSummary/2012/run-table.html (cit. on p. 123).

[217] Y. Heng, *Tau Energy Scale Uncertainties at high p_T*, [Online; accessed 26-June-2015], 2014, URL: https://indico.cern.ch/event/304091/contribution/0/material/slides/2.pdf (cit. on p. 159).

[218] D. Duschinger, *Search for New Physics in Fully Hadronic Di-tau Final States with the ATLAS Detector*, MA thesis: TU Dresden, July 2013, URL: https://cds.cern.ch/record/1630401 (cit. on pp. 160–162).

[219] ATLAS Collaboration, *A Study of Release 16 Tracking Performance in Jets Using 2010 Data*, tech. rep. ATL-COM-INDET-2011-028, CERN, June 2011, URL: https://cds.cern.ch/record/1356615 (cit. on p. 162).

[220] A.D. Martin, W.J. Stirling, R.S. Thorne, G. Watt, *Parton distributions for the LHC*, Eur. Phys. J C **63** (2009) 189–285, arXiv:0901.0002 [hep-ph] (cit. on p. 164).

[221] ATLAS Collaboration, *Search for the Standard Model Higgs boson in the $H \to \tau\tau$ decay mode with 4.7 fb^{-1} of ATLAS data at 7 TeV*, tech. rep. ATLAS-CONF-2012-014, CERN, Mar. 2012, URL: https://cds.cern.ch/record/1429662 (cit. on p. 164).

[222] A. Buckley, J. Butterworth, D. Grellscheid, H. Hoeth, L. Lonnblad, J. Monk, H. Schulz, F. Siegert, *Rivet user manual* (2010), arXiv:1003.0694 [hep-ph] (cit. on p. 164).

[223] G. Cowan, K. Cranmer, E. Gross, O. Vitells, *Asymptotic formulae for likelihood-based tests of new physics*, Eur. Phys. J. C **71** (2011) 1554, arXiv:1007.1727v2 [physics.data-an] (cit. on pp. 178–181, 185).

[224] J. Neyman, E. S. Pearson, *On the Problem of the Most Efficient Tests of Statistical Hypotheses*, Philosophical Transactions of the Royal Society of London A **231** (1933) 289–337 (cit. on p. 179).

[225] A. Wald, *Tests of Statistical Hypotheses Concerning Several Parameters When the Number of Observations is Large*, Transactions of the American Mathematical Society **54** (1943) 426–482 (cit. on p. 180).

[226] A. L. Read, *Presentation of search results: the CLs technique*, Journal of Physics G: Nuclear and Particle Physics **28** (2002) 2693 (cit. on p. 181).

[227] K. Cranmer, G. Lewis, L. Moneta, A. Shibata, W. Verkerke, *HistFactory: A tool for creating statistical models for use with RooFit and RooStats*, tech. rep. CERN-OPEN-2012-016, CERN, Jan. 2012, URL: https://cdsweb.cern.ch/record/1456844 (cit. on pp. 182, 184).

[228] ATLAS Collaboration, *Frequentist Limit Recommendation*, [Online; accessed 10-September-2015], 2015, URL: https://twiki.cern.ch/twiki/bin/view/AtlasProtected/StatisticsTools (cit. on p. 191).

[229] ATLAS Collaboration, *Modelling $Z \to \tau\tau$ processes in ATLAS with τ-embedded $Z \to \mu\mu$ data*, JINST **10** (2015) P09018, arXiv:1506.05623 [hep-ex] (cit. on p. 198).

[230] A.Elagin, P.Murat, A.Pranko, A.Safonov, *A New Mass Reconstruction Technique for Resonances Decaying to di-tau*, Nuclear Instruments and Methods in Physics Research A **654** (2011) 481–489, arXiv:1012.4686 [hep-ex] (cit. on p. 199).

APPENDIX A

Tau Identification Variables

Below, the full list of variables utilised by the BDT algorithm used for tau identification is given. The algorithm itself is described in Sec. 6.2.

Central energy fraction (f_{cent}) : Fraction of the transverse energy in the central region ($\Delta R < 0.1$) of $\tau_{\text{had-vis}}$

$$f_{\text{cent}} = \frac{\sum_{i \in \{\text{all cells}\}}^{\Delta R_i < 0.1} E_{\text{T},i}^{\text{EM}}}{\sum_{j \in \{\text{all cells}\}}^{\Delta R_j < 0.2} E_{\text{T},j}^{\text{EM}}} \tag{A.1}$$

where i and j run over all cells associated with the candidate within the ΔR indicated in the formula and computed with respect to the candidate axis. Here, the transverse energy is calibrated to the EM-scale. This variable is utilised after a correction for pile-up, for $p_{\text{T}}(\tau_{\text{had-vis}}) < 80$ GeV, by adding $\Delta f_{\text{cent}} = 0.003\, N_{\text{PV}}$, where quality criteria are applied for the selection of primary vertices. In Fig. A.1, the f_{cent} distributions for 1-prong and 3-prong candidates are shown.

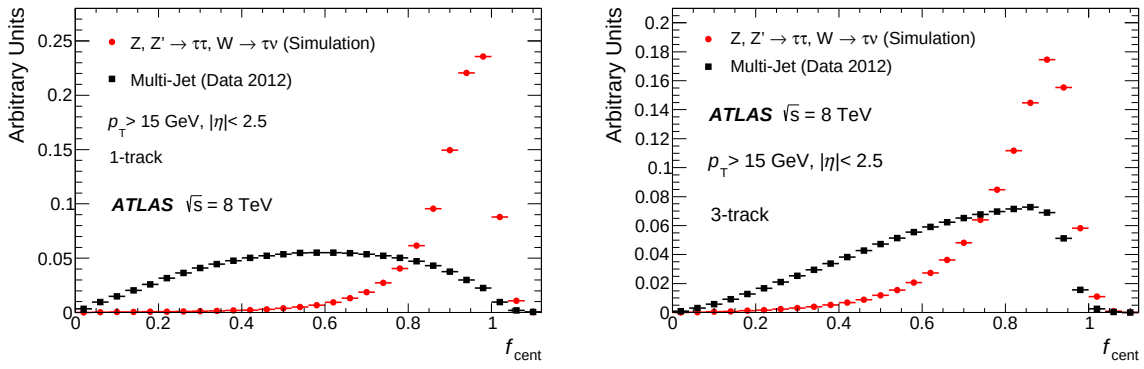

Figure A.1: Central energy fraction for 1-prong (left) and 3-prong (right) $\tau_{\text{had-vis}}$ candidates. The plots are taken from Ref. [159].

Leading track momentum fraction (f_{track}) :

$$f_{\text{track}} = \frac{p_{\text{T}}^{\text{lead track}}}{\sum_{j\in\{\text{all cells}\}}^{\Delta R_j<0.2} E_{\text{T},j}^{\text{EM}}} \tag{A.2}$$

where $p_{\text{T}}^{\text{lead track}}$ is the highest-p_{T} track of the $\tau_{\text{had-vis}}$ candidate in the core region. For 1-prong candidates, this corresponds to the momentum attributed to the track compared to the total $\tau_{\text{had-vis}}$ momentum, which is affected by the presence of neutral pions. This variable is corrected for pile-up as the previous one, and its distributions for 1-prong and 3-prong candidates are shown in Fig. A.2.

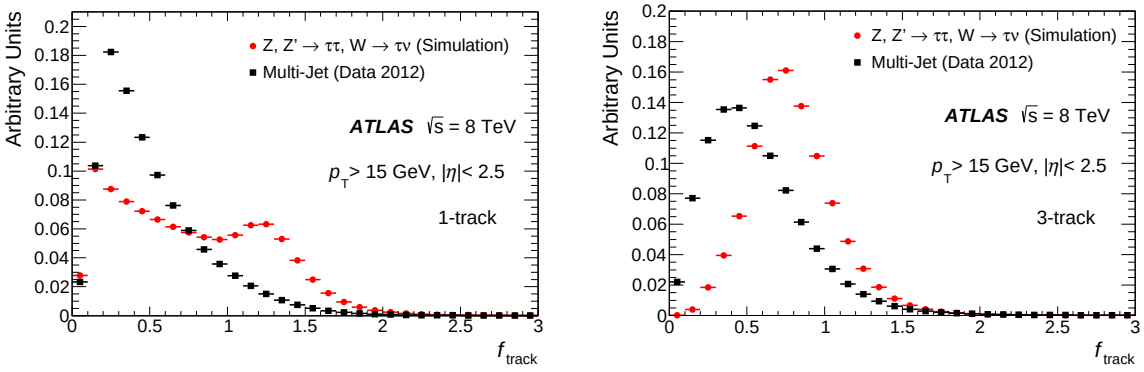

Figure A.2: Leading track momentum fraction for 1-prong (left) and 3-prong (right) $\tau_{\text{had-vis}}$ candidates. The plots are taken from Ref. [159].

Track radius (R_{track}) : Distance between the $\tau_{\text{had-vis}}$ tracks and its axis. The variable is computed using all tracks within the core and isolation regions, and weighting them with their p_{T}.

$$R_{\text{track}} = \frac{\sum_{i\in\{\text{all tracks}\}}^{\Delta R_i\leq 0.4} p_{\text{T},i}\,\Delta R_i}{\sum_{j\in\{\text{all tracks}\}}^{\Delta R_j\leq 0.4} p_{\text{T},j}} \tag{A.3}$$

The distributions are shown in Fig. A.3.

Leading track d_0 significance ($S_{\text{lead track}}$) : Significance of the impact parameter of the leading track in the core region

$$S_{\text{lead track}} = \frac{d_0}{\delta d_0} \tag{A.4}$$

where d_0 is computed with respect to the tau vertex, and δd_0 is its uncertainty. The variable is only considered for 1-prong candidates. The distributions are shown in Fig. A.4 (left).

Maximum ΔR (ΔR_{max}) : Maximum distance between a track in the core region and the $\tau_{\text{had-vis}}$ direction. Only 3-prong candidates are considered for this variable. The distributions are illustrated in Fig. A.4 (right).

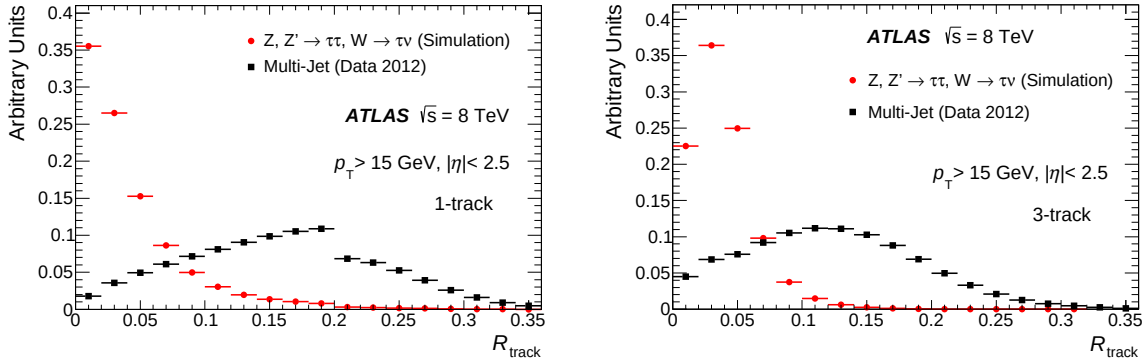

Figure A.3: Track radius for 1-prong (left) and 3-prong (right) $\tau_{\text{had-vis}}$ candidates. The plots are taken from Ref. [159].

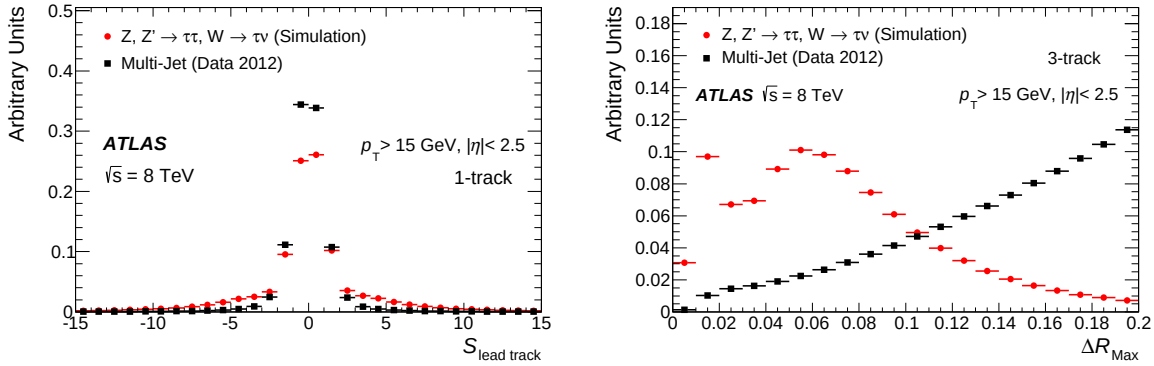

Figure A.4: Left: impact parameter significance of the leading track. This variable is only used for 1-prong candidates. Right: Maximum ΔR for 3-prong tau candidates. The plots are taken from Ref. [159].

Number of tracks in the isolation region ($N^{\text{iso}}_{\text{track}}$) : This variable is only used for 1-prong candidates. Distributions are shown in Fig. A.5.

Transverse flight path significance ($S_{\text{T}}^{\text{flight}}$) : Using only the tracks associated with the $\tau_{\text{had-vis}}$ candidate in the core region, a new vertex is determined by combining the tracks into a fit. Its distance in the transverse plane with respect to the tau vertex is called the *decay length* or *flight path* of the tau, $L_{\text{T}}^{\text{flight}}$. Its significance is

$$S_{\text{T}}^{\text{flight}} = \frac{L_{\text{T}}^{\text{flight}}}{\delta L_{\text{T}}^{\text{flight}}} \tag{A.5}$$

where $\delta L_{\text{T}}^{\text{flight}}$ is the estimated uncertainty. This variable is only defined and used for 3-prong decays. Distributions are shown in Fig. A.6 (right).

Track mass (m_{track}) : Invariant mass computed using the momenta of tracks in the core and isolation regions, assuming a pion mass for each track. The variable is only used for 3-prong candidates and is distributed as shown in Fig. A.6 (right).

Track-plus-π^0-system mass ($m_{\pi^0+\text{track}}$) : Invariant mass of the tracks plus the contribution of π^0 mesons. The signal and background separation is illustrated in Fig. A.7.

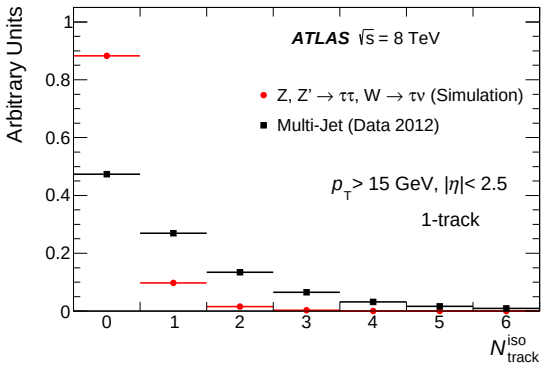

Figure A.5: Number of tracks in the isolation region for 1-prong $\tau_{\text{had-vis}}$. The plot is taken from Ref. [159].

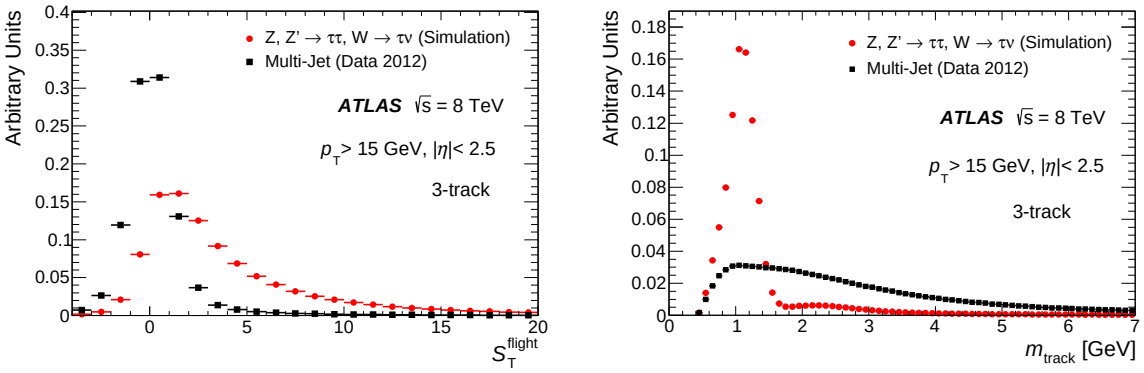

Figure A.6: Transverse flight path significance (left) and track mass (right) for 3-prong $\tau_{\text{had-vis}}$ candidates. These variables are only used for this track multiplicity. The plots are taken from Ref. [159].

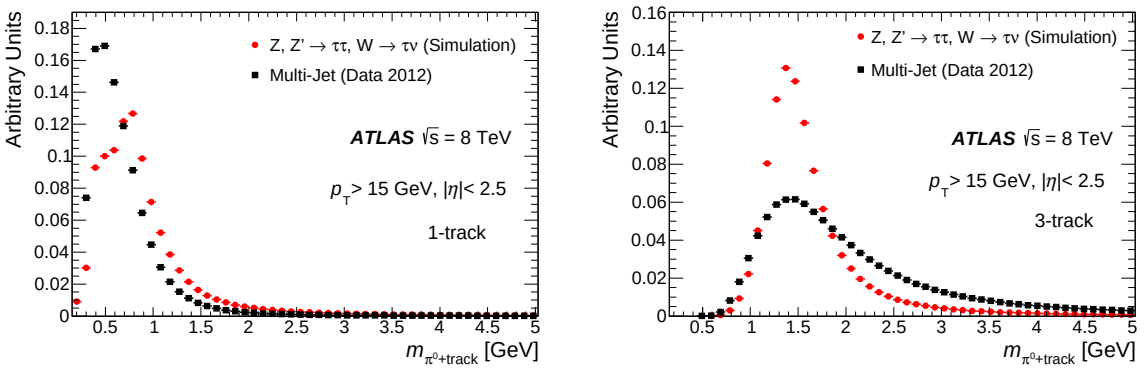

Figure A.7: Invariant mass of the track and π^0 system for 1-prong (left) and 3-prong (right) $\tau_{\text{had-vis}}$ candidates. The plots are taken from Ref. [159].

Number of π^0 mesons (N_{π^0}) : The number of π^0 mesons in the core region is used for all track multiplicities of the tau decay. The distributions are in Fig. A.8.

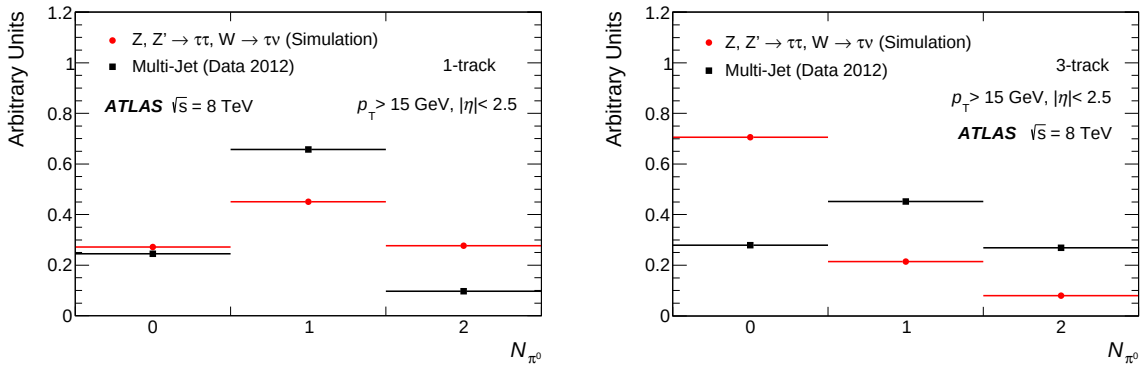

Figure A.8: Number of π^0 mesons in the decay for 1-prong (left) and 3-prong (right) $\tau_{\text{had-vis}}$ candidates. The plots are taken from Ref. [159].

Ratio of track-plus-π^0-system p_{T} ($p_{\text{T}}^{\pi^0+\text{track}}/p_{\text{T}}$) : Ratio between the p_{T} estimated using the track and π^0 information and the p_{T} determined from the calorimeter only. The distributions are in Fig. A.9.

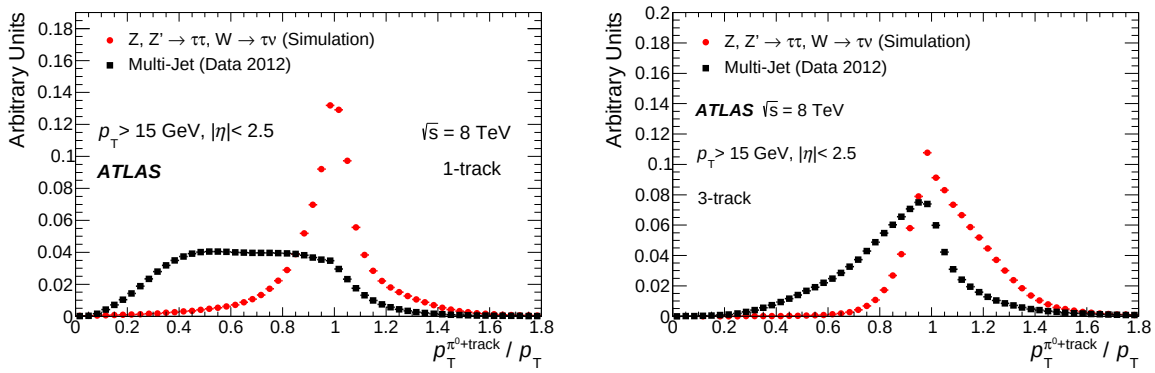

Figure A.9: Transverse momentum ratio for 1-prong (left) and 3-prong (right) $\tau_{\text{had-vis}}$ candidates. The plots are taken from Ref. [159].

APPENDIX B

Light Leptons Identification

As described for jets in Sec. 6.2, dedicated algorithms are used to separate tau candidates from electrons or muons, which are described respectively in Sec. B.0.1 and B.0.2. In Sec. B.1, the measurement for the electron veto correction factors is described.

B.0.1 Electron Veto

After jet suppression, depending on the analysis, a yet large background contamination could be present for 1-prong $\tau_{\text{had-vis}}$ candidates which can be mimicked by electrons. Several variables are combined into a BDT, which rely on the information collected by the TRT and the calorimeter. The ratio of high-threshold to low-threshold hits in the TRT is typically higher for electrons than it is for the charged pions from the tau decay. The angular distance between a track and the calorimeter-based direction of the $\tau_{\text{had-vis}}$ tends to be smaller for electrons. The ratio of the energy deposited in the EM calorimeter to the energy in the EM plus HCAL sections (*electromagnetic fraction*, f_{EM}) is also higher for the background. Also, the amount of energy leaking into the HCAL is used as a measurement of the longitudinal shower shape, and the ratio of the energy deposited in the region $0.1 < \Delta R < 0.2$ to the energy in the entire core region is used, which depends on the transverse development of the shower, which is narrower for electrons. Different BDT algorithms are used depending on the pseudo-rapidity, as the available set of variables depends on η, due to the limited coverage of the TRT system, and the reduced discriminating power of subset of variables in certain regions of the detector, which are dropped.

The signal and background efficiencies are determined by using simulated $Z \to \tau\tau$ and $Z \to ee$ events, respectively. The signal efficiency is defined by selecting reconstructed 1-prong candidates identified with the loose working point of the jet discrimination, and matched to the simulated tau within $\Delta R < 0.2$. The background efficiency is measured with respect to reconstructed electrons matched to simulated ones within $\Delta R < 0.2$. Both signal and background objects are selected above $p_{\text{T}} = 20$ GeV. Signal efficiencies of $\approx 75\%, 85\%$ and 95% are provided respectively by the tight, medium and loose working points. The inverse background efficiency as a function of the signal efficiency is shown in Fig. B.1, for the different regions in pseudo-rapidity.

B.0.2 Muon Veto

Muons are unlikely to fake a tau, as they typically deposit very little energy in the calorimeter. However, a sufficiently energetic cluster might be incorrectly associated with a muon track, and together be mis-identified as a $\tau_{\text{had-vis}}$ with one associated track. On the other hand, low energetic muons can lose

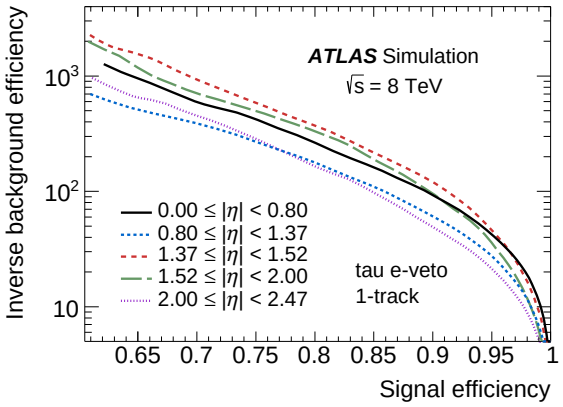

Figure B.1: Inverse background efficiency as a function of the signal efficiency for the electron veto algorithm. Simulated $Z \to \tau\tau$ events are used to measure the signal efficiency and $Z \to ee$ events for the background one. The plot is taken from Ref. [159].

significant energy in the calorimeter and be stopped in its volume, or lead to badly reconstructed tracks in the MS. Finally, inefficient regions in the MS will provide no track outside the calorimeter, making the standard muon reconstruction to fail. All these cases make the standard muon reconstruction inefficient and not suitable to reject the muon background. A muon veto has been developed, which is based on the definition of variables sensitive to the mentioned cases. Muons with high energy deposited in the calorimeter predominantly lead to showers in the HCAL, leading to low f_{EM} values. For those muons the momentum estimated from the track is usually higher than the energy deposit, leading to high f_{track} values, which is also true for clusters incorrectly assigned to a muon track. Finally, muons with very low momenta, which are stopped in the first few layers of the calorimeter, might fake a $\tau_{\text{had-vis}}$ if their energy deposit overlaps with other clusters, and are therefore characterised by high f_{EM} and lower f_{track}. A simple selection on f_{EM} and f_{track} is used to discriminate tau leptons and muon fakes. Efficiencies are determined by using simulated $Z \to \tau\tau$ events for the signal and $Z \to \mu\mu$ events for the background. In Fig. B.2, the distribution of f_{EM} for the signal and the background is shown. The efficiency achieved is better than 96%, with a corresponding reduction of muon fakes of $\approx 40\%$.

B.1 Electron Veto Efficiency in Data

Similarly to what already described in Sec. 6.4, the efficiency of the electron veto algorithm has to be measured in data using a $L_{\text{int}} = 20.1$ fb^{-1} sample collected at $\sqrt{s} = 8$ TeV. A tag-and-probe selection of $Z \to ee$ events is used in this case, where the tag and the probe are found in opposite hemispheres of the detector. The probe is required to have only one track associated with it and reconstructed as a tau, while the tag has to pass electron identification. To suppress the $Z \to \tau\tau$ background, tag electrons must have $p_{\text{T}}^{e} > 35$ GeV. Finally, probe electrons are required to not overlap geometrically with an identified electron. Different levels of jet discrimination are tested in correspondence to the different electron veto algorithms. Efficiencies in data are measured in different intervals of the $\tau_{\text{had-vis}}$ pseudo-rapidity by counting the number of reconstructed tau leptons before and after applying the veto. Background processes include $Z \to \tau\tau$, $W \to e\nu$ and $t\bar{t}$. These backgrounds are subtracted and are estimated using the simulation renormalised in dedicated control regions, with the exception of the multi-jet background which is estimated from data in a control region where the tag and the probe have the same electric charge, after subtracting the other contributions. The scale factors are measured comparing the efficiency in data

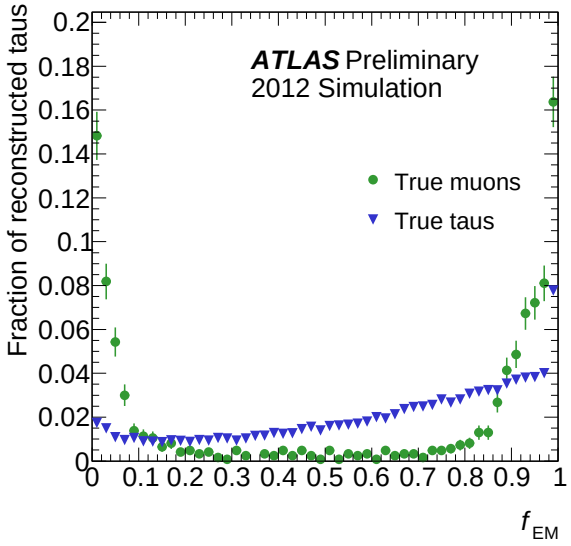

Figure B.2: Distributions of the electromagnetic fraction of 1-prong tau candidates used for the muon veto algorithm. The signal and background distributions are obtained respectively using $Z \to \tau\tau$ and $Z \to \mu\mu$ simulated events. The distributions are obtained after removing candidates that overlap with a reconstructed muon. The plot is taken from Ref. [160].

and the one measured from $Z \to ee$ events. Scale factors are close to unity and have uncertainties in the range 8 – 30%, getting larger with the tightness of the working point and are driven by the statistical component. In Fig. B.3, distributions are illustrated for the number of probe electron fakes selected before the electron veto (left) and after (right). More details about this measurement can be found in Ref. [159, 160].

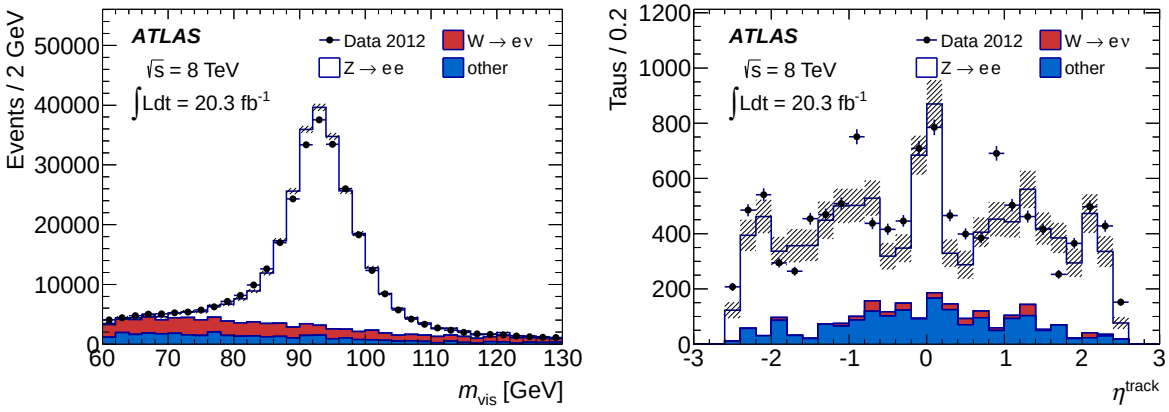

Figure B.3: Left: visible mass distribution of the tag and probe electrons before electron veto is applied. Right: pseudo-rapidity distribution of the probe electron after the loose working point of the electron veto algorithm. Medium tau identification is applied in both cases. The backgrounds labelled as others correspond to $Z \to \tau\tau$, $t\bar{t}$ and multi-jet events. The distributions are obtained using the loose working point of the tau identification algorithm. The uncertainty indicated only includes the statistical component. The plots are taken from Ref. [159].

APPENDIX C

Results of Tau Identification Efficiency in Data

In this section, the tables summarising the results for the mesurement of the tau identification efficiency scale factors are presented, for the $Z \to \tau_\mu \tau_{\text{had}}$ channel, in Tab. C.1, the $Z \to \tau_e \tau_{\text{had}}$ channel, Tab. C.2 and their combination, Tab. C.3. The measurement has been discussed in Sec. 6.4.

$Z \to \tau_\mu \tau_{\text{had}}$	Inclusive ID Efficiency SF ± syst .± stat.		
	Overall	Barrel	End-cap
Loose	1.001 ± 2.5% ± 1.3%	0.993 ± 2.7% ± 1.8%	1.000 ± 2.6% ± 2.8%
Medium	0.970 ± 2.4% ± 1.5%	0.973 ± 2.9% ± 1.9%	0.947 ± 2.5% ± 2.6%
Tight	0.895 ± 2.7% ± 1.9%	0.930 ± 3.3% ± 2.1%	0.904 ± 2.4% ± 2.6%

Table C.1: Summary of the results for the measurement of the tau identification efficiency scale factors in data in the $Z \to \tau_\mu \tau_{\text{had}}$ channel. The table is illustrating the results for inclusive track multiplicities. Measurements are presented for the overall pseudo-rapidity region, the barrel and the end-cap.

$Z \to \tau_e \tau_{\text{had}}$	Inclusive ID Efficiency SF ± syst .± stat.		
	Overall	Barrel	End-cap
Loose	1.056 ± 2.0% ± 1.5%	1.040 ± 2.2% ± 1.6%	1.001 ± 4.4% ± 1.9%
Medium	0.996 ± 3.3% ± 1.7%	0.949 ± 4.5% ± 1.9%	0.960 ± 2.7% ± 2.4%
Tight	0.954 ± 4.8% ± 2.3%	0.980 ± 5.5% ± 2.6%	0.911 ± 5.9% ± 4.0%

Table C.2: Summary of the results for the measurement of the tau identification efficiency scale factors in data in the $Z \to \tau_e \tau_{\text{had}}$ channel. The table is illustrating the results for inclusive track multiplicities. Measurements are presented for the overall pseudo-rapidity region, the barrel and the end-cap.

Combination	Inclusive ID Efficiency SF ± syst .± stat.		
	Overall	Barrel	End-cap
Loose	1.033 ± 2.0% ± 1.0%	1.021 ± 2.1% ± 1.2%	1.000 ± 2.9% ± 1.6%
Medium	0.979 ± 2.1% ± 1.1%	0.966 ± 2.8% ± 1.3%	0.954 ± 2.2% ± 1.8%
Tight	0.907 ± 2.6% ± 1.5%	0.941 ± 3.0% ± 1.6%	0.905 ± 2.4% ± 2.2%

Table C.3: Summary of the results for the measurement of the tau identification efficiency scale factors in data for the combination between the $Z \to \tau_\mu \tau_{\text{had}}$ and $Z \to \tau_e \tau_{\text{had}}$ channels. The table is illustrating the results for inclusive track multiplicities. Measurements are presented for the overall pseudo-rapidity region, the barrel and the end-cap.

APPENDIX D

Cross-sections and Simulated Samples for the $h/H/A \to \tau_{\text{had}}\tau_{\text{had}}$ analysis

This section illustrates details regarding the simulated samples used for the $h/H/A \to \tau_{\text{had}}\tau_{\text{had}}$ search. Tables are presented summarising the cross-section of the different processes, multiplied by the branching ratio of the final state previous to the hadronic decay of the tau leptons. The *effective luminosity* of the samples used is also reported which is defined as

$$\mathcal{L}_{\text{eff.}} = \frac{N_{\text{MC}}}{\sigma \times \text{BR} \times \varepsilon_{\text{filter}}} \tag{D.1}$$

where N_{MC} is the number of generated events in the simulation, $\sigma \times \text{BR}$ the cross-section of the process up to the final state and $\varepsilon_{\text{filter}}$ the efficiency of the filter applied to the generator to select a particular final state.

In Tab. D.1, D.2, D.3 and D.4 details about all simulated background processes are presented, while in Tab. D.5 details about the signal simulation are illustrated. Signal cross-sections depend on tanβ and are illustrated from Tab. D.6 to D.11 for the m_h^{max} scenario.

Sample	$\sigma \times$ BR [pb]	$\varepsilon_{\text{filter}}$	$\mathcal{L}_{\text{eff.}}$[fb^{-1}]	Generator
$Z/\gamma^* \to \tau\tau$ (inclusive)	878.04	1	17.08	Pythia
$Z/\gamma^* \to \tau\tau$ (180 GeV $< m_{\tau\tau} <$ 250 GeV)	1.25	1	120.14	Pythia
$Z/\gamma^* \to \tau\tau$ (250 GeV $< m_{\tau\tau} <$ 400 GeV)	0.44	1	343.97	Pythia
$Z/\gamma^* \to \tau\tau$ (400 GeV $< m_{\tau\tau} <$ 600 GeV)	0.07	1	20.89×10^2	Pythia
$Z/\gamma^* \to \tau\tau$ (600 GeV $< m_{\tau\tau} <$ 800 GeV)	0.01	1	12.26×10^3	Pythia
$Z/\gamma^* \to \tau\tau$ (800 GeV $< m_{\tau\tau} <$ 1000 GeV)	3.07×10^{-3}	1	47.19×10^3	Pythia
$Z/\gamma^* \to \tau\tau$ (1000 GeV $< m_{\tau\tau} <$ 1250 GeV)	1.07×10^{-3}	1	13.53×10^4	Pythia
$Z/\gamma^* \to \tau\tau$ (1250 GeV $< m_{\tau\tau} <$ 1500 GeV)	3.00×10^{-4}	1	50.04×10^4	Pythia
$Z/\gamma^* \to \tau\tau$ (1500 GeV $< m_{\tau\tau} <$ 1750 GeV)	9.52×10^{-5}	1	15.76×10^5	Pythia
$Z/\gamma^* \to \tau\tau$ (1750 GeV $< m_{\tau\tau} <$ 2000 GeV)	3.26×10^{-5}	1	46.00×10^5	Pythia
$Z/\gamma^* \to \tau\tau$ (2000 GeV $< m_{\tau\tau} <$ 2250 GeV)	1.19×10^{-5}	1	12.64×10^6	Pythia
$Z/\gamma^* \to \tau\tau$ (2250 GeV $< m_{\tau\tau} <$ 2500 GeV)	4.46×10^{-6}	1	33.66×10^6	Pythia
$Z/\gamma^* \to \mu\mu$ (inclusive)	990.00	1	10.09	PowHeg
$Z/\gamma^* \to \mu\mu$ (180 GeV $< m_{\mu\mu} <$ 250 GeV)	1.57	1	63.59	PowHeg
$Z/\gamma^* \to \mu\mu$ (250 GeV $< m_{\mu\mu} <$ 400 GeV)	0.55	1	181.90	PowHeg
$Z/\gamma^* \to \mu\mu$ (400 GeV $< m_{\mu\mu} <$ 600 GeV)	0.10	1	10.34×10^2	PowHeg
$Z/\gamma^* \to \mu\mu$ (600 GeV $< m_{\mu\mu} <$ 800 GeV)	0.02	1	66.23×10^2	PowHeg
$Z/\gamma^* \to \mu\mu$ (800 GeV $< m_{\mu\mu} <$ 1000 GeV)	3.75×10^{-3}	1	26.67×10^3	PowHeg
$Z/\gamma^* \to \mu\mu$ (1000 GeV $< m_{\mu\mu} <$ 1250 GeV)	1.29×10^{-3}	1	77.26×10^3	PowHeg
$Z/\gamma^* \to \mu\mu$ (1250 GeV $< m_{\mu\mu} <$ 1500 GeV)	3.58×10^{-4}	1	27.96×10^4	PowHeg
$Z/\gamma^* \to \mu\mu$ (1500 GeV $< m_{\mu\mu} <$ 1750 GeV)	1.12×10^{-4}	1	88.96×10^4	PowHeg
$Z/\gamma^* \to \mu\mu$ (1750 GeV $< m_{\mu\mu} <$ 2000 GeV)	3.84×10^{-5}	1	26.05×10^5	PowHeg
$Z/\gamma^* \to \mu\mu$ (2000 GeV $< m_{\mu\mu} <$ 2250 GeV)	1.39×10^{-5}	1	71.99×10^5	PowHeg
$Z/\gamma^* \to \mu\mu$ (2250 GeV $< m_{\mu\mu} <$ 2500 GeV)	5.23×10^{-6}	1	19.10×10^6	PowHeg
$Z/\gamma^* \to ee$ (inclusive)	1109.80	1	9.01	PowHeg
$Z/\gamma^* \to ee$ (180 GeV $< m_{ee} <$ 250 GeV)	1.57	1	63.65	PowHeg
$Z/\gamma^* \to ee$ (250 GeV $< m_{ee} <$ 400 GeV)	0.55	1	182.08	PowHeg
$Z/\gamma^* \to ee$ (400 GeV $< m_{ee} <$ 600 GeV)	0.10	1	10.35×10^2	PowHeg
$Z/\gamma^* \to ee$ (600 GeV $< m_{ee} <$ 800 GeV)	0.02	1	66.22×10^2	PowHeg
$Z/\gamma^* \to ee$ (800 GeV $< m_{ee} <$ 1000 GeV)	3.75×10^{-3}	1	26.67×10^3	PowHeg
$Z/\gamma^* \to ee$ (1000 GeV $< m_{ee} <$ 1250 GeV)	1.29×10^{-3}	1	77.34×10^3	PowHeg
$Z/\gamma^* \to ee$ (1250 GeV $< m_{ee} <$ 1500 GeV)	3.58×10^{-4}	1	27.93×10^4	PowHeg
$Z/\gamma^* \to ee$ (1500 GeV $< m_{ee} <$ 1750 GeV)	1.12×10^{-4}	1	84.15×10^4	PowHeg
$Z/\gamma^* \to ee$ (1750 GeV $< m_{ee} <$ 2000 GeV)	3.84×10^{-5}	1	26.05×10^5	PowHeg
$Z/\gamma^* \to ee$ (2000 GeV $< m_{ee} <$ 2250 GeV)	1.39×10^{-5}	1	71.99×10^5	PowHeg
$Z/\gamma^* \to ee$ (2250 GeV $< m_{ee} <$ 2500 GeV)	5.23×10^{-6}	1	19.13×10^6	PowHeg

Table D.1: Summary of cross-sections and effective luminosities for the simulated $Z/\gamma^* \to ll$ samples. The k-factors, not reported in the table, are mass dependent as illustrated in Sec. 7.2.2.

Sample	$\sigma \times$ BR [pb]	$\varepsilon_{\text{filter}}$	k-factor	$\mathcal{L}_{\text{eff.}}$[fb^{-1}]
$W \to l\nu+ \geq 1$ $b-$jet ($p_{\text{T}}^{W} > 0$ GeV)	11000.00	0.012	1.10	102.80
$W \to l\nu+ \geq 1$ $c-$jet ($p_{\text{T}}^{W} > 0$ GeV)	11000.00	0.048	1.10	17.21
$W \to l\nu+ \geq 1$ light jet ($p_{\text{T}}^{W} > 0$ GeV)	11000.00	0.940	1.10	3.51
$W \to l\nu+ \geq 1$ $b-$jet (70 GeV $< p_{\text{T}}^{W} <$ 140 GeV)	250.60	0.046	1.10	157.92
$W \to l\nu+ \geq 1$ $c-$jet (70 GeV $< p_{\text{T}}^{W} <$ 140 GeV)	250.60	0.199	1.10	54.72
$W \to l\nu+ \geq 1$ light jet (70 GeV $< p_{\text{T}}^{W} <$ 140 GeV)	250.60	0.755	1.10	24.03
$W \to l\nu+ \geq 1$ $b-$jet (140 GeV $< p_{\text{T}}^{W} <$ 280 GeV)	31.16	0.063	1.10	462.38
$W \to l\nu+ \geq 1$ $c-$jet (140 GeV $< p_{\text{T}}^{W} <$ 280 GeV)	31.16	0.220	1.10	264.84
$W \to l\nu+ \geq 1$ light jet (140 GeV $< p_{\text{T}}^{W} <$ 280 GeV)	31.16	0.716	1.10	81.48
$W \to l\nu+ \geq 1$ $b-$jet (280 GeV $< p_{\text{T}}^{W} <$ 500 GeV)	1.84	0.083	1.10	595.92
$W \to l\nu+ \geq 1$ $c-$jet (280 GeV $< p_{\text{T}}^{W} <$ 500 GeV)	1.84	0.233	1.10	425.22
$W \to l\nu+ \geq 1$ light jet (280 GeV $< p_{\text{T}}^{W} <$ 500 GeV)	1.84	0.684	1.10	361.69
$W \to l\nu+ \geq 1$ $b-$jet ($p_{\text{T}}^{W} >$ 500 GeV)	0.10	0.100	1.10	894.89
$W \to l\nu+ \geq 1$ $c-$jet ($p_{\text{T}}^{W} >$ 500 GeV)	0.10	0.242	1.10	368.22
$W \to l\nu+ \geq 1$ light jet ($p_{\text{T}}^{W} >$ 500 GeV)	0.10	0.660	1.10	675.60

Table D.2: Summary of cross-sections and effective luminosities for the simulated $W \to l\nu$ + jets samples. All charged leptons are considered in the final state. All processes are simulated with `Sherpa`.

Sample	$\sigma \times$ BR [pb]	$\varepsilon_{\text{filter}}$	k-factor	$\mathcal{L}_{\text{eff.}}$[fb^{-1}]	Generator
$t\bar{t}$(fully-hadronic final state)	238.06	0.457	1	11.03	`MC@NLO`
$t\bar{t}$(non-fully-hadronic final state)	238.06	0.543	1	115.99	`MC@NLO`
single-top: s-channel $W \to l\nu$	0.61	1	1	329.87	`MC@NLO`
single-top: t-channel $W \to l\nu$	9.48	1	1	31.65	`AcerMC`
single-top: Wt	22.37	1	1	89.38	`MC@NLO`

Table D.3: Summary of cross-sections and effective luminosities for the simulated samples of the top quark bakcground.

Sample	$\sigma \times$ BR [pb]	$\varepsilon_{\text{filter}}$	k-factor	$\mathcal{L}_{\text{eff.}}$[fb^{-1}]
WW inclusive	53.90	0.382	1	121.12
ZZ inclusive	7.32	0.212	1	161.36
WZ inclusive	22.30	0.305	1	146.78

Table D.4: Summary of cross-sections and effective luminosities for the simulated samples of the di-boson background. All processes are modelled with `Herwig`.

m_A[GeV]	$b\bar{b} \to \phi$			$gg \to \phi$		
	N_{MC}	$\varepsilon_{\text{filter}}$	k-factor	N_{MC}	$\varepsilon_{\text{filter}}$	k-factor
170	50000	1	1	50000	1	1
200	50000	1	1	49999	1	1
250	39999	1	1	50000	1	1
300	50000	1	1	50000	1	1
350	50000	1	1	49999	1	1
400	50000	1	1	49999	1	1
450	49999	1	1	50000	1	1
500	50000	1	1	50000	1	1
600	50000	1	1	50000	1	1
700	50000	1	1	50000	1	1
800	50000	1	1	49998	1	1
900	50000	1	1	50000	1	1
1000	50000	1	1	50000	1	1

Table D.5: Number of generated events in the simulation for each of the dominant production mechanisms of the A boson in the MSSM. The table also shows the filter efficiency $\varepsilon_{\text{filter}}$ and the k-factor featured in the simulation, always unitary for the signal samples. The $b\bar{b} \to \phi$ and $gg \to \phi$ mechanisms are respectively modelled with `Sherpa` and `Pythia`.

m_h^{max} scenario, tanβ = 5	Mass [GeV]	$\sigma(b\bar{b} \to \phi)\times\text{BR}(\phi \to \tau\tau)$[fb]	$\sigma(gg \to \phi)\times\text{BR}(\phi \to \tau\tau)$[fb]
A	170.0	$153.03\ ^{+19.68}_{-28.08}$	$73.25\ ^{+10.05}_{-9.51}$
H	178.4	$75.03\ ^{+9.56}_{-13.49}$	$197.81\ ^{+21.84}_{-22.57}$
h	120.2	$131.83\ ^{+19.57}_{-29.49}$	$1400.70\ ^{+177.09}_{-169.01}$
A	200.0	$63.00\ ^{+7.85}_{-10.84}$	$35.30\ ^{+4.78}_{-4.56}$
H	205.9	$48.50\ ^{+6.02}_{-8.27}$	$95.56\ ^{+10.78}_{-11.16}$
h	122.4	$72.28\ ^{+10.62}_{-15.98}$	$1439.59\ ^{+177.19}_{-170.92}$
A	250.0	$14.69\ ^{+1.81}_{-2.37}$	$13.49\ ^{+1.74}_{-1.72}$
H	254.1	$17.78\ ^{+2.18}_{-2.85}$	$31.06\ ^{+3.67}_{-3.75}$
h	123.9	$40.49\ ^{+5.91}_{-8.88}$	$1383.95\ ^{+167.55}_{-162.67}$
A	300.0	$2.63\ ^{+0.33}_{-0.41}$	$4.80\ ^{+0.64}_{-0.62}$
H	303.3	$5.16\ ^{+0.64}_{-0.80}$	$10.12\ ^{+1.19}_{-1.26}$
h	124.6	$29.43\ ^{+4.29}_{-6.43}$	$1322.34\ ^{+159.01}_{-154.81}$
A	350.0	$0.63\ ^{+0.08}_{-0.10}$	$4.94\ ^{+0.72}_{-0.69}$
H	352.6	$1.75\ ^{+0.22}_{-0.27}$	$5.16\ ^{+0.64}_{-0.67}$
h	124.9	$24.25\ ^{+3.53}_{-5.29}$	$1277.58\ ^{+153.09}_{-149.27}$
A	400.0	$0.32\ ^{+0.04}_{-0.05}$	$2.25\ ^{+0.29}_{-0.30}$
H	401.9	$0.62\ ^{+0.08}_{-0.09}$	$2.28\ ^{+0.26}_{-0.29}$
h	125.1	$21.34\ ^{+3.10}_{-4.65}$	$1246.16\ ^{+149.02}_{-145.42}$
A	450.0	$0.16\ ^{+0.02}_{-0.03}$	$1.07\ ^{+0.13}_{-0.14}$
H	451.4	$0.19\ ^{+0.03}_{-0.03}$	$0.73\ ^{+0.08}_{-0.09}$
h	125.3	$19.50\ ^{+2.83}_{-4.25}$	$1223.58\ ^{+146.13}_{-142.67}$
A	500.0	$0.09\ ^{+0.01}_{-0.01}$	$0.54\ ^{+0.07}_{-0.07}$
H	501.2	$0.09\ ^{+0.01}_{-0.01}$	$0.32\ ^{+0.03}_{-0.04}$
h	125.4	$18.19\ ^{+2.64}_{-3.96}$	$1207.13\ ^{+144.02}_{-140.67}$
A	600.0	$0.03\ ^{+0.00}_{-0.00}$	$0.14\ ^{+0.02}_{-0.02}$
H	601.2	$0.03\ ^{+0.00}_{-0.00}$	$0.09\ ^{+0.01}_{-0.01}$
h	125.5	$16.62\ ^{+2.41}_{-3.62}$	$1185.05\ ^{+141.21}_{-137.99}$
A	700.0	$0.01\ ^{+0.00}_{-0.00}$	$0.05\ ^{+0.01}_{-0.01}$
H	701.0	$0.01\ ^{+0.00}_{-0.00}$	$0.03\ ^{+0.00}_{-0.00}$
h	125.6	$15.87\ ^{+2.30}_{-3.45}$	$1170.54\ ^{+139.40}_{-136.25}$
A	800.0	$0.00\ ^{+0.00}_{-0.00}$	$0.02\ ^{+0.00}_{-0.00}$
H	800.8	$0.00\ ^{+0.00}_{-0.00}$	$0.01\ ^{+0.00}_{-0.00}$
h	125.6	$15.48\ ^{+2.25}_{-3.36}$	$1160.58\ ^{+138.17}_{-135.06}$
A	900.0	$0.00\ ^{+0.00}_{-0.00}$	$0.01\ ^{+0.00}_{-0.00}$
H	900.7	$0.00\ ^{+0.00}_{-0.00}$	$0.01\ ^{+0.00}_{-0.00}$
h	125.6	$15.24\ ^{+2.21}_{-3.31}$	$1153.41\ ^{+137.29}_{-134.22}$
A	1000.0	$0.00\ ^{+0.00}_{-0.00}$	$0.00\ ^{+0.00}_{-0.00}$
H	1000.5	$0.00\ ^{+0.00}_{-0.00}$	$0.00\ ^{+0.00}_{-0.00}$
h	125.7	$15.08\ ^{+2.19}_{-3.28}$	$1148.13\ ^{+136.65}_{-133.59}$

Table D.6: Cross-sections for the production and decay of A, H and h in the di-tau final state assuming the m_h^{max} scenario and tanβ = 5. The masses of the three states are also reported.

m_h^{max} scenario, tanβ = 10	Mass [GeV]	$\sigma(b\bar{b} \to \phi)\times\text{BR}(\phi \to \tau\tau)$[fb]	$\sigma(gg \to \phi)\times\text{BR}(\phi \to \tau\tau)$[fb]
A	170.0	$746.46\ ^{+95.98}_{-136.96}$	$218.44\ ^{+31.67}_{-29.79}$
H	172.6	$623.96\ ^{+80.15}_{-113.80}$	$403.95\ ^{+51.07}_{-50.67}$
h	127.2	$156.96\ ^{+22.63}_{-33.85}$	$1423.89\ ^{+179.34}_{-171.86}$
A	200.0	$368.30\ ^{+45.88}_{-63.37}$	$78.34\ ^{+11.47}_{-10.72}$
H	201.7	$359.43\ ^{+44.76}_{-61.70}$	$173.53\ ^{+22.72}_{-22.69}$
h	128.0	$72.48\ ^{+10.42}_{-15.57}$	$1382.76\ ^{+169.26}_{-164.14}$
A	250.0	$125.63\ ^{+15.45}_{-20.26}$	$17.99\ ^{+2.51}_{-2.39}$
H	251.2	$148.67\ ^{+18.25}_{-23.94}$	$56.07\ ^{+7.61}_{-7.62}$
h	128.5	$37.04\ ^{+5.31}_{-7.94}$	$1267.97\ ^{+152.79}_{-148.93}$
A	300.0	$36.15\ ^{+4.51}_{-5.61}$	$4.73\ ^{+0.70}_{-0.62}$
H	301.0	$56.64\ ^{+7.03}_{-8.76}$	$19.74\ ^{+2.61}_{-2.75}$
h	128.7	$26.08\ ^{+3.74}_{-5.58}$	$1184.91\ ^{+141.92}_{-138.60}$
A	350.0	$11.54\ ^{+1.48}_{-1.77}$	$5.46\ ^{+0.92}_{-0.83}$
H	350.7	$20.77\ ^{+2.64}_{-3.15}$	$8.25\ ^{+1.12}_{-1.17}$
h	128.8	$21.17\ ^{+3.03}_{-4.53}$	$1130.71\ ^{+135.01}_{-131.99}$
A	400.0	$5.56\ ^{+0.73}_{-0.86}$	$3.05\ ^{+0.49}_{-0.45}$
H	400.3	$8.56\ ^{+1.12}_{-1.30}$	$3.42\ ^{+0.40}_{-0.44}$
h	128.8	$18.46\ ^{+2.64}_{-3.95}$	$1094.33\ ^{+130.43}_{-127.58}$
A	450.0	$2.81\ ^{+0.38}_{-0.44}$	$1.55\ ^{+0.24}_{-0.23}$
H	450.1	$3.06\ ^{+0.42}_{-0.47}$	$1.09\ ^{+0.11}_{-0.13}$
h	128.9	$16.77\ ^{+2.40}_{-3.59}$	$1068.92\ ^{+127.24}_{-124.52}$
A	500.0	$1.50\ ^{+0.21}_{-0.24}$	$0.80\ ^{+0.12}_{-0.12}$
H	500.1	$1.41\ ^{+0.20}_{-0.22}$	$0.44\ ^{+0.04}_{-0.05}$
h	128.9	$15.56\ ^{+2.23}_{-3.33}$	$1050.76\ ^{+124.96}_{-122.33}$
A	600.0	$0.43\ ^{+0.07}_{-0.07}$	$0.21\ ^{+0.03}_{-0.03}$
H	600.3	$0.43\ ^{+0.06}_{-0.07}$	$0.10\ ^{+0.01}_{-0.01}$
h	128.9	$14.07\ ^{+2.02}_{-3.01}$	$1026.99\ ^{+121.99}_{-119.46}$
A	700.0	$0.16\ ^{+0.03}_{-0.03}$	$0.07\ ^{+0.01}_{-0.01}$
H	700.2	$0.16\ ^{+0.03}_{-0.03}$	$0.03\ ^{+0.00}_{-0.00}$
h	129.0	$13.43\ ^{+1.92}_{-2.87}$	$1011.94\ ^{+120.14}_{-117.67}$
A	800.0	$0.07\ ^{+0.01}_{-0.01}$	$0.03\ ^{+0.00}_{-0.00}$
H	800.1	$0.07\ ^{+0.01}_{-0.01}$	$0.01\ ^{+0.00}_{-0.00}$
h	129.0	$13.14\ ^{+1.88}_{-2.81}$	$1001.96\ ^{+118.93}_{-116.50}$
A	900.0	$0.03\ ^{+0.01}_{-0.01}$	$0.01\ ^{+0.00}_{-0.00}$
H	900.1	$0.03\ ^{+0.01}_{-0.01}$	$0.00\ ^{+0.00}_{-0.00}$
h	129.0	$12.96\ ^{+1.86}_{-2.77}$	$994.81\ ^{+118.07}_{-115.66}$
A	1000.0	$0.02\ ^{+0.00}_{-0.00}$	$0.01\ ^{+0.00}_{-0.00}$
H	1000.0	$0.02\ ^{+0.00}_{-0.00}$	$0.00\ ^{+0.00}_{-0.00}$
h	129.0	$12.84\ ^{+1.84}_{-2.74}$	$989.73\ ^{+117.46}_{-115.06}$

Table D.7: Cross-sections for the production and decay of A, H and h in the di-tau final state assuming the m_h^{max} scenario and tanβ = 10. The masses of the three states are also reported.

m_h^{max} scenario, tanβ = 20	Mass [GeV]	$\sigma(b\bar{b} \to \phi)\times\text{BR}(\phi \to \tau\tau)$[fb]	$\sigma(gg \to \phi)\times\text{BR}(\phi \to \tau\tau)$[fb]
A	170.0	$2987.58\ ^{+384.14}_{-548.14}$	$1021.10\ ^{+146.37}_{-139.70}$
H	170.7	$2866.59\ ^{+369.27}_{-525.34}$	$1146.05\ ^{+162.01}_{-155.51}$
h	129.4	$175.11\ ^{+25.03}_{-37.35}$	$1499.65\ ^{+188.83}_{-181.04}$
A	200.0	$1598.55\ ^{+199.14}_{-275.03}$	$409.77\ ^{+60.03}_{-57.65}$
H	200.5	$1592.84\ ^{+198.53}_{-274.00}$	$488.97\ ^{+70.93}_{-68.65}$
h	129.7	$75.11\ ^{+10.73}_{-16.00}$	$1402.27\ ^{+171.46}_{-166.22}$
A	250.0	$633.74\ ^{+77.96}_{-102.18}$	$107.75\ ^{+16.16}_{-15.78}$
H	250.4	$661.51\ ^{+81.22}_{-106.59}$	$147.94\ ^{+22.17}_{-21.71}$
h	129.8	$37.23\ ^{+5.31}_{-7.93}$	$1252.45\ ^{+150.77}_{-147.00}$
A	300.0	$259.52\ ^{+32.35}_{-40.30}$	$30.42\ ^{+4.71}_{-4.57}$
H	300.4	$296.63\ ^{+36.82}_{-45.91}$	$53.23\ ^{+8.04}_{-8.13}$
h	129.8	$25.98\ ^{+3.71}_{-5.53}$	$1156.39\ ^{+138.40}_{-135.21}$
A	350.0	$105.27\ ^{+13.47}_{-16.12}$	$11.25\ ^{+2.01}_{-1.83}$
H	350.2	$133.45\ ^{+16.97}_{-20.28}$	$21.25\ ^{+3.30}_{-3.35}$
h	129.9	$21.00\ ^{+3.00}_{-4.47}$	$1096.17\ ^{+130.80}_{-127.94}$
A	400.0	$52.84\ ^{+6.99}_{-8.17}$	$6.79\ ^{+1.29}_{-1.16}$
H	399.9	$64.56\ ^{+8.47}_{-9.84}$	$8.56\ ^{+1.25}_{-1.33}$
h	129.9	$18.26\ ^{+2.61}_{-3.89}$	$1056.71\ ^{+125.86}_{-123.19}$
A	450.0	$27.94\ ^{+3.83}_{-4.42}$	$3.53\ ^{+0.67}_{-0.62}$
H	449.8	$29.12\ ^{+3.96}_{-4.51}$	$3.10\ ^{+0.43}_{-0.47}$
h	129.9	$16.57\ ^{+2.36}_{-3.53}$	$1029.43\ ^{+122.47}_{-119.92}$
A	500.0	$15.41\ ^{+2.19}_{-2.51}$	$1.85\ ^{+0.35}_{-0.33}$
H	499.8	$14.79\ ^{+2.08}_{-2.34}$	$1.27\ ^{+0.17}_{-0.19}$
h	129.9	$15.34\ ^{+2.19}_{-3.26}$	$1010.07\ ^{+120.06}_{-117.60}$
A	600.0	$4.88\ ^{+0.74}_{-0.83}$	$0.52\ ^{+0.10}_{-0.10}$
H	600.0	$4.84\ ^{+0.73}_{-0.79}$	$0.28\ ^{+0.03}_{-0.04}$
h	129.9	$13.69\ ^{+1.95}_{-2.91}$	$985.30\ ^{+116.95}_{-114.62}$
A	700.0	$1.88\ ^{+0.31}_{-0.34}$	$0.18\ ^{+0.04}_{-0.03}$
H	700.0	$1.88\ ^{+0.31}_{-0.32}$	$0.08\ ^{+0.01}_{-0.01}$
h	129.9	$13.10\ ^{+1.87}_{-2.79}$	$969.60\ ^{+115.04}_{-112.76}$
A	800.0	$0.82\ ^{+0.14}_{-0.16}$	$0.07\ ^{+0.01}_{-0.01}$
H	799.9	$0.81\ ^{+0.14}_{-0.15}$	$0.03\ ^{+0.00}_{-0.00}$
h	129.9	$12.93\ ^{+1.84}_{-2.75}$	$958.95\ ^{+113.77}_{-111.52}$
A	900.0	$0.38\ ^{+0.07}_{-0.08}$	$0.03\ ^{+0.01}_{-0.01}$
H	899.9	$0.38\ ^{+0.07}_{-0.07}$	$0.01\ ^{+0.00}_{-0.00}$
h	129.9	$12.82\ ^{+1.83}_{-2.73}$	$951.72\ ^{+112.91}_{-110.68}$
A	1000.0	$0.19\ ^{+0.04}_{-0.04}$	$0.01\ ^{+0.00}_{-0.00}$
H	999.9	$0.19\ ^{+0.04}_{-0.04}$	$0.00\ ^{+0.00}_{-0.00}$
h	129.9	$12.74\ ^{+1.82}_{-2.71}$	$946.41\ ^{+112.28}_{-110.06}$

Table D.8: Cross-sections for the production and decay of A, H and h in the di-tau final state assuming the m_h^{max} scenario and tanβ = 20. The masses of the three states are also reported.

m_h^{max} scenario, tanβ = 30	Mass [GeV]	$\sigma(b\bar{b} \to \phi)\times\text{BR}(\phi \to \tau\tau)$[fb]	$\sigma(gg \to \phi)\times\text{BR}(\phi \to \tau\tau)$[fb]
A	170.0	$6738.89\ ^{+866.47}_{-1236.41}$	$2394.87\ ^{+341.42}_{-326.72}$
H	170.3	$6610.61\ ^{+852.07}_{-1212.66}$	$2428.56\ ^{+351.31}_{-334.39}$
h	130.0	$185.48\ ^{+26.46}_{-39.46}$	$1568.07\ ^{+197.40}_{-189.37}$
A	200.0	$3650.62\ ^{+454.77}_{-628.08}$	$987.46\ ^{+143.70}_{-138.67}$
H	200.2	$3641.86\ ^{+454.00}_{-626.73}$	$1032.64\ ^{+152.80}_{-146.70}$
h	130.0	$78.00\ ^{+11.12}_{-16.59}$	$1438.48\ ^{+175.86}_{-170.56}$
A	250.0	$1488.29\ ^{+183.08}_{-239.96}$	$275.53\ ^{+41.22}_{-40.46}$
H	250.2	$1515.12\ ^{+186.02}_{-244.19}$	$308.41\ ^{+47.07}_{-45.82}$
h	130.1	$38.35\ ^{+5.47}_{-8.15}$	$1265.46\ ^{+152.36}_{-148.57}$
A	300.0	$660.03\ ^{+82.27}_{-102.49}$	$88.03\ ^{+13.61}_{-13.46}$
H	300.3	$697.11\ ^{+86.52}_{-107.90}$	$110.40\ ^{+17.17}_{-17.11}$
h	130.1	$26.70\ ^{+3.81}_{-5.68}$	$1159.59\ ^{+138.81}_{-135.63}$
A	350.0	$295.95\ ^{+37.87}_{-45.33}$	$31.11\ ^{+5.30}_{-5.10}$
H	350.1	$334.69\ ^{+42.55}_{-50.85}$	$44.29\ ^{+7.09}_{-7.13}$
h	130.1	$21.57\ ^{+3.08}_{-4.58}$	$1094.61\ ^{+130.65}_{-127.80}$
A	400.0	$153.50\ ^{+20.30}_{-23.73}$	$16.10\ ^{+2.94}_{-2.78}$
H	399.9	$171.50\ ^{+22.50}_{-26.13}$	$18.55\ ^{+2.94}_{-3.02}$
h	130.1	$18.74\ ^{+2.67}_{-3.98}$	$1052.45\ ^{+125.39}_{-122.74}$
A	450.0	$83.76\ ^{+11.48}_{-13.25}$	$8.06\ ^{+1.50}_{-1.44}$
H	449.7	$85.91\ ^{+11.67}_{-13.30}$	$7.55\ ^{+1.19}_{-1.25}$
h	130.1	$16.99\ ^{+2.42}_{-3.61}$	$1023.40\ ^{+121.79}_{-119.26}$
A	500.0	$47.55\ ^{+6.75}_{-7.73}$	$4.16\ ^{+0.79}_{-0.77}$
H	499.7	$46.38\ ^{+6.53}_{-7.32}$	$3.36\ ^{+0.53}_{-0.57}$
h	130.1	$15.71\ ^{+2.24}_{-3.34}$	$1003.07\ ^{+119.26}_{-116.83}$
A	600.0	$16.20\ ^{+2.47}_{-2.77}$	$1.19\ ^{+0.23}_{-0.23}$
H	599.9	$16.13\ ^{+2.44}_{-2.63}$	$0.84\ ^{+0.13}_{-0.15}$
h	130.1	$13.85\ ^{+1.97}_{-2.94}$	$977.37\ ^{+116.02}_{-113.72}$
A	700.0	$6.48\ ^{+1.05}_{-1.17}$	$0.40\ ^{+0.08}_{-0.08}$
H	699.9	$6.47\ ^{+1.06}_{-1.10}$	$0.26\ ^{+0.04}_{-0.05}$
h	130.1	$13.30\ ^{+1.90}_{-2.83}$	$960.99\ ^{+114.04}_{-111.79}$
A	800.0	$2.86\ ^{+0.50}_{-0.55}$	$0.16\ ^{+0.03}_{-0.03}$
H	799.8	$2.85\ ^{+0.51}_{-0.51}$	$0.09\ ^{+0.02}_{-0.02}$
h	130.1	$13.23\ ^{+1.89}_{-2.81}$	$949.70\ ^{+112.71}_{-110.48}$
A	900.0	$1.36\ ^{+0.25}_{-0.27}$	$0.07\ ^{+0.01}_{-0.01}$
H	899.8	$1.35\ ^{+0.26}_{-0.25}$	$0.03\ ^{+0.01}_{-0.01}$
h	130.1	$13.19\ ^{+1.88}_{-2.80}$	$942.07\ ^{+111.81}_{-109.60}$
A	1000.0	$0.68\ ^{+0.14}_{-0.15}$	$0.03\ ^{+0.01}_{-0.01}$
H	999.8	$0.67\ ^{+0.15}_{-0.13}$	$0.01\ ^{+0.00}_{-0.00}$
h	130.1	$13.14\ ^{+1.87}_{-2.79}$	$936.65\ ^{+111.17}_{-108.97}$

Table D.9: Cross-sections for the production and decay of A, H and h in the di-tau final state assuming the m_h^{max} scenario and tanβ = 30. The masses of the three states are also reported.

m_h^{max} scenario, tanβ = 40	Mass [GeV]	$\sigma(b\bar{b} \to \phi)\times\text{BR}(\phi \to \tau\tau)$[fb]	$\sigma(gg \to \phi)\times\text{BR}(\phi \to \tau\tau)$[fb]
A	170.0	$12032.50\ ^{+1547.11}_{-2207.66}$	$4338.33\ ^{+617.18}_{-591.15}$
H	170.2	$11895.23\ ^{+1533.57}_{-2182.89}$	$4246.74\ ^{+619.22}_{-587.54}$
h	130.2	$194.87\ ^{+27.77}_{-41.40}$	$1636.73\ ^{+206.03}_{-197.68}$
A	200.0	$6541.44\ ^{+814.90}_{-1125.44}$	$1805.31\ ^{+262.00}_{-253.24}$
H	200.2	$6529.03\ ^{+813.97}_{-1123.77}$	$1802.33\ ^{+268.50}_{-257.00}$
h	130.3	$81.03\ ^{+11.55}_{-17.21}$	$1478.19\ ^{+180.74}_{-175.30}$
A	250.0	$2691.04\ ^{+331.03}_{-433.87}$	$514.74\ ^{+76.84}_{-75.55}$
H	250.2	$2716.67\ ^{+333.55}_{-437.86}$	$535.45\ ^{+82.20}_{-79.85}$
h	130.3	$39.61\ ^{+5.64}_{-8.41}$	$1282.49\ ^{+154.45}_{-150.61}$
A	300.0	$1226.08\ ^{+152.83}_{-190.38}$	$172.31\ ^{+26.55}_{-26.41}$
H	300.2	$1259.90\ ^{+156.37}_{-195.01}$	$191.14\ ^{+30.02}_{-29.76}$
h	130.3	$27.53\ ^{+3.92}_{-5.85}$	$1167.00\ ^{+139.75}_{-136.54}$
A	350.0	$575.35\ ^{+73.62}_{-88.12}$	$63.08\ ^{+10.43}_{-10.27}$
H	350.0	$620.67\ ^{+78.90}_{-94.31}$	$77.04\ ^{+12.46}_{-12.47}$
h	130.3	$22.22\ ^{+3.17}_{-4.72}$	$1097.54\ ^{+131.05}_{-128.18}$
A	400.0	$303.59\ ^{+40.15}_{-46.92}$	$30.59\ ^{+5.37}_{-5.23}$
H	399.8	$325.95\ ^{+42.76}_{-49.66}$	$33.05\ ^{+5.38}_{-5.47}$
h	130.3	$19.29\ ^{+2.75}_{-4.10}$	$1052.67\ ^{+125.47}_{-122.80}$
A	450.0	$168.47\ ^{+23.09}_{-26.66}$	$15.05\ ^{+2.71}_{-2.67}$
H	449.6	$171.58\ ^{+23.31}_{-26.57}$	$14.33\ ^{+2.36}_{-2.44}$
h	130.3	$17.48\ ^{+2.49}_{-3.71}$	$1022.12\ ^{+121.69}_{-119.15}$
A	500.0	$97.22\ ^{+13.81}_{-15.81}$	$7.73\ ^{+1.43}_{-1.41}$
H	499.6	$95.79\ ^{+13.49}_{-15.13}$	$6.70\ ^{+1.12}_{-1.17}$
h	130.3	$16.13\ ^{+2.30}_{-3.43}$	$1000.88\ ^{+119.04}_{-116.60}$
A	600.0	$34.63\ ^{+5.27}_{-5.91}$	$2.24\ ^{+0.43}_{-0.43}$
H	599.8	$34.56\ ^{+5.24}_{-5.64}$	$1.79\ ^{+0.31}_{-0.33}$
h	130.3	$14.05\ ^{+2.00}_{-2.98}$	$974.18\ ^{+115.67}_{-113.37}$
A	700.0	$14.16\ ^{+2.30}_{-2.56}$	$0.77\ ^{+0.15}_{-0.16}$
H	699.7	$14.16\ ^{+2.32}_{-2.41}$	$0.57\ ^{+0.10}_{-0.11}$
h	130.3	$13.54\ ^{+1.93}_{-2.88}$	$957.01\ ^{+113.59}_{-111.35}$
A	800.0	$6.35\ ^{+1.10}_{-1.22}$	$0.30\ ^{+0.06}_{-0.06}$
H	799.7	$6.34\ ^{+1.13}_{-1.13}$	$0.21\ ^{+0.04}_{-0.04}$
h	130.3	$13.58\ ^{+1.93}_{-2.88}$	$945.40\ ^{+112.24}_{-110.01}$
A	900.0	$3.05\ ^{+0.57}_{-0.61}$	$0.12\ ^{+0.03}_{-0.03}$
H	899.6	$3.03\ ^{+0.59}_{-0.56}$	$0.08\ ^{+0.02}_{-0.02}$
h	130.3	$13.60\ ^{+1.94}_{-2.89}$	$937.38\ ^{+111.31}_{-109.09}$
A	1000.0	$1.54\ ^{+0.31}_{-0.33}$	$0.06\ ^{+0.01}_{-0.01}$
H	999.6	$1.52\ ^{+0.33}_{-0.29}$	$0.04\ ^{+0.01}_{-0.01}$
h	130.3	$13.59\ ^{+1.94}_{-2.89}$	$931.73\ ^{+110.64}_{-108.44}$

Table D.10: Cross-sections for the production and decay of A, H and h in the di-tau final state assuming the m_h^{max} scenario and tanβ = 40. The masses of the three states are also reported.

m_h^{max} scenario, tanβ = 50	Mass [GeV]	$\sigma(b\bar{b} \to \phi)\times\text{BR}(\phi \to \tau\tau)$[fb]	$\sigma(gg \to \phi)\times\text{BR}(\phi \to \tau\tau)$[fb]
A	170.0	$18915.99\ ^{+2432.17}_{-3470.60}$	$6867.31\ ^{+975.94}_{-935.20}$
H	170.1	$18774.34\ ^{+2420.76}_{-3446.02}$	$6617.88\ ^{+968.50}_{-917.54}$
h	130.4	$204.44\ ^{+29.12}_{-43.39}$	$1708.44\ ^{+215.06}_{-206.35}$
A	200.0	$10294.72\ ^{+1282.46}_{-1771.18}$	$2868.57\ ^{+415.74}_{-402.14}$
H	200.1	$10281.58\ ^{+1281.86}_{-1769.85}$	$2803.32\ ^{+418.91}_{-400.41}$
h	130.4	$84.16\ ^{+11.99}_{-17.86}$	$1519.33\ ^{+185.80}_{-180.20}$
A	250.0	$4250.29\ ^{+522.83}_{-685.27}$	$825.87\ ^{+123.14}_{-121.17}$
H	250.1	$4276.17\ ^{+525.02}_{-689.26}$	$830.55\ ^{+127.85}_{-124.06}$
h	130.4	$40.89\ ^{+5.82}_{-8.68}$	$1300.57\ ^{+156.68}_{-152.77}$
A	300.0	$1959.23\ ^{+244.21}_{-304.22}$	$282.46\ ^{+43.43}_{-43.30}$
H	300.2	$1989.50\ ^{+246.92}_{-307.95}$	$295.94\ ^{+46.69}_{-46.15}$
h	130.4	$28.35\ ^{+4.04}_{-6.02}$	$1175.46\ ^{+140.81}_{-137.56}$
A	350.0	$941.47\ ^{+120.47}_{-144.19}$	$106.11\ ^{+17.28}_{-17.18}$
H	350.0	$992.33\ ^{+126.15}_{-150.78}$	$119.60\ ^{+19.43}_{-19.40}$
h	130.4	$22.87\ ^{+3.26}_{-4.85}$	$1101.38\ ^{+131.56}_{-128.66}$
A	400.0	$501.43\ ^{+66.32}_{-77.50}$	$49.94\ ^{+8.57}_{-8.46}$
H	399.7	$527.62\ ^{+69.20}_{-80.38}$	$52.03\ ^{+8.57}_{-8.68}$
h	130.4	$19.82\ ^{+2.82}_{-4.21}$	$1054.02\ ^{+125.68}_{-122.99}$
A	450.0	$280.88\ ^{+38.50}_{-44.44}$	$24.38\ ^{+4.30}_{-4.29}$
H	449.5	$285.20\ ^{+38.74}_{-44.16}$	$23.34\ ^{+3.91}_{-4.01}$
h	130.4	$17.95\ ^{+2.56}_{-3.81}$	$1021.83\ ^{+121.70}_{-119.15}$
A	500.0	$163.67\ ^{+23.25}_{-26.61}$	$12.50\ ^{+2.26}_{-2.27}$
H	499.5	$162.30\ ^{+22.86}_{-25.63}$	$11.22\ ^{+1.92}_{-1.98}$
h	130.4	$16.53\ ^{+2.35}_{-3.51}$	$999.57\ ^{+118.93}_{-116.48}$
A	600.0	$59.85\ ^{+9.11}_{-10.22}$	$3.66\ ^{+0.70}_{-0.70}$
H	599.7	$59.89\ ^{+9.07}_{-9.78}$	$3.11\ ^{+0.56}_{-0.58}$
h	130.4	$14.23\ ^{+2.03}_{-3.02}$	$972.08\ ^{+115.43}_{-113.14}$
A	700.0	$24.85\ ^{+4.04}_{-4.49}$	$1.26\ ^{+0.25}_{-0.25}$
H	699.6	$24.88\ ^{+4.07}_{-4.24}$	$1.02\ ^{+0.19}_{-0.20}$
h	130.4	$13.75\ ^{+1.96}_{-2.92}$	$954.30\ ^{+113.30}_{-111.05}$
A	800.0	$11.25\ ^{+1.96}_{-2.16}$	$0.49\ ^{+0.10}_{-0.10}$
H	799.5	$11.24\ ^{+2.00}_{-2.01}$	$0.38\ ^{+0.08}_{-0.08}$
h	130.4	$13.90\ ^{+1.98}_{-2.95}$	$942.09\ ^{+111.89}_{-109.66}$
A	900.0	$5.43\ ^{+1.01}_{-1.10}$	$0.20\ ^{+0.04}_{-0.05}$
H	899.4	$5.41\ ^{+1.05}_{-1.00}$	$0.16\ ^{+0.03}_{-0.03}$
h	130.4	$13.99\ ^{+1.99}_{-2.97}$	$933.85\ ^{+110.94}_{-108.71}$
A	1000.0	$2.76\ ^{+0.56}_{-0.59}$	$0.09\ ^{+0.02}_{-0.02}$
H	999.4	$2.73\ ^{+0.59}_{-0.53}$	$0.07\ ^{+0.01}_{-0.02}$
h	130.4	$14.01\ ^{+2.00}_{-2.98}$	$927.97\ ^{+110.25}_{-108.04}$

Table D.11: Cross-sections for the production and decay of A, H and h in the di-tau final state assuming the m_h^{max} scenario and tanβ = 50. The masses of the three states are also reported.

APPENDIX E

Summary Tables of the $h/H/A \rightarrow \tau_{\text{had}}\tau_{\text{had}}$ Analysis Results

	Pre-selection	$p_{\text{T}}(\tau_{\text{lead/sub-lead}}) > 50$ GeV	Opposite-sign	$\lvert\Delta\phi(\tau_{\text{lead}}, \tau_{\text{sub-lead}})\rvert > 2.7$
$b\bar{b} \rightarrow A$ ($\tan\beta = 20$)				
$m_A = 170$ GeV	4006 ± 44	2253 ± 41	2129 ± 39	1705 ± 35
$m_A = 200$ GeV	3153 ± 29	1943 ± 27	1835 ± 27	1512 ± 24
$m_A = 250$ GeV	1722 ± 15	1132 ± 15	1066 ± 14	905 ± 13
$m_A = 300$ GeV	836 ± 5.9	572.8 ± 6.1	541.6 ± 5.9	466.4 ± 5.5
$m_A = 350$ GeV	377.2 ± 2.5	257.6 ± 2.6	243.4 ± 2.5	213.8 ± 2.3
$m_A = 400$ GeV	204.9 ± 1.3	143.8 ± 1.4	134.8 ± 1.3	119.3 ± 1.2
$m_A = 450$ GeV	112.60 ± 0.71	77.89 ± 0.73	73.3 ± 0.71	65.73 ± 0.67
$m_A = 500$ GeV	63.98 ± 0.40	44.45 ± 0.41	41.73 ± 0.39	37.58 ± 0.38
$m_A = 600$ GeV	20.95 ± 0.13	14.67 ± 0.13	13.67 ± 0.13	12.50 ± 0.12
$m_A = 700$ GeV	8.160 ± 0.050	5.726 ± 0.051	5.338 ± 0.049	4.906 ± 0.047
$m_A = 800$ GeV	3.526 ± 0.022	2.469 ± 0.022	2.270 ± 0.021	2.104 ± 0.020
$m_A = 900$ GeV	1.5478 ± 0.0082	1.1467 ± 0.0091	1.0543 ± 0.0087	0.9852 ± 0.0084
$m_A = 1000$ GeV	0.7445 ± 0.0045	0.5489 ± 0.0049	0.5020 ± 0.0048	0.4675 ± 0.0046

Table E.1: Event yields for the $b\bar{b} \rightarrow A$ signal after pre-selection and the application of topological and kinematic requirements as discussed in Sec. 7.3.1 and 7.3.2, respectively. The table includes the statistical uncertainty. The cross-section used to normalise the signal corresponds to $\tan\beta = 20$ in the m_h^{max} scenario.

	Pre-selection	$p_{\text{T}}(\tau_{\text{lead/sub-lead}}) > 50$ GeV	Opposite-sign	$\lvert\Delta\phi(\tau_{\text{lead}}, \tau_{\text{sub-lead}})\rvert > 2.7$
$gg \to A$ ($\tan\beta = 20$)				
$m_A = 170$ GeV	1446.18 ± 15.5	837.0 ± 14.4	752.5 ± 13.7	449.8 ± 10.6
$m_A = 200$ GeV	789.6 ± 7.2	489.8 ± 7.0	448.8 ± 6.7	294.3 ± 5.4
$m_A = 250$ GeV	291.7 ± 2.2	191.0 ± 2.2	176.5 ± 2.2	125.0 ± 1.8
$m_A = 300$ GeV	97.5 ± 0.7	66.53 ± 0.71	61.71 ± 0.68	46.62 ± 0.59
$m_A = 350$ GeV	40.15 ± 0.27	28.02 ± 0.27	25.99 ± 0.26	20.47 ± 0.23
$m_A = 400$ GeV	25.85 ± 0.17	18.07 ± 0.17	16.76 ± 0.17	13.65 ± 0.15
$m_A = 450$ GeV	14.135 ± 0.090	9.961 ± 0.093	9.294 ± 0.089	7.72 ± 0.081
$m_A = 500$ GeV	7.644 ± 0.048	5.428 ± 0.049	5.034 ± 0.048	4.209 ± 0.044
$m_A = 600$ GeV	2.185 ± 0.013	1.561 ± 0.014	1.561 ± 0.014	1.232 ± 0.012
$m_A = 700$ GeV	0.7632 ± 0.0047	0.5452 ± 0.0048	0.4972 ± 0.0046	0.4233 ± 0.0042
$m_A = 800$ GeV	0.2923 ± 0.0018	0.2070 ± 0.0018	0.1887 ± 0.0018	0.1645 ± 0.0016
$m_A = 900$ GeV	0.12140 ± 0.00064	0.08877 ± 0.00069	0.08031 ± 0.00067	0.07024 ± 0.00062
$m_A = 1000$ GeV	0.05400 ± 0.00032	0.03907 ± 0.00035	0.03513 ± 0.00033	0.03094 ± 0.00031

Table E.2: Event yields for the $gg \to A$ signal after pre-selection and the application of topological and kinematic requirements as discussed in Sec. 7.3.1 and 7.3.2, respectively. The table includes the statistical uncertainty. The cross-section used to normalise the signal corresponds to $\tan\beta = 20$ in the m_h^{max} scenario.

		DTT Selection			
	Di-tau trigger	$p_{\text{T}}(\tau_{\text{lead}}) < 150$ GeV	Medium tau-ID	$E_{\text{T}}^{\text{miss}} > 10$ GeV	$\Sigma E_{\text{T}} > 160$ GeV
$b\bar{b} \to A$ ($\tan\beta = 20$)					
$m_A = 170$ GeV	754 ± 24	752 ± 23	548 ± 20	432 ± 18	370 ± 16
$m_A = 200$ GeV	655 ± 16	651 ± 16	482 ± 13	407 ± 12	371 ± 12
$m_A = 250$ GeV	422.1 ± 9.2	415.1 ± 9.1	312.2 ± 7.8	276.3 ± 7.4	264.9 ± 7.2
$m_A = 300$ GeV	210.9 ± 3.7	194.5 ± 3.5	147.8 ± 3.1	132.9 ± 2.9	129.3 ± 2.8
$m_A = 350$ GeV	102.7 ± 1.6	76.3 ± 1.4	58.2 ± 1.2	52.2 ± 1.1	51.3 ± 1.1
$m_A = 400$ GeV	59.28 ± 0.88	33.47 ± 0.66	25.80 ± 0.58	23.67 ± 0.55	23.37 ± 0.55
$m_A = 450$ GeV	32.31 ± 0.47	14.02 ± 0.31	10.91 ± 0.27	9.89 ± 0.26	9.82 ± 0.26
$m_A = 500$ GeV	19.24 ± 0.27	6.54 ± 0.16	5.00 ± 0.14	4.58 ± 0.13	4.49 ± 0.13

Table E.3: Event yields for the $b\bar{b} \to A$ signal at each stage of the selection in the DTT category selection. The table includes only the statistical uncertainty at each stage. The cross-section used to normalise the signal corresponds to $\tan\beta = 20$ in the m_h^{max} scenario. Only the relevant signal masses for the DTT category are considered.

	DTT Selection				
	Di-tau trigger	$p_T(\tau_{lead}) < 150$ GeV	Medium tau-ID	$E_T^{miss} > 10$ GeV	$\Sigma E_T > 160$ GeV
$gg \to A$ (tan$\beta = 20$)					
$m_A = 170$ GeV	196.0 ± 7.1	191.7 ± 7.0	129.8 ± 5.7	104.9 ± 5.1	94.5 ± 4.9
$m_A = 200$ GeV	131.5 ± 3.7	129.3 ± 3.6	94.7 ± 3.1	79.9 ± 2.9	75.4 ± 2.8
$m_A = 250$ GeV	56.3 ± 1.2	54.3 ± 1.2	38.9 ± 1.0	34.71 ± 0.96	33.97 ± 0.95
$m_A = 300$ GeV	21.45 ± 0.41	19.16 ± 0.38	14.42 ± 0.33	13.16 ± 0.31	13.02 ± 0.31
$m_A = 350$ GeV	9.69 ± 0.16	7.10 ± 0.14	5.25 ± 0.12	4.811 ± 0.11	4.80 ± 0.11
$m_A = 400$ GeV	6.47 ± 0.10	3.530 ± 0.078	2.665 ± 0.067	2.473 ± 0.064	2.472 ± 0.064
$m_A = 450$ GeV	3.686 ± 0.057	1.504 ± 0.036	1.127 ± 0.031	1.058 ± 0.031	1.055 ± 0.030
$m_A = 500$ GeV	2.039 ± 0.030	0.668 ± 0.017	0.492 ± 0.015	0.460 ± 0.014	0.458 ± 0.014

Table E.4: Event yields for the $gg \to A$ signal at each stage of the selection in the DTT category selection. The table includes only the statistical uncertainty at each stage. The cross-section used to normalise the signal corresponds to tan$\beta = 20$ in the m_h^{max} scenario. Only the relevant signal masses for the DTT category are considered.

	STT Selection		
	Single-tau trigger	$p_T(\tau_{lead}) > 150$ GeV	Loose tau-ID
$b\bar{b} \to A$ (tan$\beta = 20$)			
$m_A = 250$ GeV	27.5 ± 2.3	6.9 ± 1.1	4.56 ± 0.92
$m_A = 300$ GeV	57.7 ± 1.9	21.5 ± 1.2	15.35 ± 0.97
$m_A = 350$ GeV	54.6 ± 1.2	35.16 ± 0.95	26.71 ± 0.82
$m_A = 400$ GeV	42.78 ± 0.74	32.97 ± 0.65	25.31 ± 0.56
$m_A = 450$ GeV	28.13 ± 0.44	23.85 ± 0.41	18.69 ± 0.35
$m_A = 500$ GeV	18.32 ± 0.26	16.30 ± 0.25	12.95 ± 0.22
$m_A = 600$ GeV	7.069 ± 0.092	6.628 ± 0.089	5.263 ± 0.078
$m_A = 700$ GeV	3.002 ± 0.037	2.887 ± 0.037	2.339 ± 0.032
$m_A = 800$ GeV	1.332 ± 0.016	1.295 ± 0.016	1.295 ± 0.016
$m_A = 900$ GeV	1.295 ± 0.016	0.6313 ± 0.0068	0.5116 ± 0.0060
$m_A = 1000$ GeV	0.3023 ± 0.0037	0.2960 ± 0.0037	0.2392 ± 0.0032

Table E.5: Event yields for the $b\bar{b} \to A$ signal at each stage of the selection in the STT category selection. The table includes only the statistical uncertainty at each stage. The cross-section used to normalise the signal corresponds to tan$\beta = 20$ in the m_h^{max} scenario. Only the relevant signal masses for the STT category are considered.

	Selection		
	Single-tau trigger	$p_{\text{T}}(\tau_{\text{lead}}) > 150$ GeV	Loose tau-ID
$gg \to A$ ($\tan\beta = 20$)			
$m_A = 250$ GeV	5.77 ± 0.39	2.23 ± 0.24	1.25 ± 0.17
$m_A = 300$ GeV	6.58 ± 0.22	3.05 ± 0.15	2.12 ± 0.12
$m_A = 350$ GeV	5.49 ± 0.12	3.579 ± 0.099	2.593 ± 0.083
$m_A = 400$ GeV	4.914 ± 0.090	3.873 ± 0.080	2.926 ± 0.068
$m_A = 450$ GeV	3.407 ± 0.054	2.924 ± 0.050	2.228 ± 0.043
$m_A = 500$ GeV	2.058 ± 0.031	1.826 ± 0.028	1.401 ± 0.024
$m_A = 600$ GeV	0.6998 ± 0.0094	0.6547 ± 0.0091	0.5076 ± 0.0079
$m_A = 700$ GeV	0.2527 ± 0.0033	0.2427 ± 0.0032	0.1892 ± 0.0028
$m_A = 800$ GeV	0.1049 ± 0.0013	0.1023 ± 0.0013	0.0796 ± 0.0011
$m_A = 900$ GeV	0.04521 ± 0.00050	0.04428 ± 0.00049	0.03442 ± 0.00043
$m_A = 1000$ GeV	0.02005 ± 0.00025	0.01968 ± 0.00024	0.01517 ± 0.00021

Table E.6: Event yields for the $gg \to A$ signal at each stage of the selection in the STT category selection. The table includes only the statistical uncertainty at each stage. The cross-section used to normalise the signal corresponds to $\tan\beta = 20$ in the m_h^{max} scenario. Only the relevant signal masses for the STT category are considered.

$b\bar{b} \rightarrow A$	DTT Systematic Uncertainties [%]							
m_A[GeV]	170	200	250	300	350	400	450	500
TES true tau	+8.9	+5.3	+2.8	+0.3	-0.9	-3.9	-4.3	-6.0
	-6.8	-7.7	-2.4	-1.1	+2.0	+3.4	+4.8	+5.4
TES fake tau	-	-0.07	-	-0.07	-0.09	-	-0.07	-
	-	+0.1	-	-0.01	+0.1	-	+0.01	-
Trigger low-p_T	+20.2	+19.4	+14.7	+11.3	+9.7	+8.8	+8.5	+7.7
	-21.2	-20.3	-15.9	-12.5	-10.9	-10.1	-9.8	-9.2
Trigger high-p_T	+0.4	±1.52	+5.04	+8.2	+9.6	+10.2	+10.6	+10.6
	-0.3		-4.92	-7.9	-9.2	-9.7	-10.04	-10.1
Tau-ID	+6.6	+6.8	+6.6	+6.7	+6.6	+6.5	+6.5	+6.3
	-6.4	-6.6	-6.4	-6.5	-6.4	-6.3	-6.3	-6.1
Mis-ID reweighting	±0.04	±0.02	±0.02	±0.03	±0.01	±0.02	±0.01	±0.01
JES	+1.8	+0.3	+0.5	+0.05	+0.5	+0.4	+0.24	+0.2
	-2.6	-0.9	-0.4	-0.38	-0.2	-0.8	-0.01	-0.1
E_T^{miss} resolution	-0.1	-0.3	-0.54	+0.5	-0.2	-0.38	-0.2	+0.01
	+0.5	-0.4	+0.04	-0.3	+0.5	-0.07	+0.3	+0.15
E_T^{miss} scale	+0.6	-0.14	-0.19	-0.3	+0.04	-0.09	-0.27	-0.16
	+0.5	+0.09	+0.02	+0.1	+0.26	-0.10	+0.06	-0.04
Acceptance	±6.4	±6.4	±6.4	±4.7	±4.7	±4.7	±4.7	±5.2

Table E.7: Systematic uncertainties in the DTT category presented as a relative variation in the expected number of events for each $b\bar{b} \rightarrow A$ signal hypothesis. The upward and downward variations in the event yield are shown in the upper and lower rows respectively, when a systematic effect is not symmetric. Cross-section uncertainties depend on tanβ and are illustrated in App. D.

$gg \to A$	DTT Systematic Uncertainties [%]							
m_A[GeV]	170	200	250	300	350	400	450	500
TES true tau	+6.9	+6.1	+2.4	-0.06	-2.4	-2.5	-5.1	-5.9
	-10.6	-5.9	-3.8	-0.81	+2.5	+3.2	+3.8	+4.6
TES fake tau	-	+0.01	-	-0.18	-0.05	-0.12	-0.08	-
	-	+0.03	-	-	+0.10	-	+0.04	-
Trigger low-p_{T}	+20.5	+18.6	+15.1	+11.5	+9.6	+9.1	+7.9	+7.9
	-21.5	-19.9	-16.4	-12.9	-10.9	-10.5	-9.4	-9.3
Trigger high-p_{T}	±0.4	±1.5	+4.8	+7.7	+9.6	+9.8	+10.8	+10.9
			-4.7	-7.5	-9.2	-9.4	-10.3	-10.3
Tau-ID	+6.9	+6.7	+6.7	+6.6	+6.6	+6.5	+6.5	+6.3
	-6.6	-6.5	-6.4	-6.4	-6.4	-6.3	-6.3	-6.1
Mis-ID reweighting	±0.16	±0.06	±0.04	±0.02	±0.02	±0.03	±0.03	±0.03
JES	+1.4	+0.51	-0.2	+0.04	-0.02	-0.07	+0.1	+0.01
	-0.8	-0.08	-0.4	-0.18	-0.41	-0.06	-0.2	-0.75
$E_{\text{T}}^{\text{miss}}$ resolution	-0.98	+0.3	-0.03	-0.3	+0.3	-0.4	-0.11	-0.39
	-0.05	-0.1	-0.13	+0.5	-0.5	+0.1	+0.03	+0.05
$E_{\text{T}}^{\text{miss}}$ scale	+0.1	-0.3	+0.35	+0.11	+0.1	-0.21	-0.20	-0.02
	+0.2	+0.2	-0.09	+0.02	-0.2	+0.02	-0.19	-0.20
Acceptance	±1.3	±1.3	±1.3	±1.3	±1.8	±1.8	±1.7	±1.7

Table E.8: Systematic uncertainties in the DTT category presented as a relative variation in the expected number of events for each $gg \to A$ signal hypothesis. The upward and downward variations in the event yield are shown in the upper and lower rows respectively, when a systematic effect is not symmetric. Cross-section uncertainties depend on tanβ and are illustrated in App. D.

$b\bar{b} \rightarrow A$	STT Experimental Uncertainties [%]										
m_A[GeV]	250	300	350	400	450	500	600	700	800	900	1000
TES true tau	+23.1	+27.5	+9.9	+6.1	+4.3	+3.4	+1.5	+0.9	+0.8	+0.7	+0.4
	-38.5	-19.8	-11.8	-6.7	-5.2	-3.2	-2.0	-1.4	-0.7	-0.8	-0.7
TES fake tau	-0.01	-	-0.06	∓0.05	-0.07	-	-0.02	-0.06	-0.03	-0.04	∓0.02
	-	-	-		+0.09	-	-	-	+0.02	+0.02	
Trigger high-p_T	±10.0	±10.0	±10.0	±10.0	±10.0	±10.0	±10.0	±10.0	±10.0	±10.0	±10.0
Tau-ID	+6.9	+6.5	+6.5	+6.5	+6.5	+6.5	+6.6	+6.7	+6.8	+6.9	+7.0
	-6.7	-6.3	-6.3	-6.3	-6.3	-6.3	-6.4	-6.5	-6.6	-6.7	-6.8
Mis-ID reweighting	±0.02	±0.05	±0.03	±0.01	±0.01	±0.01	±0.02	±0.01	±0.02	±0.02	±0.02
Track reco. eff.	±0.2	±0.2	±0.2	±0.4	±0.6	±0.8	±1.2	±1.5	±2.1	±2.4	±2.6
Acceptance	±28.2	±13.2	±13.2	±13.2	±13.2	±3.0	±3.0	±2.8	±2.8	±2.8	±2.8

Table E.9: Systematic uncertainties in the STT category presented as a relative variation in the expected number of events for each $b\bar{b} \rightarrow A$ signal hypothesis. The upward and downward variations in the event yield are shown in the upper and lower rows respectively, when a systematic effect is not symmetric. Cross-section uncertainties depend on tanβ and are illustrated in App. D.

$gg \to A$	STT Experimental Uncertainties [%]										
m_A[GeV]	250	300	350	400	450	500	600	700	800	900	1000
TES true tau	+22.0	+18.1	+9.8	+6.5	+3.7	+3.1	+1.7	+0.8	+0.8	±0.6	+0.5
	-14.3	-18.4	-12.0	-5.9	-4.0	-3.3	-1.6	-1.3	-1.0		-0.7
TES fake tau	+0.01	-	-	-0.06	-0.02	-	-	-0.03	-	-0.02	-0.02
	-	+0.25	-	+0.05	+0.09	+0.03	+0.02	+0.02	+0.03	+0.01	-
Trigger high-p_{T}	±10.0	±10.0	±10.0	±10.0	±10.0	±10.0	±10.0	±10.0	±10.0	±10.0	±10.0
Tau-ID	+6.9	+6.5	+6.4	+6.4	+6.4	+6.5	+6.5	+6.6	+6.8	+6.9	+7.0
	-6.7	-6.3	-6.2	-6.2	-6.2	-6.3	-6.3	-6.4	-6.6	-6.7	-6.7
Mis-ID reweighting	±0.52	±0.19	±0.03	±0.03	±0.04	±0.03	±0.02	±0.03	±0.03	±0.03	±0.03
Track reco. eff.	±0.32	±0.24	±0.3	±0.4	±0.6	±0.8	±1.1	±1.5	±2.0	±2.3	±2.5
Acceptance	±8.3	±8.3	±8.3	±1.5	±1.5	±1.2	±1.2	±1.2	±1.2	±1.2	±1.2

Table E.10: Systematic uncertainties in the STT category presented as a relative variation in the expected number of events for each $gg \to A$ signal hypothesis. The upward and downward variations in the event yield are shown in the upper and lower rows respectively, when a systematic effect is not symmetric. Cross-section uncertainties depend on tanβ and are illustrated in App. D.

APPENDIX F

Supporting Material for Exclusion Limits

F.0.1 Pull Distributions

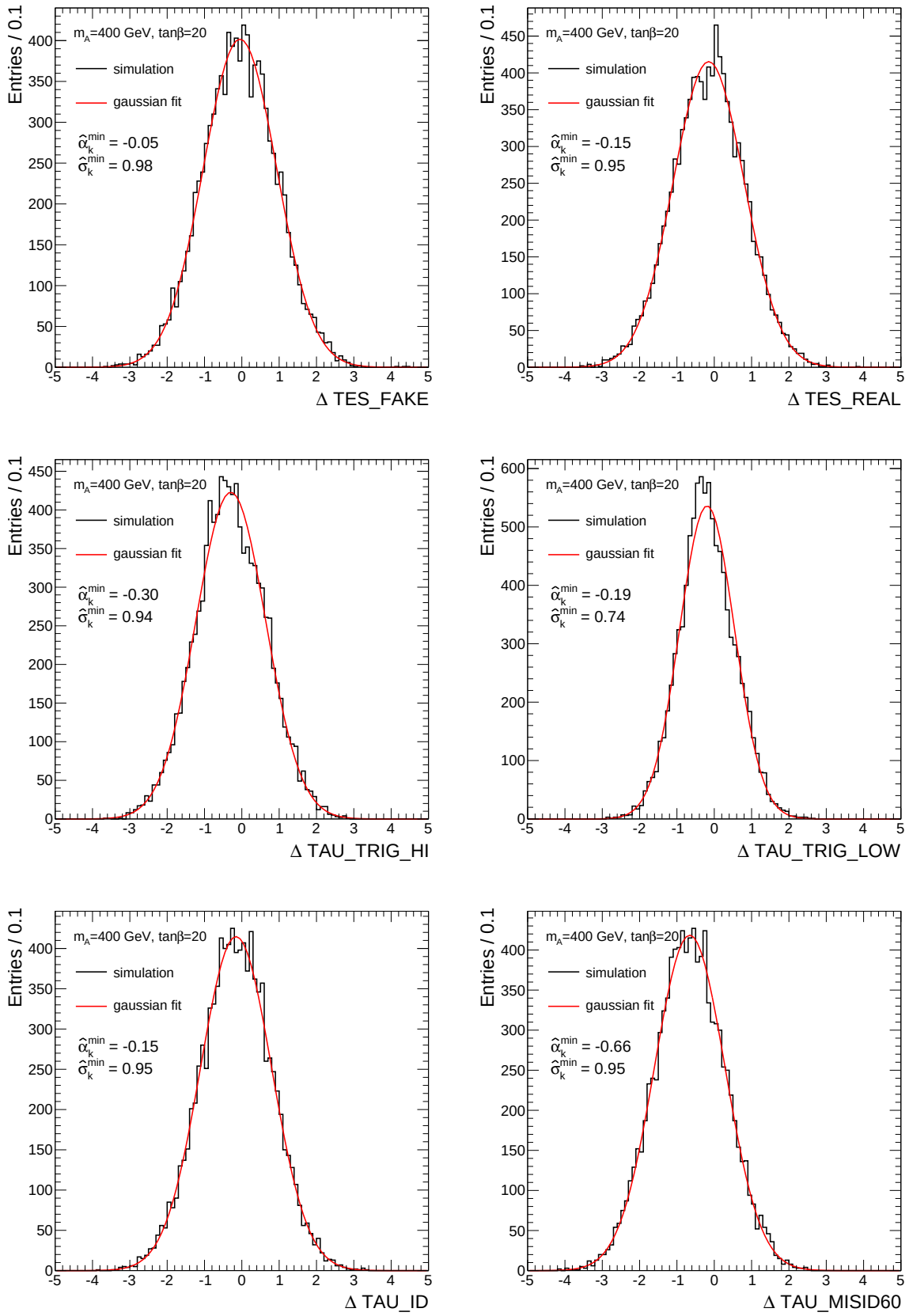

Figure F.1: Distributions of the fit pulls for all systematic uncertainties in the $h/H/A \to \tau_{\text{had}}\tau_{\text{had}}$ analysis

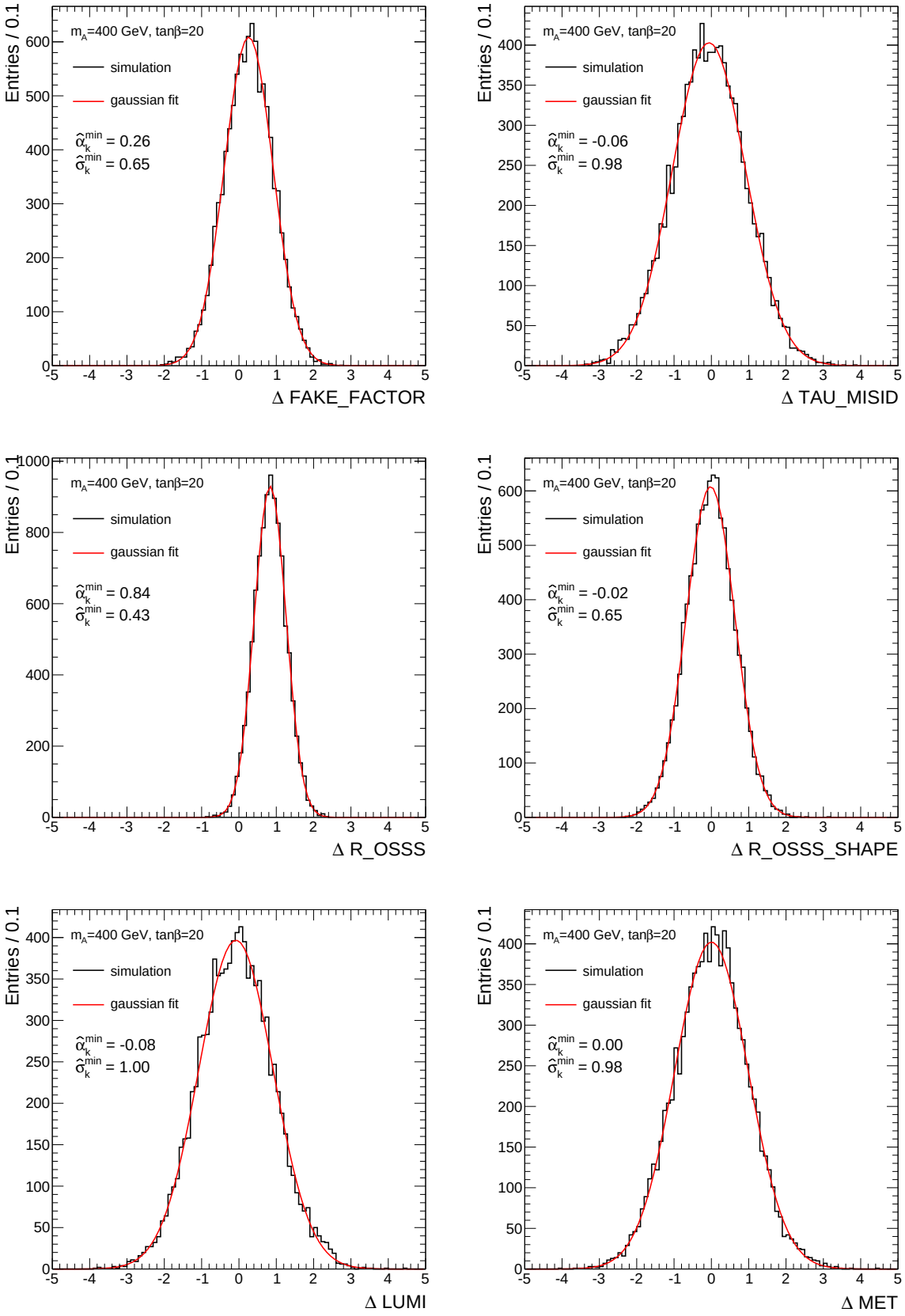

Figure F.2: Distributions of the fit pulls for all systematic uncertainties in the $h/H/A \rightarrow \tau_{\text{had}}\tau_{\text{had}}$ analysis

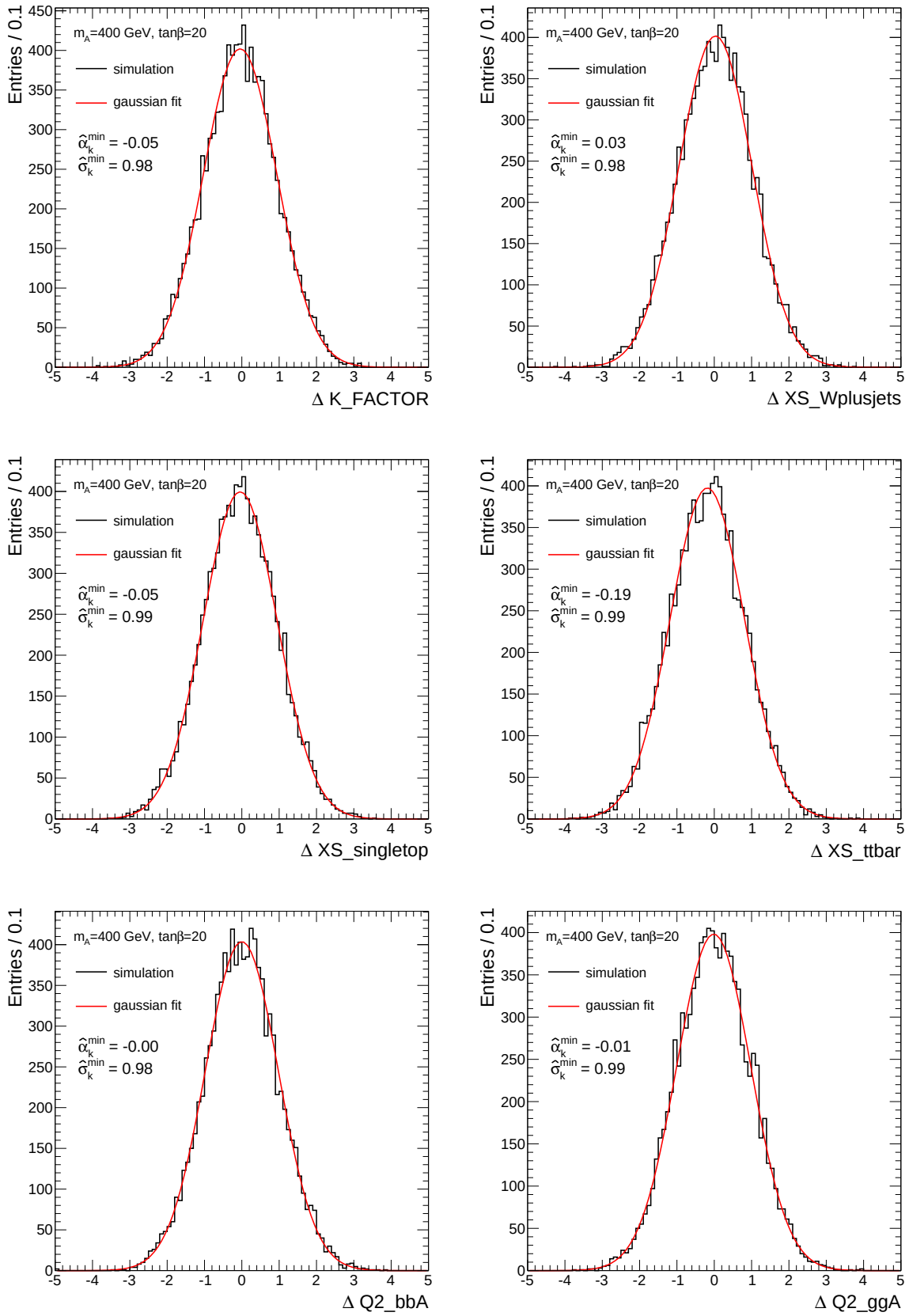

Figure F.3: Distributions of the fit pulls for all systematic uncertainties in the $h/H/A \to \tau_{\text{had}}\tau_{\text{had}}$ analysis

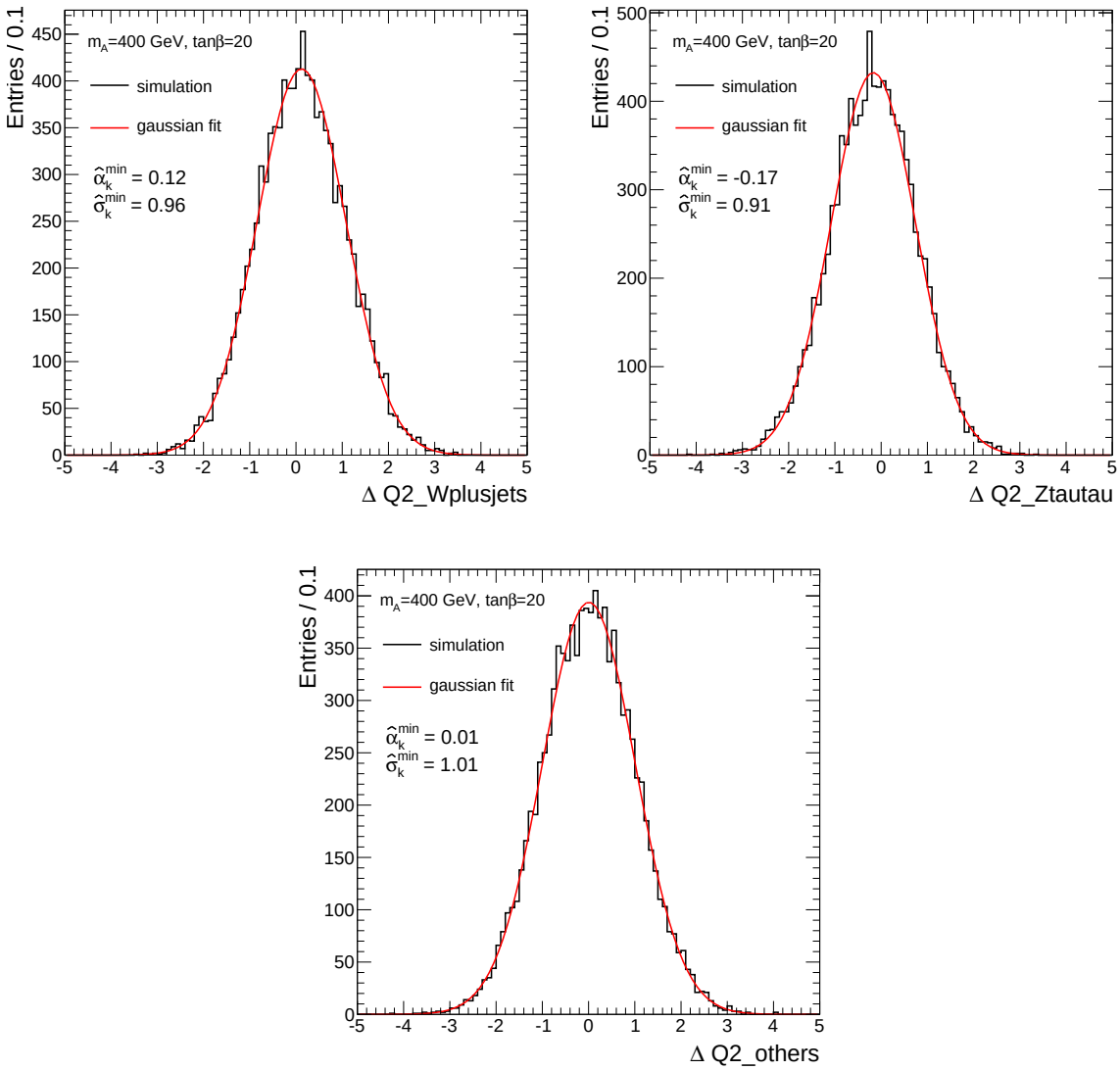

Figure F.4: Distributions of the fit pulls for all systematic uncertainties in the $h/H/A \rightarrow \tau_{\text{had}}\tau_{\text{had}}$ analysis

F.0.2 Exclusion Limits in Additional MSSM Scenarios

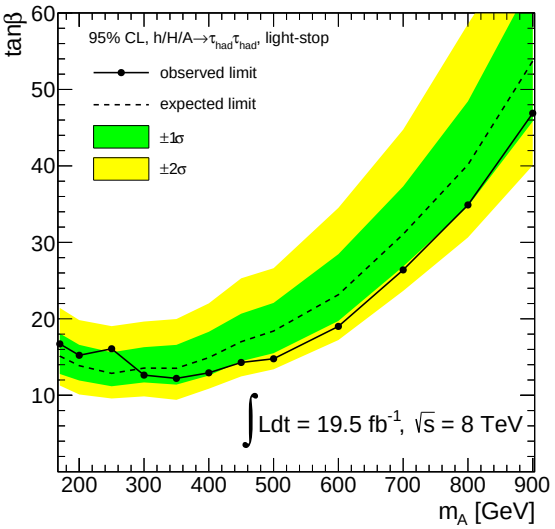

Figure F.5: Exclusion limit in the *light − stop* scenario of the MSSM. The area above each curve is excluded at 95% CL.

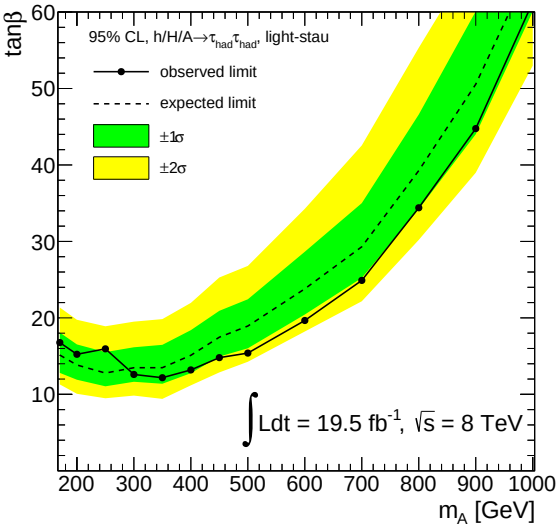

Figure F.6: Exclusion limit in the *light − stau* scenario of the MSSM. The area above each curve is excluded at 95% CL.

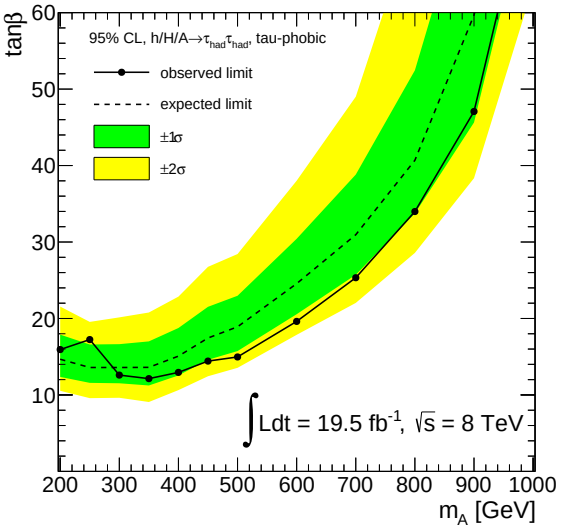

Figure F.7: Exclusion limit in the *tau − phobic* scenario of the MSSM. The area above each curve is excluded at 95% CL.

F.0.3 Ranking of Systematic Uncertainties

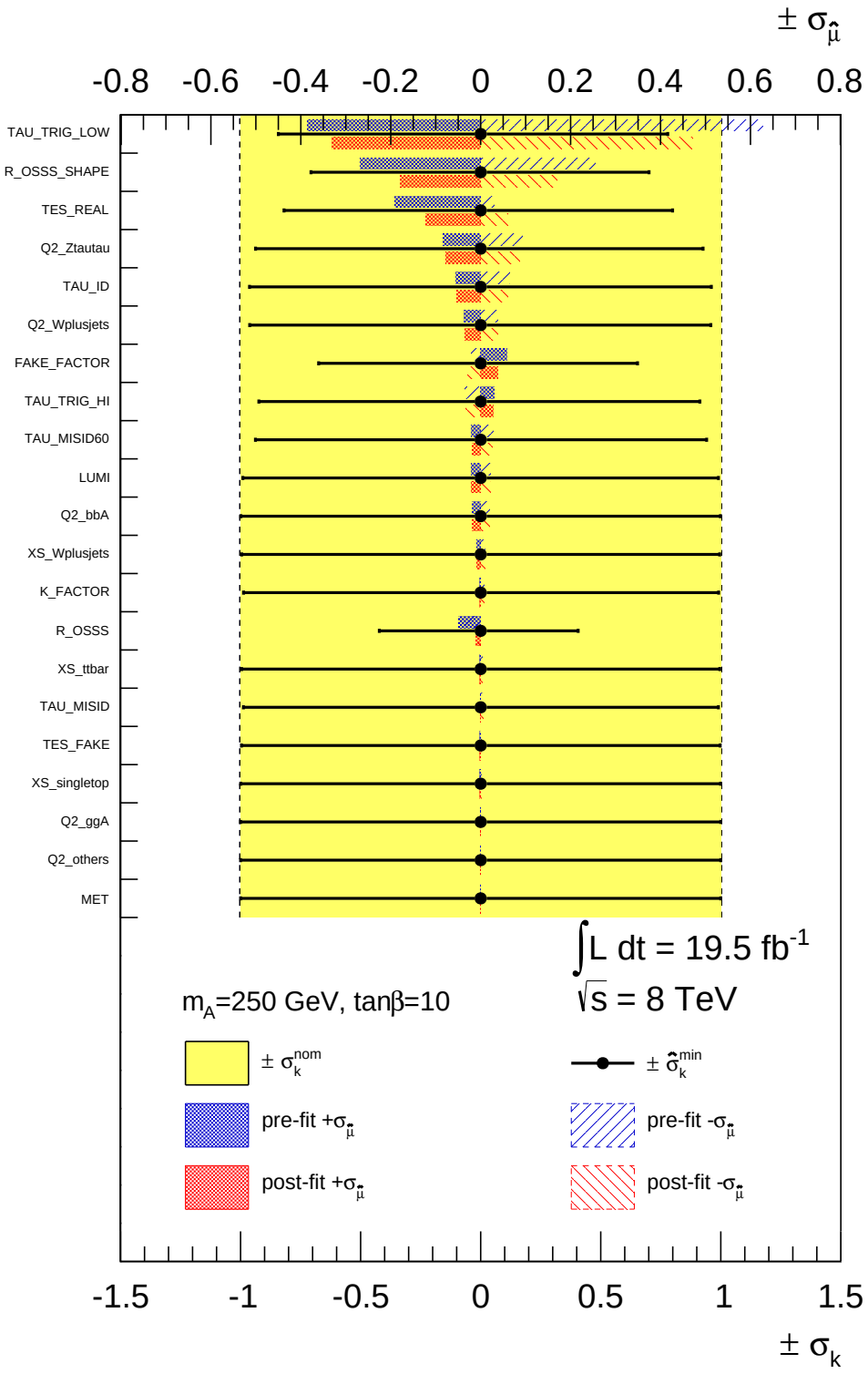

Figure F.8: Summary of the impact of systematic uncertainties on $\hat{\mu}$ determined from an unconditional fit to the Asimov dataset. The point $m_A = 250$ GeV and $\tan\beta = 10$ has been used. Systematic uncertainties are ranked from top to bottom on the left axis according to the post-fit impact shown in red. The upper axis illustrates the scale of $\sigma_{\hat{\mu}}$. The plot also includes the values of $\hat{\sigma}_k^{\text{min}}$, shown in black, determined from the post-fit likelihood contours. The nominal pre-fit bound on each nuisance parameter is also shown and represented by the yellow region. The scale of the post-fit and pre-fit systematic contours is shown by the lower axis.

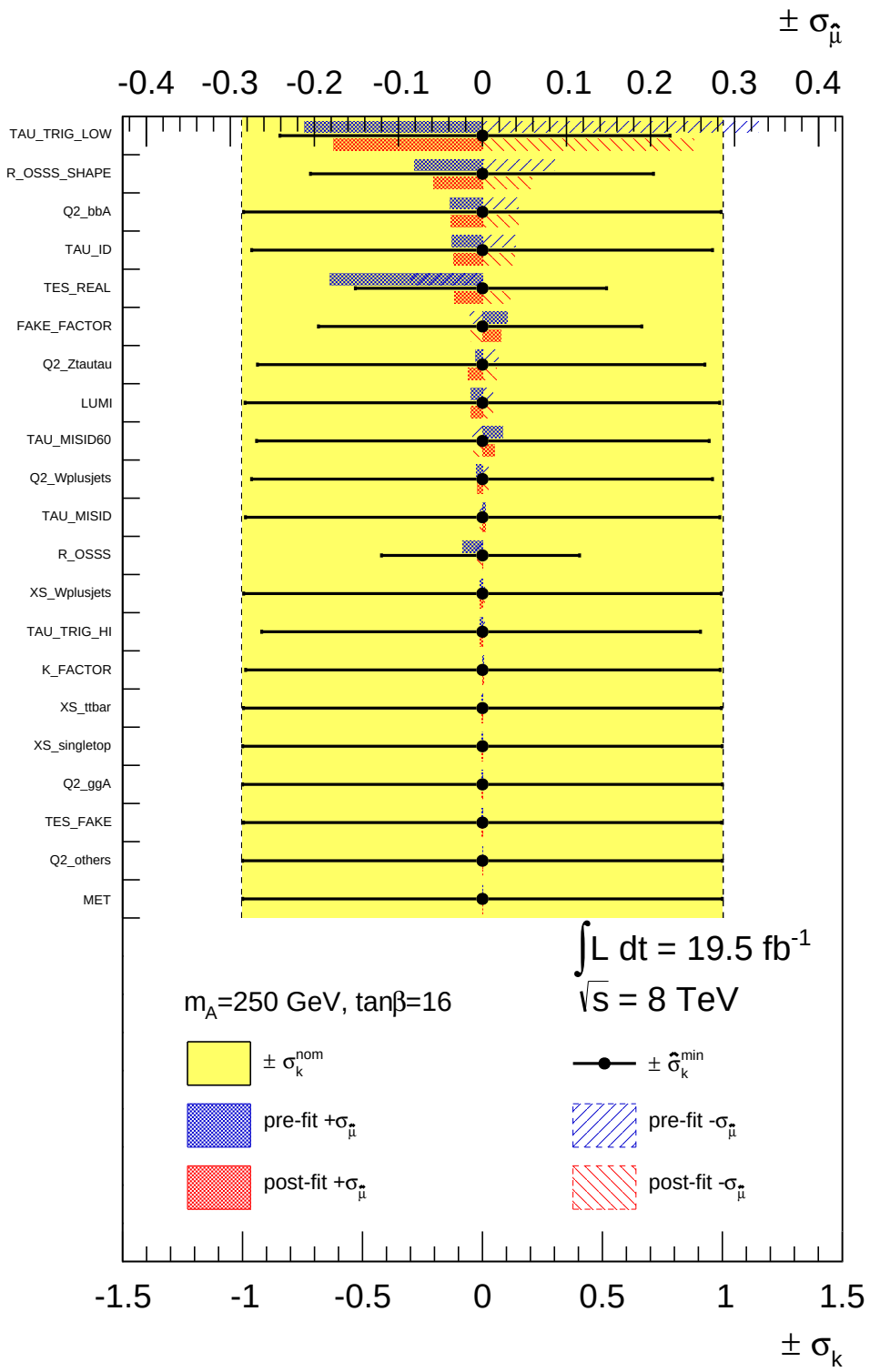

Figure F.9: Summary of the impact of systematic uncertainties on $\hat{\mu}$ determined from an unconditional fit to the Asimov dataset. The point $m_A = 250$ GeV and $\tan\beta = 16$ has been used. Systematic uncertainties are ranked from top to bottom on the left axis according to the post-fit impact shown in red. The upper axis illustrates the scale of $\sigma_{\hat{\mu}}$. The plot also includes the values of $\hat{\sigma}_k^{\text{min}}$, shown in black, determined from the post-fit likelihood contours. The nominal pre-fit bound on each nuisance parameter is also shown and represented by the yellow region. The scale of the post-fit and pre-fit systematic contours is shown by the lower axis.

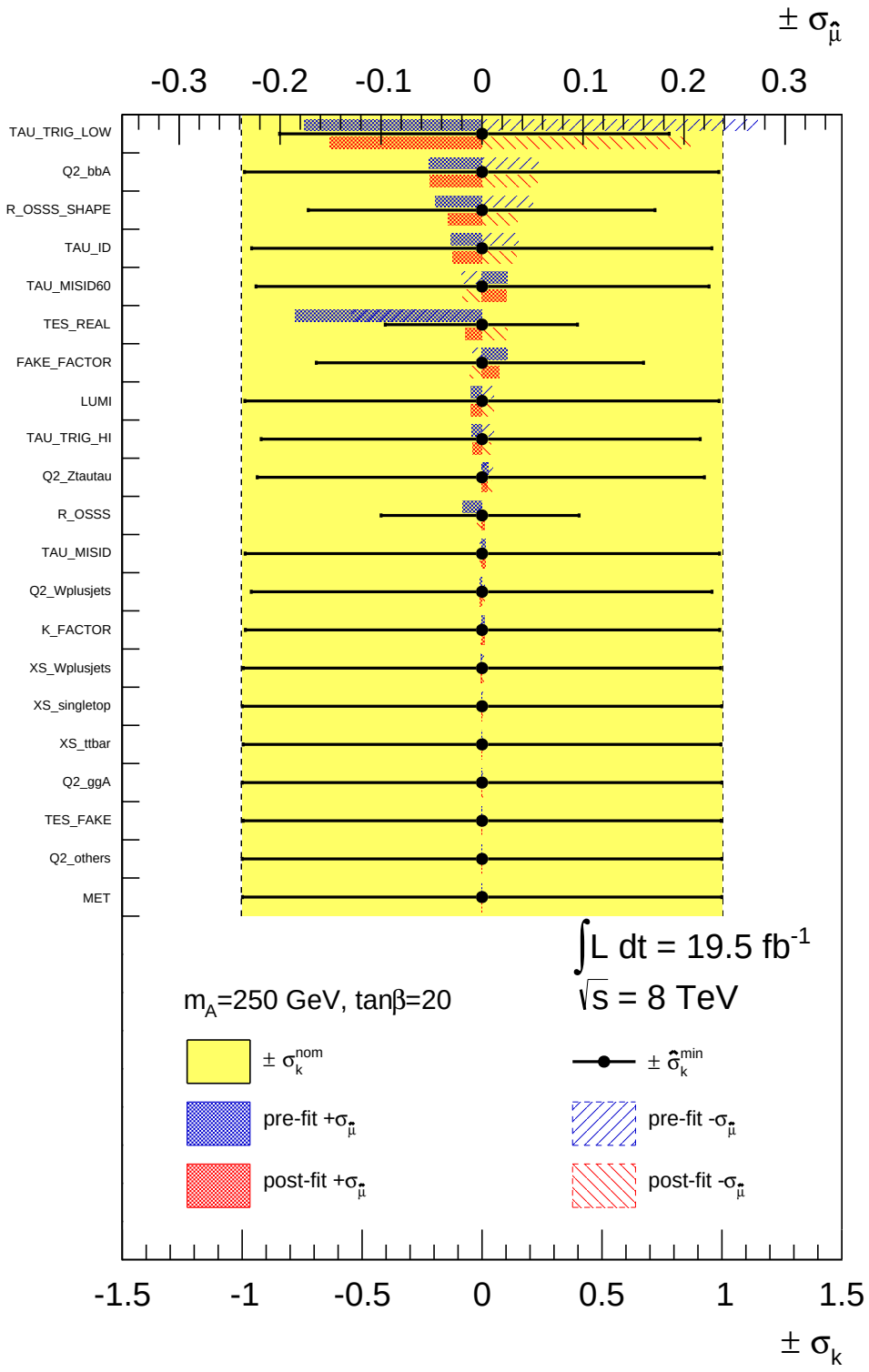

Figure F.10: Summary of the impact of systematic uncertainties on $\hat{\mu}$ determined from an unconditional fit to the Asimov dataset. The point $m_A = 250$ GeV and $\tan\beta = 20$ has been used. Systematic uncertainties are ranked from top to bottom on the left axis according to the post-fit impact shown in red. The upper axis illustrates the scale of $\sigma_{\hat{\mu}}$. The plot also includes the values of $\hat{\sigma}_k^{\text{min}}$, shown in black, determined from the post-fit likelihood contours. The nominal pre-fit bound on each nuisance parameter is also shown and represented by the yellow region. The scale of the post-fit and pre-fit systematic contours is shown by the lower axis.

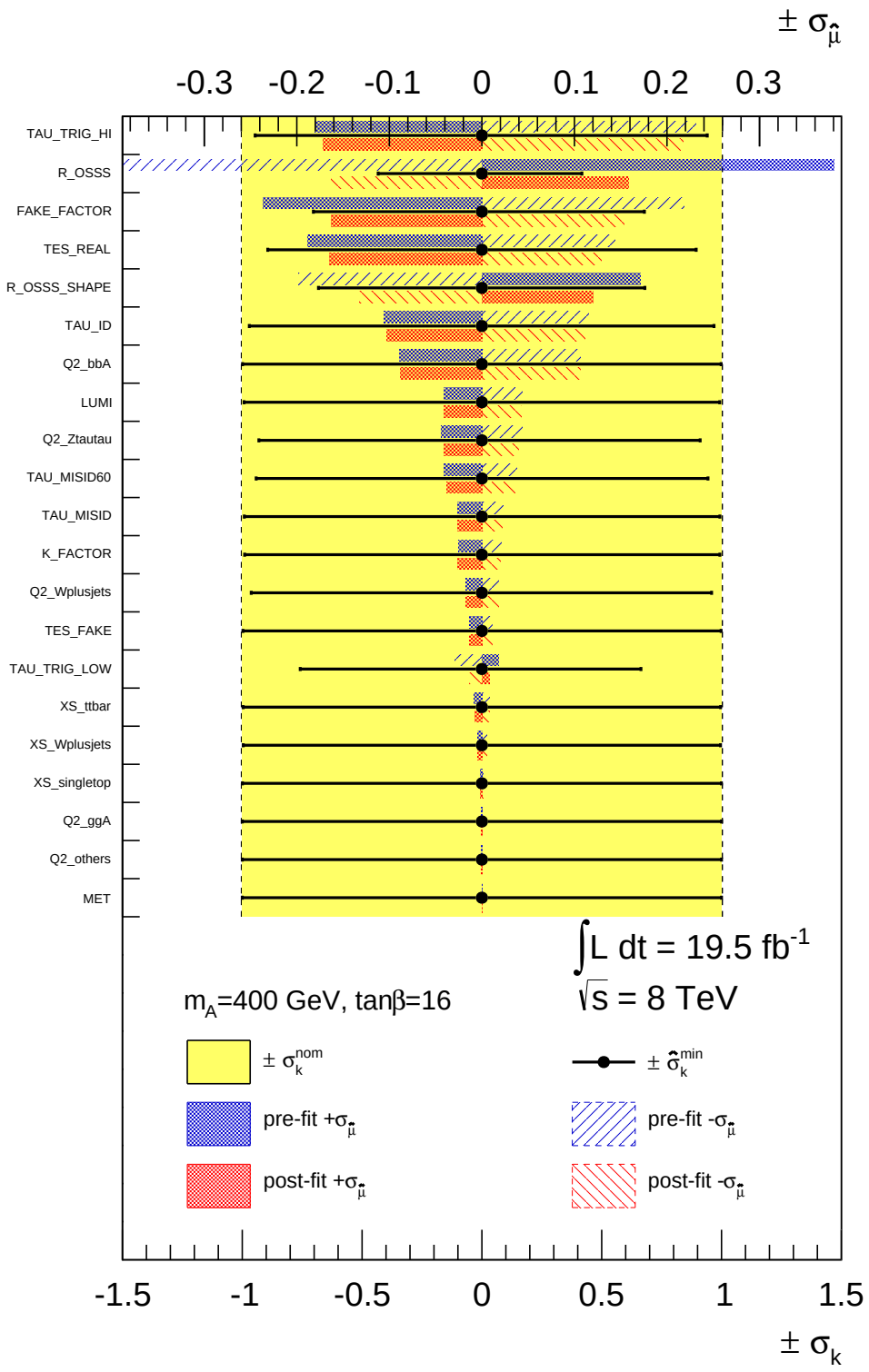

Figure F.11: Summary of the impact of systematic uncertainties on $\hat{\mu}$ determined from an unconditional fit to the Asimov dataset. The point $m_A = 400$ GeV and $\tan\beta = 16$ has been used. Systematic uncertainties are ranked from top to bottom on the left axis according to the post-fit impact shown in red. The upper axis illustrates the scale of $\sigma_{\hat{\mu}}$. The plot also includes the values of $\hat{\sigma}_k^{\text{min}}$, shown in black, determined from the post-fit likelihood contours. The nominal pre-fit bound on each nuisance parameter is also shown and represented by the yellow region. The scale of the post-fit and pre-fit systematic contours is shown by the lower axis.

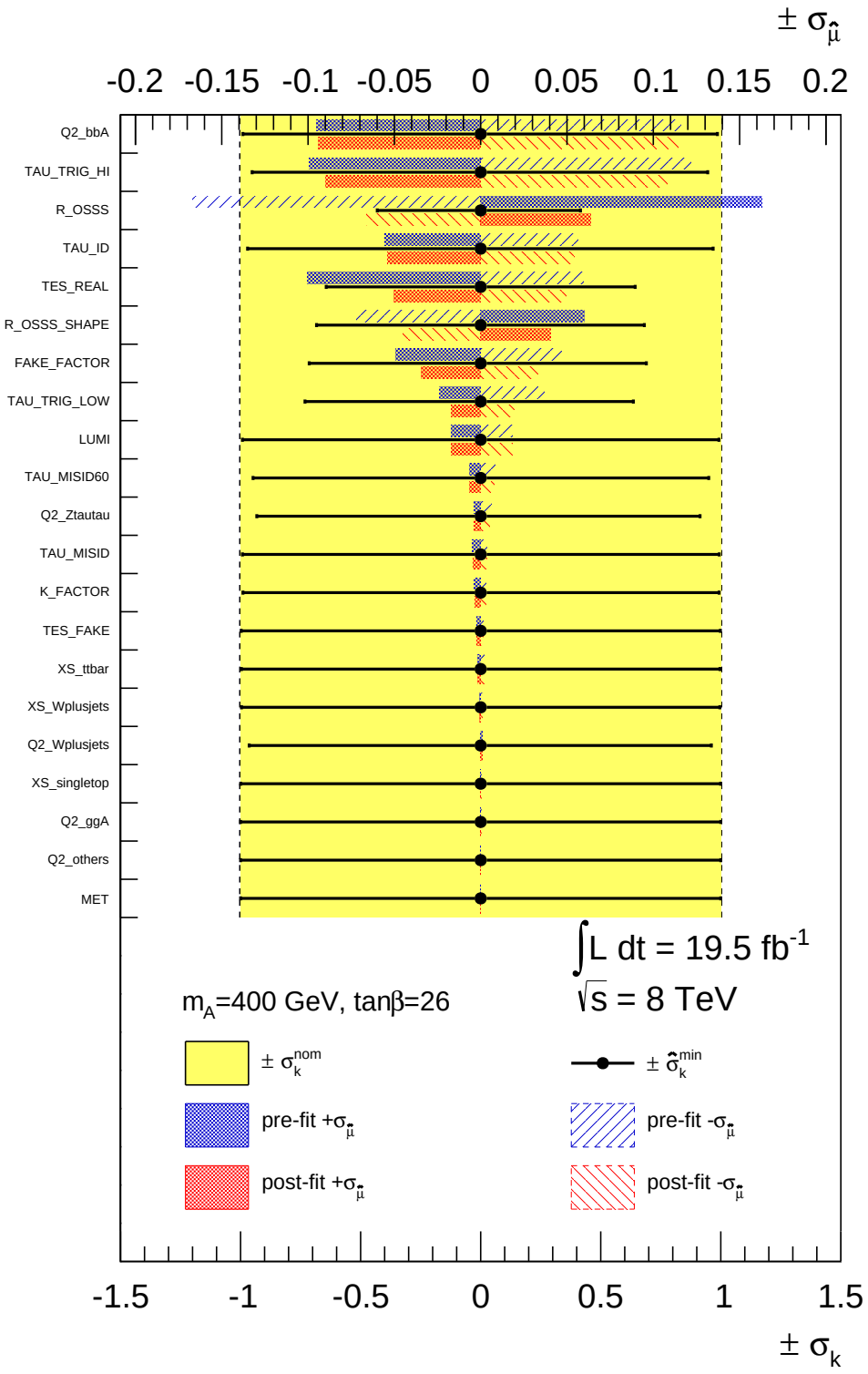

Figure F.12: Summary of the impact of systematic uncertainties on $\hat{\mu}$ determined from an unconditional fit to the Asimov dataset. The point $m_A = 400$ GeV and $\tan\beta = 26$ has been used. Systematic uncertainties are ranked from top to bottom on the left axis according to the post-fit impact shown in red. The upper axis illustrates the scale of $\sigma_{\hat{\mu}}$. The plot also includes the values of $\hat{\sigma}_k^{\min}$, shown in black, determined from the post-fit likelihood contours. The nominal pre-fit bound on each nuisance parameter is also shown and represented by the yellow region. The scale of the post-fit and pre-fit systematic contours is shown by the lower axis.

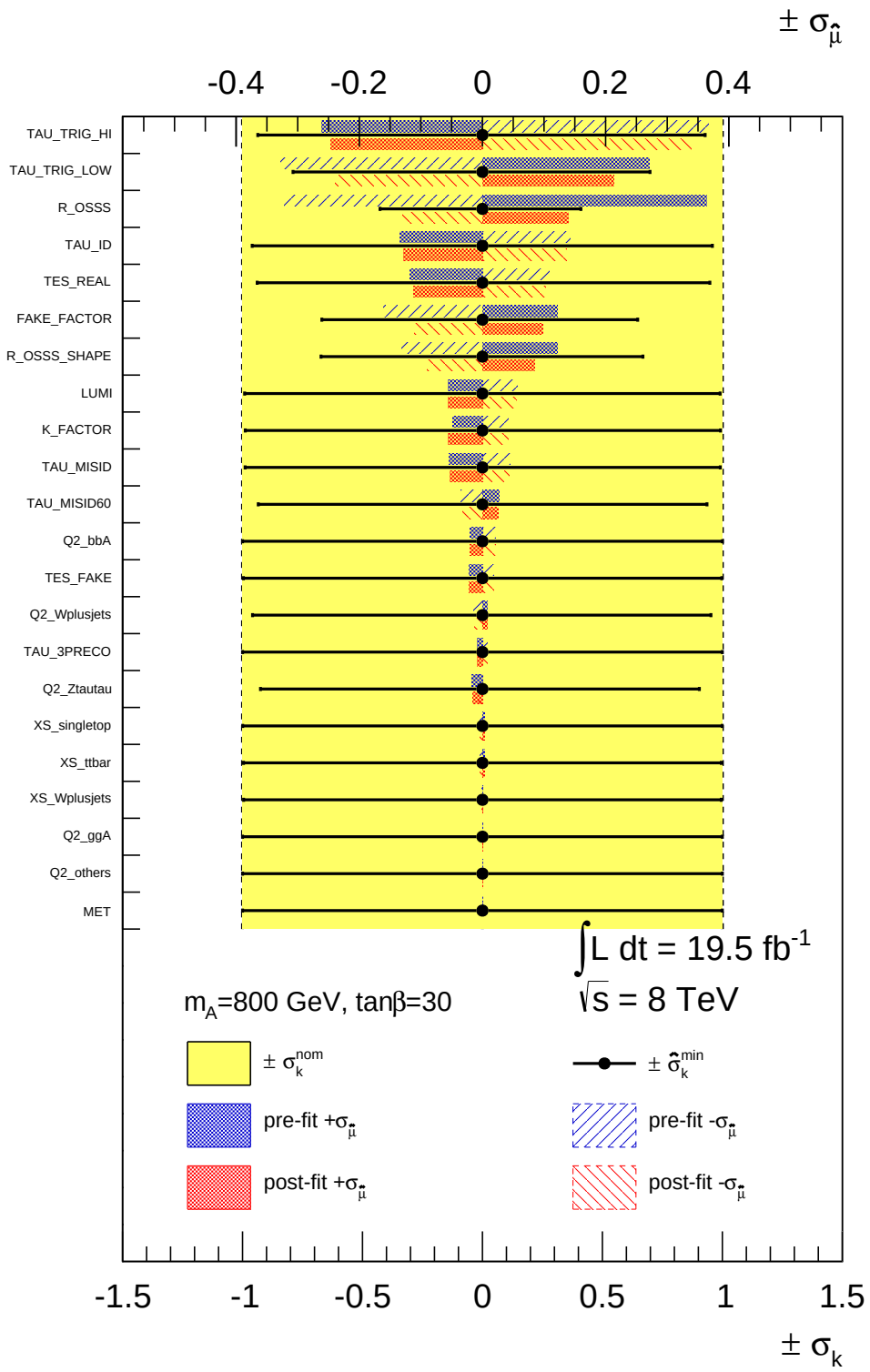

Figure F.13: Summary of the impact of systematic uncertainties on $\hat{\mu}$ determined from an unconditional fit to the Asimov dataset. The point m_A = 800 GeV and tanβ = 30 has been used. Systematic uncertainties are ranked from top to bottom on the left axis according to the post-fit impact shown in red. The upper axis illustrates the scale of $\sigma_{\hat{\mu}}$. The plot also includes the values of $\hat{\sigma}_k^{\text{min}}$, shown in black, determined from the post-fit likelihood contours. The nominal pre-fit bound on each nuisance parameter is also shown and represented by the yellow region. The scale of the post-fit and pre-fit systematic contours is shown by the lower axis.

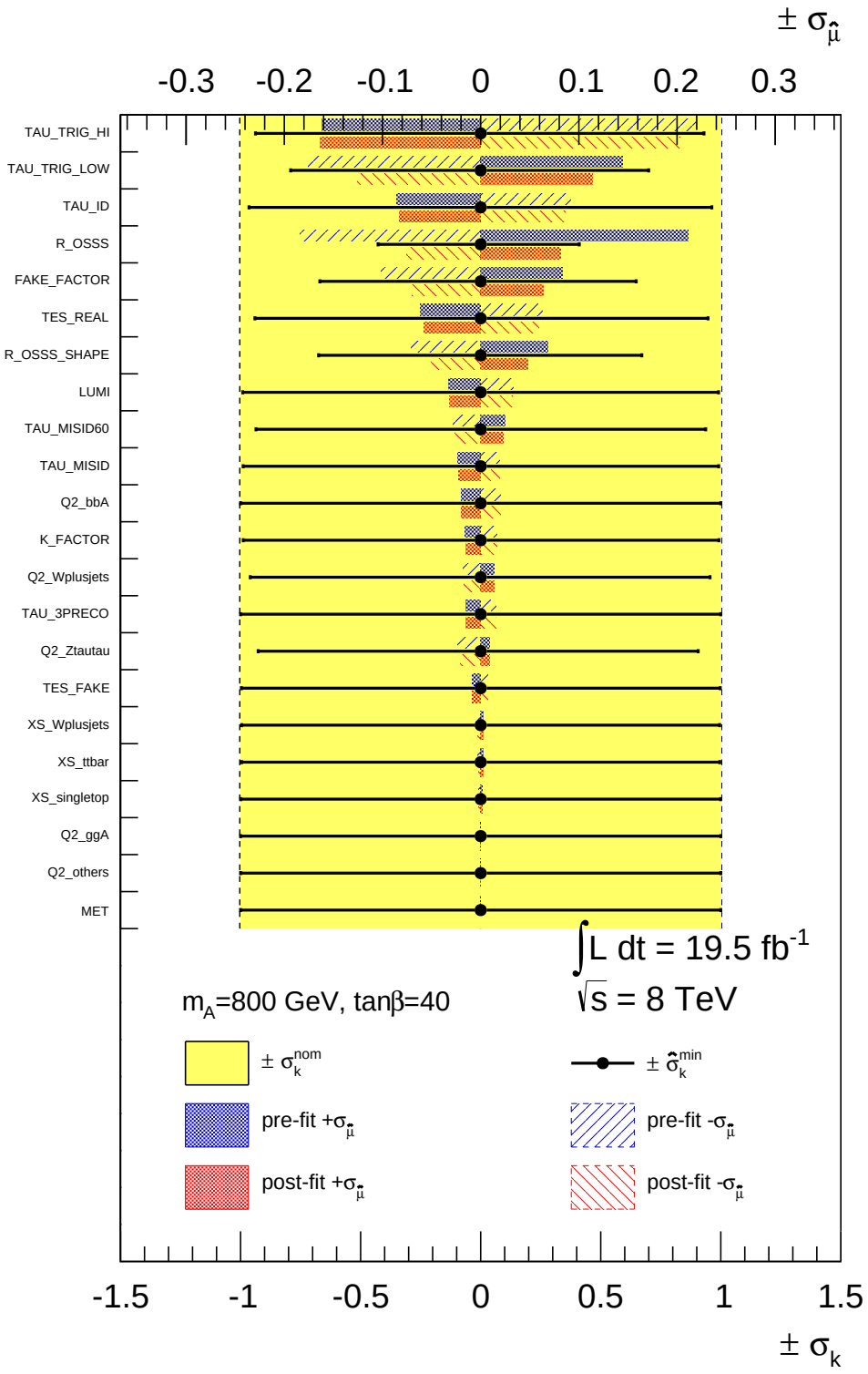

Figure F.14: Summary of the impact of systematic uncertainties on $\hat{\mu}$ determined from an unconditional fit to the Asimov dataset. The point $m_A = 800$ GeV and $\tan\beta = 40$ has been used. Systematic uncertainties are ranked from top to bottom on the left axis according to the post-fit impact shown in red. The upper axis illustrates the scale of $\sigma_{\hat{\mu}}$. The plot also includes the values of $\hat{\sigma}_k^{\min}$, shown in black, determined from the post-fit likelihood contours. The nominal pre-fit bound on each nuisance parameter is also shown and represented by the yellow region. The scale of the post-fit and pre-fit systematic contours is shown by the lower axis.

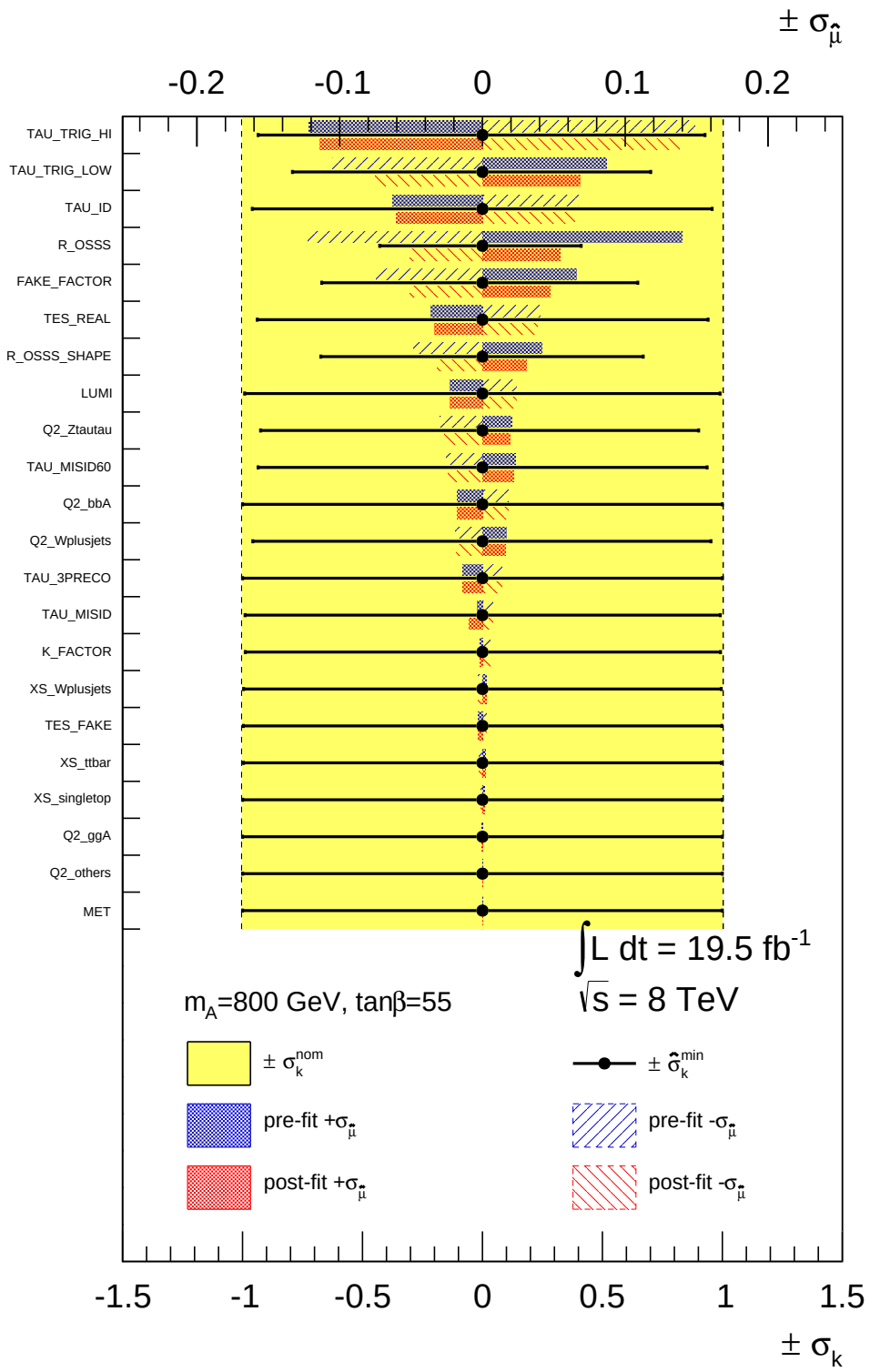

Figure F.15: Summary of the impact of systematic uncertainties on $\hat{\mu}$ determined from an unconditional fit to the Asimov dataset. The point m_A = 800 GeV and tanβ = 55 has been used. Systematic uncertainties are ranked from top to bottom on the left axis according to the post-fit impact shown in red. The upper axis illustrates the scale of $\sigma_{\hat{\mu}}$. The plot also includes the values of $\hat{\sigma}_k^{\text{min}}$, shown in black, determined from the post-fit likelihood contours. The nominal pre-fit bound on each nuisance parameter is also shown and represented by the yellow region. The scale of the post-fit and pre-fit systematic contours is shown by the lower axis.

Acknowledgements

The work documented in this thesis would not have been possible without the wise lead and inestimable support of my advisor Prof. Jochen Dingfelder. Working in your group has been a wonderful experience of my life, which made me grow professionally and humanly. I would also like to express my deep gratitude to Dr. Will Davey for supervising my work tirelessly and collaborating with me with inspiring enthusiasm.

A big thanks to all the people involved in tau related studies in the ATLAS Tau Working Group during 2011 and 2012, especially to the conveners Stefania Xella, Stan Lai and Martin Flechl. Thanks also to Soshi Tsuno, Daniele Zanzi, Yuki Sakurai, Pierre-Olivier de Viveiros, Almut Maria Pingel, Guilherme Nunes Hanninger and the many other tau-passionate physicists I had the pleasure to collaborate with.

I thank also the fellow analysers involved in the $h/H/A \to \tau\tau$ search: Julian Glatzer, Marcus Mattias Morgenstern, Sebastian Wahrmund, Felix Friedrich, John Stakely Keller, Tan Wang, Alessandro Manfredini, Matthew Beckingham, Stephen Sekula and Jianming Qian with a special thanks to Nikolaos Rompotis. Thanks also to the members of the ATLAS editorial board of the $h/H/A \to \tau\tau$ analysis, who helped getting the final result in good shape, Tony Liss, Mogens Dam, Jaehoon Yu and Keith Baker.

These years in Bonn have been great also thanks to the good company of my office mates Christian Oswald, Luis Pesantez, Jan Hasenbusch, Benedict Winter and Stephanie Yuen. It has been wonderful to know you all.

Finally, I wish to express the deepest gratitude to my parents Maria Antonietta and Silvano, for their infinite support and understanding, often of super-human nature. My last thank you goes to Flavia, my *Mimi*, for making my life rich and preparing cake with me.